

AD/A-007 157

**RAIN IMPACT DAMAGE TO SUPERSONIC
RADOMES**

Ray Kinslow, et al

Tennessee Technological University

Prepared for:

Army Missile Command

October 1974

DISTRIBUTED BY:

NTIS

**National Technical Information Service
U. S. DEPARTMENT OF COMMERCE**

A.D/M-007157

Unclassified
Exempt Classification

DOCUMENT CONTROL DATA - R & D

(Security classification of title, body of abstract and indexing annotation must be entered when the overall report is classified)

1. ORIGINATING ACTIVITY (Corporate author) Tennessee Technological University Cookeville, Tennessee 38501	2a. REPORT SECURITY CLASSIFICATION Unclassified
	2b. GROUP

3. REPORT TITLE

Rain Impact Damage of Supersonic Radomes

4. DESCRIPTIVE NOTES (Type of report and inclusive dates)
Final Report (Nov. 17, 1971, through June 30, 1974)

5. AUTHOR(S) (First name, middle initial, last name)
Ray Kinslow (with 7 appendices by: Dallas G. Smith, Vireshwar Sahai, Leland L. Long, John Peddieson, Jr., Ju-chin Huang, George R. Buchanan, Peter Hsu, Jer-Shong Ueng, Mikkilineni Chowdary, and Chung-Hsein Lyu)

6. REPORT DATE October 1974	7a. TOTAL NO. OF PAGES 468	7b. NO. OF REFS 32(+ 74 in appendices)
--------------------------------	-------------------------------	---

8a. CONTRACT OR GRANT NO. DAAH01-72-C-0375	8b. ORIGINATOR'S REPORT NUMBER(S) TTU-ES-74-3
8c. PROJECT NO.	8d. OTHER REPORT NO(S) (Any other numbers that may be assigned this report)

10. DISTRIBUTION STATEMENT

Approved for public release; distribution unlimited.

11. SUPPLEMENTARY NOTES	12. SPONSORING MILITARY ACTIVITY GE&M Directorate RDE & MSL U. S. Army Missile Command Redstone Arsenal, Alabama 35809
-------------------------	--

13. ABSTRACT

The research described has been directed toward a better understanding of raindrop damage to vehicles traveling at very high velocities with emphasis upon the erosion of ceramic-type radomes. An accelerator capable of impacting targets with short water jets at speeds up to Mach 5 is described. The validity of using high-speed liquid jets to simulate raindrop impact is demonstrated.

Topics covered include: drop energy-crater volume relations; oblique and multiple impacts; erosion rates; internal fracturing and spallation caused by stress waves; radome coatings; information from rocket sled tests; a theoretical analysis of the cratering process; motion of raindrops in the supersonic shock layer; probability modeling of erosion; and spatial and temporal variations of pressure exerted on the target surface by liquid impacts.

Reproduced by
NATIONAL TECHNICAL
INFORMATION SERVICE
U.S. Department of Commerce
Springfield VA 22151

Unclassified
Security Classification

13. KEY WORDS	LINK A		LINK B		LINK C	
	ROLE	WT	ROLE	WT	ROLE	WT
Rain erosion						
Erosion mechanics						
Erosion rate						
High-velocity impact						
Theory of cratering						
Stress waves						
Spallation						
Radomes						
Jet pressure distribution						
Liquid jet accelerators						
Fused silica						

ia

Unclassified
Security Classification

DISPOSITION INSTRUCTIONS

DESTROY THIS REPORT WHEN IT IS NO LONGER NEEDED. DO NOT RETURN IT TO THE ORIGINATOR.

DISCLAIMER

THE FINDINGS IN THIS REPORT ARE NOT TO BE CONSTRUED AS AN OFFICIAL DEPARTMENT OF THE ARMY POSITION UNLESS SO DESIGNATED BY OTHER AUTHORIZED DOCUMENTS.

TRADE NAMES

USE OF TRADE NAMES OR MANUFACTURERS IN THIS REPORT DOES NOT CONSTITUTE AN OFFICIAL INDORSEMENT OR APPROVAL OF THE USE OF SUCH COMMERCIAL HARDWARE OR SOFTWARE.

ACCESSION FOR	
NTIS	White Section <input checked="" type="checkbox"/>
DDIC	Buff Section <input type="checkbox"/>
UNCLASSIFIED	<input type="checkbox"/>
JUSTIFICATION	
BY	
DISTRIBUTION/AVAILABILITY CODES	
Dist.	Avail. and/or SPECIAL
A	

if

ACKNOWLEDGMENTS

The work presented in this report was performed by Dr. R. Kinslow, Dr. D. G. Smith, Dr. J. C. Huang, Dr. G. R. Buchanan, Dr. J. Peddieson, Mr. P. Hsu, Mr. J. S. Ueng, Mr. M. Chowdary and Mr. C. H. Lyu all of the Engineering Science Department, Tennessee Technological University, Cookeville, Tennessee 38501.

Credit is also due Professor L. L. Long of the Mathematics Department at Tennessee Tech for his work in developing the Probability Model for Rain Erosion Damage.

This work was performed with the technical direction and administrative support of Dr. B. R. Mullinix of the US Army Missile Command, AMSMI-RLP, Redstone Arsenal, Alabama 35809.

Expressions of gratitude are also due Mr. W. A. Lewis of the Ground Equipment and Materials Directorate and all levels of supervision of the US Army Missile Command for their support to this project.

ic

CONTENTS

<u>Section</u>	<u>Page</u>
I. INTRODUCTION	1
II. WATER JET ACCELERATOR	6
III. JET SIMULATION OF RAINDROP IMPACT	11
IV. CRATERING OF SLIP-CAST FUSED SILICA	14
V. OBLIQUE IMPACTS	18
VI. MULTIPLE IMPACTS	22
VII. SPALLATION AND SUBSURFACE FRACTURE	27
VIII. RADOME COATINGS	39
IX. ROCKET SLED TESTS	44
X. CONCLUSIONS	49
REFERENCES	51

ILLUSTRATIONS

<u>Figure</u>
1. REGIMES OF IMPACT PHENOMENA
2. SCHEMATIC OF WATER EJECTION FROM NOZZLE
3. DETAILS OF HIGH-PRESSURE CYLINDER AND PISTON
4. EXPLODED VIEW OF JET ACCELERATOR
5. PHOTOGRAPHS OF JET ACCELERATOR
6. PHOTOGRAPHS OF WATER JET
7. JET AND FRACTURE DIAMETERS
8. JET PENETRATION OF A LEAD TARGET
9. DAMAGE TO A 0.25-INCH LEAD PLATE
10. FRACTURES IN VARIOUS MATERIALS

11. WATER IMPACT DAMAGE TO LUCITE TARGETS
12. PROFILE AND DEPTH CONTOURS OF CRATER IN LUCITE
13. BULLET VELOCITIES
14. EFFECT OF NOZZLE DIAMETER UPON JET VELOCITY
15. RELATION BETWEEN BULLET ENERGY AND JET VELOCITY
16. AMOUNTS OF WATER EJECTED FROM NOZZLE
17. EFFECT OF NOZZLE-TARGET DISTANCE
18. EFFECT OF THE AMOUNT OF WATER IN PRESSURE CHAMBER
19. EFFECT OF SHOCK WAVE ON WATER DROPS (AFTER REFERENCE 9)
20. STRESSES RESULTING FROM LIQUID IMPACT
21. STRESS HISTORY AT A POINT
22. STRESSES RESULTING FROM REFLECTED WAVES
23. MAXIMUM TENSILE STRESSES
24. WATER IMPACT DAMAGE TO FUSED SILICA TARGETS
25. CRATER CROSS-SECTIONS (FUSED SILICA)
26. CRATER DEPTH CONTOURS (FUSED SILICA)
27. CRATERS IN SLIP-CAST FUSED SILICA
27. CRATERS IN SLIP-CAST FUSED SILICA (Continued)
28. RELATION BETWEEN CRATER DIMENSIONS AND JET VELOCITY
29. VOLUME-AREA-ENERGY RELATIONS (ORIGINAL AMC-SCFS TARGETS)
30. ENERGY-VOLUME RELATIONS FOR DIFFERENT TARGETS (LOG SCALE)
31. ENERGY-VOLUME RELATIONS FOR DIFFERENT TARGETS (RECT COORD)
32. VOLUME-AREA-ENERGY RELATIONS (SCFS TARGET NO. 1)
33. CRATERS RESULTING FROM LEAD PELLET IMPACTS
34. CRATERS RESULTING FROM SHOTGUN PELLET IMPACTS
35. DEFLECTION OF RAINDROPS BY THE RADOME SHOCK WAVE

36. PHOTOGRAPHS OF CRATERS FORMED BY NORMAL AND OBLIQUE IMPACTS
37. CRATER CONTOURS
38. EFFECT OF IMPACT ANGLE ON CRATER VOLUME
39. COMPARISON OF CRATER PROFILES
40. CRATER CAUSED BY SHOTS 829 AND 830
41. CRATER CAUSED BY SHOTS 806 AND 831
42. CRATERS CAUSED BY SHOTS 827 AND 832
43. CRATERS CAUSED BY SHOTS 828 AND 833
44. EFFECTS OF DISTANCE BETWEEN IMPACTS
45. CRATERS CAUSED BY SHOTS 807 AND 837
46. CRATERS CAUSED BY SHOTS 834 AND 838
47. CRATERS CAUSED BY SHOTS 836 AND 840
48. CRACK THROUGH CRATER 769 CAUSED BY SHOT 770
49. MULTIPLE IMPACTS - SCFS
50. EFFECT OF PERCENT OF SURFACE ERODED ON VOLUME OF MATERIAL REMOVED
51. EROSION RATE AS A FUNCTION OF DISTANCE TRAVELED IN RAIN FIELD
52. RAIN FIELD LENGTH REQUIRED FOR 100 PERCENT SURFACE EROSION
53. RELATION BETWEEN EROSION RATE AND VELOCITY
54. SUBSURFACE FRACTURES IN SCFS
55. INTERNAL FRACTURES AND REAR SURFACE SPALL
56. FRACTURES IN DEFECTIVE TARGETS
57. FRACTURE CONE FROM PERFORATED SCFS TARGET
58. FRACTURE LOCATIONS
59. REAR SURFACE OF PERFORATED TARGET - SHOT 810
60. FRACTURES CAUSED BY REFLECTED STRESS WAVES
61. PHOTOGRAPHS OF CRATER AND SPALL - SHOT 702

62. CRATER AND SPALL PROFILES
63. PHOTOGRAPHS OF CRATER AND SPALL - SHOT 826
64. PHOTOGRAPHS OF CRATER AND SPALL - SHOT 809
65. PHOTOGRAPHS OF CRATER AND INCIPIENT SPALL - SHOT 706
66. KINETIC ENERGY REQUIRED FOR SPALLATION
67. PRINCIPAL STRESSES PRODUCED BY IMPACT
68. EFFECT OF MATERIAL PROPERTIES UPON MAXIMUM TENSILE STRESS
69. MAXIMUM RADIAL TENSILE STRESS AS FUNCTION OF MATERIAL PROPERTIES
70. MAXIMUM TENSILE STRESS ALONG AXIS OF 0.75-INCH TARGET
71. CONTOURS OF MAXIMUM TENSILE STRESS IN A 0.75-INCH TARGET
72. EFFECT OF TARGET THICKNESS UPON MAXIMUM TENSILE STRESS
73. SPALLATION THRESHOLD AS A FUNCTION OF VELOCITY FOR A 0.434-INCH-THICK RADOME COLLIDING WITH AN 8-MM RAINDROP
74. DROP DIAMETER-DISTANCE-PROBABILITY RELATION (RFR = 2.5 IN/HR)
75. DROP DIAMETER-DISTANCE-PROBABILITY RELATION (RFR = 5.0 IN/HR)
76. MAXIMUM TENSILE STRESS DUE TO REFLECTED WAVES RESULTING FROM SIMULTANEOUS IMPACTS
77. DEPENDENCE OF MAXIMUM STRESS UPON DISTANCE AND TIME BETWEEN IMPACTS
78. EFFECT OF IMPEDANCE MISMATCH UPON TRANSMITTED AND REFLECTED PULSE AMPLITUDES
79. TRANSMITTED WAVES IN SUBSTRATE PRODUCED BY MULTIPLE REFLECTIONS IN COATING
80. WAVE IN SUBSTRATE PRODUCED BY 0.05-INCH PULSE IN COATING
81. EFFECT OF THE PULSE LENGTH UPON THE TRANSMITTED WAVE IN THE SUBSTRATE
82. STRESS WAVE PROFILES IN COATED RADOMES
83. STRESS HISTORY AT A POINT IN A COATED RADOME
84. MAXIMUM TENSILE STRESSES IN COATED RADOMES

- 85. MAXIMUM TENSILE STRESS AS A FUNCTION OF K AND Δt
- 86. RADOME ON SLED AFTER TEST AT HOLLOWAN AFB
- 87. RADOME AND CLOSE-UP OF CRATERS - 7RB1
- 88. DIMENSIONS OF RADOME
- 89. PHOTOGRAPHS OF CRATERS NEAR BASE - 7RB1
- 90. PHOTOGRAPHS OF CRATERS NEAR MID-SECTION - 7RB1
- 91. PHOTOGRAPHS OF CRATERS NEAR TIP - 7RB1
- 92. MEASURING CRATER DEPTHS
- 93. CRATER CROSS-SECTIONS
- 94. DEPTH CONTOURS
- 95. CRATER CROSS-SECTIONS
- 96. DEPTH CONTOURS
- 97. COMPOSITE OF PHOTOGRAPHS MADE OF ERODED SURFACE OF RADOME 7RD1
- 98. VIEWS OF ERODED SURFACE OF RADOME 7RD1
- 99. ERODED TIP SURFACE OF RADOME 7RF2

TABLES

Table

- 1 MULTIPLE IMPACTS - SCFS
- 2 CALCULATED RADOME DAMAGE - 2500 FT/SEC
- 3 CALCULATED RADOME DAMAGE - 5000 FT/SEC
- 4 CALCULATED RADOME DAMAGE - 7500 FT/SEC
- 5 SLED TEST INFORMATION (FROM REFERENCE 32)
- 6 CALCULATED EROSION OF RADOME 7RB1

APPENDICES

Appendix

- A. PRESSURE DUE TO HIGH-VELOCITY IMPACT OF A WATER JET by Dallas G. Smith and Ray Kinslow
- B. HYDRODYNAMIC MODELS FOR HIGH-SPEED LIQUID IMPACT by Vireshwar Sehgal, Peter Hsu, and Jer-Sheng Ueng
- C. FRACTURE TOUGHNESS OF SCFS by Dallas G. Smith and Nikkilineni Chowdary
- D. PROBABILITY MODEL FOR RAIN EROSION DAMAGE by Leland L. Long
- E. GAS-PARTICLE FLOW IN SUPERSONIC SHOCK LAYERS by John Peddieon, Jr. and Chung-Hsein Lyu
- F. COMPUTER CODE FOR STRESS ANALYSIS OF HYPERVELOCITY IMPACT by George R. Buchanan and Ju-chin Huang
- G. COMPUTER CODE FOR CALCULATING RAIN EROSION OF MISSILE RADONES AT SUPERSONIC SPEEDS (RENRASS) by Ju-chin Huang

SECTION I

INTRODUCTION

The requirement of an all-weather capability for high-speed aircraft, space shuttles, rockets, and missiles has made the protection of these systems from rain erosion a vital design factor. Supersonic collisions with raindrops pose a serious threat to both the structural integrity and electromagnetic performance of ceramic radomes.

A large number of papers and reports on this subject have been published over the past few years, including the proceedings of three international conferences on rain erosion and associated phenomena. Many of them have contributed toward a better qualitative understanding of the mechanism of rain erosion and its relationship to material properties. With the exception of some rocket sled tests, most of the research has been limited to relatively low velocities. In a state-of-the-art survey of raindrop erosion, Wheelahan [1] in 1967 found very little quantitative information available on damage caused by raindrops impacting at supersonic velocities. This is generally true today also. Published reports have included a great deal of experimental data and considerable theoretical work. Many of the theories, however, have been deduced from rather arbitrary assumptions. Contradictory empirical relations have been formulated. One only needs to read the discussions following many of the papers in the proceedings of the various rain erosion conferences to see that there is much disagreement among those who are working on this problem. There is considerable disagreement as to the forces that are actually responsible for the cratering and erosion resulting from liquid-solid interactions. According to Eisenburg [2], "There remains the mystery of which mechanism, shock waves or jet formation, is responsible for actual damage." Engel [3], Fyall [4], and others believe that the damage is produced by the introduction of shear and tensile stresses as a consequence of the high localized compressive forces exerted by the liquid.

Regimes of Impact Velocity

The various theories may not be as contradictory as they first appear. In the case of solid-solid impact, there are at least three, and perhaps

four, regimes of the impact phenomena as the projectile velocity increases. These are illustrated by the rather idealized curve of Figure 1 which shows the effect of velocity upon the penetrating power of projectiles into a ductile target. In the low-velocity range the penetration is strongly influenced by the strength of the two materials. In this region the penetration appears to increase as the $4/3$ power of the velocity. A negligible amount of the projectile energy is converted into stress waves. As the projectile velocity is increased, there is greater deformation and fragmentation of the projectile. At some point there is no increase in crater depth with increased velocity; in fact the depth actually decreases, although the crater volume may continue to increase. There comes a point where the depth begins to again increase with velocity. The crater becomes more hemispherical in shape and the penetration is now roughly proportional to the $2/3$ power of the velocity. It is clear that a transition region has been crossed. The new regime is usually called the hypervelocity-impact range. The most common criterion for the beginning of this regime is when the ratio of projectile velocity to that of a stress wave in the target material exceeds unity. At these velocities the stresses developed by the projectile's deceleration are much greater than the yield strength of either the projectile or target and the materials' densities affect the cratering process more than that of the other properties such as target and projectile strengths. If the velocity is further increased, an impact region is reached that is, as yet, relatively unexplored. It is called the range of impact explosions, for the tremendous amount of energy becomes sufficient to vaporize both the projectile and a small volume of the target. The partitioning of the projectile's kinetic energy among such items as mechanical deformation, heat generated, stress waves, ejected material, and perhaps vaporization; the influence of material properties; the effects of stress waves; and the mechanism of penetration and cratering are entirely different for the various impact regimes. It is apparent that there are also different mechanisms of erosion and cratering for liquid-solid impacts at various velocities. Wheelahan [1] suggests that in the velocity range of 1000 to 3000 ft/sec, erosion rather than cratering is the dominant form of damage, but as the impact velocity is increased above a few Mach numbers the damage is primarily by cratering. Somewhere between these two types of damage there is obviously a region of transition. Those apparently

contradicting models mentioned may not be contradictory at all but each may apply at various impact velocities and for different materials. For a particular target material, the velocity-damage curves would be very different for liquid and solid projectiles but would probably converge in the hypervelocity range. If this be true, it will be possible to simulate the higher velocity liquid impacts with solid projectiles.

Scope of This Research

It is believed that the greatest insight into the mechanics of rain erosion is to be gained from experimental and semi-empirical investigations. This is sometimes called the quasi-theoretical approach. Experimental results are certainly necessary to establish the validity or limitations of theoretical analyses.

The major effort of this research has been directed toward an understanding of the erosion damage to ceramic-type radome materials under various environmental conditions. A large number of 5-inch-square slip-cast fused silica (SCFS) targets of various thicknesses were furnished by Mr. Philip Ormsby of the Army Missile Command, Redstone Arsenal. These were used in most of the experimental work which served as the basis for the majority of the empirical relations given in this report. Because of the relatively small size and sharp corners of these targets, they would crack under high-energy impact loads. Larger and thicker targets were requested so that larger raindrop sizes and higher radome velocities could be simulated. Four 12-inch-diameter, disk-shaped targets 1 inch thick were furnished by the Engineering Experiment Station at Georgia Institute of Technology. These targets were much softer than the original AMC targets. Craters in one of these targets, for example, averaged six times the volume of those in the original targets for identical impact conditions. This is mentioned because the reader may notice the wide differences in the data presented. Data determined from one of these targets could not be combined with those from another target, but data such as the effects of the impact angle or of multiple impacts are given when all are from the same target.

Two water jet accelerators were designed and constructed for use in the experiments. These are described in detail in Section II of this report. Both experimental and theoretical results are presented in

Section III to demonstrate the validity of using high-speed liquid jets to simulate raindrop impact.

Experiments to determine the spatial and temporal variations of the normal pressures exerted on the target surface by high-velocity liquid impacts are described in Appendix A. This information is essential to an understanding of the mechanics of cratering. Craters created by single high-speed jet impacts of SCFS targets are described and energy-volume relations are derived in Section IV. A theoretical model of the cratering process is presented in Appendix B, and fracture toughness--an important property of radome materials--is discussed in Appendix C.

Because rain-erosion damage to high-speed structures is caused by collisions with a large number of drops and because the eroded surface is usually at an angle to the direction of motion, oblique and multiple impacts are discussed in Sections V and VI. As the erosion rate is a function of the drop size distribution in a given rain field, and as any design criterion must be based upon the probability of failure, the derivations and analyses of these factors are given in Appendix D.

Although the rain field may be defined in terms of drop size distribution, velocity, direction, and duration, it cannot be assumed that this describes the conditions in the region between the shock wave of the supersonic radome and the radome surface. It has been shown that water drops passing through the shock wave may be fragmented, slowed down, and deflected before colliding with the surface. Appendix E gives a description of the motion of raindrops in the shock layer.

A high-velocity impact drives a stress wave into the structure. This wave may contribute to fractures at or near the point of impact, or may produce damage by reflection as a tensile wave from the target's rear surface. This problem is analyzed in Section VII and Appendix F. The effects of radome coatings on the potential damage resulting from the stress waves are discussed in Section VIII.

Three radomes that have been eroded by rocket sled tests in simulated rain fields at Holloman Air Force Base, New Mexico, have been examined. The damage has been analyzed, and the results are compared with the relations derived in this study. This is given in Section IX.

The findings of this research are summed up and conclusions stated in Section X. Areas in which more information is needed and recommended

further work are also included. The combined results of all phases of this work are included in the computer code REMRASS given in Appendix G.

It must be emphasized that the seven appendices are essential parts of this report. They were placed in a separate section because some of them were of necessity rather lengthy and because all persons reading this report may not be interested in all of the details given in all the various appendices. As these were prepared by different individuals, some variations in symbols and forms of equations will be found; however, the meanings of all symbols are defined in the text, and there should be no confusion on the part of the reader.

SECTION II

WATER JET ACCELERATOR

Accelerator Description

Devices similar to the one employed by Bowden and Brunton [5] of Cambridge University are used to accelerate small masses of water in the form of short supersonic jets [6]. Velocities as high as 5000 ft/sec are easily attainable, these being limited only by the physical strength of the apparatus.

The heart of the gun is the high-pressure cylinder, and its operation is illustrated schematically in Figure 2. As shown in the first drawing, a nylon piston (P) is inserted into the chamber, and the remainder of the chamber is filled with water (W). It has been found that efficiency and repeatability of this water gun require a tight fit between the piston and chamber. The front end of the piston is flared slightly, and it is pressed into the chamber as shown. The chamber is next filled with water, using a small hypodermic needle inserted in the nozzle. With the nozzle turned upward, water is injected until all air is expelled.

The piston is accelerated by means of a 0.22-caliber bullet (B) striking its base as shown in the second sketch, compressing the water to a very high pressure. This water pressure is so great that even cylinders made of stainless steel were deformed, and the chamber was expanded to the extent that it could not be used more than a few times, and repeatable results were not possible. Tool steel was next used, but it was too hard and the nozzle fractured on the first shot. After much experimentation, cylinders were finally made from a nickel-chrome steel truck axle and then hardened by heating and quenching in oil. These proved satisfactory and could be used for several hundred shots with good repeatability.

As the water is suddenly compressed, a very high-velocity jet is ejected through the nozzle, but before very much can escape, the pressure on the base of the piston is relieved, causing both the remaining water and the piston to rebound as shown in the last sketch. Only a small fraction of the water originally in the chamber is ejected through the nozzle, unless its diameter is very large, in which case the jet velocity would be small.

Details of the high-pressure cylinder and nylon piston are shown in Figure 3. An exploded view and photographs of the jet accelerator are shown in Figures 4 and 5, respectively. The closed box is between the gun muzzle and the high-pressure cylinder so that there will be no danger from the bullet as it ricochets. Holes are in the bottom of the box to permit the escape of gas from the blast.

Jet Damage

Photographs of the high-velocity jet are shown in Figure 6. The jet itself is not seen in these photographs as it is surrounded by vapor and small droplets as the water evaporates at this high velocity. Diameters of the jet and the vapor cloud at various distances from the nozzle are shown in Figure 7. In this case the jet velocity was about 3200 ft/sec, and the nozzle diameter was 0.0625 inch. The approximate limits of the vapor cloud were determined from photographs of the jet. The liquid jet diameter is assumed to be approximately that of the fracture diameter in Lucite. As seen, the cloud increases with the distance from the nozzle, and the water core decreases as more and more of it evaporates. In this case no visible fracture could be seen in the Lucite at distances greater than 3 inches from the nozzle.

In attempts to determine more accurately the liquid jet diameter, 0.25-inch lead plates were used as targets. Shadowgraphs of the jet penetration of a lead plate are shown in Figure 8. An interesting phenomenon can be observed in these pictures; namely, the flash of light visible in the first and third photograph. It must have been rather bright in order to be visible through the back jetting of the liquid. Two photographs of the lead targets are shown in Figure 9. The target in the lower photograph was approximately 1 inch from the nozzle. In this case of a lead target, the diameters of both the liquid core and the vapor cloud can be determined. Although the droplets in the cloud damaged the surface somewhat, it was very minor compared to the sharp perforation of the thick lead plate. The upper photograph shows the damage produced at a distance of 1.5 inches. The damage resulting from the cloud was less severe but covered a larger area, and the hole punched by the liquid was smaller than in the case of a 1-inch nozzle-target distance.

The type of damage caused by a jet varies with different materials, as illustrated in Figure 10 for targets of copper, aluminum, and Lucite. Figure 11 shows the familiar ring fractures on the surface of a Lucite target. The center portion of the surface was not affected. The lower photograph is of the sectioned target so that the depth of fracture can be seen. The photograph, cross-section, and depth contours of another crater in Lucite are shown in Figure 12.

Bullet Velocities

It was originally thought that better control of bullet velocities could be maintained by using hand-loaded shells. It was found, however, that the use of commercial shells gives satisfactory results except when higher jet velocities are required. Bullet velocities available from seven commercial and three hand-loaded shells are given in Figure 13. The maximum, minimum, and average velocities from approximately ten shots with each shell are shown. It was found that the Hy-Score 22BB caps (average velocity 925 ft/sec), the ELEY 22-LR TENEX (average velocity 1064 ft/sec), the Western SX22LR (average velocity 1283 ft/sec), and the hand-loaded Winchester cases with 4.2 grains of Unique powder (average velocity 1440 ft/sec) gave the velocity range required for most of the experiments.

Effect of Nozzle Diameter

Water velocities resulting from ELEY TENEX bullets striking 0.25-inch-diameter pistons were determined for various nozzle diameters ranging from 0.03125 to 0.09375 inch. The results are shown in Figure 14. The jet velocities decrease for larger diameters as expected. The velocities also decrease in the case of very small diameters, due probably to increased friction. The maximum velocity was reached with a 0.0625-inch nozzle. This diameter has been used in the majority of the experiments, not only because it gives the maximum jet velocity, but because any small variations in its size have negligible effect upon the results. The ratio of water to bullet velocity is 3.2 for these conditions. When larger jets are needed, a nozzle diameter of 0.09375 inch has been used. In this case the water-bullet velocity ratio is 2.8.

Relation Between Bullet Energy and Jet Velocity

The ratios of water to bullet velocities may be of interest, but because of the variation in bullet weights (18 to 45 grains), the relation between the kinetic energy of the bullet and the jet velocity is more significant. When the squares of the jet velocities were plotted as functions of bullet energies, the results were practically linear for piston diameters of 0.25 and 0.375 inch, as shown in Figure 15. It is seen that the greater jet velocities are generated with the smaller piston. As it is not practical to use pistons smaller than the bullets, the 0.25-inch diameter has been used in all experiments described in this report unless otherwise specified.

Amounts of Water Ejected from Nozzle

The water ejected was measured by simply placing the opening of a small can containing cotton over the nozzle, catching the water, and weighing it on a sensitive analytic balance. Immediately following each shot, the can opening was sealed to prevent the loss of any vapor. The container was weighed before and after each shot. The very small variation in weight for each condition was surprising. The results are shown on Figure 16. Each point represents one shot and shows the amount of water in the chamber and the amount ejected. The amount in the chamber was accurately determined by using a calibrated hypodermic needle to fill the nozzle. Most of the shots were made using 0.25-inch pistons, and nozzle diameters were 0.0625 and 0.09375 inch. The shells used are indicated. The water in the chamber averaged 0.5 gm, varying between 0.4 and 0.6. Because of the negligible variation in the amounts of water ejected, it was decided to fire some shots using pistons having a diameter of 0.375 inch and various lengths so that different amounts of water could be injected into the chamber. The results obtained were not as expected. Using ELEY TENEX bullets and a nozzle diameter of 0.0625 inch, the amount of water in the chamber was varied from about 0.4 to 1.2 grams but the amount of water ejected varied only from about 0.07 to 0.08 gram. As previously mentioned, only a small fraction of the water in the chamber is ejected from the nozzle. For the shots shown in this figure, this fraction ranged from about 5% when using the larger piston and smaller nozzle, to about 40% when using the larger nozzle and accelerating the smaller piston with a 204-ft-lb-kinetic-energy bullet.

Deflection of Steel Plates

Because of the very rough and irregular craters produced in materials such as Lucite and ceramics, and because their volumes depend greatly upon whether or not a piece of the fractured material remains in the crater or falls out, considerable variations in crater size are to be expected. For evaluating the effects of various parameters such as the distance between nozzle and target and the amount of water in the high-pressure chamber, it was believed that the deflections of metal plates that did not crater might give more reliable results than the volumes of craters. It was decided to use targets of stainless steel and to measure the displacement of the back surface. The photographs in Figure 17 show sections of two plates after jet impact. The lower plate was perforated by the jet.

The curves in Figure 17 show the deflection of the rear surface of 0.035-inch stainless steel plates as a function of the distance between the nozzle and the target. Western SX22LR and ELEY TENEX 22LR bullets were used. It is seen that this distance is very critical. A small difference in the target location would cause a large difference in the amount of damage. High-speed photographs show the jet velocity to be the same at the various distances. This difference in damage must, therefore, be due to the change in the amount of water in the jet due to evaporation and the change in its diameter. The curves could not be extended for shorter nozzle-target distances as these targets were perforated.

The amount of water in the chamber was controlled by the piston length. The effect of the chamber water volume upon the plate deflection is shown in Figure 18. This shows that the amount of water injected into the chamber has negligible effect on the target damage unless the amount is so small that a well formed jet is not possible. This confirms the fact that the amount of water ejected is independent of the amount in the chamber.

SECTION III

JET SIMULATION OF RAINDROP IMPACT

Simulation Technique

There is perhaps no substitute for actual in-flight testing to determine the rain-erosion resistance of various materials. Because of the great number of problems encountered in such testing, a wide variety of simulation techniques have been developed. Multiple-impact methods such as those employing whirling arms, sleds, wind tunnels, and ballistics, as well as single-drop techniques, have been described by Fyall [7].

Because rain damage to high-speed structures is caused by collisions with a large number of drops, multiple-impact techniques would better simulate actual conditions. However, before a reliable design criterion for the protection of high-speed aircraft and missiles can be formulated, the fundamental mechanics of the erosion process must be investigated. Before the relations between rain damage and various parameters such as material properties, relative speeds, angles of impact, rainfall rates, and drop size distribution can be determined, the damage sustained by the impact of a single drop must be understood.

In single-impact studies, a drop of the liquid may either be placed in the path of a moving target or the liquid may be accelerated against the target material. Smith and Fyall [8] have achieved excellent results by the first method for velocities up to about 1000 ft/sec. The target material forms the nose section of a lightweight projectile fired from a compressed-gas gun at a drop suspended on an artificial web.

The accelerating of a liquid drop against the target poses several difficulties. In the first place, it is not possible to accelerate a sphere of water the size of a raindrop to a high velocity without the aerodynamic forces causing the drop to break up or shatter into a fine spray of small droplets. Even if the drop integrity could be maintained, it would probably not be desirable to do so. A short water jet may better represent the drop after passing through the shock wave of a supersonic radome than would a perfectly spherical drop. The excellent photograph of water drops between the shock wave and the target in Figure 19 was made by

Lankford and Leverance of the Naval Ordnance Laboratory [9]. These drops certainly have the appearance of jets. Similar photographs have been made by Ranger and Nicholls [10] and by Reinecke and Waldman [11].

Experimental Justification

The high velocities attainable with the jet gun make it a very attractive research tool for determining the erosion resistance of materials, and it seems that the use of the jet for simulating raindrop impact may be justified. First, the appearance of craters formed by the suspended drop method, those on radomes following sled tests, and those formed by jets are all very similar in appearance. Secondly, Brunton [12] has shown that only the head of the jet is responsible for damage to the target and that the diameter of the jet determines the duration of the load. Also, the length of the jet may not be as great as has been estimated. While it is true that water can be seen coming from the nozzle for a rather long period of time (Figures 6 and 8), this may be a negligible volume at a low velocity. If the measured ejected water (Figure 16) were concentrated into spherical drops, their "diameters" would be approximately the same as the diameters of the holes punched in the lead plates (Figure 9) when the targets were placed near the nozzle, so that impact occurred before there could be a breakup of the jet by aerodynamic forces. This seems to strongly suggest that the effective length of the jet is about the same as its diameter. This may also explain why the mass of the jet is independent of the amount of water in the high-pressure chamber.

Theoretical Results

The question may also arise as to the effect the jet length might have on the internal target stresses caused by shock waves. To answer this, the amplitudes of stresses resulting from a drop or very short jet were computed and compared with those resulting from a very long jet by the methods described in Section VII and Appendix B.

The compressive forces exerted on the target by the drop were represented by the equation

$$p = 603[\exp(-0.57t) - \exp(-4.85t)] \quad (1)$$

where the time (t) is in microseconds and the pressure (p) is in 1000 psi. This function, shown in Figure 20, reaches a peak compressive force of 400,000 psi in 0.5 microsecond and then decays to 60,000 psi in 4 microseconds. The maximum pressure corresponds to the shock pressure for a drop velocity of about 5000 ft/sec. The jet pressure was represented by the equation

$$p = 412[1 - \exp(-7t)] \quad (2)$$

This relation is also shown in Figure 20. The pressure in this case also reaches a magnitude of 400,000 psi in 0.5 microsecond but does not decay as it did in the case of the drop. In fact, it represents a jet of infinite length, always increasing slightly in amplitude. The tangential stresses generated at the surface are also shown. The maximum tensile stress is approximately 300,000 psi for both the drop and jet. The stress histories at a point 0.15 inch from the point of impact in a 0.20-inch Lucite target are shown in Figure 21 for both the drop and jet. The stress waves in the 0.20-inch target are shown in Figure 22 at a time of 1.9 microseconds, just before they reach the rear surface of the target, and also at 2.2 microseconds after the waves have been reflected from the rear surface. The maximum tensile stresses in the target are shown in Figure 23. It can be seen that there is practically no difference between the stresses generated by the drop and by the jet.

In view of both experimental and theoretical results, it is concluded that the high-velocity jet is a useful research tool for simulating rain-drop impact.

SECTION IV

CRATERING OF SLIP-CAST FUSED SILICA

Both surfaces of some SCFS targets were painted with black ink before impact so that the extent of any fractures could be more easily seen. The photographs at the top of Figure 24 show the damage to a 0.25-inch target. It was completely penetrated. The fracture as viewed from the back is interesting. The lower photographs of this figure show the damage to a slightly thicker target. The familiar ring crater is seen on the front, and a crack is detected on the rear surface. The ink was not removed from the central area of the crater. Typical cross-sections of this crater are shown in Figure 25. The maximum depth is about 0.0085 inch. Unlike the ring crater in Lucite, the central undamaged portion shows a permanent set. It may be, however, that the material is not compressed but that the crack whose boundaries are seen on the rear surface extend internally to the front crater and that this entire cone of material is pushed backward. Internal and subsurface material failures are discussed in Section VII. Crater contours are shown in Figure 26.

Typical craters in SCFS targets are shown in Figure 27. These vary from small ring craters with undamaged central area, such as Nos. 582, 699, 705, and 706, to large deep craters with chunks of the material removed, such as No. 423. The scale divisions shown in the photographs are millimeters. Some of the craters and conditions of impact will be described later.

Experimental Conditions

After analyzing the results of many shots made under various conditions, it was decided that for a study of the cratering of SCFS targets, the following would be used:

Nozzle-target distance - 1.0 inch

Piston diameter - 0.25 inch

Nozzle diameters - 0.065 and 0.09375 inch

Jet Velocity and Crater Size Relations

Average crater volume and diameter as functions of jet velocity and nozzle diameter are shown in Figure 28. Each point represents the

average volume or diameter of several craters with the exception of the largest crater (volume = 25.0×10^{-4} in³, diameter = 0.49 inch). These values were the result of a single shot, as it was the only one that did not destroy the thickest target (0.75 inch) available at that time.

Crater Size as Function of Jet Energy

The jet velocity-crater size relation depends upon the nozzle diameter, but it was found that the relation between the kinetic energy of the jet and the crater volume was independent of the nozzle size. Not only that, but the energy-volume relation plots as a straight line on logarithmic paper (Figure 29), and the crater volume (V) can be expressed as a simple function of the jet energy (E), this being

$$V = 1.66 \times 10^{-6} E^{1.44} \tag{3}$$

where the volume is given in cubic inches when the energy is expressed in foot-pounds. A plot of the crater areas is also shown. The energy-area relation can be represented by the equation

$$A = 0.00741 E^{0.55} \tag{4}$$

giving the area, A, in square inches.

These relations were based upon crater dimensions obtained by impacting a large number of the original targets furnished for use in this research. When four larger and thicker targets were received, the plans were to extend these curves to higher velocities and energies. When the first of these new targets (No. 1) was impacted, it was found that the crater volumes were approximately six times larger than those in the original targets. When the average volumes and areas for different impact energies were plotted, it was found that the lines through the points had the same slopes as the original curves, giving the same exponent but that the relations had different coefficients (Figure 30). Each of the three points represents the average of several shots, but there was much less scatter than in the case of the original targets, because all craters were in one target, whereas several targets were used in the original experiment. The energy-volume curve for the second of the new targets (No. 2) fell between that for the original data and the one for target No. 1.

An important question at this point is, "Which, if either, of these energy-volume relations can be used to predict the damage to SCFS radomes in a specified rain field?" They are

$$\text{For the original targets} - V = 1.66 \times 10^{-6} E^{1.44} \quad (3)$$

$$\text{For target No. 1} \quad - V = 10.1 \times 10^{-6} E^{1.44} \quad (5)$$

$$\text{and, For target No. 2} \quad - V = 3.32 \times 10^{-6} E^{1.44} \quad (6)$$

These relations plotted on rectangular coordinate paper in Figure 31 give a better comparison of the results obtained by use of the different targets.

It is assumed that better quality control will be maintained in the manufacture of the radomes than was done in the casting of the targets used in these experiments. If some targets of the actual radome material could be supplied, the coefficients of the equations could be more accurately determined. Meanwhile, it seems reasonable to use Eq. (5) for the softest of the targets as a basis for further relations derived in this research. In Section IX of this report, the computed results will be compared with the observed damage to radomes eroded in rocket sled tests.

The energy-volume curve for this target is repeated and the energy-crater area relation

$$A = 0.022 E^{0.55} \quad (7)$$

is shown in Figure 32.

Craters Resulting from Lead Impact

Another target (No. 4) was used in experiments to determine the relation between the energy of lead shot and crater volume. This is also shown in Figure 30. For this curve, each point represents an individual shot and not the average of several shots as in the case of the water jet. It appears that a curve through these points might have the same slope as the curves representing water impact. If so, this would indicate that the exponent of the equation is perhaps dependent upon the target material and independent of the projectile properties. It also seems to indicate that lead pellets might be used to simulate liquid impact as has been suggested by Walton [13]. The crater characteristics are very similar

in the two cases. Some photographs of these craters are shown in Figure 33. As the properties of target No. 4, in which the lead pellets were fired, are perhaps different from the other targets, no comparisons of results can be made. It appears, however, that lead pellets having kinetic energies of from 3 to 10 percent of those of water jets could be used to simulate liquid impact. The craters shown in Figure 34 resulted from a shotgun impact. The No. 7-1/2 lead pellets having velocities of about 1500 ft/sec hit the target at an angle of 30 degrees with its surface.

SECTION V

OBLIQUE IMPACTS

The data presented in the previous sections of this report were determined from experiments in which the direction of the liquid jet was normal to the target surface. In general, the relative velocity vector of a raindrop is not perpendicular to the radome surface. The effect of the impact angle is therefore of great importance.

Effect of Shock Layer Upon Impact Angle

The angle at which a drop impinges upon the radome surface is determined primarily by the radome geometry. It is also affected by its passage through the supersonic shock layer. It was shown in Figure 19 that there is a distortion and fragmentation of the drop. This shattering or fragmenting will have little effect if the time to traverse the shock layer is less than the breakup time. There will also be a deflection or change in the direction of the drop as it passes through the shock layer. If the deflection angles are of sufficient magnitude, the total number of impacts will be reduced. If the raindrops have sufficient momentum to prevent them from being deflected, all drops in the path of the radome will impact. Appendix E is an analysis of the motion of raindrops in the shock layer. Figure 3B shows the effect of the shock on the motion of drops 0.5 and 5.0 mm in diameter at Mach 2.0 and 10.0 for a 15-degree conical radome. In this case, the deflection was very small. For other angles and conditions, the results may be significant.

Effect of Impact Angle Upon Crater Volume

Photographs and average volumes of craters in SCFS formed by 110-ft-lb jets making angles of 90, 70, 52, and 45 degrees with the target surface are shown in Figure 36. Contours of these craters are shown in Figure 37, and the effect of the impact angle upon crater volume is given by the lower curve of Figure 38. It was surprising to find that the crater volume created by normal impact was less than the volume formed by a 70-degree oblique impact. A look at Figure 37 reveals that there are central plateaus in the craters resulting from normal impact. These are not as

distinct as the ring craters formed by lower jet velocities, but the shaded areas shown are surrounded by regions of greater depth. The craters formed by the 70-degree jets do not have these plateaus. Cross-sections of two of the craters show this difference more clearly (Figure 39). It may be that the 70-degree jet simply "washed out" the central high region, thereby eroding out a greater volume than did the normal jet.

If this explanation is correct, it may provide a clue to the high central regions and the apparently unaffected areas in some craters. When a drop or the head of a jet strikes a target at high velocity normal to its surface, the extremely high pressure causes a compression of the liquid. This compressed volume serves to deflect the remainder of the liquid so that it impinges upon the target at an angle to the normal, eroding or washing out a circular ring crater.

This seems to be in agreement with Field's explanation as to why there is no decrease in crater volume until angles greater than 20 degrees with the normal are reached [14]. Investigators have also observed that the angle at which micron-size particles strike a target influences the erosion rate and that the maximum does not occur with normal impact [15].

The upper curve of Figure 38 shows the crater volume for different impact angles of 160-ft-lb jets. The difference in the two curves of this figure is not due primarily to the difference in jet energy, but results from the difference in the properties of the two targets. Normal impact of target No. 2 destroyed the target, and the point shown was determined by extrapolating the curve for this target on Figure 30.

It is apparent that the relation between impact angle and crater volume cannot be determined from these data. One might conclude from these curves that no cratering would occur at impact angles of less than about 30 degrees. This certainly is not the case. Using higher velocities, craters have been formed on some targets at angles of 30 degrees or less, but, because of their small size, the targets were cracked when the angle was increased. Substantial cratering occurs when 15-degree SCFS radomes are sled-tested in a simulated rain field.

As the oblique impact experiments did not give the necessary information, it is necessary to take either an analytical approach or turn to the experiments of others.

Heymann [16] says that the consensus appears to be that the normal component of the impact velocity is primarily responsible for the damage, with the tangential component playing a secondary role, if any.

If it is assumed that cratering at a given angle is governed by the normal velocity component, then by combining this hypothesis with Eq. (5),

$$V = 10.1 \times 10^{-6} E^{1.44}$$

the volume of a crater in a similar target impacted at an angle θ with the target surface is given by the relation

$$V = (3.73 \times 10^{-6})(m)^{1.44}(v \sin \theta)^{2.88} \quad (8)$$

where m and v are the jet mass in slugs and velocity in ft/sec, respectively. The volume may also be expressed as

$$V = (7.07 \times 10^{-17}) D^{4.32}(v \sin \theta)^{2.88} \quad (9)$$

where D is the drop diameter in millimeters.

Smith and Fyall question this basic hypothesis concerning the effect of the impact angle [8], and it is not in agreement with the empirical relations derived by Schmitt [17].

It was shown in Section IV that the crater volume resulting from normal liquid impact is a function of the projectile kinetic energy. It was also demonstrated that the crater volume is a function of the kinetic energy of lead projectiles. It has also been shown that the volume of craters in metal targets is a function of the kinetic energy of solid projectiles [18]. This seems to indicate that the mechanics of cratering is very similar for both liquid and solid impacts. It would seem reasonable to assume that the crater volume dependence upon impact angle would also be similar. In the case of solid projectile impact, the crater volume is a linear function of the sine of the impact angle [19].

Because of the results of solid projectile impact experiments and also because it is in agreement with the empirical relations developed by Schmitt [17], who has perhaps analyzed this problem as thoroughly as anyone, it is assumed that the crater volume is also a linear function of the sine of the impact angle of liquid projectiles.

The relation used in this study for determining the erosion of SCFF radomes is, therefore,

$$V = (7.07 \times 10^{-17}) D^{4.32} v^{2.88} \sin \theta \quad (10)$$

Effect of Impact Angle Upon Crater Area

Just as the oblique impact experiments did not provide sufficient information to determine the crater volume dependence upon the impact angle, they were of little help in determining the effect of the impact angle upon the crater area. About all that could be learned from these experiments was that the crater area becomes smaller as the angle with the target surface is decreased but not at as rapid a rate. The craters also became relatively more shallow as the impact angle was decreased.

Reinecke [20] says that a spherical drop impacting a plane surface at an angle θ gives an elliptical "imprint" with an area of $\pi R^2/\sin \theta$, where R is the drop radius. This undoubtedly does not refer to the actual crater area, as it would mean a larger area for very acute angles. For example, the drop "imprint" on a 15-degree radome would have an area almost four times as large as for normal impact, and its major axis would likewise be 3.9 times as long as the drop diameter, which is obviously not the case.

If the crater volume is a linear function of the sine of the impact angle, the area of geometrically similar craters would be a function of the 2/3 power of the sine of the angle. Although none of the oblique impact experiments supply sufficient information to determine this power empirically, the crater contours of Figure 37 do show that the area does not decrease as rapidly as the depth, as the impact angle θ decreases. In other words, as the angle decreases, the craters become relatively more shallow. It seems that a value of one-half might be a reasonable value to use for this exponent.

It is believed that the approximate crater area for the SCFS being considered can be found by applying this factor to Eq. (7), giving

$$A = 0.022E^{0.55}(\sin \theta)^{0.5} \tag{11}$$

or, in terms of drop diameter (mm) and velocity (ft/sec),

$$A = (1.21 \times 10^{-6})D^{1.65}v^{1.10}(\sin \theta)^{0.5} \tag{12}$$

SECTION VI

MULTIPLE IMPACTS

This research has been directed largely toward an investigation of cratering resulting from single high-velocity liquid impacts. It is realized, however, that radome damage will result from collisions with many raindrops and that one of the problems that must be dealt with is the interaction of stresses developed by multiple-drop impacts.

Some experimental results and illustrations of dual impacts will be given. Shot No. 829 created a crater having a volume of 0.000203 in^3 in the SCFS target. An identical shot (830) impacting the previous crater increased its volume by a factor of 2.7 to 0.000557 in^3 . Photographs and dimensions are given in Figure 40. Repeating this experiment, crater 806 was increased by a factor of 3.18 by a second shot (831) as shown in Figure 41. When reference is made to "identical" shots, it simply means that the same type bullets, nozzle sizes, amounts of water, and nozzle-target distances were employed. Shots 806 and 829, for example, were "identical" but the crater volumes were 0.000146 and 0.000203 in^3 , respectively. There is no way of knowing what the results of shots 830 and 831 would have been had they not impacted the previous craters. Conclusions can, therefore, only be based upon the averages of a number of shots. Similar craters are shown in Figure 42 except that the centers of the first (827) and second (832) shots were separated by a distance almost equal to a crater diameter. The combined volumes of the two shots were 2.74 times as great as the first. The craters shown in Figure 43 were separated a greater distance. The first shot (828) resulted in a crater having a volume of 0.000123 in^3 . The second shot (833) created a crater having a 0.000150-in^3 volume, but of most interest, it caused the volume of the first crater to increase by 30 percent to a volume of 0.000171 in^3 . From these data, the relation between the increase in crater volume caused by the second shot and the distance between impact points is shown in Figure 44. From this limited amount of data, it seems that the second impact will have no effect upon the volume of the first crater if the distance between crater centers is at least twice the diameter of the craters.

Figures 45, 46, and 47 show the results of similar experiments using higher velocity jets. In the first two of these, the crater volume increase due to the second impact was 2.46 and 2.85, which agrees very

well with the previous data. The final total volume for the third case was only 2.09 times as great as the first crater volume. It should be noted that the second shot (840) created a crater volume of only 0.000619 in³ as compared with that of the first (836) of 0.000715 in³, but that it caused the volume of the first crater to increase 22 percent. Finally, Figure 48 illustrates the fact that, although the impacts are sufficiently far apart so as not to affect the volume of the first, the first crater may serve as a stress raiser causing fracture of the target. The crack through No. 769 did not occur until No. 770 was fired.

Why is the total crater volume resulting from two impacts greater than twice that of one crater? When the craters coincide or overlap, the target surface is not the same for the second shot as for the first. Experiments have demonstrated that the momentum transfer from jet to target is greater for the second shot. Also, it has been pointed out that one reason for the relatively wide variations in crater size in brittle material is that some of the fractured material may not be completely broken loose but remains in the crater. It is likely that the stress waves from the second shot may detach some of this material, causing an increase in volume.

Radomes will, of course, be eroded by many collisions with drops as they pass through rain fields. The effect of several impacts is illustrated in Figure 49. The average volume of a single isolated crater in this target under the impact conditions of the experiment was 10.2×10^{-4} in³ per crater. After five impacts the average volume was 13.3×10^{-4} in³, an average increase of 30 percent per crater. Approximately 14 percent of the total surface area was covered by craters.

The number of shots was increased in steps of five until approximately 70 percent of the surface area was covered, by which time the average crater volume had increased about 90 percent. The ratio of average crater volume to that of a single isolated crater is plotted as a function of the percent of the target surface covered in Figure 50. The empirical relation

$$V/V_1 = 2 - \exp[-3P/(132-P)] \quad (13)$$

passes through the experimental points very well and indicates that when the total target surface is covered with craters that the average crater

volume will be approximately twice that of a single crater. This relation will be incorporated in the calculations of damage to SCFS radomes. These data are given in Table 1.

Calculation of the Total Volume of Radome Material Removed by Erosion

The three basic equations derived up to this point are Eqs: (10), (12), and (13). The volume and area of a single crater have been designated by V and A. As this study will now be concerned with the total volume and area, these designations for a single crater will be changed to V_1 and A_1 . Also, the direction of the projectile velocity vector with respect to the target surface has been designated as the angle θ . In the case of supersonic radomes, this impact angle will not be θ but will be the difference between the radome angle and the deflection angle due to the shock layer, $(\theta - \delta)$, as shown in Figure 35.

Equations (10) and (12) now become

$$V_1 = (7.07 \times 10^{-17}) D^{4.32} v^{2.88} \sin(\theta - \delta) \quad (14)$$

and

$$A_1 = (1.21 \times 10^{-6}) D^{1.65} v^{1.10} [\sin(\theta - \delta)]^{0.5} \quad (15)$$

It should be kept in mind that the constant coefficients in these equations apply only for SCFS having the properties of the Georgia Tech target No. 1.

These equations together with the probability model derived in Appendix D will be used to calculate the erosion of radomes. It will be noted that the exponents of $\sin(\theta - \delta)$ in Eqs. (14) and (15) are different from those derived in Appendix D. The reasons for these changes were given in Section V.

The drop size is based upon the well-known Marshall-Palmer exponential distribution function [21].

$$p(D) = 8000 \exp(4.1R^{-0.21}) \quad (16)$$

when D is the drop size in millimeters and R is the rainfall rate in millimeters/hour.

The percent of the area eroded in a traveled distance of S feet through the rain field is

$$P = Sv^{1.1} \sin\theta [\sin(\theta - \delta)]^{0.5} \int_{D_0}^{D_{\max}} D^{1.65} p(D) dD \quad (17)$$

and the total volume of material eroded per unit area (in^3/in^2) of radome surface is

$$V_t = [2 - \exp(-3P/(132-P))]Sv^{2.88} \sin\theta \sin(\theta - \delta) \int_{D_0}^{D_{\max}} D^{4.32} P(D) dD \quad (18)$$

It is believed that raindrops less than 0.5 mm in diameter will have negligible effect upon the erosion of radomes; therefore, the lower limit of D (D_0) in the above integral is taken as this value. The upper limit (D_{\max}) is given a value of 10 mm. It has been shown that the terminal velocities of raindrops larger than about 6 mm in diameter are sufficiently great to cause them to break up or disintegrate into smaller drops [7]. By extending the upper limit to a value of 10, a slight factor of safety is provided; however, according to the Marshall-Palmer distribution, there would be such a small number of the large drops that taking this upper limit as infinity changes the calculated erosion rate less than 1 percent.

The reader is referred to Appendix D for details of the derivations and the calculation of the various constants and to Appendix G for the computer program used for calculating the various numerical values.

Calculation of Erosion Rate

The rate at which the surface is eroded (ER) in inches/second will be the total volume of radome material removed per unit area divided by the time in the rain field. Substituting $S = vt$ in Eq. (18) and dividing by t gives

$$ER = [2 - \exp(-3P/(132 - P))]v^{3.88} \sin\theta \sin(\theta - \delta) \int_{D_0}^{D_{\max}} D^{4.32} P(D) dD \quad (19)$$

Numerical Results

Equations (17), (18), and (19) have been solved for rainfall rates of 1, 2, 3, 4, 5, and 6 in/hr; radome angles of 15, 30, 45, 60, 75, and 90 degrees; and velocities of 2500, 5000, and 7500 ft/sec; for distances up to 5000 ft. The deflection of the drops in the shock layer has been neglected.

Tables 2, 3, and 4 give numerical values of the percent of radome surface cratered; the volume of material removed per unit area; the erosion rate; and the erosion rate divided by $\sin^2\theta$.

Erosion rates for a 15-degree radome with a velocity of 5000 ft/sec are shown in Figure 51. It is seen that the rate of erosion increases

until the radome surface is entirely covered with craters, after which it remains constant. Figure 52 gives the distance that a radome must travel through a given rain field before its surface is 100 percent eroded. For example, a 30-degree conical SCFS radome moving at a speed of 5000 ft/sec through a 2.5-in/hr rain would travel only 350 feet before being entirely covered with craters.

Erosion Equations

The volume of radome material removed and the erosion rates were computed by solving Eqs. (18) and (19) by numerical integration. The material volume and rate of erosion after the radome is entirely covered by craters can be expressed by the following relations:

$$V = 1.76 \times 10^{-16} R^{1.12} v^{2.88} \sin^2 \theta \tag{20}$$

and

$$ER = 1.76 \times 10^{-16} R^{1.12} v^{3.88} \sin^2 \theta \tag{21}$$

Values of ER/sin²θ for various rainfall rates are shown in Figure 53.

This ER is equivalent to the MDPR (mean depth penetration rate) of Schmitt [17]. He has developed empirical relations based upon ten 5500-ft/sec firings on the rocket sled track at Holloman Air Force Base, New Mexico, and previous work which covered velocities from about 1500 ft/sec to 4000 ft/sec.

It is interesting to compare Eq. (21), determined by water jet gun experiments conducted in the laboratory and the theoretical drop size distribution, with the results based upon rocket sled tests in a simulated rain field. For 7941 fused silica, Schmitt found the erosion rate-velocity dependence relation to be

$$MDPR(\text{cm/sec}) = 9.22 \times 10^{-17} v^{4.48} \sin^2 \theta \tag{22}$$

for a rainfall rate of 4.6 in/hr. This relation converted to in/sec is also shown on Figure 53. The properties of the fused silica used in these sled tests may have been quite different from the targets used in the research described in this report.

SECTION VII

SPALLATION AND SUBSURFACE FRACTURE

Up to this point the research described in this report has dealt primarily with cratering and erosion of the radome surface. It is very likely, however, that the most catastrophic damage may be due to subsurface fractures or to spallation of the inner surface as a result of the reflection of stress waves.

Description of Fractures

Figure 54 shows fractures beneath the craters of three SCFS targets. In general these cracks run radially from the surface crater. This can be seen in the photographs of two 0.75-inch targets in Figure 55. Both also show rear surface spall resulting in the complete detachment of material in the lower photograph and the cracks parallel to the rear surface in the upper picture. The large fracture seen at the left of the lower target was caused by a crack through a nearby crater caused by this impact. Both of these targets, as well as those in Figure 56, show defective planes at the center, caused perhaps in the casting process. In most cases the radial cracks extend across this central plane, except in the upper target of this figure the cracks seem to originate at the center.

The fracture of the 0.40-inch target shown in Figure 57 is very similar to the one shown in Figure 24 except for the rear surface spall directly behind the impact point and that the circular crack was somewhat more pronounced. Shortly after the first photographs were made, the entire rear portion shown in the last two photographs of this figure became detached. Upon examination of these fractures, Figure 58 was drawn.

A Possible Explanation of the Target Fracture

The cracks indicated by A, B, and C of Figure 58 are of interest as either of them would cause greater damage to a radome than the ring crater, from either a structural or an electromagnetic viewpoint.

Initially, the path of crack A is determined by the tensile stresses around the immediate impact area. As suggested by Yoffee [22], the crack propagates into the plate normal to the maximum tangential stress near the crack tip. If this maximum stress is caused to shift from its original direction, the direction of the crack propagation would be expected to change. This could be caused by the stress waves generated by the impact and is probably the reason for A not following a straight line. The maximum speed of the crack propagation was analytically determined by Yoffee to be approximately 0.6 times the velocity of the shear wave. This agrees very well with the value of 0.38 times the dilatational wave velocity as observed by Küppers [23] in experiments with glass.

It is apparent that the stress wave associated with the impact travels through the plate and reflects from the rear surface, intersecting the crack before it has time to propagate through the target. It is computed that the crack reaches the first point of branching in approximately 3.5 μsec and that the reflected dilatational wave reaches the same point in approximately the same time. The stresses associated with the arrival of this wave will cause a change in the state of stress around the propagating crack tip and is probably the cause of the branching which creates crack C. As the reflected shear wave velocity is less than that of the dilatational wave, it will intersect crack A at a later time and would be expected to cause another branching such as crack B.

Spallation Resulting from Reflected Stress Waves

The fact that considerable damage can result from the reflection of stress waves from the inner surface of a radome has been alluded to several times. This source of potential danger will now be looked at in more detail. First, some experimental results and empirical relations will be considered, and next, the methods of stress calculation will be described.

In addition to creating a crater, a high-velocity impact will drive a strong shock wave into a structure. If the impacted structure, or "target," is sufficiently thin, a puncture will result (Figures 24 and 59). If the target is relatively thick, the shock will rapidly decay into an elastic stress wave. When such a wave encounters a free surface, it is reflected--generally as a tensile wave--and its amplitude may be of sufficient magnitude to produce fractures near the rear surface. When such

fractures do occur, they usually cause spallation or detachment of considerable material, producing greater damage than failure at the point of impact. This is an important problem in radome design, as it may dictate the required thickness. Such fractures may appear as granular cracks near the surface, as rear surface bulges, or as a complete detachment of target material, creating a shrapnel effect. An example of each is shown in Figure 60 for copper, aluminum, and steel targets. Fractures in a transparent acrylic resin (trade names of Lucite or Plexiglas) are also shown in this figure.

Photographs of sections of SCFS targets that fractured as a result of the reflected stress waves have been shown in Figures 55 and 56. Figure 61 shows photographs of both the front and rear surfaces of a 0.5-inch-thick SCFS target that has been impacted with a water jet. As shown in Figure 62, the crater volume is 0.001626 in^3 while the volume of material removed by the spall was 0.01868 in^3 , or approximately twelve times the volume of the crater.

A backing plate was placed behind target 826 which prevented the complete detachment of the fractured material, but which eventually fell out. Figure 63 shows the craters on the front of the target and the rear surface before and after the material was detached. Target 809, shown in Figure 64, was not only damaged by the cratering of the front surface and spallation of the rear surface, but it was also damaged by large cracks through the point of impact. The rear surface of target 706 was fractured as shown in Figure 65.

Drop Energy Required to Cause Spallation

The water jet kinetic energies and target thicknesses were plotted for the fifteen targets that had spalled in the course of these experiments. This information was also plotted for eleven other targets that showed no evidence of spallation. It is seen in Figure 66 that except for thin targets a straight line can be drawn separating the spall from no-spall points. This seems to indicate that the target thickness and jet energy are the major factors determining whether or not this type of failure will occur. The empirical relation shown says that spall in SCFS is likely to occur when

$$E > \frac{T-0.3}{0.0043} \quad (23)$$

where T is the target thickness in inches and E is the energy in ft-lbs.

Stress Relations for Spherical Waves

Spherical dilatational wave propagation in a homogeneous, isotropic material can be specified by the equation

$$\partial^2 \phi / \partial t^2 = C_1^2 [\partial^2 \phi / \partial r^2 + (2/r) \partial \phi / \partial r] \quad (24)$$

where ϕ is a scalar displacement potential, C_1 is the wave velocity, r is the radius vector, and t is time.

A computer program for the solution of this equation is given in Appendix F.

Model for Generating Stress Waves

The mathematical model for generating spherical elastic waves is that described by the author in Reference [24]. To summarize briefly, it is assumed that a time-varying pressure or forcing function is applied to the surface of an imaginary hollow spherical cavity, generating stress waves in the material. This cavity may be located entirely within the material as in the case of simulating underground explosions; with its center on the surface as is usually done in simulating hypervelocity impact of small solid particles such as micrometeorites; or outside the boundary of the target in the case of liquid impacts being considered in this research. The radius of this imaginary cavity (R_0) is determined by correlating the solutions of the stress wave equation with experimental results.

The pressure applied to the surface of the cavity is an impulse described by the relation

$$p/p_0 = K(\exp \alpha_1 t - \exp \alpha_2 t) \quad (25)$$

where p_0 is the maximum pressure, α_1 and α_2 are decay constants, t is the elapsed time, and K is a constant. By the proper choice of the values of α_1 and α_2 , various wave forms can be generated.

Reflected Stress Waves

The simplest example of the reflection of an elastic dilatation wave from a free surface occurs when the wave strikes normal to the surface. Since the resulting surface stress must be zero, a compressive wave must,

therefore, always be reflected as a tensile wave, and a tensile wave must be reflected as a compressive wave. When such a wave strikes a free surface at an oblique angle, the situation is much more complex. Not only will waves of dilatation be reflected but there will also be generated distortional or shear waves. From an analysis of these waves reflected from a plane surface, it seems that only the incident and reflected dilatation waves need to be considered in determining the maximum tensile stress except at points some distance from the normal axis where fracture is not likely to occur. For this reason, the amplitudes of the reflected shear waves are not computed in this analysis, although their existence is recognized and taken into account in the computation of the magnitude of the reflected dilatation waves.

Relative values of computed principal stresses soon after the wave reflection from a plane surface are shown in Figure 67. Compressive stresses are considered as positive and tensile stresses as negative. At the time shown, the maximum tensile stress has a value of -61 units. It can be seen, however, that this is not the maximum tension that will be created, as at a slightly later time this reflected tensile wave will combine with the tensile "tail" of the incident wave to generate a much higher tensile stress at a somewhat greater distance from the rear surface.

Effects of Material Properties upon Maximum Tensile Stress

Before considering the stress in a SCFS radome material, it might be well to see how the stresses are influenced by the various material properties. This may serve as a guide in the selection of material that will be subject to high-velocity impact. The maximum surface pressure, the pulse rise time and decay time, the imaginary cavity radius, the target thickness, and all other variables remain the same with only Young's modulus (E), Poisson's ratio (ν), and material density (ρ) being varied.

The maximum tensile stresses are shown in Figure 68. In the upper set of curves, the values of ρ and ν remain constant and the value of E is varied from 5×10^6 to 40×10^6 psi. The influence of Young's modulus is apparent. The maximum tensile stress near the rear surface of this 0.7-inch target is an inverse function of E . It will also be noted that these are radial stresses and if the strength of the target material is exceeded, the cracks will be perpendicular to the stress direction or

parallel to the rear surface. It will also be noted that the tangential components of the tensile stresses are maximum through approximately the first one-half of the target thickness and that any cracks will be radiating from the region of impact. This was observed to be the case in Figure 54. The middle set of curves represent constant values of E and ν , but with the density varying from 0.10×10^{-3} to 0.50×10^{-3} lb- $\mu\text{sec}^2\text{-in}^{-4}$. As the value of ρ increases, so does the maximum tensile stress. The lower set of curves show the dependence of the maximum tensile stress upon Poisson's ratio as it varies from 0.1 to 0.4, while values of E and ρ remain constant. Values of the maximum radial tensile stresses near the target's rear surface are shown in Figure 69, as each of the three material properties E , ρ , and ν is varied one at a time while the other two remain at the values indicated by their point of intersection.

Decay Constants in Terms of Drop Diameter

The function, $p/p_0 = K[\exp(-\alpha_1 t) - \exp(-\alpha_2 t)]$, expressed by Eq. (25) can be used to describe a pressure pulse of practically any form by the proper choice of decay constants, α_1 and α_2 . This was seen in Figure 20 when the pressures resulting from the impact of a liquid drop and an infinitely long jet were simulated. Pressure-time curves have been determined experimentally, and typical ones are shown in Appendix A that describe both spatial and temporal distributions of pressure resulting from an impinging jet. The forms of these curves can be described by the above relation if $\alpha_2/\alpha_1 = 4.5$. If this ratio is denoted by A , the relation becomes, for the purpose of this study,

$$p/p_0 = K[\exp(-\alpha_1 t) - \exp(-A\alpha_1 t)] \quad (26)$$

The pulse rise time has been calculated by Huang [25] to be approximately 0.25 of the ratio D/c , where D is the drop diameter and c is the wave velocity in the drop. As c of water is about 1.52 mm/ μsec , this relation becomes

$$t_R = 0.16D \quad (27)$$

where t_R is the pulse rise time in μsec and the diameter, D , is expressed in millimeters.

The value of t_R can be found by differentiating Eq. (26) with respect to t and equating to zero. This gives

$$t_R = \frac{\ln A}{\alpha_1(A-1)} \quad (28)$$

or, for a value of A of 4.5,

$$t_R = \frac{0.430}{\alpha_1} \quad (29)$$

In terms of drop size, D ,

$$\alpha_1 = 2.69/D \quad (30)$$

Maximum Impact Pressure

It was determined experimentally in Appendix A that the maximum value of the liquid impact pressure occurs at the center of the impact area and has a value of approximately 90 percent of the water hammer pressure, or

$$p_0 = 0.9\rho v c \quad (31)$$

Substituting the values of density and wave velocity of water gives

$$p_0 = 60.6v \quad (32)$$

where the pressure is in lb/in^2 when the velocity v is expressed in ft/sec .

The constant K in Eq. (26) has the value that makes the maximum magnitude of p equal to p_0 . This is found by substituting the value of t_R as given by Eq. (28) for t , giving

$$K[\exp(-\ln A/(A-1)) - \exp(-A \ln A/(A-1))] = 1 \quad (33)$$

If $A = 4.5$, $K = 1.98$.

The pressure, p , in lb/in^2 can now be expressed in terms of radome velocity (ft/sec) and drop diameter (mm) as

$$p = 119.7v[\exp(-2.69t/D) - \exp(-12.11t/D)] \quad (34)$$

To solve this equation for cases of oblique impact, the velocity v is simply replaced by its normal component, $v \sin \theta$ [19].

Values of the Radius, R_0

The radius of the imaginary cavity to which the preceding forcing function is applied can best be determined empirically if sufficient experimental information is available. Its value is chosen so that the computed results will be in as close agreement as possible with observed experimental data. When this is done for one set of data, it has been found that it usually gives results that are in fair agreement with those of other experiments involving the same materials [27]. When the derived quasi-theoretical relations are found to give answers that are in agreement with the results of several experiments, they can then be used with confidence to solve similar problems without the expenditure of time and money that would be required to conduct additional experiments.

It was found that the value of R_0 is dependent primarily upon the size of the impacting raindrops, its radius being slightly less than one-half of the drop radius. To express R_0 in inches and the drop diameter in millimeters, the relation used is

$$R_0 = 0.0085D \quad (35)$$

Some Numerical Examples

The 0.75-inch targets shown in cross-section in Figure 55 and the lower photograph in Figure 56 were impacted by 0.20-gm jets of water at velocities averaging 4170 ft/sec. This mass of water is equivalent to a 7.26-mm-diameter raindrop.

The following values were computed by the relations previously derived: (1) Pulse rise time, $t_R = 1.16\mu\text{sec}$ (Eq. (27)); (2) Decay constants, α_1 and $\alpha_2 = 0.37$ and $1.66\mu\text{sec}^{-1}$, respectively (Eq. (30)); (3) Maximum pressure, $p_0 = 252,700$ psi (Eq. (32)); and (4) The cavity radius, $R_0 = 0.062$ in (Eq. (35)). The "cavity" was placed so as to just touch the target surface. This produced surface pressures that were in close agreement with pressure distribution determined experimentally in Appendix A. The resulting stresses throughout the target were computed by use of the program described in Appendix F.

The maximum tensile stresses along the target's normal axis are shown in Figure 70. The tensile strength of SCFS is reported as ranging from about 4000 psi to 6000 psi [28]. As the computed tensile stress was slightly

greater than 6000 psi at a point approximately 0.1 inch from the rear surface, cracks parallel to the surface and spallation would be expected. Also, from the computed stresses, cracks radiating from the impact crater would also be expected. A two-dimensional plot of the maximum tensile stresses is shown in Figure 71.

The tensile stresses resulting from equivalent impact energies of 119.6 ft-lb on targets of various thicknesses are shown in Figure 72. If the tensile strength of this material is 5000 psi, there would be no spallation of targets thicker than about 0.85 inch.

The 0.5-inch-thick target shown in the upper photograph of Figure 56 was impacted with a 0.19-gm jet of water at a velocity of approximately 3270 ft/sec. The maximum tensile stress was computed to be 6300 psi at a point 0.07 inch from the rear surface. The spallation would have been predicted.

One SCFS radome being considered had a wall thickness of 0.434 inch. Conditions that would cause this radome to fail by spallation will be investigated. First, collision with a rather large, 8-mm-diameter raindrop is considered. For this size drop, the cavity radius, R_0 , is 0.068 in (Eq. (35)) and the decay constants, α_1 and α_2 , are 0.336 and 1.519 μsec^{-1} (Eq. (30)), respectively. For these conditions, it was found by use of the program of Appendix F that the maximum tensile stress near the rear surface of a SCFS target of 0.434-inch wall thickness could be related to the velocity and impact angle by the simple equation

$$\sigma_{\min} = 2.34 v \sin \theta \quad (36)$$

If the tensile strength of this material is 5000 psi, this relation says that for a 15-degree radome to fail by colliding with an 8-mm raindrop, its velocity must be 8,250 ft/sec or greater. The velocity-angle-stress relations for this radome colliding with an 8-mm raindrop are shown in Figure 73.

If the maximum diameter is assumed to be 7 mm, the velocity of this 15-degree, 0.434-inch-thick radome must have a velocity of 10,000 ft/sec or greater before spallation failure would be expected to occur.

Probability Relations

In the preceding section reference was made to the fact that the raindrop diameter would probably not exceed 6 mm [7], but in computing the erosion rate it made little difference what this upper limit was assumed to be. In calculating the stresses that may cause spallation of the radome's inner surface, however, the maximum probable drop size must be taken into consideration. The 6-mm maximum diameter was apparently determined for rainfall near the earth's surface, but it may not be the maximum at higher altitudes where the drops may not have reached terminal velocities and the aerodynamic forces caused by the rarefied atmosphere may permit larger drops to form. Because of the lack of information about maximum raindrop sizes at higher altitudes, it seems reasonable to assume an upper limit of 10 mm.

The probabilities of collision under various conditions are discussed in Appendix D. Figures 74 and 75 show the drop size-distance traveled-probability relations for a radome having a base diameter of 18 inches moving through rainfalls of 2.5 and 5.0 inches per hour. From Figure 74, for example, it can be seen that in a 2.5 in/hr rain the probability is 0.20 that this radome will encounter a raindrop as large as 8 mm in diameter in a distance of 1000 feet.

If the allowable probability of failure and the expected rainfall (both rate and extent) are specified, the largest raindrop that a radome of a given size is likely to encounter can be computed. The required wall thickness necessary to prevent spallation of its inner surface for a specified radome angle and velocity can then be computed by the method described and by use of the computer program of Appendix F.

Stresses Resulting from Multiple Impacts

One of the problems that must be dealt with in the analysis of radome damage resulting from rain impact is the effect of multiple drops and the interaction of the stress waves developed by the individual drops. The equations are derived and a computer program is given in Appendix F by which the stresses in a target produced by a number of raindrop collisions can be calculated.

The effect of multiple impacts upon the total crater volumes has been analyzed. The effects of the distance and time between impacts will now be analyzed with respect to the tensile stresses created by reflected waves.

The stresses computed are relative values only, and dimensionless units of time and dimensions are employed. The radome thickness is denoted by T , the stress by $\bar{\sigma}$, and the time by \bar{t} . A pressure wave typical of high-velocity impact is employed.

First, two impacts at the same time are considered. The maximum tensile stress resulting from two impacts will be generated either directly beneath the points of impact or on an axis midway between these points. Figure 76 gives the values of the tensile stress for different distances between the impact points. The maximum tensile stress for a single impact has a relative value of $\bar{\sigma} = 115$. If two drops are very close together at the same time, the resulting stress will obviously be twice this value, or 230. As the distance between drops is increased, the developed stress will decrease. In this case of simultaneous impacts, it can be seen that the maximum stress occurs along the axis between the two points. At a distance of about $0.8 T$, the stresses directly beneath the impact points have decreased to those resulting from a single drop, but the stress on the z-axis has a value of almost 200. The stress on this axis continues to decrease as the distance between drops increases. At a distance of approximately $1.8 T$, the stress on this axis has decreased to the value created by a single impact. This means that if the distance between two drops is greater than twice the thickness of the target, the maximum stress can probably be determined by computing the stress developed by a single drop and that the interaction of the stress waves can be neglected.

The effect of time ($\Delta\bar{t}$) between drops will now be considered. The stresses developed by two drops impacting the same point are shown in the first graph of Figure 77. As pointed out, the tensile stress will have a value of 230 for zero time between impacts. As the time increases, the stress decreases up to a relative time of 0.50, beyond which the stress is the same as for the impact of a single drop. If the distance between drops is $0.4 T$, the tensile stress for various times ($\Delta\bar{t}$) is given in the

second graph of Figure 77. The first impact is P_1 and the later impact is P_2 . The other curves give this information for various distances between impacts.

Further studies have indicated that the probability of a second impact occurring near the first before the amplitude of the first stress wave has decayed to a negligible value is so small that it can be neglected. For this reason, this phase of the research was pursued no further.

SECTION VIII

RADOME COATINGS

Radome surfaces are frequently covered with thin coatings as protection against rain erosion. Many experimental investigations have been conducted to provide information concerning the effects of specific coating-substrate combinations. Others, such as Engel [29] and Springer [30], have made analytical contributions to this subject.

In this analysis, no specific coatings have been considered, but SCFS substrates are assumed. The effects of coating upon the stress waves and the resulting tensile stresses that may cause subsurface fractures or spallation are analyzed. The effect upon cratering and erosion is not considered except to note the interface stresses that may cause the coating to become separated from the substrate.

Pulse Behavior at an Interface

An abrupt change in the physical properties of a material will result in the modification of a pressure pulse as it encounters this change. In general, a portion of the pulse will be transmitted, and a portion will be reflected. The relations which describe the modification of a pulse are based upon the boundary conditions of continuity of pressure and continuity of particle velocity across the interface between the two materials [31]. These relations depend upon the value of ρc , called the "characteristic impedance." If $\rho_o c_o$ is for the first and $\rho_t c_t$ is for the second laminate, and P_o is the pulse amplitude in the first, the amplitude of the transmitted component is

$$P_t = \left[\frac{2\rho_t c_t}{\rho_t c_t + \rho_o c_o} \right] P_o \quad (37)$$

and the reflected component is

$$P_r = \left[\frac{\rho_t c_t - \rho_o c_o}{\rho_t c_t + \rho_o c_o} \right] P_o \quad (38)$$

These relations are somewhat simplified by letting

$$K = \frac{\rho_t c_t}{\rho_o c_o} \quad (39)$$

giving

$$P_t = \left[\frac{2K}{K+1} \right] P_o \quad (40)$$

and

$$P_r = \left[\frac{K-1}{K+1} \right] P_o \quad (41)$$

Figure 78 gives the relative values of the transmitted and reflected pulse amplitudes as functions of K.

Effect of Pulse Length and Coating Thickness

A 5-mil-thick coating (C) on a substrate (S) is shown in Figure 79. The coating does not represent any particular material, but it is assumed that the impedance mismatch between the coating and the water drop (K_1) and between the coating and the SCFS substrate (K_2) have the values shown. It is also assumed that the ratio of the pulse velocity in the substrate to that in the coating (c_s/c_c) is 1.2.

The impact pressure is represented by P. Equations (40) and (41) are used to calculate the transmitted and reflected stresses at the interface between the coating and substrate, if no attenuation of the pressure pulse is considered. The pulse having an amplitude of $\sigma_1 = 0.352P$ will be transmitted into the radome. The tensile pulse reflected from this interface will have an amplitude of $-0.648P$. A portion of this reflected pulse will then be transmitted, $\sigma_1' = -0.042P$, into the liquid drop and a pulse having an amplitude of $0.606P$ will be reflected back through the coating. Upon reaching the substrate interface, another pulse, $\sigma_2 = 0.213P$, will be transmitted into the radome. This will continue with decreasing amplitudes.

The amplitudes of the respective stresses transmitted into the radome wall are given by the equation

$$\sigma_n = \left[\frac{(K_2-1)(K_1-1)}{(K_2+1)(K_1+1)} \right]^{n-1} \left[\frac{2K_2}{K_2+1} \right] P \quad (42)$$

If the thickness of the coating is sufficiently small or if the pulse length sufficiently large, the train of transmitted pulses will merge into a single wave. For this to occur, the pulse length in the coating, λ_c , must be equal to or greater than twice the coating thickness.

In this example, the pulse must have a length, λ_C , of at least 0.01 in. before they will merge into a single wave. Suppose, for example, a square pulse or step function having a length, λ_C , of 0.05 in. is generated by the collision with the liquid. This pulse will have a length, λ_S , of 0.06 in. in the substrate because of the increase in velocity according to the relation

$$\lambda_S = \frac{c_S}{c_C} \lambda_C \quad (43)$$

The pulse of amplitude σ_1 will be followed by the second pulse of amplitude σ_2 . The distances between these pulse fronts in the substrate will be 0.012 in. These will be followed by the other pulses at equal intervals. These would combine to form the wave front, O to A, in Figure 80. The front of the sixth pulse will pass through the coating-substrate interface at the same time as the "tail" of the first pulse. There will, therefore, be a sudden decrease in amplitude equal to $\sigma_1 - \sigma_6$ from the peak of 0.819F. The arrival of the tails of later pulses continues to cause step decreases until the wave decays as shown. Figure 80 then represents the resulting shape of the wave transmitted into the substrate.

It is seen that the amplitude of the wave transmitted into the substrate will depend not only upon the properties of the coating material but upon its thickness and the pulse length generated by the liquid impact. The effect of the pulse length, λ_C , upon the profile of the transmitted wave is shown in Figure 81. If, for example, $n = 1$, λ_n is greater than $0.01(n-1) = 0$, and equal to or less than $0.01n = 0.05$. In this case the transmitted wave would consist of separate and distinct pulses having the amplitudes shown in Figure 79. These amplitudes are indicated by the points on the curve λ_1 of Figure 81.

If λ is greater than 0.01 in. and equal to or less than 0.02., the pulses will overlap, and the transmitted wave will rise in a stepwise manner to a value 0.565P and then decay as shown by the points on the curve λ_2 . If λ is greater than 0.05 in. and equal to or less than 0.05 in., $n = 5$ and the transmitted wave would rise in amplitude to point A and then decay as indicated by λ_5 . This was the case previously considered and shown in Figure 80. If the generated pulse length is very long, the amplitude of the transmitted wave would approach a value of about 0.9P as shown.

Instead of assuming the impact pressures to be step functions, more realistic impact pressure-time functions as used in Section VII, Eq. (25), will now be considered, together with the decay of the stress wave as it moves through the target and is reflected from the rear surface.

The thickness of the coating, T_C , will be expressed in terms of the pulse velocity in the coating, C_C , and the time, Δt , separating the wave fronts in the substrate. These are related by the equation

$$\Delta t = \frac{2T_C}{C_C} \quad (44)$$

The stress wave profiles just prior to reaching the rear surface of a 0.5-in. target are shown in Figure 82 for an impedance mismatch of 0.5. The curve for $\Delta t = 0$ is that for no coating. When $\Delta t = 0.10$, the amplitude is somewhat less, and its shape is changed but little. When $\Delta t = 0.25$, the effect of the separate pulses becomes evident. The maximum stress is dependent upon the amplitude of the first two transmitted waves, but not upon the others. For a value of $\Delta t = 0.5$, the maximum stress depends only upon the amplitude of the first transmitted wave, and the remaining waves contribute only to the wave length. Also shown in Figure 82 are the curves for an impedance mismatch of 2.0. In this case, the stress amplitude reaches a value much greater than that of an uncoated target.

The stress histories at a given point 0.42 in. from the target's front surface for values of Δt equal to 0.1 and 0.5 and impedance mismatch values of 0.5 and 2.0 are shown in Figure 83. The front of the reflected wave reached the point at a time of approximately 3.2 μsec , causing the large tensile stresses. For $K = 0.5$ and 2.0, the maximum tensile stresses developed in a 0.5-in. target are shown in Figure 84. Figure 85 summarizes the effects of K and Δt on the peak stresses occurring in a 0.5-inch substrate.

From these examples it is seen that the use of coatings on radome surfaces sometimes causes a decrease and sometimes an increase in the maximum tensile stresses in the material. If the impedance of the coating is greater than the substrate ($K < 1$), the stress in the substrate will be lowered; whereas, if the impedance of the coating is smaller than the substrate ($K > 1$), the stress in the substrate can be considerably greater than the no-coating value. This is a factor that should be taken into consideration when designing an all-weather radome. If the radome wall is

sufficiently thick or the angle of impact is small, spallation may not be a problem at all, and the coating should be designed for erosion and micro-wave effects only. For thin-wall radomes, the stress resulting from reflected waves may be a factor.

SECTION IX
ROCKET SLED TESTS

A rocket sled test program was conducted at Holloman Air Force Base, New Mexico, to determine the rain erosion resistance of slip-cast fused silica at velocities above 5000 ft/sec. The fabrication techniques used at the Georgia Institute of Technology to slip-cast, heat-treat, and flame-glaze the radomes; a description of the test facilities; and the results of six sled tests have been described by Walton and Harris [32]. Radomes from three of these tests have been examined in the course of the present work, and some observations will be made concerning the damages sustained by each. The damage will also be compared with that predicted by the relations of Section VI. Sled test information from Reference [32] is summarized in Table 5.

Radome No. 7RB1

Figure 86 is a photograph of the radome of run No. 2. The rain intensity was reported as 2.5 inches/hour, and the average drop size was said to be between 1.5 and 2.0 mm in diameter. The average velocity was about 5300 ft/sec, and the rain field length was 400 ft. A view of the radome with its metal tip broken off and a closer view of some of the craters are shown in Figure 87. The radome dimensions as well as the locations of the centers of the photographs of Figures 89, 90, and 91 are given in Figure 88.

The photographs of Figure 89 were taken around the circumference at 45-degree intervals at a distance of 11.6 inches from the tip. By counting all craters that could be detected, it was found that they averaged 27.1 per square inch. Those of Figure 90 were 8.3 inches from the tip and averaged 40.4 craters per square inch. At a distance of 3.0 inches from the tip, the photographs overlapped (Figure 91), and the number of craters averaged 25.1 per square inch. The radome appearance is certainly different near the tip. Erosion rather than cratering seems to have been the major source of damage. It may be that the craters were largely removed by the high temperatures and fusion caused by aerodynamic heating, or the high temperature may have first fused the surface, and cratering is different in material heated to very high temperatures. No

explanation is offered for the higher density of craters near the middle of the radome surface. Based upon these photographs, it was estimated that for the entire radome there was an overall average of 30 craters per square inch and that about 40 percent of the radome surface was covered. This radome had been flame-glazed by the use of a plasma jet to fuse the surface and to provide a coating of non-porous fused silica that served to seal the surface. Walton and Harris reported that the thickness of the fused layer varied from 0.03 to 0.04 inch near the tip to less than 0.005 inch near the base.

The depths of some of the craters were measured, and their volumes were computed. The purpose of this was to learn more of the nature of the fractures and to determine the extent to which drop impacts can be simulated by the use of the water jet accelerator and by solid projectile impacts. Crater measurements are being made in Figure 92. Cross-sections of a somewhat larger-than-average crater near the base of the radome are shown in Figure 93. The depths were measured from the curved surface. The first profiles were taken outside the crater and indicate the roughness and irregularities of the surface. As it is impossible to recognize the actual crater boundaries from the measurements (although they can be seen visually) because of the surface roughness, the depths shown in Figure 94 start with the 0.001-inch contour. The volume of this crater was found to be $5.6 \times 10^{-5} \text{ in}^3$, and average diameter was about 0.20 inch. Profiles and crater contours of another crater located near the midpoint of the radome surface are given in Figures 95 and 96. Although the area of this crater is less than the previous one, its depth is somewhat greater. It appeared to be about an average-size crater, and its volume was $3.1 \times 10^{-5} \text{ in}^3$, and average diameter was about 0.125 in.

Comparing the depth contours of these craters with those of Figures 25 and 26, several similarities and differences are noted. In both cases there is a central plateau surrounded by areas of greater depth containing several rather deep pits. The primary differences are that the radome craters were more irregular in shape (although the actual boundaries are not shown), and the crater surface is rougher. Also, the central plateau of the jet-produced crater was of the original surface, and it is apparent that some of the original radome material had been removed. The jet impact

was normal to the target's surface at a velocity of about 2000 ft/sec and that of the drop was at an angle of about 16 degrees at a speed of 5300 ft/sec. This slight difference in the shape of the craters produced by normal and oblique impacts was seen in Figure 36.

Although both targets were of SCFS, the surfaces were entirely different. The radome surface was much rougher, and it had also been provided with a coating of non-porous fused silica. Walton had observed that once the impact pressure was sufficient to cause damage to the glazed surface, there was a tendency to chip out a portion of the glaze extending beyond the actual area of impact.

In view of the differences in the material properties of the target impacted by the jet and the radome eroded by raindrops and the great difference in the impact angles, the similarities in the craters are more than would have been expected.

The direction of impact seems to make little difference in the crater's general appearance. It appears that the simulation of a high-velocity impact at a small angle with the surface can be accomplished with a lower velocity impact at a different angle as long as the normal velocity components are the same. For example, the velocity of 5000 ft/sec at 15 degrees with the surface could probably be simulated with a velocity of 2000 ft/sec at an angle of 40 degrees.

Estimates of Erosion

It was previously mentioned that a careful study of the radome photographs indicated that there was an average of about 30 craters per square inch and that approximately 40 percent of its surface was covered. Neglecting the overlapping of craters, this gives an average crater area of 0.0133 in^2 , or an average diameter of 0.13 in. This confirms the fact that the second crater measured ($d = 0.125 \text{ in}$, $V = 3.1 \times 10^{-5} \text{ in}^3$) was perhaps one of average size. If this is assumed, the total volume of material removed in the 400-ft rain field was $(30 \times 3.1 \times 10^{-5})$, or $9.3 \times 10^{-4} \text{ in}^3/\text{in}^2$, and the average rate of erosion up to that time was $1.23 \times 10^{-2} \text{ in}/\text{sec}$.

Radome No. 7RD1

Figure 97 is a mosaic or composite of photographs made of the surface of the radome of run No. 4. The average rocket velocity was about 4900 ft/sec. The rain field was equivalent to 3000 ft of length at a rate of 2.5 in/hr. The surface had been flame-glazed the same as No. 7RB1. The entire surface was covered with craters, and it was not possible to determine crater volumes or the extent of the erosion. Views of this radome are shown to a larger scale in Figure 98.

Radome No. 7RF2

Only the tip of this radome of run No. 7 survived, as it apparently hit a bird during coast-out after traveling through the same equivalent rain field as run No. 4. The average velocity through the rain was about 5100 ft/sec. The tip is shown in Figure 99. This radome was unglazed, and, although the entire surface was eroded, it did not appear to be as severe as that of No. 7RD1. Because of the eroded surface, it was impossible to measure the crater volumes with any high degree of accuracy.

Comparison of Rocket Test Results with Predicted Values

Equations (17), (18), and (19) have been solved by the computer code REMRASS for the conditions of Holloman run No. 2 ($R = 2.5$ in/hr and $v = 5300$ ft/sec) and also taking into consideration the deflection of the drops in the shock layer. The results are shown in Table 6. These calculations indicate that at a distance of 400 ft, 43.2 percent of the radome will be covered with craters, that 6.76×10^{-4} in³/in² of the material will have been removed, and that the average erosion rate up to that time has been 8.96×10^{-3} inches/sec.

The following gives a direct comparison of the results:

	<u>Percent of Area Eroded</u>	<u>Volume (In³/In²)</u>	<u>Erosion Rate (In/Sec)</u>
Calculated values	43.2	6.76×10^{-4}	8.96×10^{-3}
Estimated from radome examination	40.0	9.3×10^{-4}	1.23×10^{-2}

Keeping in mind the fact that the properties of the radome material and target material are probably not the same, that the surface of the radome had been flame-glazed, increasing its susceptibility to cratering, and that the actual rainfall rate may have been somewhat greater than

2.5 in/hr for the sled tests, it is surprising that the results are in such close agreement.

It was not possible to obtain a similar comparison for the radomes of runs Nos. 4 and 7, as their surfaces were completely covered with craters after traveling through 2000-ft rain fields. The computed results indicate that the radomes would be 100 percent covered at a distance of 925 ft in the rain.

SECTION X

CONCLUSIONS

It has been shown that the water jet accelerator is a valuable tool for simulating the damage caused by collisions of supersonic radomes with raindrops. Cratering and erosion data obtained by use of the accelerator, together with theoretical considerations, give relations that can be employed in the design of high-speed vehicles that must possess all-weather capabilities.

When the rain field is described (i.e., rate, duration, and extent) and the radome profile, wall thickness, velocity, and allowable probability of failure are specified, the methods described in this report can be used to determine the probable damage, provided that the radome material properties and their relations to cratering resistance are known.

It must be remembered that the equations derived and the numerical values computed in this study were based upon only one of the SCFS targets. This target experienced the greatest damage of any of those finished for use in this research; therefore, the use of these relations in radome design would probably be on the side of safety.

The craters in the weakest of the targets averaged six times the volume of those in the strongest targets (Figure 30). It is not known which of the material properties has the greatest influence on the target's resistance to cratering. The effects of such properties as hardness, porosity, modulus of rupture, Young's modulus, surface finish, and the compressive, tensile, and shear strengths upon the material's resistance to erosion and cratering can be determined by the use of the jet accelerator. Such information would certainly be of great value to the engineer in preparing the radome material and fabrication specifications.

The water jet accelerator is an economical tool for comparing the erosion resistance of different materials as well as determining the effects of coating, laminates, and surface conditions.

Although much has been learned about high-speed liquid impact, it is apparent that much more information is needed. Empirical relations have been derived that will give the probable rain damage to SCFS radomes, but

relatively little is known about the actual mechanics of cratering. The maximum tensile stress has been assumed to be the governing factor relating to subsurface fracture and spallation. This is probably not entirely correct. Other theories of fracture should be investigated. As the required radome wall thickness depends upon the maximum probable raindrop size, more information concerning the drop size distribution is needed, especially for rainfall at various altitudes.

REFERENCES

- [1] Wheelahan, E. J. (1967), "State-of-the-Art Survey of Raindrop Erosion," U. S. Army Missile Command Report No. RS-TR-67-13, Redstone Arsenal, Alabama.
- [2] Eisenberg, P. (1970), "Cavitation and Impact Erosion - Concepts, Correlations, Controversies," Characterization and Determination of Erosion Resistance, ASTM STP 474, p. 3.
- [3] Engel, O. (1957), "Mechanism of Rain Erosion, Part X: A Review and Evaluation of the Present State of the Problem," National Bureau of Standards, Washington, D. C., WADC TR-53-192X, AD-142 240.
- [4] Fyall, A. A. (1970), "Rain Erosion--A Special Radome Problem," Chapter 8, Radome Engineering Handbook, J. D. Walton, editor, Marcel Dekker, Inc., New York.
- [5] Bowden, F. P., and Brunton, J. H. (1958), "Damage to Solids by Liquid Impact at Supersonic Speeds," Nature, Vol. 181, pp. 873-875.
- [6] Kinslow, R., Sahai, Vireshwar, and Peddieson, John, Jr. (1972), "Preliminary Investigation of High-Velocity Liquid Impact Damage," p. 50, Tenn. Tech. Univ., TTU-ES-72-2, AD-753 381.
- [7] Fyall, A. A. (1967), "Single Impact Studies with Liquids and Solids," Rain Erosion and Associated Phenomena, Royal Aircraft Establishment, Farnborough, England, N88-19401-427, pp. 428-433.
- [8] Smith, P., and Fyall, A. A. (1969), "Single Impact Studies of Rain Erosion," Royal Aircraft Establishment Tech. Report 69086.
- [9] Lankford, J. L., and Leverance, R. A. (1971), "Determination of Threshold Damage in Radome Materials by Discrete Impact in a Ballistics Range," Naval Ordnance Laboratory, NOLTR71-113.
- [10] Ranger, A. A., and Nicholls, J. A. (1970), "Water Droplet Breakup in High Speed Airstreams," Proc. of the Third Internatl. Conf. on Rain Erosion and Associated Phenomena, pp. 601-628.
- [11] Reinecke, W. G., and Waldman, G. D. (1970), "An Investigation of Water Drop Disintegration in the Region Behind Strong Shock Waves," Proc. of the Third Internatl. Conf. on Rain Erosion and Associated Phenomena, pp. 629-658.
- [12] Brunton, J. H. (1961), "Deformation of Solids by Impact of Liquids at High Speeds," Symposium on Erosion and Cavitation, p. 83, ASTM Special Tech. Pub. No. 307.

- [13] Walton, J. D., Jr., and Gorton, C. W. (1970), "Evaluation of Ceramic Coatings for Rain Erosion Protection," Proc. of the Third Internatl. Conf. on Rain Erosion and Associated Phenomena, pp. 209-220.
- [14] Field, J. E. (1966), "Stress Waves, Deformation, and Fracture Caused by Liquid Impact," Phil. Trans. Royal Society (London), Vol. 260A, pp. 86-93.
- [15] Grant, G., and Tabakoff, G. (1973), "An Experimental Investigation of the Erosive Characteristics of 2024 Aluminum Alloy," Univ. of Cincinnati Report No. 73-37.
- [16] Heymann, F. J. (1967), "A Survey of Clues to the Relationship Between Erosion Rate and Impact Parameters," Proc. of the Second Conf. on Rain Erosion and Associated Phenomena, Meersburg, Germany.
- [17] Schmitt, G. F., Jr. (1972), "Rain Erosion Behavior of Materials at 5500 Feet Per Second," AFML-TR-72-64, Air Force Materials Laboratory, Wright-Patterson Air Force Base, Ohio.
- [18] Halperson, S. M., and Atkins, W. W. (1961), "Observation of Hypervelocity Impact," Proc. of the Fifth Symposium on Hypervelocity Impact.
- [19] Bryan, G. M. (1961), "High Velocity Oblique Impacts," Proc. of the Fifth Symposium on Hypervelocity Impact.
- [20] Reinecke, W. G. (1974), "Rain Erosion at High Speeds," presented at the Fourth Internatl. Conf. on Rain Erosion and Related Phenomena, Meersburg, Germany.
- [21] Marshall, J. S., and Palmer, W. McK. (1948), "The Distribution of Raindrops with Size," Journal of the Atmospheric Sciences, v. 5, pp. 165-166.
- [22] Yoffee, E. H. (1951), "The Moving Griffith Crack," Philosophical Magazine, series 7, v. 42, pp. 739-750.
- [23] Koppers, H. (1967), "The Initial Course of Crack Velocity in Glass Plates," International Journal of Fracture Mechanics 3, No. 1, p. 13.
- [24] Kinslow, R. (1963), "Properties of Spherical Stress Waves Produced by Hypervelocity Impact," AEDC-TDR-63-197 (AD-421 578).
- [25] Huang, Y. C., et al (1971), "Impact of Spherical Water Drop on Flat Rigid Surface," Mich. Univ., Ann Arbor, PB-203 385.
- [26] Springer, G. S., and Baxi, C. H. (1972), "A Model for Rain Erosion of Homogeneous Materials," AFML-TR-72-106, Air Force Materials Laboratory, Wright-Patterson Air Force Base, Ohio.

- [27] Kinslow, R. (1973), "Bumper-Protected Laminated Spacecraft Mainwalls," NASA CR-2262.
- [28] Crmsby, P. A., et al (1971), "Ceramic Materials Research - Status Report 1971," U. S. Army Missile Command, Redstone Arsenal, Alabama, AD-728 816.
- [29] Engel, O. G. (1971), "Investigation of Composite-Coating Systems for Rain-Erosion Protection," Univ. of Dayton, AD-737 661.
- [30] Springer, G. S., et al (1973), "Analysis of Rain Erosion of Coated Materials," AFML-TR-73-227, Air Force Materials Laboratory, Wright-Patterson Air Force Base, Ohio.
- [31] Kinslow, R. (1967), "Stress Waves in Laminated Materials," AIAA Paper No. 67-140, 5th Aerospace Sciences Meeting, N.Y., N.Y.
- [32] Walton, J. D., and Harris, J. N. (1966), "Rain Erosion Sled Testing of Slip-Cast Fused Silica Radomes," Final Technical Report, Part I, Project A-925; prepared for U. S. Army Missile Command, Redstone Arsenal, Alabama; Georgia Inst. of Technology.

54<

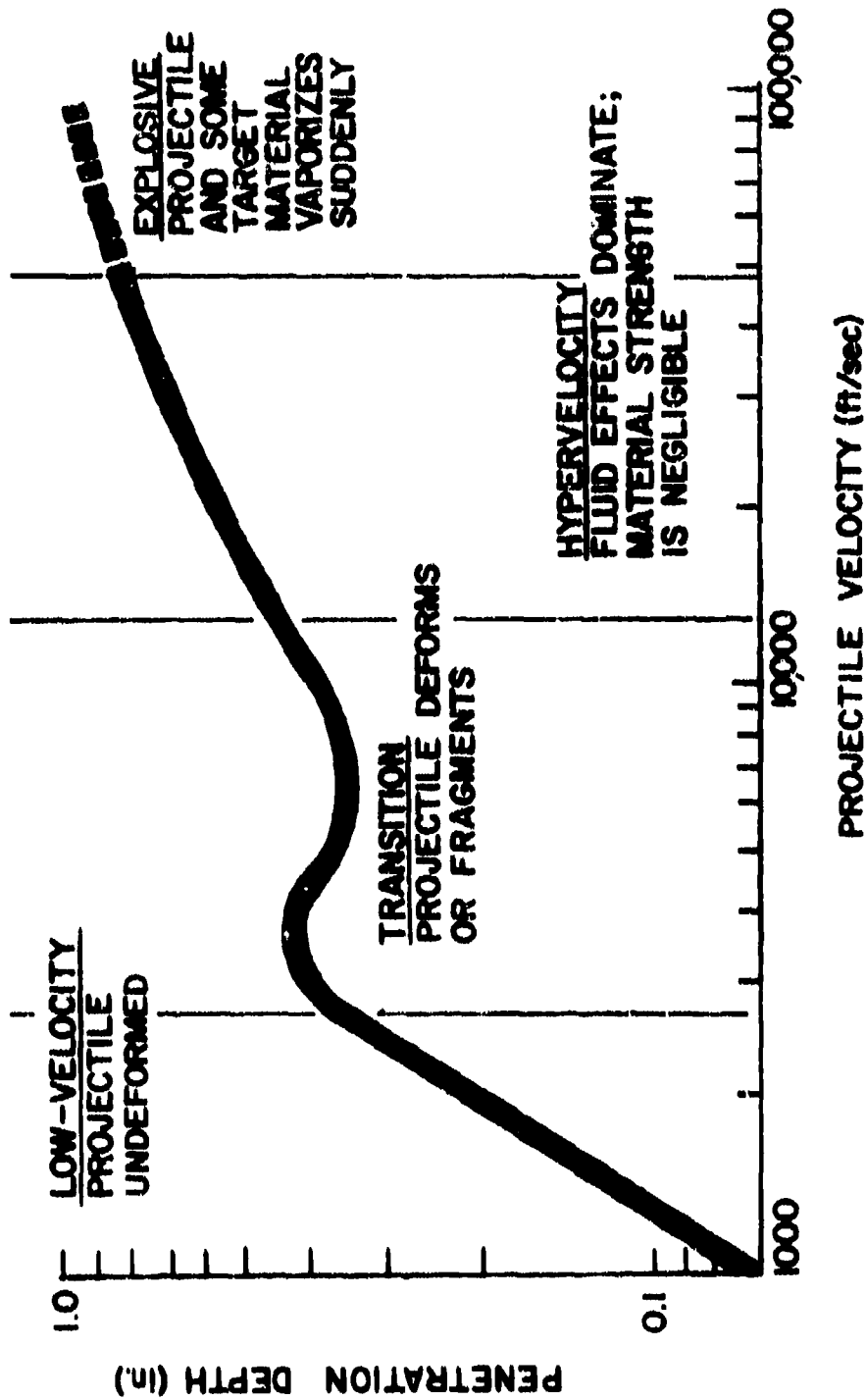


FIGURE 1. REGIMES OF IMPACT PHENOMENA

55<

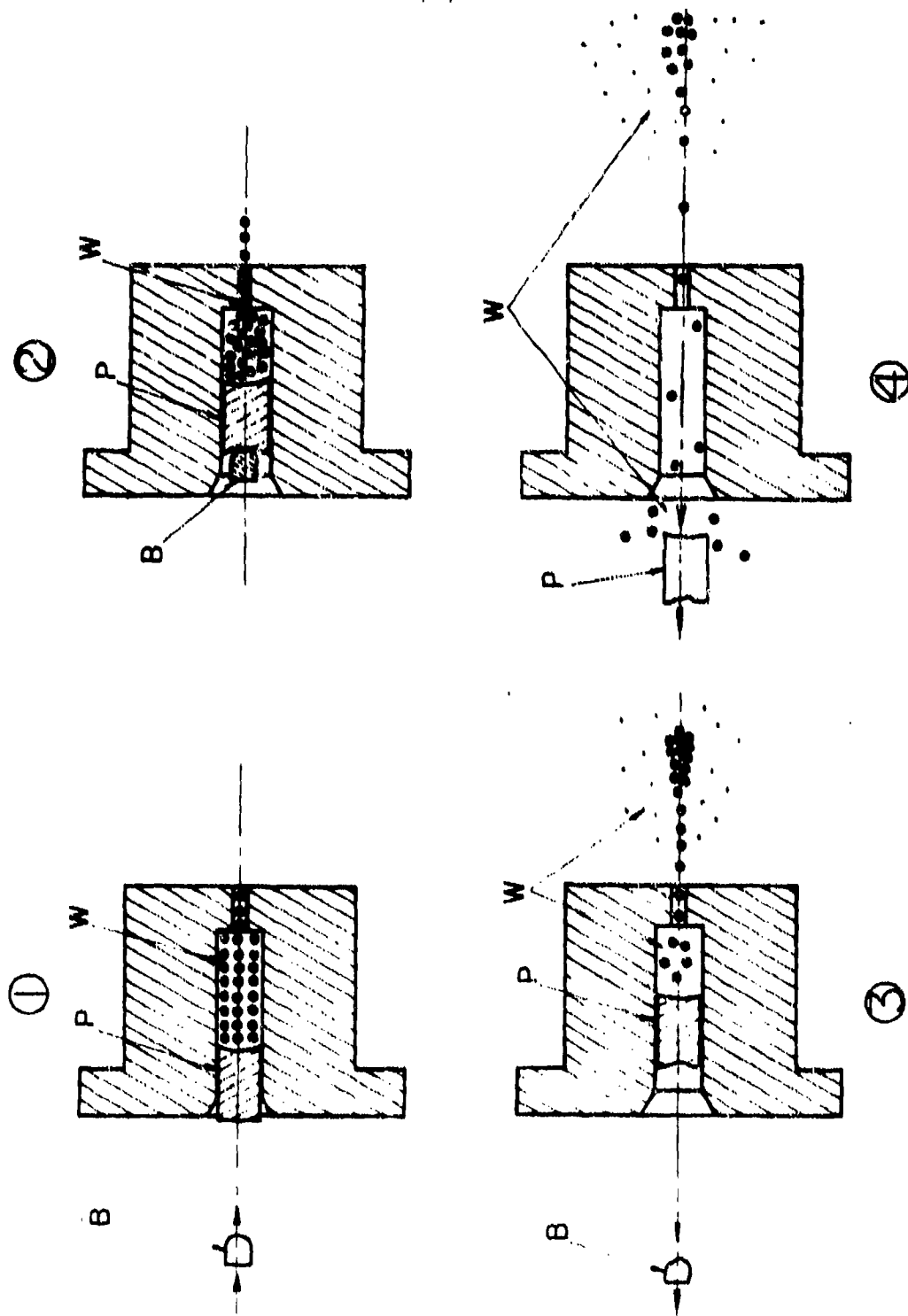
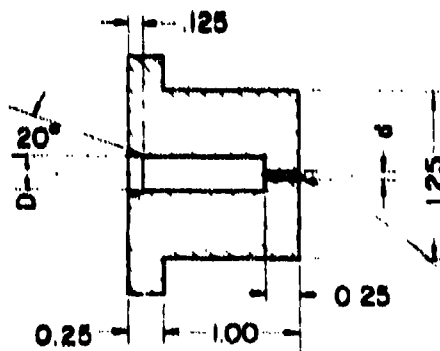
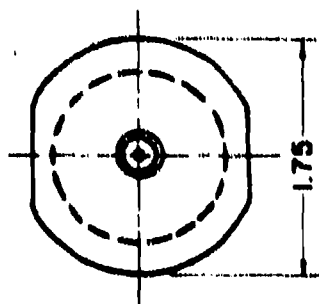
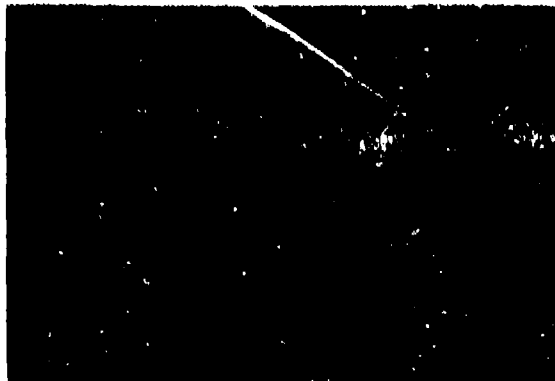
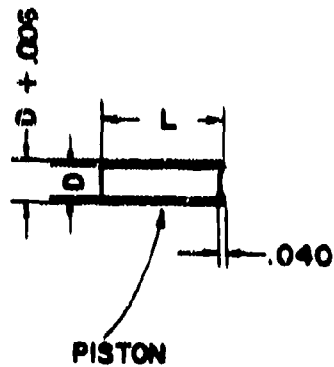


FIGURE 2. SCHEMATIC OF WATER EJECTION FROM NOZZLE

56<



NOZZLE

FIGURE 3. DETAILS OF HIGH-PRESSURE CYLINDER AND PISTON

57<

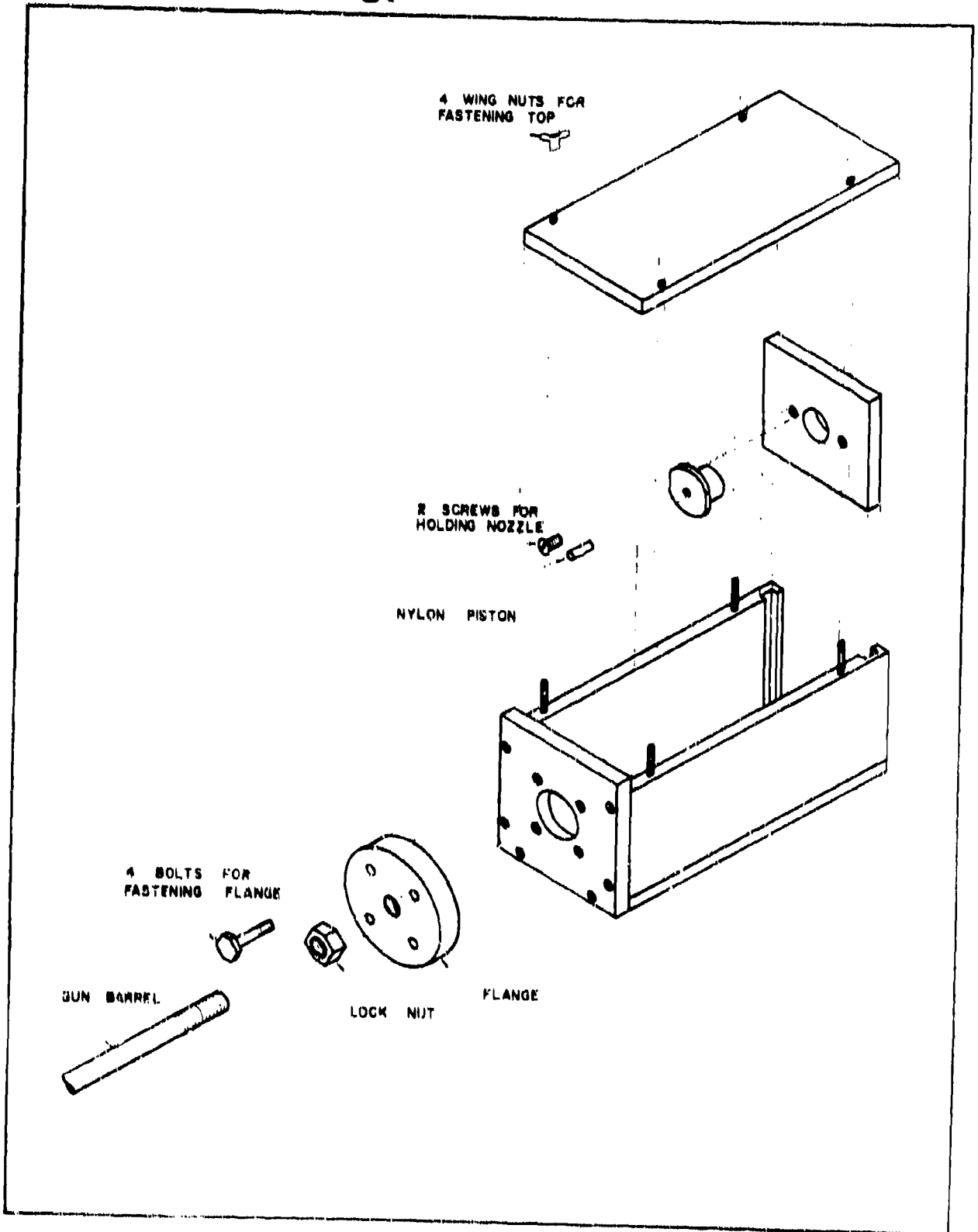


FIGURE 4. EXPLODED VIEW OF JET ACCELERATOR

58<

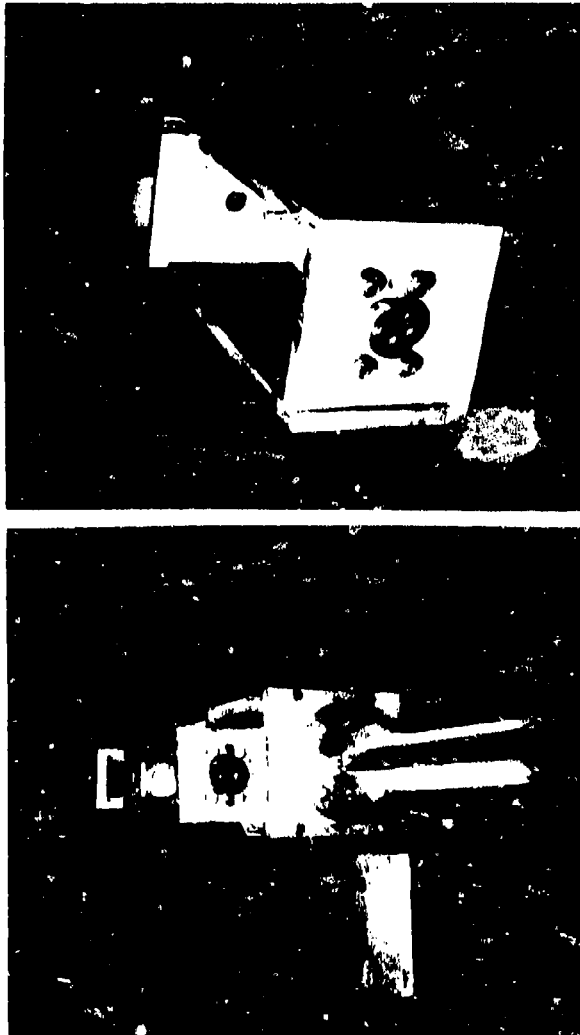


FIGURE 5. PHOTOGRAPHS OF JET ACCELERATOR

59<

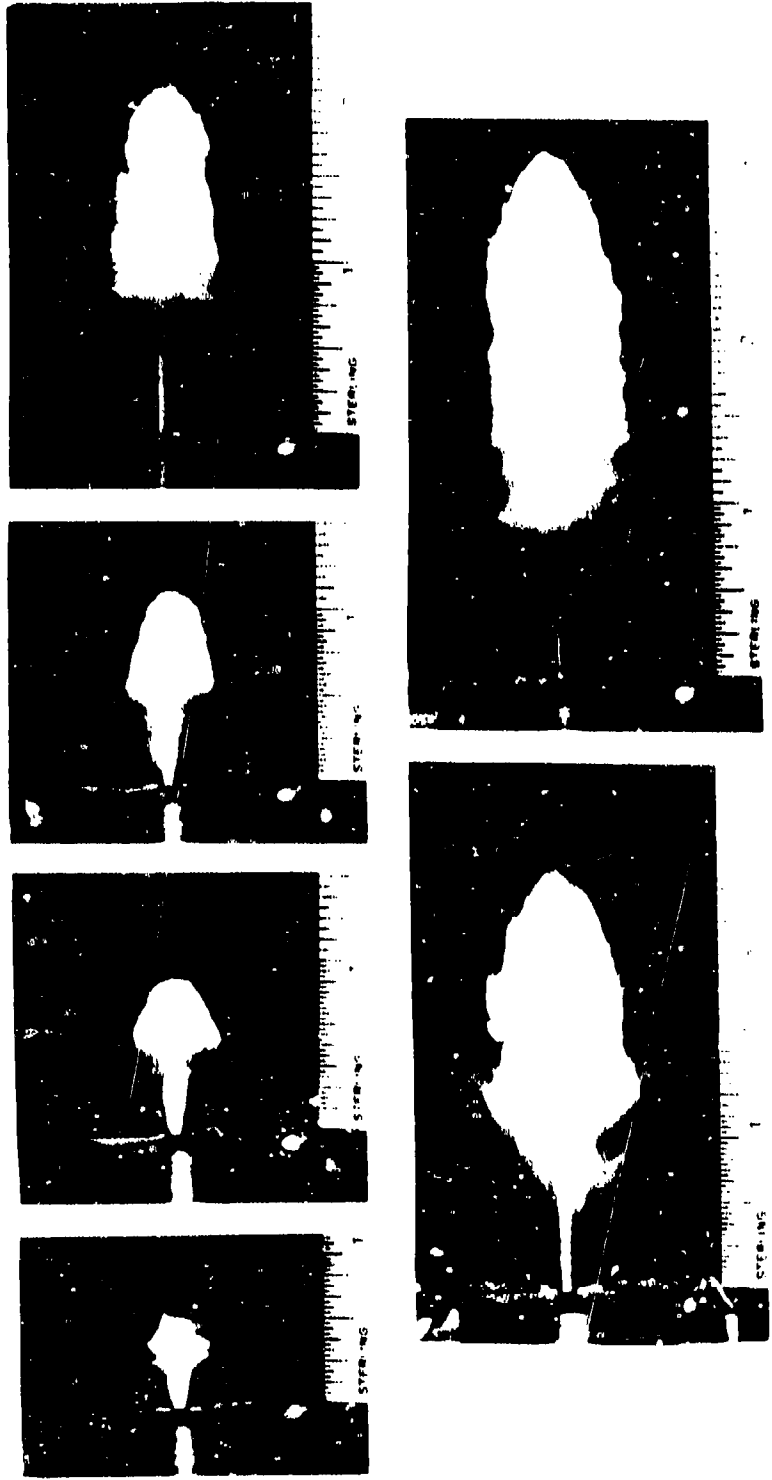


FIGURE 6. PHOTOGRAPHS OF WATER JET

60<

JET VELOCITY APPROXIMATELY 3200 ft/sec

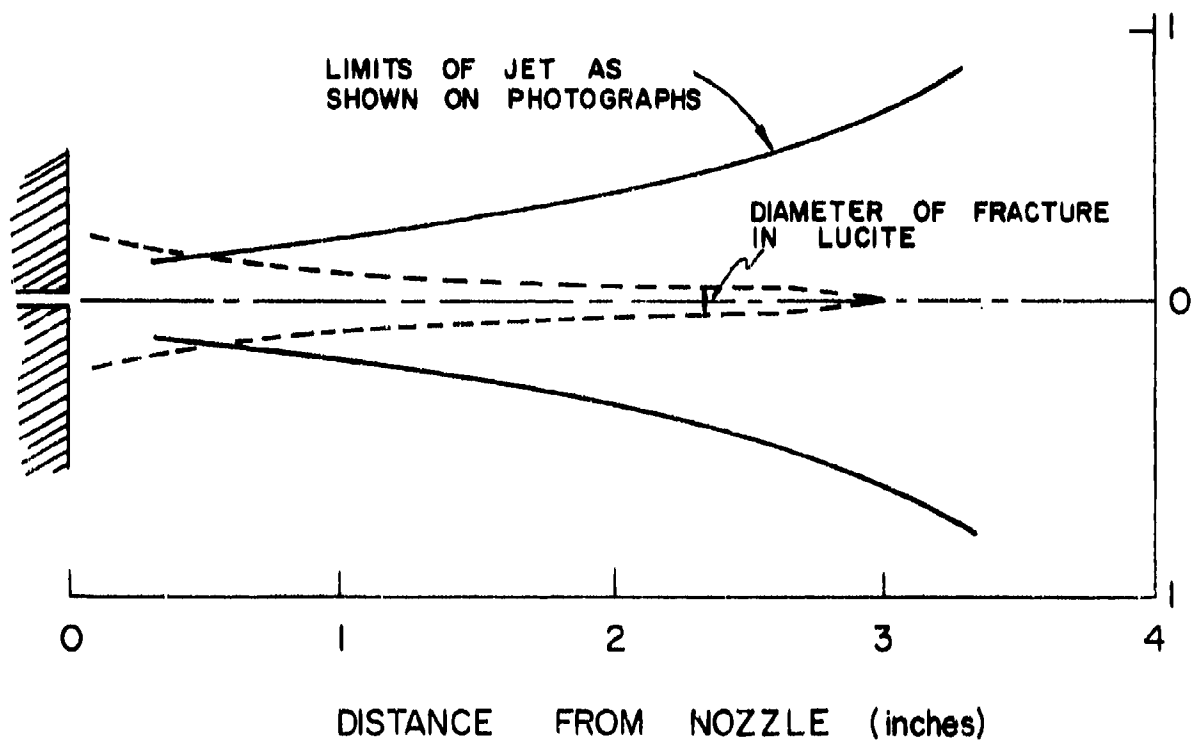


FIGURE 7. JET AND FRACTURE DIAMETERS

61<

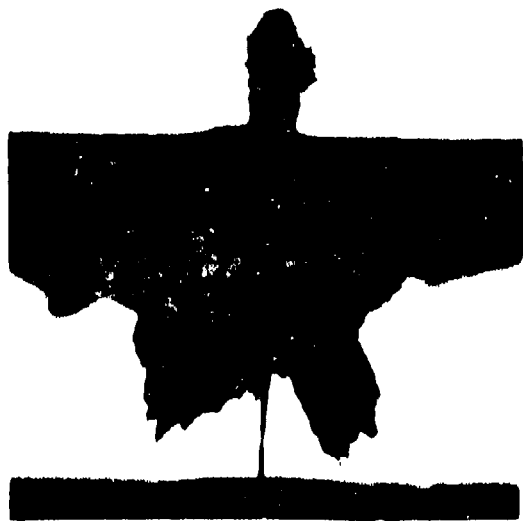
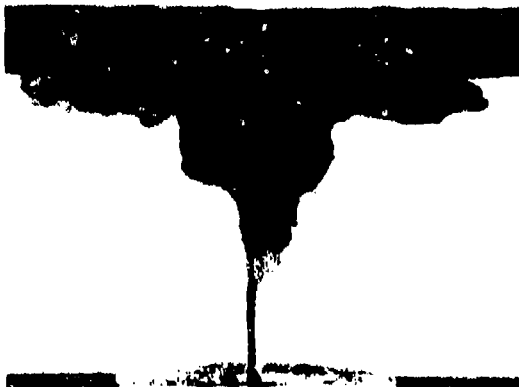


FIGURE 8. JET PENETRATION OF A LEAD TARGET

62<

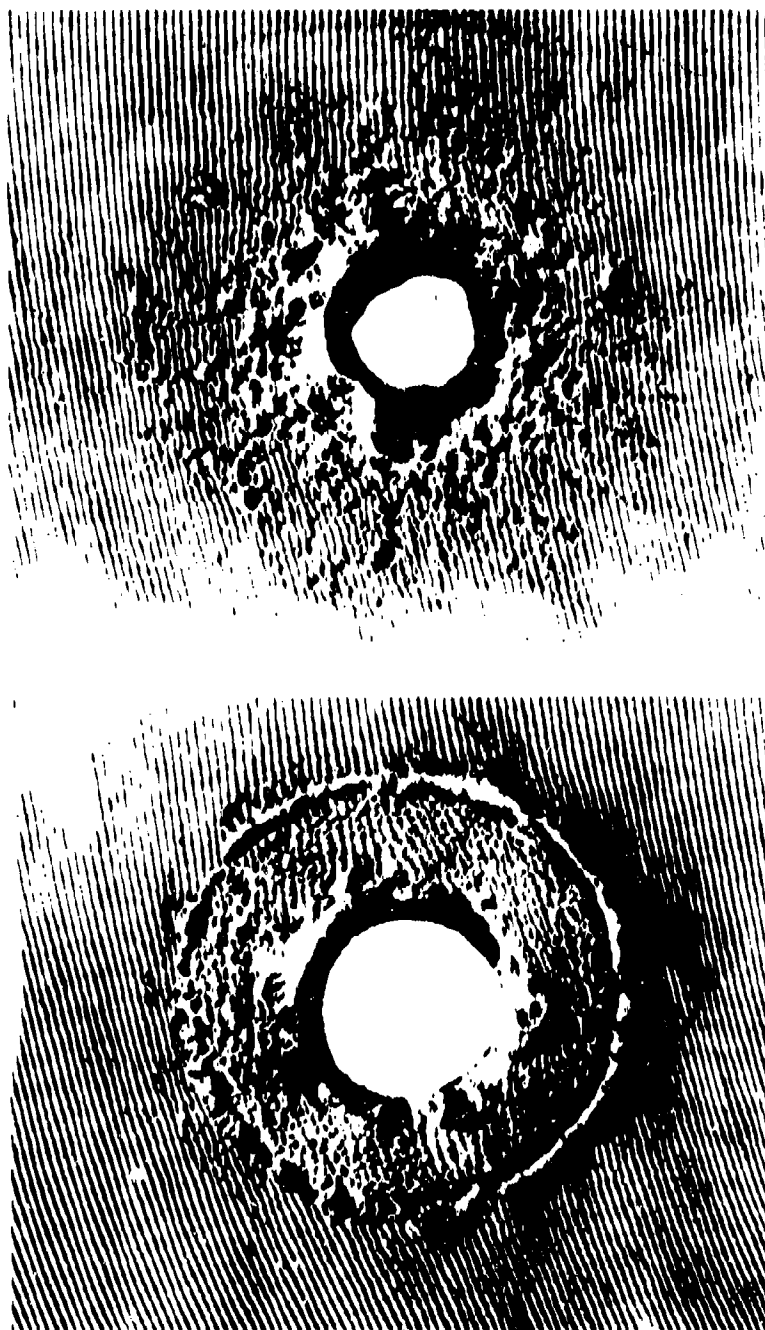


FIGURE 9. DAMAGE TO A 0.25-INCH LEAD PLATE

63<

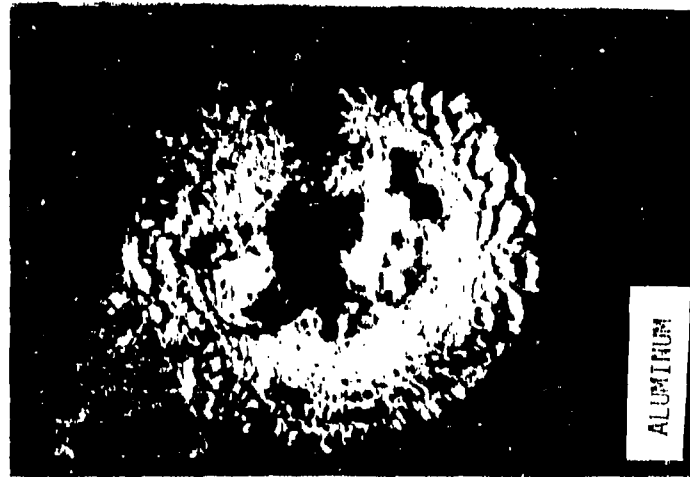
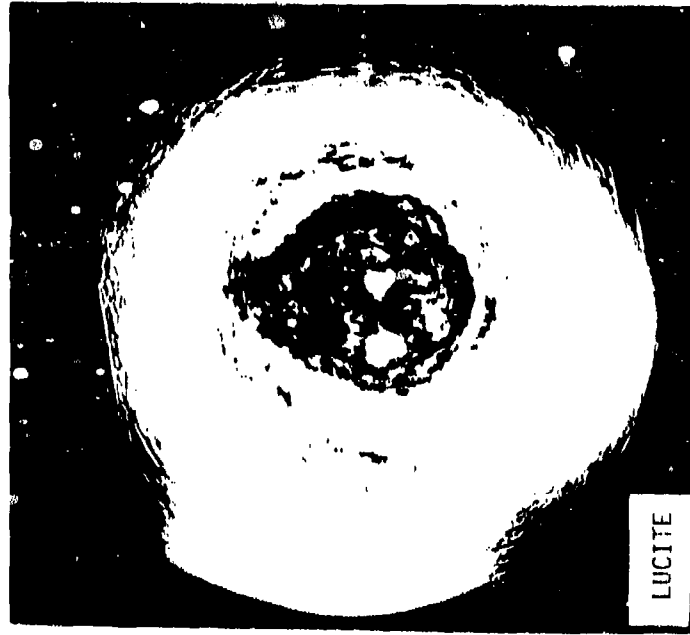


FIGURE 10. FRACTURES IN VARIOUS MATERIALS

64<



Reproduced from
best available copy.

FIGURE 11. WATER IMPACT DAMAGE TO LUCITE TARGETS

65<

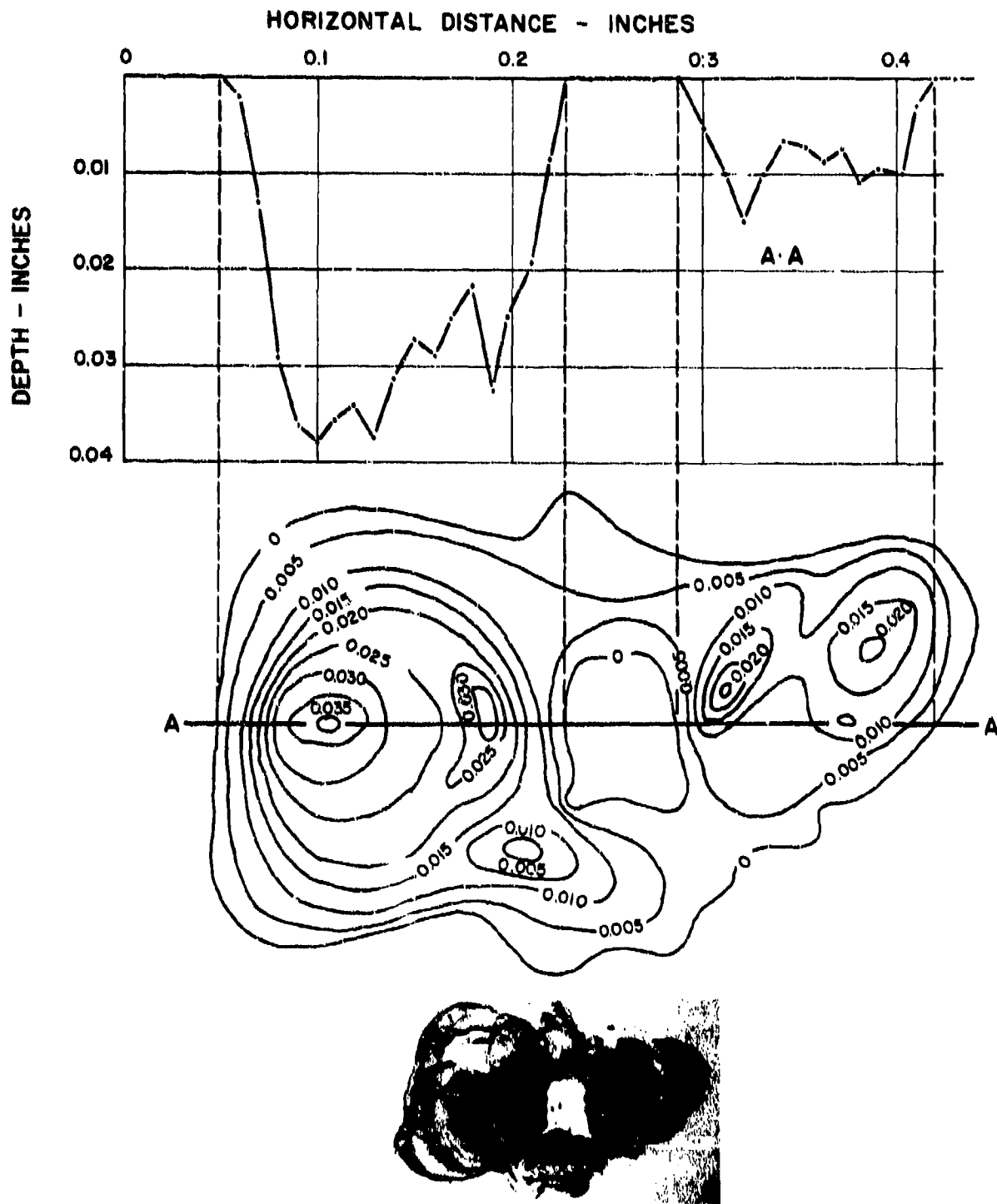
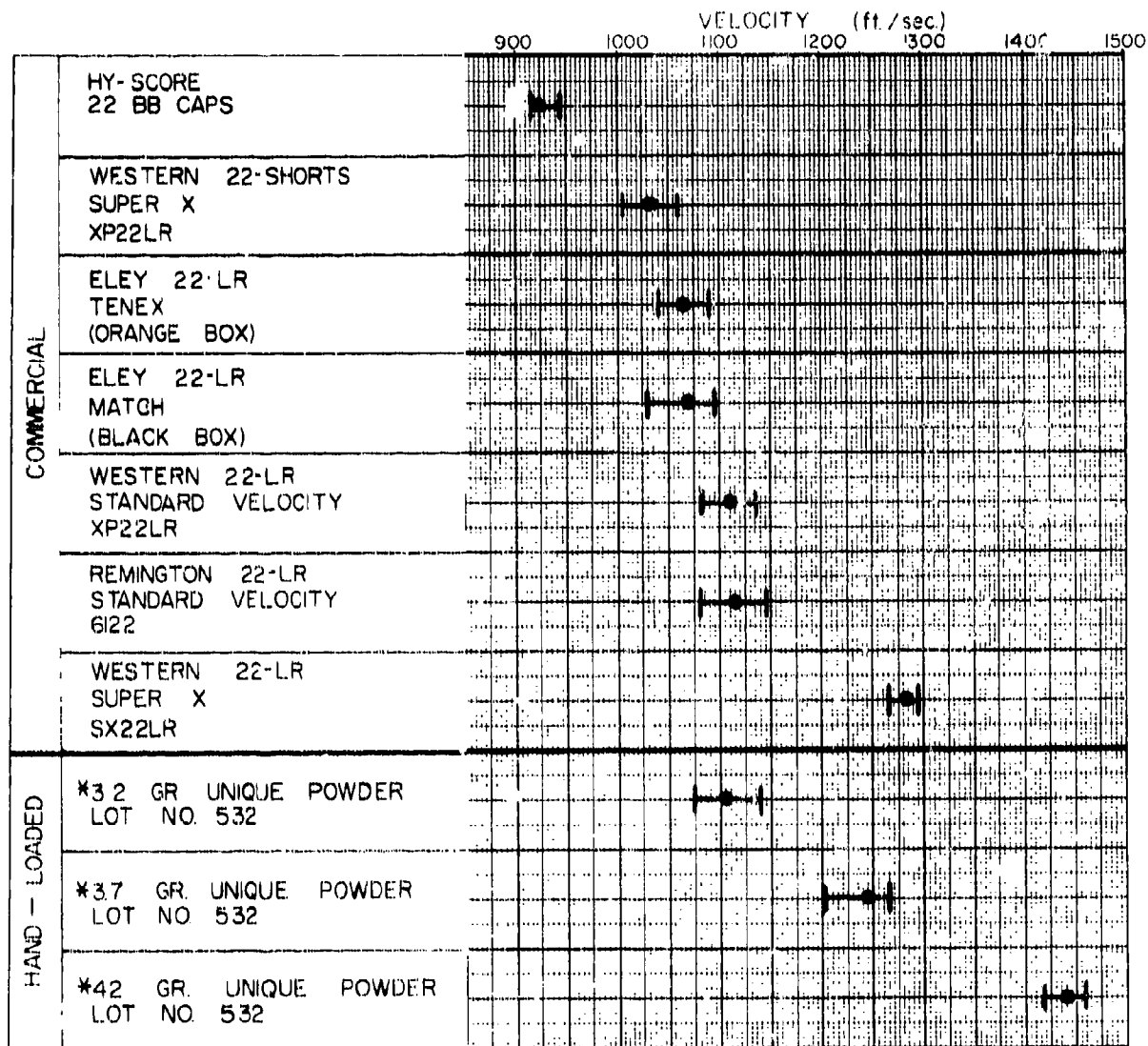


FIGURE 12. PROFILE AND DEPTH CONTOURS OF CRATER IN LUCITE

66<



NOTE: Velocity is measured at 100 yds.
 The test was conducted in accordance with
 the standard procedure for
 determining muzzle velocity.

FIGURE 13. BULLET VELOCITIES

67<

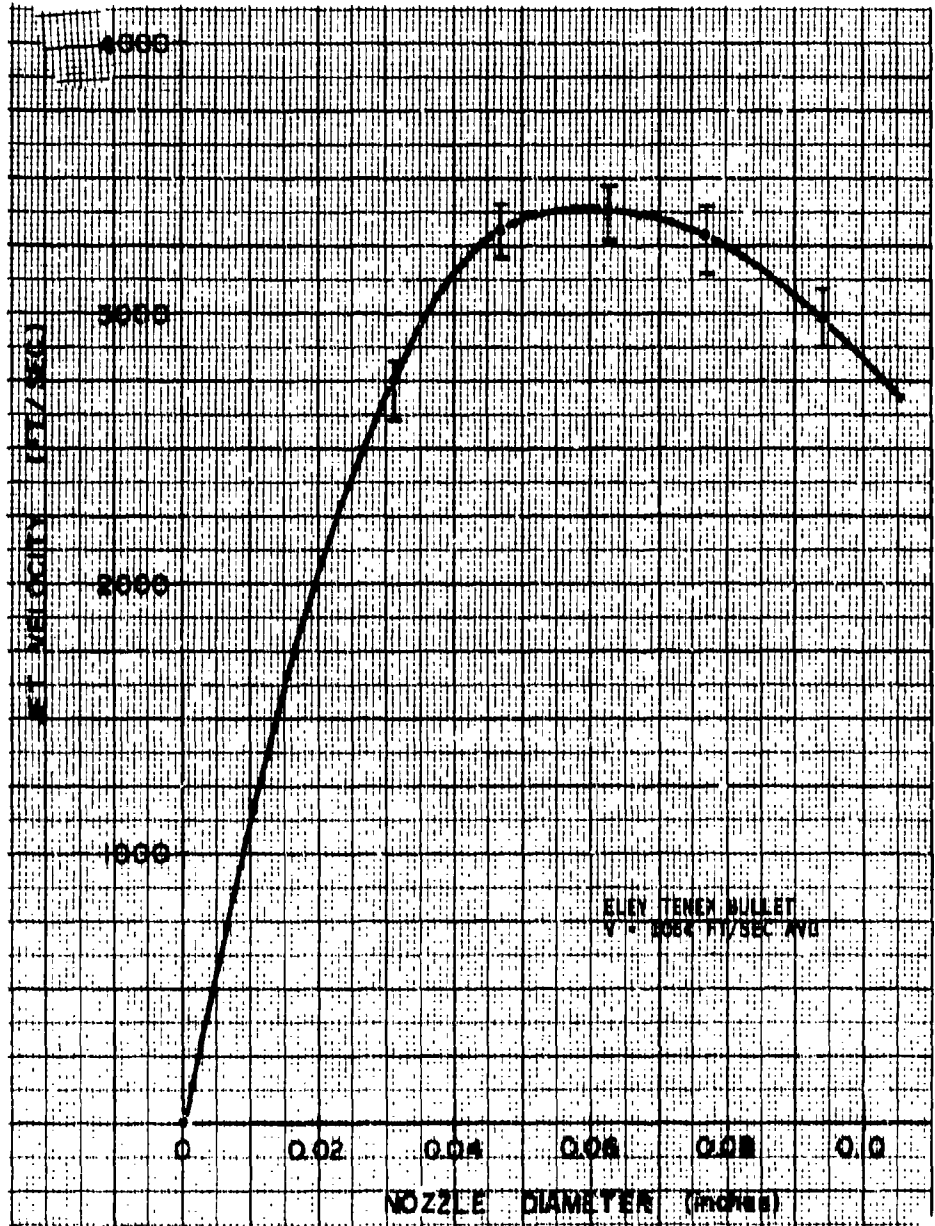


FIGURE 14. EFFECT OF NOZZLE DIAMETER UPON JET VELOCITY

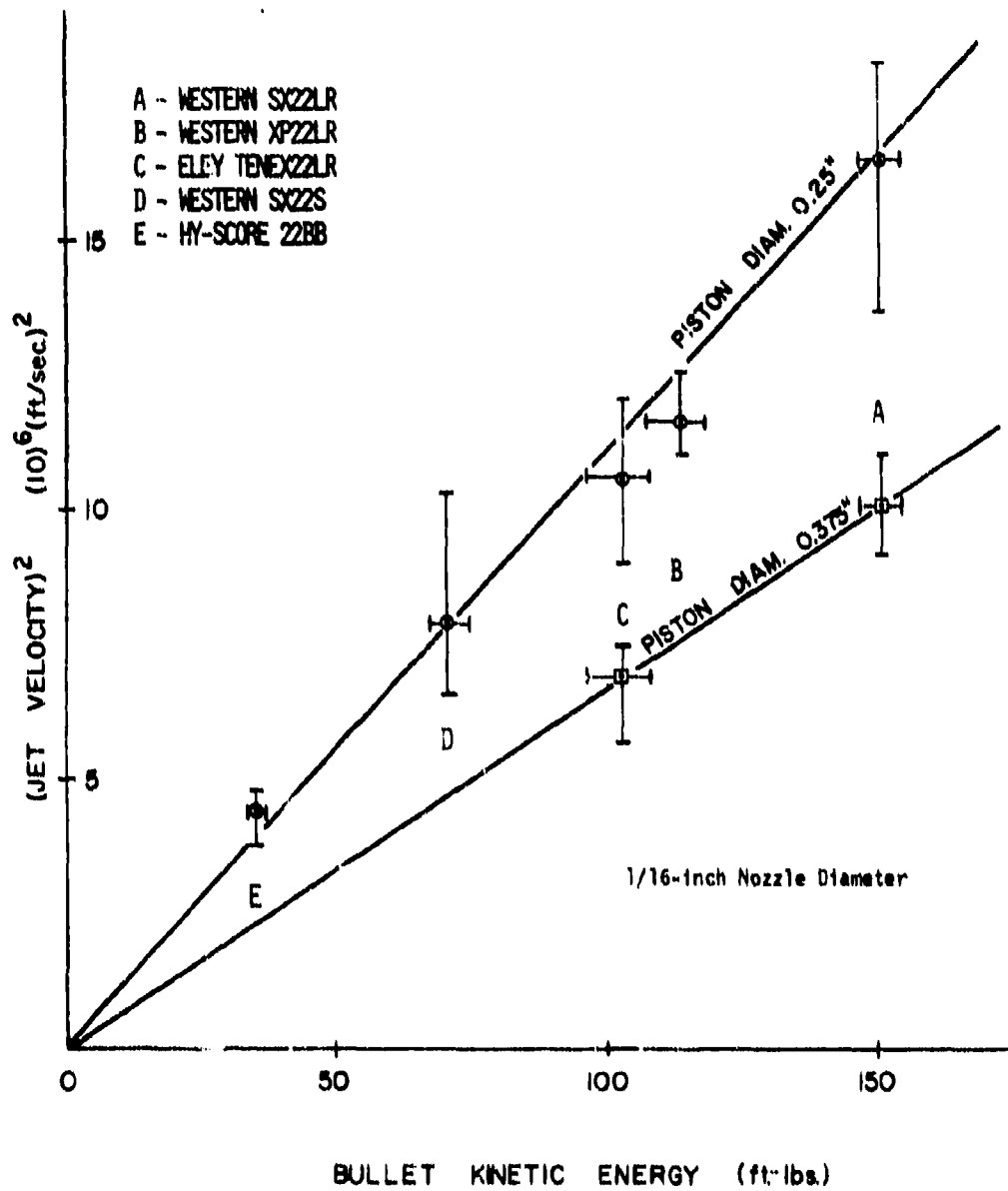


FIGURE 15. RELATION BETWEEN BULLET ENERGY AND JET VELOCITY

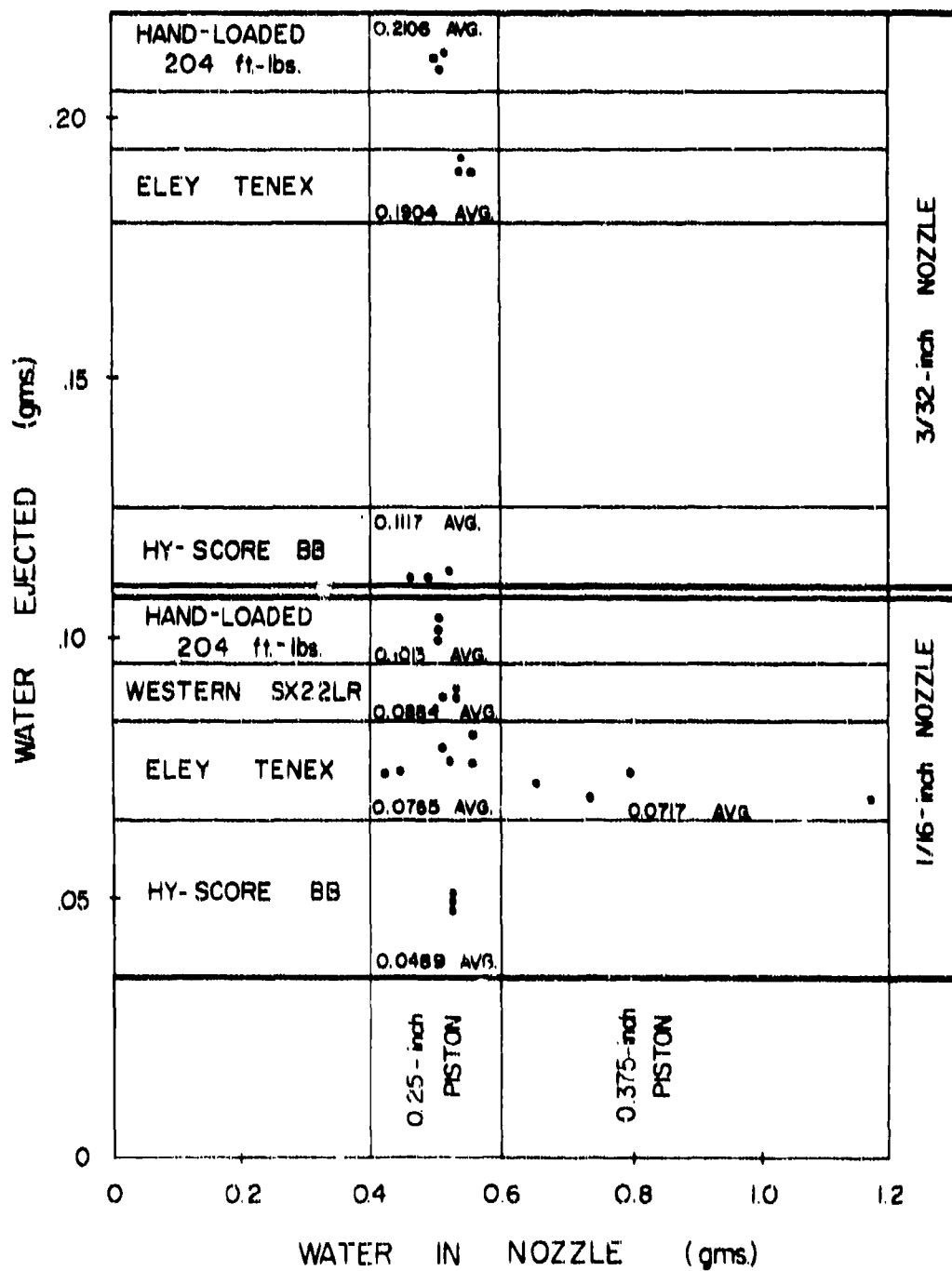


FIGURE 16. AMOUNTS OF WATER EJECTED FROM NOZZLE

70<

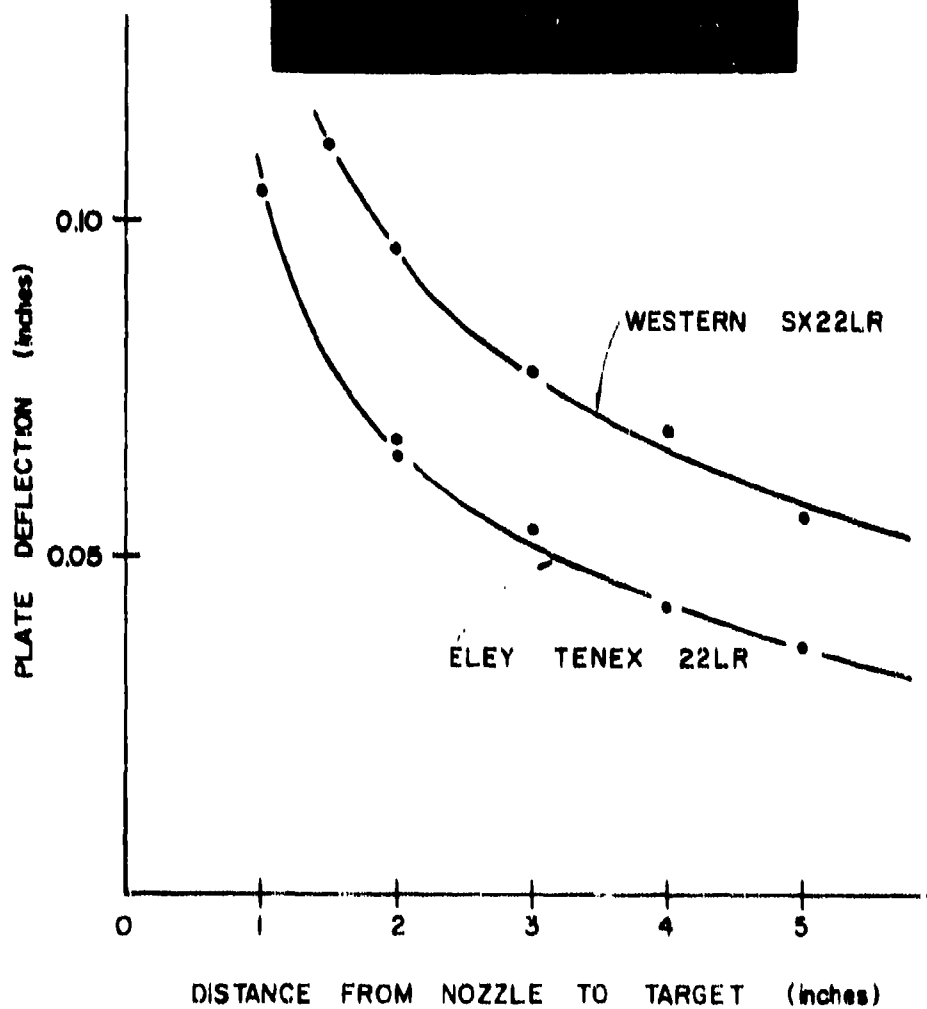


FIGURE 17. EFFECT OF NOZZLE-TARGET DISTANCE

71<

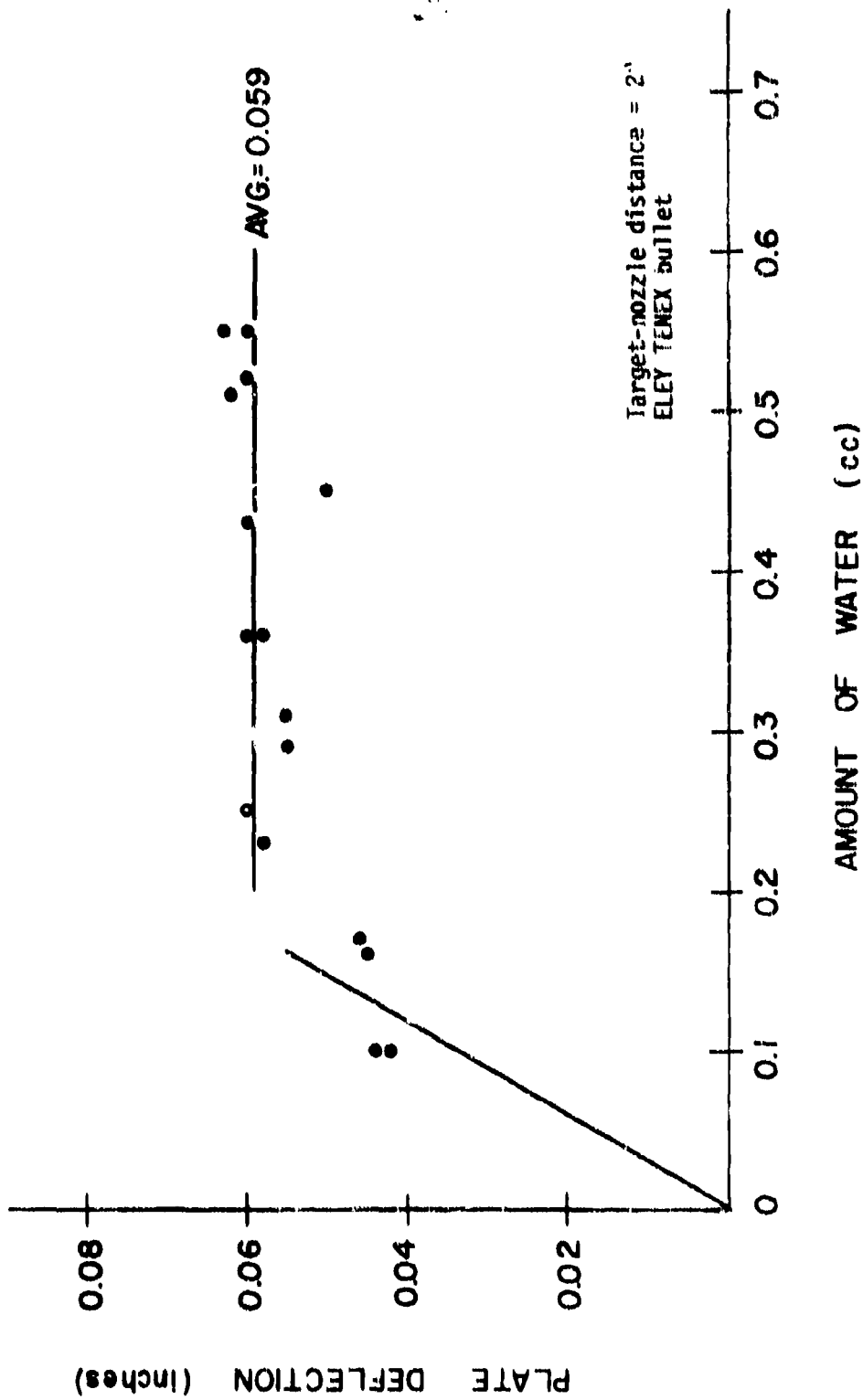
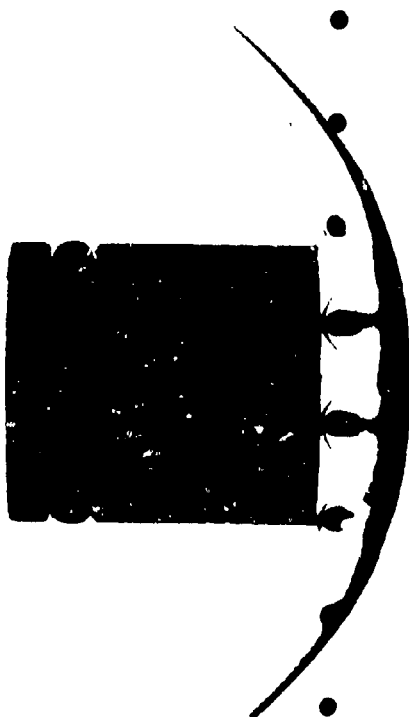


FIGURE 18. EFFECT OF THE AMOUNT OF WATER IN PRESSURE CHAMBER

72<



118
760 TORR
2970 F/S
 $D_0 = 1.12 \text{ MM}$

73<

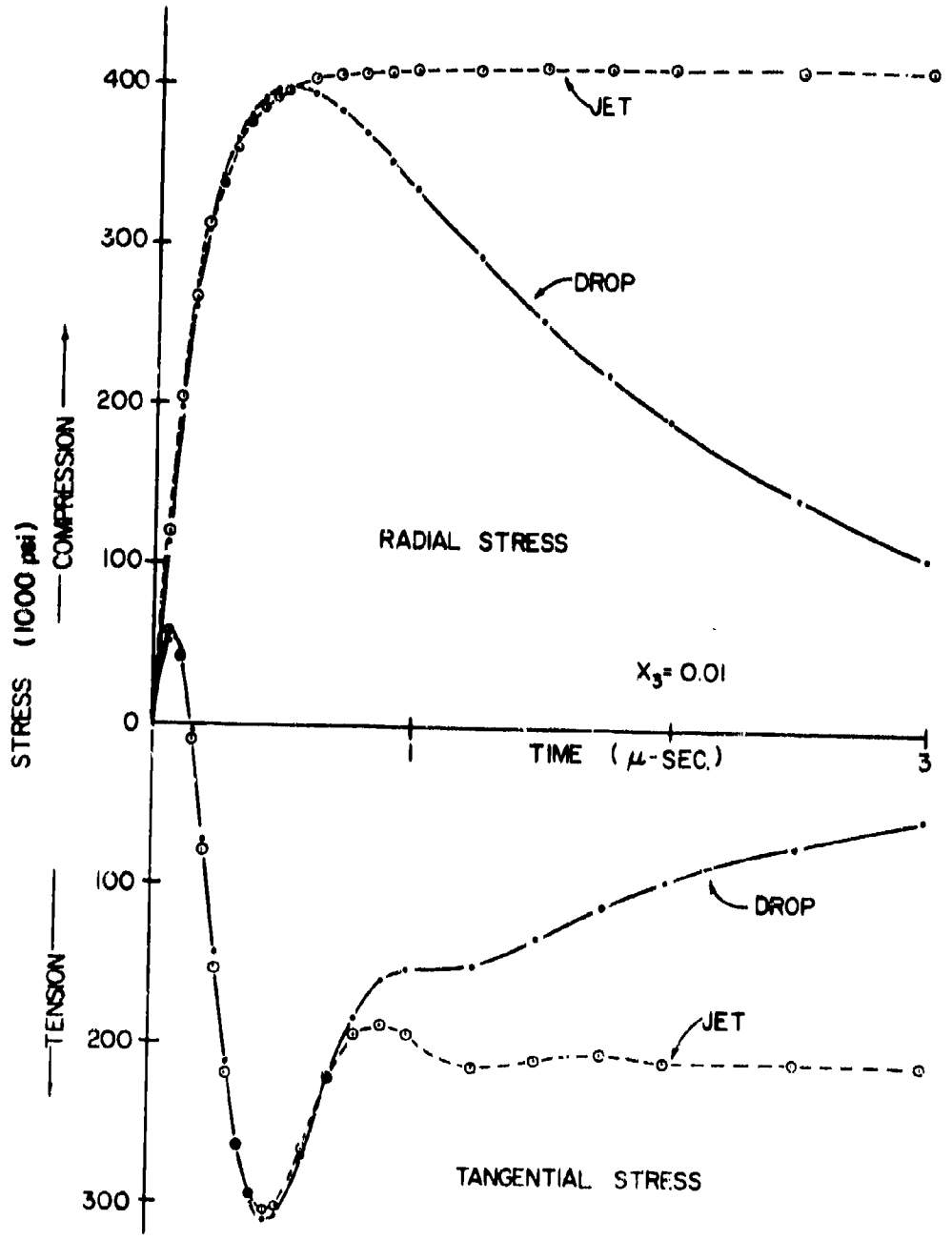


FIGURE 20. STRESSES RESULTING FROM LIQUID IMPACT

74<

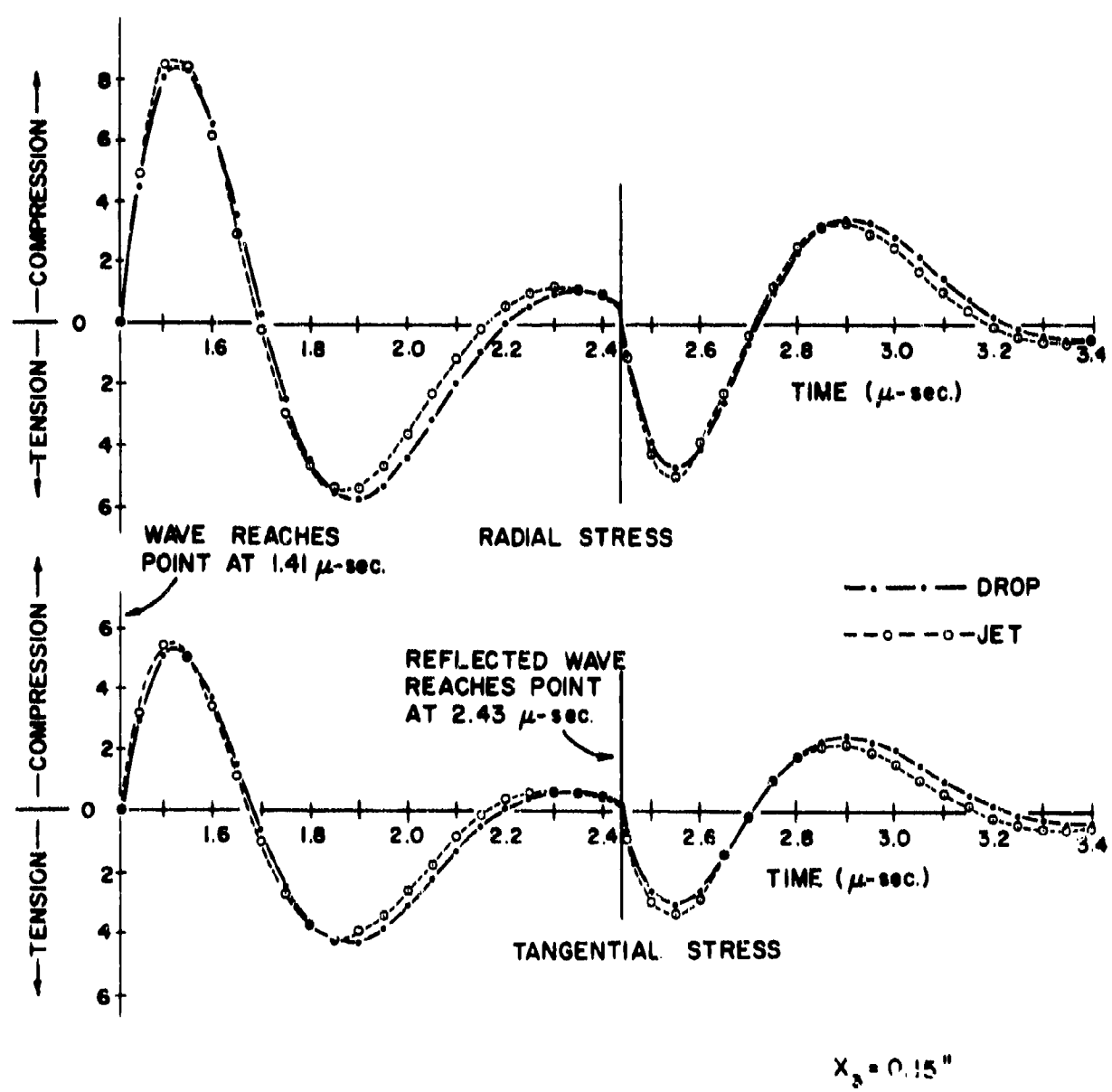


FIGURE 21. STRESS HISTORY AT A POINT

75<

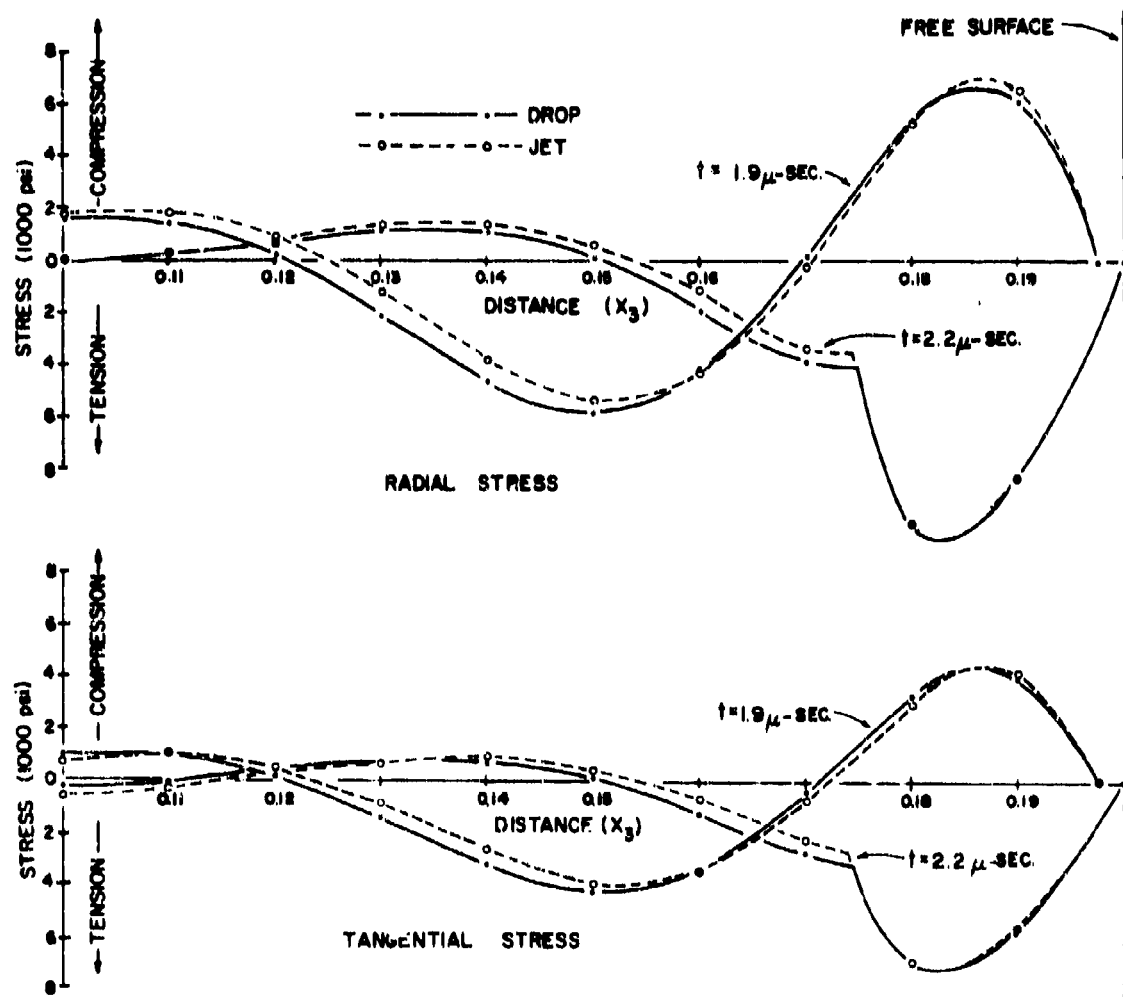


FIGURE 22. STRESSES RESULTING FROM REFLECTED WAVES

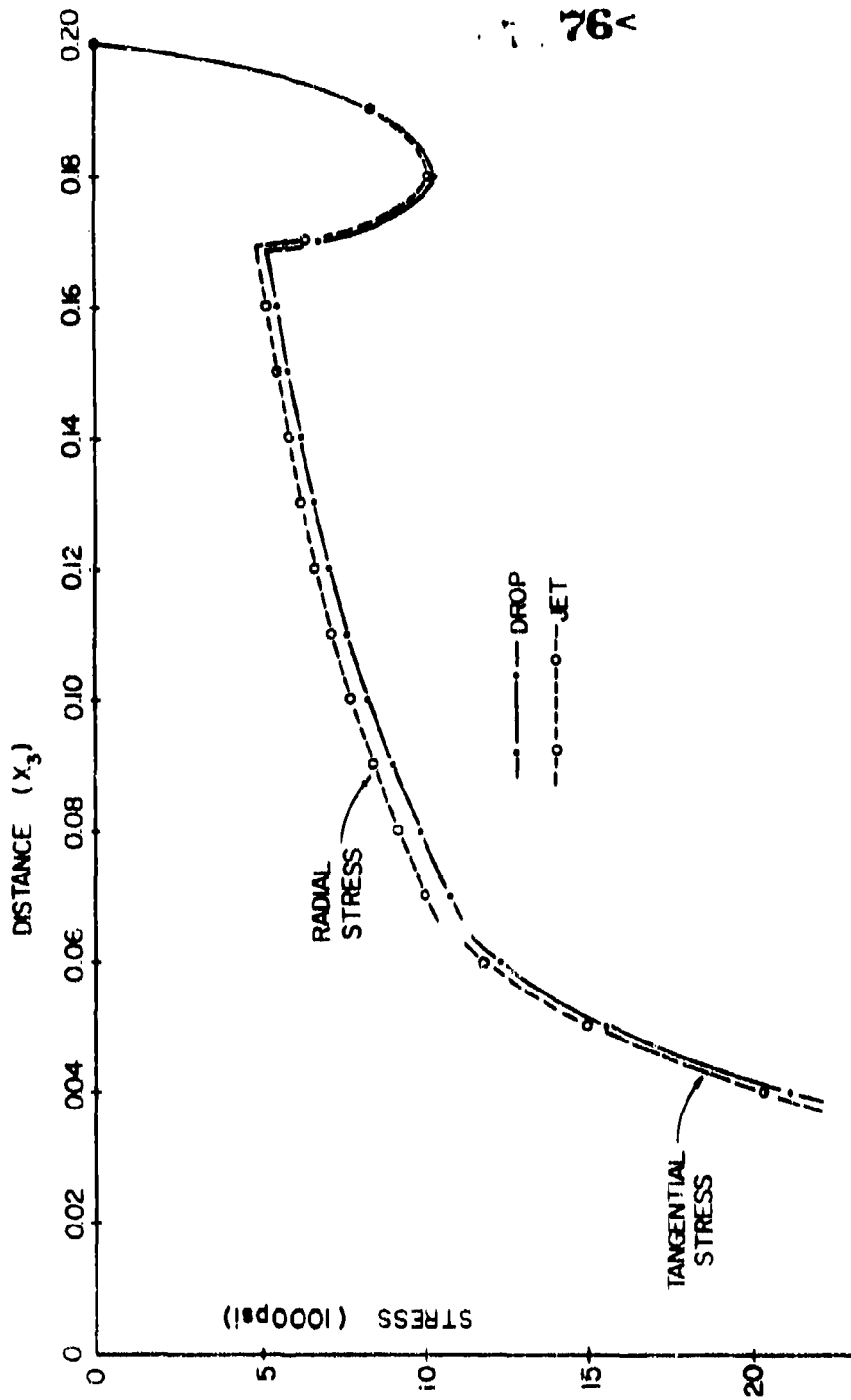


FIGURE 23. MAXIMUM TENSILE STRESSES

77<

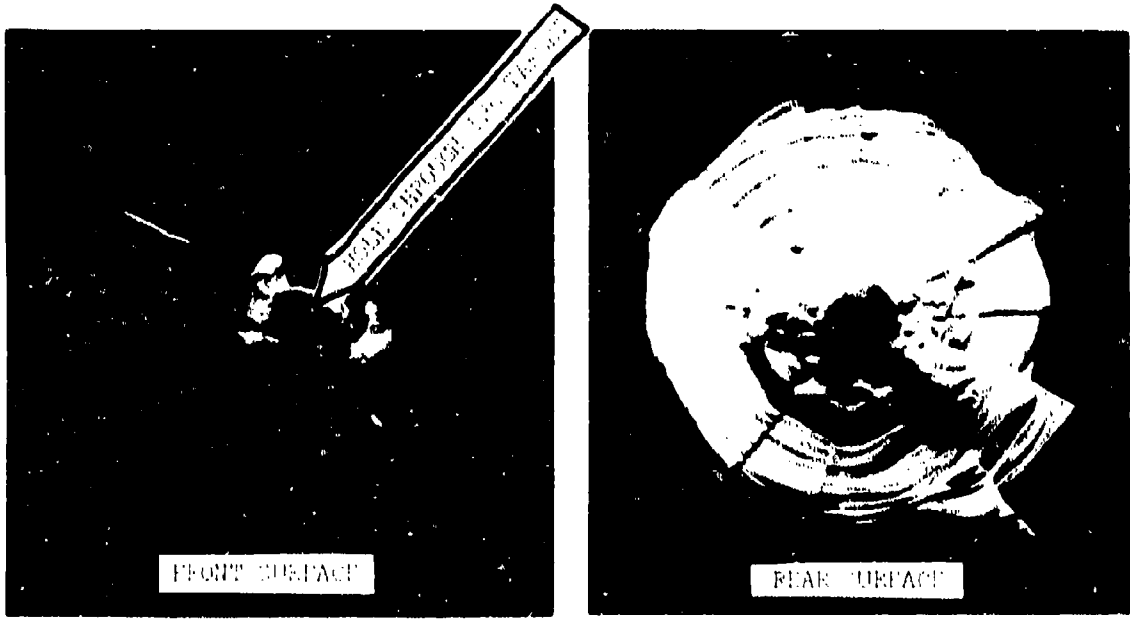


FIGURE 20. WATER IMPACT DAMAGE TO FUSED SILICA TARGETS

78<

DISTANCE - X (INCHES)

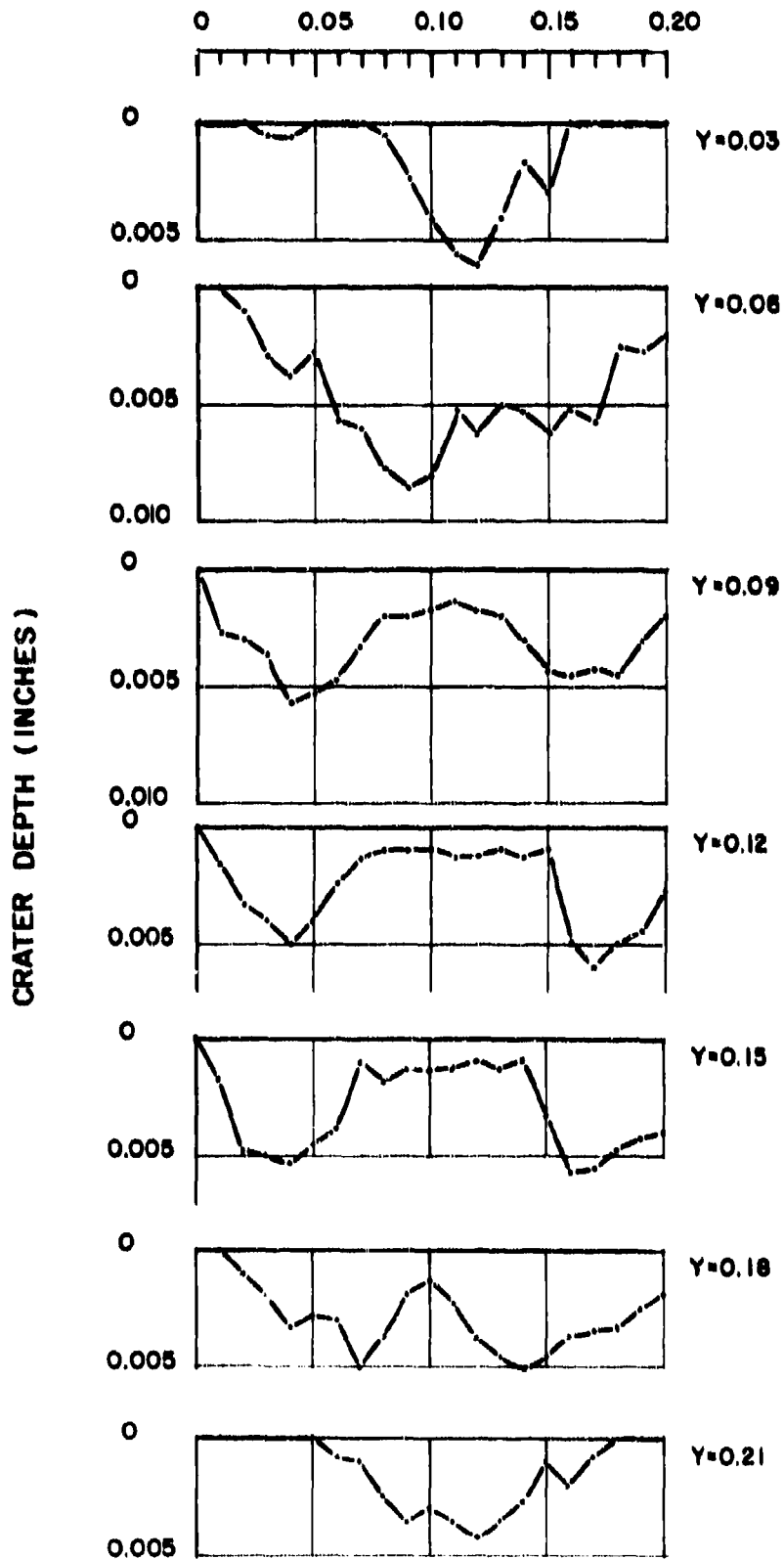


FIGURE 25. CRATER CROSS-SECTIONS (FUSED SILICA)

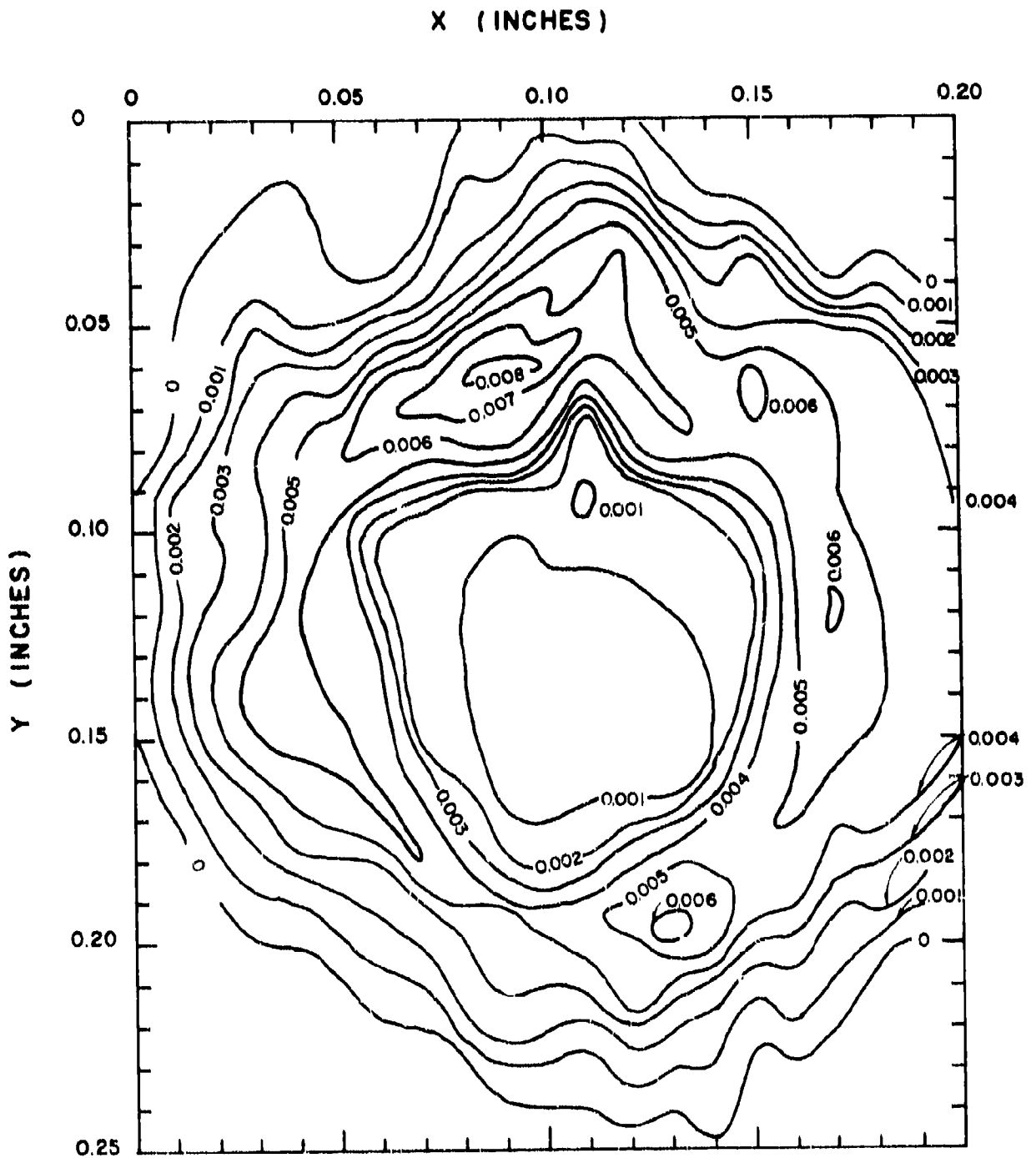


FIGURE 26. CRATER DEPTH CONTOURS (FUSED SILICA)

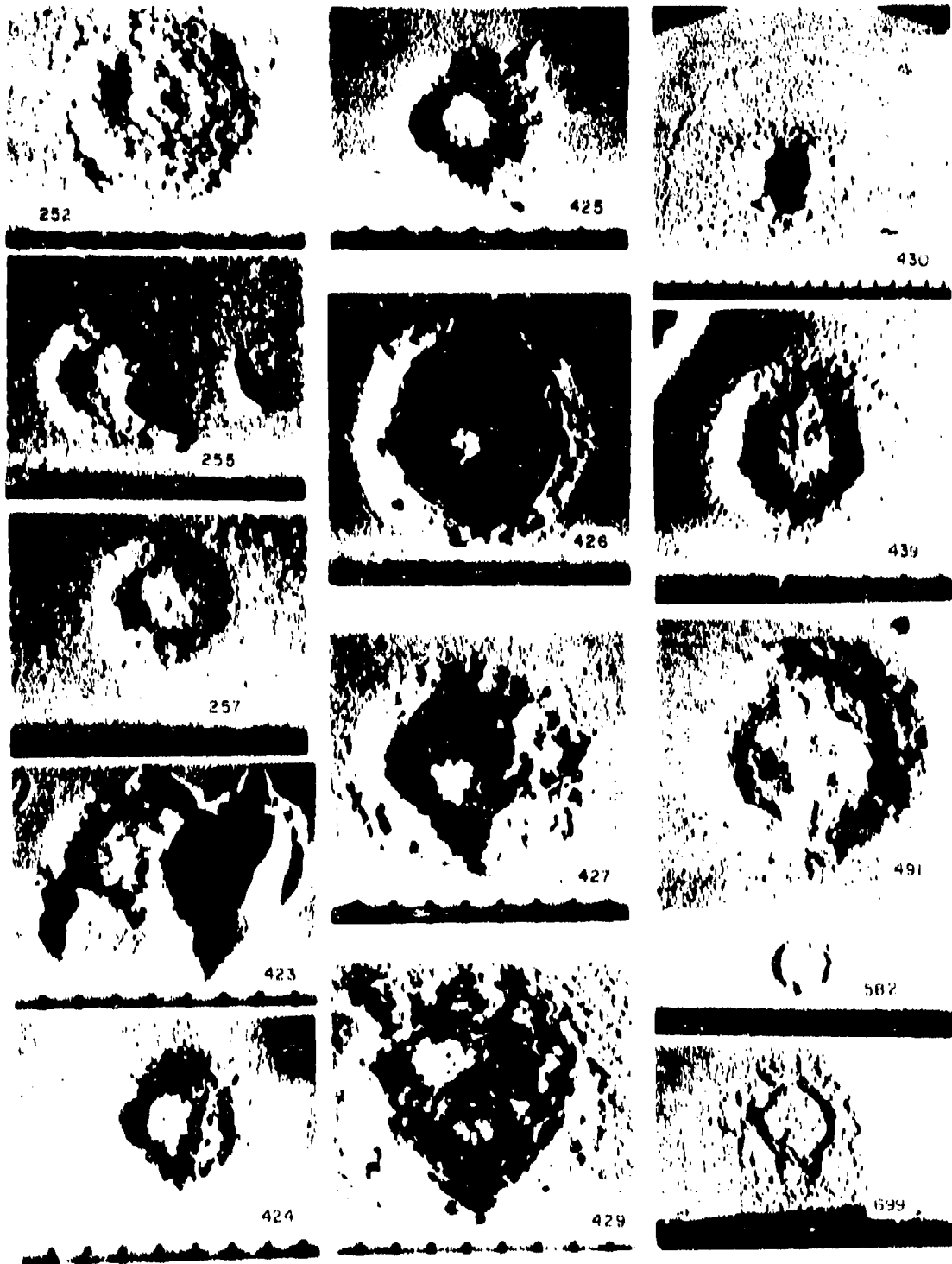
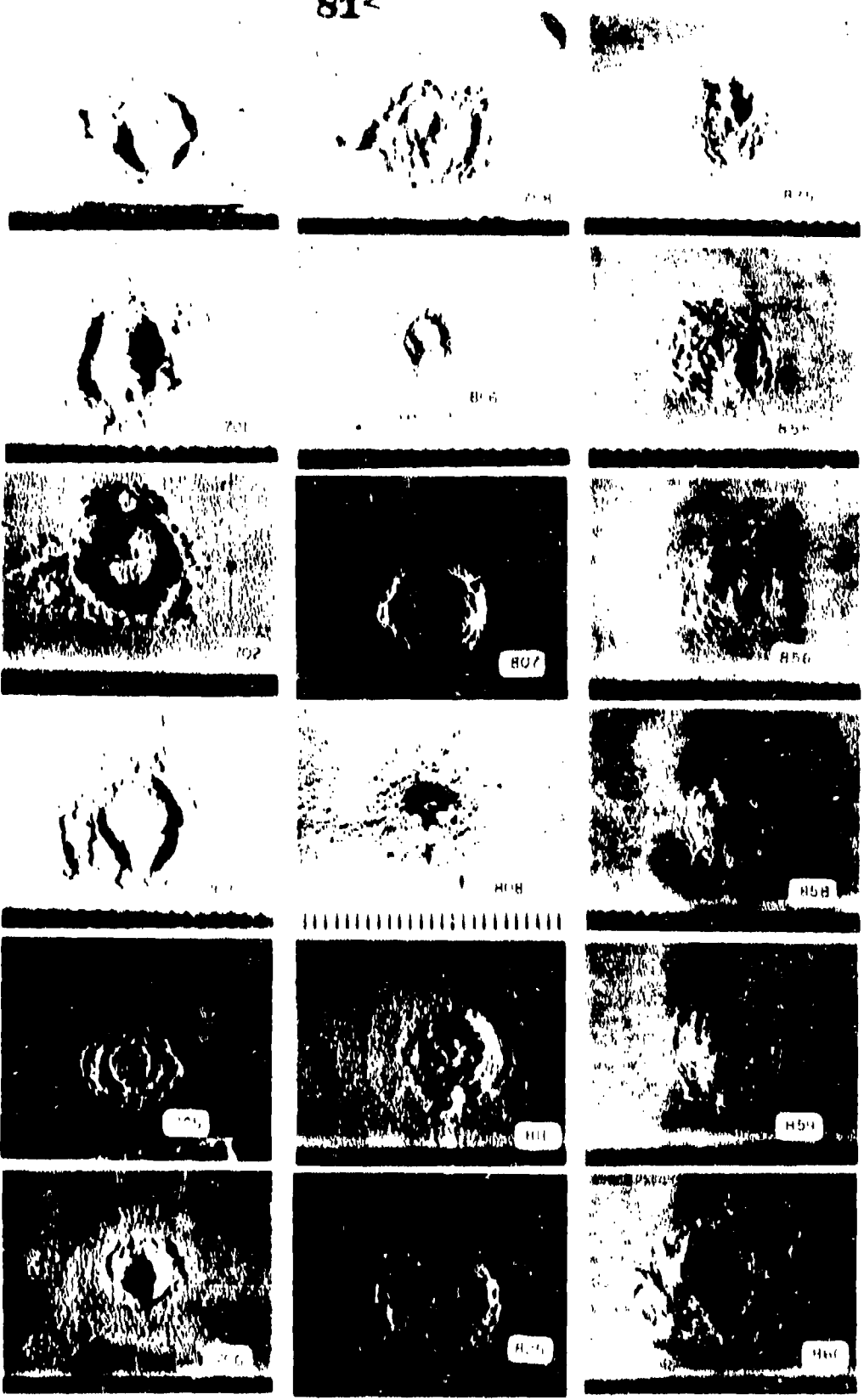


FIGURE 27. CRATERS IN MELT-CAST FUSED SILICA

81<



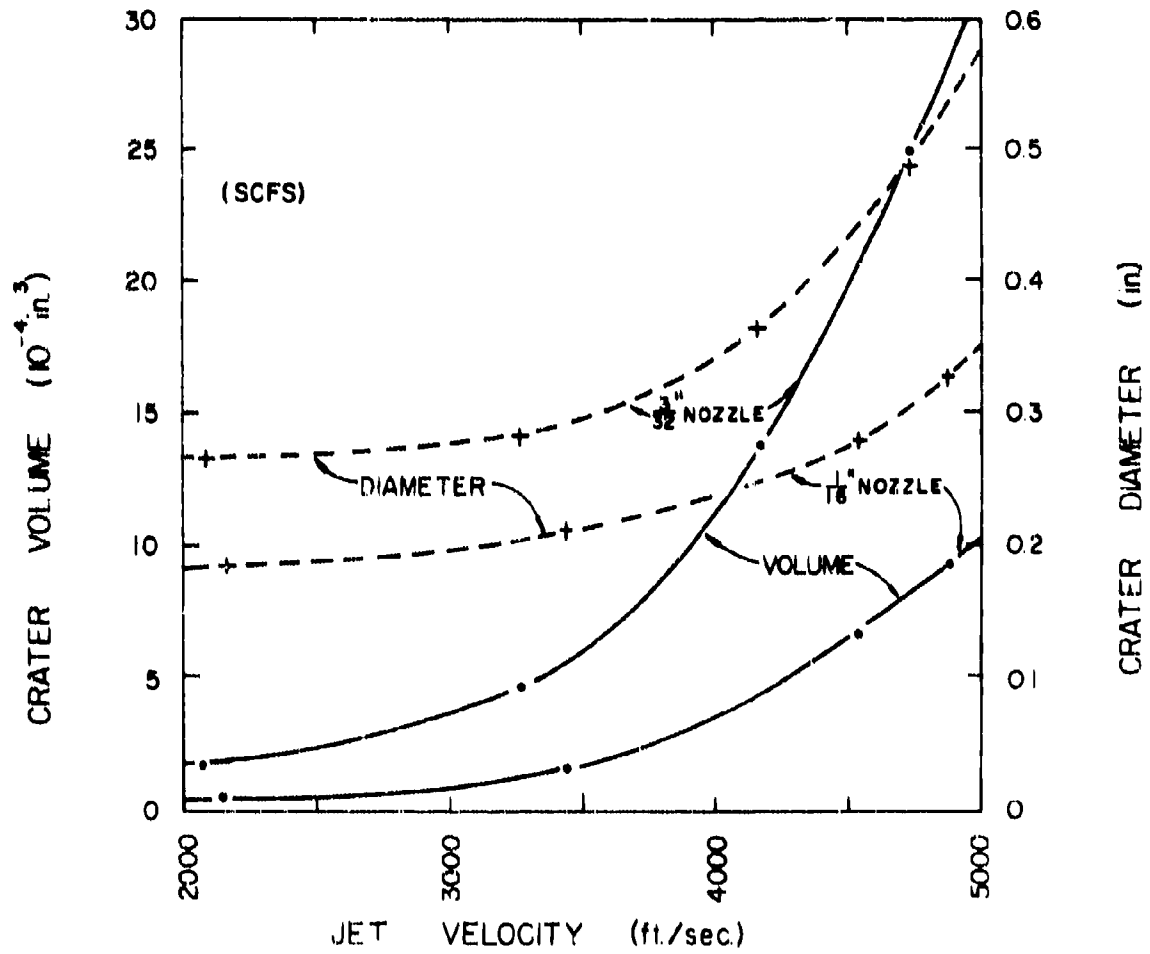


FIGURE 28. RELATION BETWEEN CRATER DIMENSIONS AND JET VELOCITY

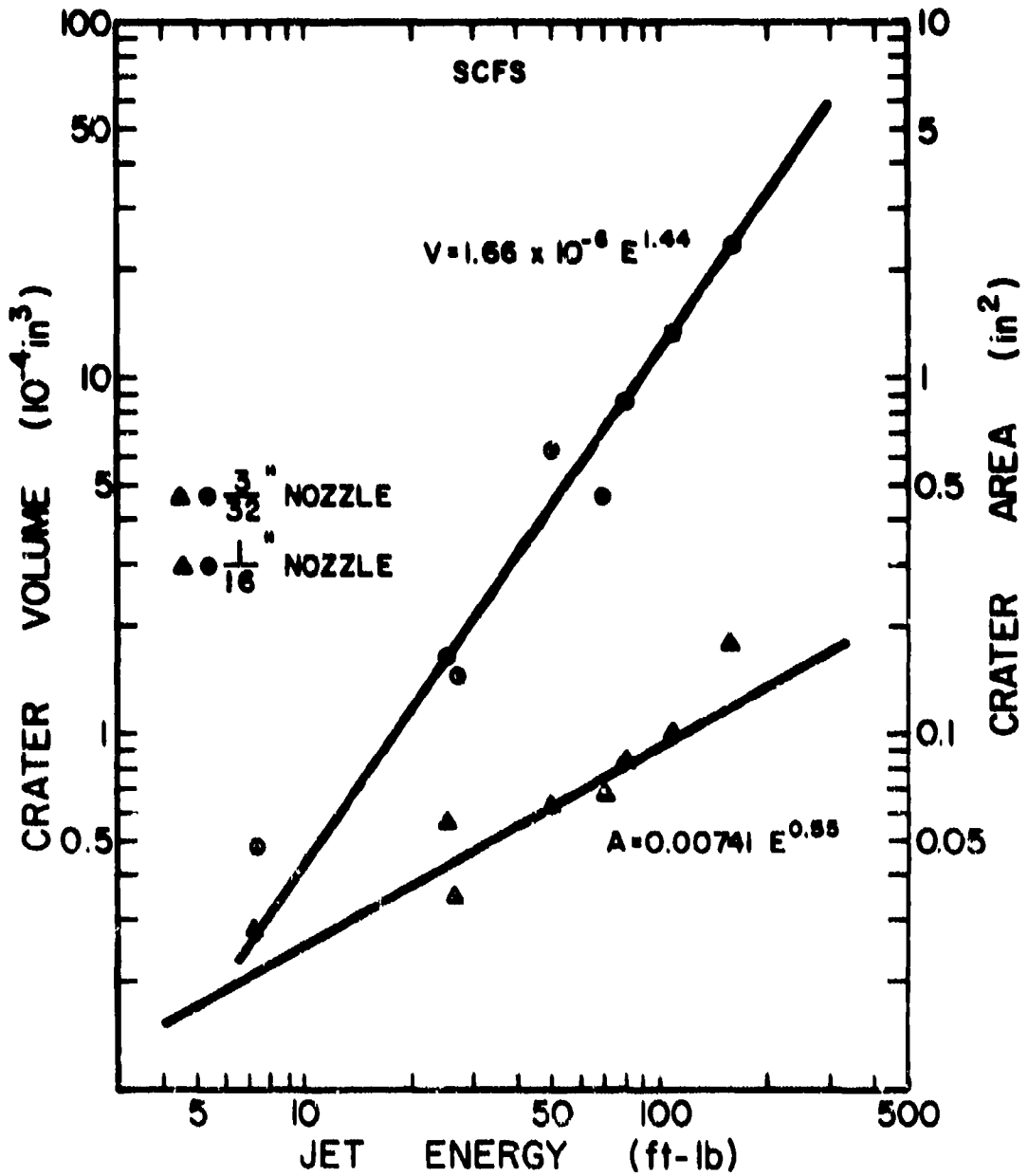


FIGURE 29. VOLUME-AREA-ENERGY RELATIONS (ORIGINAL AMC-SCFS TARGETS)

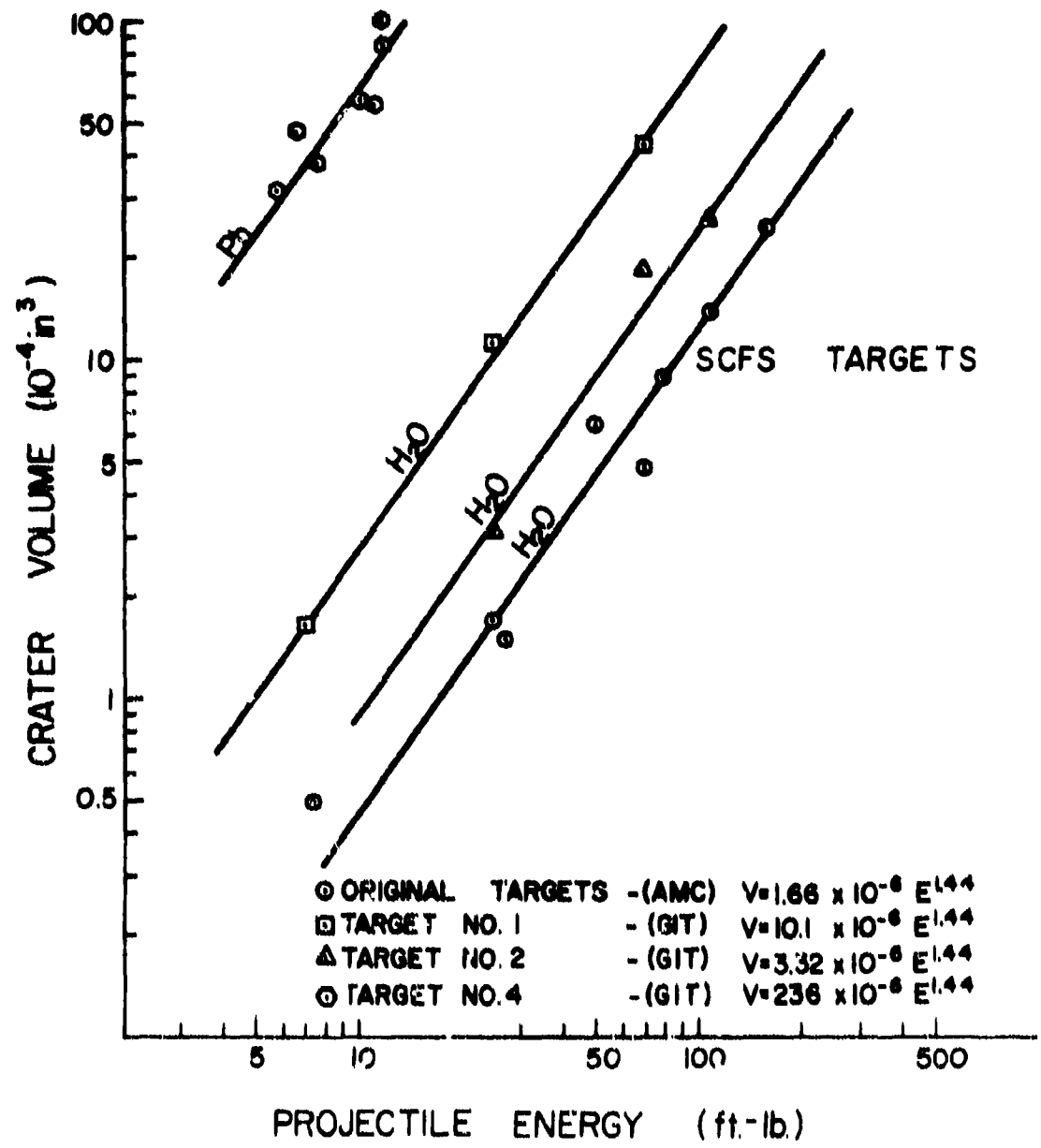


FIGURE 30. ENERGY-VOLUME RELATIONS FOR DIFFERENT TARGETS (LOG SCALE)

85<

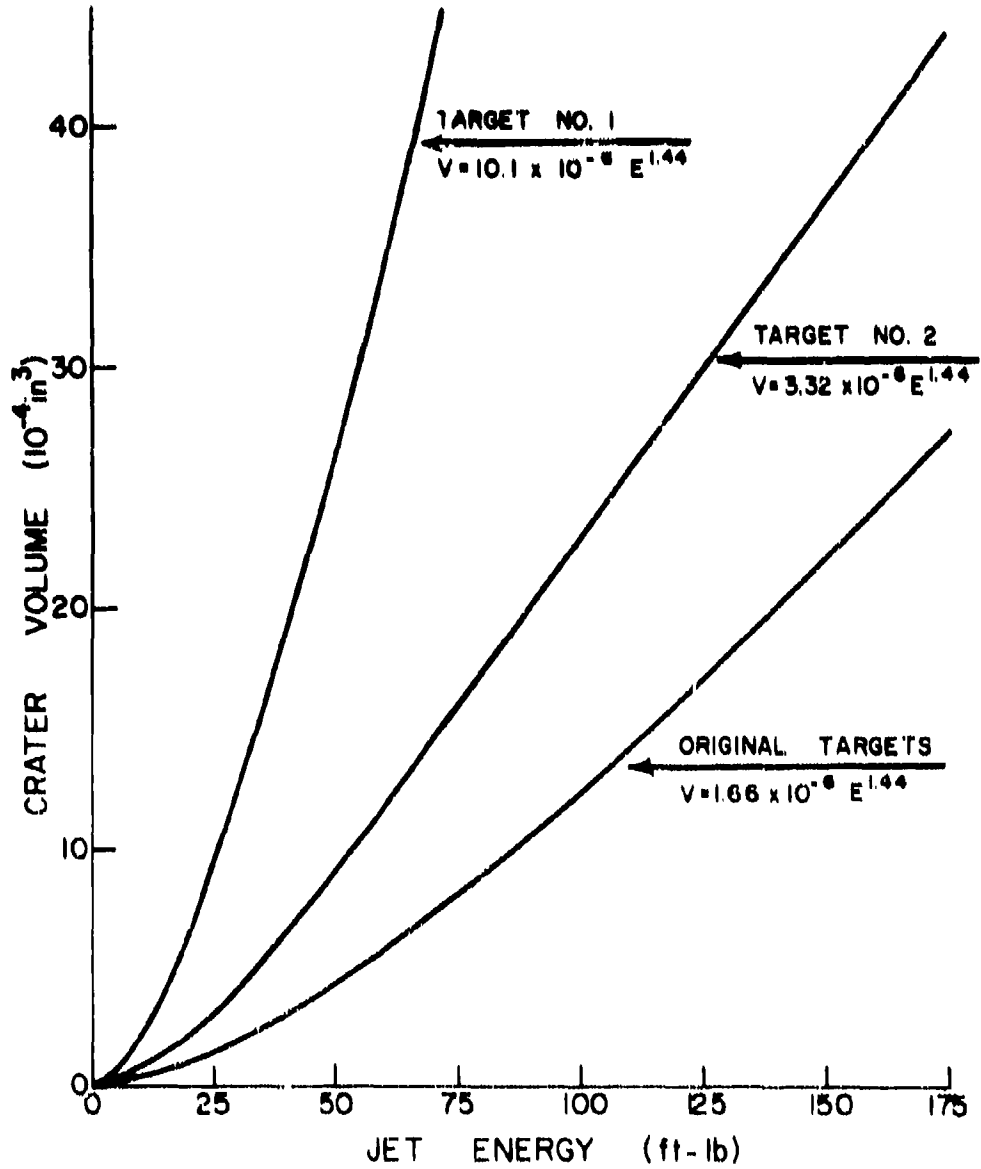


FIGURE 11. ENERGY VOLUME RELATION FOR DIFFERENT TARGET TYPES

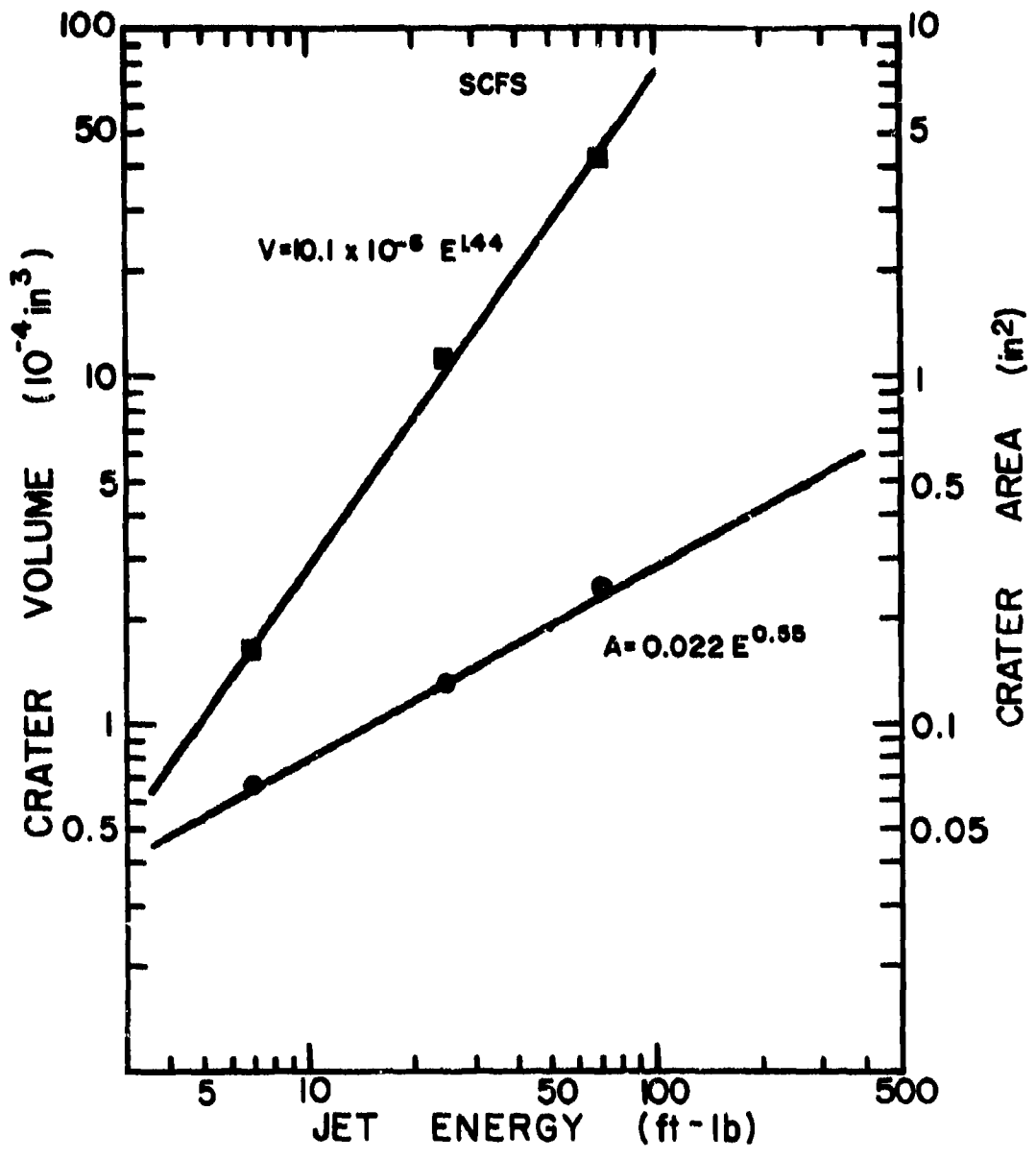


FIGURE 32. VOLUME-AREA-ENERGY RELATIONS (SCFS TARGET NO. 1)

87<



FIGURE 33. CRATERS RESULTING FROM LEAD PELLET IMPACTS

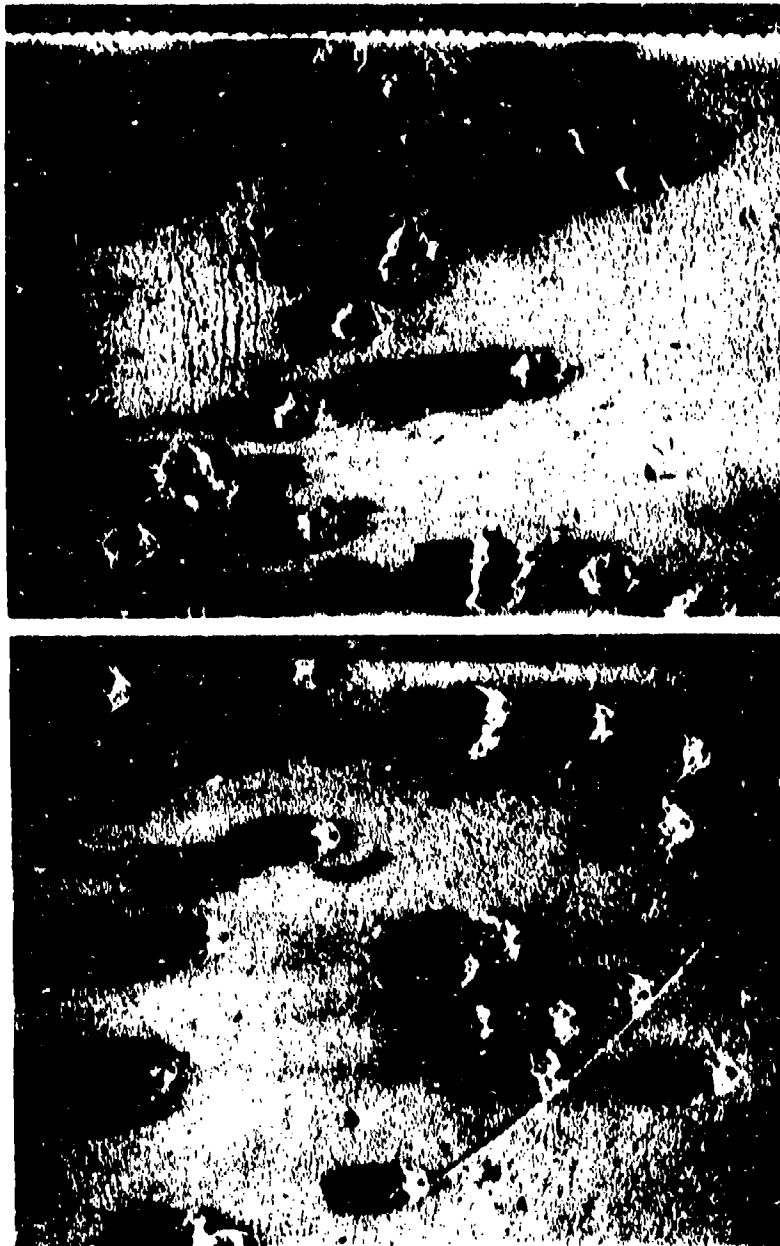


FIGURE 34. COATING DISRUPTION FROM SHOT AND PELLET IMPACTS

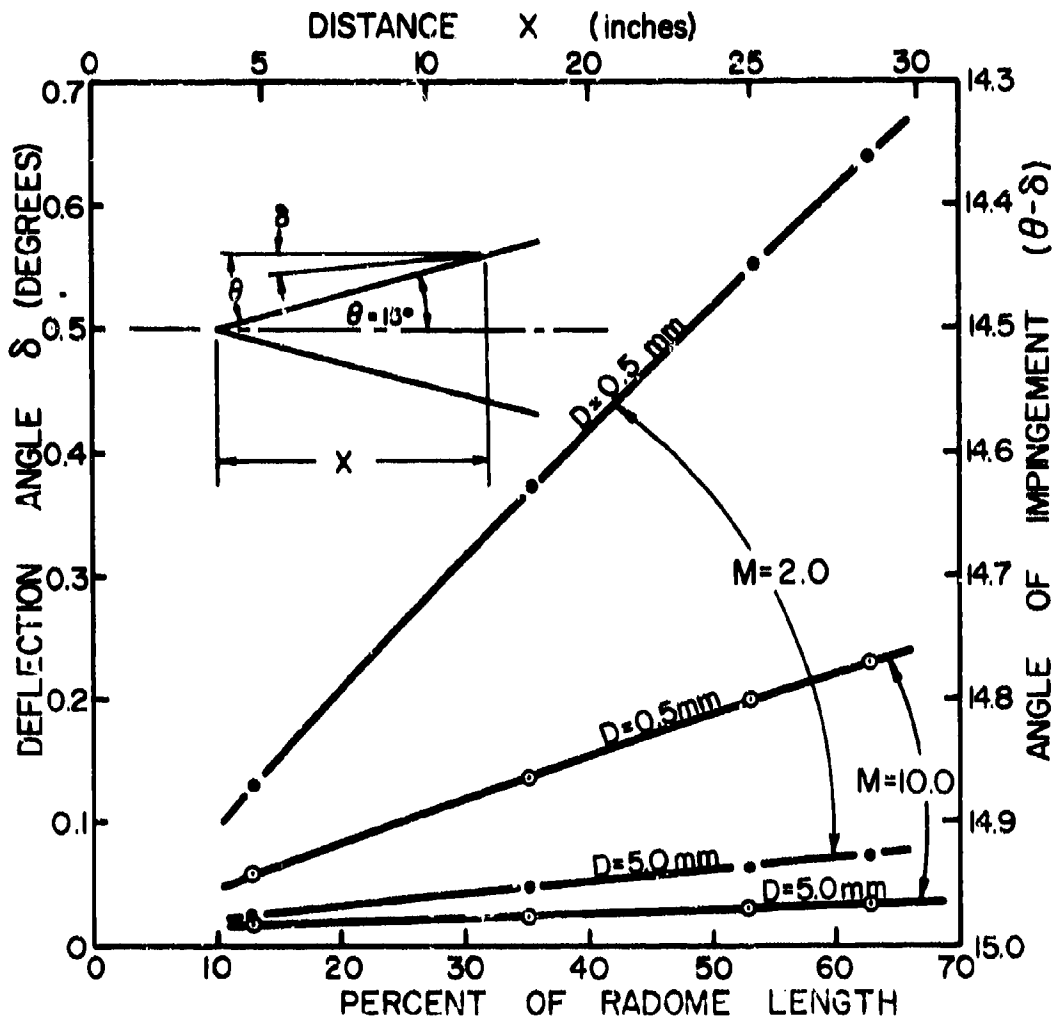
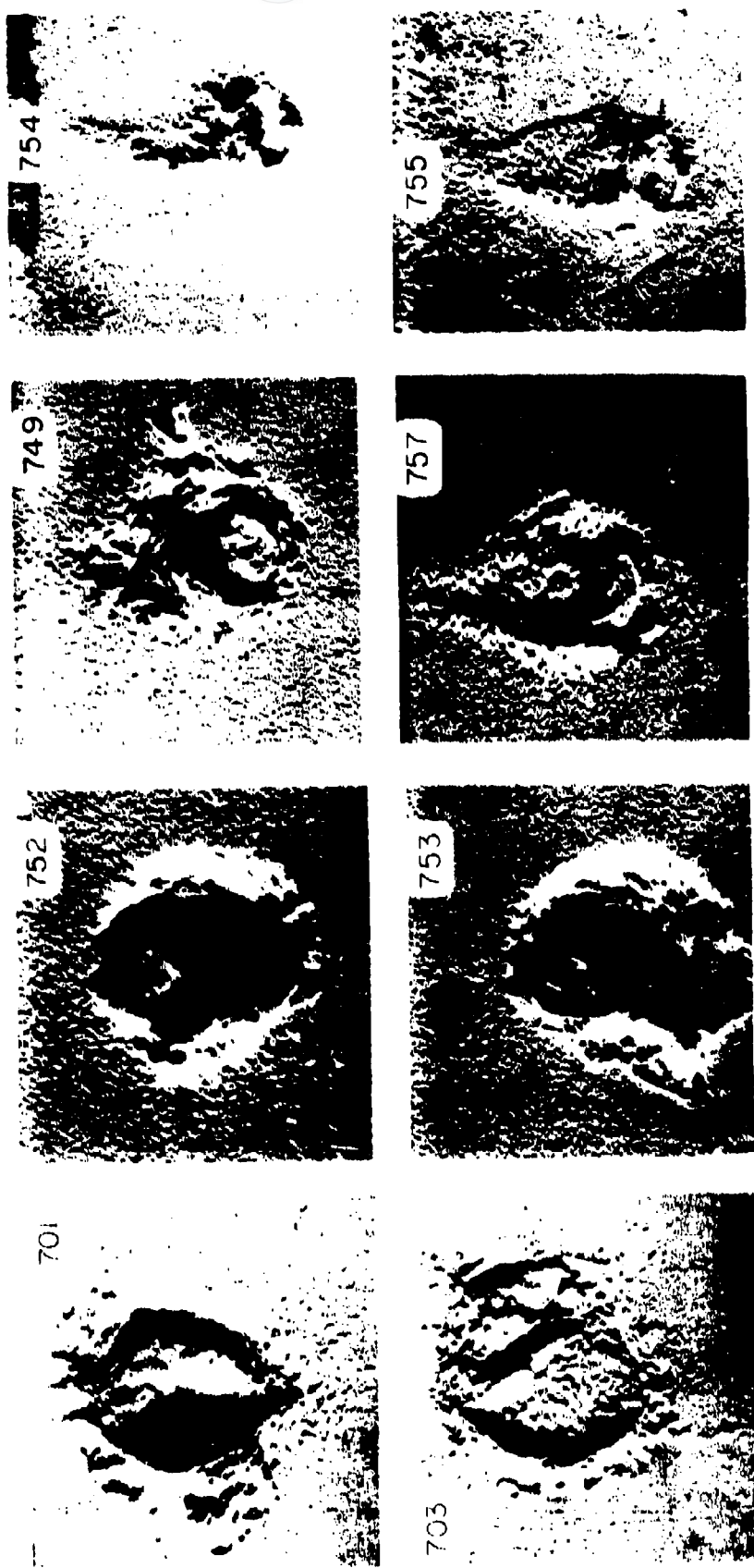


FIGURE 35. DEFLECTION OF RAINDROPS BY THE RADOME SHOCK WAVE

90<



90 degrees (normal)
Avg. Vel. 14.6×10^{-4} cu. in.

70 degrees
Avg. Vel. 18.8×10^{-4} cu. in.

52 degrees
Avg. Vel. 6.01×10^{-4} cu. in.

45 degrees
Avg. Vel. 2.06×10^{-4} cu. in.

FIGURE 36. PHOTOGRAPHS OF CRATERS FORMED BY NORMAL AND OBLIQUE IMPACTS

91<

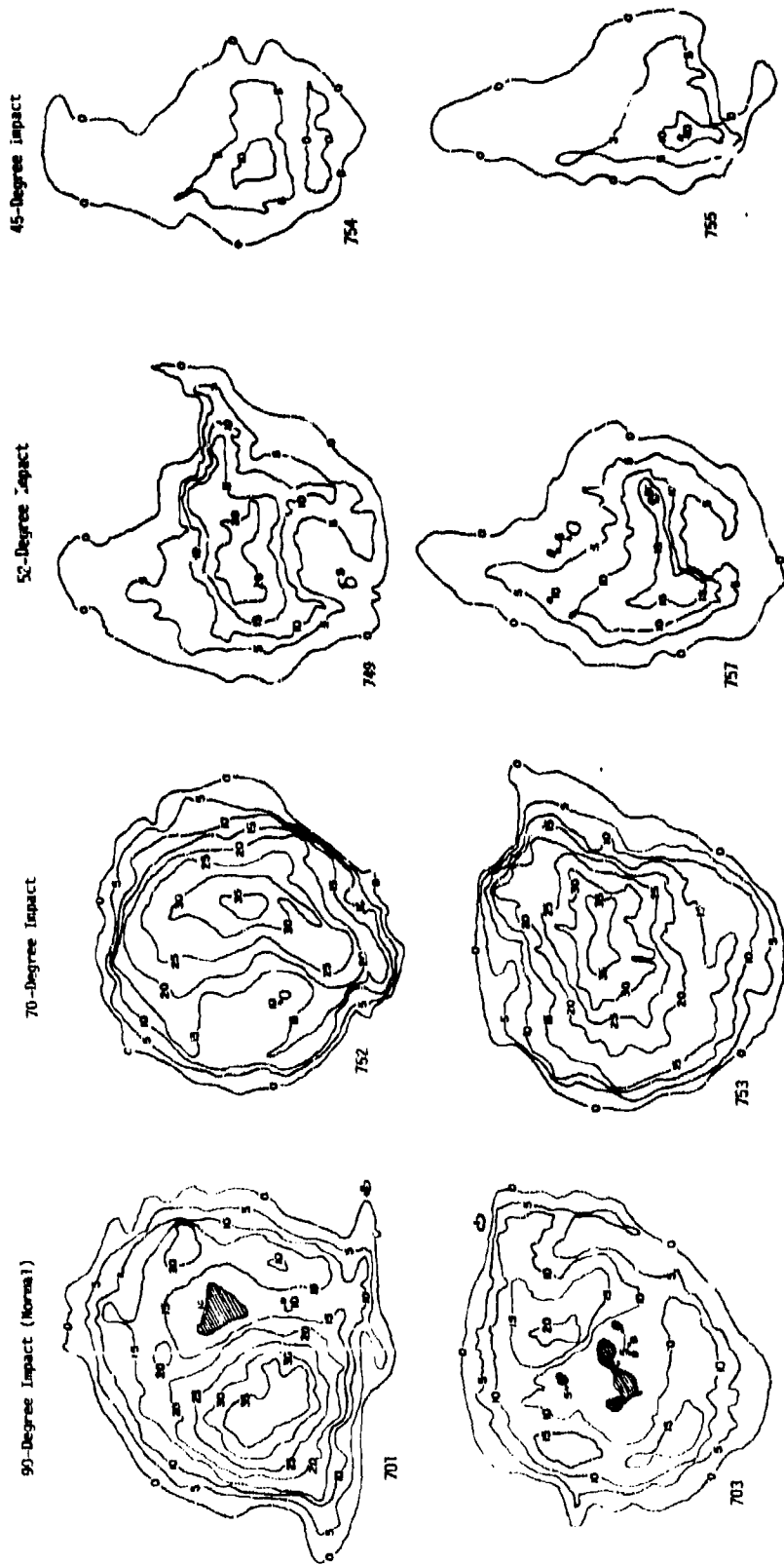


FIGURE 37. CRATER CONTOURS

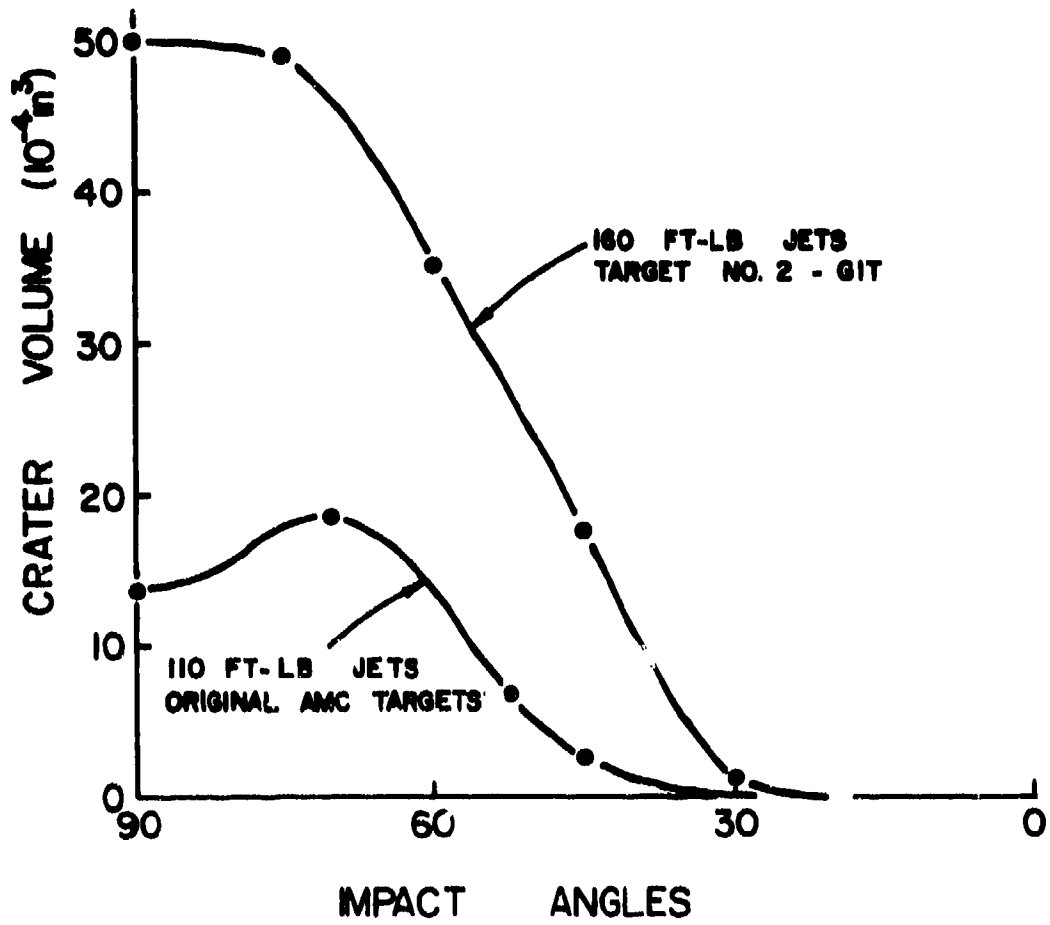


FIGURE 38. EFFECT OF IMPACT ANGLE ON CRATER VOLUME

93<

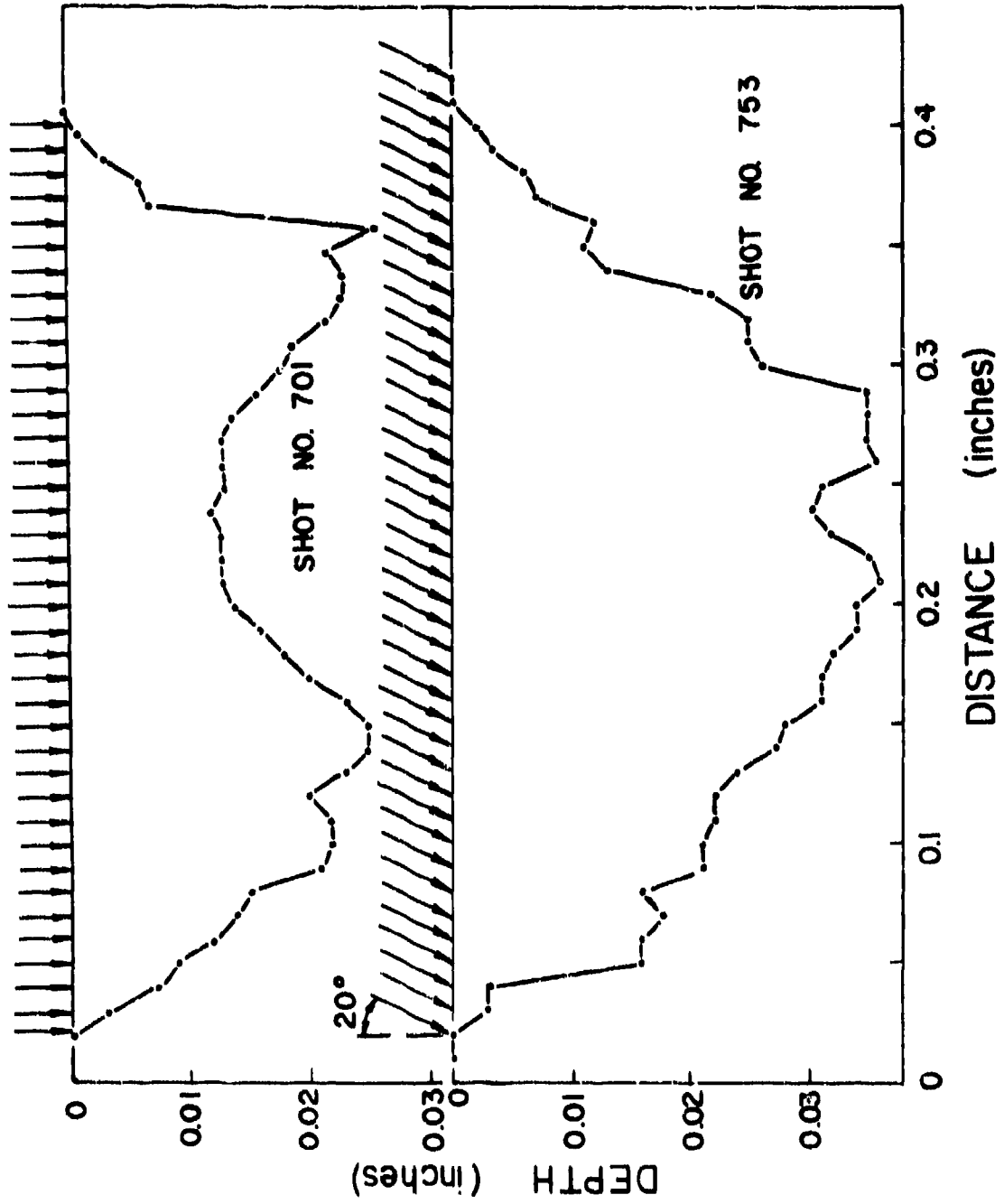


FIGURE 39. COMPARISON OF CRATER PROFILES

94<

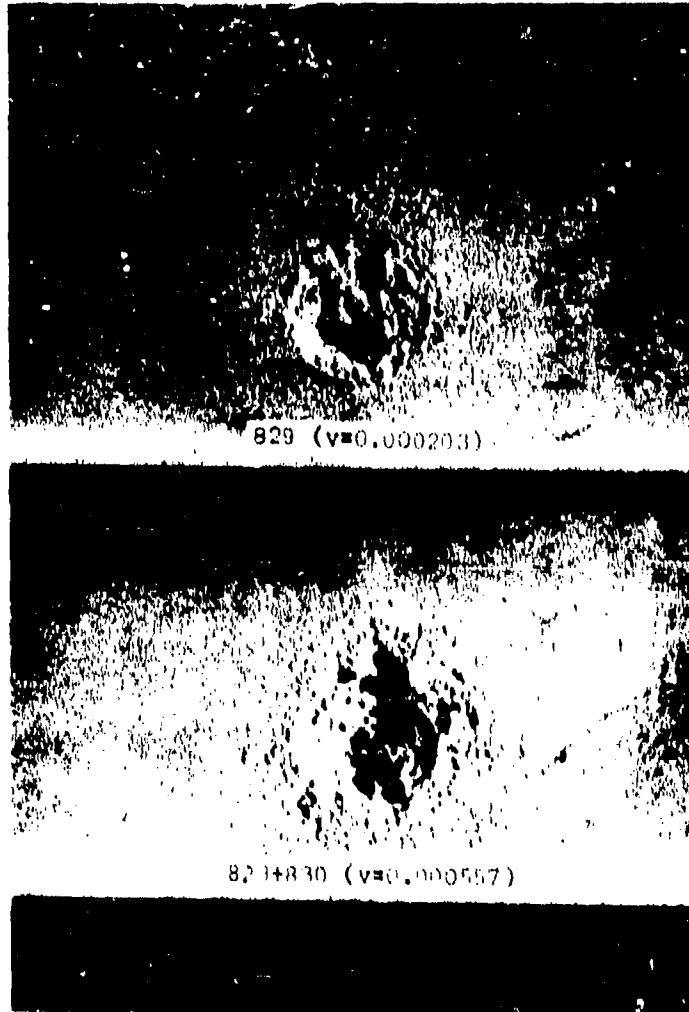


FIGURE 40. CRATER CAUSED BY SHOTS 829 AND 830

95<

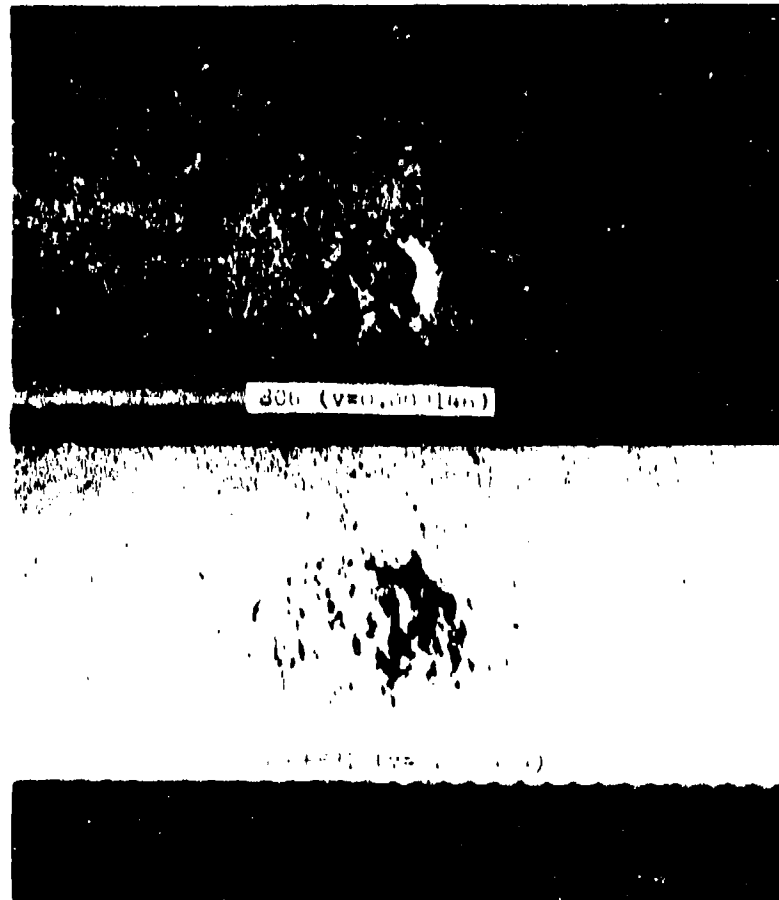


FIGURE 41. CRATER CAUSED BY SHOTS 806 AND 811

97<

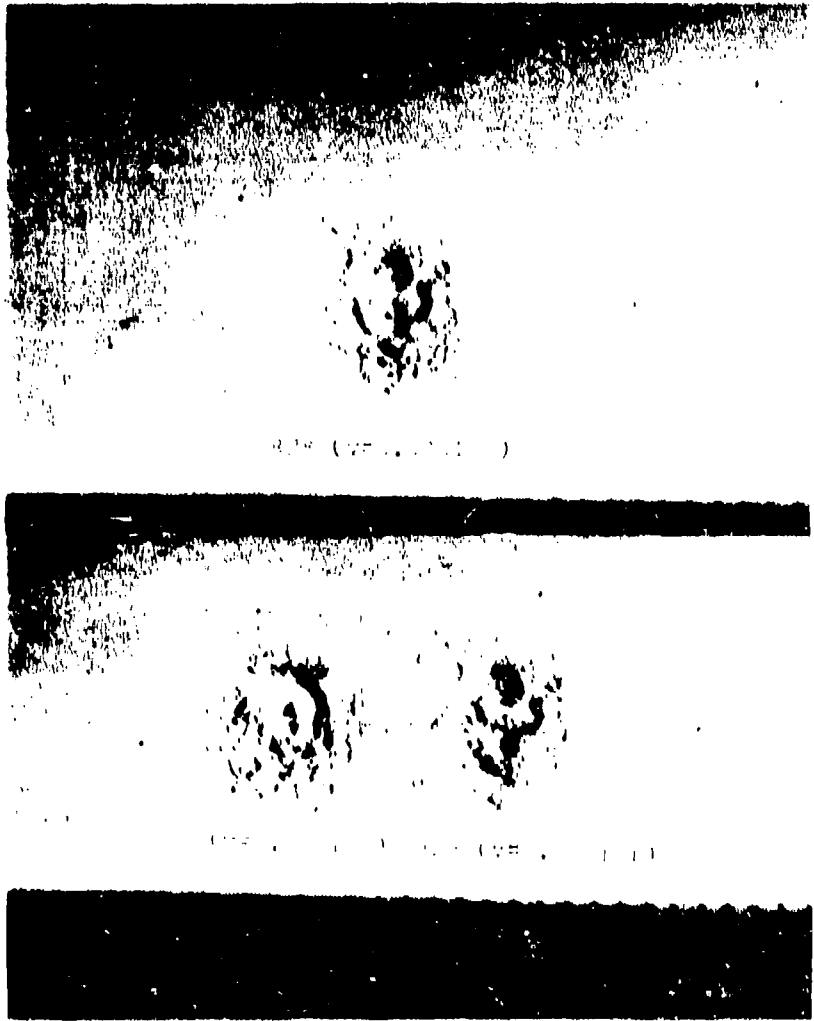


FIGURE 43. CRATERS CAUSED BY CHIPS 828 AND 833

98<

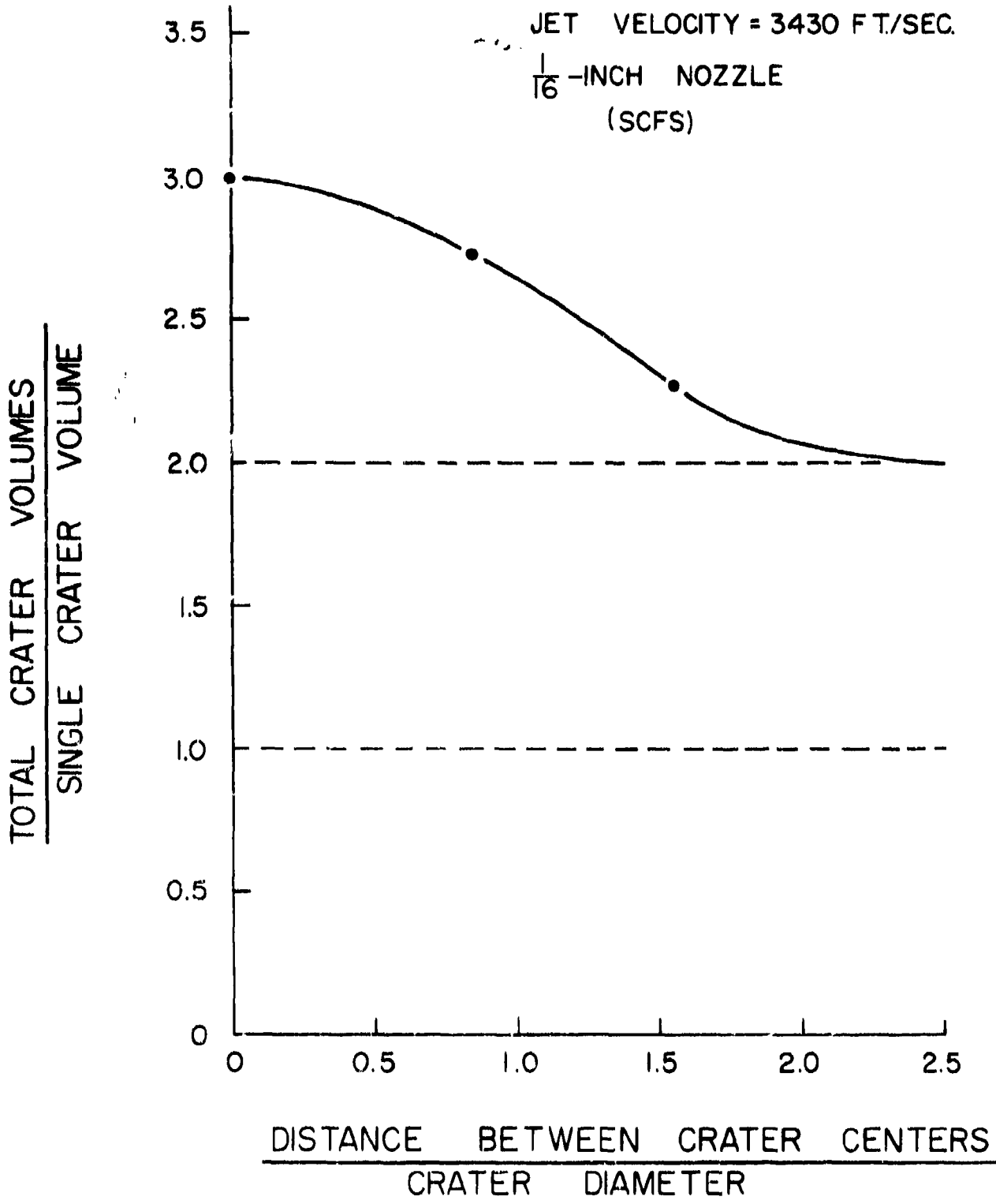


FIGURE 44. EFFECTS OF DISTANCE BETWEEN IMPACTS

99<

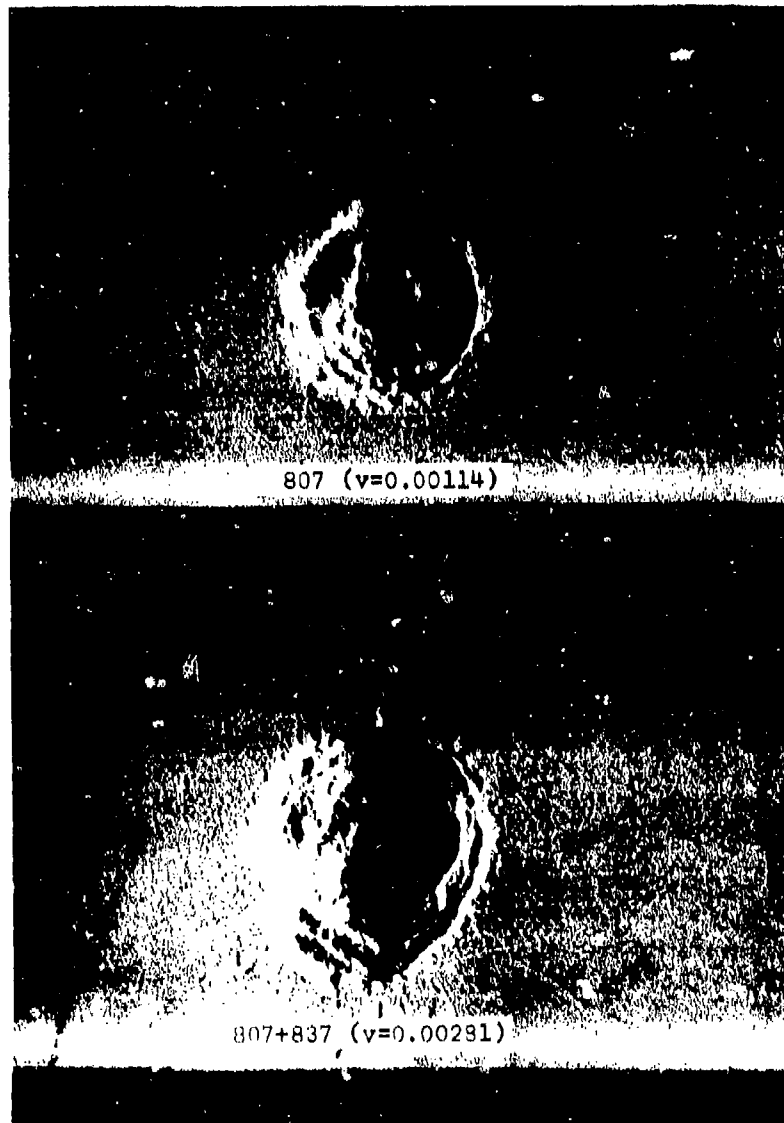


FIGURE 45. CRATERS CAUSED BY SHOTS 807 AND 837

100<

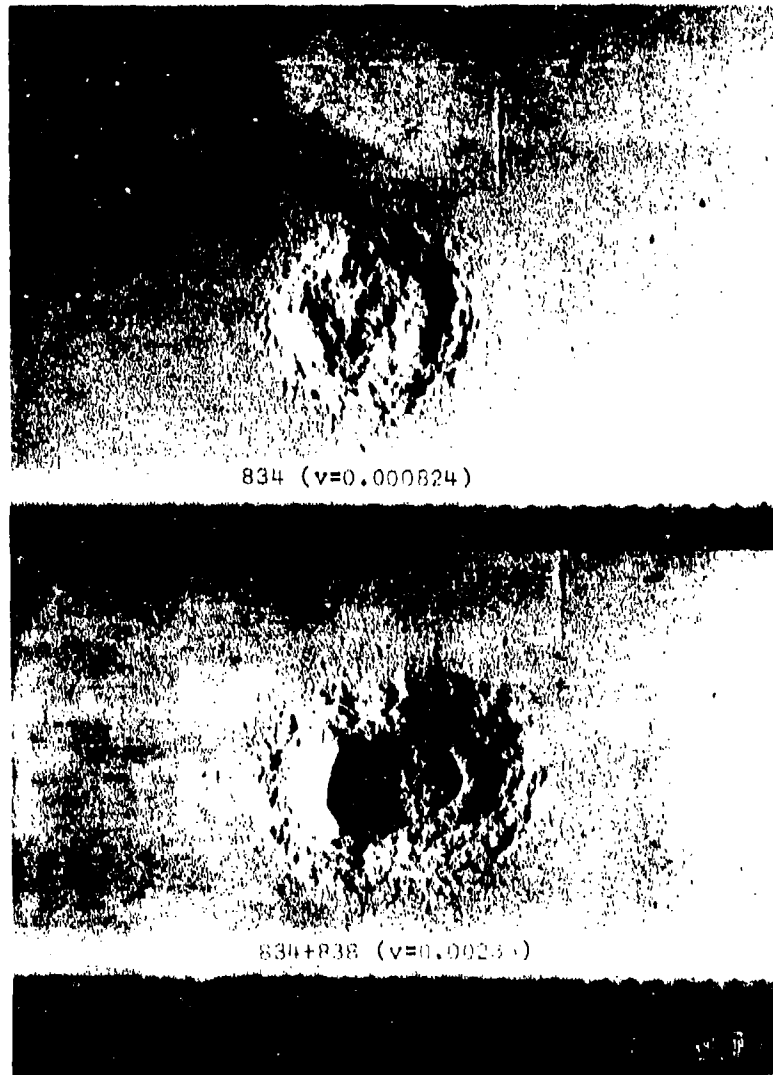


FIGURE 46. CRATERS CAUSED BY SHOTS 834 AND 838

101<

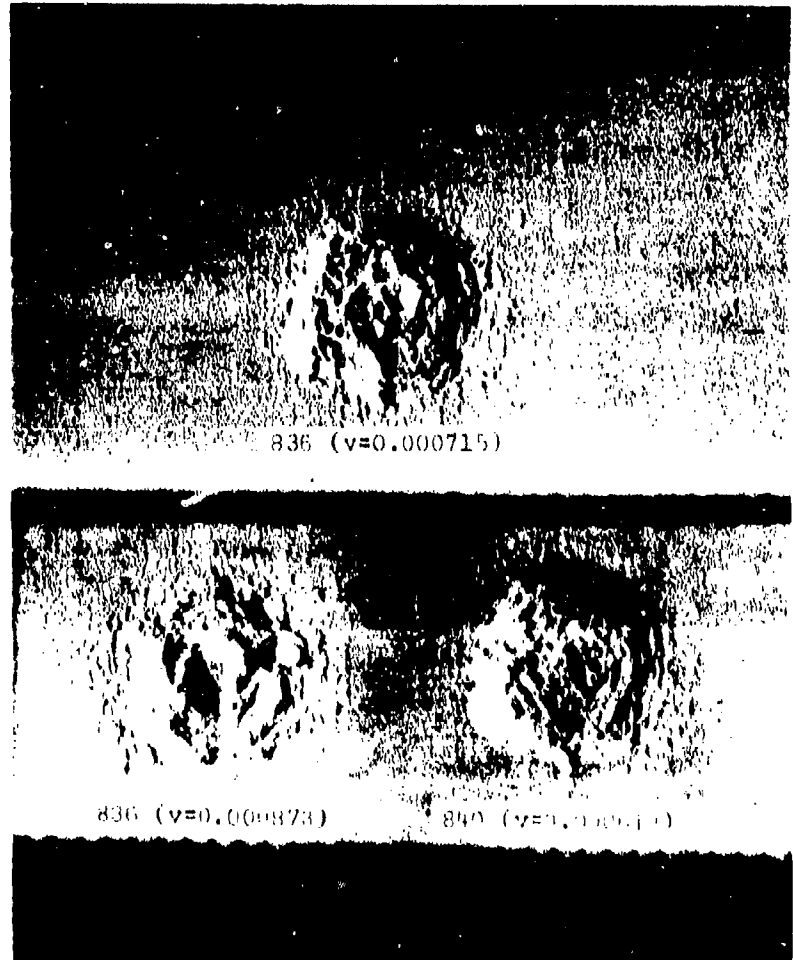


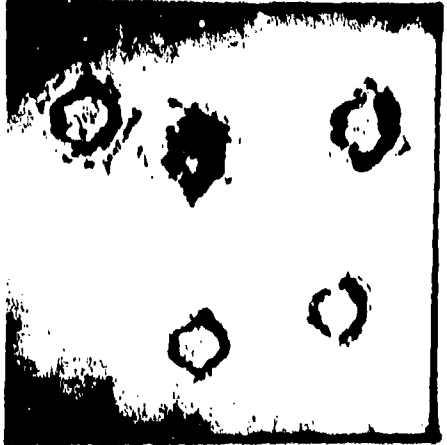
FIGURE 47. CRATERS CAUSED BY SHOTS 836 AND 840

102<



FIGURE 48. CRACK THROUGH CRATER 769 CAUSED BY SHOT 770

103<



104<

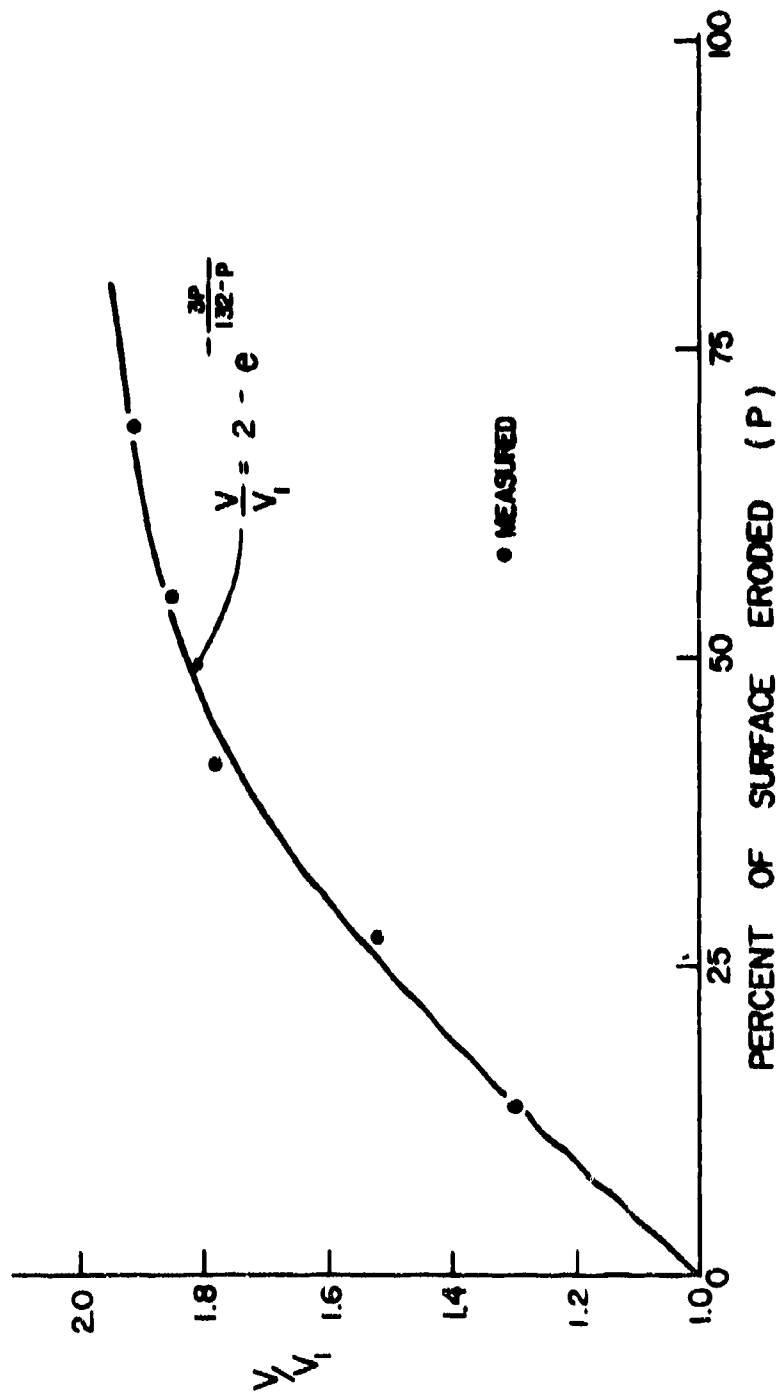


FIGURE 50. EFFECT OF PERCENT OF SURFACE ERODED ON VOLUME OF MATERIAL REMOVED

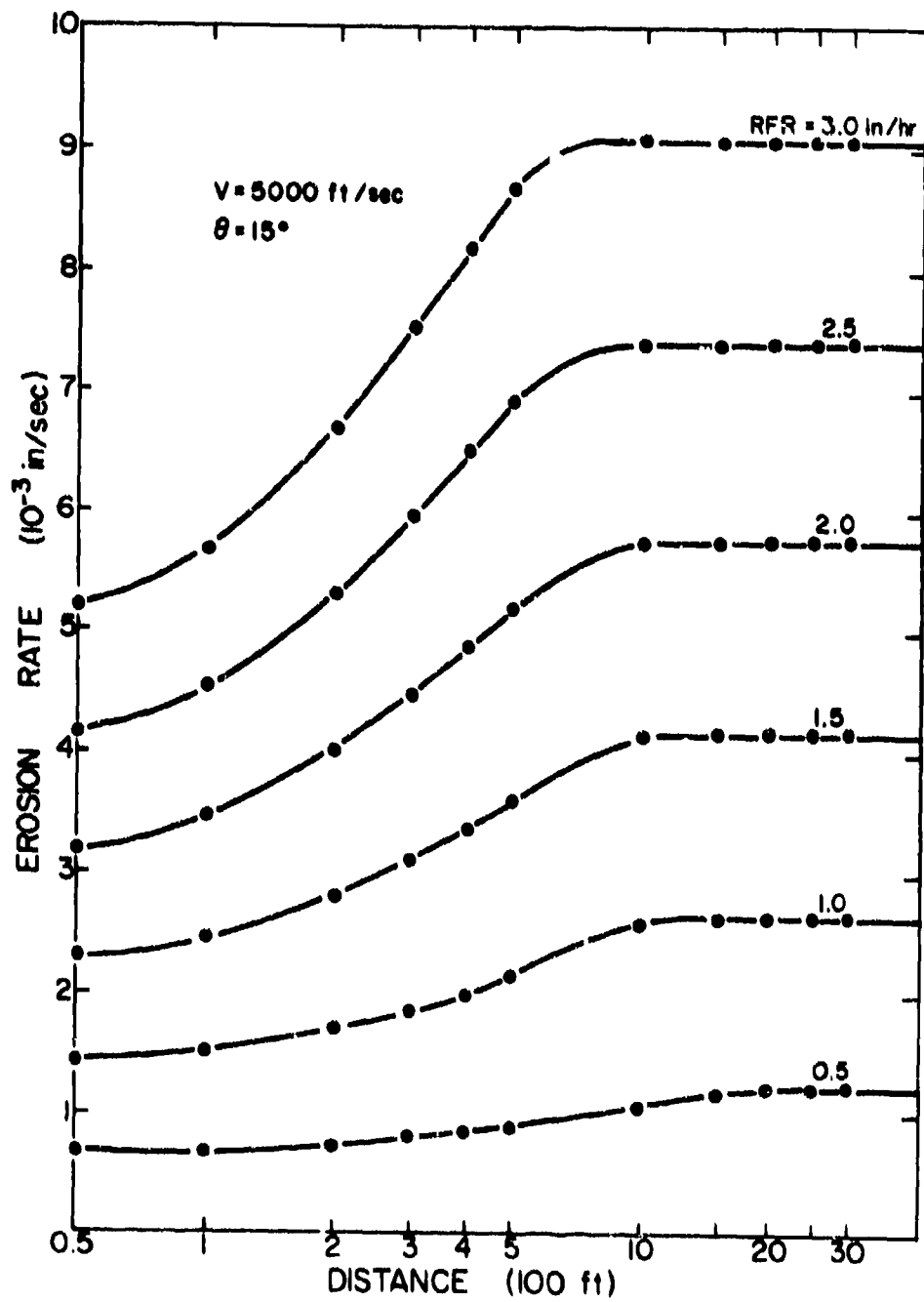


FIGURE 51. EROSION RATE AS A FUNCTION OF DISTANCE TRAVELED IN RAIN FIELD

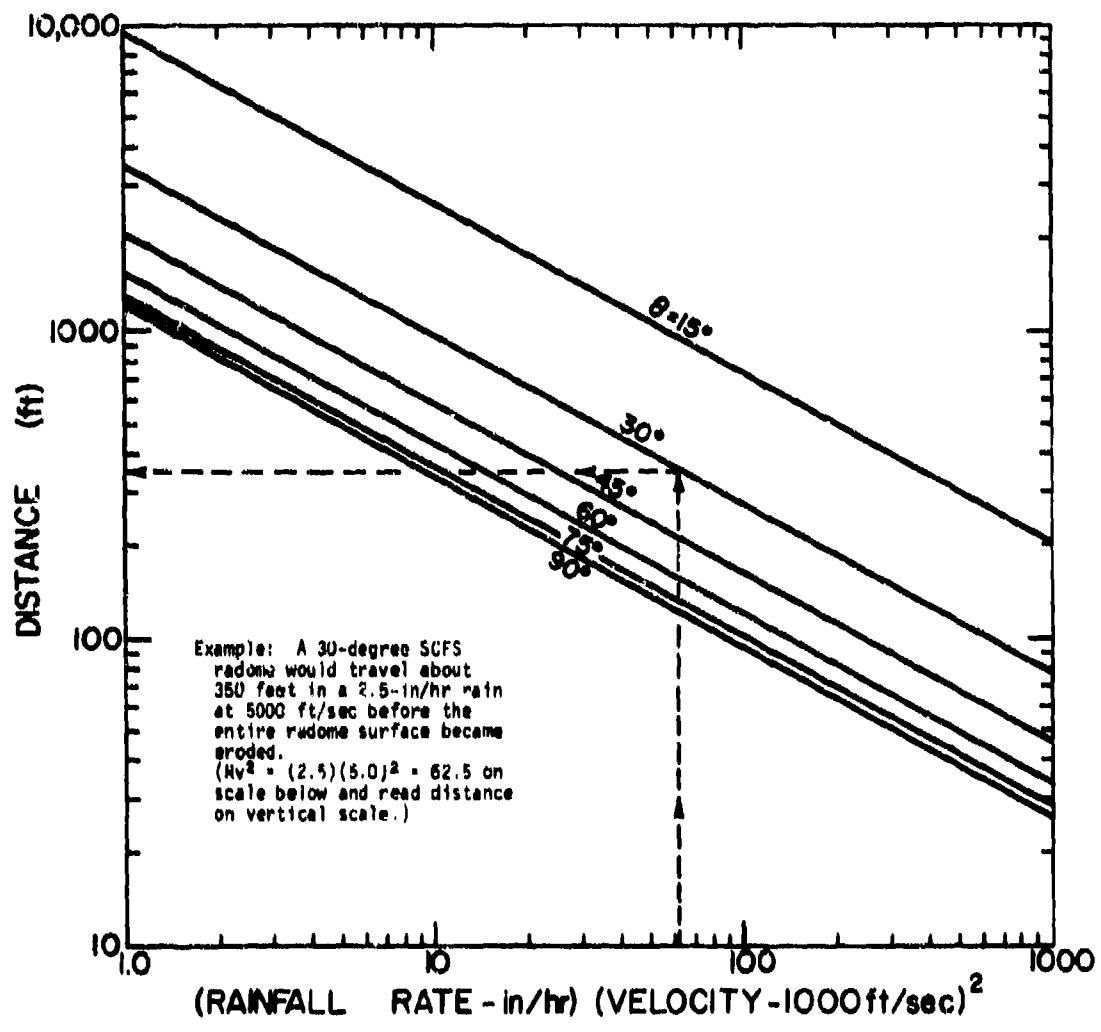


FIGURE 52. RAIN FIELD LENGTH REQUIRED FOR 100 PERCENT SURFACE EROSION

107<

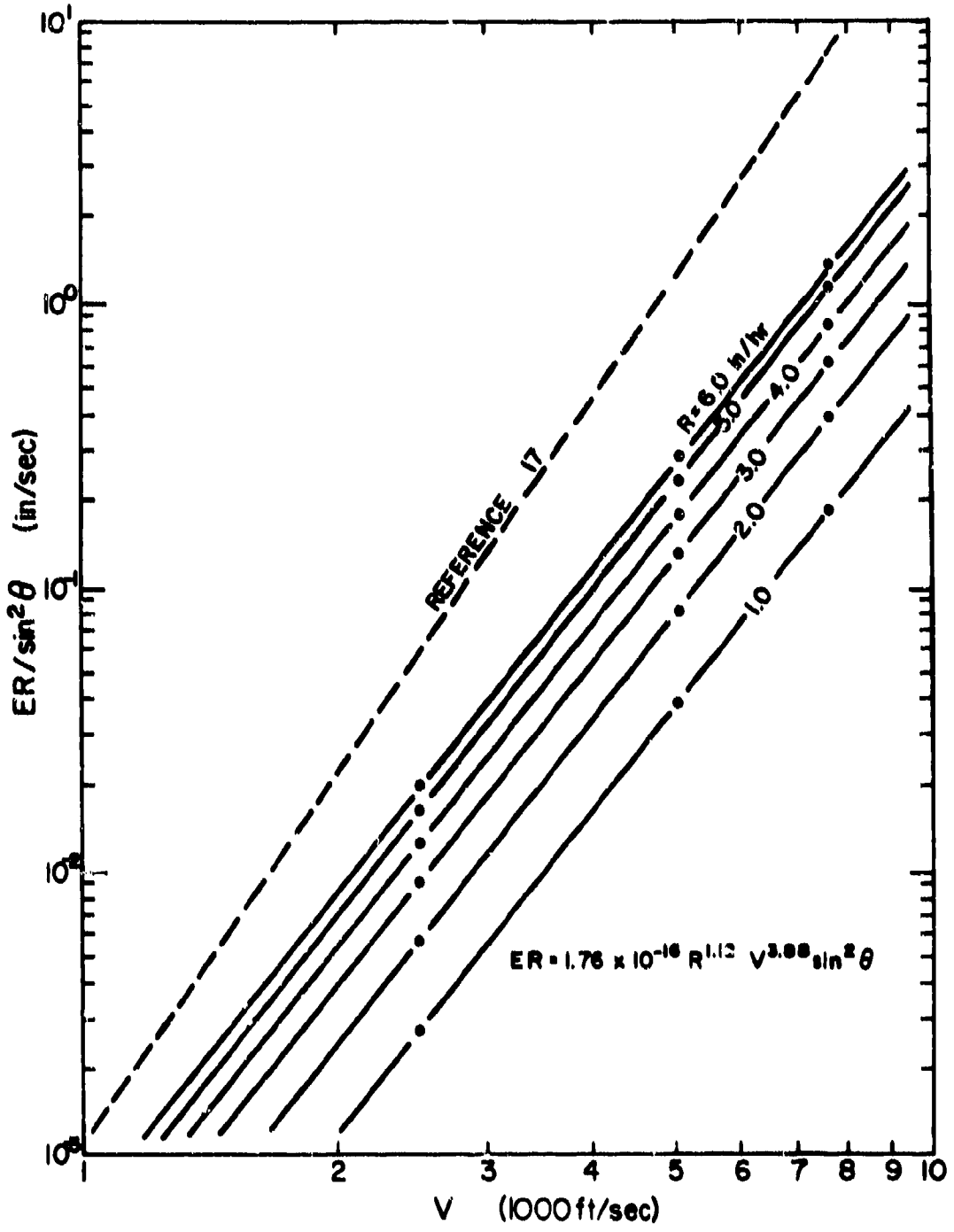


FIGURE 53. RELATION BETWEEN EROSION RATE AND VELOCITY

108<



4x

109<

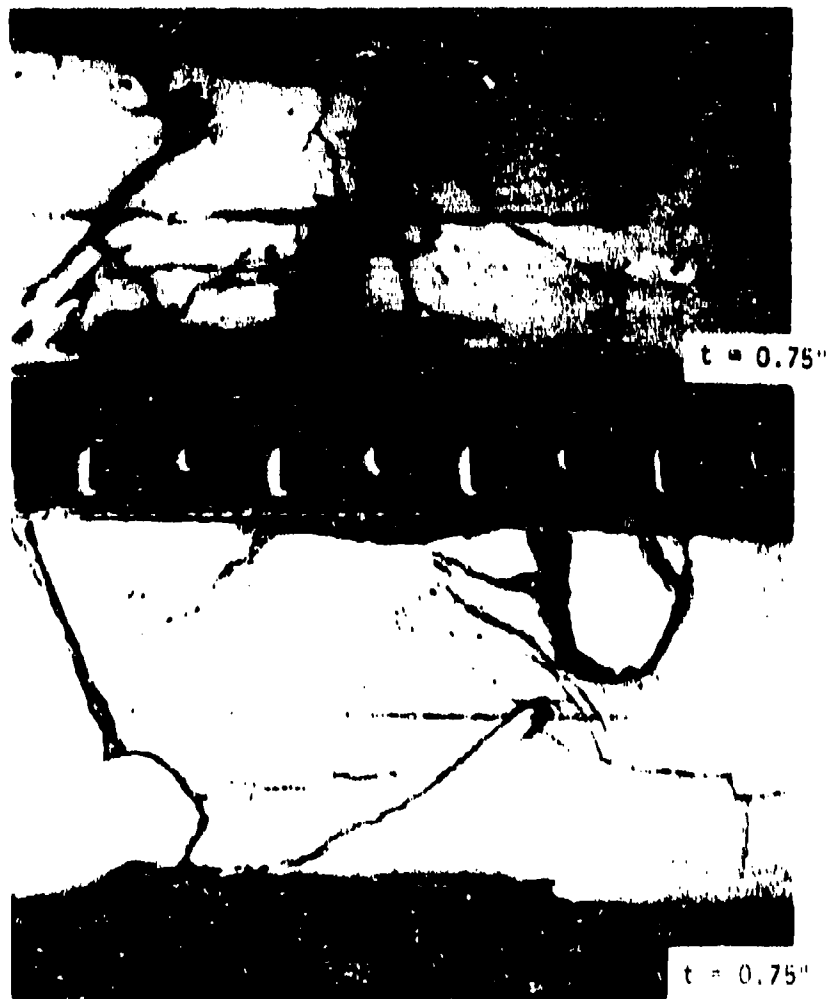


FIGURE 55. INTERNAL FRACTURES AND REAR SURFACE SPALL.

110<

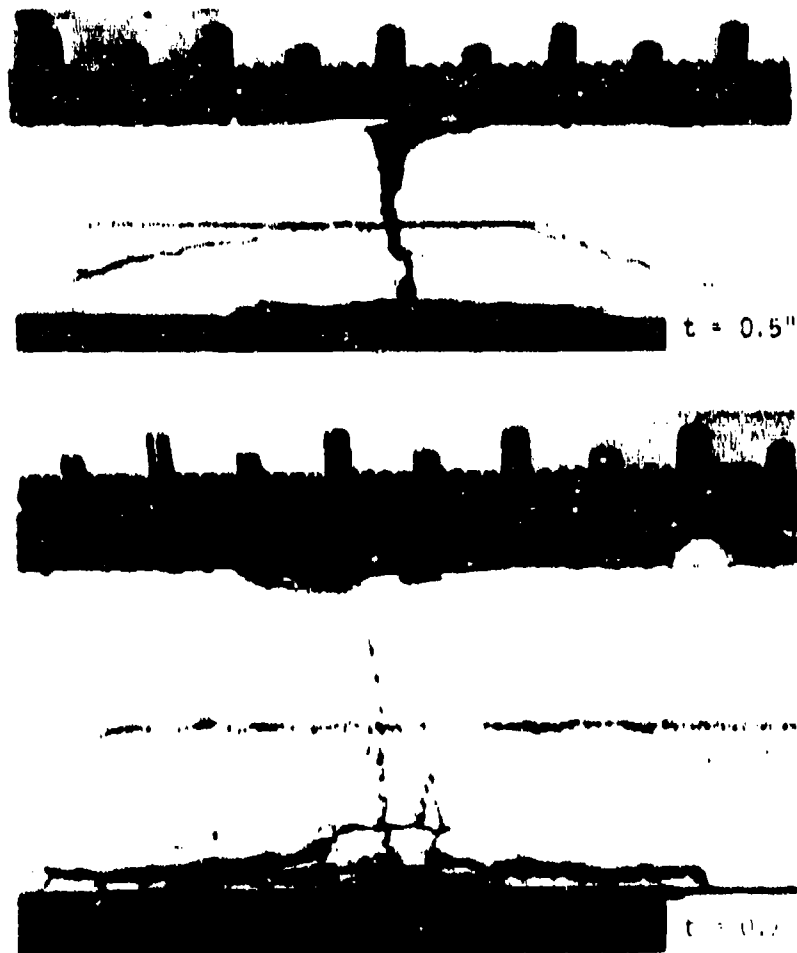


FIGURE 56. CRACKS IN DEFECTIVE TARGETS

111<

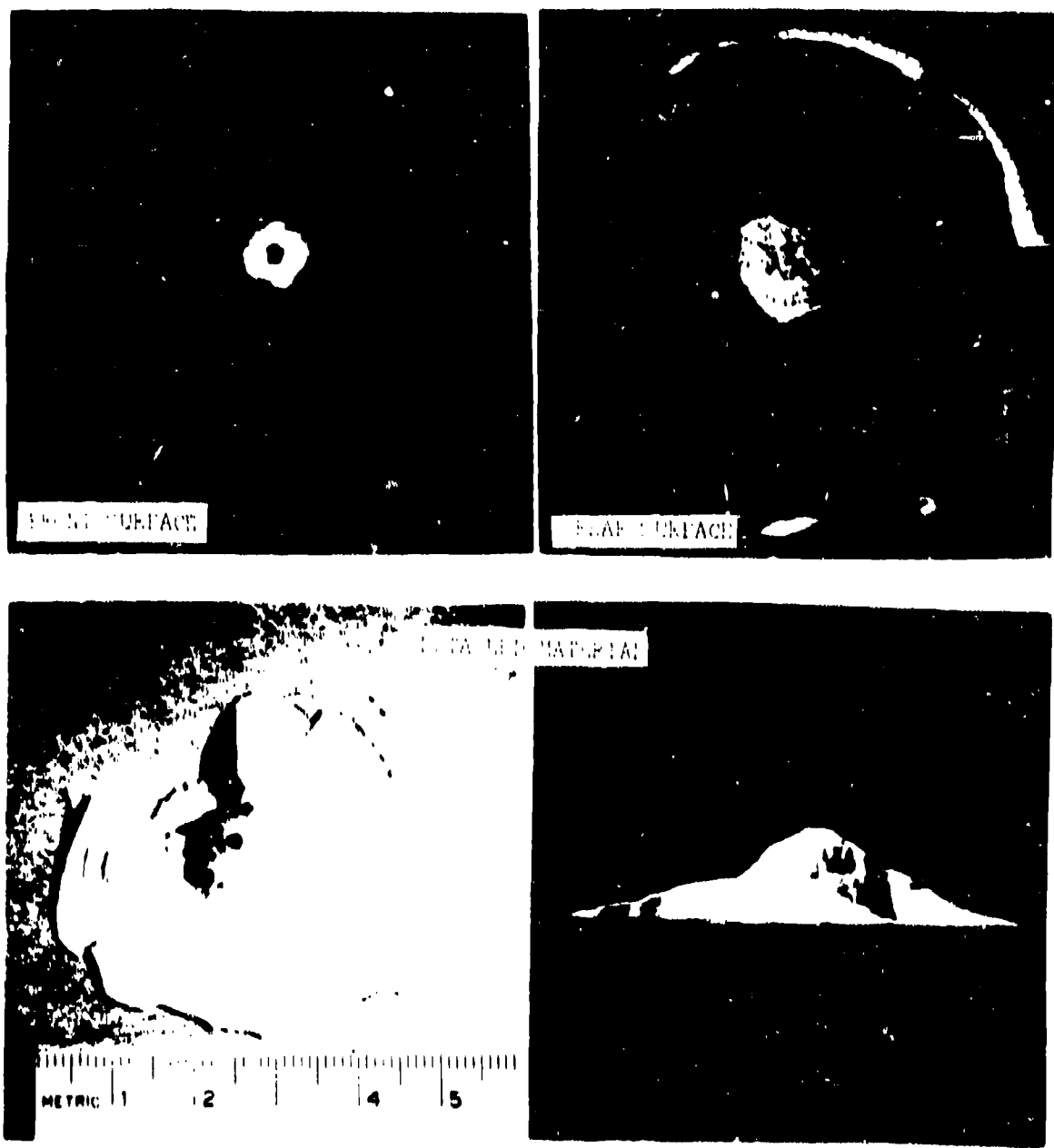


FIGURE 57. FRACTURE CONE FROM PERFORATED SCF'S TARGET

11C<

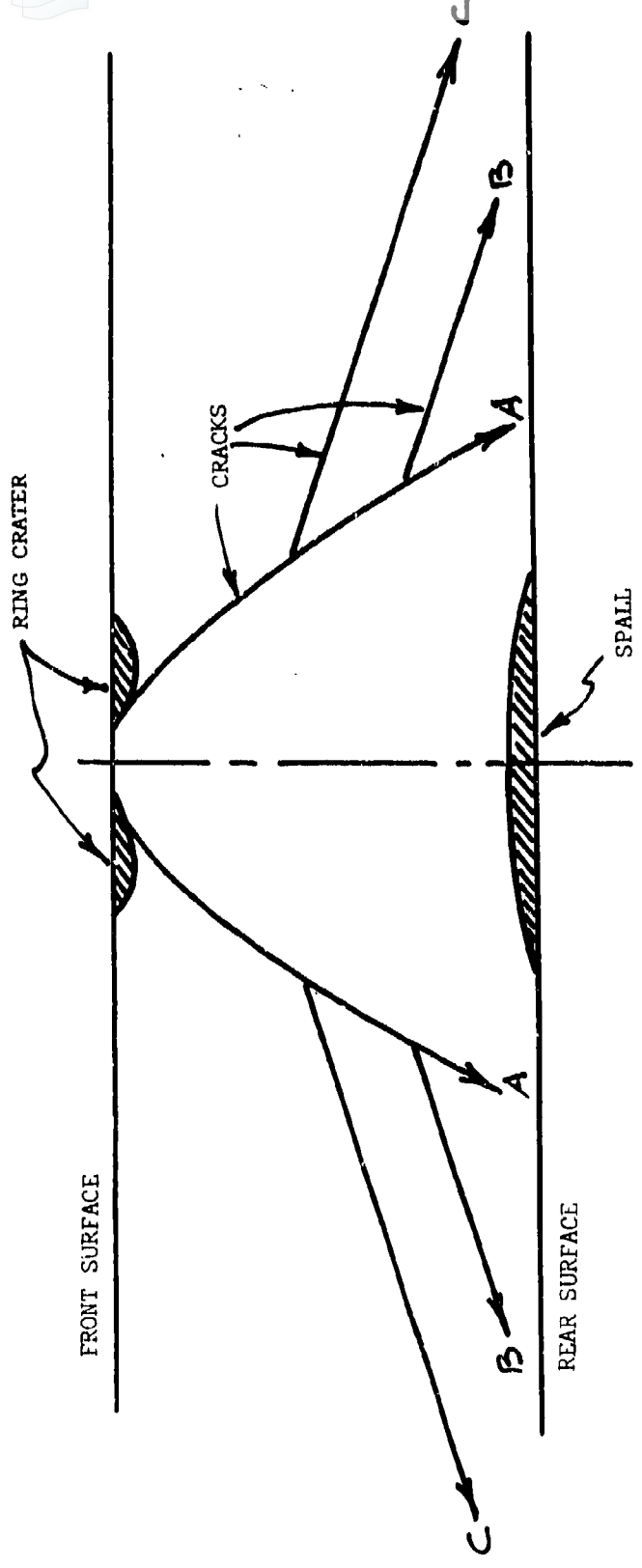


FIGURE 58. FRACTURE LOCATIONS

113<

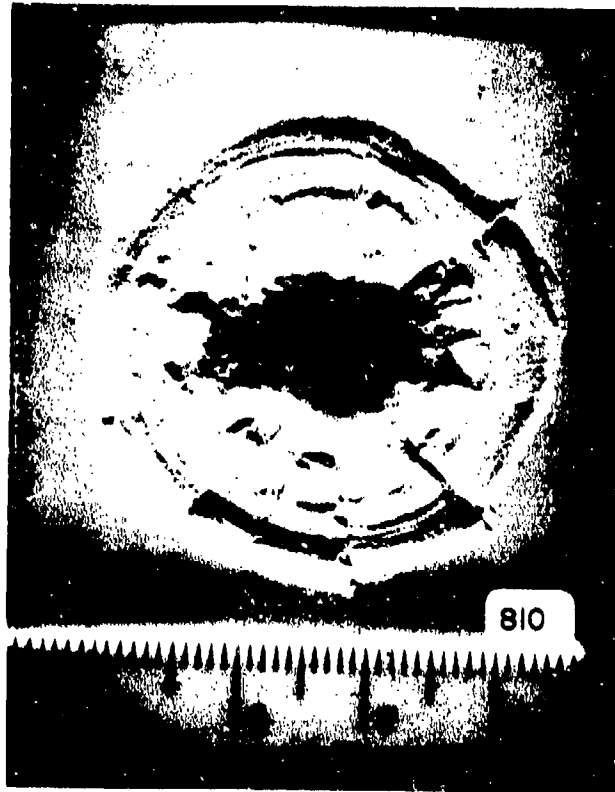


FIGURE 59. REAR SURFACE OF PERFORATED TARGET - SHOT 810

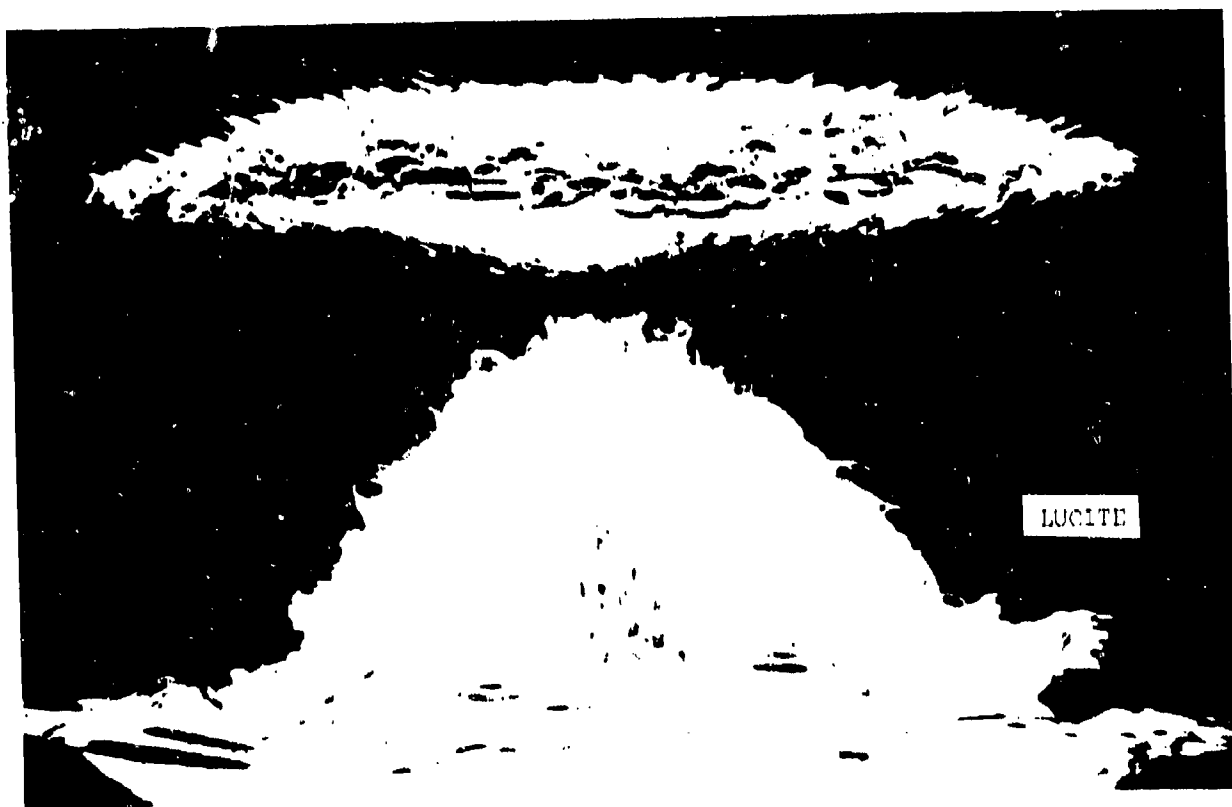
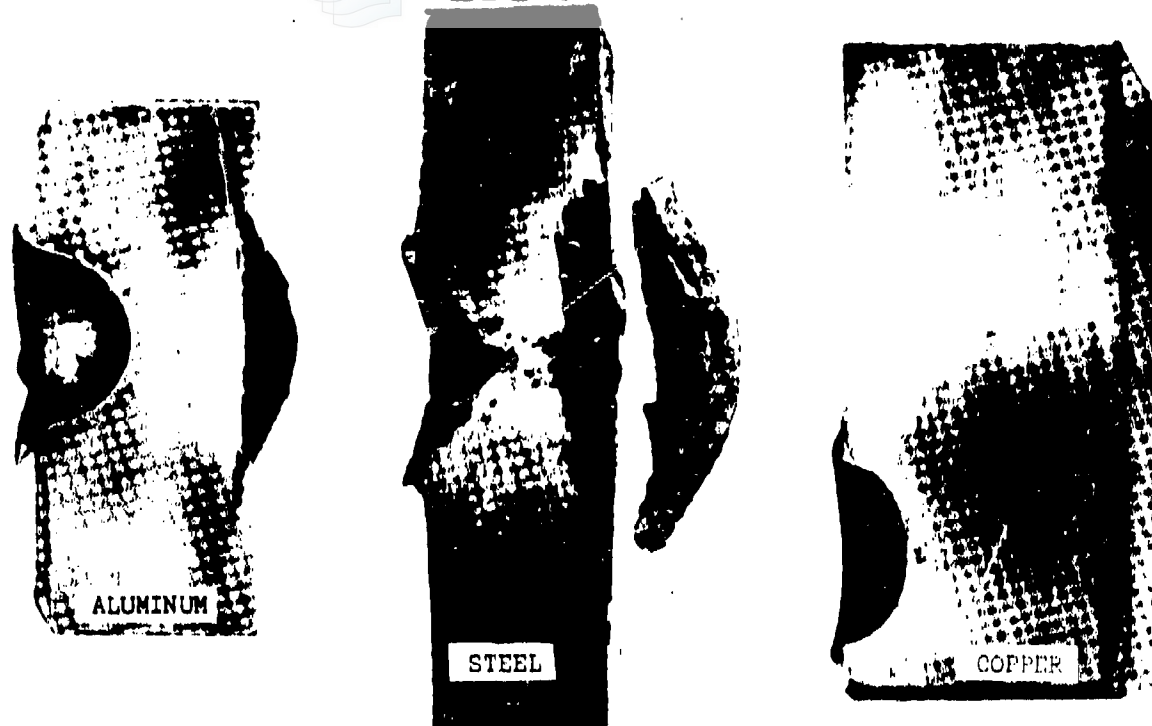


FIGURE 60. FRACTURES CAUSED BY REFLECTED STRESS WAVES

115<

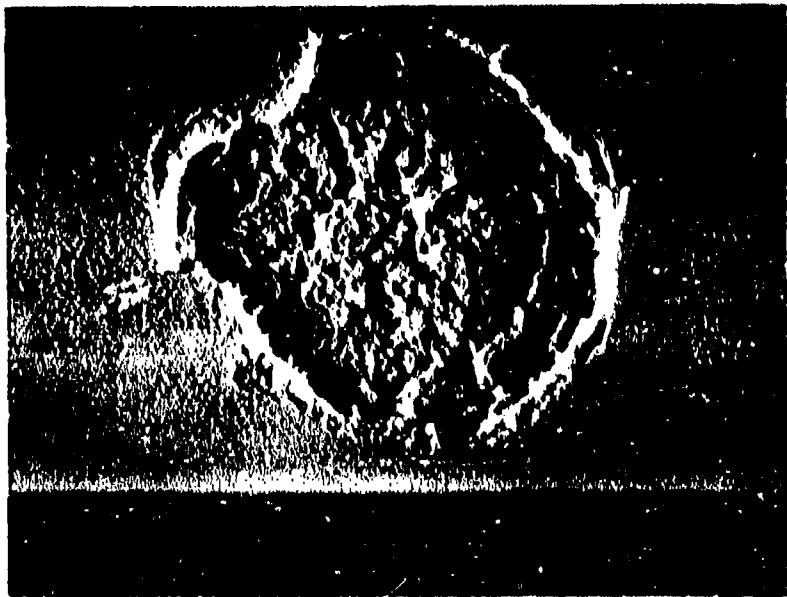


FIGURE 61. PHOTOGRAPHS OF CRATER AND SPALL - SHOT 702

116<

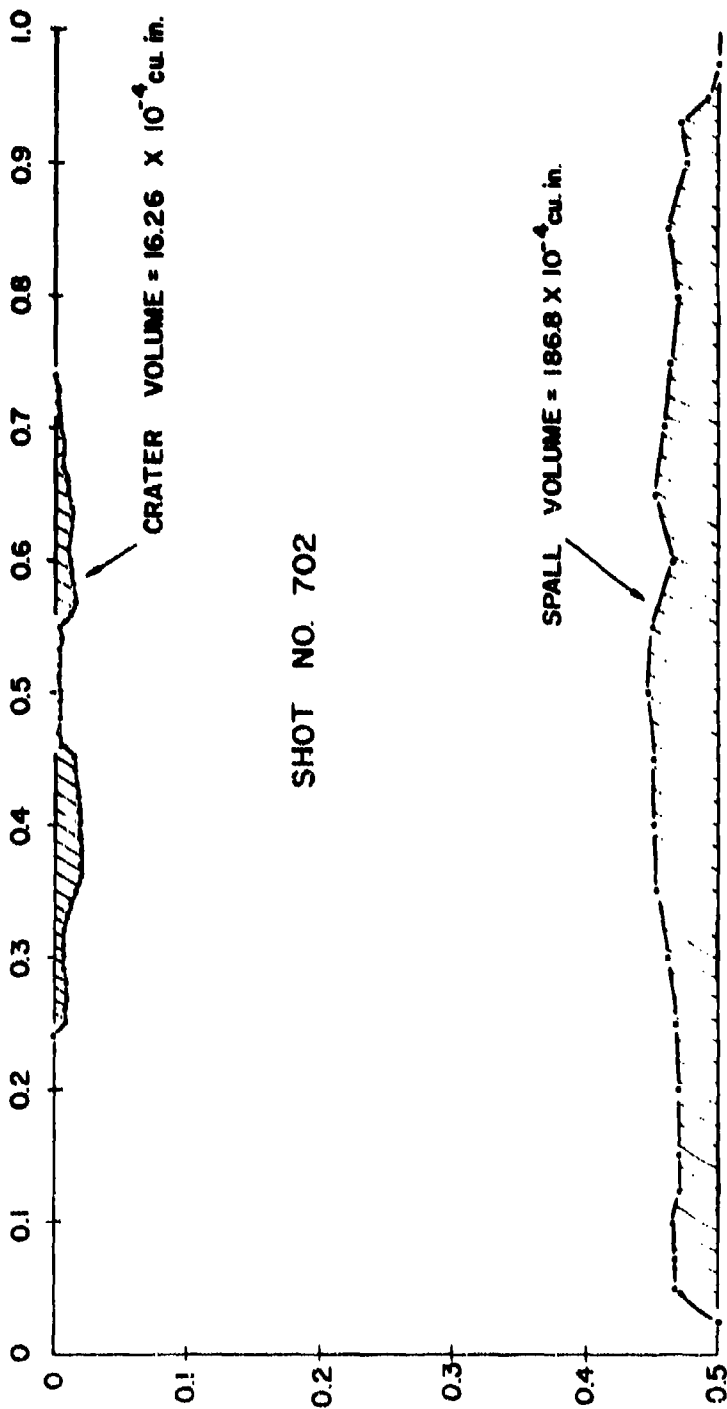


FIGURE 62. CRATER AND SPALL PROFILES

117<

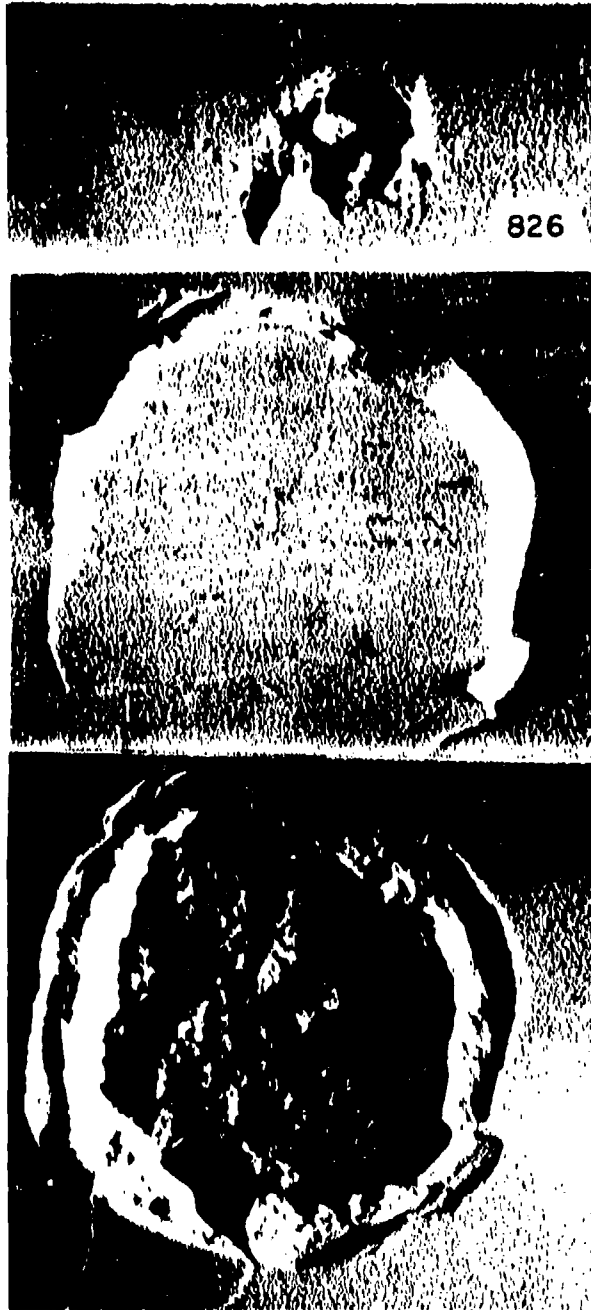


FIGURE 63. PHOTOGRAPHS OF CRATER AND SPALL - SHOT 826

118<

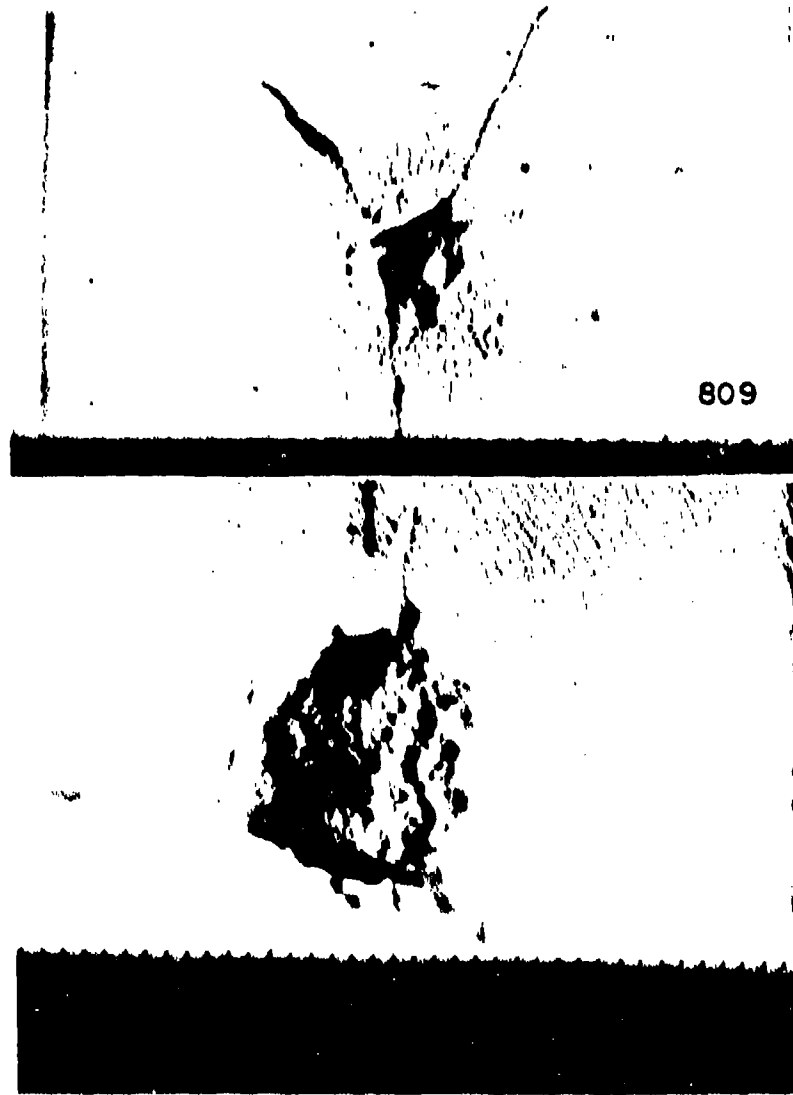


FIGURE 64. PHOTOGRAPHS OF CRATER AND SPALL - SHOT 809

119<

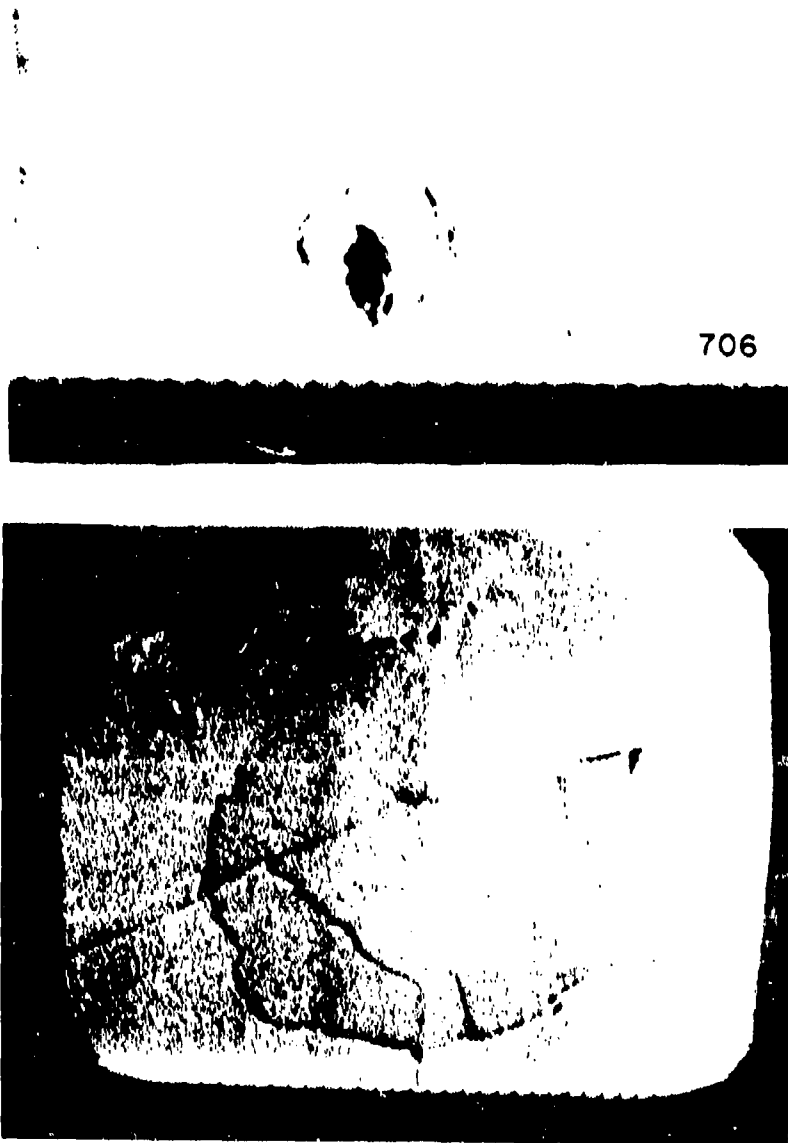


FIGURE 65. PHOTOGRAPHS OF CRATER AND INCIPIENT SPALL. - SHOT 706

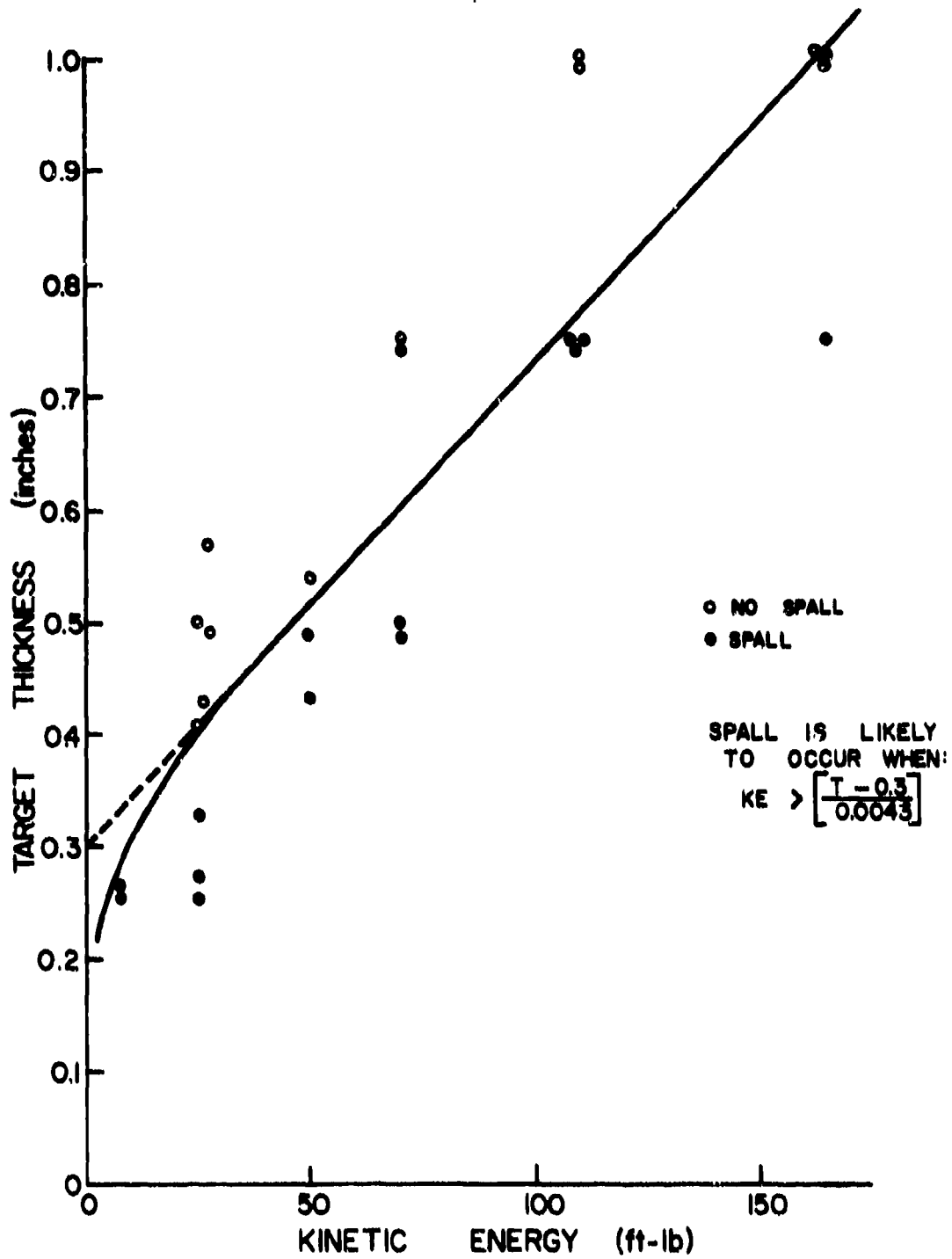


FIGURE 66. KINETIC ENERGY REQUIRED FOR SPALLATION

121<

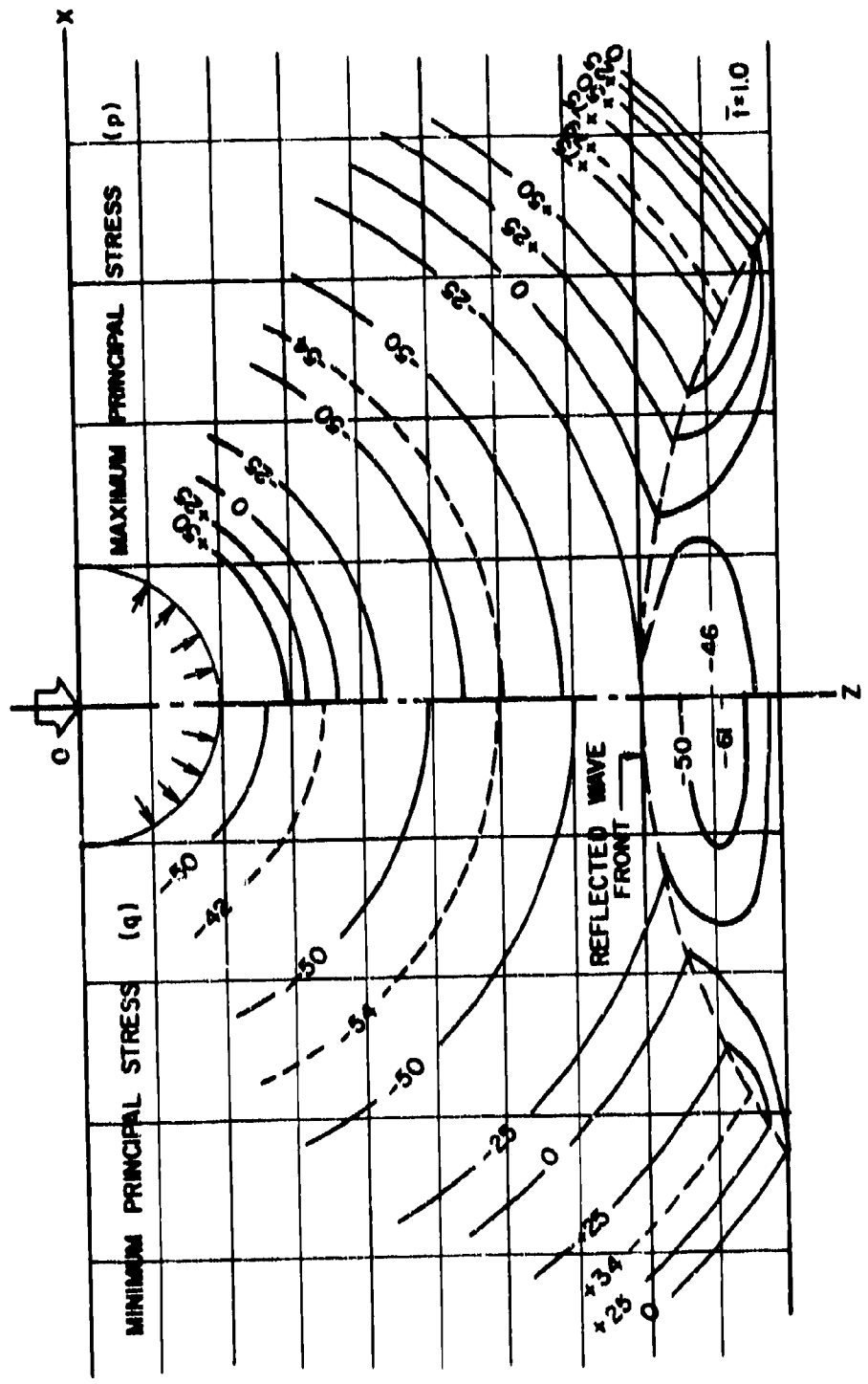


FIGURE 67. PRINCIPAL STRESSES PRODUCED BY IMPACT

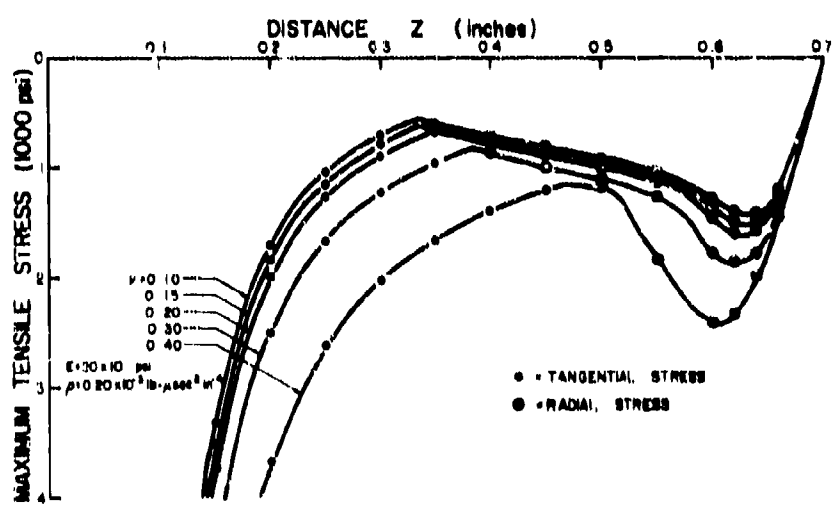
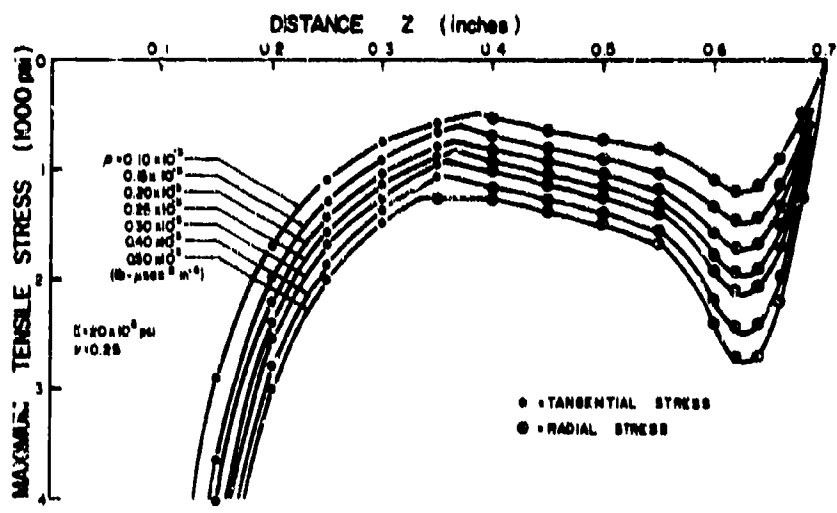
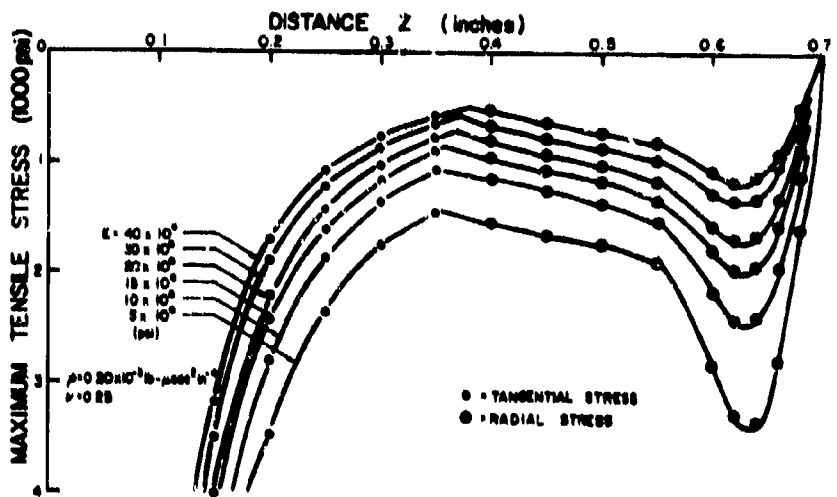


FIGURE 68. EFFECT OF MATERIAL PROPERTIES UPON MAXIMUM TENSILE STRESS

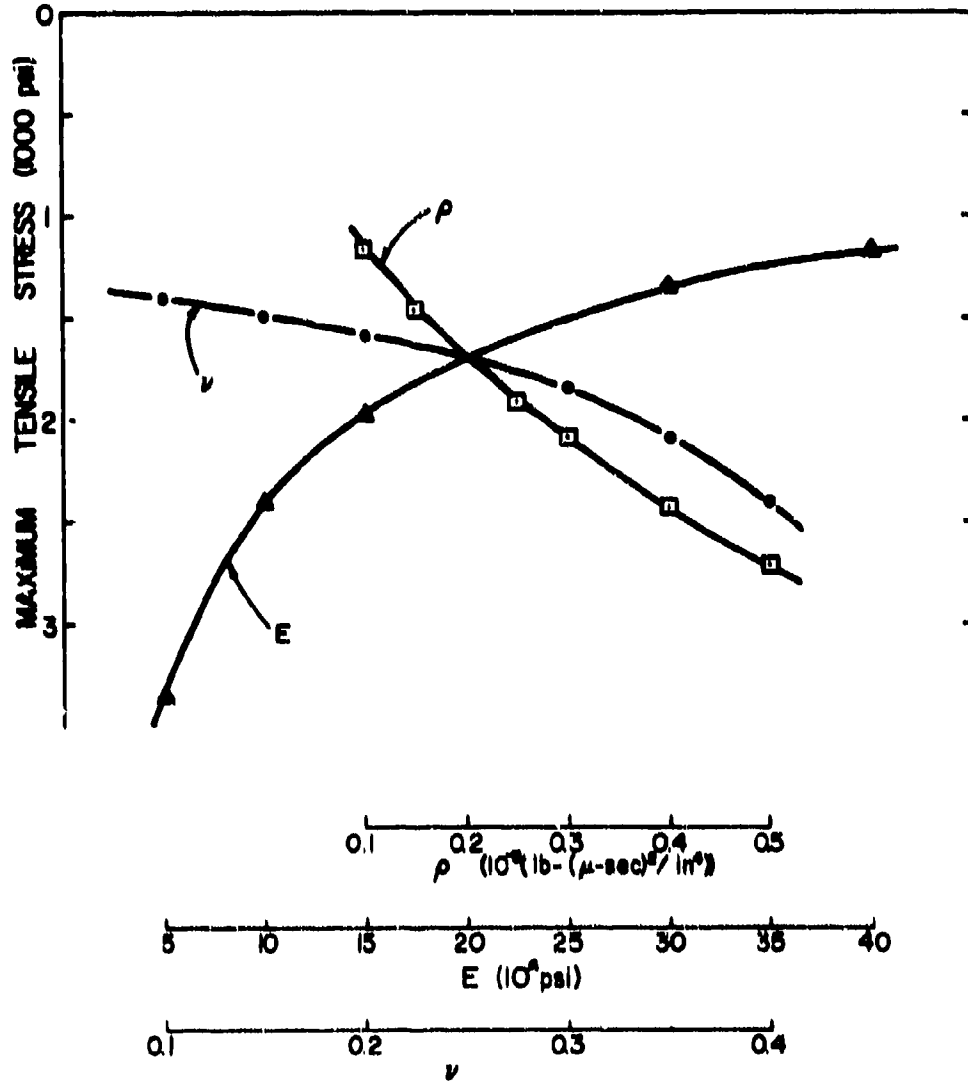


FIGURE 69. MAXIMUM RADIAL TENSILE STRESS AS FUNCTION OF MATERIAL PROPERTIES

124<

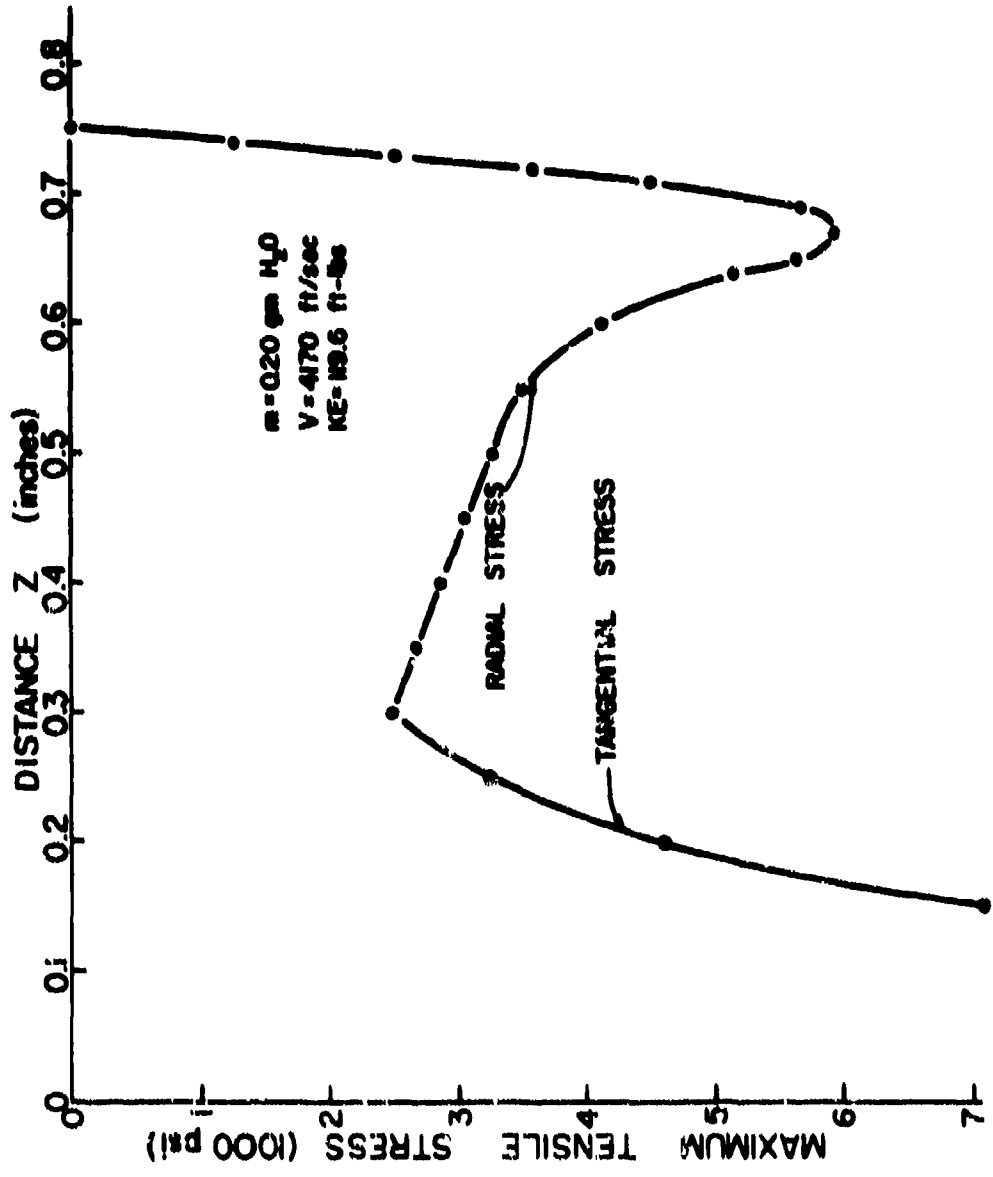


FIGURE 70. MAXIMUM TENSILE STRESS ALONG AXIS OF 0.75-INCH TARGET

125<

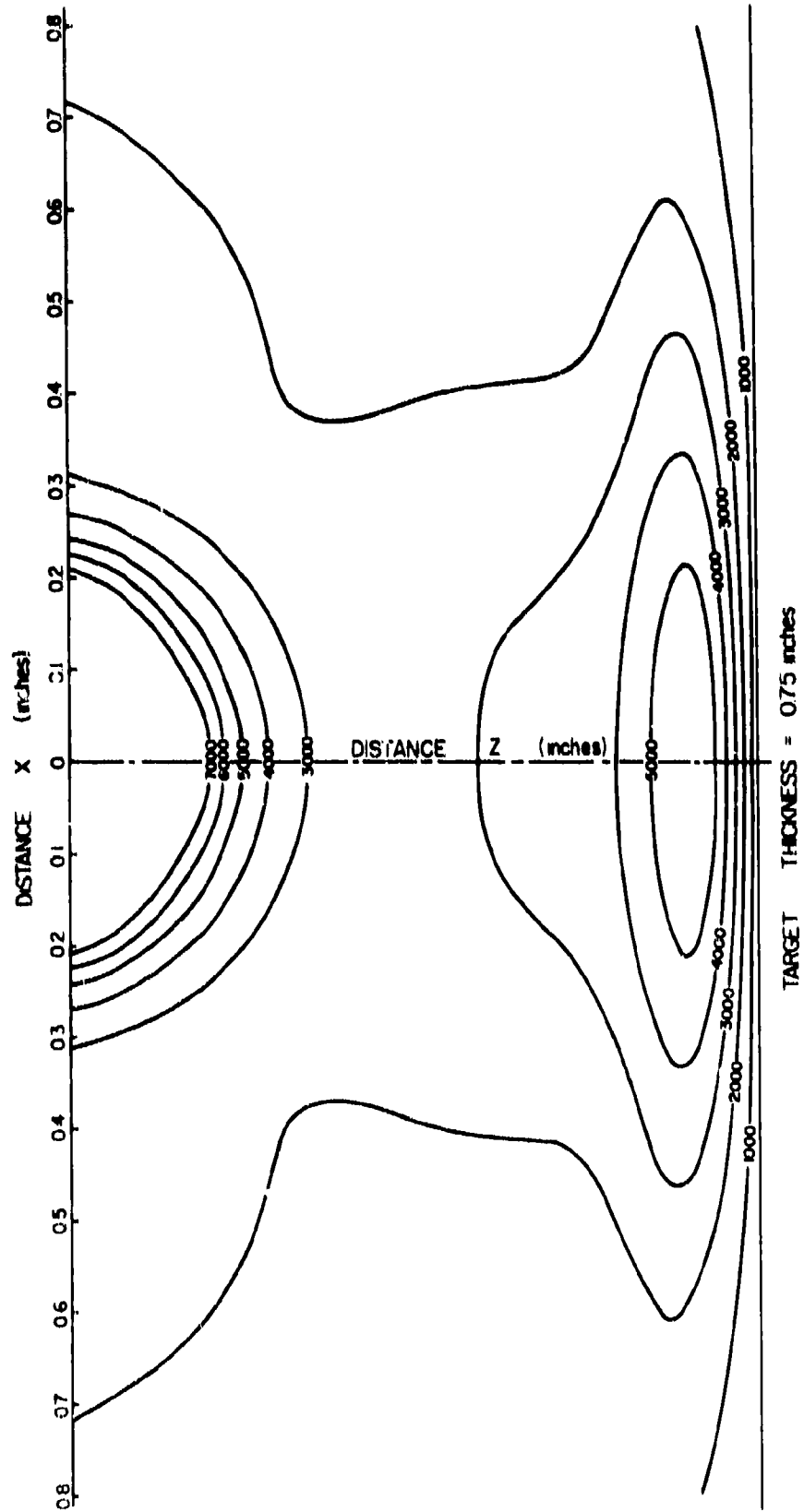


FIGURE 71. CONTOURS OF MAXIMUM TENSILE STRESS IN A 0.75-INCH TARGET

126<

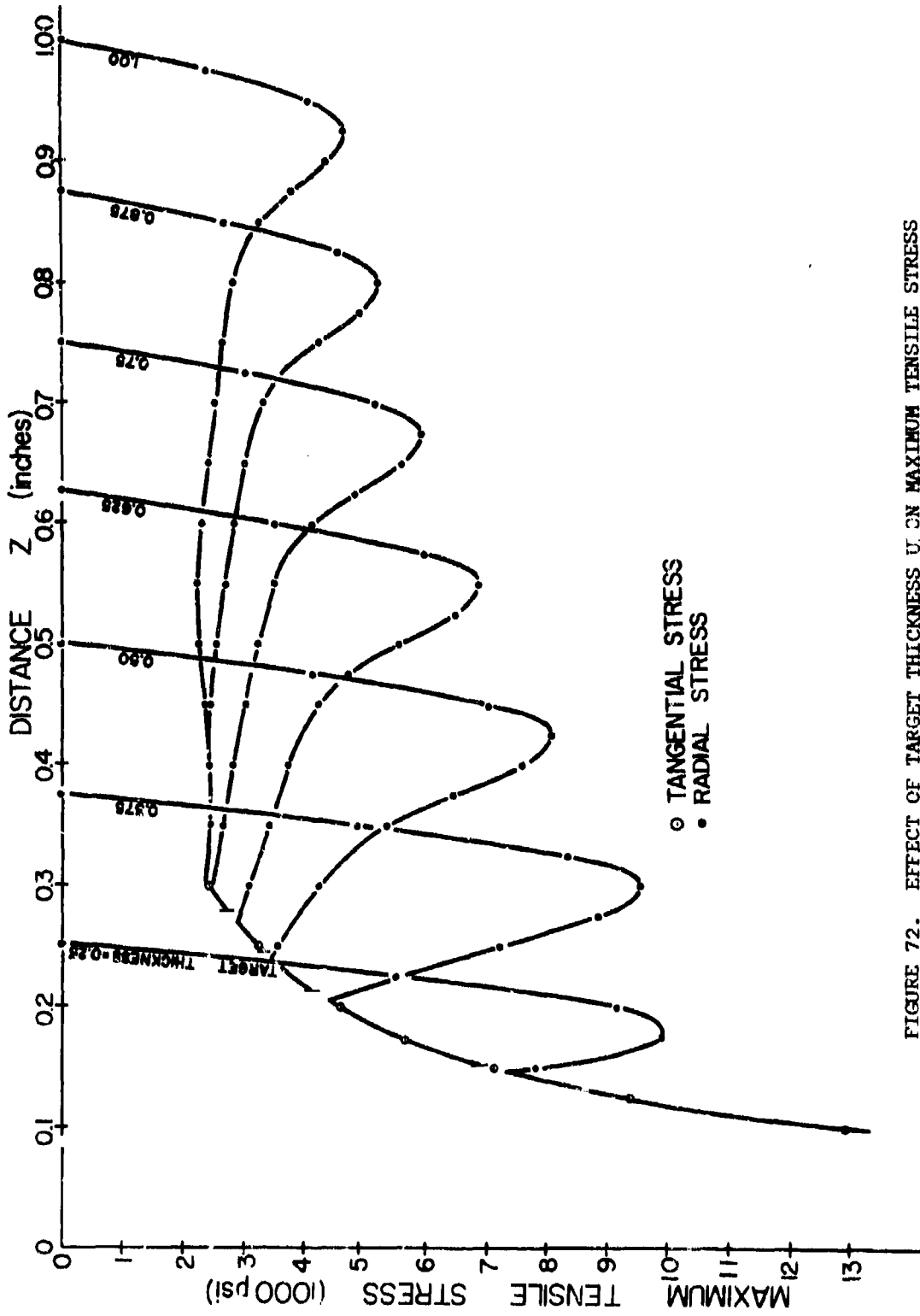


FIGURE 72. EFFECT OF TARGET THICKNESS U ON MAXIMUM TENSILE STRESS

127<

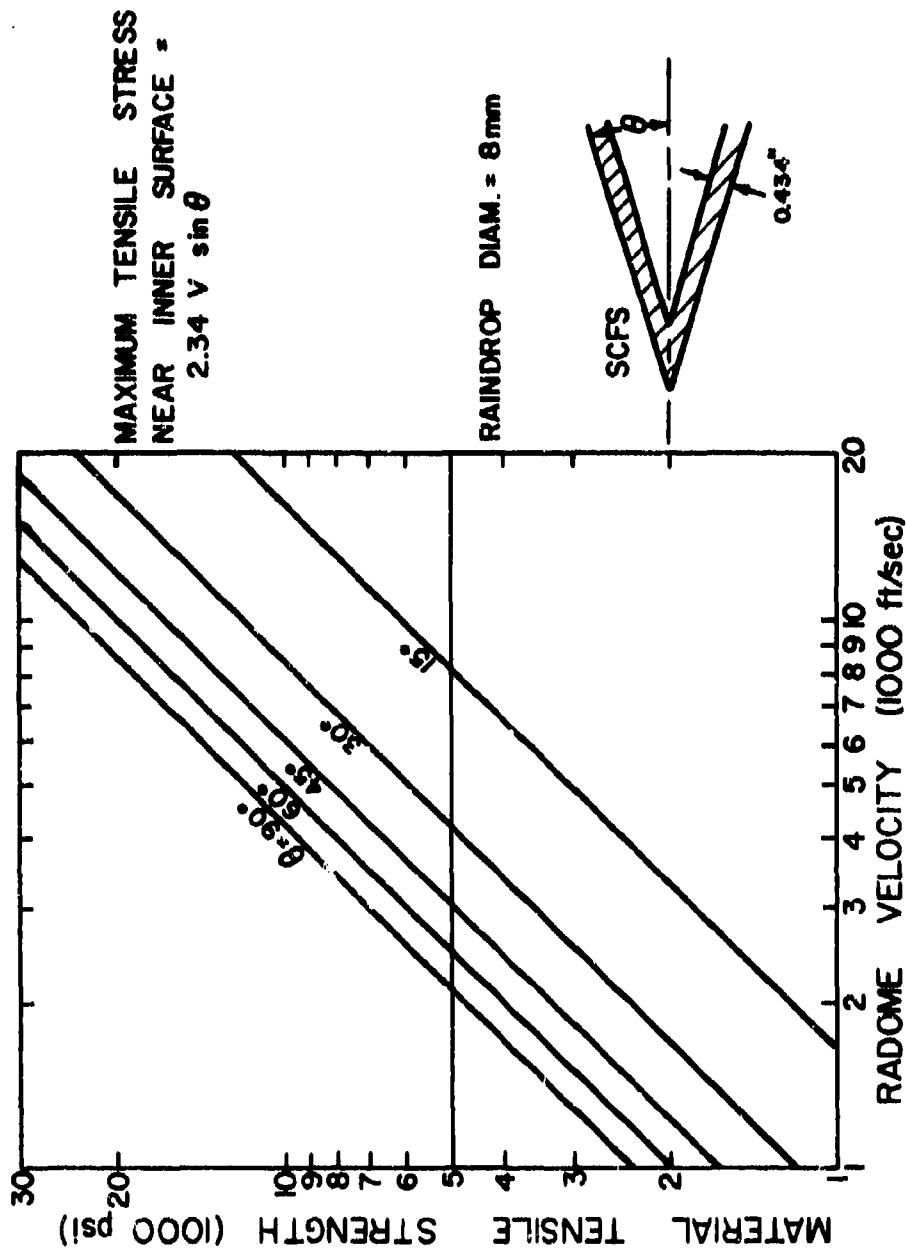


FIGURE 73. SPALLATION THRESHOLD AS A FUNCTION OF VELOCITY FOR A 0.434-INCH-THICK
 RADOME COLLIDING WITH AN 8-MM RAINDROP

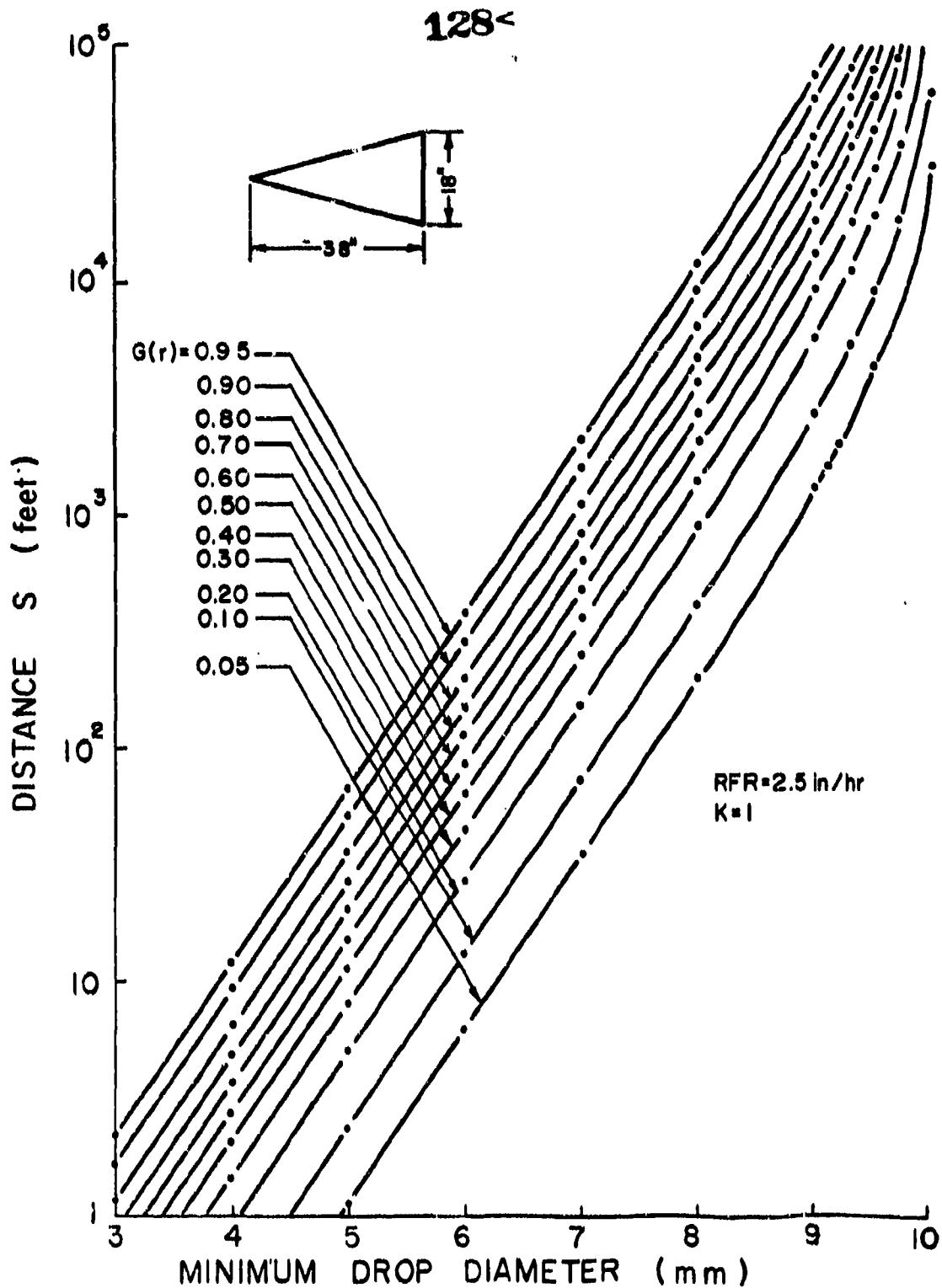


FIGURE 74. DROP DIAMETER-DISTANCE-PROBABILITY RELATION (RFR = 2.5 IN/HR)

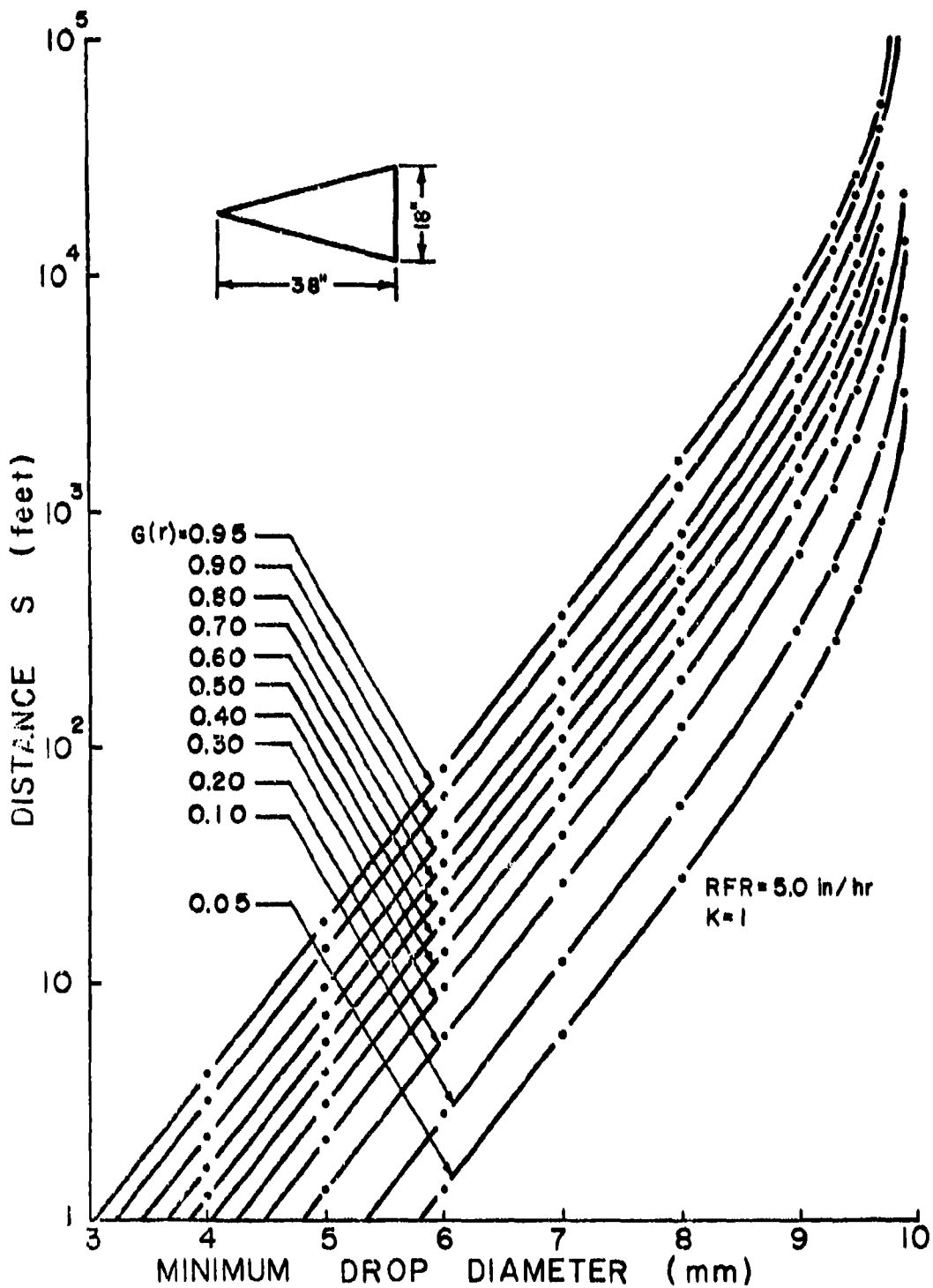


FIGURE 75. DROP DIAMETER-DISTANCE-PROBABILITY RELATION (RFR = 5.0 IN/HR)

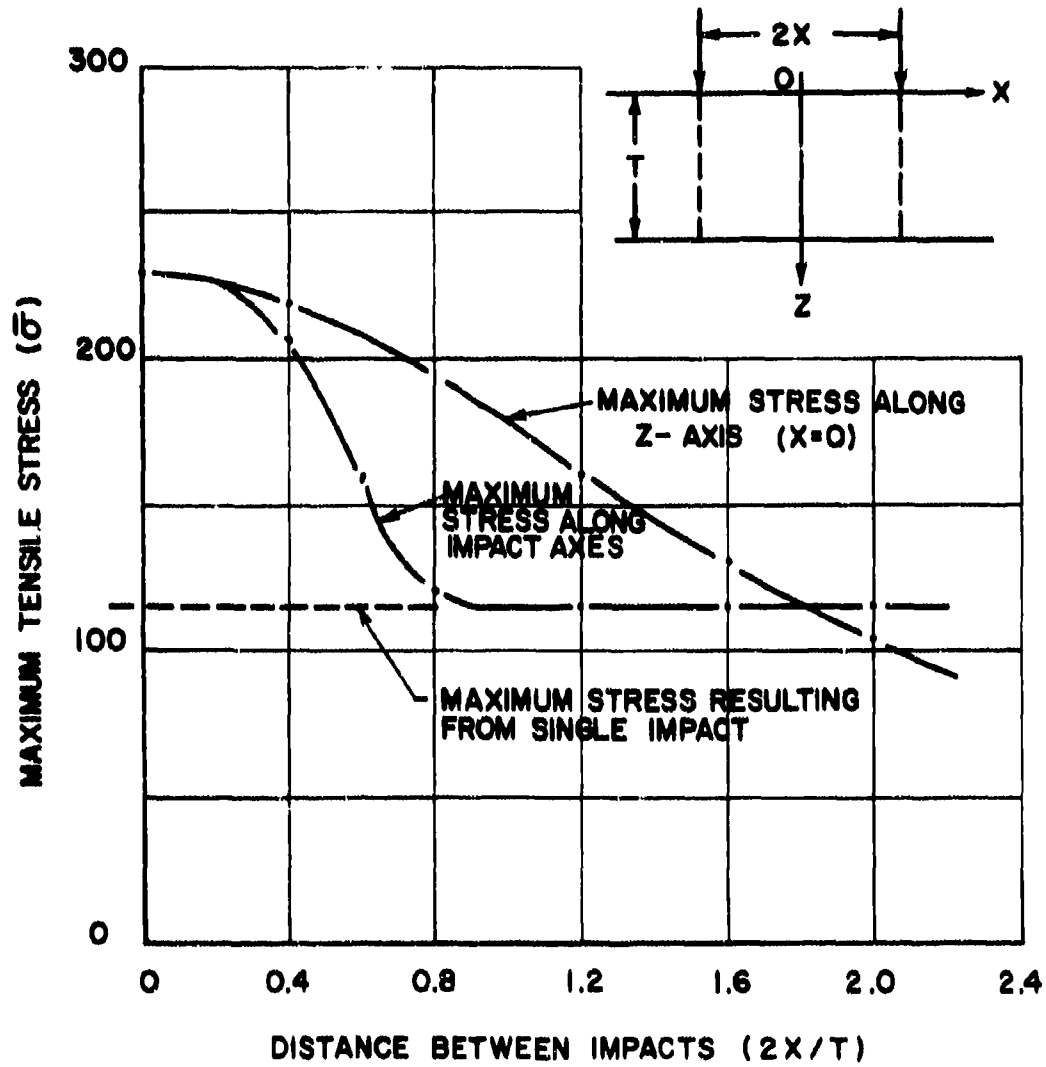


FIGURE 76. MAXIMUM TENSILE STRESS DUE TO REFLECTED WAVES RESULTING FROM SIMULTANEOUS IMPACTS

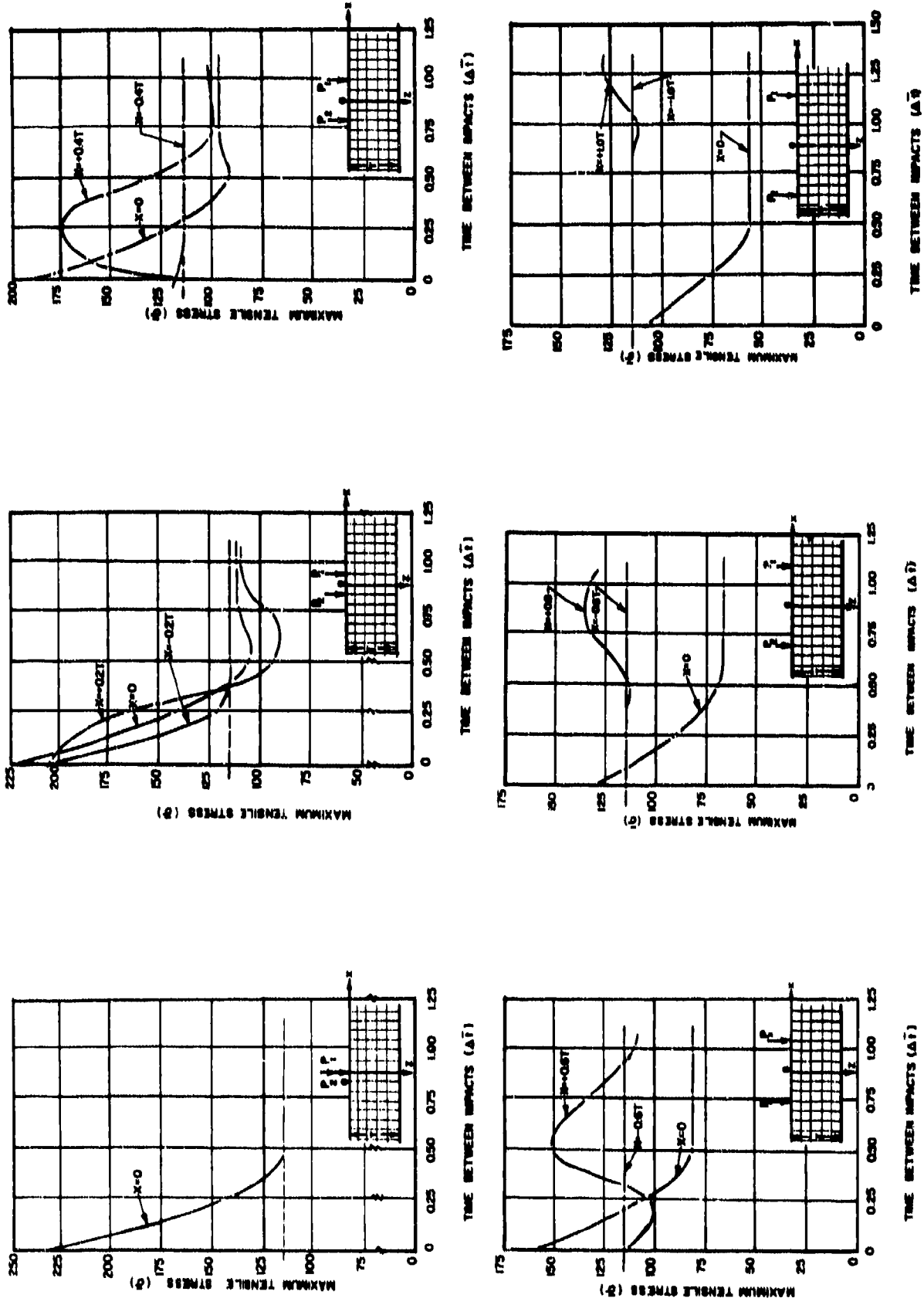


FIGURE 77. DEPENDENCE OF MAXIMUM STRESS UPON DISTANCE AND TIME BETWEEN IMPACTS

132<

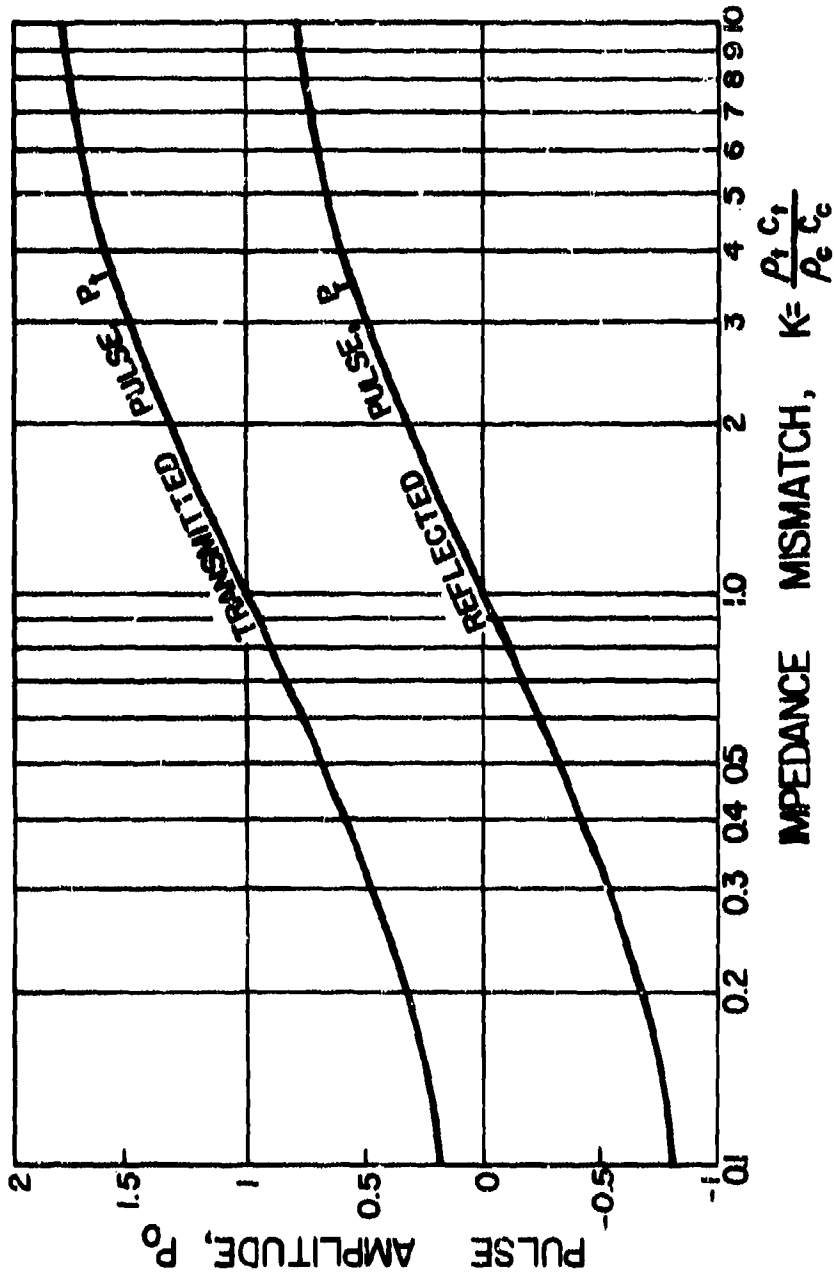


FIGURE 78. EFFECT OF IMPEDANCE MISMATCH UPON TRANSMITTED AND REFLECTED PULSE AMPLITUDES

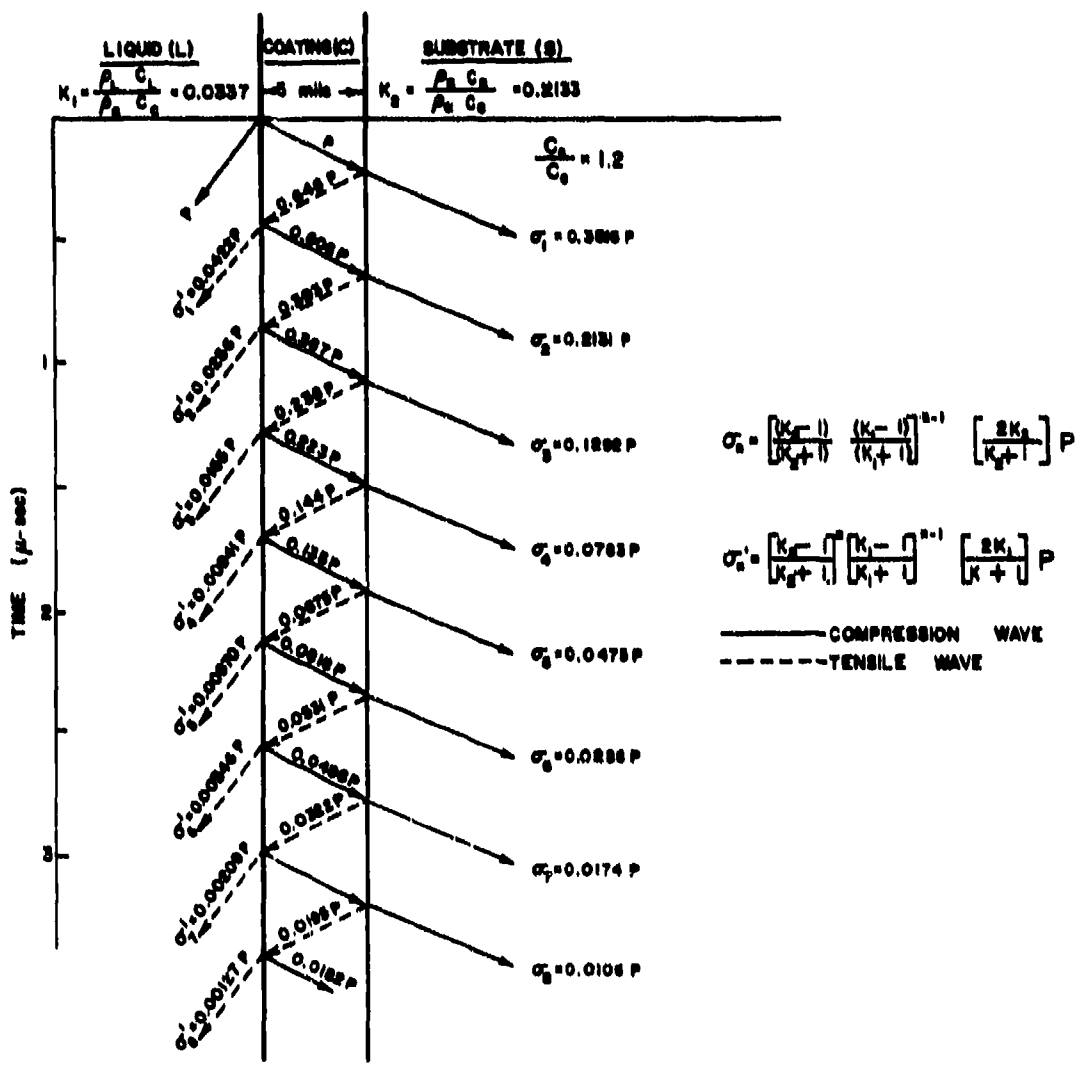


FIGURE 79. TRANSMITTED WAVES IN SUBSTRATE PRODUCED BY MULTIPLE REFLECTIONS IN COATING

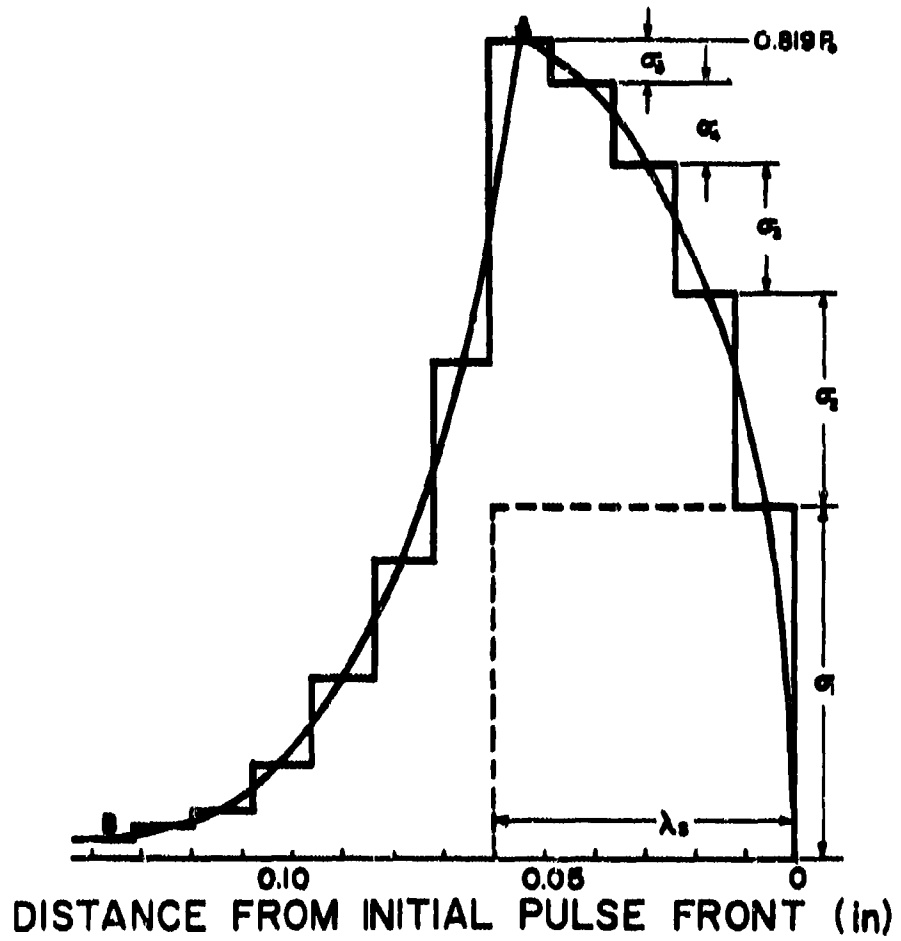


FIGURE 80. WAVE IN SUBSTRATE PRODUCED BY 0.05-INCH PULSE IN COATING

135<

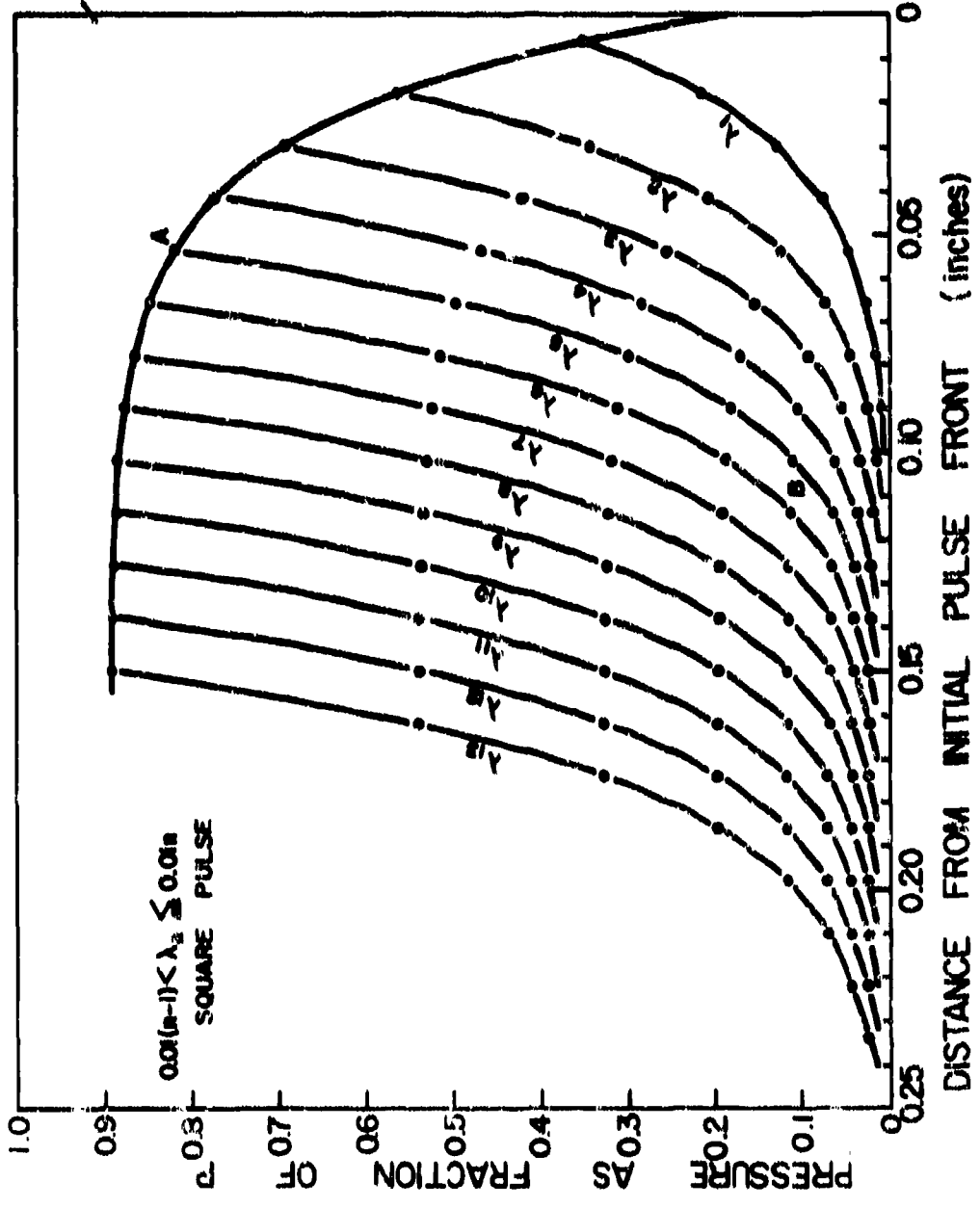


FIGURE 81. EFFECT OF THE PULSE LENGTH UPON THE TRANSMITTED WAVE IN THE SUBSTRATE

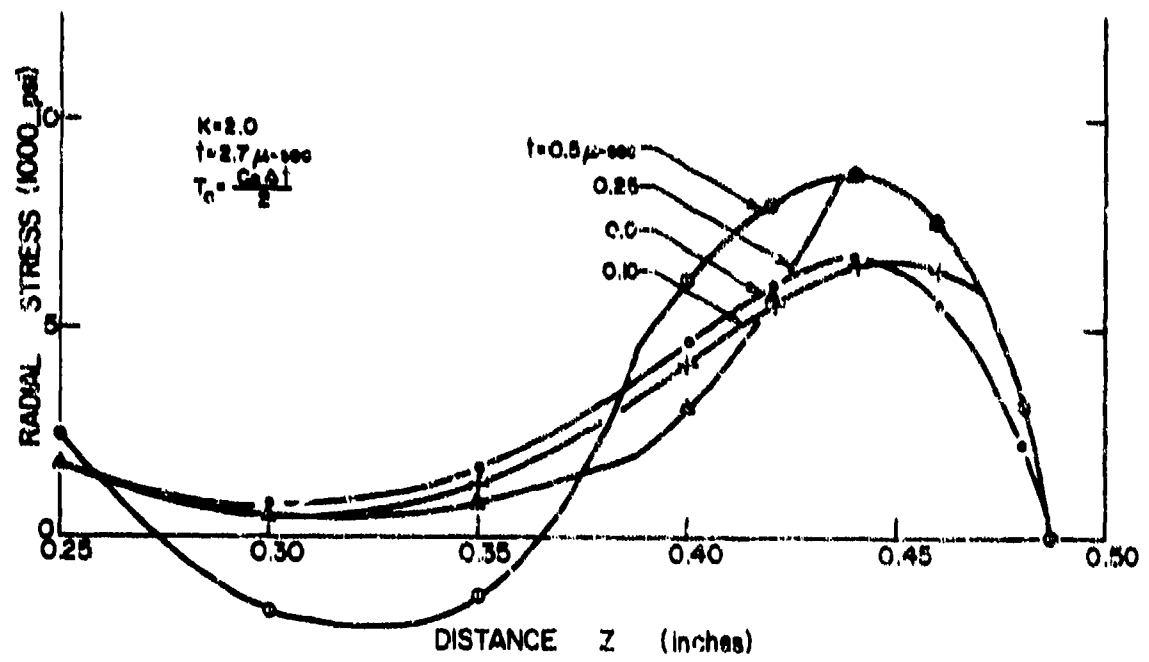
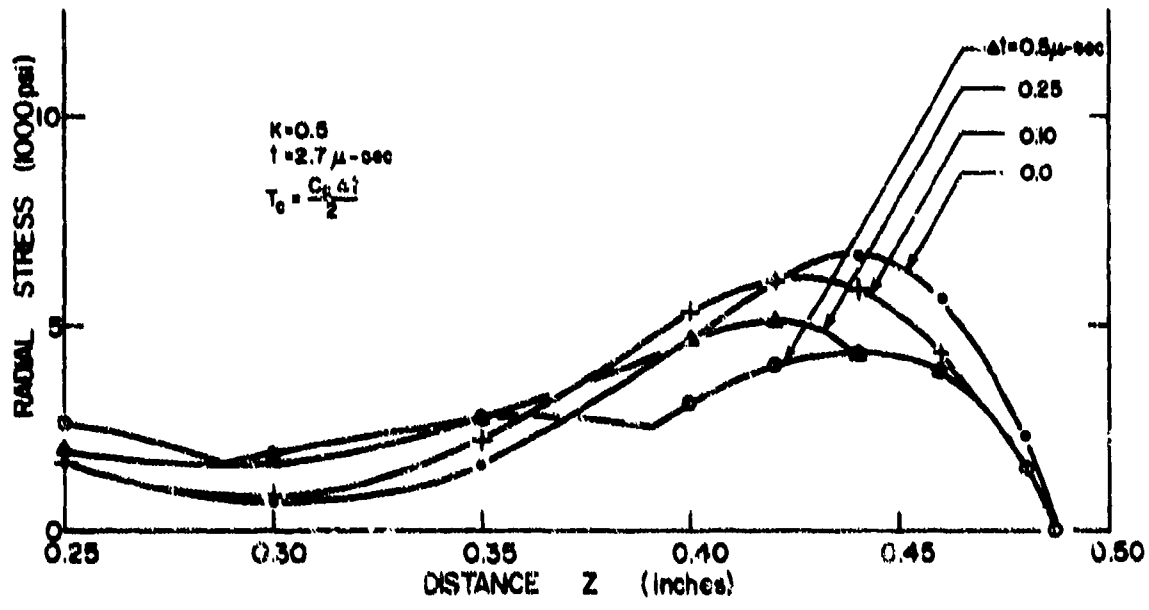


FIGURE 82. STRESS WAVE PROFILES IN COATED RADOMES

137<

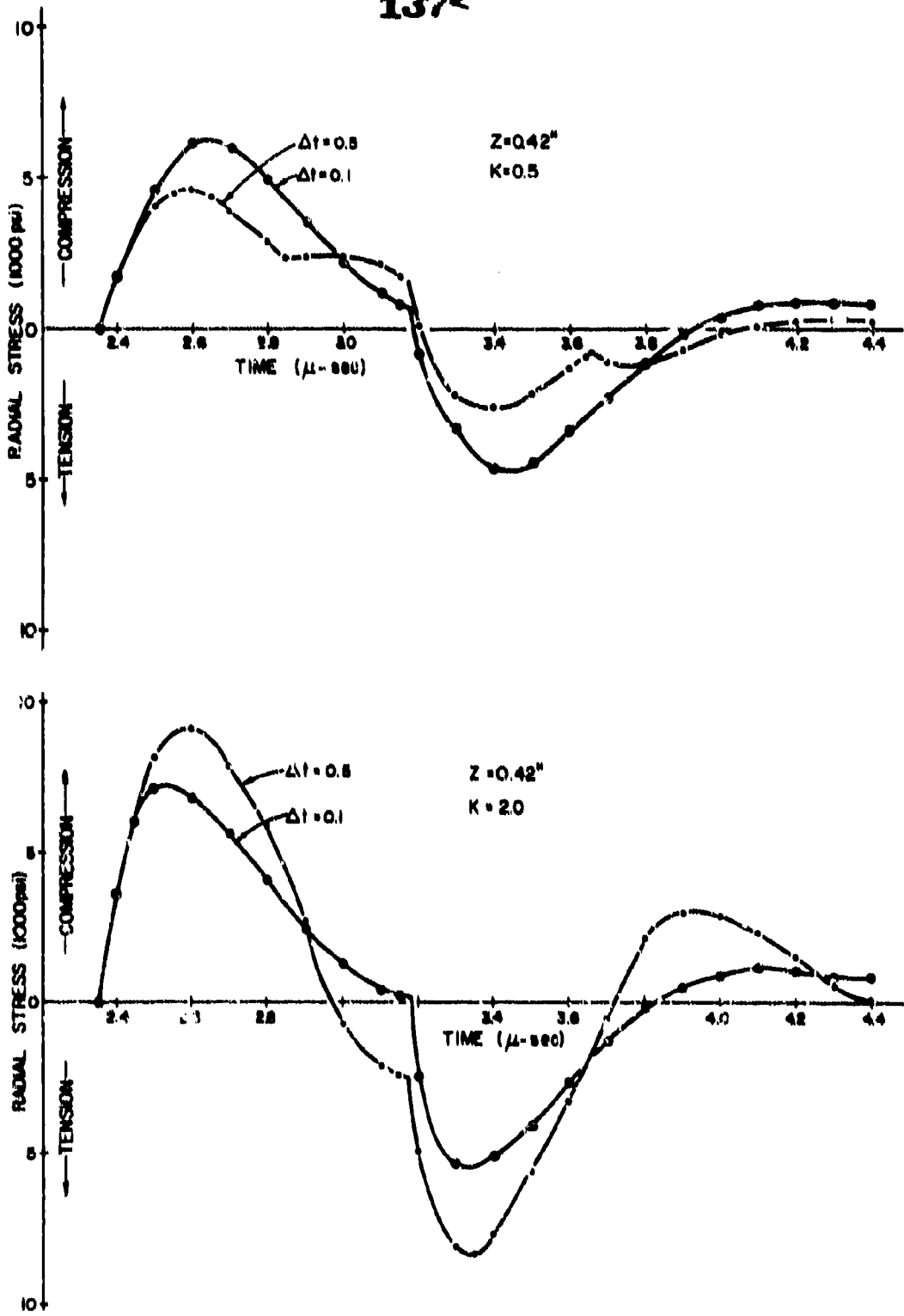


FIGURE 83. STRESS HISTORY AT A POINT IN A COATED RADOME

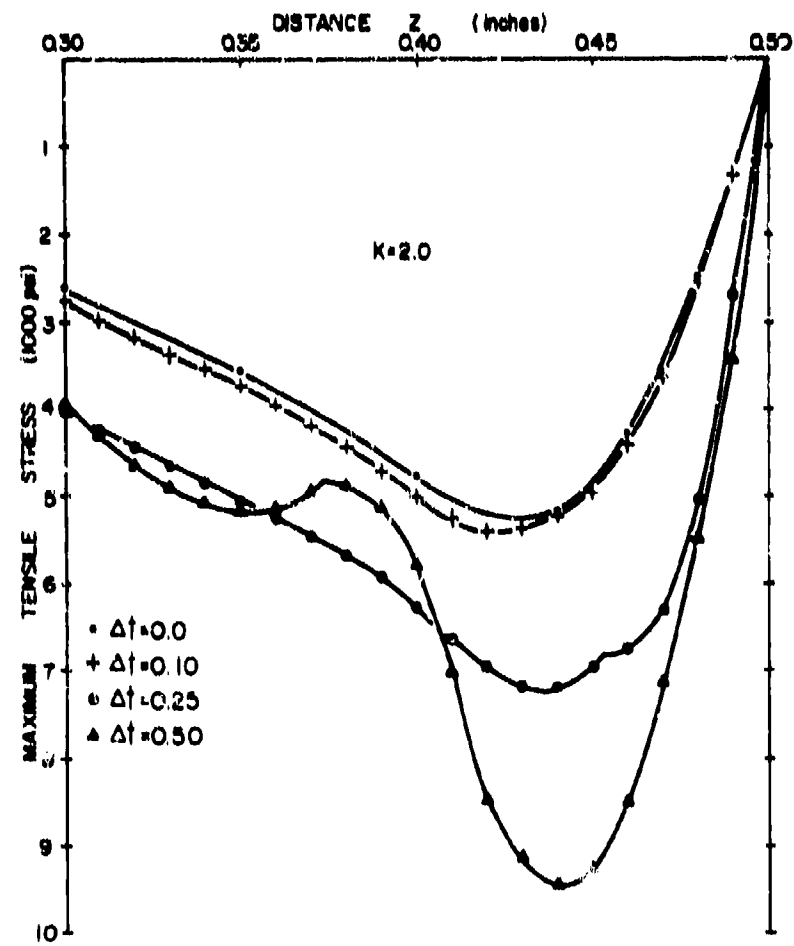
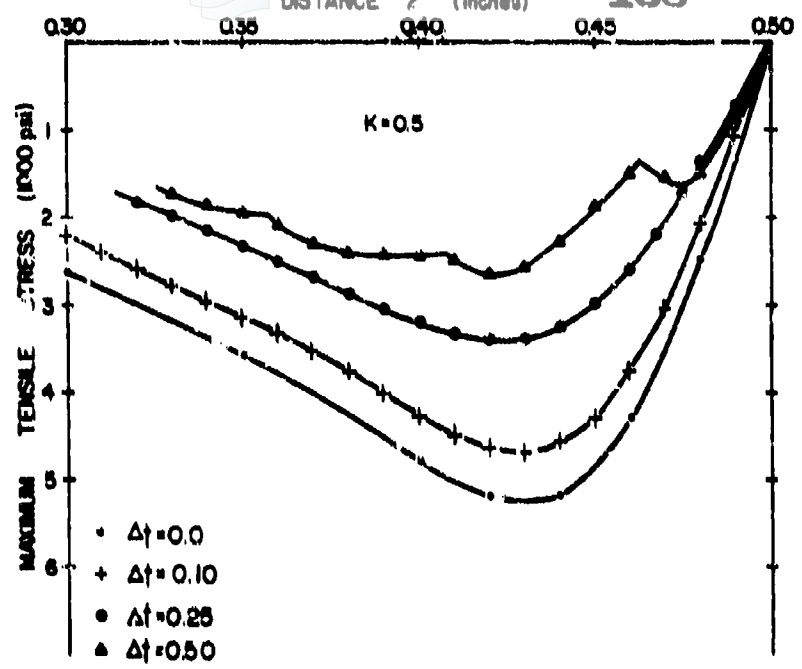


FIGURE 84. MAXIMUM TENSILE STRESSES IN COATED RADOMES

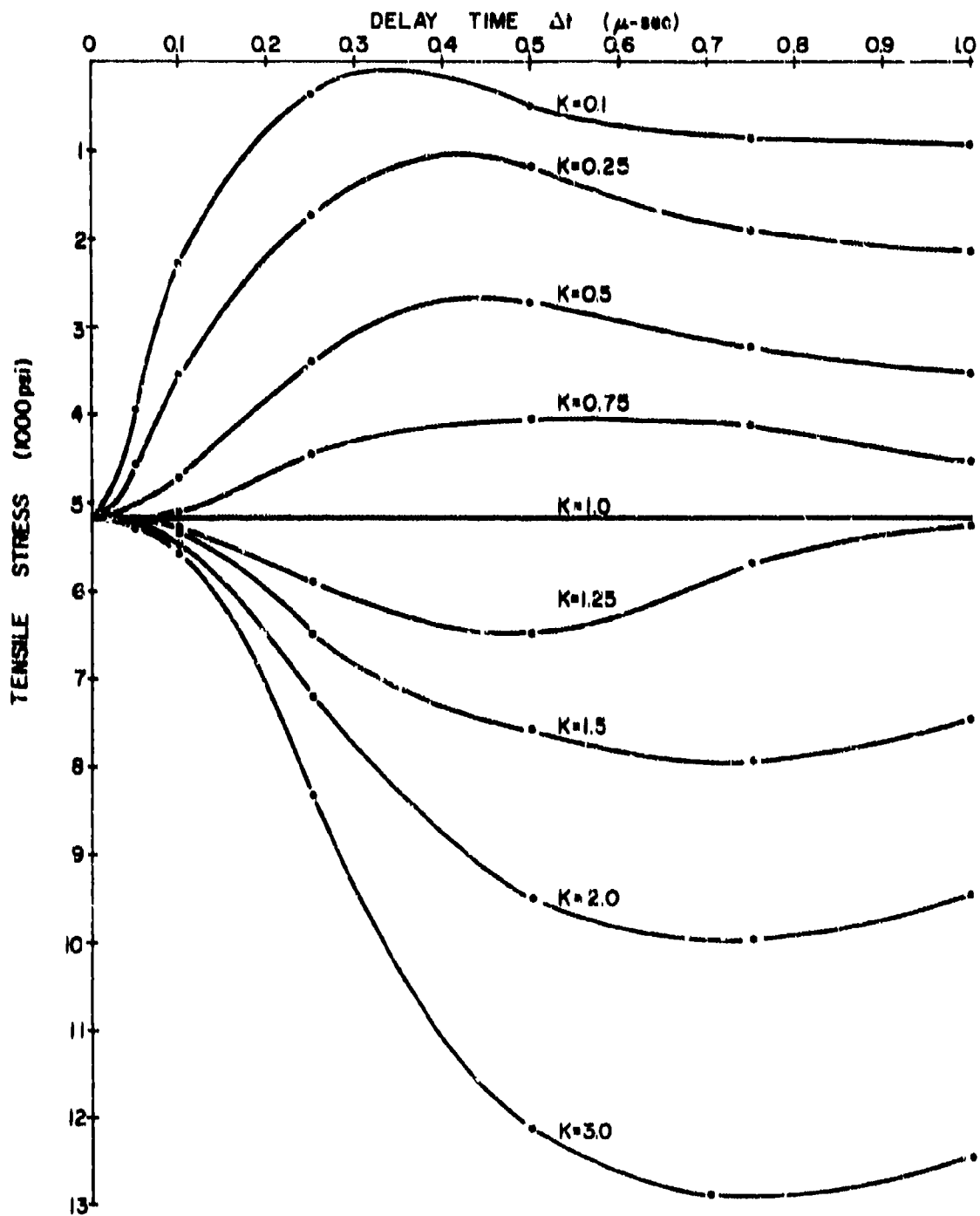


FIGURE 95. MAXIMUM TENSILE STRESS AS A FUNCTION OF K AND Δt

140<



FIGURE 86. RADOME ON SLED AFTER TEST AT HOLLOMAN AFB

141<

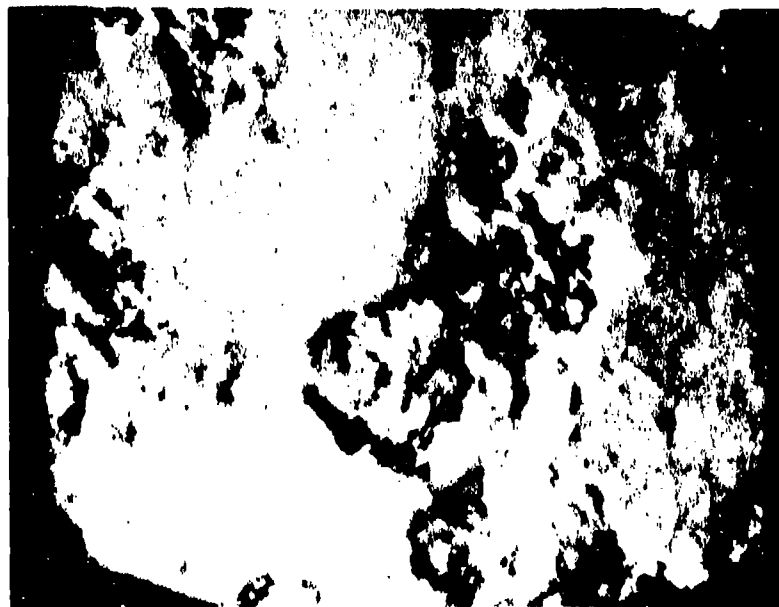


FIGURE 87. RA80ME AND CLOSE-UP OF CRATERS - 7RB1

142<

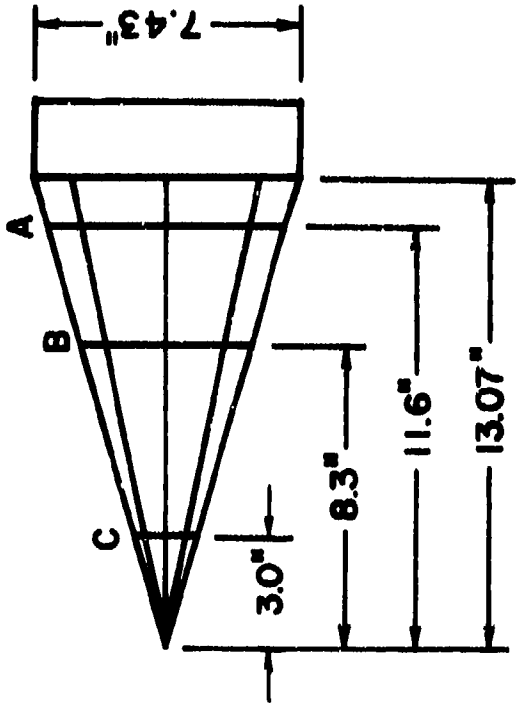
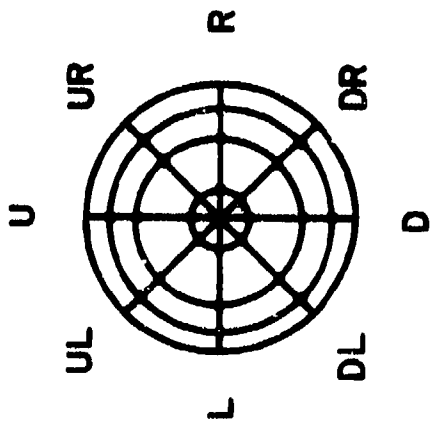
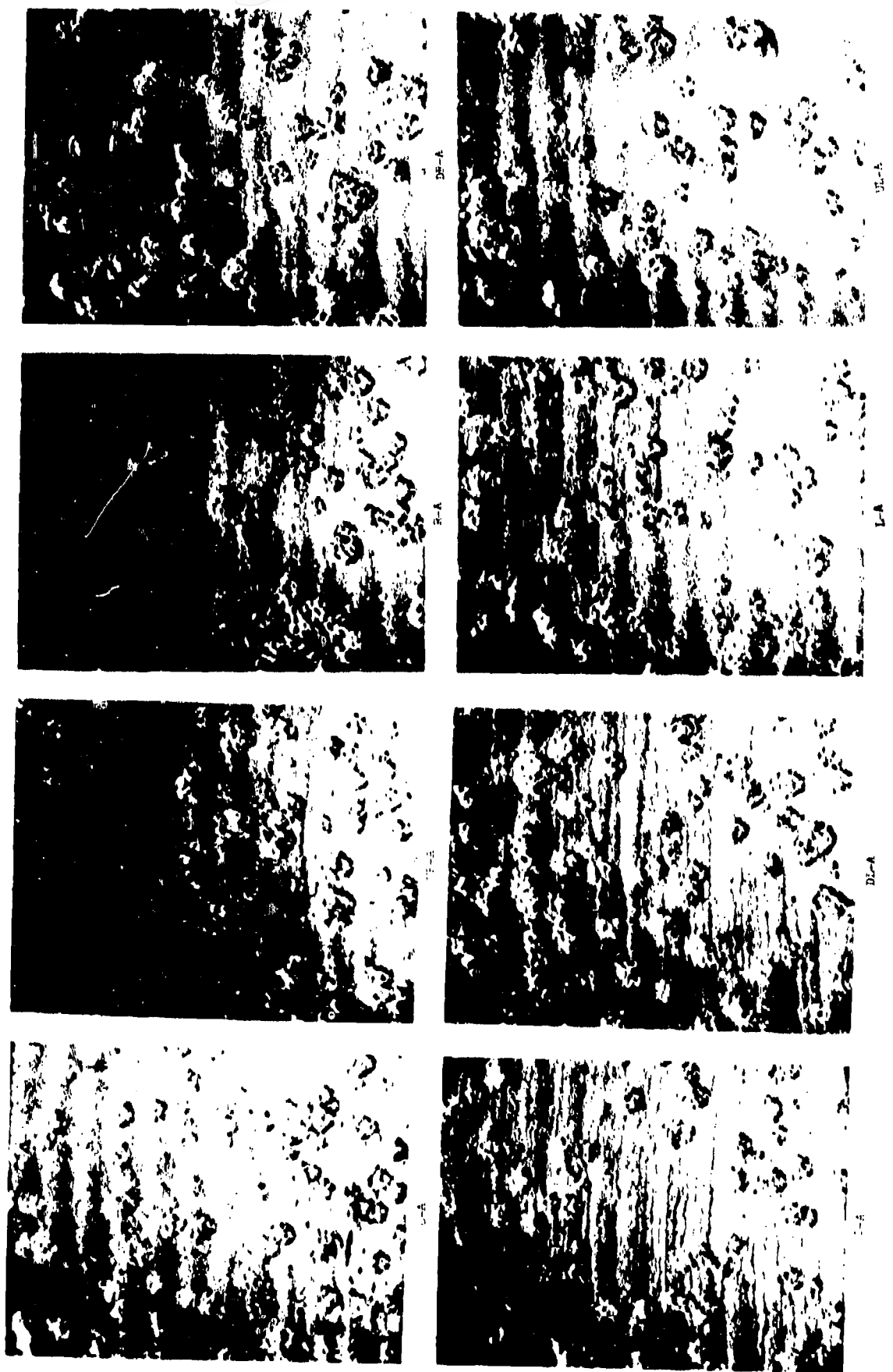


FIGURE 88. DIMENSIONS OF RADOME

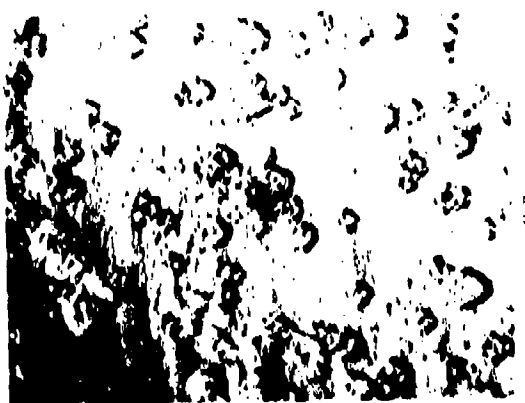
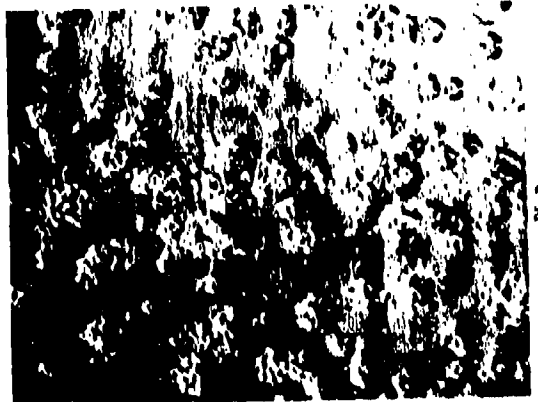
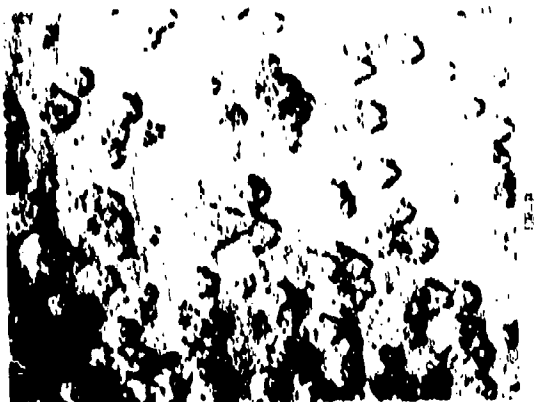
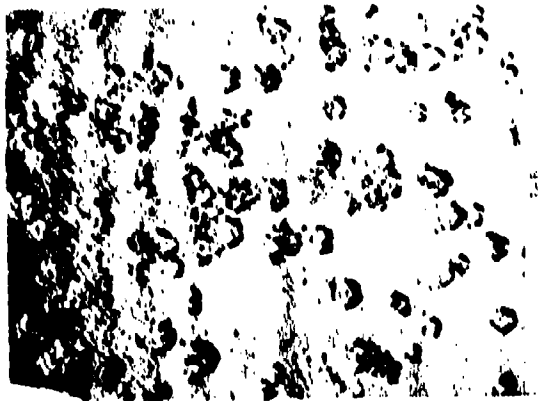
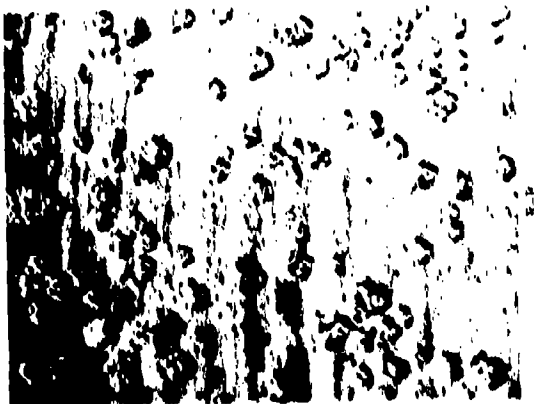
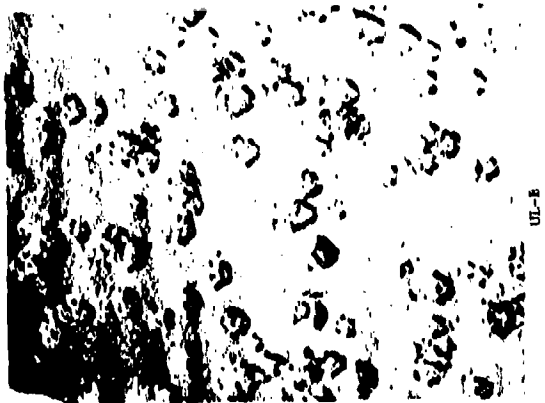
143<



1 of 10

FIGURE 89. PHOTOGRAPHS OF CRATERS NEAR BASE - 7RB1

144<



144
144-B

FIGURE 90. PHOTOGRAPHS OF CRATERS NEAR MID-SECTION - 7RBI

1.15<



FIGURE 91. PHOTOGRAPHS OF CRATERS NEAR TIP - 7RB1

146-



Reproduced from
best available copy.

FIG. 1. MECHANICAL PARTS OF THE

147<

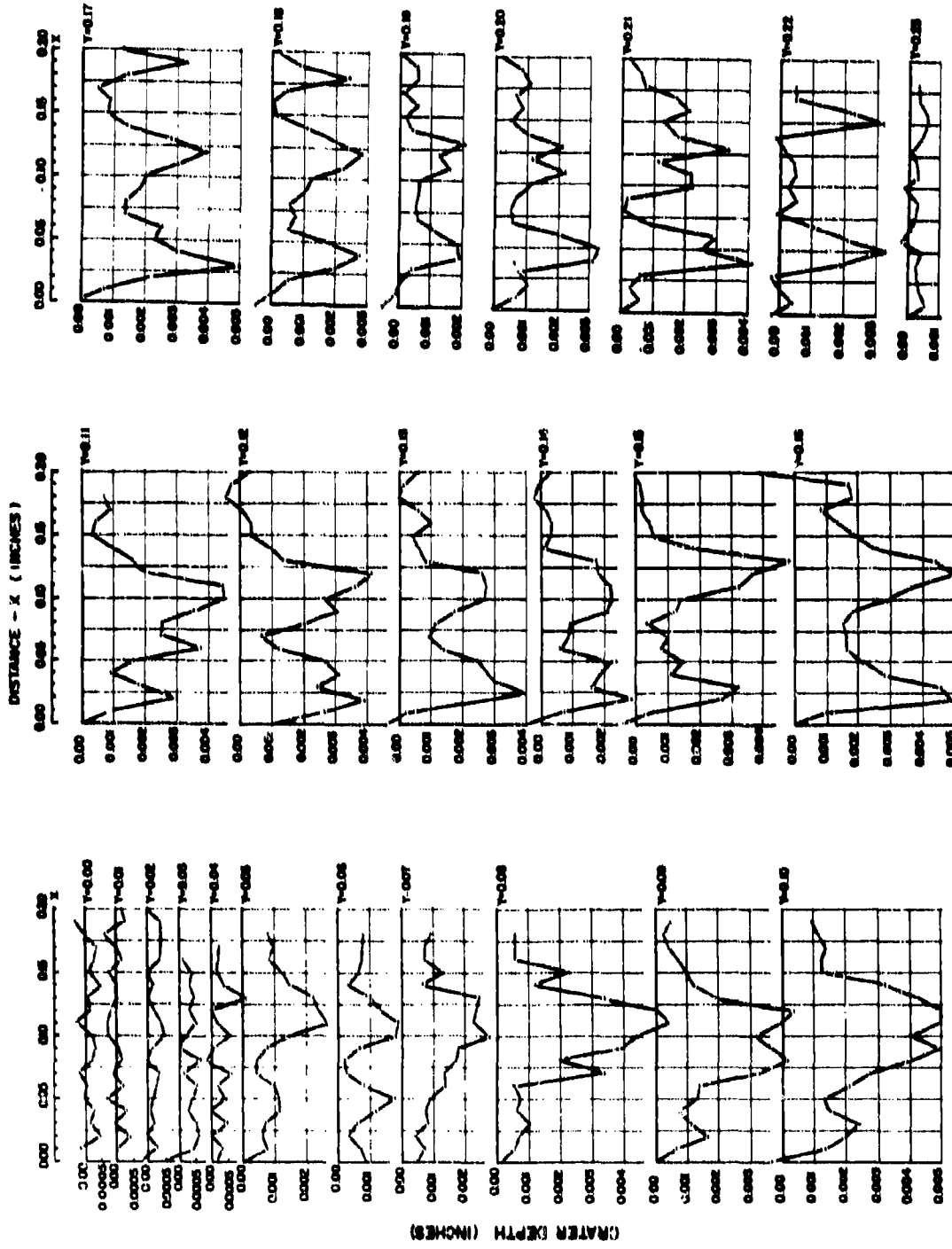


FIGURE 93. CRATER CROSS-SECTIONS

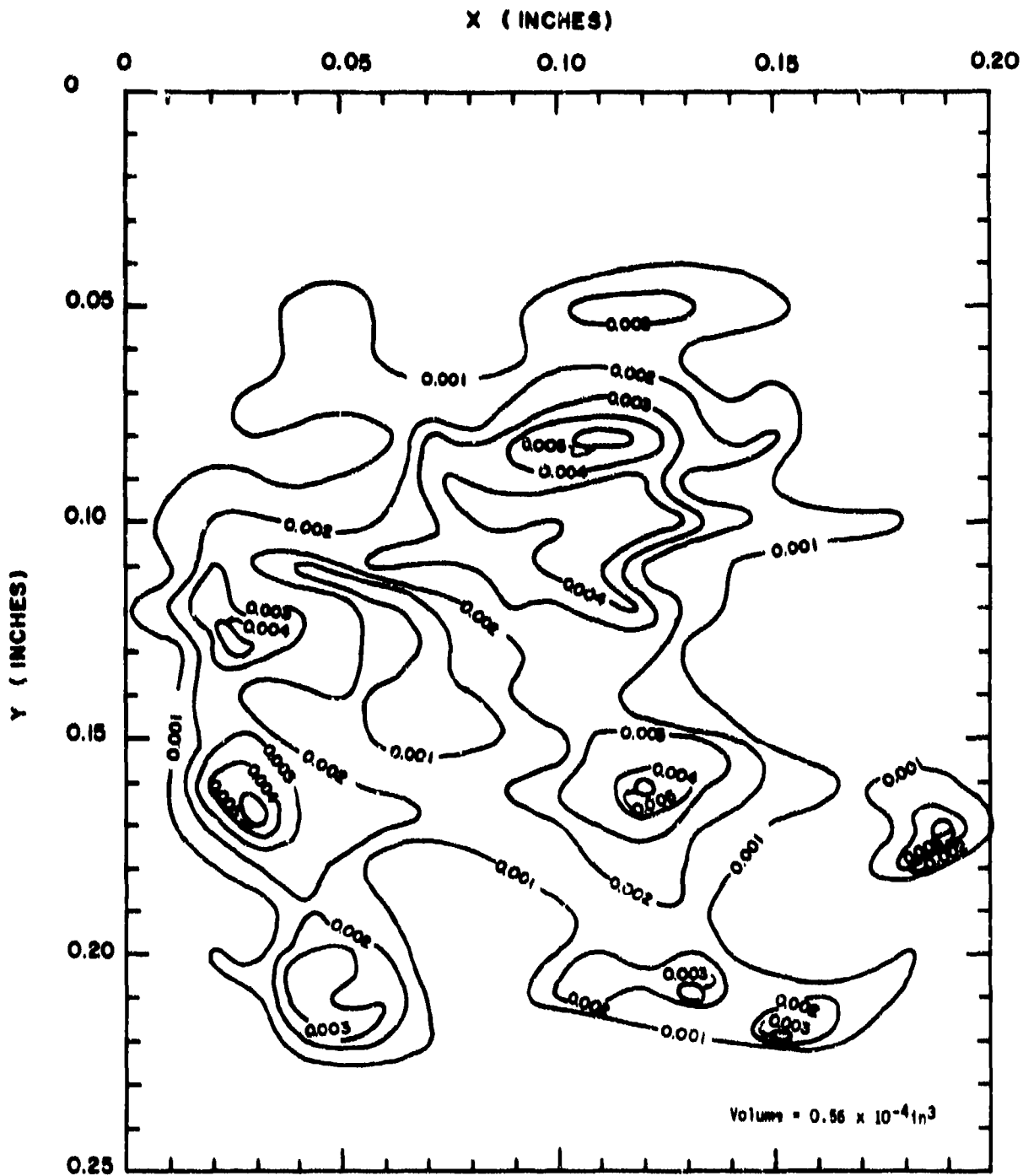


FIGURE 94. DEPTH CONTOURS

149<

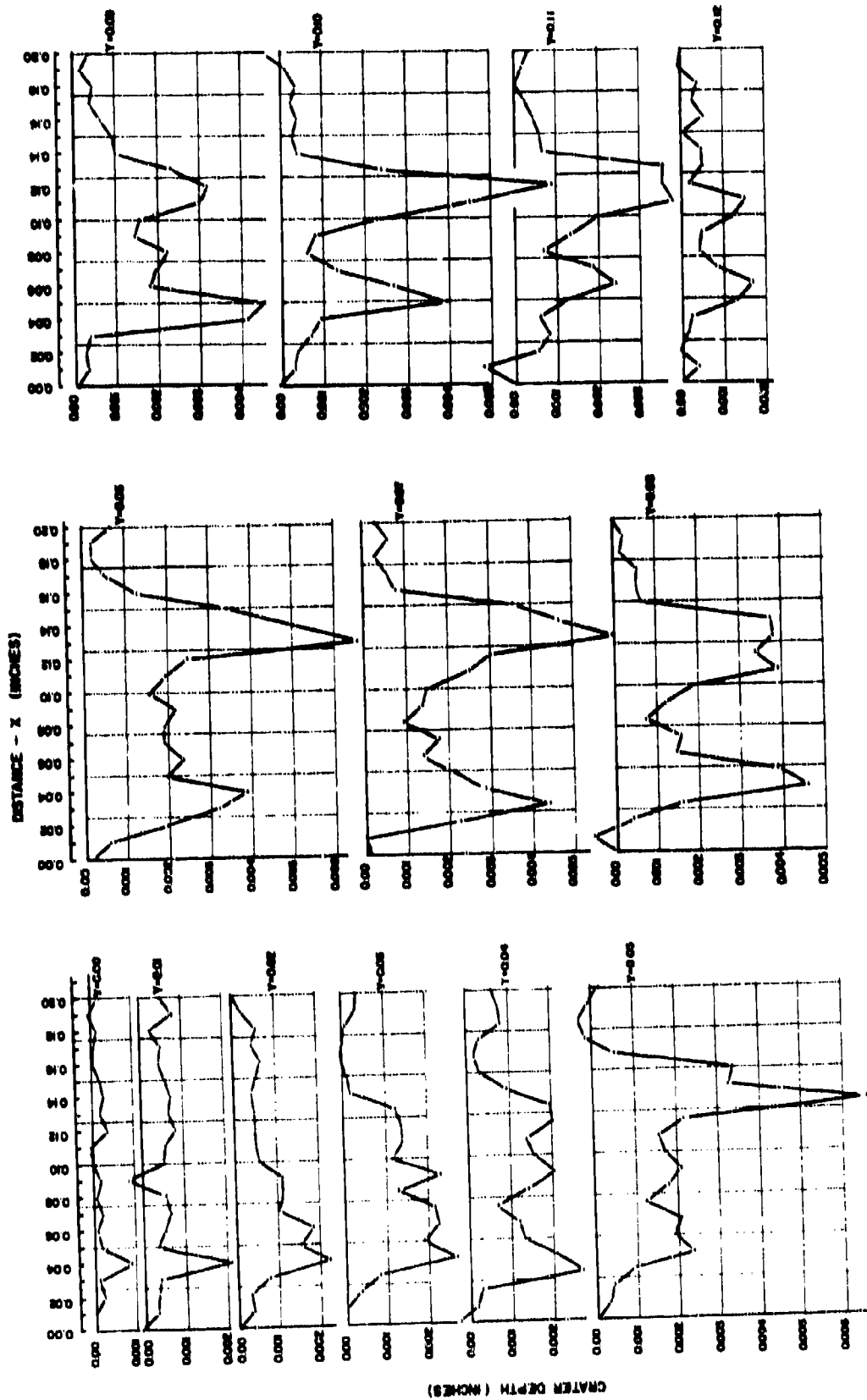


FIGURE 95. CRATER CROSS-SECTIONS

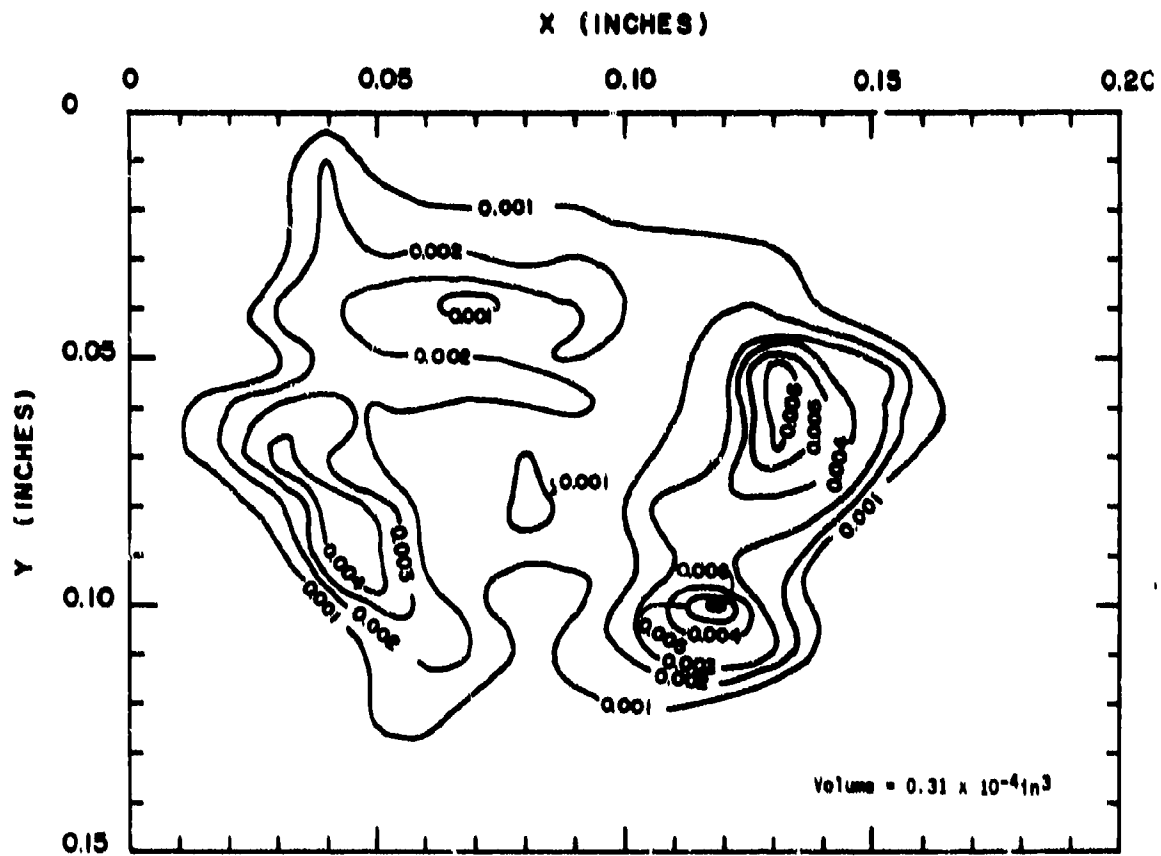


FIGURE 96. DEPTH CONTOURS

151<

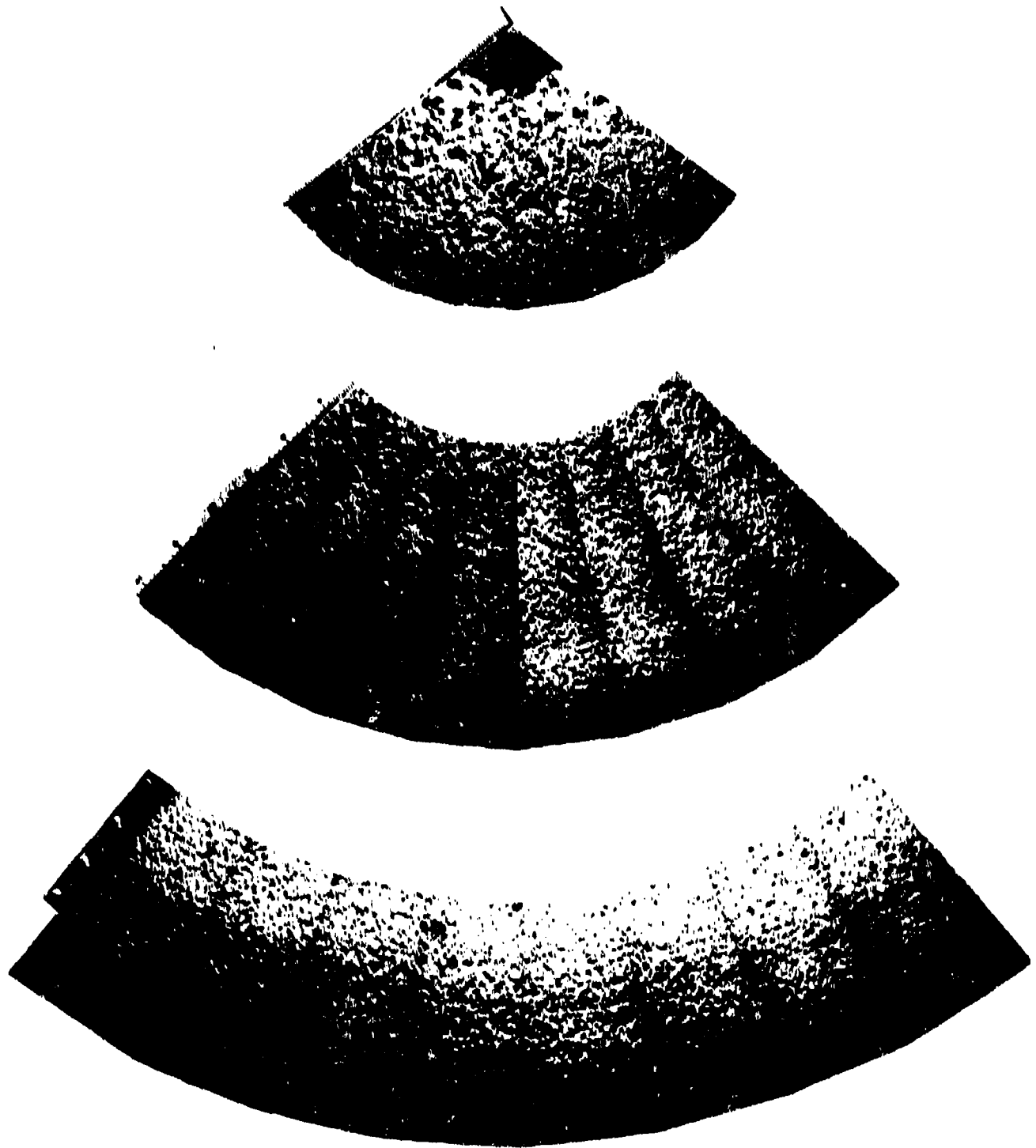


FIGURE 97. COMPOSITE OF PHOTOGRAPH MADE OF ERODED SURFACE OF RADOME 7RD1

152<

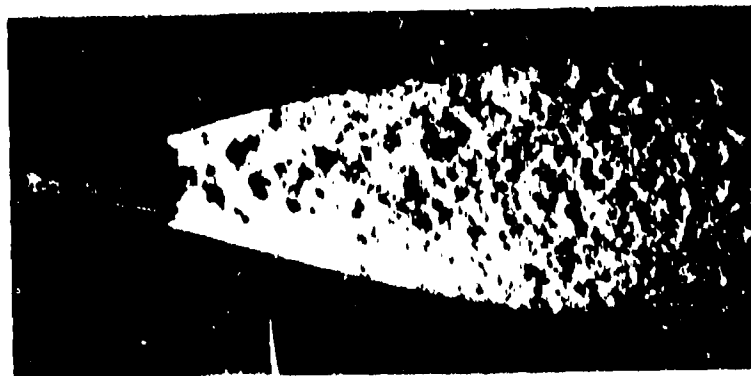
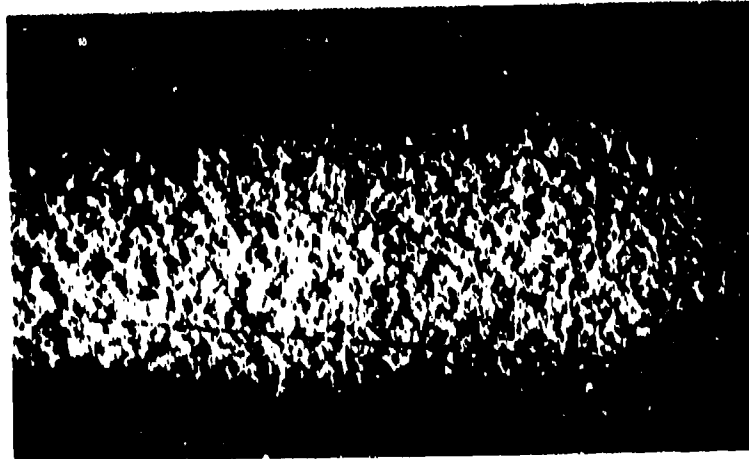
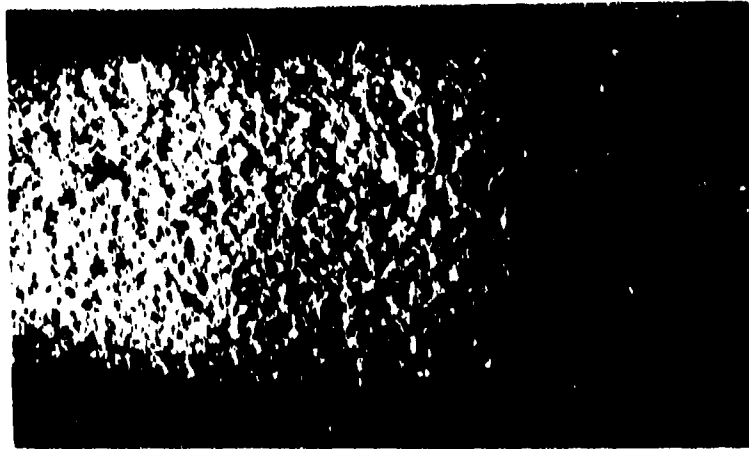


FIG. 1

FIG. 2

153<

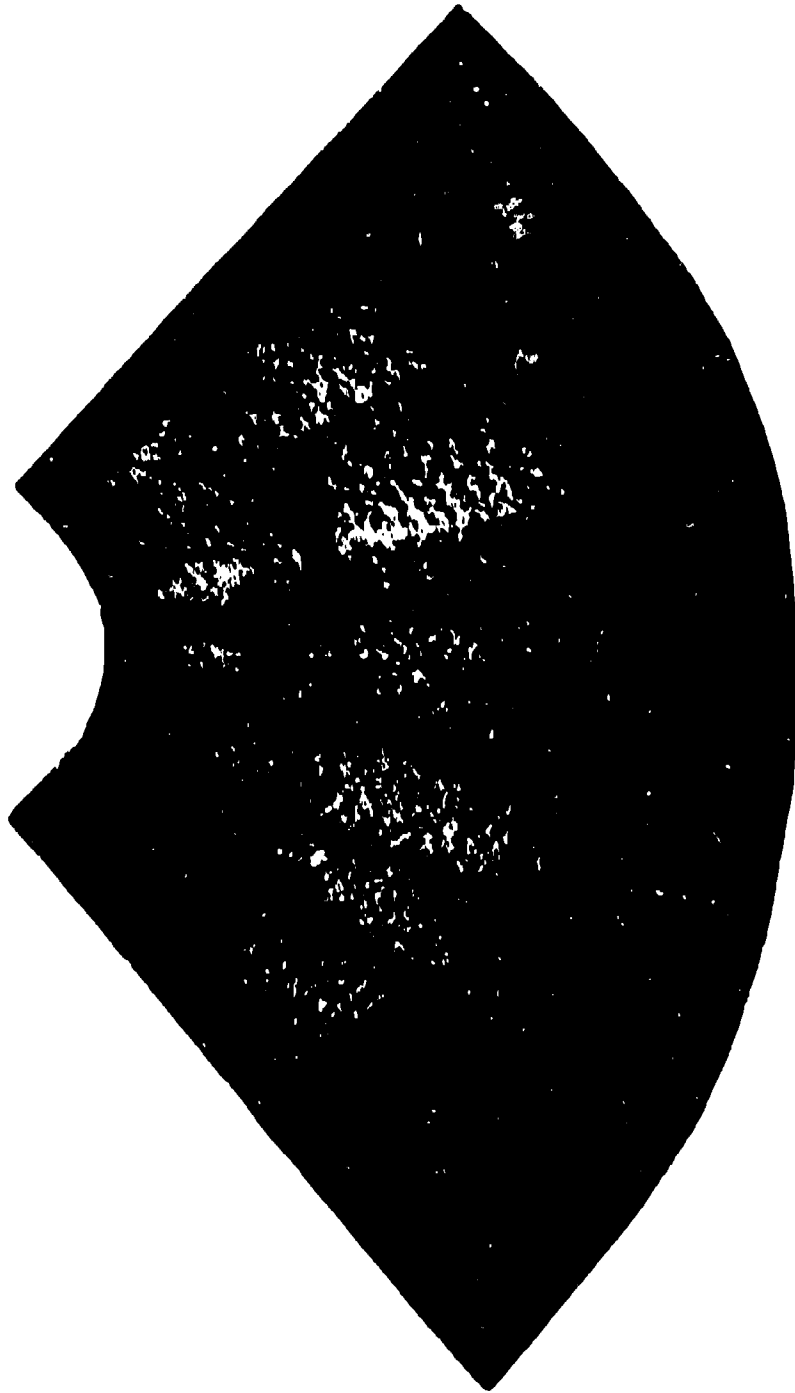


FIGURE 10. 100X. 11. 100X. 100X. 100X. 100X. 100X. 100X. 100X. 100X. 100X.

154<

TABLE 1
 MULTIPLE IMPACTS - SCFS

<u>Number of Impacts</u>	<u>Fraction of Total Surface Eroded</u>	<u>Volume of Material Removed (10^{-4}in^3)</u>	<u>Average Volume per Impact (V)</u>	<u>V/V₁ Measured</u>	<u>V/V₁ Computed</u>
5	0.138	66.5	13.30	1.30	1.29
10	0.275	154.5	15.45	1.52	1.55
15	0.413	271.5	18.10	1.78	1.74
20	0.550	377.2	18.86	1.85	1.88
25	0.687	487.9	19.52	1.91	1.96

Notes: Target #1

Jet Energy = 25 ft-lb

V₁ = Volume of a single isolated crater ($10.2 \times 10^{-4} \text{in}^3$)

TABLE 2. VARIATION OF CALCULATED RADOME EROSION WITH RAINFIELD LENGTH AND INTENSITY

VELOCITY=2500 FT/SEC THETA=15 DEGREES

RPM	1-400 RPM		2-400 RPM		3-400 RPM		4-400 RPM	
	DISTANCE (FT)	WT. AMT	DISTANCE (FT)	WT. AMT	DISTANCE (FT)	WT. AMT	DISTANCE (FT)	WT. AMT
1000	1000	1.00	1000	1.00	1000	1.00	1000	1.00
1100	1100	1.10	1100	1.10	1100	1.10	1100	1.10
1200	1200	1.20	1200	1.20	1200	1.20	1200	1.20
1300	1300	1.30	1300	1.30	1300	1.30	1300	1.30
1400	1400	1.40	1400	1.40	1400	1.40	1400	1.40
1500	1500	1.50	1500	1.50	1500	1.50	1500	1.50
1600	1600	1.60	1600	1.60	1600	1.60	1600	1.60
1700	1700	1.70	1700	1.70	1700	1.70	1700	1.70
1800	1800	1.80	1800	1.80	1800	1.80	1800	1.80
1900	1900	1.90	1900	1.90	1900	1.90	1900	1.90
2000	2000	2.00	2000	2.00	2000	2.00	2000	2.00
2100	2100	2.10	2100	2.10	2100	2.10	2100	2.10
2200	2200	2.20	2200	2.20	2200	2.20	2200	2.20
2300	2300	2.30	2300	2.30	2300	2.30	2300	2.30
2400	2400	2.40	2400	2.40	2400	2.40	2400	2.40
2500	2500	2.50	2500	2.50	2500	2.50	2500	2.50
2600	2600	2.60	2600	2.60	2600	2.60	2600	2.60
2700	2700	2.70	2700	2.70	2700	2.70	2700	2.70
2800	2800	2.80	2800	2.80	2800	2.80	2800	2.80
2900	2900	2.90	2900	2.90	2900	2.90	2900	2.90
3000	3000	3.00	3000	3.00	3000	3.00	3000	3.00
3100	3100	3.10	3100	3.10	3100	3.10	3100	3.10
3200	3200	3.20	3200	3.20	3200	3.20	3200	3.20
3300	3300	3.30	3300	3.30	3300	3.30	3300	3.30
3400	3400	3.40	3400	3.40	3400	3.40	3400	3.40
3500	3500	3.50	3500	3.50	3500	3.50	3500	3.50
3600	3600	3.60	3600	3.60	3600	3.60	3600	3.60
3700	3700	3.70	3700	3.70	3700	3.70	3700	3.70
3800	3800	3.80	3800	3.80	3800	3.80	3800	3.80
3900	3900	3.90	3900	3.90	3900	3.90	3900	3.90
4000	4000	4.00	4000	4.00	4000	4.00	4000	4.00

TABLE 2. VARIATION OF CALCULATED RADOME EROSION WITH
RAINFIELD LENGTH AND INTENSITY (CONTINUED)

VELOCITY-2500 FT/SEC THETA-60 DEGREES

RPM	4000 FT/SEC		VOLUME (1/100000000)	DR (1/100000)	ENVIRONMENTAL INDEX	DR (1/100000)	VOLUME (1/100000000)	5000 FT/SEC		ENVIRONMENTAL INDEX
	DEPTH (FT)	WT (LBS)								
3000	3.00	15.00	1.00	1.00	1.00	1.00	1.00	3.00	15.00	1.00
3100	3.10	15.50	1.05	1.05	1.05	1.05	1.05	3.10	15.50	1.05
3200	3.20	16.00	1.10	1.10	1.10	1.10	1.10	3.20	16.00	1.10
3300	3.30	16.50	1.15	1.15	1.15	1.15	1.15	3.30	16.50	1.15
3400	3.40	17.00	1.20	1.20	1.20	1.20	1.20	3.40	17.00	1.20
3500	3.50	17.50	1.25	1.25	1.25	1.25	1.25	3.50	17.50	1.25
3600	3.60	18.00	1.30	1.30	1.30	1.30	1.30	3.60	18.00	1.30
3700	3.70	18.50	1.35	1.35	1.35	1.35	1.35	3.70	18.50	1.35
3800	3.80	19.00	1.40	1.40	1.40	1.40	1.40	3.80	19.00	1.40
3900	3.90	19.50	1.45	1.45	1.45	1.45	1.45	3.90	19.50	1.45
4000	4.00	20.00	1.50	1.50	1.50	1.50	1.50	4.00	20.00	1.50
4100	4.10	20.50	1.55	1.55	1.55	1.55	1.55	4.10	20.50	1.55
4200	4.20	21.00	1.60	1.60	1.60	1.60	1.60	4.20	21.00	1.60
4300	4.30	21.50	1.65	1.65	1.65	1.65	1.65	4.30	21.50	1.65
4400	4.40	22.00	1.70	1.70	1.70	1.70	1.70	4.40	22.00	1.70
4500	4.50	22.50	1.75	1.75	1.75	1.75	1.75	4.50	22.50	1.75
4600	4.60	23.00	1.80	1.80	1.80	1.80	1.80	4.60	23.00	1.80
4700	4.70	23.50	1.85	1.85	1.85	1.85	1.85	4.70	23.50	1.85
4800	4.80	24.00	1.90	1.90	1.90	1.90	1.90	4.80	24.00	1.90
4900	4.90	24.50	1.95	1.95	1.95	1.95	1.95	4.90	24.50	1.95
5000	5.00	25.00	2.00	2.00	2.00	2.00	2.00	5.00	25.00	2.00

160<

TABLE 2. VARIATION OF CALCULATED RADOME EROSION WITH
 RAINFIELD LENGTH AND INTENSITY (CONTINUED)

VELOCITY-2500 FT/SEC THETA-90 DEGREES

RANGE DISTANCE (FT)	1-400 FT/SEC		5-20 FT/SEC		30-100 FT/SEC		150-200 FT/SEC	
	PERCENT AREA	PERCENT EROSION	PERCENT AREA	PERCENT EROSION	PERCENT AREA	PERCENT EROSION	PERCENT AREA	PERCENT EROSION
100	1.00	0.00	1.00	0.00	1.00	0.00	1.00	0.00
200	1.00	0.00	1.00	0.00	1.00	0.00	1.00	0.00
300	1.00	0.00	1.00	0.00	1.00	0.00	1.00	0.00
400	1.00	0.00	1.00	0.00	1.00	0.00	1.00	0.00
500	1.00	0.00	1.00	0.00	1.00	0.00	1.00	0.00
600	1.00	0.00	1.00	0.00	1.00	0.00	1.00	0.00
700	1.00	0.00	1.00	0.00	1.00	0.00	1.00	0.00
800	1.00	0.00	1.00	0.00	1.00	0.00	1.00	0.00
900	1.00	0.00	1.00	0.00	1.00	0.00	1.00	0.00
1000	1.00	0.00	1.00	0.00	1.00	0.00	1.00	0.00
1100	1.00	0.00	1.00	0.00	1.00	0.00	1.00	0.00
1200	1.00	0.00	1.00	0.00	1.00	0.00	1.00	0.00
1300	1.00	0.00	1.00	0.00	1.00	0.00	1.00	0.00
1400	1.00	0.00	1.00	0.00	1.00	0.00	1.00	0.00
1500	1.00	0.00	1.00	0.00	1.00	0.00	1.00	0.00
1600	1.00	0.00	1.00	0.00	1.00	0.00	1.00	0.00
1700	1.00	0.00	1.00	0.00	1.00	0.00	1.00	0.00
1800	1.00	0.00	1.00	0.00	1.00	0.00	1.00	0.00
1900	1.00	0.00	1.00	0.00	1.00	0.00	1.00	0.00
2000	1.00	0.00	1.00	0.00	1.00	0.00	1.00	0.00
2100	1.00	0.00	1.00	0.00	1.00	0.00	1.00	0.00
2200	1.00	0.00	1.00	0.00	1.00	0.00	1.00	0.00
2300	1.00	0.00	1.00	0.00	1.00	0.00	1.00	0.00
2400	1.00	0.00	1.00	0.00	1.00	0.00	1.00	0.00
2500	1.00	0.00	1.00	0.00	1.00	0.00	1.00	0.00
2600	1.00	0.00	1.00	0.00	1.00	0.00	1.00	0.00
2700	1.00	0.00	1.00	0.00	1.00	0.00	1.00	0.00
2800	1.00	0.00	1.00	0.00	1.00	0.00	1.00	0.00
2900	1.00	0.00	1.00	0.00	1.00	0.00	1.00	0.00
3000	1.00	0.00	1.00	0.00	1.00	0.00	1.00	0.00
3100	1.00	0.00	1.00	0.00	1.00	0.00	1.00	0.00
3200	1.00	0.00	1.00	0.00	1.00	0.00	1.00	0.00
3300	1.00	0.00	1.00	0.00	1.00	0.00	1.00	0.00
3400	1.00	0.00	1.00	0.00	1.00	0.00	1.00	0.00
3500	1.00	0.00	1.00	0.00	1.00	0.00	1.00	0.00
3600	1.00	0.00	1.00	0.00	1.00	0.00	1.00	0.00
3700	1.00	0.00	1.00	0.00	1.00	0.00	1.00	0.00
3800	1.00	0.00	1.00	0.00	1.00	0.00	1.00	0.00
3900	1.00	0.00	1.00	0.00	1.00	0.00	1.00	0.00
4000	1.00	0.00	1.00	0.00	1.00	0.00	1.00	0.00
4100	1.00	0.00	1.00	0.00	1.00	0.00	1.00	0.00
4200	1.00	0.00	1.00	0.00	1.00	0.00	1.00	0.00
4300	1.00	0.00	1.00	0.00	1.00	0.00	1.00	0.00
4400	1.00	0.00	1.00	0.00	1.00	0.00	1.00	0.00
4500	1.00	0.00	1.00	0.00	1.00	0.00	1.00	0.00
4600	1.00	0.00	1.00	0.00	1.00	0.00	1.00	0.00
4700	1.00	0.00	1.00	0.00	1.00	0.00	1.00	0.00
4800	1.00	0.00	1.00	0.00	1.00	0.00	1.00	0.00
4900	1.00	0.00	1.00	0.00	1.00	0.00	1.00	0.00
5000	1.00	0.00	1.00	0.00	1.00	0.00	1.00	0.00

TABLE 3. VARIATION OF CALCULATED RADOME EROSION WITH
 RAINFIELD LENGTH AND INTENSITY (CONTINUED)

VELOCITY-5000 FT/SEC THETA-45 DEGREES

RANGE (FT)	RFL (FT)	EROSION (IN)		RANGE (INCHES)	RFL (IN)	EROSION (IN)		RANGE (INCHES)	RFL (IN)	EROSION (IN)	
		1000	2000			1000	2000			1000	2000
1000	1000	0.00	0.00	1000	1000	0.00	0.00	1000	1000	0.00	0.00
1000	1500	0.00	0.00	1000	1500	0.00	0.00	1000	1500	0.00	0.00
1000	2000	0.00	0.00	1000	2000	0.00	0.00	1000	2000	0.00	0.00
1000	2500	0.00	0.00	1000	2500	0.00	0.00	1000	2500	0.00	0.00
1000	3000	0.00	0.00	1000	3000	0.00	0.00	1000	3000	0.00	0.00
1000	3500	0.00	0.00	1000	3500	0.00	0.00	1000	3500	0.00	0.00
1000	4000	0.00	0.00	1000	4000	0.00	0.00	1000	4000	0.00	0.00
1000	4500	0.00	0.00	1000	4500	0.00	0.00	1000	4500	0.00	0.00
1000	5000	0.00	0.00	1000	5000	0.00	0.00	1000	5000	0.00	0.00
1000	5500	0.00	0.00	1000	5500	0.00	0.00	1000	5500	0.00	0.00
1000	6000	0.00	0.00	1000	6000	0.00	0.00	1000	6000	0.00	0.00
1000	6500	0.00	0.00	1000	6500	0.00	0.00	1000	6500	0.00	0.00
1000	7000	0.00	0.00	1000	7000	0.00	0.00	1000	7000	0.00	0.00
1000	7500	0.00	0.00	1000	7500	0.00	0.00	1000	7500	0.00	0.00
1000	8000	0.00	0.00	1000	8000	0.00	0.00	1000	8000	0.00	0.00
1000	8500	0.00	0.00	1000	8500	0.00	0.00	1000	8500	0.00	0.00
1000	9000	0.00	0.00	1000	9000	0.00	0.00	1000	9000	0.00	0.00
1000	9500	0.00	0.00	1000	9500	0.00	0.00	1000	9500	0.00	0.00
1000	10000	0.00	0.00	1000	10000	0.00	0.00	1000	10000	0.00	0.00
1500	1000	0.00	0.00	1500	1000	0.00	0.00	1500	1000	0.00	0.00
1500	1500	0.00	0.00	1500	1500	0.00	0.00	1500	1500	0.00	0.00
1500	2000	0.00	0.00	1500	2000	0.00	0.00	1500	2000	0.00	0.00
1500	2500	0.00	0.00	1500	2500	0.00	0.00	1500	2500	0.00	0.00
1500	3000	0.00	0.00	1500	3000	0.00	0.00	1500	3000	0.00	0.00
1500	3500	0.00	0.00	1500	3500	0.00	0.00	1500	3500	0.00	0.00
1500	4000	0.00	0.00	1500	4000	0.00	0.00	1500	4000	0.00	0.00
1500	4500	0.00	0.00	1500	4500	0.00	0.00	1500	4500	0.00	0.00
1500	5000	0.00	0.00	1500	5000	0.00	0.00	1500	5000	0.00	0.00
1500	5500	0.00	0.00	1500	5500	0.00	0.00	1500	5500	0.00	0.00
1500	6000	0.00	0.00	1500	6000	0.00	0.00	1500	6000	0.00	0.00
1500	6500	0.00	0.00	1500	6500	0.00	0.00	1500	6500	0.00	0.00
1500	7000	0.00	0.00	1500	7000	0.00	0.00	1500	7000	0.00	0.00
1500	7500	0.00	0.00	1500	7500	0.00	0.00	1500	7500	0.00	0.00
1500	8000	0.00	0.00	1500	8000	0.00	0.00	1500	8000	0.00	0.00
1500	8500	0.00	0.00	1500	8500	0.00	0.00	1500	8500	0.00	0.00
1500	9000	0.00	0.00	1500	9000	0.00	0.00	1500	9000	0.00	0.00
1500	9500	0.00	0.00	1500	9500	0.00	0.00	1500	9500	0.00	0.00
1500	10000	0.00	0.00	1500	10000	0.00	0.00	1500	10000	0.00	0.00
2000	1000	0.00	0.00	2000	1000	0.00	0.00	2000	1000	0.00	0.00
2000	1500	0.00	0.00	2000	1500	0.00	0.00	2000	1500	0.00	0.00
2000	2000	0.00	0.00	2000	2000	0.00	0.00	2000	2000	0.00	0.00
2000	2500	0.00	0.00	2000	2500	0.00	0.00	2000	2500	0.00	0.00
2000	3000	0.00	0.00	2000	3000	0.00	0.00	2000	3000	0.00	0.00
2000	3500	0.00	0.00	2000	3500	0.00	0.00	2000	3500	0.00	0.00
2000	4000	0.00	0.00	2000	4000	0.00	0.00	2000	4000	0.00	0.00
2000	4500	0.00	0.00	2000	4500	0.00	0.00	2000	4500	0.00	0.00
2000	5000	0.00	0.00	2000	5000	0.00	0.00	2000	5000	0.00	0.00
2000	5500	0.00	0.00	2000	5500	0.00	0.00	2000	5500	0.00	0.00
2000	6000	0.00	0.00	2000	6000	0.00	0.00	2000	6000	0.00	0.00
2000	6500	0.00	0.00	2000	6500	0.00	0.00	2000	6500	0.00	0.00
2000	7000	0.00	0.00	2000	7000	0.00	0.00	2000	7000	0.00	0.00
2000	7500	0.00	0.00	2000	7500	0.00	0.00	2000	7500	0.00	0.00
2000	8000	0.00	0.00	2000	8000	0.00	0.00	2000	8000	0.00	0.00
2000	8500	0.00	0.00	2000	8500	0.00	0.00	2000	8500	0.00	0.00
2000	9000	0.00	0.00	2000	9000	0.00	0.00	2000	9000	0.00	0.00
2000	9500	0.00	0.00	2000	9500	0.00	0.00	2000	9500	0.00	0.00
2000	10000	0.00	0.00	2000	10000	0.00	0.00	2000	10000	0.00	0.00

165<

TABLE 3. VARIATION OF CALCULATED RADOME EROSION WITH
RAINFIELD LENGTH AND INTENSITY (CONTINUED)

VELOCITY-5000 FT/SEC THETA-75 DEGREES

NO.	1-40	40-80	80-120	120-160	160-200	200-240	240-280	280-320	320-360	360-400	400-440	440-480	480-520	520-560	560-600	600-640	640-680	680-720	720-760	760-800	
1-40	1-40	40-80	80-120	120-160	160-200	200-240	240-280	280-320	320-360	360-400	400-440	440-480	480-520	520-560	560-600	600-640	640-680	680-720	720-760	760-800	
40-80	1-40	40-80	80-120	120-160	160-200	200-240	240-280	280-320	320-360	360-400	400-440	440-480	480-520	520-560	560-600	600-640	640-680	680-720	720-760	760-800	
80-120	1-40	40-80	80-120	120-160	160-200	200-240	240-280	280-320	320-360	360-400	400-440	440-480	480-520	520-560	560-600	600-640	640-680	680-720	720-760	760-800	
120-160	1-40	40-80	80-120	120-160	160-200	200-240	240-280	280-320	320-360	360-400	400-440	440-480	480-520	520-560	560-600	600-640	640-680	680-720	720-760	760-800	
160-200	1-40	40-80	80-120	120-160	160-200	200-240	240-280	280-320	320-360	360-400	400-440	440-480	480-520	520-560	560-600	600-640	640-680	680-720	720-760	760-800	
200-240	1-40	40-80	80-120	120-160	160-200	200-240	240-280	280-320	320-360	360-400	400-440	440-480	480-520	520-560	560-600	600-640	640-680	680-720	720-760	760-800	
240-280	1-40	40-80	80-120	120-160	160-200	200-240	240-280	280-320	320-360	360-400	400-440	440-480	480-520	520-560	560-600	600-640	640-680	680-720	720-760	760-800	
280-320	1-40	40-80	80-120	120-160	160-200	200-240	240-280	280-320	320-360	360-400	400-440	440-480	480-520	520-560	560-600	600-640	640-680	680-720	720-760	760-800	
320-360	1-40	40-80	80-120	120-160	160-200	200-240	240-280	280-320	320-360	360-400	400-440	440-480	480-520	520-560	560-600	600-640	640-680	680-720	720-760	760-800	
360-400	1-40	40-80	80-120	120-160	160-200	200-240	240-280	280-320	320-360	360-400	400-440	440-480	480-520	520-560	560-600	600-640	640-680	680-720	720-760	760-800	
400-440	1-40	40-80	80-120	120-160	160-200	200-240	240-280	280-320	320-360	360-400	400-440	440-480	480-520	520-560	560-600	600-640	640-680	680-720	720-760	760-800	
440-480	1-40	40-80	80-120	120-160	160-200	200-240	240-280	280-320	320-360	360-400	400-440	440-480	480-520	520-560	560-600	600-640	640-680	680-720	720-760	760-800	
480-520	1-40	40-80	80-120	120-160	160-200	200-240	240-280	280-320	320-360	360-400	400-440	440-480	480-520	520-560	560-600	600-640	640-680	680-720	720-760	760-800	
520-560	1-40	40-80	80-120	120-160	160-200	200-240	240-280	280-320	320-360	360-400	400-440	440-480	480-520	520-560	560-600	600-640	640-680	680-720	720-760	760-800	
560-600	1-40	40-80	80-120	120-160	160-200	200-240	240-280	280-320	320-360	360-400	400-440	440-480	480-520	520-560	560-600	600-640	640-680	680-720	720-760	760-800	
600-640	1-40	40-80	80-120	120-160	160-200	200-240	240-280	280-320	320-360	360-400	400-440	440-480	480-520	520-560	560-600	600-640	640-680	680-720	720-760	760-800	
640-680	1-40	40-80	80-120	120-160	160-200	200-240	240-280	280-320	320-360	360-400	400-440	440-480	480-520	520-560	560-600	600-640	640-680	680-720	720-760	760-800	
680-720	1-40	40-80	80-120	120-160	160-200	200-240	240-280	280-320	320-360	360-400	400-440	440-480	480-520	520-560	560-600	600-640	640-680	680-720	720-760	760-800	
720-760	1-40	40-80	80-120	120-160	160-200	200-240	240-280	280-320	320-360	360-400	400-440	440-480	480-520	520-560	560-600	600-640	640-680	680-720	720-760	760-800	
760-800	1-40	40-80	80-120	120-160	160-200	200-240	240-280	280-320	320-360	360-400	400-440	440-480	480-520	520-560	560-600	600-640	640-680	680-720	720-760	760-800	

166<

TABLE 3. VARIATION OF CALCULATED RADOME EROSION WITH
 RAINFIELD LENGTH AND INTENSITY (CONTINUED)

VELOCITY=5000 FT/SEC THETA=90 DEGREES

RAINFIELD LENGTH (FT)	INTENSITY (INCHES)	EROSION (MILLI METERS)	RAINFIELD LENGTH (FT)	INTENSITY (INCHES)	EROSION (MILLI METERS)	RAINFIELD LENGTH (FT)	INTENSITY (INCHES)	EROSION (MILLI METERS)
100	0.1	0.0001	100	0.2	0.0004	100	0.3	0.0009
100	0.4	0.0016	100	0.6	0.0036	100	0.9	0.0081
100	1.0	0.0100	100	1.5	0.0225	100	2.0	0.0400
100	2.0	0.0400	100	3.0	0.0900	100	4.0	0.1600
100	3.0	0.0900	100	4.0	0.1600	100	5.0	0.2500
100	4.0	0.1600	100	5.0	0.2500	100	6.0	0.3600
100	5.0	0.2500	100	6.0	0.3600	100	7.0	0.4900
100	6.0	0.3600	100	7.0	0.4900	100	8.0	0.6400
100	7.0	0.4900	100	8.0	0.6400	100	9.0	0.8100
100	8.0	0.6400	100	9.0	0.8100	100	10.0	1.0000
100	9.0	0.8100	100	10.0	1.0000	100	11.0	1.2100
100	10.0	1.0000	100	11.0	1.2100	100	12.0	1.4400
100	11.0	1.2100	100	12.0	1.4400	100	13.0	1.6900
100	12.0	1.4400	100	13.0	1.6900	100	14.0	1.9600
100	13.0	1.6900	100	14.0	1.9600	100	15.0	2.2500
100	14.0	1.9600	100	15.0	2.2500	100	16.0	2.5600
100	15.0	2.2500	100	16.0	2.5600	100	17.0	2.8900
100	16.0	2.5600	100	17.0	2.8900	100	18.0	3.2400
100	17.0	2.8900	100	18.0	3.2400	100	19.0	3.6100
100	18.0	3.2400	100	19.0	3.6100	100	20.0	4.0000
100	19.0	3.6100	100	20.0	4.0000	100	21.0	4.4100
100	20.0	4.0000	100	21.0	4.4100	100	22.0	4.8400
100	21.0	4.4100	100	22.0	4.8400	100	23.0	5.2900
100	22.0	4.8400	100	23.0	5.2900	100	24.0	5.7600
100	23.0	5.2900	100	24.0	5.7600	100	25.0	6.2500
100	24.0	5.7600	100	25.0	6.2500	100	26.0	6.7600
100	25.0	6.2500	100	26.0	6.7600	100	27.0	7.2900
100	26.0	6.7600	100	27.0	7.2900	100	28.0	7.8400
100	27.0	7.2900	100	28.0	7.8400	100	29.0	8.4100
100	28.0	7.8400	100	29.0	8.4100	100	30.0	9.0000
100	29.0	8.4100	100	30.0	9.0000	100	31.0	9.6100
100	30.0	9.0000	100	31.0	9.6100	100	32.0	10.2400
100	31.0	9.6100	100	32.0	10.2400	100	33.0	10.8900
100	32.0	10.2400	100	33.0	10.8900	100	34.0	11.5600
100	33.0	10.8900	100	34.0	11.5600	100	35.0	12.2500
100	34.0	11.5600	100	35.0	12.2500	100	36.0	12.9600
100	35.0	12.2500	100	36.0	12.9600	100	37.0	13.6900
100	36.0	12.9600	100	37.0	13.6900	100	38.0	14.4400
100	37.0	13.6900	100	38.0	14.4400	100	39.0	15.2100
100	38.0	14.4400	100	39.0	15.2100	100	40.0	16.0000
100	39.0	15.2100	100	40.0	16.0000	100	41.0	16.8100
100	40.0	16.0000	100	41.0	16.8100	100	42.0	17.6400
100	41.0	16.8100	100	42.0	17.6400	100	43.0	18.4900
100	42.0	17.6400	100	43.0	18.4900	100	44.0	19.3600
100	43.0	18.4900	100	44.0	19.3600	100	45.0	20.2500
100	44.0	19.3600	100	45.0	20.2500	100	46.0	21.1600
100	45.0	20.2500	100	46.0	21.1600	100	47.0	22.0900
100	46.0	21.1600	100	47.0	22.0900	100	48.0	23.0400
100	47.0	22.0900	100	48.0	23.0400	100	49.0	24.0100
100	48.0	23.0400	100	49.0	24.0100	100	50.0	25.0000

TABLE 4. VARIATION OF CALCULATED RADOME EROSION WITH RAINFIELD LENGTH AND INTENSITY (CONTINUED)

VELOCITY=7500 FT/SEC THETA=45 DEGREES

RPM = 1.00 (700)				RPM = 3.00 (700)				RPM = 6.00 (700)			
DISTANCE (FT)	PCT AREA	VOLUME (CUBIC FEET)	EVAPORATION (LBS)	DISTANCE (FT)	PCT AREA	VOLUME (CUBIC FEET)	EVAPORATION (LBS)	DISTANCE (FT)	PCT AREA	VOLUME (CUBIC FEET)	EVAPORATION (LBS)
100-100	24.88	11281.22	13273.00	100-100	14.13	6182.14	7298.00	100-100	7.07	3091.07	3669.00
100-125	24.88	14346.53	17121.00	100-125	14.13	7915.18	9498.00	100-100	7.07	4011.43	4813.50
100-150	24.88	17411.84	20969.00	100-150	14.13	9648.22	11697.00	100-100	7.07	4931.78	5937.00
100-175	24.88	20477.15	24817.00	100-175	14.13	11381.26	13896.00	100-100	7.07	5852.13	7041.00
100-200	24.88	23542.46	28665.00	100-200	14.13	13114.30	16095.00	100-100	7.07	6772.48	8145.00
100-225	24.88	26607.77	32513.00	100-225	14.13	14847.34	18294.00	100-100	7.07	7692.83	9249.00
100-250	24.88	29673.08	36361.00	100-250	14.13	16580.38	20493.00	100-100	7.07	8613.18	10353.00
100-275	24.88	32738.39	40209.00	100-275	14.13	18313.42	22692.00	100-100	7.07	9533.53	11457.00
100-300	24.88	35803.70	44057.00	100-300	14.13	20046.46	24891.00	100-100	7.07	10453.88	12561.00
100-325	24.88	38869.01	47905.00	100-325	14.13	21779.50	27090.00	100-100	7.07	11374.23	13665.00
100-350	24.88	41934.32	51753.00	100-350	14.13	23512.54	29289.00	100-100	7.07	12294.58	14769.00
100-375	24.88	45000.00	55601.00	100-375	14.13	25245.58	31488.00	100-100	7.07	13214.93	15873.00
100-400	24.88	48065.31	59449.00	100-400	14.13	26978.62	33687.00	100-100	7.07	14135.28	16977.00
100-425	24.88	51130.62	63297.00	100-425	14.13	28711.66	35886.00	100-100	7.07	15055.63	18081.00
100-450	24.88	54195.93	67145.00	100-450	14.13	30444.70	38085.00	100-100	7.07	15975.98	19185.00
100-475	24.88	57261.24	71000.00	100-475	14.13	32177.74	40284.00	100-100	7.07	16896.33	20289.00
100-500	24.88	60326.55	74848.00	100-500	14.13	33910.78	42483.00	100-100	7.07	17816.68	21393.00
100-525	24.88	63391.86	78696.00	100-525	14.13	35643.82	44682.00	100-100	7.07	18737.03	22497.00
100-550	24.88	66457.17	82544.00	100-550	14.13	37376.86	46881.00	100-100	7.07	19657.38	23601.00
100-575	24.88	69522.48	86392.00	100-575	14.13	39109.90	49080.00	100-100	7.07	20577.73	24705.00
100-600	24.88	72587.79	90240.00	100-600	14.13	40842.94	51279.00	100-100	7.07	21498.08	25809.00
100-625	24.88	75653.10	94088.00	100-625	14.13	42575.98	53478.00	100-100	7.07	22418.43	26913.00
100-650	24.88	78718.41	97936.00	100-650	14.13	44309.02	55677.00	100-100	7.07	23338.78	28017.00
100-675	24.88	81783.72	101784.00	100-675	14.13	46042.06	57876.00	100-100	7.07	24259.13	29121.00
100-700	24.88	84849.03	105632.00	100-700	14.13	47775.10	60075.00	100-100	7.07	25179.48	30225.00
100-725	24.88	87914.34	109480.00	100-725	14.13	49508.14	62274.00	100-100	7.07	26100.00	31329.00
100-750	24.88	90979.65	113328.00	100-750	14.13	51241.18	64473.00	100-100	7.07	27020.52	32433.00
100-775	24.88	94044.96	117176.00	100-775	14.13	52974.22	66672.00	100-100	7.07	27941.04	33537.00
100-800	24.88	97110.27	121024.00	100-800	14.13	54707.26	68871.00	100-100	7.07	28861.56	34641.00
100-825	24.88	100175.58	124872.00	100-825	14.13	56440.30	71070.00	100-100	7.07	29782.08	35745.00
100-850	24.88	103240.89	128720.00	100-850	14.13	58173.34	73269.00	100-100	7.07	30702.60	36849.00
100-875	24.88	106306.20	132568.00	100-875	14.13	59906.38	75468.00	100-100	7.07	31623.12	37953.00
100-900	24.88	109371.51	136416.00	100-900	14.13	61639.42	77667.00	100-100	7.07	32543.64	39057.00
100-925	24.88	112436.82	140264.00	100-925	14.13	63372.46	79866.00	100-100	7.07	33464.16	40161.00
100-950	24.88	115502.13	144112.00	100-950	14.13	65105.50	82065.00	100-100	7.07	34384.68	41265.00
100-975	24.88	118567.44	147960.00	100-975	14.13	66838.54	84264.00	100-100	7.07	35305.20	42369.00
100-1000	24.88	121632.75	151808.00	100-1000	14.13	68571.58	86463.00	100-100	7.07	36225.72	43473.00

TABLE 4. VARIATION OF CALCULATED RADOME EROSION WITH
RAINFIELD LENGTH AND INTENSITY (CONTINUED)

VELOCITY=7500 FT/SEC THETA=90 DEGREES

DEPTH	0-25 INCH	0-50 INCH	0-75 INCH	1-00 INCH	1-25 INCH	1-50 INCH	1-75 INCH	2-00 INCH	2-25 INCH	2-50 INCH	2-75 INCH	3-00 INCH	3-25 INCH	3-50 INCH	3-75 INCH	4-00 INCH	4-25 INCH	4-50 INCH	4-75 INCH	5-00 INCH
1.00	1.00	1.00	1.00	1.00	1.00	1.00	1.00	1.00	1.00	1.00	1.00	1.00	1.00	1.00	1.00	1.00	1.00	1.00	1.00	1.00
1.25	1.25	1.25	1.25	1.25	1.25	1.25	1.25	1.25	1.25	1.25	1.25	1.25	1.25	1.25	1.25	1.25	1.25	1.25	1.25	1.25
1.50	1.50	1.50	1.50	1.50	1.50	1.50	1.50	1.50	1.50	1.50	1.50	1.50	1.50	1.50	1.50	1.50	1.50	1.50	1.50	1.50
1.75	1.75	1.75	1.75	1.75	1.75	1.75	1.75	1.75	1.75	1.75	1.75	1.75	1.75	1.75	1.75	1.75	1.75	1.75	1.75	1.75
2.00	2.00	2.00	2.00	2.00	2.00	2.00	2.00	2.00	2.00	2.00	2.00	2.00	2.00	2.00	2.00	2.00	2.00	2.00	2.00	2.00
2.25	2.25	2.25	2.25	2.25	2.25	2.25	2.25	2.25	2.25	2.25	2.25	2.25	2.25	2.25	2.25	2.25	2.25	2.25	2.25	2.25
2.50	2.50	2.50	2.50	2.50	2.50	2.50	2.50	2.50	2.50	2.50	2.50	2.50	2.50	2.50	2.50	2.50	2.50	2.50	2.50	2.50
2.75	2.75	2.75	2.75	2.75	2.75	2.75	2.75	2.75	2.75	2.75	2.75	2.75	2.75	2.75	2.75	2.75	2.75	2.75	2.75	2.75
3.00	3.00	3.00	3.00	3.00	3.00	3.00	3.00	3.00	3.00	3.00	3.00	3.00	3.00	3.00	3.00	3.00	3.00	3.00	3.00	3.00
3.25	3.25	3.25	3.25	3.25	3.25	3.25	3.25	3.25	3.25	3.25	3.25	3.25	3.25	3.25	3.25	3.25	3.25	3.25	3.25	3.25
3.50	3.50	3.50	3.50	3.50	3.50	3.50	3.50	3.50	3.50	3.50	3.50	3.50	3.50	3.50	3.50	3.50	3.50	3.50	3.50	3.50
3.75	3.75	3.75	3.75	3.75	3.75	3.75	3.75	3.75	3.75	3.75	3.75	3.75	3.75	3.75	3.75	3.75	3.75	3.75	3.75	3.75
4.00	4.00	4.00	4.00	4.00	4.00	4.00	4.00	4.00	4.00	4.00	4.00	4.00	4.00	4.00	4.00	4.00	4.00	4.00	4.00	4.00
4.25	4.25	4.25	4.25	4.25	4.25	4.25	4.25	4.25	4.25	4.25	4.25	4.25	4.25	4.25	4.25	4.25	4.25	4.25	4.25	4.25
4.50	4.50	4.50	4.50	4.50	4.50	4.50	4.50	4.50	4.50	4.50	4.50	4.50	4.50	4.50	4.50	4.50	4.50	4.50	4.50	4.50
4.75	4.75	4.75	4.75	4.75	4.75	4.75	4.75	4.75	4.75	4.75	4.75	4.75	4.75	4.75	4.75	4.75	4.75	4.75	4.75	4.75
5.00	5.00	5.00	5.00	5.00	5.00	5.00	5.00	5.00	5.00	5.00	5.00	5.00	5.00	5.00	5.00	5.00	5.00	5.00	5.00	5.00

173<

TABLE 5
 SLED TEST INFORMATION (FROM REFERENCE 32)

	Run No. 2	Run No. 4	Run No. 7
Holloman No.	7RB1	7RD1	7RF2
Serial No.	2723	3430	1745
Length of Rain Field	400 ft	2000 ft	2000 ft
Rainfall Rate	2.5 in/hr	See comments	Same as Run No. 4
Average Drop Size	1.5 to 2.0 mm	1.5 to 2.0 mm	1.5 to 2.0 mm
Velocity Entrance Maximum Exit	5250 ft/sec 5443 ft/sec 5350 ft/sec	5050 ft/sec 5100 ft/sec 4600 ft/sec	4570 ft/sec 5430 ft/sec 5190 ft/sec
Comments	Surface dimples covered about 50% of surface. Practically every drop caused some surface damage. Flame-glazed 0.035 in. at tip to 0.005 in. near base.	Rainfall equivalent to 3000 ft at 2.5 in/hr, 4000 ft of natural rain at 2.5 in/hr. Factor of 18/13 due to difference in terminal velocity. Moderate surface erosion over entire surface. Maximum damage to forward 5 in. Flame-glazed same as No. 7RB1.	Unglazed. Erosion much less than No. 7RD1. Hit bird during coast-out.

174<

TABLE 6

CALCULATED EROSION OF RADOME 7R81

Distance (Ft)	Pct Area	Volume (In ³ /In ²)	ER (In/Sec)
50.00	5.40	.535852E-04	.568003E-02
100.00	10.80	.118118E-03	.625027E-02
150.00	16.19	.192697E-03	.680864E-02
200.00	21.53	.276297E-03	.732186E-02
250.00	26.99	.367770E-03	.779673E-02
300.00	32.39	.465863E-03	.823024E-02
350.00	37.78	.569225E-03	.861970E-02
400.00	43.13	.676448E-03	.896293E-02
450.00	48.58	.786099E-03	.925850E-02
500.00	53.98	.896784E-03	.950591E-02
1000.00	100.00	.191364E-02	.101423E-01
1500.00	100.00	.287046E-02	.101423E-01
2000.00	100.00	.382729E-02	.101423E-01
2500.00	100.00	.478411E-02	.101423E-01
3000.00	100.00	.574093E-02	.101423E-01
3500.00	100.00	.669775E-02	.101423E-01
4000.00	100.00	.765457E-02	.101423E-01
4500.00	100.00	.861139E-02	.101423E-01
5000.00	100.00	.956822E-02	.101423E-01

A-i

APPENDIX A

Pressure Due to High-Velocity Impact of a Water Jet

**The transient pressure distribution across the impact
area of a small high-velocity water jet is studied
by means of a pressure transducer technique**

by

**Dallas Smith and Ray Kinslow
Assistant Professor and Professor, respectively**

**Department of Engineering Science
Tennessee Technological University
Cookeville, Tennessee 38501**

Abstract

A pressure transducer technique was developed for determining the transient distribution of pressure on a surface caused by the impact of a high-velocity jet. Jet parameters known to be effective in producing ring craters were selected for the study. The average jet velocity was 2100 ft/s (640 m/s) and its approximate diameter was 0.26 in. (0.66 cm). A hardened, small-diameter (0.039 in., 0.099 cm) "pressure pin" was used to transmit the pressure from the impact surface to the pressure transducer. The average pressure was thus found over an area of 0.001192 in.² (0.007690 cm²) at several locations within the impact area.

Results show the greatest pressure to occur at the center of the impact area. These results refute the idea that ring craters are produced by the existence of higher pressures near the jet edge.

Introduction

To explain cratering or fracturing due to high-velocity impact of water drops or jets, knowledge is needed of the spatial and temporal variation of the normal pressure exerted on the target surface due to the impact. With this information an attempt can be made to determine the transient state of stress within the solid. Combining the stresses with the correct fracture criterion may eventually lead to a better understanding of the cratering mechanism. In practice, cratering due to drop rather than jet impact is of primary importance, but since jets have been used considerably in the laboratory to simulate drop impact, it is important to understand the pressure due to a jet impact.

When a jet impinges on a flat solid, an initial pressure occurs which is comparable to the water hammer pressure of Cook.¹

$$P = \rho v c \tag{1}$$

where P is the pressure, ρ is the liquid density, c is the sonic velocity in the liquid, and v is the impact velocity. The initial high pressure given by equation (1) decays very rapidly due to release waves propagating into the jet from its circumference followed by lateral jetting. If impingement continues until a steady state is reached, the pressure approaches the hydrodynamical pressure,

$$P = \frac{1}{2} \rho v c^2 \tag{2}$$

By taking account of the compressibility of the solid being impacted as well as the properties of the jet, DeHaller² showed that equation (1) would be modified slightly to contain the density and sonic velocity of the solid.

For the impingement of a spherical liquid drop, Engel³ proposed

$$P = \frac{\alpha}{2} \rho v c \tag{3}$$

where the factor α depends on the impact velocity and approaches unity for high velocities. The maximum pressure proposed by Engel would thus be $\frac{1}{2} \rho v c$.

In an experimental study Brunton⁴ impacted a water jet onto a pressure trans-

ducer. The resulting pressure peak exhibited a rise time of $1 \mu\text{s}$ and decayed in a time of less than $3 \mu\text{s}$, which was somewhat greater than the time required for release waves to propagate from the circumference to the center of the jet. The longer decay times were believed to be due to the fact that the head of the jet was neither flat nor parallel to the surface. The jet velocity was 2400 ft/s (731.7 m/s) and the jet diameter was 0.17 in. (0.43 cm). The average pressure exerted over the impact area was $134,000 \text{ psi}$ (924 MN/m^2) whereas equation (1) yields $153,000 \text{ psi}$ (1058 MN/m^2). Thus the average pressure found by Brunton was 0.874 pvc . Brunton's experiment permitted the determination of average pressure only, rather than the actual distribution of pressure. High-speed photographs made by Brunton showed that fracturing due to the jet impact was completed within the first $3 \mu\text{s}$ of impact. Therefore, the initial peak of high pressure is of primary interest and the small remaining pressure after decay is of little consequence.

While equations such as (3) provide an estimate of the maximum pressure exerted by the jet, they give no information about the distribution of pressure or its variation with time. Recent numerical solutions by Huang^{5, 6, 7, 8} provide results for both spatial and temporal variations of pressure due to the impact of drops of various geometries onto a flat surface. He used a numerical scheme known as the Compressible-Cell-and-Marker technique. Both slip and non-slip boundary conditions between the drop and the surface have been considered. His results confirm the rapid rise and decay times observed by Brunton. With a free-slip boundary condition and a water velocity of 980 ft/s (299 m/s) the maximum pressure ranged approximately from 0.7 pvc for a spherical drop to 1.2 pvc for a finite-length cylindrical jet. Results were slightly higher for the non-slip boundary condition. As a percentage of pvc, results were also greater for higher impact velocities. In all cases the maximum pressure occurred at the center of impact.

Recent experimental results by Johnson and Vickers⁹ showed the maximum pres-

sure to occur near the edge of the jet. The pressure was approximately 0.67 pvc near the center and jumped to 1.5 pvc near the edge of the jet. This does not agree with Huang's prediction of maximum pressure at the center. The velocity used by Johnson and Vickers was 151 ft/s (46 m/s), and the jet diameter was 1.97 in. (50 mm). Both parameters are one order of magnitude removed from those usually considered relative to drop impact.

A recent experiment by Rochester and Brunton¹⁰ for the impact of a liquid disk and cylinder agrees with Johnson and Vickers in finding a ring of high pressure. A thin rectangular bullet containing a small piezoelectric ceramic was fired into a water disk held between two Perspex windows or into a vertical water jet. Impact velocity was 328 ft/s (100 m/s). The greatest pressure at the center and in the annular region at a distance 0.2 of the disk radius from the center was 0.7 pvc and 1.8 pvc, respectively.

There is considerable disagreement between the analytical and experimental results. It was thus felt that an experimental investigation should be undertaken using the actual jet geometries and velocities, which have recently been used in the laboratory to simulate drop cratering¹¹. An experimental program was undertaken for one set of jet test parameters. The aim was twofold: (1) to check analytical predictions of the pressure distribution, and (2) to provide, for one test case, the dynamic loads required as input in theories for determining the transient stress state in the impacted solid, ultimately leading to methods of predicting the extent of fracturing due to high-velocity drop impacts.

Experimental Method

The experiment employed a pressure transducer which provided a voltage output displayed on an oscilloscope screen. The pressure transducer was mounted in a plate which could be moved accurately by means of a micrometer so that the impact area could be traversed. Figure 1 shows three views of the pressure transducer

assembly. The first photograph shows the transducer positioned in front of the water jet accelerator box, the oscilloscope, and the transducer power source mounted on top of the oscilloscope. The last two photographs show the back and front sides, respectively, of the pressure transducer assembly. The pressure transducer was Model 101A03, manufactured by PCB Piezotronics, Inc., of Buffalo, New York. The transducer had a rise time of 1 μ s, a natural frequency of 400 KHz, a sensitivity of 0.5 ± 0.05 mv/psi, and a range of 10,000 psi for a 5-volt output.

The pressure was transmitted to the transducer by means of a small cylindrical pin mounted in a hole in the impact plate, Figure 2. The diameter of the small end of the pressure pin was 0.039 in. (0.099 cm). Hence, the average pressure was determined over an area of only 0.001197 in.² (0.00769 cm²), small enough to approximate the pressure at a point. The nominal dimensions of the pin are shown in Figure 2. The final length of the pin was determined by assembling the pin, surface plate, and transducer, and machining the protruding end of the pin flush with the impact plate. A flat, smooth impacting surface was thus provided for the impingement of the water jet.

In the initial stages of the investigation stainless steel was used for the impact plate and the pressure pin. Stainless steel proved to be too soft. After a few impacts the pin became plastically compressed; thus, the end of the pin gradually receded into the hole in the impact plate and the diameter of the pin increased slightly. The stainless steel impact plate after a few shots became dented on the surface in the impacting area. A solution for the impact plate was found by replacing the stainless steel with tool steel which was hardened by heating and quenching in oil. Pins were machined from drill rod and hardened in the same way. These pins proved to be too brittle, fracturing at the junction of the small diameter part with the base after only one impact. This problem was finally solved by heating and hardening only the small diameter part of the pin. Thus an impact plate and

pressure pin evolved which would withstand several impacts before suffering any visual damage or measurable change in dimensions. Figure 3 shows a photograph of two views of an impact plate with the pressure pin removed.

The experiment was conducted by accurately positioning the pressure transducer in line with the water jet nozzle 1 inch from the nozzle. The water was accelerated by impacting a nylon piston in a water-filled nozzle with a Hy-Score BB cap bullet, Figure 2. The average velocity of the head of the water jet was 2100 ft/s (640 m/s). The diameter of the jet core was 0.094 in. (0.238 cm) and the diameter of the jet head was 0.25 in. (0.66 cm). These parameters have been used extensively for making craters in slip-cast fused silica targets. More details of the water jet accelerator are given in Section II of this report.

A trace of the transducer voltage output was obtained on the oscilloscope screen for each shot. The oscilloscope was triggered internally by the transducer output. The impact area was traversed by means of the micrometer, Figure 1, using increments of 0.040 in. (0.102 cm). In order to get an average value of the pressure at any given point, several shots were made at each setting of the micrometer. Considerable scatter was experienced from shot to shot. Some of the scatter is due to the fact that, as pointed out by Brunton⁴, not all jet heads will be equally well formed. After each shot the pressure pin was removed and dried. The diameter of the pressure pin was measured frequently with a micrometer to determine if any deformation had occurred.

Results and Discussion

Figure 4 shows a sample of the oscilloscope trace of the transducer output at various distances from the center of impact. The vertical dimensions represent voltage output which, by means of the transducer calibration, was converted to pressure on the transducer. Pressure on the transducer was converted to pressure at the impact surface by multiplying the transducer pressure by the ratio of the transducer area

and pin area. The rise time was approximately 3 μ s and the decay time was 5 to 6 additional μ s.

Figure 5 shows the distribution of pressure (transducer voltage) across the impact area obtained by plotting the peak pressure for each location, r . The effects of scatter were minimized by obtaining several data points at each location. The broken line is drawn through the mean of peak pressures obtained at each point. It is evident that the largest pressure occurs at the center of the impact area and not near the edge. The profiles of two ring craters made in slip-cast fused silica with the same jet parameters are included in Figure 5. Figure 6 shows photographs of the same two craters. It has been suggested by Engel¹² that ring craters may be due to larger pressures near the edge of the impact area. From Figure 5 it appears that this may not be the correct explanation for the formation of ring craters.

The observation of largest pressures at the center agrees with the calculations of Huang^{5,6,7,8}. For large times after the initial impact, Huang's results show that the center pressure decays and that for those times the pressure near the edge may exceed the center pressure, but this pressure is much smaller than the maximum pressure which initially existed at the center.

It must be remembered that the curve in Figure 7 represents the mean of peak pressures that occurred at each location. With the present experimental arrangement the pressure at all locations for some constant time after the initial impact could not be obtained. Since the oscilloscope was triggered internally by the transducer output, then, for say a semi-spherical jet front, triggering for points remote to the center would occur later than for points near the center.

The distribution shown in Figure 5 should ideally be symmetric about the center. The averages shown approximate symmetry to a surprising degree, considering the amount of scatter encountered. To enforce symmetry, the mean voltage of

all equal-distance points was computed before converting voltage to pressure. The resulting pressure envelope, nondimensionalized by $\rho v c$ and R , the jet head radius, is shown in Figure 7. It was fortuitous that the normal distribution curve

$$\frac{P}{\rho v c} = 0.915e^{-1.22\left(\frac{r}{R}\right)^2} \quad (4)$$

where r is distance from the center, represented the experimental points almost exactly. The normal distribution was used by Banks and Chandrasekhar¹³ for the steady state impact of a liquid jet. The maximum pressure is 0.915 $\rho v c$ or 125,100 psi (862.8 MN/m²). This compares with the results of Huang^{5,6} of 0.70 $\rho v c$ for a spherical drop and 1.12 $\rho v c$ for a cylindrical jet. Some of Huang's results, taken from the graphs in references 5 and 6, are also plotted in Figure 7. The present results fall between the results of Huang for a spherical drop and a cylindrical jet. Since the jet used in the present experiment corresponds to neither a spherical drop nor a flat-ended cylinder, it seems reasonable that the experimental results should fall between the results for those two cases. The jet speed used by Huang was 980 ft/s (299 m/s) whereas the speed in the present experiment was 2100 ft/s (640 m/s). For the non-slip boundary condition, reference 8, Huang's results are somewhat higher for higher speeds. The pressures measured by the transducer may have been attenuated somewhat by the transfer of pressure through the pin. Certainly it seems that some energy could have been dissipated in the pin, but it is pointed out that a pin typically withstood many shots with no measurable deformation. Considering the above, it is felt that the present results support the magnitude of pressures found by Huang.

Contrary to the results of Johnson and Vickers⁹, no ring of high pressure was found in the present study. The ring of high pressure found by Johnson and Vickers was at the edge of the jet. In the present experiment this corresponds to the edge of the jet core ($r = 0.047$ in.), not the jet head ($r = 0.13$ in.). It may be that the radial increment ($\Delta r = 0.04$ in.) used in the present study

was too coarse to detect the ring, but it also seems possible at the present velocity of 2100 ft/s (640 m/s) that the formation of the jet head is considerably different from that of the Johnson and Vickers study, where the velocity was only 151 ft/s (46 m/s). A recent theoretical development by Huang¹⁴ may resolve the difference in the two experiments. His theory indicates that for a rigid target material the maximum pressure will occur at the center whereas for a deformable material the maximum pressure may shift to an annular region. In the present experiment a hardened tool steel was used for the target.

The rise times observed in the present experiment were relatively large, Figure 4. A typical value is 3 μ s. The response time of the transducer in the present experiment would account for 1 μ s of the rise time and the rise time may have also been affected by the behavior of the stress waves in the pin. The reason for the large rise times is not completely understood at the present, but because of the larger jet in this experiment, a pressure pulse of approximately twice that observed by Brunton would be expected.

Conclusions

Using a pressure transducer, the spatial distribution of peak pressures due to high-velocity jet impact of a rigid target has been determined. The observed rise time was approximately 3 μ s followed by a 6 μ s decay. The maximum pressure was 0.915 pvc, and occurred at the center of the impact area rather than near the edge, even though the jet had been used to make numerous ring craters in slip-cast fused targets. The present results support those of Huang.

REFERENCES

1. Cook, S. S., "Erosion by Water-Hammer," Proceedings, Royal Society, London, Series A, 119, 481-488 (1928).
2. DeHaller, P., "Investigation of Corrosion Due to Cavitation," Schweizerische Bauzeitung, 101 (22), 260-264 (1933).
3. Engel, O. G., "Waterdrop Collision with Solid Surfaces," Journal of Research of the National Bureau of Standards, 54 (5), 281-298 (1955).
4. Brunton, J. H., "Deformation of Solids by Impact of Liquids at High Speeds," Symposium on Erosion and Cavitation, ASTM Special Tech. Pub. No. 307, 83-89 (1961).
5. Huang, Y. C., Hammitt, F. G., and Yang, W. J., "Normal Impact of a Finite Cylindrical Liquid Jet on a Flat Rigid Plane," Univ. of Mich. Report No. UMICH 03371-9-T (August 1970).
6. Huang, Y. C., Hammitt, F. G., and Yang, W. J., "Impact of Spherical Water Drop on Flat Rigid Surface," Univ. of Mich. Report No. UMICH 033710-10-T (August 1971).
7. Huang, Y. C., Hammitt, F. G., and Yang, W. J., "Computer Simulation of High Speed Collision with Rain Drop (Combined Spherical-Cylindrical Shape)," Univ. of Mich. Report No. UMICH 03371-12-T (Sept. 1971).
8. Huang, Y. C., Hammitt, F. G., and Yang, W. J., "Spherical Droplet Impingement on Flat Rigid Surface Non-Slip Boundary Condition," Univ. of Mich. Report No. UMICH 03371-14-T (Nov. 1971).
9. Johnson, W., and Vickers, G. W., "Transient Stress Distribution Caused by Water-Jet Impact," Journal of Mechanical Engineering Science, 15 (4), 302-310 (1973).
10. Rochester, M. C., and Brunton, J. H. "Surface Pressure Distribution During Drop Impingement," CUED/C-Mat/TR.15 (1974), University of Cambridge. Presented at 4th International Conference on Rain Erosion and Related Phenomena, Meersburg, The Federal German Republic, 8-10 May, 1974.
11. Kinslow, R., Smith, D. G., and Sahai, V. "High-Velocity Liquid Impact Damage (1973 Progress Report), TTU-ES-74-1, Tennessee Technological University, January 1974. AD-724 275/2WM.
12. Engel, O. G., "Damage Produced by High-Speed Liquid-Drop Impacts," Journal of Applied Physics, 44 (2), 692-704 (Feb. 1973).
13. Banks, R. B., and Chandrasekhara, D. V., "Experimental Investigation of the Penetration of a High-Velocity Gas Jet Through a Liquid Surface," Journal of Fluid Mechanics, 15, 13-34 (1963).
14. Huang, Y. C., "Three Stage Impact Process in Liquid Impingement." Presented at the 4th International Conference on Rain Erosion and Related Phenomena, Meersburg, The Federal German Republic, 8-10 May, 1974.

List of Figures

- Figure 1. Pressure transducer assembly, power source, and oscilloscope
- Figure 2. Impact plate, pressure pin, transducer, and jet nozzle
- Figure 3. Photograph of impact plate and pressure pin
- Figure 4. Oscillograms of pressure transducer output
- Figure 5. Pressure distribution compared with crater cross-sections
- Figure 6. Photographs of ring craters
- Figure 7. Peak pressure distribution across the impact area

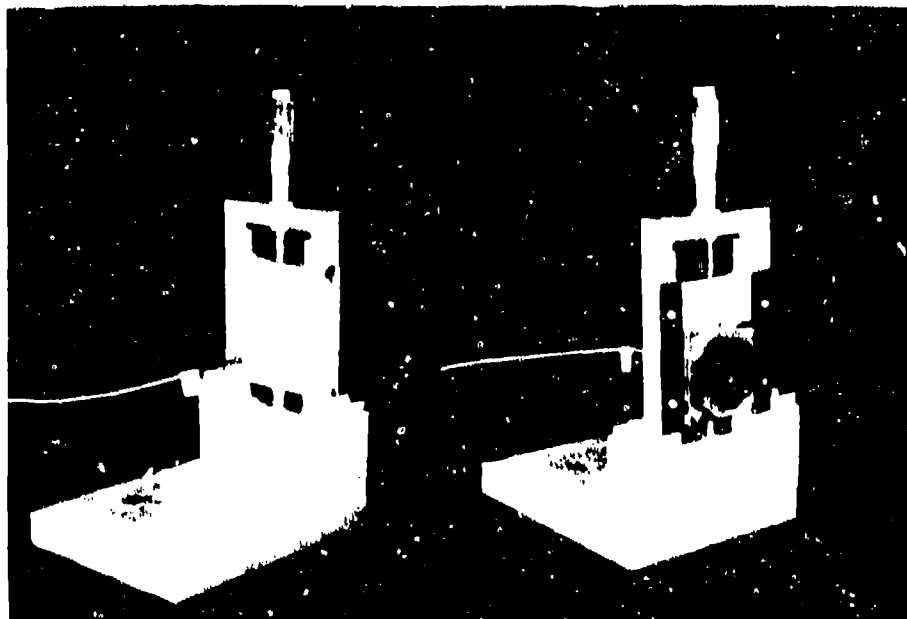
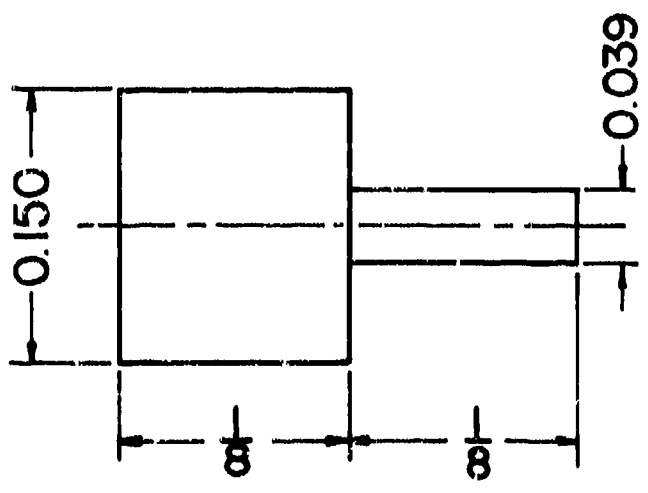
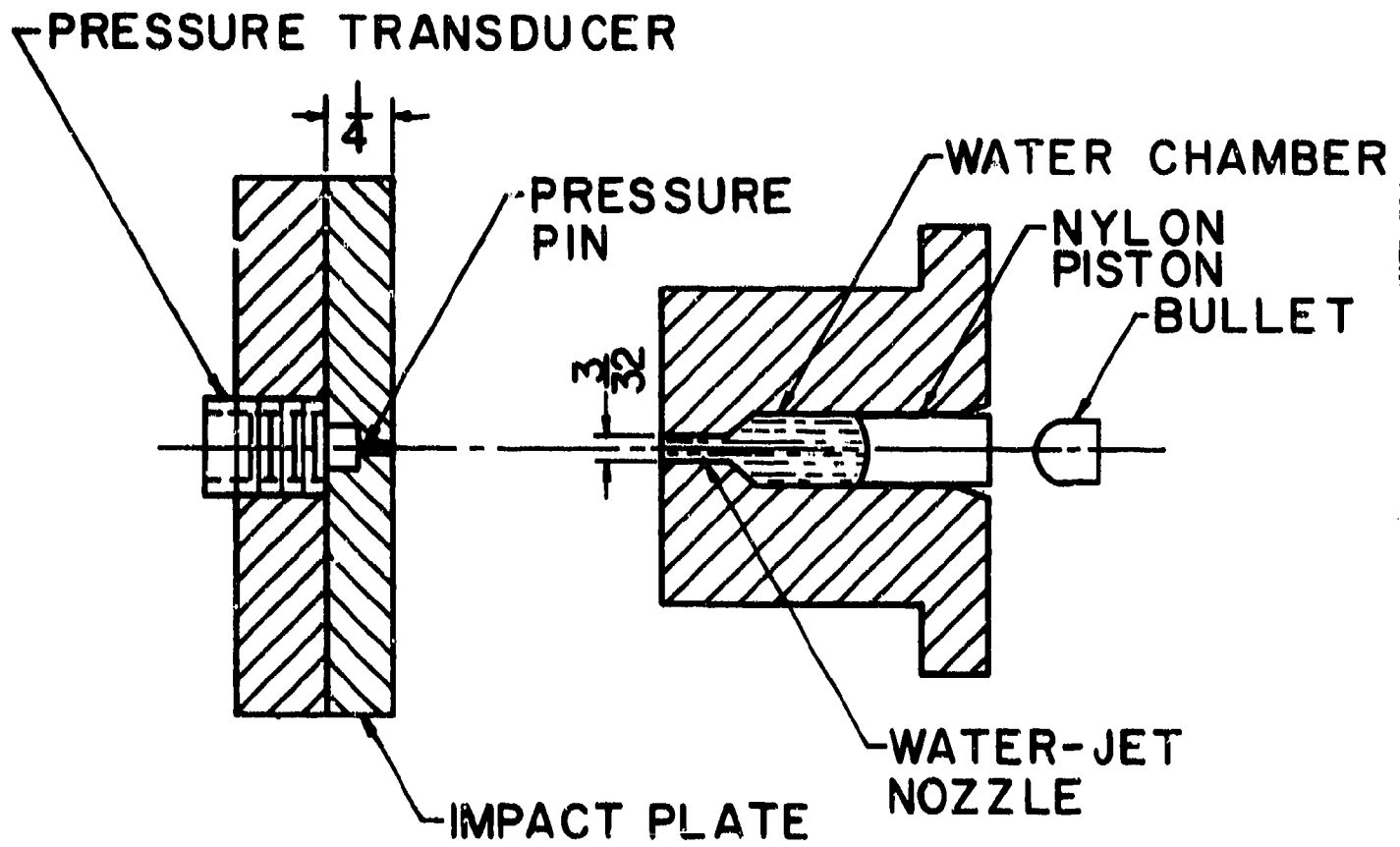


Figure 1

PRESSURE TRANSDUCER ASSEMBLY,
POWER SOURCE, AND OSCILLOSCOPE



PRESSURE PIN

Figure 2
IMPACT PLATE, PRESSURE PIN, TRANSDUCER, AND JET NOZZLE

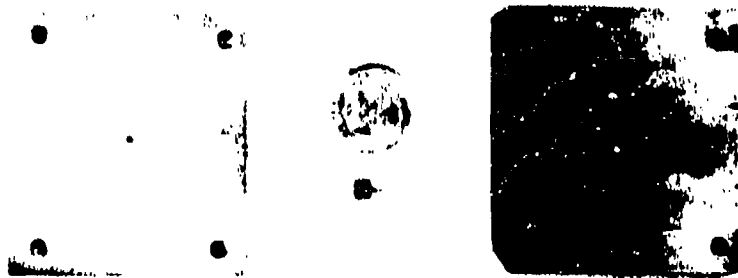
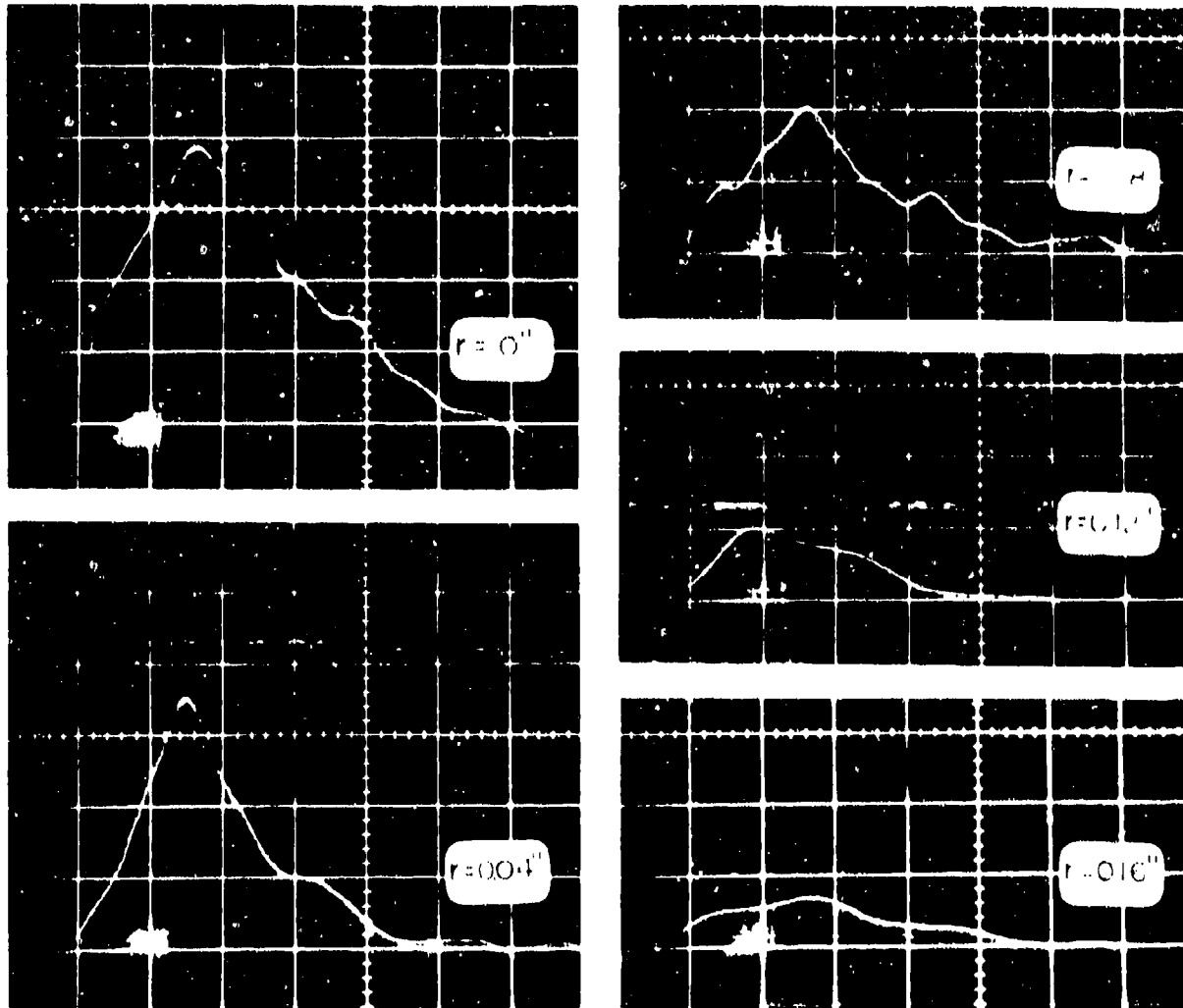


Figure 3

PHOTOGRAPH OF IMPACT PLATE AND PRESSURE PIN



SCALES-Horizontal: 2 microsec./division
Vertical: 28,900 psi / division

Figure 4

OSCILLOGRAMS OF PRESSURE TRANSDUCER OUTPUT

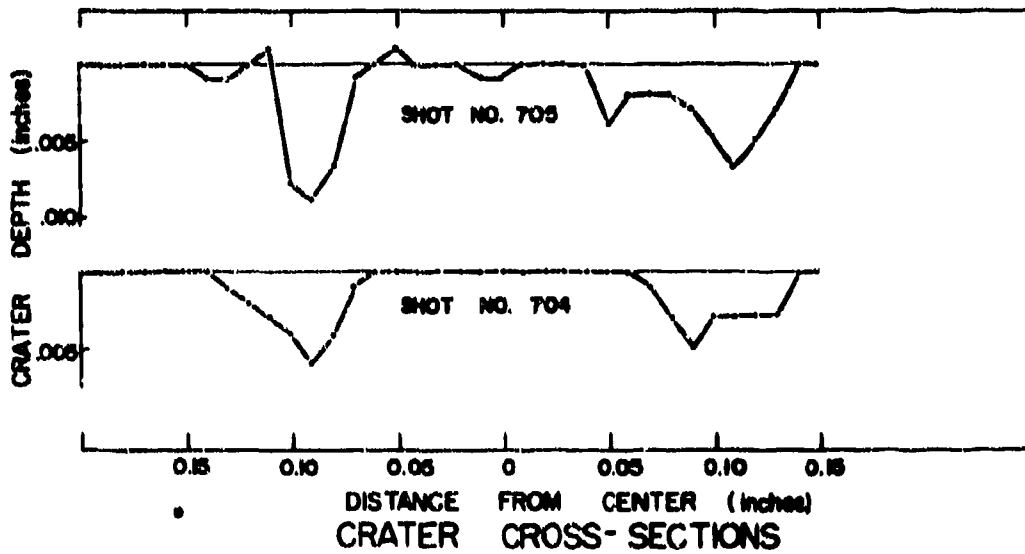
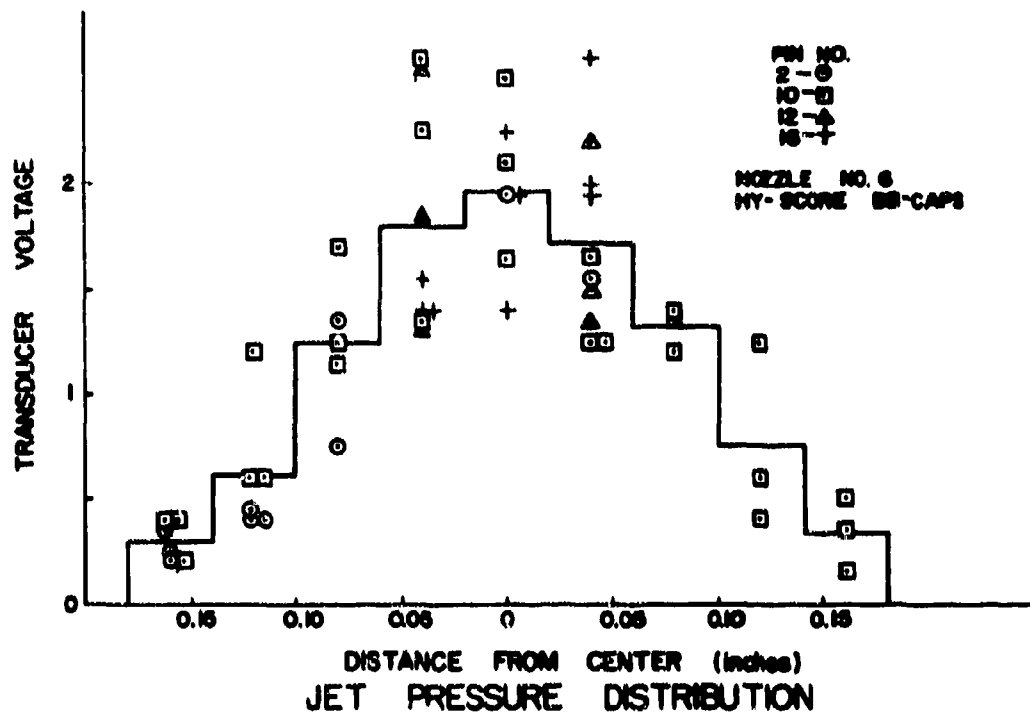


Figure 5
 PRESSURE DISTRIBUTION COMPARED WITH
 CRATER CROSS-SECTIONS

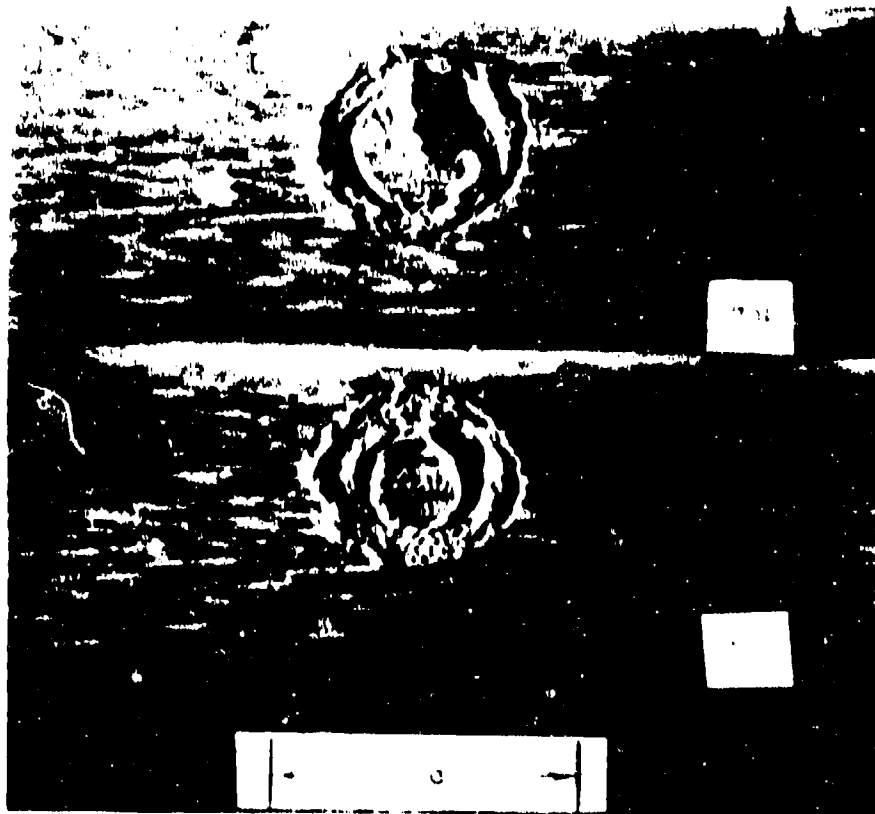


Figure 6
PHOTOGRAPHS OF RING CRATERS

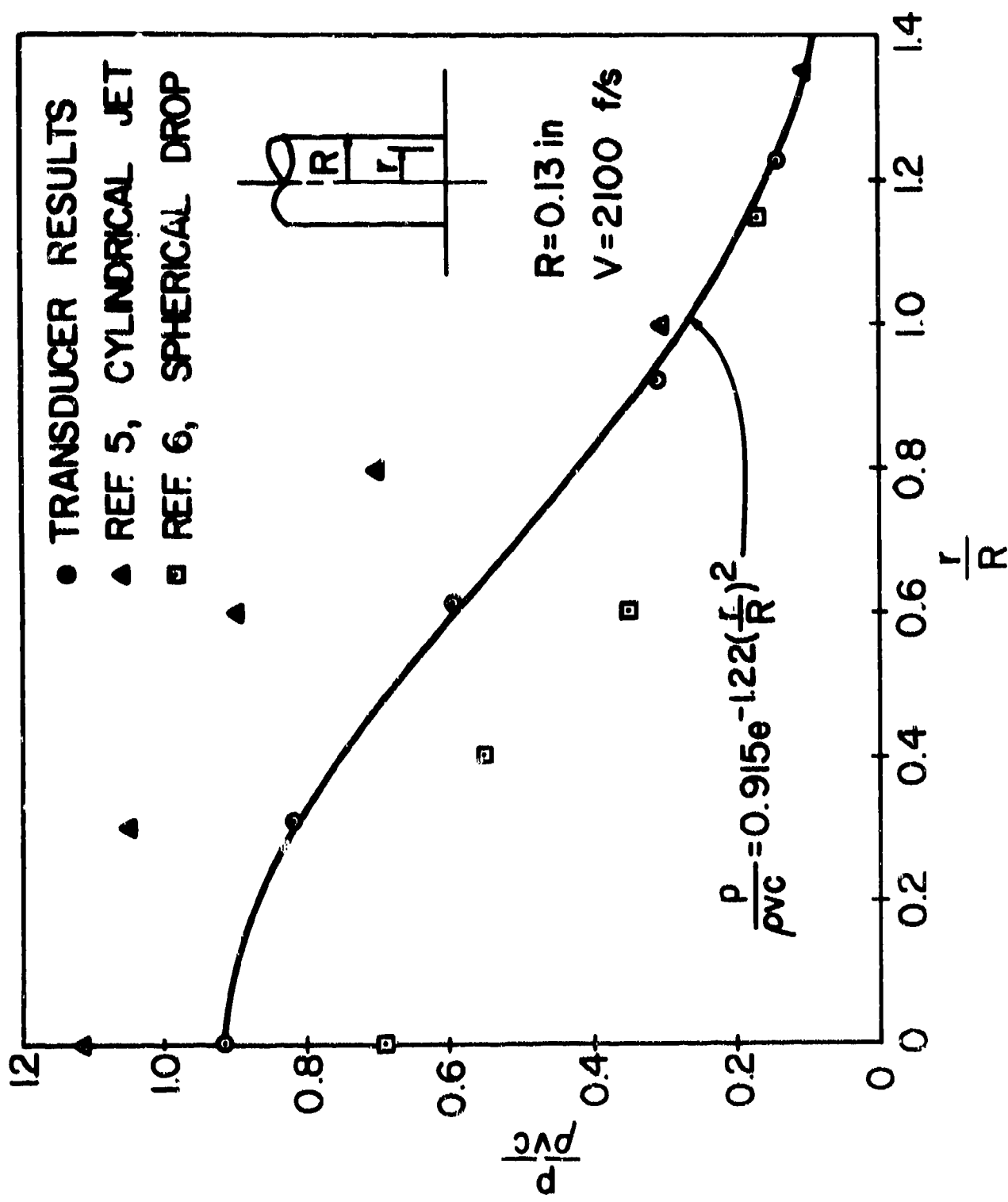


Figure 7

PEAK PRESSURE DISTRIBUTION ACROSS THE IMPACT AREA

B:

APPENDIX B

HYDRODYNAMIC MODELS FOR HIGH-SPEED LIQUID IMPACT

by

Vireshwar Sahai, Peter Hsu, and Jer-Shong Ueng
Associate Professor and Former Graduate Students, Respectively

Department of Engineering Science
Tennessee Technological University
Cookeville, Tennessee 38501

APPENDIX B

HYDRODYNAMIC MODELS FOR HIGH-SPEED LIQUID IMPACT

by Vireshwar Sahai, Peter Hsu, and Jer-Shong Ueng

INTRODUCTION

Cratering due to liquid droplet impingement on solid surfaces is a serious and limiting problem in the design of objects that fly at high speed through rain. A review of literature (for recent comprehensive surveys, see Heymann [1], Eisenberg [2], and Field [3]) has shown that there have been many recent advances toward an understanding of liquid impact damage. However, while an impressive amount of experimental data has been generated, very little work has been done toward the development of a physical theory for quantitative prediction of erosion damage. This is understandable in view of the very complex nature of the damage mechanism. The theoretical analysis described below is not in itself expected to quantitatively predict all the rain erosion characteristics of materials; nevertheless, it is hoped that it will provide a better understanding of the mechanism of cratering due to liquid impact.

As indicated in Appendix A, the pressure distribution over the contact area that is produced when a liquid drop strikes a solid surface is not yet known with certainty. It is, however, generally accepted that a sharp peak of pressure, of the order of magnitude of the water hammer pressure, occurs in the initial stages of impact. The models proposed in the present study are based upon the assumption that this initial impact pressure and its rate of application are high enough to cause the target material to be liquified in the neighborhood of the impact area. This assumption allows the target material to be treated as a fluid during the cratering process.

Such a fluid-fluid impact model was first conceived by Opik [4]. Recently this model was studied both experimentally and analytically by Engel [5, 6]. Her analytical study, however, was semi-empirical, and it involved an arbitrary assumption with regard to partition of the energy of the impacting drops.

Two fluid-fluid impact models will be considered in the present study. The first model is based on an analogy with the impingement of a high-speed liquid jet on a liquid surface. The formulation of this model was prompted by a remark by Cheslak et al [7] that the cavities formed by the impingement of high-speed jets on a liquid surface bear a striking resemblance to those formed on solid surfaces by high-speed impact. While high-speed jets are commonly used to simulate rain erosion, little theoretical work has been done to exploit this analogy.

In the jet model considered here, an equation developed by Rosler and Stewart [8] in connection with their study of capillary jet impingement on liquid surfaces will be used. They developed the governing equation for the cavity profile using the principle of conservation of momentum. In the present study, the Rosler-Stewart equation will be used to determine the size and shape of the cavities formed in not only liquid-liquid impacts but in liquid-solid impacts as well.

The second model is based upon the concept of apparent mass which deals with a body moving through an infinite stationary mass of fluid. As is the case with all hydrodynamic models of high-velocity impact, it is assumed here as well that the target material behaves as a liquid in the vicinity of the point of impact. The concept of apparent mass allows the flow of the target material around the projectile to be described in rather simple terms. Although the concept is being

overextended somewhat in the present application, it is hoped, nevertheless, that it will provide an appropriate simple picture of the high-velocity impact phenomenon.

The apparent mass model was first conceived by Ludloff [9]. A major portion of his work was devoted to the resolution of an apparent discrepancy in results obtained from momentum and energy considerations. He was also concerned with the kinetic energy of the ejected mass of the target material. Only a limited amount of comparison was made with experimental results for impact of solid projectiles on solid targets.

The purpose of the present study is to apply the Ludloff model not only to solid-solid impacts but also to liquid-solid impacts. One of the very attractive features of this model is that it describes the impact cratering as a time-dependent process. In addition to the prediction of maximum crater depth, it also allows the calculation of the rate of crater growth. This latter feature of the apparent mass model will be exploited in the present work.

A problem that confronts all cratering theories, especially those involving hydrodynamic models, is the determination of the proper value to be used for target strength. The problem is further complicated by the fact that the material strength is likely to vary in different phases of the cratering process. Fortunately it was possible, however, to determine simple strength criteria for the two models considered here, which adequately and consistently predict the cratering characteristics.

Because of the nature of the models, the theory is most directly applicable when the target material is ductile. The validity of the models will therefore be checked against available experimental results for impact against metal surfaces. Hydrodynamic models cannot completely

characterize the cratering process in brittle materials such as ceramics used in the construction of radomes. It will be demonstrated, however, that the jet model, under certain circumstances, can adequately predict the maximum depths and volumes of the craters formed in slip-cast fused silica (SCFS) targets due to liquid impact.

Even though the models considered here are of doubtful validity in the case of brittle materials used in radome construction, the analyses presented below are significant in two respects. First, the results may be directly applicable because some designs of radomes suggest that metals may be incorporated in the attachment to the afterbody of the vehicle or in the nose as a protection against rain erosion. Microwave engineers have shown that such a use of metals is possible without serious detriment to radar performance. Second, the development of a reliable theory must be based upon materials on which the test data is repeatedly reproducible. Metals are such materials.

JET MODEL

As indicated earlier, this model is based upon the assumption that for high speeds of impact, the initial pressure developed is high enough to liquify the target material allowing the impact to be categorized as a fluid-fluid impact. Based on the arguments of Plesset and Chapman [10] and others, it is assumed, however, that the high contact pressure due to the initial impact decays very soon and is reduced to the stagnation level. The calculations of Plesset and Chapman showed that the duration of the stagnation pressure pulse is an order of magnitude higher than the period over which the initial water hammer pressure acts. They further expressed the opinion that this longer acting stagnation pressure pulse may be the primary source of damage caused by fluid impact.

Based upon the above-mentioned arguments, a simple idealized model of steady-state impingement of a cylindrical liquid jet on a liquid surface will be used. The drop is replaced by a cylindrical jet in order to simplify mathematical analysis. This simplification is prompted by the fact that jets are often used with success to simulate rain erosion. Because of its importance in industrial processes (such as the oxygen conversion process in the steel industry), the jet impingement on liquid surfaces has been studied extensively both experimentally and analytically. Some of this work is described below.

Banks and Chandrasekhara [11] presented an experimental investigation of normal penetration of a high-velocity gas jet through a liquid surface. Banks and Bhavamai [12] extended this study to a more general one--experimental study of the impingement of a liquid jet on the surface of a heavier liquid. Some 300 experiments were made to measure the sizes of cavities formed due to impact of oil jets on water and water jets on carbon tetrachloride.

From the viewpoint of the present application, the most useful analytical study of the problem is by Rosler and Stewart [8]. They derived the governing differential equation for the cavity profile using a steady-state force analysis. However, since their eventual purpose was to explore the instability of the indentation formed by the impact, they did not verify their equation against experimental results such as those cited above. In what follows, a general form of the Rosler-Stewart equation, applicable to any given pressure and shear distribution on the liquid surface, will be derived. After testing the theory against experimental results of Banks and Bhavamai [12] for the case of impact of a liquid jet against a liquid surface, it will be applied to determine the crater sizes in the high-speed

impingements of water and mercury drops against metals. Attempts will be made to determine the correspondence of surface tension with some strength property of the target material. Experimental results of Engel [13, 14] will be used for this purpose. An approximate form of the Rosler-Stewart equation and its solution will also be presented. In addition it will be shown that, even though the governing assumptions are not entirely valid for a brittle target material, the model is capable of yielding good results for SCFS if a suitable value is used for the strength parameter.

Governing Equations

It is assumed that the cavity formed by normal impact is axisymmetric. The configuration of the cavity and the coordinate system used are shown in Figure 1. The forces acting on an infinitesimal segment ds along the cavity profile are shown in Figure 2. Here

- p = pressure difference across the interface
- τ = shear stress on the interface
- σ = surface tension of the target liquid
- W = weight of the impinging jet occupying the cavity
- B = buoyant force

For the cavity to be in equilibrium, the sum of the vertical components of these forces must vanish. Hence

$$2\pi r ds p \cos\theta + 2\pi[r\sigma\sin\theta]_r = 2\pi r ds \tau \sin\theta + 2\pi r dr(\rho_1 - \rho_2)gh + 2\pi[r\sigma\sin\theta]_{r+dr} = 0$$

Here ρ_1 and ρ_2 are jet and target densities respectively, g is the gravitational constant, and θ is the angle between ds and a horizontal line. Noting that $ds = dr/\cos\theta$ and taking the limit results in

$$p - \tau \tan\theta = (\rho_2 - \rho_1)gh + (\sigma/r)d/dr(r \sin\theta) \quad (1)$$

Finally, if the trigonometric relation $\tan\theta = -dh/dr$ and a corresponding one for $\sin\theta$ are used, Eq. (1) becomes

$$h'' + (h'/r)[1+(h')^2] = (1/\sigma)[(\rho_2 - \rho_1)gh - p - \tau h'] [1 + (h')^2]^{3/2} \quad (2)$$

Here h and r are coordinates describing the cavity profile (see Figure 1) and the primes denote differentiation with respect to r . Equation (2) is the governing equation for the cavity profile and is to be solved subject to the following boundary conditions:

$$h' = 0 \text{ at } r = 0 \text{ and at } r \rightarrow \infty \text{ both } h' \text{ and } h \rightarrow 0 \quad (3)$$

Equation (2) is a highly nonlinear second order differential equation. The input information needed for its solution includes the two densities, the surface tension of the target fluid, and the pressure and shear distributions along the cavity profile. Unfortunately no analytical forms of pressure and shear distributions are available for high-speed impacts. Approximate forms based on experimental results will therefore be needed.

Before discussing the possible forms of pressure and shear distributions for the solution of Eq. (2), it will be convenient to nondimensionalize the equation. The following relationships are used for this purpose:

$$h^* = h/\beta R, \quad r^* = r/\beta R, \quad p^* = p/(\frac{1}{2}\rho_1 V^2), \quad \tau^* = \tau/(\frac{1}{2}\rho_1 V^2) \quad (4)$$

Here R is the jet radius, V is the impact velocity, and β is an adjustable nondimensional parameter chosen so that $r^* = 1$ will be the location of zero pressure point. The starred quantities are nondimensional. The dimensionless form of Eq. (2) can then be written as follows:

$$h^{*''} + (h^*/r^*)[1 + (h^{*'})^2] = [Ah^* - B(p^* + \tau^* h^{*'})][1 + (h^{*'})^2]^{3/2} \quad (5)$$

Here $A = [(\rho_2 - \rho_1)g\beta^2 R^2]/\sigma$ and $B = (\frac{1}{2}\rho_1 V^2 \beta R)/\sigma$. A and B are both dimensionless parameters. Approximate forms of the pressure and shear distributions will now be described in terms of the new dimensionless variables.

Pressure Distribution

In view of the assumptions stated above, the form of pressure distribution needed is that for steady-state impact of a liquid jet on a flat surface. Banks and Chandrasekhara [11] used a normal distribution $p^* = \exp(-Kr^{*2})$ (6)

which served as a fair approximation to the measured data of Gibson [15]. This distribution, however, does not take the possible negative pressure near the cavity edge into account. Rosler and Stewart [8] used a different distribution to fit Gibson's data, a modified form of which is given by

$$p^* = F \sin(1-r^*)\pi/2 \tag{7}$$

$$\text{where } F = \begin{cases} 1 & , \quad 0 \leq r^* < 1 \\ 0.015 (r^*-1), & 1 \leq r^* < 3 \\ 0 & , \quad 3 \leq r^* \end{cases}$$

This sectionally continuous distribution does take the negative pressure near the cavity edge into account. A conservation of momentum analysis showed that the parameter β in the definition of $r^*(r^* = r/\beta R)$ must be equal to 2.72. However, a value of $\beta = 2.0$ provides a better fit with the experimental data of Gibson. The pressure distributions given by Eq. (6) and Eq. (7) with $\beta = 2.0$ and $\beta = 2.72$ are compared with Gibson's results in Figure 3a.

Another useful equation for pressure distribution is that by Leech and Walker [16]. They carried out an extensive set of experiments and fitted their results with the following polynomial:

$$p^* = 1 - 3r^{*2} + 2r^{*3}, \quad \beta = 2.6 \tag{8}$$

Their results however do not differ significantly from those of Gibson. A pressure distribution which is close to that of Leech and Walker and

which takes negative pressures near the cavity edge into account is given by the equation

$$p^* = (1 - r^{*2}) \exp(-r^{*2}), \quad \beta = 2.6 \quad (9)$$

The pressure distributions given by Eqs. (7), (8), and (9) are compared with each other in Figure 3b.

Shear Distribution

Banks and Chandrasekhara [11] and Cheslak, et al [7] concluded from their experimental results that the viscosity of the impinging jet has a negligible effect on stable cavities on liquid surfaces. In the impact of drops on solid surfaces, however, the shear stresses may not be negligible because the velocity of the lateral flow is expected to be very large. To take the shear stresses into account, the following approximate distribution suggested by Rosler and Stewart [8] will be used:

$$r^* = (\alpha^2)(0.664/Re_g^{1/2})(1 - \exp[-(s/R)^2]) \quad (10)$$

Here $Re_g = \rho_1 \alpha V_s / \mu$ is the local Reynolds number based on the distance s along the cavity profile. μ is the viscosity of the jet fluid. The numerical factor α (to be called the shear factor) has been introduced to take care of the possibility that the lateral flow velocity may be larger than the normal impact velocity. In the case of liquid-solid impacts, several experimenters (see, for example, Heymann [1]) have found the lateral flow velocity to be several times the velocity of impact.

Numerical Solution

A generalized program (for a listing of the program, see Hsu [17]) using a fourth-order Hamming's method based on an interval-halving iterative technique was developed to solve the governing equations on a Xerox

Sigma 6 computer. This program was used to determine the cavity shapes and sizes in the case of jet impingement on liquid surfaces as well as liquid drop impact on solid surfaces.

Because the nonlinear nature of the governing equation and the nature of the boundary condition made convergence difficult, several subroutines were written to take care of the various difficulties. The final form of the computer program seems to provide fast and stable convergence in all cases under consideration.

Discussion of Results

First, the effect of various parameters in the governing equation was investigated. For simplicity, the center line velocity of the jet was assumed to remain unchanged upon impact, thus neglecting the effect of jet spreading. The parameters used were those for impact of an air jet on water. As shown in Figure 4, the cavity depth increases with increasing velocity. When the velocity exceeds a certain limit, the cavity shape is no longer shallow, and a cavity lip is created. Both the cavity depth and the lip height continue to grow until a maximum cavity size is reached at a critical velocity. Beyond this value the cavity depth starts to decrease while the lip height continues to increase. It might be mentioned, however, that the pressure distribution used becomes less and less accurate as the cavity gets deeper.

In Figure 5, the effect of increasing the shear factor α on the cavity size is presented. The shear factor seems to have a more significant influence on deep cavities than on shallow cavities. Note also that the numerical solution is capable of providing the cavity profile as well as the cavity depth. Figure 5 also shows the presence of a cavity lip in the case of deep cavities.

Next, the effect of increasing the surface tension was investigated. As expected, the depth of the cavity decreases as the surface tension is increased. The effect of changing the parameter β in the pressure distribution will be discussed later.

The theory was then checked against experimental results of Banks and Bhavamai [12] for impacts of oil jets against water and water jets against carbon tetrachloride. The effect of turbulent spreading of the jet was taken into account in this case.

Figure 6 presents the results for the case of the impact of an oil jet on water. The coordinates used are the same as those used by Banks and Bhavamai. The ordinate h_{\max}^* is the cavity depth nondimensionalized with respect to the jet elevation. The abscissa M^* represents nondimensional jet momentum. The experimental points of Banks and Bhavamai for various nozzle elevations are plotted on this graph. Also plotted are the calculated results of the present theory using pressure distribution Eq. (7) with $\beta = 2.72$ and $\beta = 2.0$. In view of the considerable scatter in the experimental data, the agreement seems to be satisfactory.

An empirical equation obtained by Banks and Bhavamai which fits their experimental data is compared with the present theory in Figures 7 and 8 for oil-water and water-carbon tetrachloride impacts respectively. The ordinate used here represents a normalized cavity depth defined in Banks and Bhavamai [12] or Hsu [17]. Specific comparisons with experimental results showed that the higher value of β is better for cases of deep penetration while lower values of β are more suitable for shallow cavities.

This model was also applied to the case of the impact of a water drop on water surface. This case was considered by Engel [5] as a model for

high-speed liquid-solid impingements. In Figure 9 her experimental results are compared with those computed from the present theory. The agreement is satisfactory.

The fluid-fluid impact model was then applied to the impact of liquid drops on solid surfaces. The premise on which this model is based has already been discussed earlier. In this analysis, the pressure distributions given by both Eqs. (7) and (9) were used, but no significant difference was noted. As far as the shear distribution given by Eq. (10) is concerned, it was found that increasing the shear factor α to a value up to 4 does not significantly change the results; therefore, α was fixed at a value of 1. In fact, it was found that the shear term in Eq. (5) is small compared with other terms in the equation.

One of the difficulties in applying the proposed model to liquid-solid impacts is that of relating the surface tension parameter σ to some strength property of the solid. Experimental results of Engel [13, 14] were used to roughly test the order of magnitude of σ by a backward integrating process. After considerable experimentation, it was found that the use of dynamic compressive yield strength as the strength parameter yields the most consistent results.

Figures 10, 11, 12, and 13 present the calculated results for the impact of 2-mm water and mercury drops on copper and aluminum targets at high velocities. Engel [14] carried out experiments to measure pit depths in such impacts. Mercury drops were used because they are capable of imparting large momenta due to their high densities. Experimental results of Engel are also plotted on the figures for comparison. Calculated results seem to be surprisingly good in view of the crude nature of the model used. Because of the assumption that the target

material behaves as a fluid, the model should be more applicable at higher values of the momentum. This is apparent from the figures; the correspondence between calculated and measured pit depths is better for the mercury impact than for the water impact. Also, in the case of water impact, the calculated results get closer to the measured data as the impingement velocity increases.

Approximate Solution

Examination of the relative importance of the various parameters in the nondimensional form of the governing equation (Eq. (5)) revealed the possibility of a simple approximate solution. In the case of liquid-solid impacts σ is very large and consequently the nondimensional parameter A is very small. The first term on the right-hand side is therefore negligible in comparison with other terms. As suggested earlier, the shear term makes an insignificant contribution. In addition, the cavities are expected to be shallow, therefore $(h^*)^2 \ll 1$. With these approximations, Eq. (5) simplifies to

$$h^{*''} + h^*/r^* = -B\rho^* \tag{11}$$

An exact solution to Eq. (11) can be obtained if the approximate form of the pressure distribution given by Eq. (9) is used. The solution of Eq. (11) subject to the proper boundary conditions (Eq. (3)) is then, simply,

$$h^* = (B/4) \exp(-r^{*2}) \tag{12}$$

The maximum cavity depth which occurs at $r^* = 0$ is given, in dimensional form, by the following expression:

$$h_{\max} = \rho_1 v^2 \beta^2 R^2 / 8\sigma \tag{13}$$

The approximate solution given by Eq. (13) is compared with the numerical solution of the entire equation and with the experimental

results of Engel in Figures 14 and 15 for impacts of mercury drops against 2024-O aluminum and steel respectively. It can be concluded that the approximate solution is quite adequate. Similar correspondence was found in other cases not presented here.

Cratering of Slip-Cast Fused Silica

The mechanism of cratering in a brittle material such as SCFS is significantly different from that in ductile materials. The assumptions associated with the jet model therefore are not completely valid for SCFS. It is interesting, nevertheless, to investigate if the model can yield meaningful results for such a material.

One of the difficulties in applying the model to SCFS is to determine the appropriate value to be used for the strength parameter. It will be recalled that in the case of metals, their dynamic compressive yield strength, which is an order of magnitude higher than the ordinary static strength value, was used. In the case of SCFS a corresponding value of dynamic strength is not available. It was decided therefore to use a value for the strength parameter equal to ten times the value of ordinary fracture strength for SCFS.

The results obtained by solving the governing Eq. (5) for the jet model are presented in Figures 16 and 17. These results correspond to the test conditions of the experiments carried out by Dr. R. Kinslow, the results of which are presented in Section IV of the report. Figure 16 presents the variation of the maximum crater depth with the jet velocity. No comparison has been made with experimental results since there was a wide variation in measured values under apparently the same test conditions. There was considerable variation in values of crater volumes

measured under the same test conditions, but the averages of these values are more likely to be representative of the true conditions. These average values of the crater volumes are plotted along with the computed values in Figure 17. The agreement seems fair and even surprising in view of the nature of the model used. The inapplicability of the model to brittle materials, however, must be kept in mind; therefore, the results described above should be used with care.

APPARENT MASS MODEL

The apparent mass model, just like the jet model, is a rough, approximate hydrodynamic model. This model, based on a concept first used by Ludloff [9] in connection with his study of hypervelocity impact, is characterized by the following assumptions:

1. As in all other hydrodynamic theories of high-velocity impact, it is assumed here as well that the target behaves as a fluid in the immediate vicinity of the point of impact.
2. Upon impact a fraction of the initial kinetic energy of the projectile is expended in melting the target material surrounding the point of impact. This material is in a highly compressed state. While the projectile is penetrating through the target, this stressed and liquified target material is set in motion. The crater grows until the material strength, which resists this motion, is finally able to stop the penetration.
3. Based upon the penetration mechanism described above, the flow of the target material will be represented in terms of a fluid mass set in motion due to a body moving through it.

Such a motion can be described most conveniently in terms of the apparent mass associated with the moving body. The concept of apparent mass is often used in impulsive motion problems (see for example Batchelor [18], page 471).

4. Based upon experimental evidence (see, for example, Engel [19]) it is assumed that the crater formed is approximately hemispherical.
5. The force resisting the penetration is taken to be $-2\pi r^2 S$ where r is the radius of the growing hemispherical crater and S is a parameter representing some measure of strength of the target material. Correspondingly the energy expended in forming the crater is assumed to be $\frac{2}{3} \pi r^3 S$.

According to the concept of apparent mass, the equation of motion governing the flow of the target material is given by

$$\frac{d}{dt} [(m + m')r] + 2\pi r^2 \dot{S} = 0 \quad (14)$$

Here m is the mass of the projectile and m' is its associated apparent mass. The dot denotes differentiation with respect to time. It is assumed that the motion is axially symmetrical.

Two cases will be considered. In the first case, the apparent mass will be treated as a constant. This treatment comes closest to the fluid dynamics definition of apparent mass. However, this case is an oversimplification because it does not consider the growing size of the crater in which the apparent mass moves with the projectile. In reality, the apparent mass should vary while the size of the crater is growing. However, the assumption of constant apparent mass will give a simple model for the high-velocity impact problem.

The second case deals with the more realistic problems of variable apparent mass. This does take into account the growth of the crater.

Constant Apparent Mass

As indicated earlier, the constant apparent mass case does not take into account the growing size of the crater in which the flow takes place. The assumption of constant apparent mass, however, simplifies the governing equations considerably. Two shapes of projectile will be considered in this simplified case--spherical and disc-shaped. The purpose of using two different shapes for the projectile is to consider the effect of the shape of the projectile on the cratering process. The common shape for both solid and liquid projectiles is spherical. However, the projectile is expected to be flattened by impact and thus assume a disc-like shape.

Spherical projectile. The apparent mass associated with the motion of a sphere (see Batchelor [18]) is given by

$$m' = (2\pi/3)\rho_t a^3$$

and the mass of the projectile is

$$m = (4\pi/3)\rho_p a^3$$

where a is the radius of the sphere and ρ_p and ρ_t are respectively the densities of the projectile and target materials. Substitution of these expressions in Eq. (14) results in the following equation:

$$(4\pi a^3/3)(\rho_p + \rho_t/2)r^{\cdot\cdot} + 2\pi r^2 S = 0 \tag{15}$$

This equation may be integrated to yield

$$(2\pi a^3/3)(\rho_p + \rho_t/2)r^{\cdot 2} + (2\pi/3)r^3 S = (2\pi a^3/3)\rho_p V^2 \tag{16}$$

where the integration constant on the right-hand side represents the given initial kinetic energy, $\frac{1}{2} mV^2$, of the projectile. Here V is the velocity of impact. When the projectile comes to rest, the following condition applies:

$$\dot{r} = h_{\max} \quad \text{and} \quad \ddot{r} = 0$$

Using the above condition, the maximum crater depth is determined from Eq. (16) to be

$$h_{\max} = a(\rho_p V^2/S)^{1/3} \quad (17)$$

It is now convenient to express Eq. (16) in terms of a dimensionless coordinate $y = r/h_{\max}$. Equation (16) then becomes

$$(1 + \rho_t/2\rho_p)(a/V)^2(\rho_p V^2/S)^{2/3} \dot{y}^2 = 1 - y$$

This equation can be integrated directly to give

$$\bar{T} = ak(1 + \rho_t/2\rho_p)^{1/2}(h_{\max}/SV)^{1/3} \quad (18)$$

Here \bar{T} is the "penetration time" defined to be the period of time measured from the beginning of penetration to the end of penetration. The constant k is given by

$$k = \int_0^1 (1 - y^3)^{-1/2} dy = 1.376$$

Disc-shaped projectile. The apparent mass for a disk with radius a and thickness h is given by (see Batchelor [18])

$$m' = \frac{8}{3} \rho_t a^3$$

and the mass of disk projectile is

$$m = \rho_p \pi h a^2$$

The momentum Eq. (14) becomes, in this case,

$$(\pi a^2 h \rho_p + \frac{8}{3} a^3 \rho_t) \ddot{r} + 2\pi S r^2 = 0 \quad (19)$$

Integration of this equation results in the following energy equation:

$$\frac{1}{2}(\pi a^2 h \rho_p + \frac{8}{3} a^3 \rho_t) \dot{r}^2 + \frac{2}{3} \pi S r^3 = \frac{1}{2} \pi a^2 h \rho_p V^2 \quad (20)$$

Where the integration constant on the right-hand side is the given initial kinetic energy of the projectile with V as the impact velocity. When the projectile comes to rest, it has made a crater of final penetration depth h_{\max} in the target. This condition can be written as

$$r = h_{\max} \quad \text{when} \quad \dot{r} = 0$$

The penetration depth h_{\max} can now be calculated from Eq. (20) by using the above condition. It is given by

$$h_{\max} = (3a^2 h_p v^2 / 4S)^{1/3} \tag{21}$$

It is convenient again to introduce dimensionless coordinate

$y = r/h_{\max}$ where h_{\max} is given by Eq. (21). Then the momentum and energy equations become, respectively,

$$(3\pi a^2 h_p \rho_p + 8a^3 \rho_t) / (\ddot{y} / 2S h_{\max}) = -3y^2 \tag{22}$$

$$(3\pi a^2 h_p \rho_p + 8a^3 \rho_t) / (\dot{y}^2 / 4\pi S h_{\max}) = 1 - y^3 \tag{23}$$

The penetration time is given by

$$\bar{T} = k(3\pi a^2 h_p \rho_p + 8a^3 \rho_t)^{1/2} (4\pi S h_{\max})^{-1/2} \tag{24}$$

Here the constant k is again equal to 1.375.

As indicated earlier, it is of interest to consider the effect of the shape of projectile on cratering. For the purpose of comparison, consider a disc-shaped projectile having the same volume as a spherical projectile of equal radius. Thus

$$\pi a^2 h = \frac{4}{3} \pi a^3$$

or

$$h = \frac{4}{3} a$$

Then the maximum crater depth given by Eq. (21) reduces to

$$h_{\max} = a(\rho_p v^2 / S)^{1/3}$$

Thus a disc-shaped projectile produces the same maximum crater depth as a spherical projectile of equal volume. For this equivalent disc projectile the penetration time is given by

$$\bar{T} = ka(1 + \frac{2}{\pi} \frac{\rho_t}{\rho_p})^{1/2} (h_{\max} / SV)^{1/3} \tag{25}$$

A comparison of this equation with Eq. (18) shows that the only difference in the two equations is in the coefficient of ρ_t / ρ_p . This results in a

slightly greater time of penetration of the disc as compared to that for the sphere, but the difference is not very significant in most cases.

Variable Apparent Mass

One of the primary objectives of Ludloff [9], the proposer of the apparent mass model, was to determine the momentum and kinetic energy of the ejected mass. He found that the constant apparent mass model gives an expression for the energy of ejecta which is in contradiction with the experimental results. He, therefore, proposed a modified model in which the apparent mass was assumed to be variable and proportional to r^3 , where r is the radius of the growing crater. This latter assumption makes the model more realistic inasmuch as it takes the growth of the crater into account. Ludloff, however, found that this modified model leads to an apparent discrepancy. As will be shown below, the momentum and energy approaches lead to two different results. A major portion of Ludloff's work was devoted to the resolution of this discrepancy.

In the present work, an arbitrary factor α will be introduced in the expression for the variable apparent mass. A major part of the effort here will be directed towards using this model to characterize crater growth as a time-dependent process. Ludloff's primary effort was directed towards the determination of the energy of the ejected material.

For simplicity only a spherical projectile will be considered. It has been shown in the case of constant apparent mass that the shape of the projectile has a very little effect on the results. Furthermore, inclusion of the adjustable parameter α in the expression for the variable apparent mass makes the results applicable to other shapes as well.

In accordance with the variable apparent mass model described above, the apparent mass associated with a translating sphere can be written as

$$m' = a \frac{2}{3} \rho_t \pi r^3$$

Equation (14) then becomes

$$\frac{d}{dt} \left[\left(\frac{4}{3} \pi a^3 \rho_p + a \rho_t \frac{2\pi}{3} r^3 \right) \dot{r} \right] + 2\pi S r^2 = 0$$

where $2\pi S r^2$ is the force of resistance to penetration. This equation can be expanded to

$$\left(\frac{4}{3} \pi a^3 \rho_p + a \rho_t \frac{2\pi}{3} r^3 \right) \ddot{r} + a \rho_t 2\pi r^2 \dot{r}^2 + 2\pi S r^2 = 0 \quad (26)$$

The maximum crater depth may be found by integrating Eq. (26) subject to the condition $\dot{r} = h_{\max}$ when $r = 0$ and is given by

$$\left(\frac{h_{\max}}{a} \right)^3 = \left(\frac{2}{a} \right) \left(\rho_p / \rho_t \right) \left\{ \left(1 + a \rho_t v^2 / S \right)^{1/2} - 1 \right\} \quad (27)$$

The penetration time \bar{T} is obtained by a second integration of Eq. (26) subject to the condition $\dot{r} = v$ when $r = 0$ and is given by

$$\bar{T} = \left(a \rho_t / S \right)^{1/2} h_{\max} \int_0^1 \left\{ \left[\frac{(1+B)}{(y^3+B)} \right]^2 - 1 \right\}^{-1/2} dy \quad (28)$$

Here y is the dimensionless coordinate defined earlier and B is a constant given by

$$B = \left(2a^3 \rho_p \right) / \left(a h_{\max}^3 \rho_t \right)$$

As indicated earlier, the energy approach gives results that are somewhat different than the momentum approach described above. The total moving mass, as before, is given by

$$\left(\frac{2\pi}{3} \right) \left(2a^3 \rho_p + a \rho_t r^3 \right)$$

The application of the energy conservation principle then gives

$$m v^2 / 2 = \left(\frac{\pi}{3} \right) \left(2a^3 \rho_p + a \rho_t r^3 \right) v^2 + \left(\frac{2\pi}{3} \right) S r^3 \quad (29)$$

The condition $\dot{r} = 0$ where $r = h_{\max}$ then yields the maximum crater depth to be

$$h_{\max} = a \left(\rho_p v^2 / S \right)^{1/3}$$

This crater depth equation is the same as that derived for the case of constant apparent mass; however, it differs from the one obtained by the momentum approach above (Eq. (28)).

The penetration time \bar{T} can be obtained by integrating Eq. (29) and is given by

$$\bar{T} = C \int_0^1 [(1 + h_{\max} y^3)/(1 - y^3)]^{1/2} dy \quad (30)$$

where $C = (\rho_p v^2/S)^{1/3} (a/V)$. The details of integration for both momentum and energy approaches may be found in Ueng [20].

In order to establish the validity of the apparent mass model, the results obtained from equations derived above need to be compared with available experimental data. These comparisons of results are presented below.

Discussion of Results

In order to make numerical computations, the values of the densities ρ_p and ρ_t , the size of the projectile, impact velocity, and the strength parameter S are needed. While the values of the first three parameters are easily available, the determination of the proper value to be used for target strength is not so straightforward. This is a problem that confronts all cratering theories, especially those involving hydrodynamic models. The problem is further complicated by the fact that the material strength is likely to vary in different phases of the cratering process.

The problem is less acute in the determination of the maximum crater depth since in this case the process is represented on an integrated, average basis. Still, however, the problem remains as to which strength criterion should be used. Ludloff [9], the proposer of the models presently under consideration, has suggested the use of latent heat of melting (or

fusion) as a strength parameter. The argument involved is that, at high-velocity impact, the target material changes from the solid state to the liquid state (melting) and then from the liquid state to the solid state (fusion) at a very fast rate. It stands to reason then that the energy expended in melting and fusion is related to the latent heat of the material. A discussion of the role of melting and vaporization in hypervelocity impact may be found in Olshaker and Bjork [21].

In the present work, latent heat will be used as a strength parameter in the determination of the maximum crater depth. The energy E expended in melting a hemispherical crater of varying penetration depth r is assumed to be equal to the latent heat of fusion for the mass of the instantaneous hemispherical crater. This is given by

$$E = \frac{2}{3} \pi r^3 \rho_t H_m$$

where H_m is the latent heat of fusion per unit mass. Let the strength of the material S be expressed in terms of the latent heat of fusion as follows

$$S = \rho_t H_m$$

Then

$$E = \frac{2}{3} \pi r^3 S$$

Table 1 presents some typical values of the strength of the material S calculated in terms of the latent heat of fusion. As indicated, the strength of the target material is not expected to remain constant over the entire period of impact. This suggests that in the determination of crater depth as a function of time, one should use a time-dependent constitutive relationship for the target material. Even if such a relationship could be found, it would complicate the analysis, so as to negate

the main advantage of the model--its simplicity. Efforts were therefore directed towards finding a measure of strength that is easily available and yet gives a good verification of the experimental results on an average basis. It was found that the dynamic yield strength (also used as a strength parameter in the jet model) serves this purpose in an adequate manner.

Table 1

Some Typical Values of the Strength of the Material S
 Calculated in Terms of the Latent Heat of Fusion

Material	Latent heat *(H _m , cal/GFW)	Density *(ρ _t , gm/cm ³)	Material Strength (S, dyne/cm ²)
Aluminum	2550	2.70	0.107 x 10 ¹¹
Copper	3120	8.96	0.184 x 10 ¹¹
Iron	3670	7.87	0.217 x 10 ¹¹
Lead	1101	11.34	0.261 x 10 ¹⁰
Nickel	4210	8.90	0.267 x 10 ¹¹
Platinum	4700	21.45	0.216 x 10 ¹¹
Tantalum	7500	16.60	0.288 x 10 ¹¹
Tin	1720	7.30	0.443 x 10 ¹⁰
Titanium	3700	4.50	0.146 x 10 ¹¹
Zinc	1765	7.14	0.807 x 10 ¹⁰

*Elliot [22]

Numerical results will now be presented for maximum crater depth, penetration time, and instantaneous crater depth for several different cases. Whenever possible, these results will be compared with available experimental data.

Maximum penetration depth. Two equations have been derived for maximum penetration depth. The constant apparent mass model and the energy approach for the variable apparent mass model yield identical results given by Eq. (17). On the other hand, in the case of the momentum approach for the variable apparent mass model, the maximum crater depth is given by Eq. (27). Equation (17) gives higher value of penetration depth than Eq. (27). However, in the range of low impact velocities (impact velocities under 40,000 cm/sec) these two equations give almost the same result. The results of present theory will now be compared with experimental data by means of the crater-depth-versus-velocity curves.

The model applies most directly in the case of impact of solid projectile against solid targets. Figures 18 and 19 present some representative results. The results computed from Eq. (17) are compared with the experimental results of Engel [23] in Figure 18 for the impact of steel spheres against aluminum. Similar comparisons with experimental data of Engel [19] for the case of impact of copper spheres against copper targets are presented in Figure 19. In each case the theory seems to fit the experimental results fairly well. A more extensive comparison with available experimental data may be found in Ueng [20].

At high velocities of impact, the only properties of the projectile that materially affect the crater depth are the velocity and density. This indicates that the results of studies of the effects of impacts of solid on solid can be used to predict the effects of high-velocity impacts of liquid drops on solid. Unfortunately, very little experimental data is available for single impacts of liquid drops on solid targets at velocities over 10×10^4 cm/sec. This is undoubtedly because of the experimental difficulties associated with accelerating liquid drops to very high

velocities. Engel [13] partly overcame this problem by using mercury drops which, because of their density, are capable of generating a high value of momentum even at low velocities of impact.

The present theory will be compared with the experimental data of Engle [13] in Figures 20, 21, and 22. The crater-depth-versus-velocity curves calculated by use of Eqs. (17) and (27) for collision of 0.10-cm drops against lead are shown in Figure 20. It can be seen that the two curves fit the experimental data of Engel fairly well. The calculated curves for collisions of 0.10-cm mercury drops against aluminum plates are shown in Figure 21. It would appear that near the impact velocity of about 40,000 cm/sec, the present theory gives good predictions, but a curve that would fit the experimental data would have a slope considerably more than that of the calculated curves. Figure 22 shows calculated curves of Eq. (17) for collisions of mercury drops of two sizes against plates of copper. It can be seen that the present theory is in good agreement with the experimental data. It must be noted, however, that the present model is somewhat inferior to the jet model in the prediction of crater depths.

Time of penetration. For the case of constant apparent mass, two different shapes for the projectile were considered. The penetration time for a spherical projectile is given by Eq. (18) and the penetration time for a disc projectile having the same volume as a spherical projectile of equal radius is given by Eq. (24). As observed earlier, the results obtained from the two equations are not expected to be significantly different. This is corroborated by the results presented in Figure 23 which gives the penetration times produced in impacts of aluminum projectiles ($D_p = 0.635$ cm) against aluminum targets obtained by using Eqs. (18) and (24).

The approach of constant apparent mass does not give satisfactory results for penetration time. For this reason, an improved model using variable apparent mass was developed. For this model, the momentum and energy approaches yield two different results. The equations for penetration time for momentum approach and energy approach of variable apparent mass are, respectively, Eqs. (28) and (30).

In Figure 24 the penetration time produced in impacts of mercury spheres $D_p = 0.10$ cm against copper plates are plotted. It can be seen that the time of penetration obtained by using the energy approach of variable apparent mass model keeps increasing with increasing impact velocities, while the corresponding values obtained by using the momentum approach tend to level off.

As far as the authors are aware, measurements have not been made for penetration time for impact of liquid drops against solids. However, the time of penetration shown in Figure 24 (2 microseconds) checks out with the usual impact times reported in the literature (1-3 microseconds). For the impact of solids against solids, there is some experimental data available which treats the penetration as a time-dependent process. However, comparison with experimental data can best be made in terms of the instantaneous crater depth expressed as a function of time. These results are presented below.

Instantaneous crater depth. There were three differential equations derived earlier, the solution of which will yield crater depth expressed as a function of time. Equation (16) is based on the constant apparent mass model, while the variable apparent mass model gives two equations, Eqs. (26) and (29), based on momentum and energy approaches, respectively.

onsiderable amount of testing with the help of available experimental ata was done to determine which one might yield the best results. It was ound that Eq. (16) based on the constant apparent mass model was unsatis- actory in all cases tested. This is to be expected in view of the restric- ive assumptions made with respect to this model.

While the energy approach of the variable apparent mass model is cap- ble of giving satisfactory results in a few of the cases, Eq. (26) obtained y using the momentum approach gives the most consistent results. The esults presented in the following discussion are all based upon this equa- ion. The differential equation was integrated by using a fourth-order unge-Kutta procedure.

An important factor, already discussed, that affects the results ignificantly is the value of the strength parameter S . For reasons tated earlier, dynamic yield strength will be used for calculations of nstantaneous crater growth. In Figure 25, however, results using two ifferent values of S (dynamic yield strength and latent heat value) are ompared for the case of impact of aluminum spheres ($D_p = 0.635$ cm) gainst aluminum plates with two different impact velocities. Here R s the instantaneous crater depth and D_p is the diameter of the projectile. he coefficient of variable apparent mass α has been taken to be 0.5. In he same figure, the results of the present theory are also compared with he computed results of Rosenblatt [24]. Rosenblatt used a sophisticated umerical procedure using a rather complicated constitutive equation. In iew of the simplicity of the apparent mass model, the present results rom Eq. (26) seem to be satisfactory.

As far as the author is aware, Kineke [25] and Kineke and Vitali [26] re the only ones who have made extensive and careful measurements of

crater depth as a function of time. In what follows, the calculated results from the present theory will be compared with their experimental results. Figures 26 and 27 present results for the impact of 0.18 gram steel disc against lucite and aluminum targets, respectively. The impact velocity for the aluminum target, was 5.01 km/sec and for lucite it was 4.6 km/sec. As indicated earlier, the effect of the shape of projectile is not significant. Therefore, results were calculated from Eq. (26) using a spherical projectile of equal weight. In these cases the present theory has been compared with the experimental results of Kineke [25].

In Figures 28, 29, 30, and 31, results are presented for the cases of four different weights of steel projectile, impacting with different impact velocities against lead targets. In these cases the present theory has been compared with the experimental results of Kineke and Vitali [26].

In the variable apparent mass model, the value of α is adjustable. It is seen from Figures 26 through 31 that, for most cases, the optimum value of α lies between 0.1 and 0.5.

Fair agreement between the theory and the experimental result was obtained in all of the cases tested. This is gratifying in view of the crudeness of the model used in the calculations.

REFERENCES

1. Heymann, F. J., "Eine Übersicht von Schlüssen zu den Verhältnissen zwischen der Erosionsgeschwindigkeit und Aufschlags-Parametern," Proceedings of the 2nd Conference on Rain Erosion and Associated Phenomena, Meersburg, German, p. 98, 1967.
2. Eisenberg, P., "Cavitation and Impact Erosion-Concepts, Correlations, Controversies," Characterization and Determination of Erosion Resistance, ASTM STP 474, p. 3, 1970.
3. Field, J. E., "High Velocity Liquid Impact and Cavitation," IUTAM Symposium on Non-steady Flow of Water at High Speeds, Leningrad, 1971.
4. Opik, E. J., "Researches on the Physical Theory of Meteor Phenomena: I. Theory of the Formation of Meteor Craters," Tartu Ulikool Sternwarte Publications, Publications de l'Observatoire Astronomique de l'Universite de Tartu, 28, p. 1, 1936 (abstract).
5. Engel, O. G., "Crater Depths in Fluid Impacts," Journal of Applied Physics 37, p. 1798, 1966.
6. Engel, O. G., "Initial Pressure, Initial Flow Velocity, and the Time Dependence of Crater Depth in Fluid Impacts," Journal of Applied Physics 38, p. 3935, 1967.
7. Choslak, F. R., Nicholls, J. A., and Sichel, M., "Cavities Formed on Liquid Surface by Impinging Gas Jets," Journal of Fluid Mechanics 36, p. 55, 1969.
8. Rosler, R. S., and Stewart, G. H., "Impingement of Gas Jets on Liquid Surfaces," Journal of Fluid Mechanics 31, p. 163, 1968.
9. Ludloff, K. G., "A Hydrodynamic Model for Hypervelocity Impact," Ph.D. Dissertation, U.C.L.A., 1967.
10. Plesset, M. S., and Chapman, R. B., "Collapse of an Initially Spherical Vapor Cavity in the Neighborhood of a Solid Boundary," Journal of Fluid Mechanics 47, p. 283, 1971.
11. Banks, R. B., and Chandrasekhara, D. V., "Experimental Investigation of the Penetration of a High-Velocity Gas Jet through a Liquid Surface," Journal of Fluid Mechanics 15, p. 13, 1963.
12. Banks, R. B., and Bhavanai, A., "Experimental Study of the Impingement of a Liquid Jet on the Surface of a Heavier Liquid," Journal of Fluid Mechanics 23, p. 229, 1965.
13. Engel, O. G., "Pits in Metal Caused by Collision with Liquid Drops and Soft Metal Spheres," Journal of Research of National Bureau of Standards 62, p. 229, 1959.

14. Engel, O. G., "Pits in Metal Caused by Collision with Liquid Drops and Rigid Steel Spheres," Journal of Research of National Bureau of Standards 64A, p. 61, 1960.
15. Gibson, A. H., Hydraulics and Its Application, Constable, 1934.
16. Leach, S. J., and Walker, G. L., "The Application of High Speed Liquid Jet to Cutting," Phil. Trans., Roy. Soc. (London) 260A, p. 295, 1966.
17. Hsu, P. W., "Jet Model of High Speed Liquid Solid Impacts," M.S. Thesis, Tennessee Technological University, 1972.
18. Batchelor, G. K., An Introduction to Fluid Dynamics, Cambridge University Press, 1967.
19. Engel, O. G., "Collisions of Liquid Drops with Liquids," Technical Report WADD-TR-60-475, Part III, 1966.
20. Ueng, Jer-Shong, "Apparent Mass Model for High-Velocity Impact," M.S. Thesis, Tennessee Technological University, 1974.
21. Olshaker, A. E., and Bjork, R. L., "Role of Melting and Vaporization," Proceedings of the 5th Symposium on Hypervelocity Impact, p. 225, 1962.
22. Elliott, J. F., Thermochemistry for Steelmaking, Reading, Mass., Addison-Wesley Pub. Co., 1960.
23. Engel, O. G., "Basic Research on Liquid-Drop-Impact Erosion," NASA CR 1559, 1970.
24. Rosenblatt, M., "Numerical Calculations of Hypervelocity Impact Crater Formation in Hard and Soft Aluminum Alloys," AFML-TR-70-254, Wright-Patterson AFB, Ohio, 1971.
25. Kineke, J. H., Jr., "Observations of Crater Formation in Ductile Materials," Proceedings of the 5th Symposium on Hypervelocity Impact, p. 339, 1962.
26. Kineke, J. H., Jr., and Vitali, R., "Transient Observations of Crater Formation in Semi-Infinite Targets," Proceedings of the 6th Symposium on Hypervelocity Impact, p. 457, 1963.

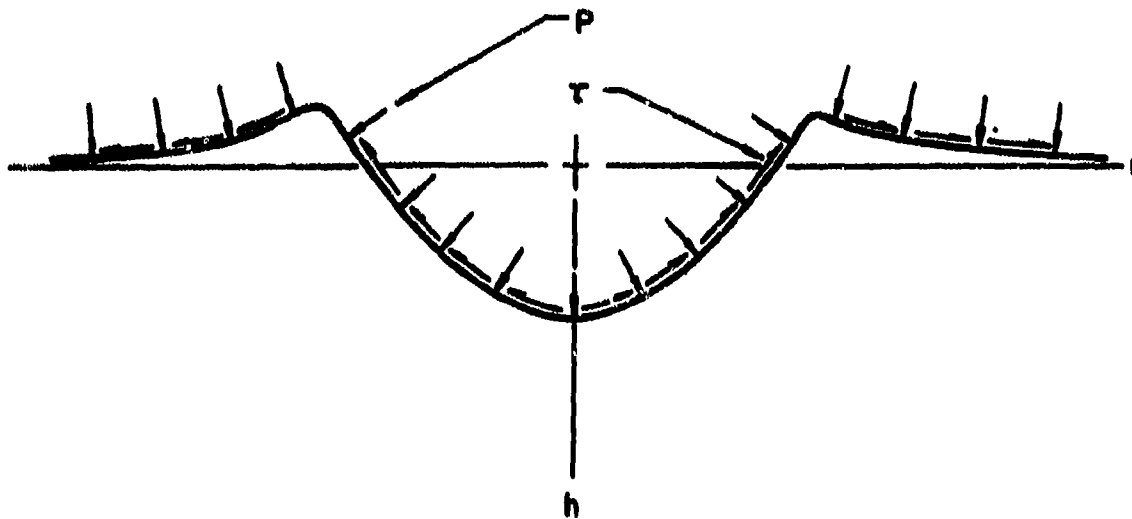


FIGURE 1. CAVITY CONFIGURATION

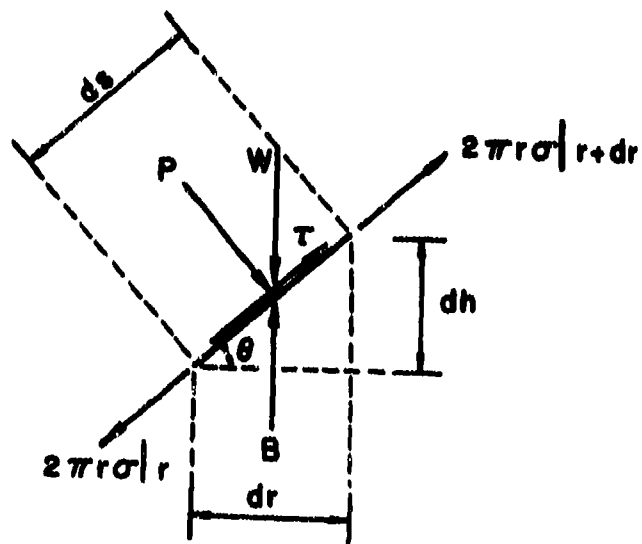


FIGURE 2. FORCE BALANCE ON AN INFINITESIMAL ELEMENT

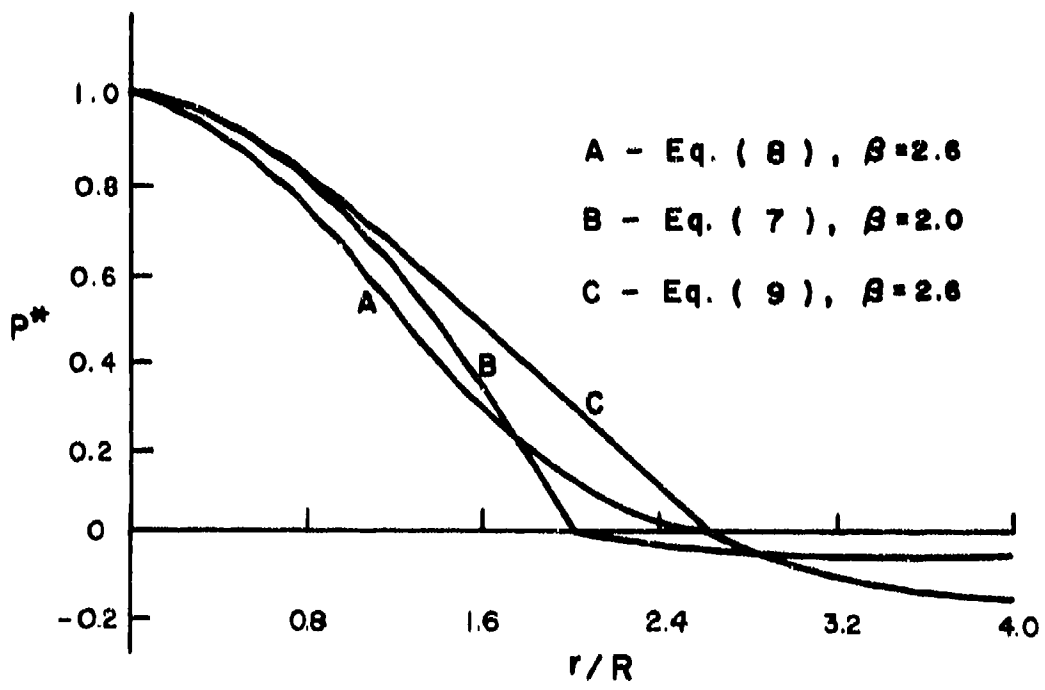
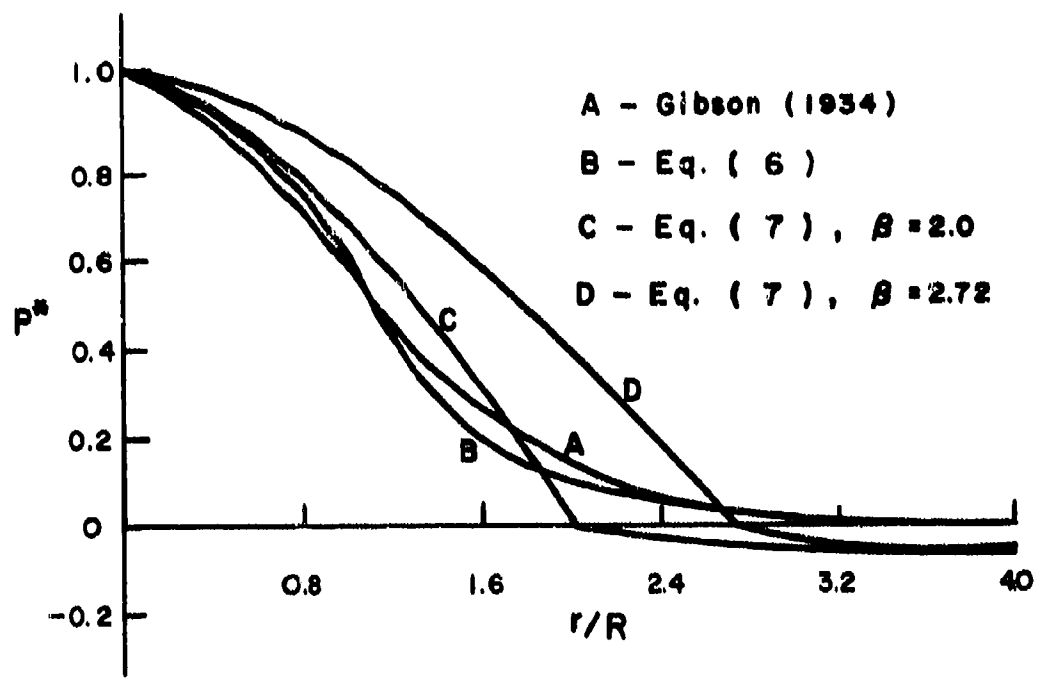


FIGURE 3. PRESSURE DISTRIBUTIONS

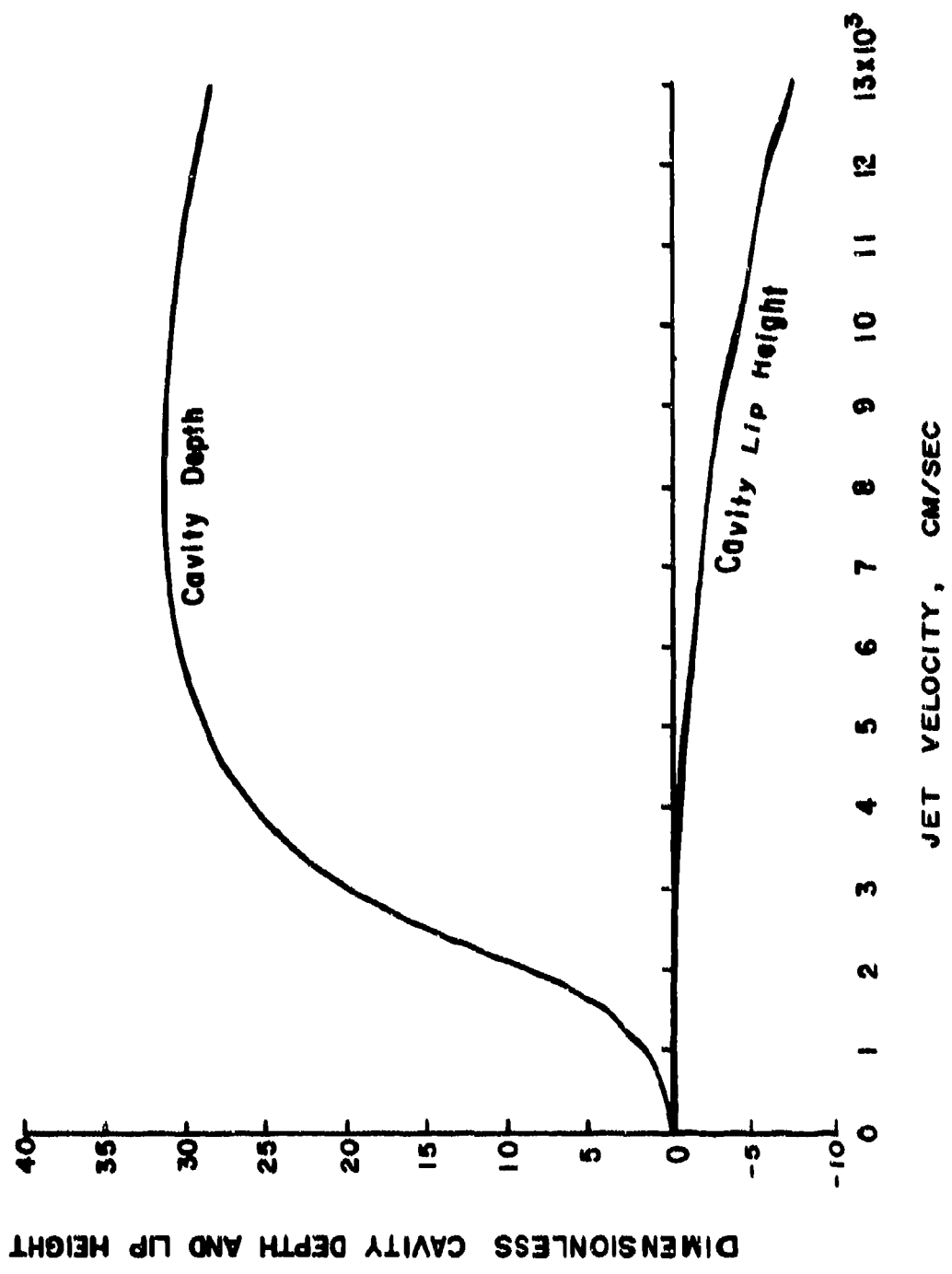


FIGURE 4. VELOCITY EFFECT

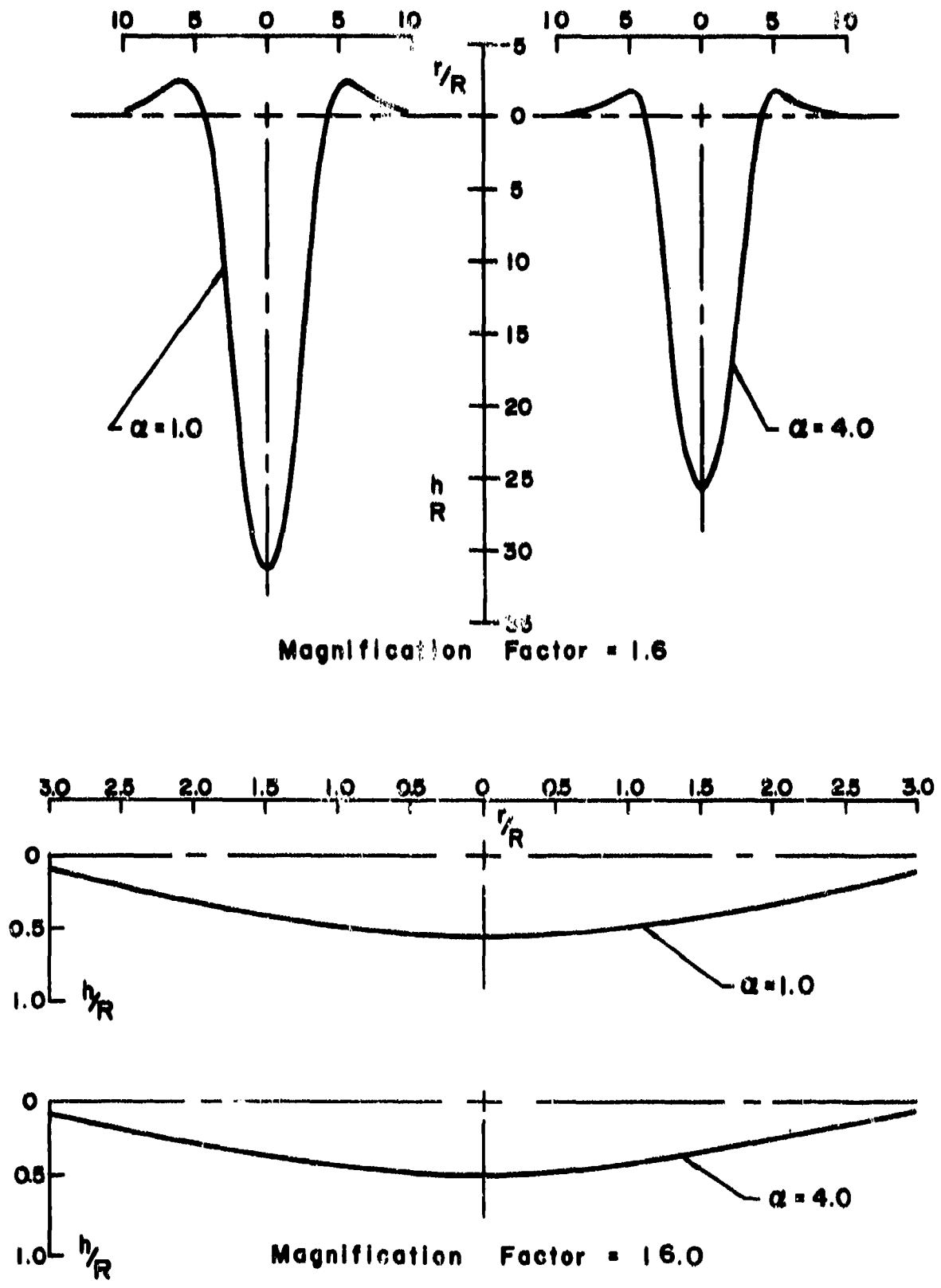
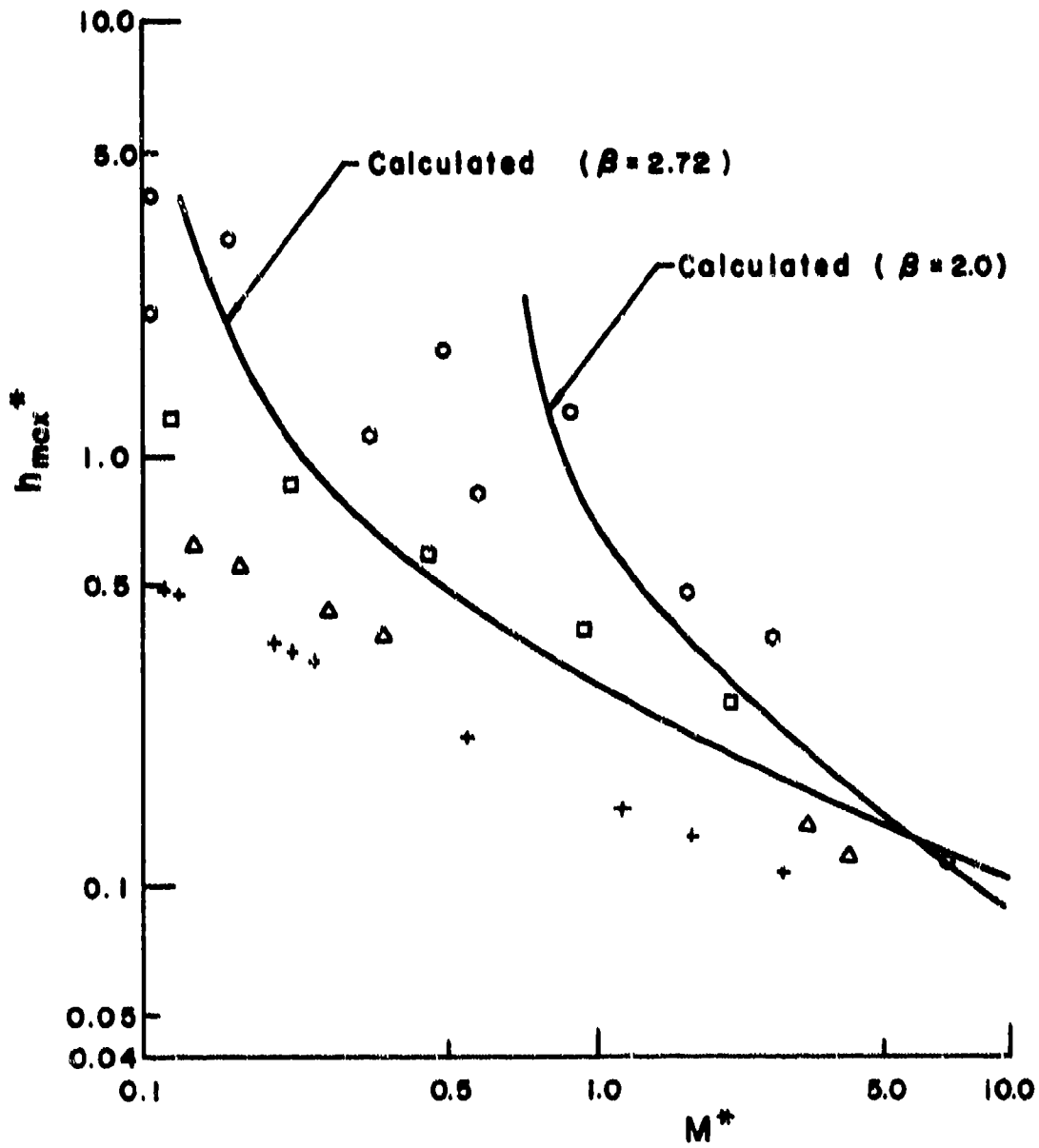


FIGURE 5. SHEAR FACTOR EFFECTS IN STRONG PENETRATION (V=8000 CM/SEC) AND WEAK PENETRATION (V=600 CM/SEC)



Experimental Data, Banks & Bhavamal (1965)

- | | | | |
|---|-----------|---|----------|
| ○ | H = 1 cm, | ○ | H = 2 cm |
| □ | H = 4 cm, | △ | H = 8 cm |
| + | H = 12 cm | | |

FIGURE 6. IMPACT OF OIL JET ON WATER SURFACE

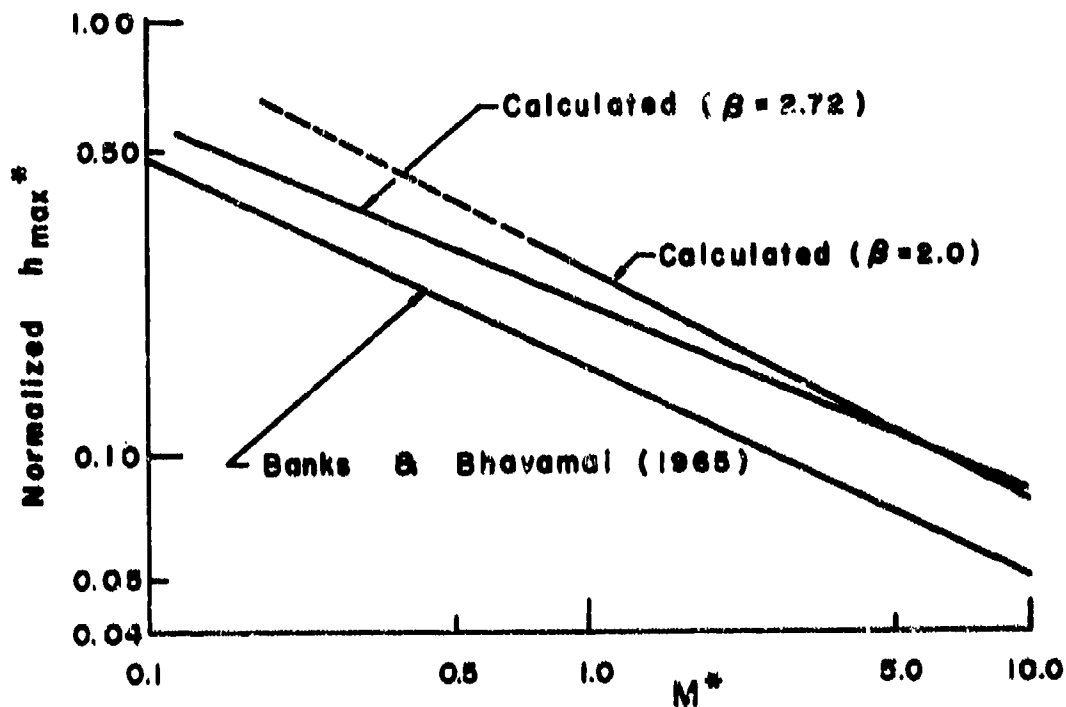


FIGURE 7. IMPACT OF OIL JET ON WATER SURFACE

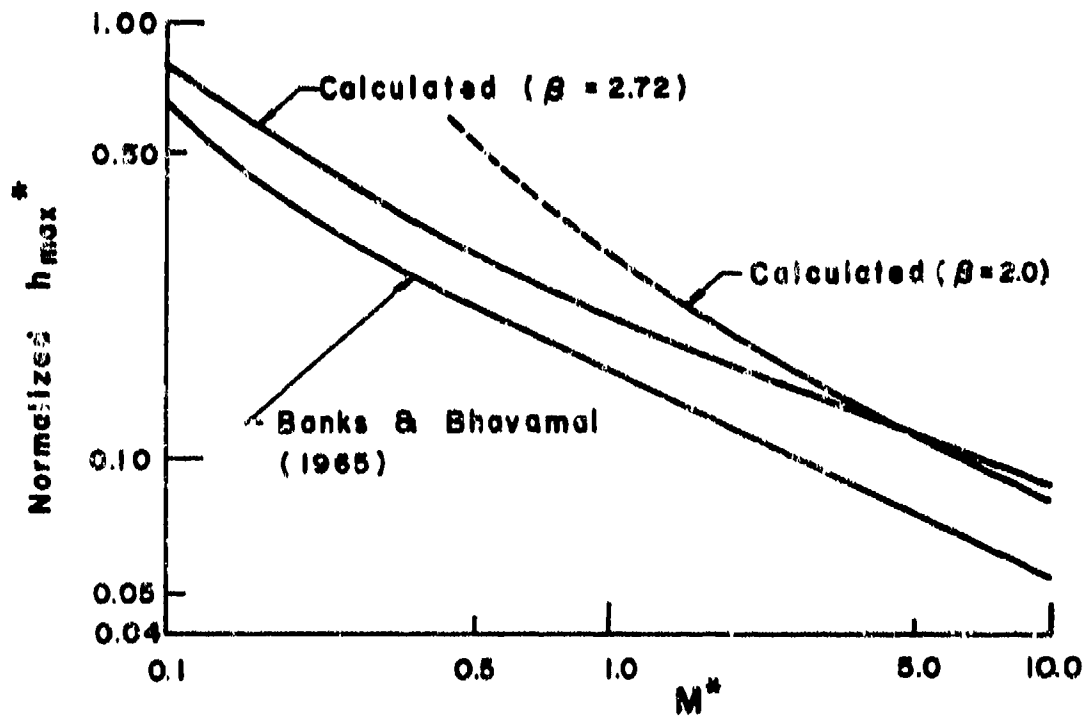


FIGURE 8. IMPACT OF WATER JET ON CARBON TETRACHLORIDE SURFACE

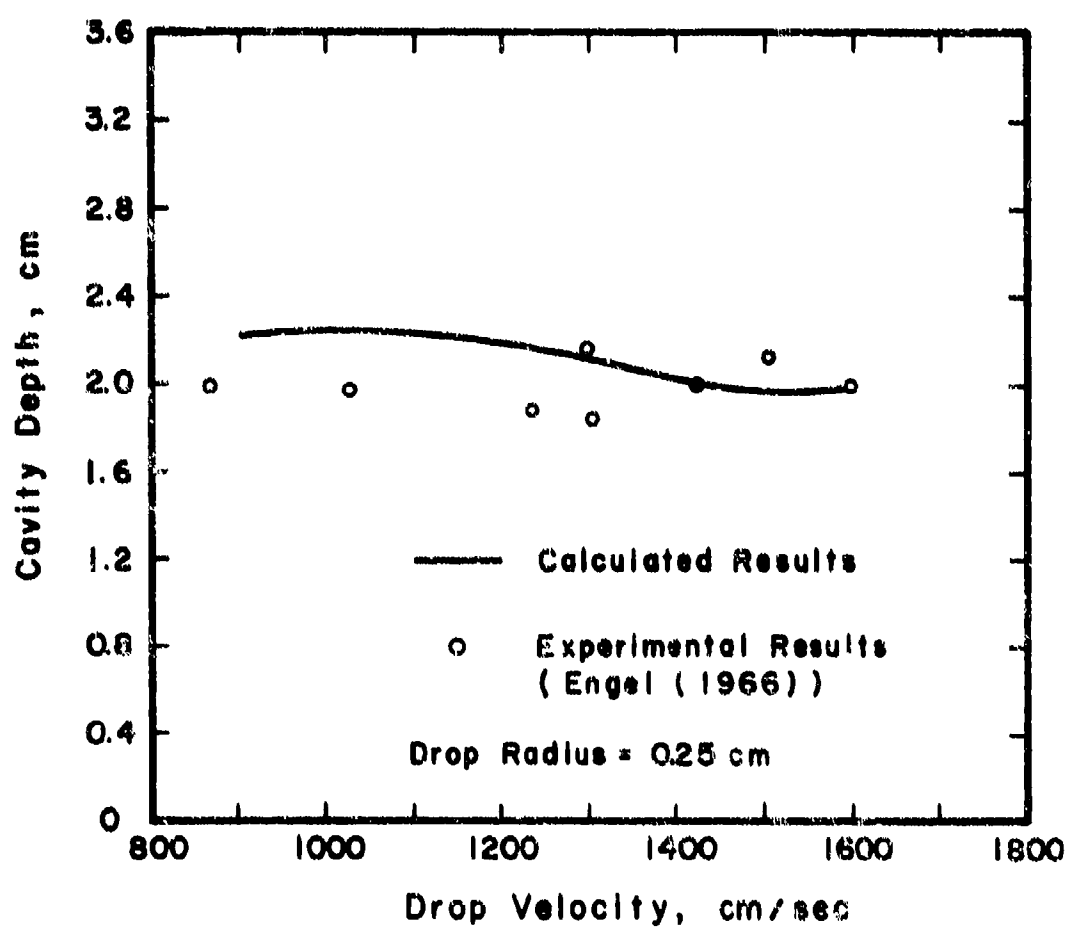


FIGURE 9. MAXIMUM CAVITY DEPTH PRODUCED BY IMPACT OF A WATER DROP AGAINST WATER

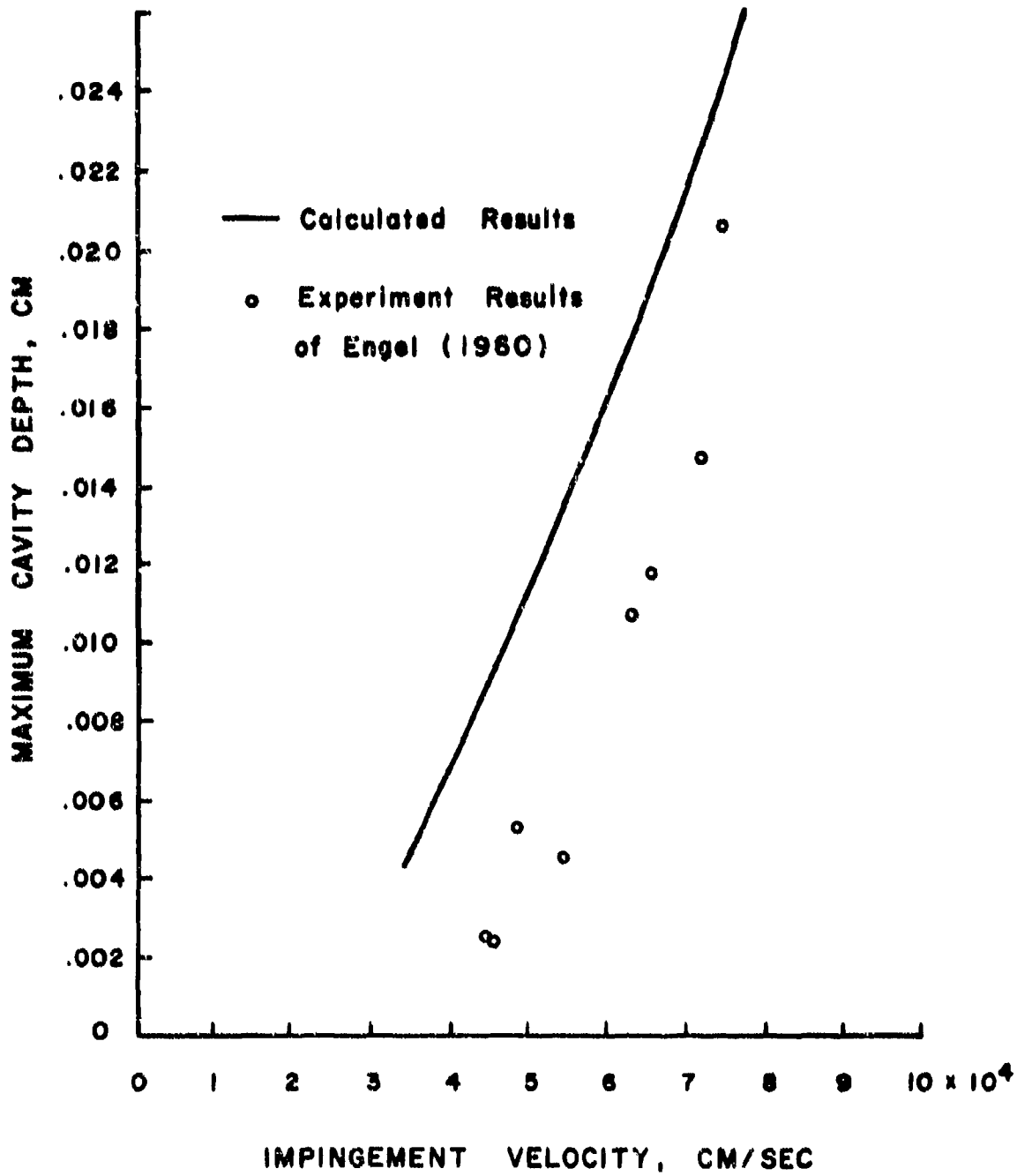


FIGURE 10. IMPACT OF WATER DROPS ON 2024-O ALUMINUM

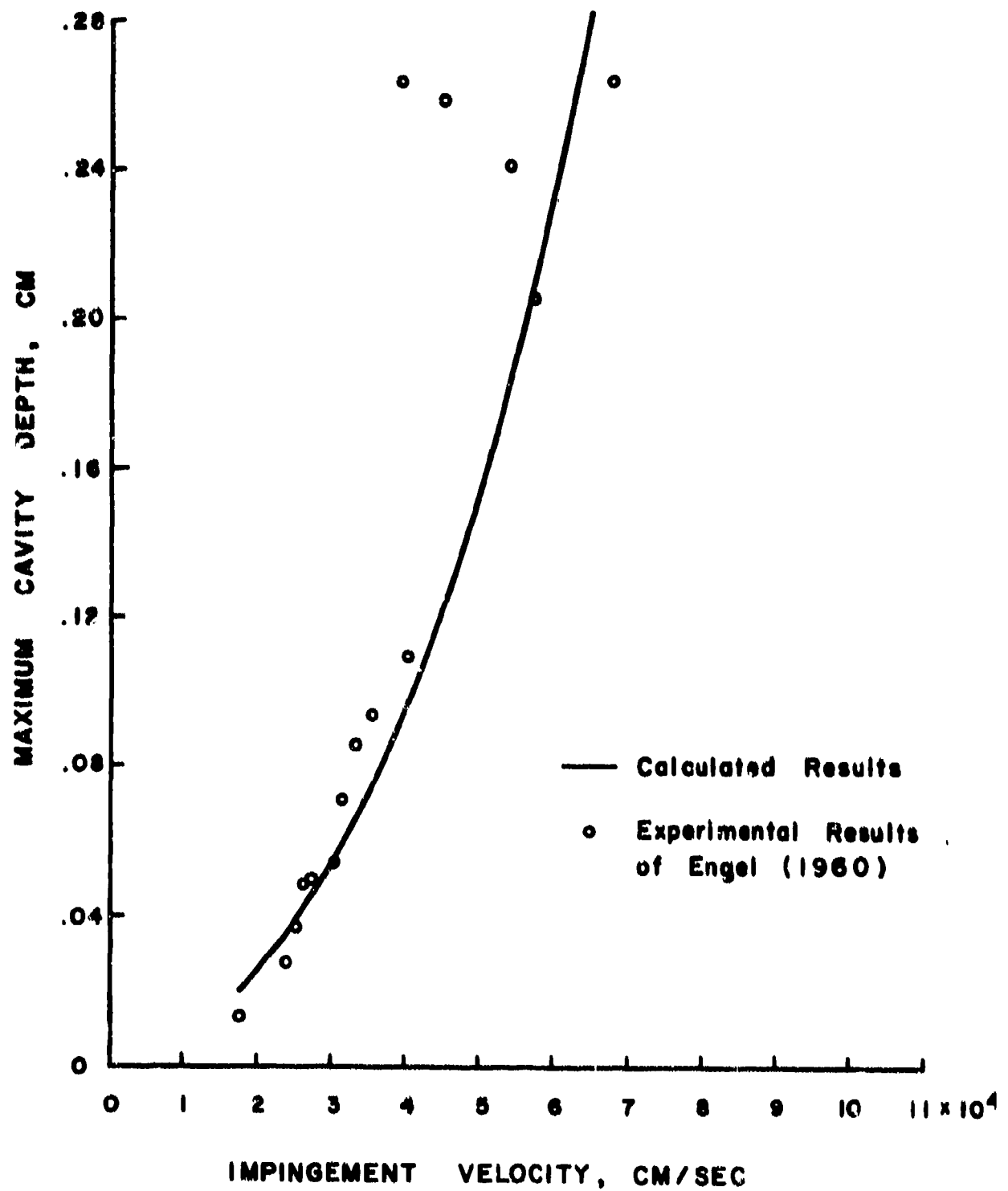


FIGURE 11. IMPACT OF MERCURY DROPS ON 2024-O ALUMINUM

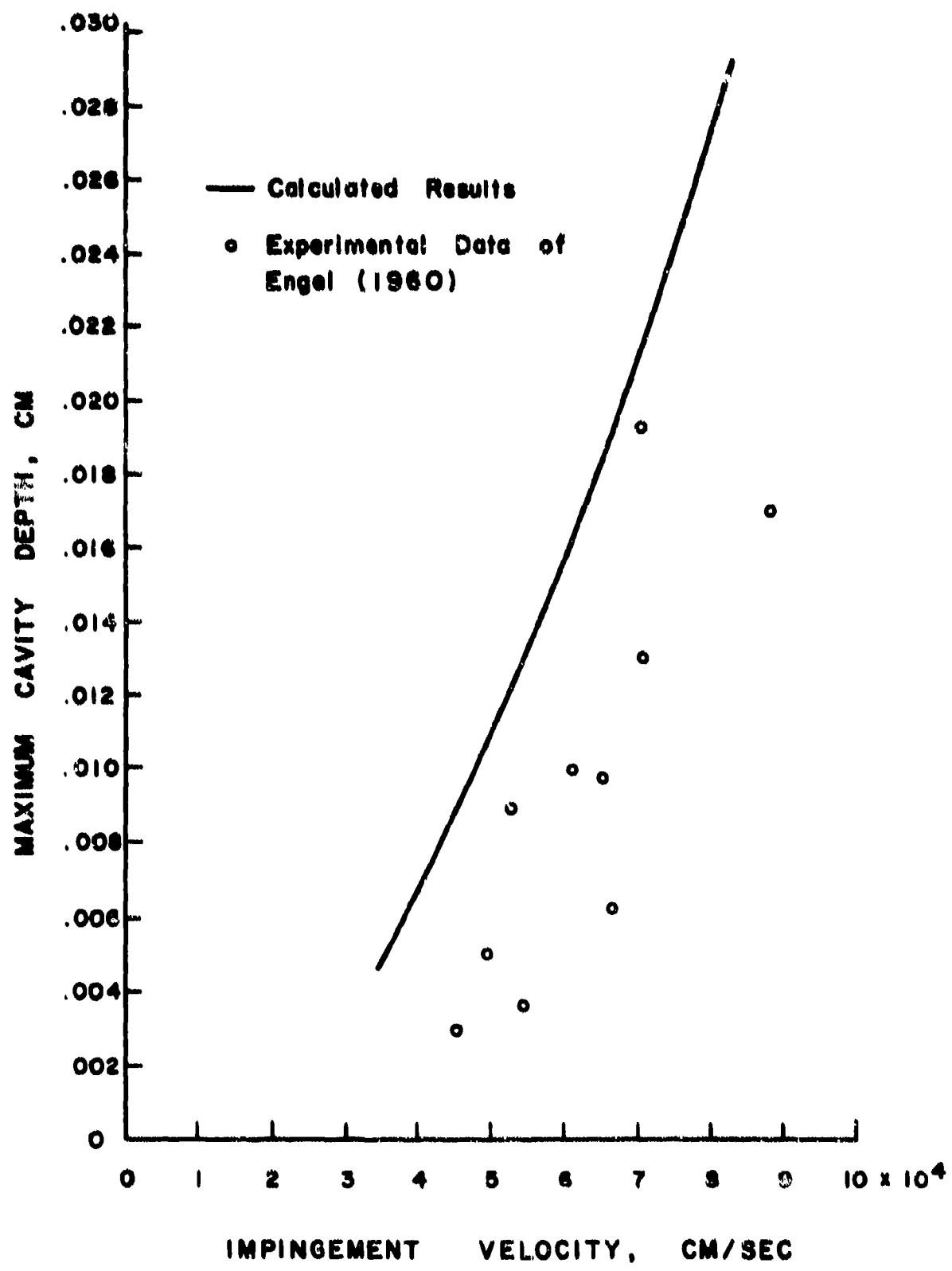


FIGURE 12. IMPACT OF WATER DROPS ON COPPER

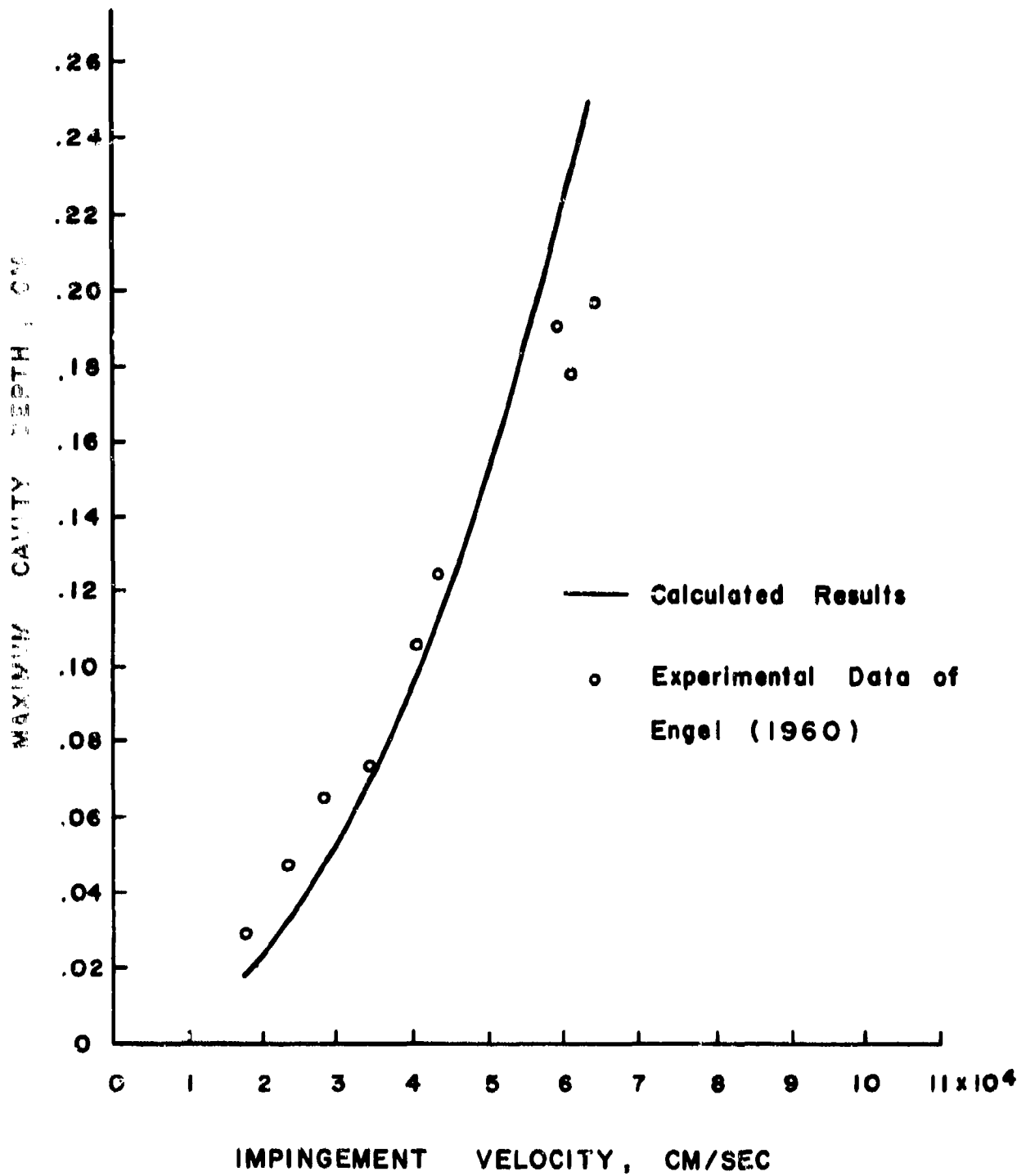


FIGURE 13. IMPACT OF MERCURY DROPS ON COPPER

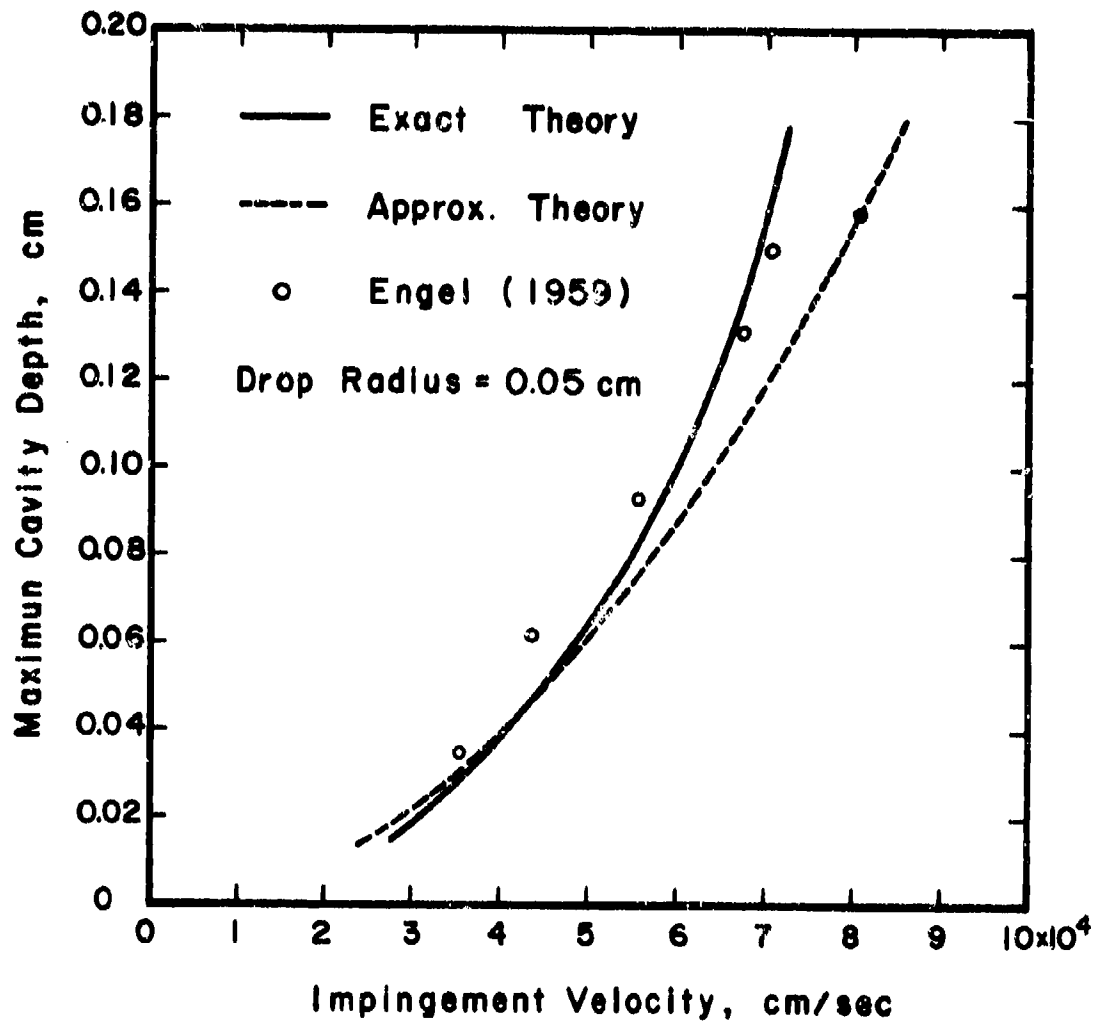


FIGURE 14. IMPACT OF MERCURY DROPS AGAINST 2024-O ALUMINUM

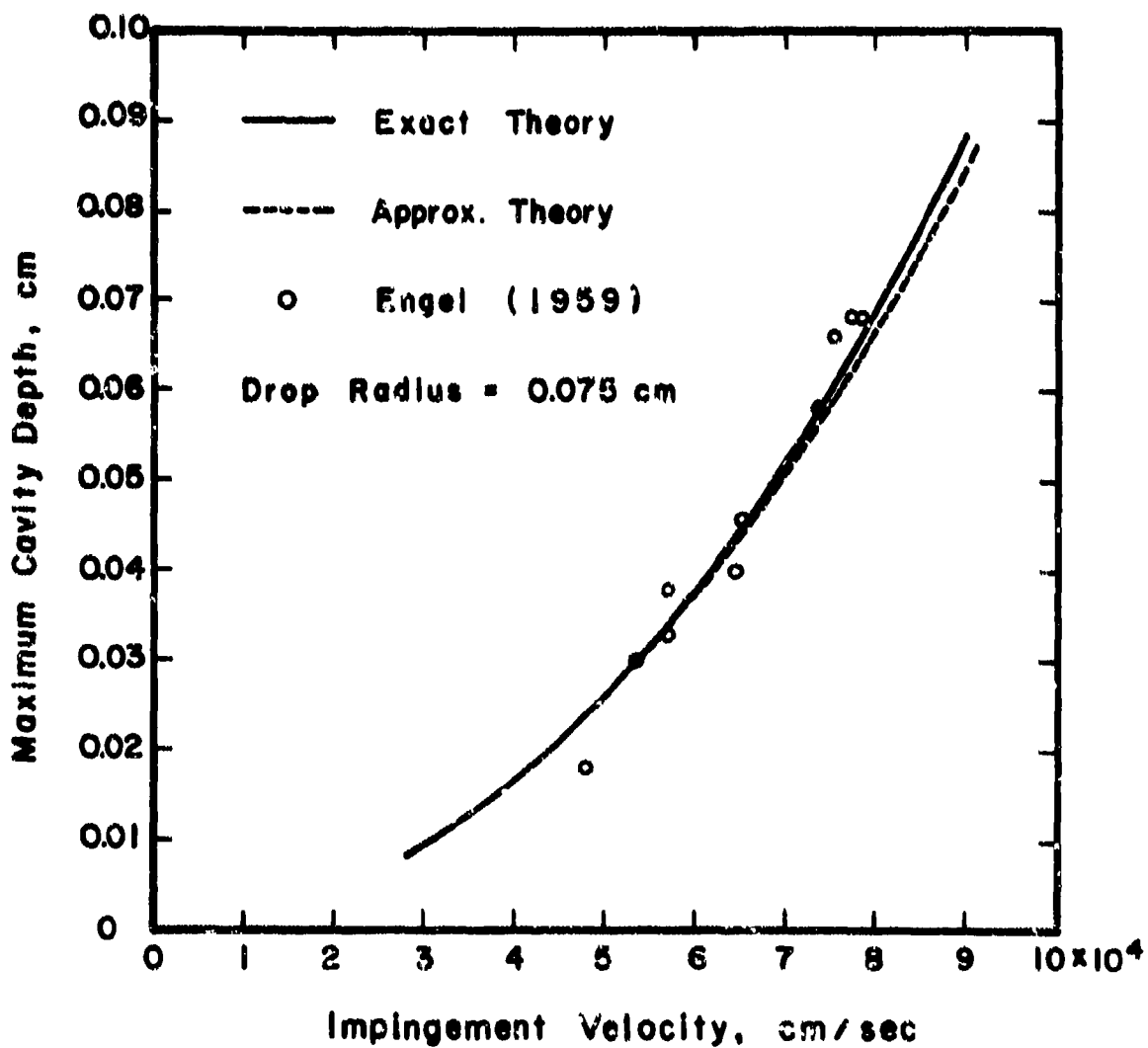


FIGURE 15. IMPACT OF MERCURY DROPS AGAINST STEEL

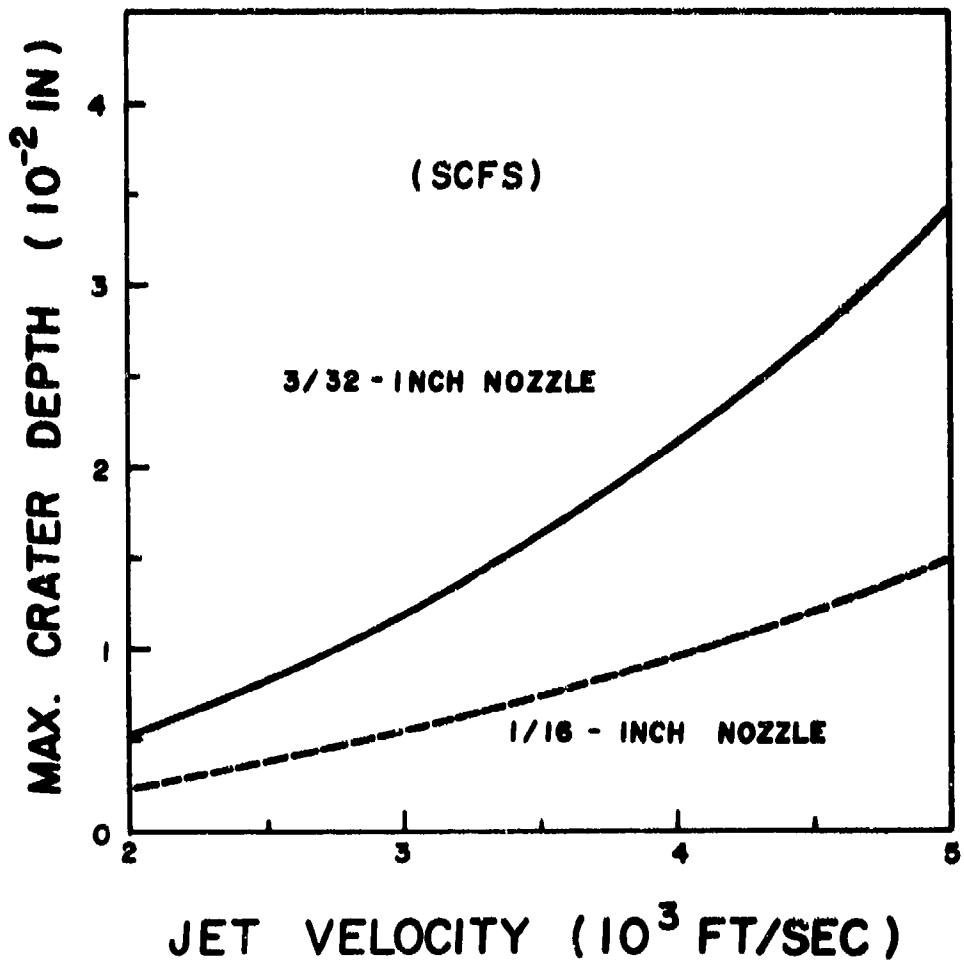


FIGURE 16. RELATION BETWEEN MAXIMUM CRATER DEPTH AND JET VELOCITY FOR SCFS

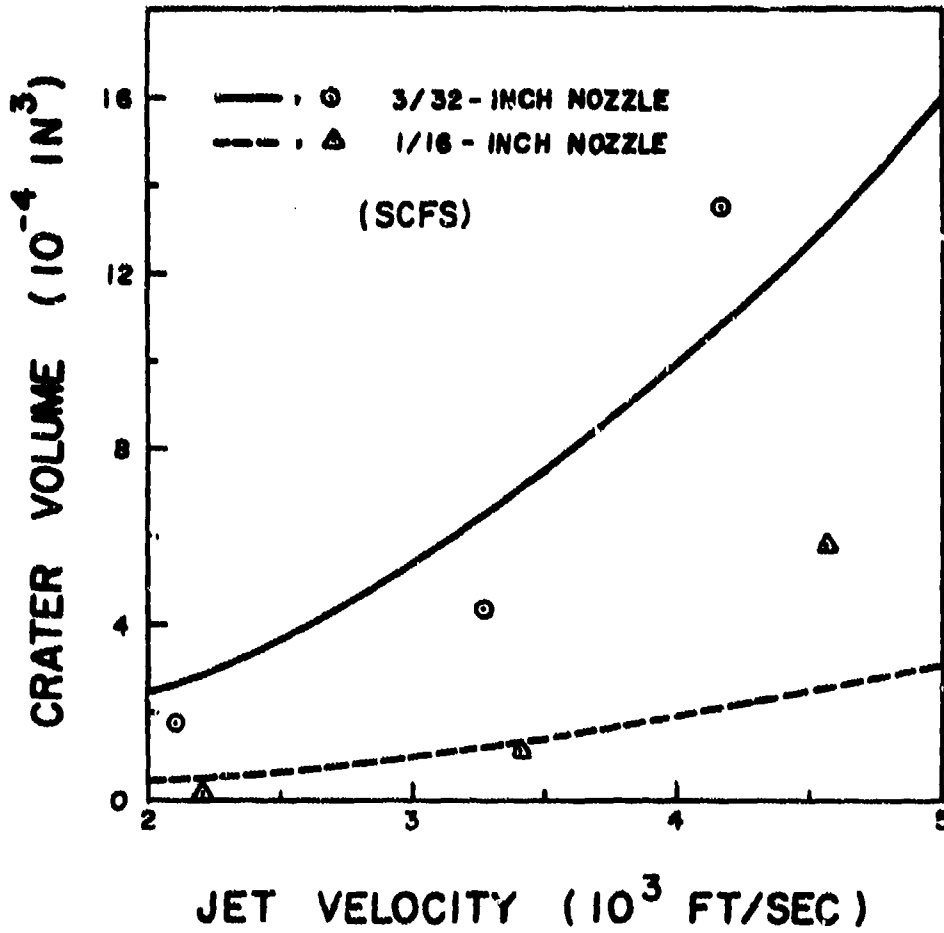


FIGURE 17. RELATION BETWEEN CRATER VOLUME AND JET VELOCITY FOR SCFS

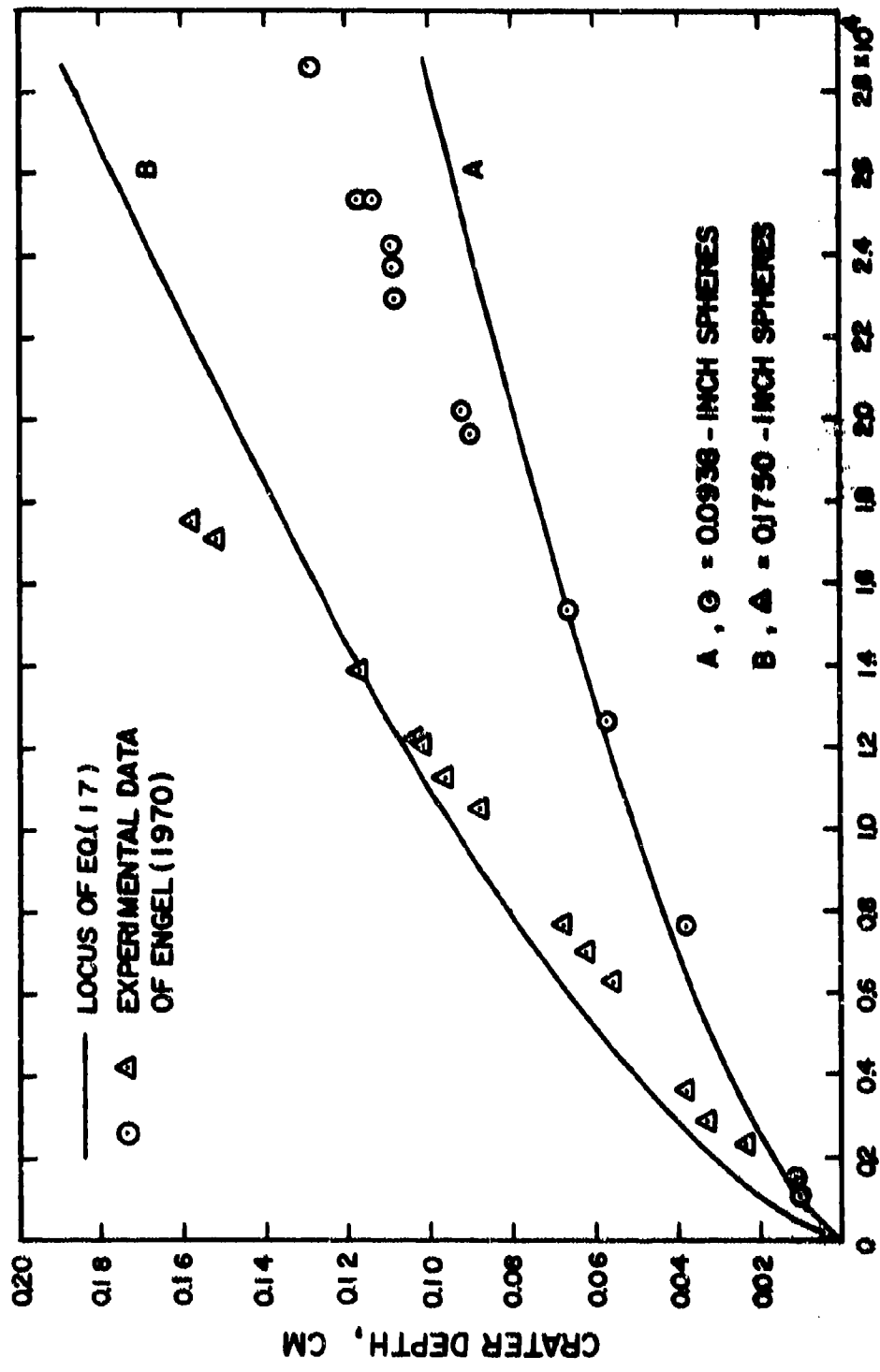


FIGURE 18. IMPACTS OF STEEL SPHERES AGAINST ALUMINUM

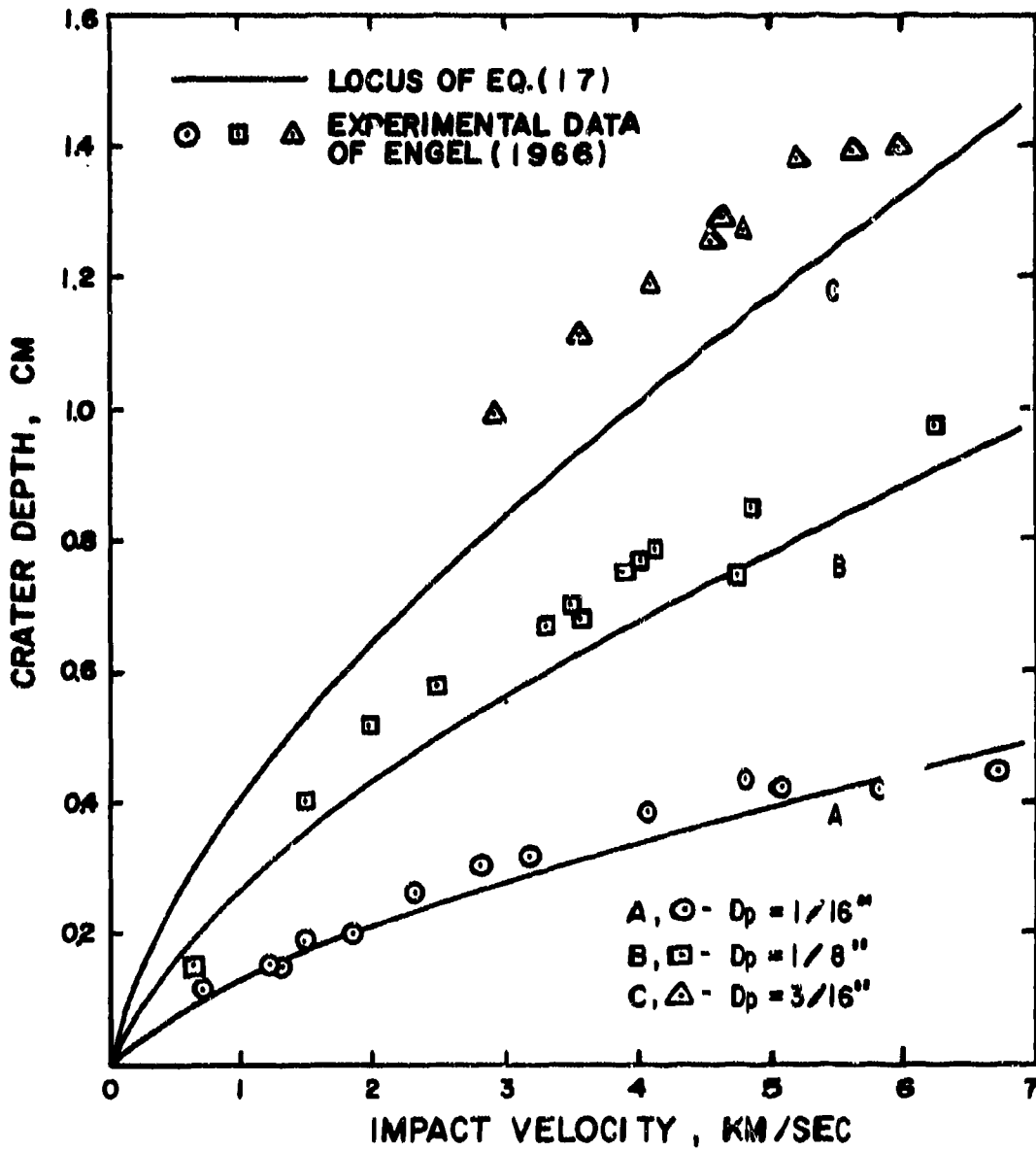


FIGURE 19. IMPACTS OF COPPER SPHERES AGAINST COPPER

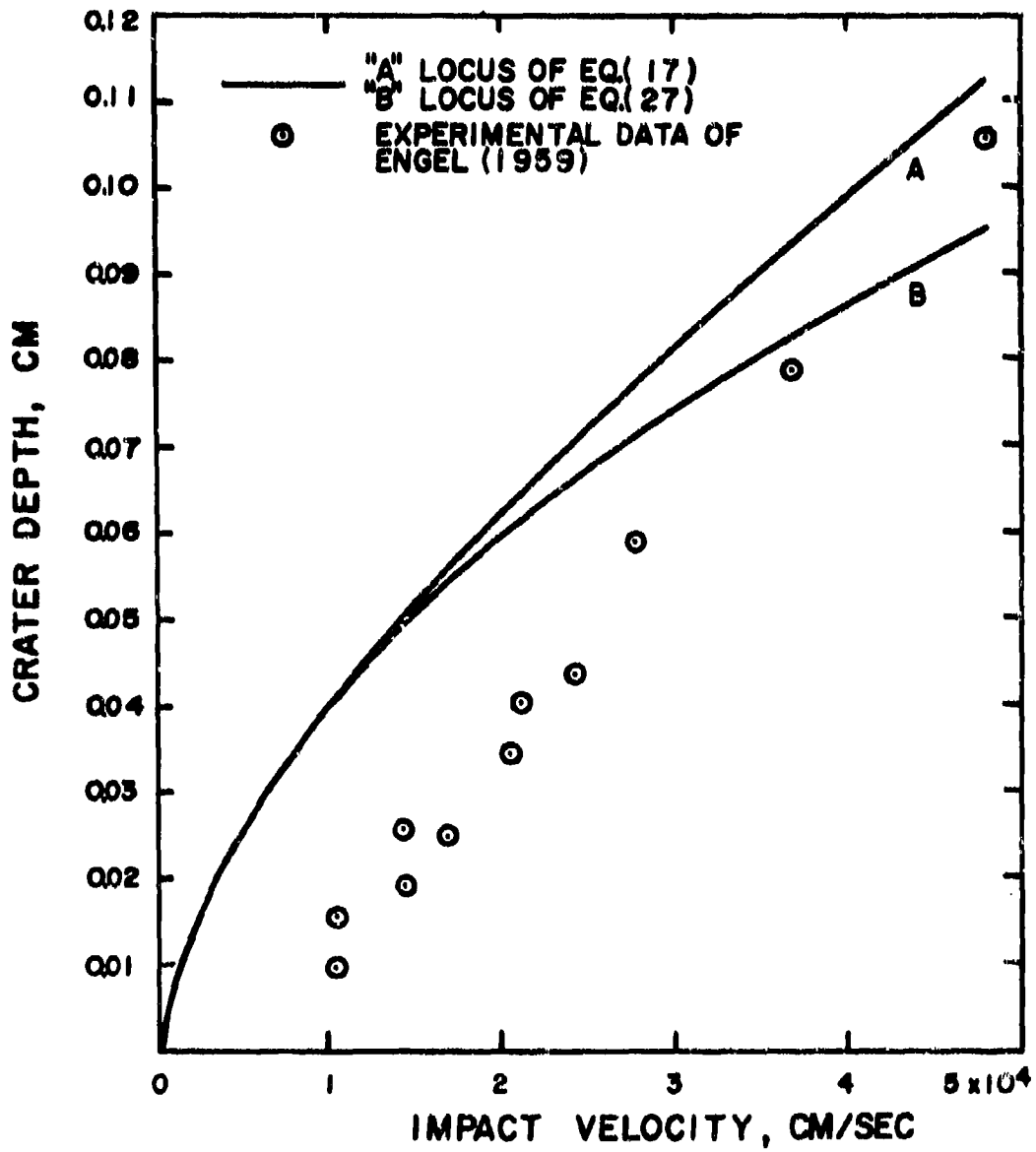


FIGURE 20. IMPACTS OF MERCURY DROPS ($D_p = 0.10$ CM) AGAINST LEAD

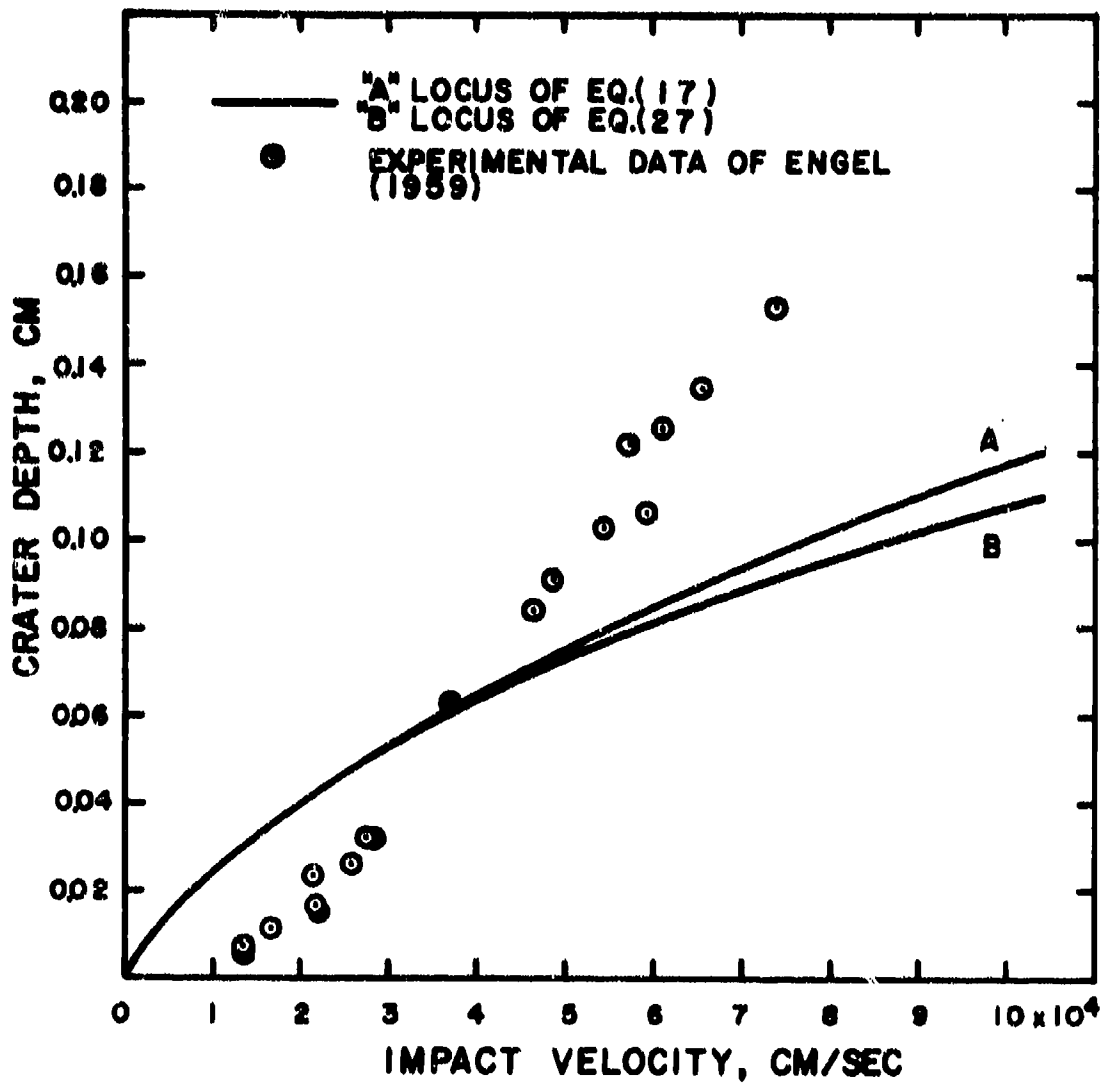


FIGURE 21. IMPACTS OF MERCURY DROPS ($D_p = 0.10$ CM) AGAINST ALUMINUM

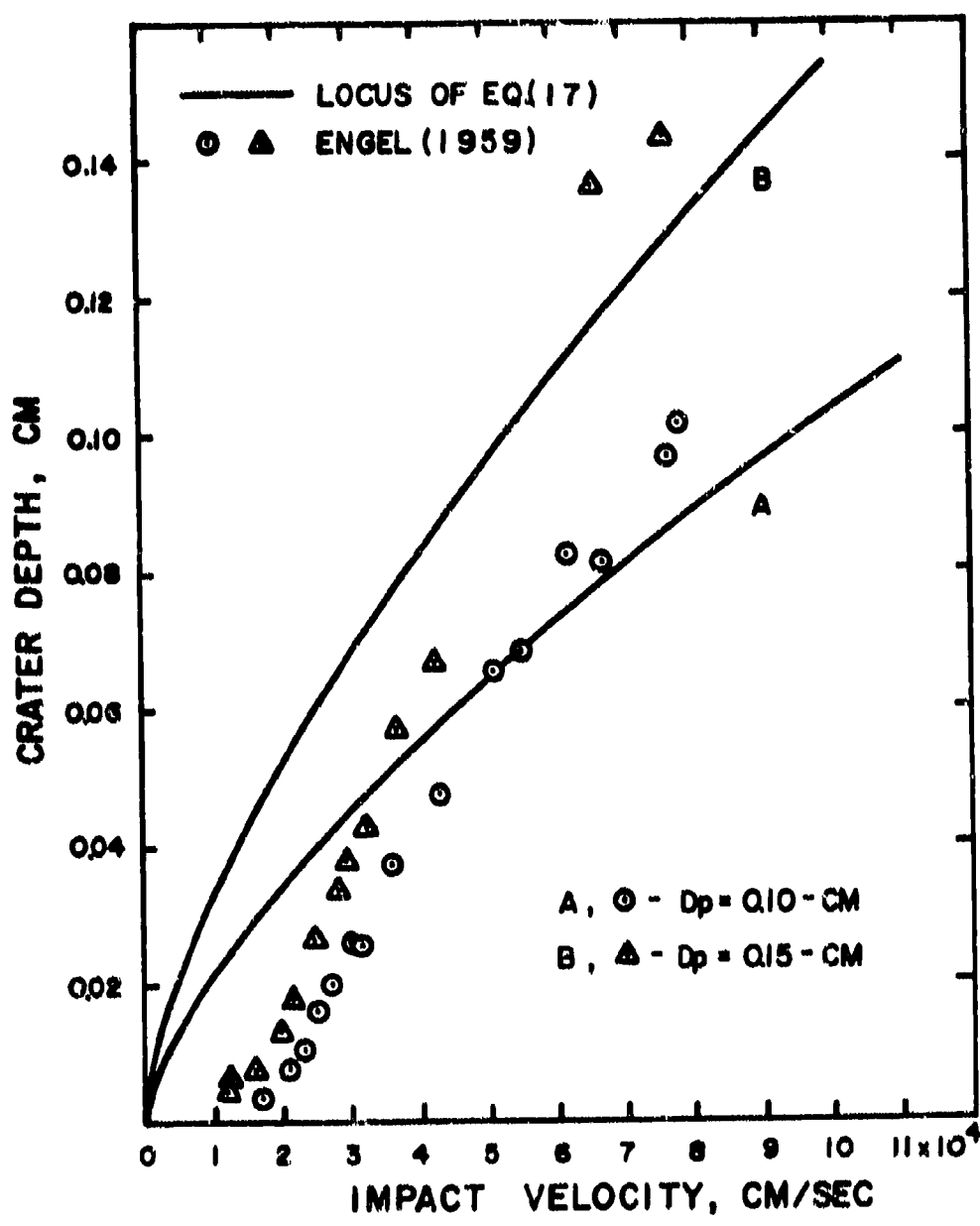


FIGURE 22. IMPACTS OF MERCURY DROPS AGAINST COPPER

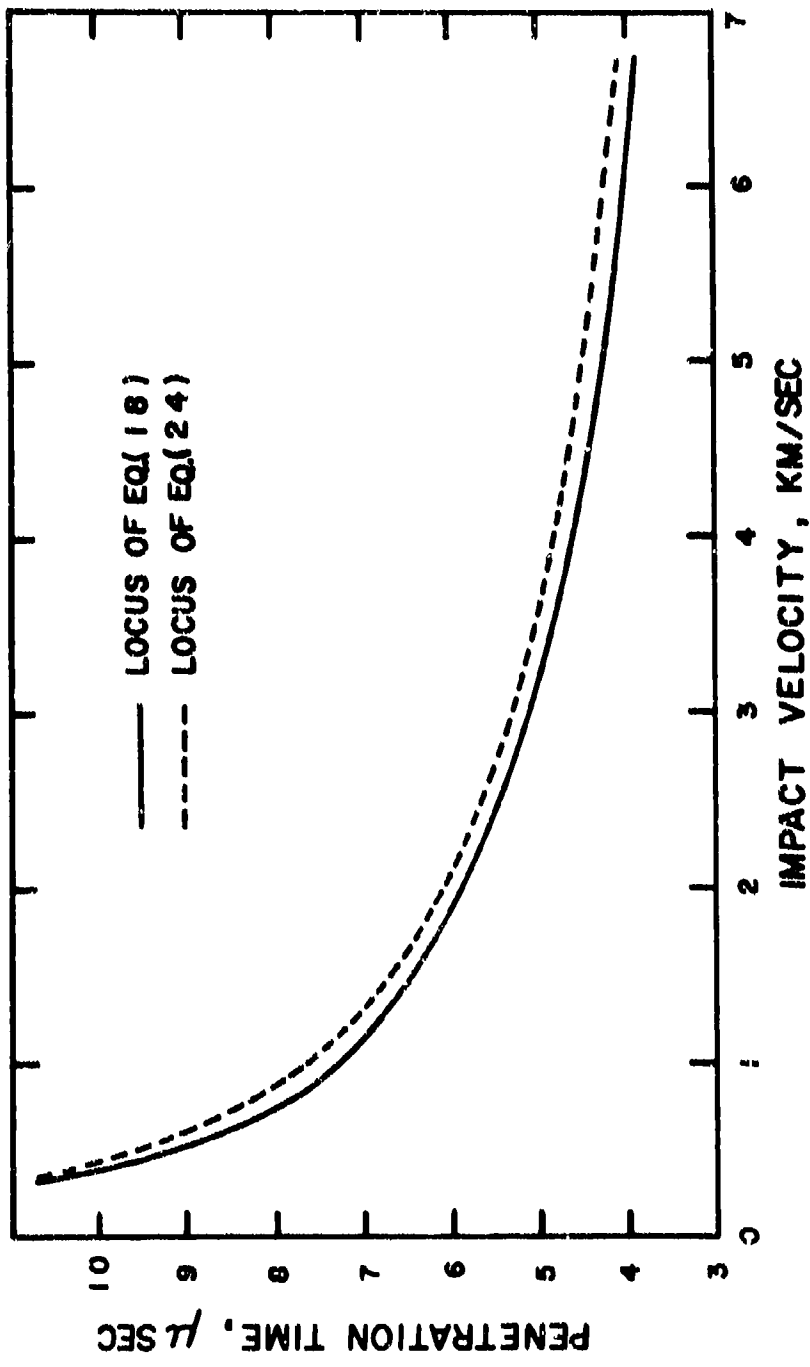


FIGURE 23. PENETRATION TIME IN IMPACTS OF TWO SHAPES OF ALUMINUM PROJECTILES
($D_p = 0.635$ CM, AGAINST ALUMINUM)

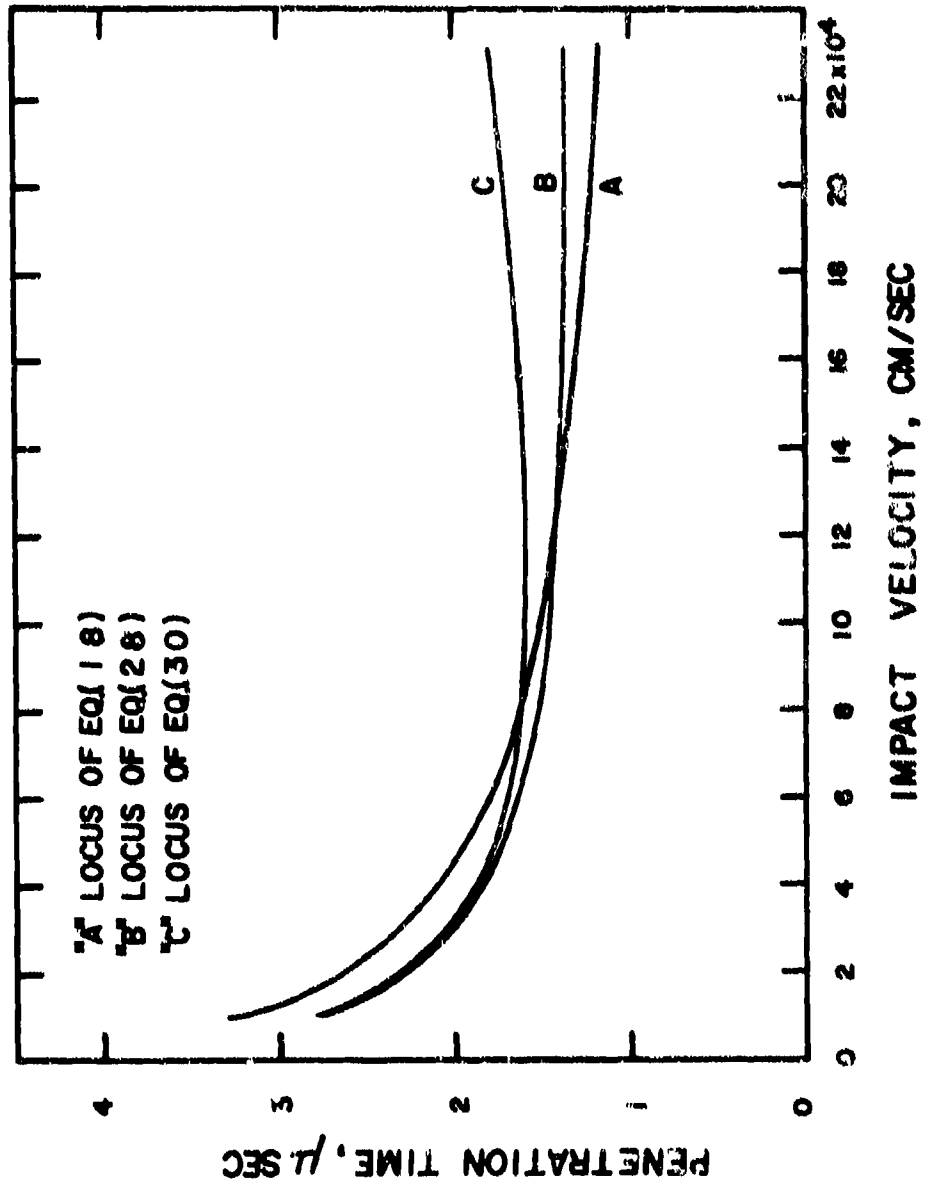


FIGURE 24. PENETRATION TIME IN IMPACTS OF MERCURY SPHERES ($D_p = 0.10$ CM) AGAINST COPPER

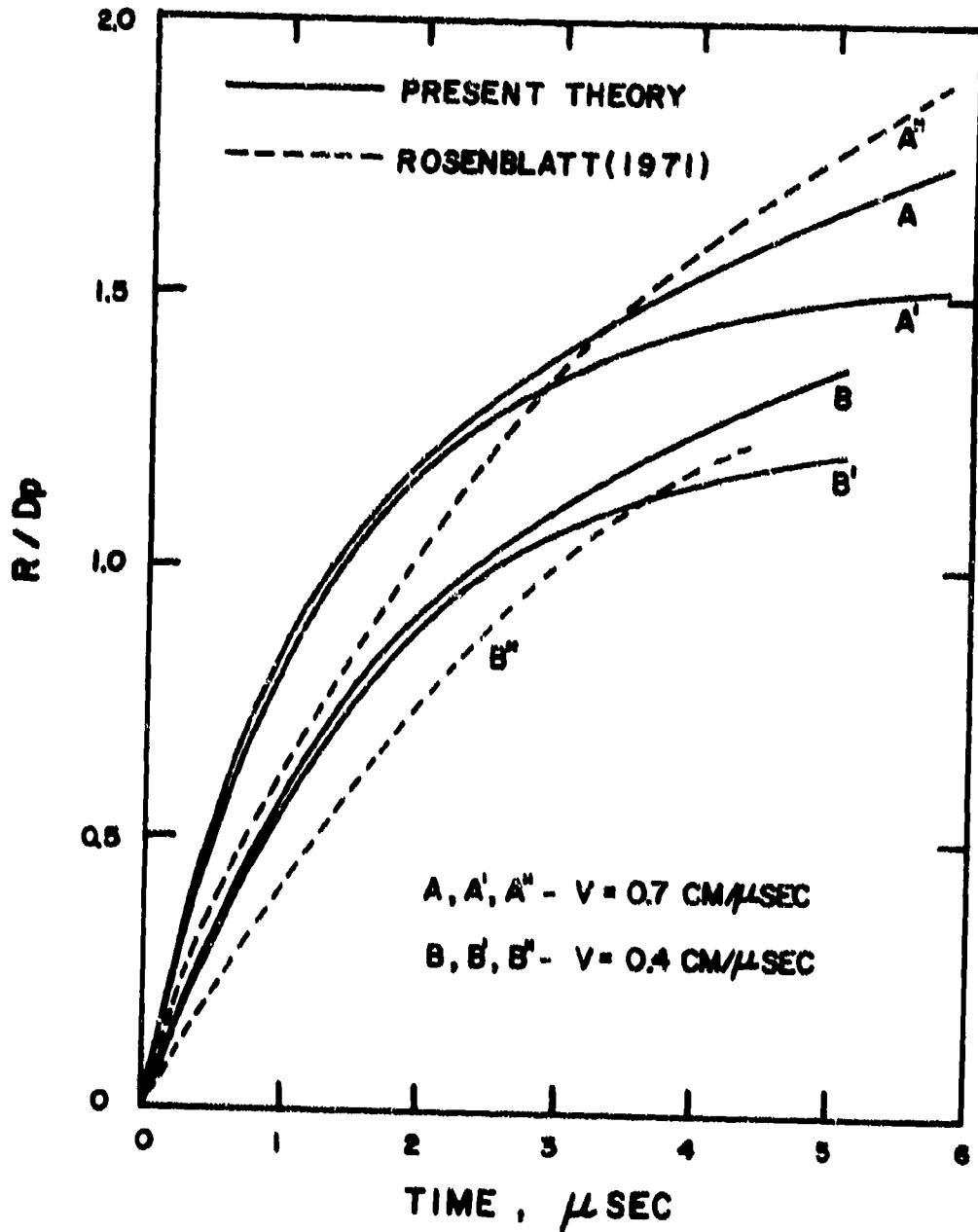


FIGURE 25. INSTANTANEOUS CRATER DEPTH IN IMPACTS OF ALUMINUM SPHERES ($D_p = 0.635 \text{ CM}$) AGAINST ALUMINUM (CURVES A, B ARE BASED ON DYNAMIC YIELD STRENGTH AND A'B' ARE BASED ON LATENT HEAT)

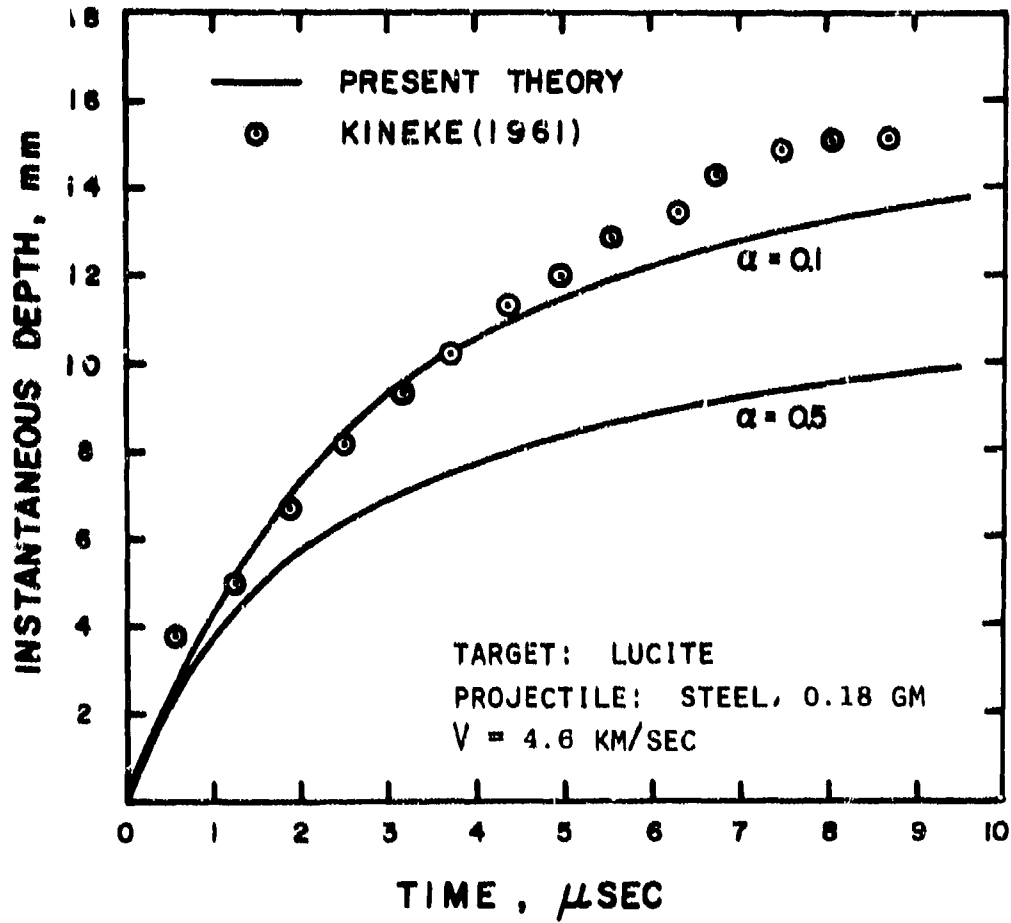


FIGURE 26. INSTANTANEOUS CRATER DEPTH IN IMPACTS OF STEEL PROJECTILES AGAINST LUCITE

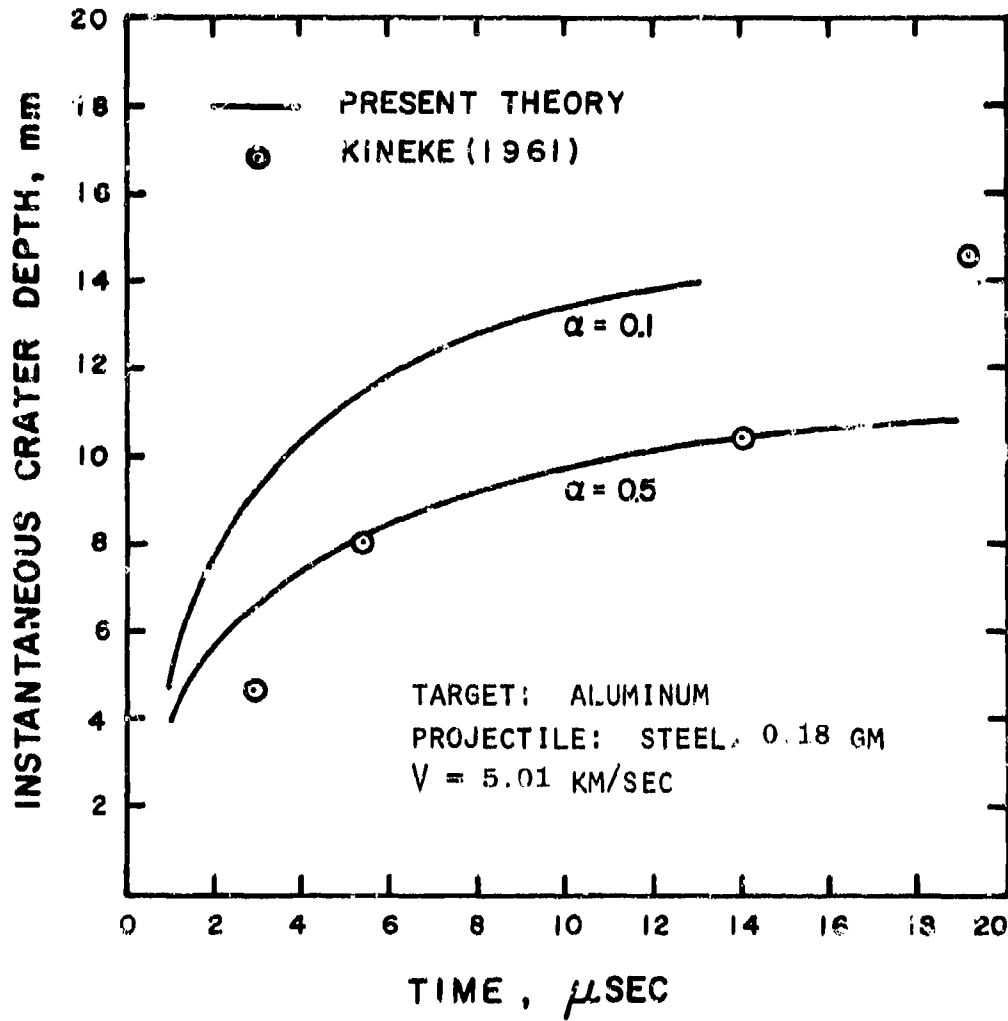


FIGURE 27. INSTANTANEOUS CRATER DEPTH IN IMPACTS OF STEEL PROJECTILES AGAINST ALUMINUM

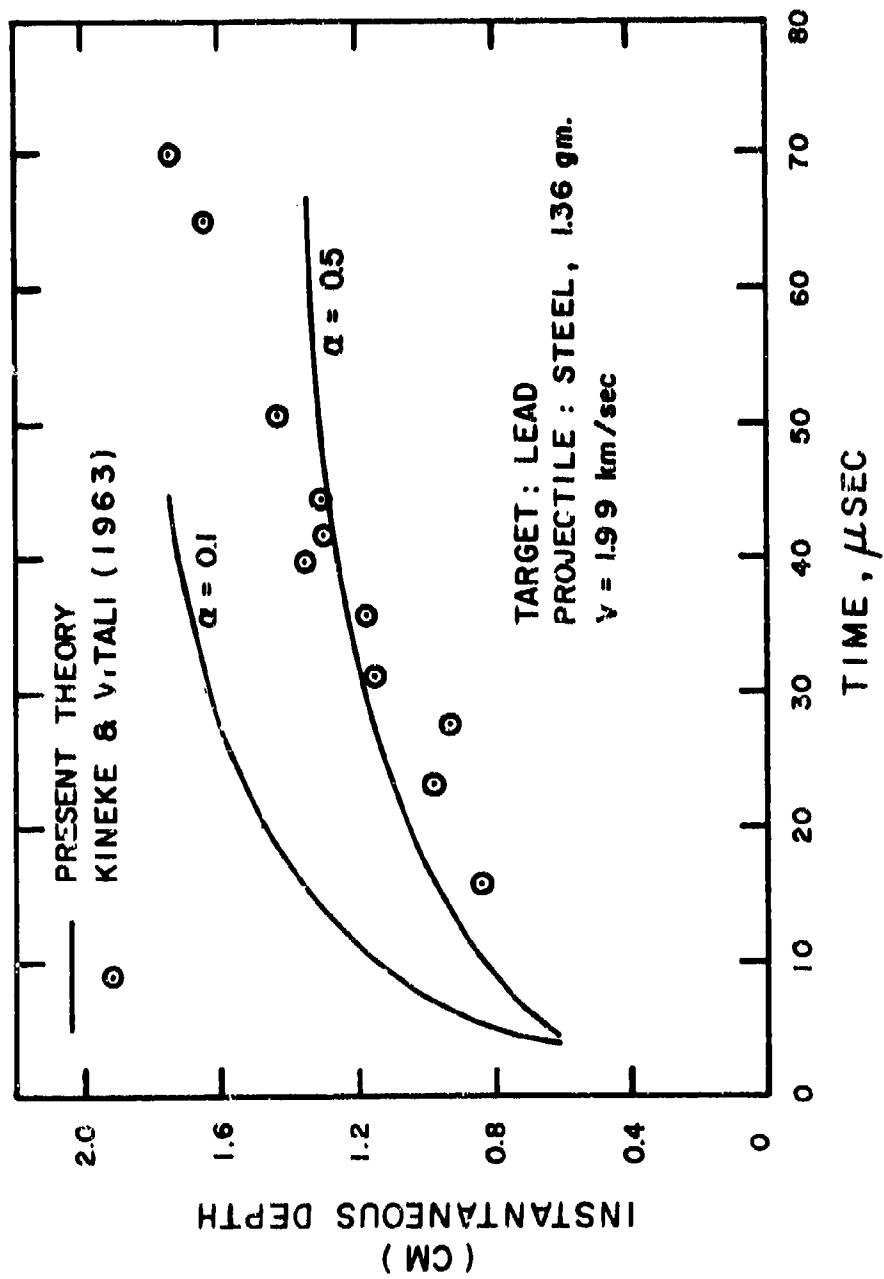


FIGURE 28. INSTANTANEOUS CRATER DEPTH IN IMPACTS OF STEEL PROJECTILES AGAINST LEAD

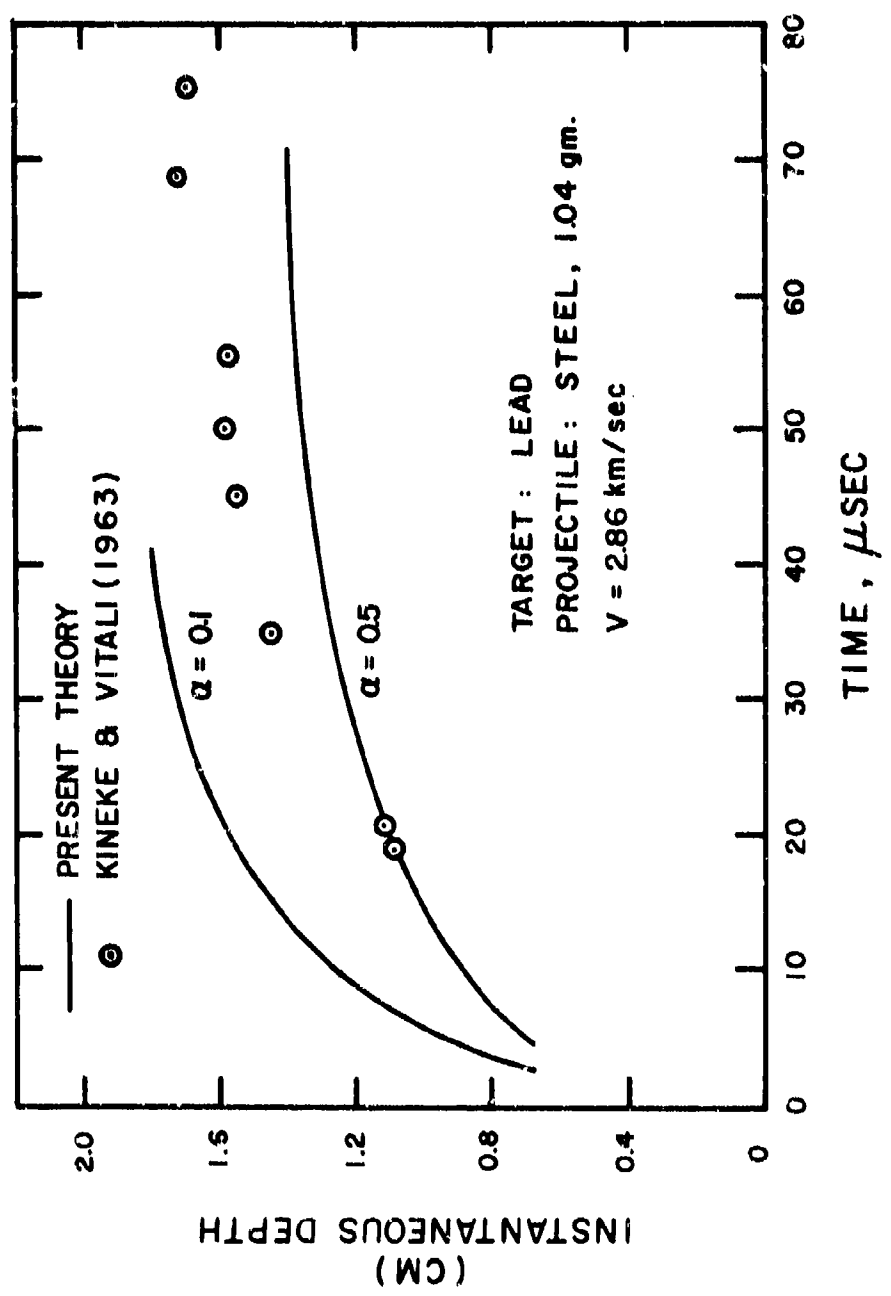


FIGURE 29. INSTANTANEOUS CRATER DEPTH IN IMPACTS OF STEEL PROJECTILES AGAINST LEAD

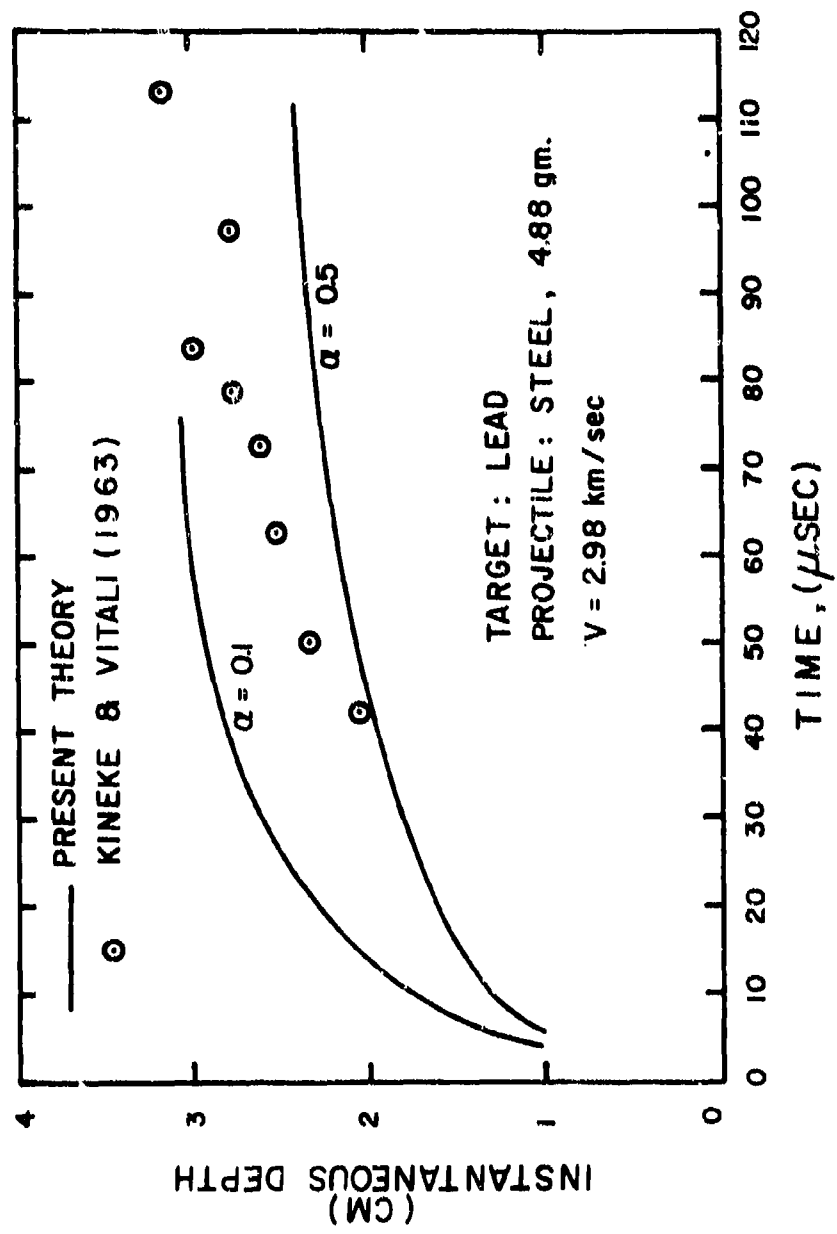


FIGURE 30. INSTANTANEOUS CRATER DEPTH IN IMPACTS OF STEEL PROJECTILES AGAINST LEAD

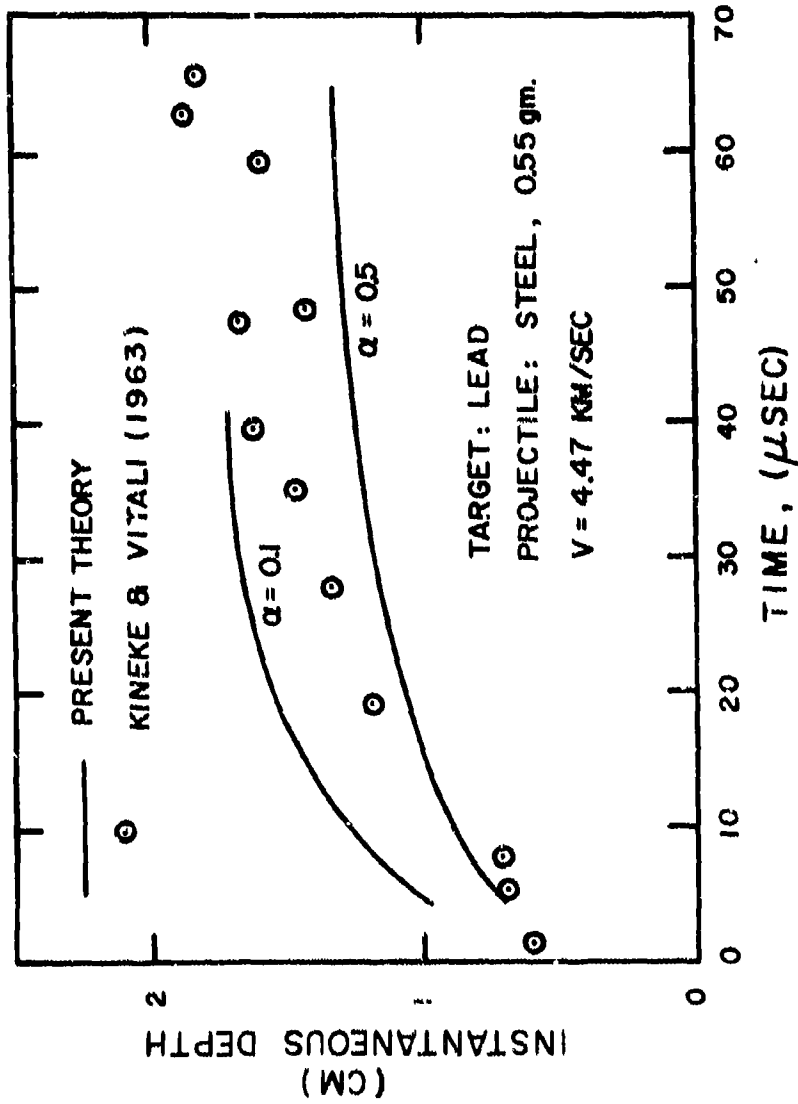


FIGURE 31. INSTANTANEOUS CRATER DEPTH IN IMPACTS OF STEEL PROJECTILES AGAINST LEAD

ci

APPENDIX C

FRACTURE TOUGHNESS OF SCFS

by

Dallas Smith and Mikkilineni Chowdary
Assistant Professor and Graduate Student, Respectively

Department of Engineering Science
Tennessee Technological University
Cookeville, Tennessee 38501

C1

APPENDIX C

FRACTURE TOUGHNESS OF SCFS

by Dallas Smith and Mikkilineni Chowdary

INTRODUCTION

This appendix is concerned with the fracture toughness of the slip-cast fused silica (SCFS). While this material has been intensively investigated as a missile radome material, its fracture toughness has not been determined. This quantity, an intrinsic property of the material, is a measure of the resistance of the material to brittle fracture. It serves as a useful basis of comparison of the fracture properties of the material with those of other materials and as an indication of the influence of certain fabrication variables, such as firing temperature, etc., on the fracture behavior of the material. The immediate object of the investigation was to determine the plane-strain critical stress intensity factor K_{IC} and to demonstrate the possibility of increasing the fracture strength by impregnating the material with a fluid known as Almag oil.

For most ceramics and glasses the theoretical cohesive strength is approximately 100 times the normal engineering strength [1]. This discrepancy was first explained by Griffith [2]. Griffith postulated that a brittle material contains a population of fine cracks prior to loading which produce a stress concentration of sufficient magnitude so that the theoretical cohesive strength is reached in localized regions at a nominal stress which is well below the theoretical value. The fracture criterion developed by Griffith can be applied not only to micro-cracks but to large cracks and flaws as well.

Different approaches have been used to apply Griffith's fracture criterion, but the stress intensity factor (SIF) approach is the one which is most widely accepted. The plane-strain stresses near the tip of a crack loaded by tension forces are [3]

$$\sigma_x = \frac{K_I}{\sqrt{2\pi r}} \cos \frac{\theta}{2} \left[1 - \sin \frac{\theta}{2} \sin \frac{3\theta}{2} \right]$$

$$\sigma_y = \frac{K_I}{\sqrt{2\pi r}} \cos \frac{\theta}{2} \left[1 + \sin \frac{\theta}{2} \sin \frac{3\theta}{2} \right]$$

$$\tau_{xy} = \frac{K_I}{\sqrt{2\pi r}} \sin \frac{\theta}{2} \cos \frac{\theta}{2} \cos \frac{3\theta}{2}$$

$$\sigma_z = \nu(\sigma_x + \sigma_y); \quad \tau_{xy} = \tau_{yz} = 0 \quad (1)$$

where K_I is the stress intensity factor for the opening mode (mode I), r and θ are polar coordinates, and the stress components are given in Figure 1. The stress intensity factor does not depend on the coordinates, r and θ , hence it controls the intensity of the stress field but not the distribution. The stress intensity factor is a function of geometry of the specimen, crack geometry, and type of loading. In general the SIF is given by

$$K_I = \alpha \sigma (\pi a)^{1/2} \quad (2)$$

where σ is the stress, a is crack length, and α is a geometric factor which can be determined by solving the appropriate equations of elasticity for a particular geometry. Fracture occurs when the value of K_I calculated from Eq. (2) approaches K_{IC} , the critical value of K_I . The critical strain energy rate G_{IC} of Irwin [4] is given in terms of K_{IC} by

$$G_{IC} = \frac{(1-\nu^2)K_{IC}^2}{E} \quad (3)$$

where E is Young's modulus and ν is Poisson's ratio. The critical strain energy release rate is just twice the surface energy γ

$$G_{IC} = 2 \gamma \quad (4)$$

where γ represents the work per unit area required to create fracture surface. The surface energy γ is the sum of the thermodynamic free energy, γ_s , and the surface energy associated with plastic work along the fracture surface, γ_p ,

$$\gamma = \gamma_s + \gamma_p \quad (5)$$

To find K_{IC} a cracked specimen is tested for which K_I is known, the failure load or stress is observed, and K_{IC} is calculated from Eq. (2). The values of G_{IC} and γ then follow from Eqs. (3) and (4).

TEST METHOD

Fracture studies of ceramics have traditionally focused on the surface energy. Primarily, two different methods have been used: the double cantilever beam method and the integral work of fracture method. Explanations of the double cantilever beam method are given by Gillis and Gilman [5] and Wiederhorn et al [6]. The integral work of fracture method, used by Nakayama [7] and Simpson and Wasylyshyn [8], employs a three-point bend specimen with a special-shaped crack which allows stable crack extension. For stable extension all the work expended goes to the creation of fracture surfaces. This demands that energy losses such as stored energy in the testing machine, kinetic energy of the fragments, etc. must be kept to a minimum. To find γ , the total work expended is divided by the area of fracture surfaces created. The main disadvantage lies in the possibility of energy losses occurring during unstable crack extension.

In the present work the three-point bend specimen recommended by ASTM [9] for fracture toughness testing of metals was used. This specimen has the advantage that it has been thoroughly investigated and K_{Ic} is accurately known as a function of load and dimensions. It is universally accepted for the testing of brittle metals. Swartzberg [10] used this specimen for the testing of fused silica glass. One disadvantage is the necessity of having an actual crack in the specimen prior to the test.

The SCFS plates, 5 inches by 5 inches, from which the specimens were machined, were fabricated and supplied by the U. S. Army Missile Command. The silica slip was prepared by wet grinding fused silica to a particle size in the range 1-50 microns with an average size of 7.5-8 microns. The slip was poured into plaster molds of the required dimensions and allowed to harden throughout. The firing treatment given to the castings was as follows: The castings were heated to 1800° F in a period of 3 hours and held for 30 to 45 minutes at that temperature. Then the castings were heated to 2310° to 2320° F in 2-3/4 hours and soaked at that temperature for 30-45 minutes. The castings were then air-cooled in the furnace to room temperature in a period of approximately 17 to 18 hours. The total amount of impurity is 200 ppm. For the above firing the amount of cristobalite is approximately 1 percent. The approximate properties of the SCFS at room temperature are:

Young's modulus	6.5×10^6 psi
Modulus of Rupture	5.0×10^3 psi
Poisson's ratio	0.155
Density	$0.186 \times 10^{-3} \frac{\text{lb-sec}^2}{\text{in}^4}$
Percent porosity	13 percent

The effects of firing temperature and firing time on the properties of SCFS have been studied extensively by Walton and Poulos [11].

A photograph of a beam ready for testing is shown in Figure 2. The beams were prepared of three nominal thicknesses--0.25, 0.40, and 0.50 inch. The first two were the thickness of the castings; the last was machined to 0.50 inch from a 0.75-inch casting. The depth and length of the beams were 1.0 inch and 4.5 inches, respectively. The beams were machined to size by means of a 20-inch-diameter diamond-impregnated saw. The saw thickness was 0.075 inch and the speed was 1725 rpm. Water was used as a cutting lubricant.

The crack-starter slot was introduced into the specimens by using a circular diamond-impregnated saw blade of 4-inch diameter. The blade speed was 200 rpm. The notch width was 0.04 inch, and the depth was maintained within the limits of 0.45 inch to 0.50 inch to meet ASTM requirements. It is important that the notch terminate with a sharp crack. The following procedure was used to accomplish this. The slot was extended an additional 0.02 inch by means of an 0.008-inch diamond-impregnated wire saw. A hacksaw blade--ground as a sharp knife edge along the sides of the teeth--was used to further extend the notch. The hacksaw notch extended an additional 0.02 inch, terminating in a tip radius of approximately 0.002 inch. This last cut caused small cracks to extend a distance of 0.01 to 0.02 inch. This procedure was developed by using glass so that the crack-tip could be observed. Figure 3 shows photographs of two typical crack tips taken at 45° through the sides of the glass beams. That the small notch-root cracks existed in the SCFS specimens as well as in glass specimens was verified by inspection of the SCFS fracture surfaces after each test. Figure 4 shows the approximate shape of the final crack tip

An autographic curve of load versus crack-opening-displacement (COD) is required by ASTM to establish the critical load. A standard COD gage

was attached across the notch, Figure 2, by means of knife edges cemented to the SCFS beam with epoxy. The load rate was controlled by means of a spring of suitable stiffness (85 lb/in) inserted between the specimen and the cross head, Figure 2. Using a cross head speed of 0.1 inch/minute, the resulting load rate was approximately 8.5 lbs/minute. This resulted in a test duration of approximately the same as for a typical metal when using the load rate specified by ASTM. A 1000-lb-capacity load cell was used for the tests. The 0-20-lb range was used for 0.25-inch-thick specimens, and the 0-50-lb range was used for the 0.40- and 0.50-inch-thick specimens. The load fixture was machined in accordance with the ASTM specimens.

To obtain an average, at least three dry samples of each thickness were tested. To avoid any environmental effects on the crack tip, the final crack tip was made just prior to the test. Several samples were also tested after being soaked for different periods in Almag oil (a metal-working lubricant manufactured by the Texaco Company). In this case the final crack was made just before immersing the specimen in the oil.

The precise crack length was measured after specimen fracture. With the crack length, specimen dimensions, and critical load known, the critical stress intensity factor K_{IC} was calculated by the following formula

[9]

$$K_{IC} = \frac{P_C S}{BW^{3/2}} f\left(\frac{a}{W}\right) \quad (6)$$

- where: P_C = the critical load,
 H = thickness of the beam, inch,
 S = span length = 4 inches,
 W = depth of the beam, inch,
 a = crack length, inch, and

$$f\left(\frac{a}{W}\right) = 2.9\left(\frac{a}{W}\right)^{1/2} - 4.6\left(\frac{a}{W}\right)^{3/2} + 21.8\left(\frac{a}{W}\right)^{5/2} - 37.6\left(\frac{a}{W}\right)^{7/2} + 38.7\left(\frac{a}{W}\right)^{9/2}$$

RESULTS

The individual and average values determined for K_{IC} and G_{IC} for all the dry and oil-impregnated samples are shown in Table I. For the dry samples the average values of K_{IC} are 644, 638, and 692 psi-in^{1/2} for the 0.25-, 0.4-, and 0.5-inch-thick specimens, respectively.

Contrary to the usual behavior in metals, the highest value occurred for the thickest specimen. There is a simple explanation for this. The 0.25-0.40-inch-thick beams were the same thickness as the castings; the sides of the beams contained the original casting surfaces. The casting surfaces were noticed to be of poorer quality than the average; in some cases chipping and flaking occurred. The presence of these surfaces lowered the value of K_{IC} for the thinner specimens. The 0.50-inch-thick specimens were machined from casting 0.75 inch thick, and hence did not contain the original casting surfaces. Thus, the value of fracture toughness believed to be representative of slip-cast fused silica is 692 psi-in^{1/2}.

Another material fabrication effect was noticed. A layer of material at the mid-plane of the castings apparently had properties different from the average. This layer was easily visible in the oil-soaked samples. The photograph in Figure 5 clearly shows the layer. The properties of the mid-plane layer, if significantly different from the average, would exert a strong influence on the strength of the thinner beams.

In general, scatter was low except for the 0.40-inch-thick beams. These beams exhibited a considerable thickness variation from one end to

the other, sometimes varying as much as 0.06 inch. This tapering probably explains the scatter encountered for the 0.40-inch-thick beams. This thickness variation resulted from inaccurate casting.

The increase in K_{IC} due to soaking the SCFS in Almag oil is also shown in Table I. For the 0.25-inch-thick specimens the increase is 12.5 percent for 12 hours of soaking and 17 percent for 15 hours. The increase was not as great for the specimens soaked for 24 hours. This may have been due to the high humidity in the laboratory on the day these samples were tested. The relative humidity on that day was 73 percent, whereas the average relative humidity was near 40 percent. Even after 24 hours of soaking the 0.25-inch beams were not completely impregnated with oil. The oil gives the SCFS a yellowish appearance, but after fracture a whitish region could be observed at the interior of the beam where the oil had not penetrated. Two 0.50-inch-thick beams were soaked for 60 hours. They show an average K_{IC} value of 17 percent more than the 0.50-inch-thick dry specimen. These specimens, too, were not impregnated at the interior. Figure 6 displays the improvement in fracture strength of SCFS due to impregnation with Almag oil.

Almag oil was an example fluid chosen primarily because of its penetrating characteristics. Impregnation--perhaps with other materials such as epoxy--appears to be a promising way to increase the fracture strength of SCFS. A silicone resin has been used on some SCFS radomes. Unfortunately, depletion of the test material prevented a more thorough study of the effects of impregnation.

The mechanism by which impregnation with Almag oil increases the fracture toughness of SCFS is not understood at this time. A number of reasons, however, can be suggested. By chemical reaction the oil may blunt the tip of the crack slightly, decreasing the stress concentration, thus requiring

and higher load for fracture. In soaking into the SCFS, the oil fills the pores. It is not inconceivable that this permits the transfer of stress across pores in such a way as to redistribute the stress and decrease microscopic stress concentrations.

Photographs of fracture surfaces made by the scanning electron microscope, Figures 7 and 8, show a striking difference in the dry and oil-soaked samples. The fracture surfaces of the oil-soaked samples have the appearance of numerous small globules. Dark angular particles of fused silica 10-20 μ in size are visible on the surfaces of the dry samples. These large particles in general are not visible in the oil-soaked samples. This suggests that in the dry samples the crack progressed around the boundaries of the large particles, while in the oil-soaked samples the crack passed through the large particles, breaking them into rough surfaces. This would effectively increase the fracture surface area, thus increasing K_{IC} . Why the oil would cause this behavior is not known.

All the above explanations for the increase in K_{IC} due to soaking in Almag oil are tentative. Further research is needed to settle this question and to suggest other ways to enhance K_{IC} .

CONCLUSIONS

The ASTM three-point bend specimen was used to find the fracture toughness of slip-cast fused silica. The critical stress intensity factor K_{IC} was determined to be 692 psi-in^{1/2}. Some material inhomogeneities due to the casting technique caused slightly lower values for thinner specimens.

It was observed that the fracture toughness was increased by impregnating the specimens with Almag cutting oil. The amount of increase depended upon specimen thickness and time of soaking in oil. The greatest

increase observed in K_{IC} was approximately 17 percent. An inadequate supply of material prevented an extensive investigation.

As a missile radome material, SCFS has one main disadvantage: its relatively low resistance to cratering due to rain impact. This property limits the maximum speed of missiles flying through rain fields. To obtain higher velocities a way must be found to increase the capability of the SCFS to resist rain erosion. It is an important finding of this research that oil impregnation is one way to do this. Since a significant increase in fracture toughness was observed due to oil soaking, a similar increase in erosion resistance would be expected. Considerably more research is needed on this topic.

In order to find the fluid which provides the greatest permanent increase in toughness, experiments are needed using impregnating materials other than Almag oil. For a given fluid, studies of the impregnation technique will be required. Such a program might eventually lead to a greatly improved radome, permitting much higher all-weather missile velocities.

REFERENCES

1. Wiederhorn, S. M., "Fracture of Ceramics," Mechanical and Thermal Properties of Ceramics, edited by J. D. Wachtman, Jr., National Bureau of Standards Special Publication No. 303, 1969, p. 217.
2. Griffith, A. A., "The Phenomena of Rupture and Flow in Solids," Philosophical Transactions, Royal Society (London), Series A, Vol. 221, 1920, pp. 163-198.
3. Paris, P. C., and Sih, G. C., "Stress Analysis of Cracks," Fracture Toughness Testing and Its Applications, ASTM STP No. 381, American Society of Testing Materials, 1966, pp. 30-81.
4. Irwin, G. R., "Analysis of Stresses and Strains Near the End of a Crack," Journal of Applied Mechanics, Vol. 24, 1957, p. 361.
5. Gillis, P. P., and Gilman, J. J., "Double-Cantilever Cleavage Method of Crack Propagation," Journal of Applied Physics, Vol. 35, 1964, p. 647.

6. Wiederhorn, S. M., et al, "Critical Analysis of the Theory of the Double Cantilever Method of Measuring Fracture-Surface Energies," Journal of Applied Physics, Vol. 39, 1968, p. 1569.
7. Nakayama, J., "Direct Measurement of Fracture Energies of Brittle Heterogeneous Materials," Journal of The American Ceramic Society, Vol. 48, No. 11, 1965, p. 583.
8. Simpson, L. A., and Wasylyshyn, A., "The Measurement of Work of Fracture in High Strength Brittle Materials," Atomic Energy of Canada Limited, Report No. 3677, Pinawa, February 1972.
9. "Tentative Method of Test for Plane Strain Fracture Toughness of Metallic Materials (ASTM Designation E 399-70T)," Review of Developments in Plane Strain Fracture Toughness Testing, ASTM STP No. 463, American Society of Testing Materials, 1970, pp. 249-269.
10. Schwartzberg, F. R., (Martin Marietta Corporation, Denver), Private Communication to Smith, D. G., July 12, 1973.
11. Walton, J. D., and Poulos, N. E., "Slip Cast Fused Silica," Georgia Institute of Technology Special Report No. 43, 1964.

TABLE I.
 EXPERIMENTAL VALUES OF K_{IC}

<u>Condition</u>	<u>Thickness, Inches</u>	<u>R.H.</u>	<u>Temp °F</u>	<u>K_{IC} PSI-In^{1/2}</u>	<u>Avg K_{IC} PSI-In^{1/2}</u>	<u>Avg G_{IC} lb-In/In²</u>
Dry	0.2716	45	69	657	644	0.0623
	0.2702	40.5	69	623		
	0.2702	40.5	69	658		
	0.2678	40.5	69	639		
Dry	0.4090	60	70	737	638	0.0611
	0.4513	48	68	649		
	0.4527	48	68	540		
	0.4652	48	65	624		
Dry	0.4912	53.5	70	682	692	0.0719
	0.4942	53	70	698		
	0.5120	48	68	695		
Soaked for 12 hours	0.2677	44	70	781	721	0.0780
	0.2586	50.5	70	663		
	0.2612	50.5	70	718		
Soaked for 15 hours	0.2752	42	69	742	753	0.0851
	0.2605	42	69	756		
	0.2694	49	65	761		
Soaked for 24 hours	0.2710	73	69	735	716	0.0770
	0.2734	73	69	697		
Soaked for 60 hours	0.5010	65	70	807	812	0.0990
	0.5016	65	70	817		

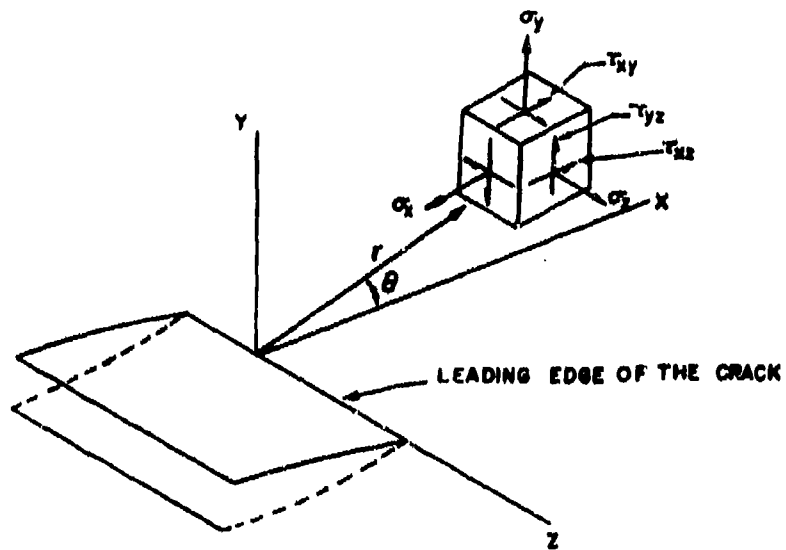


Figure 1. Coordinates measured from the leading edge of a crack and the stress components in the crack tip stress field.

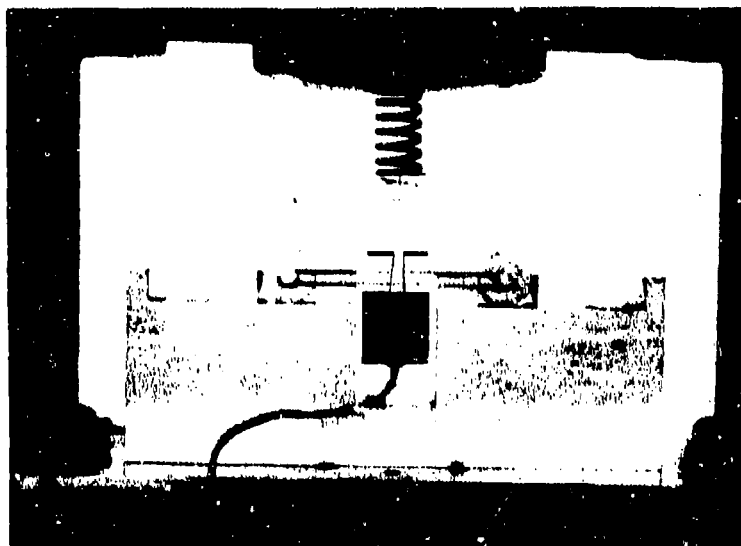


Figure 2. View of the loading setup.

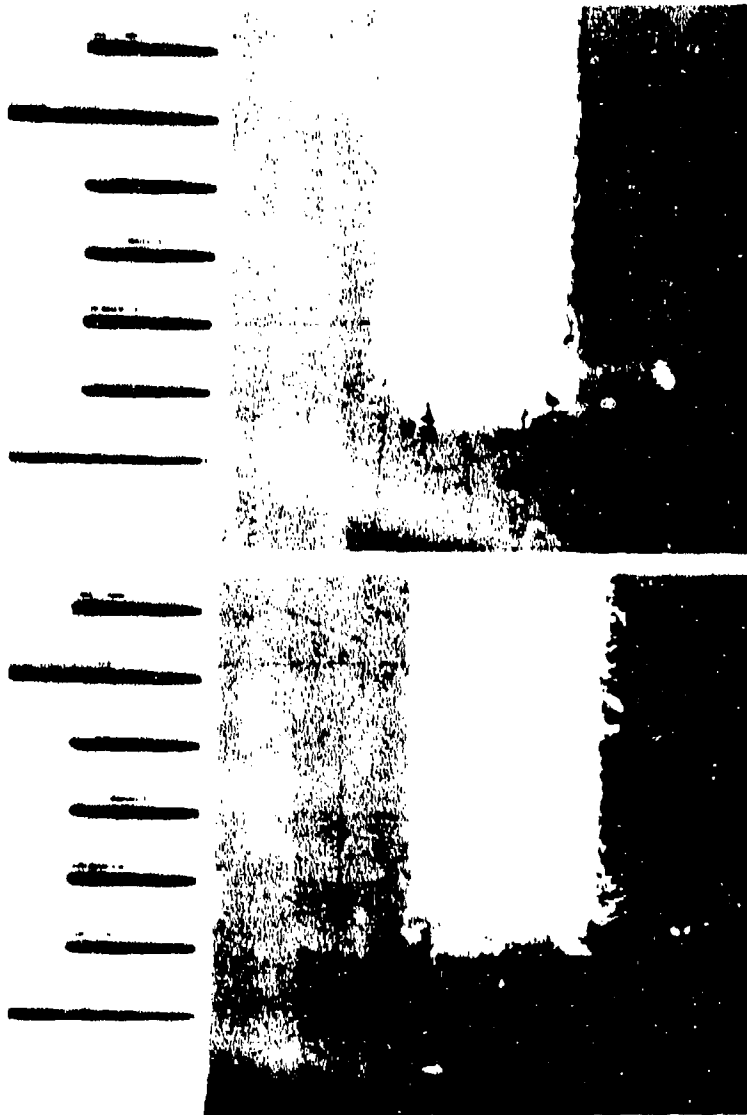


Figure 3. Two typical crack tips observed at 45° through the sides of the glass beam.

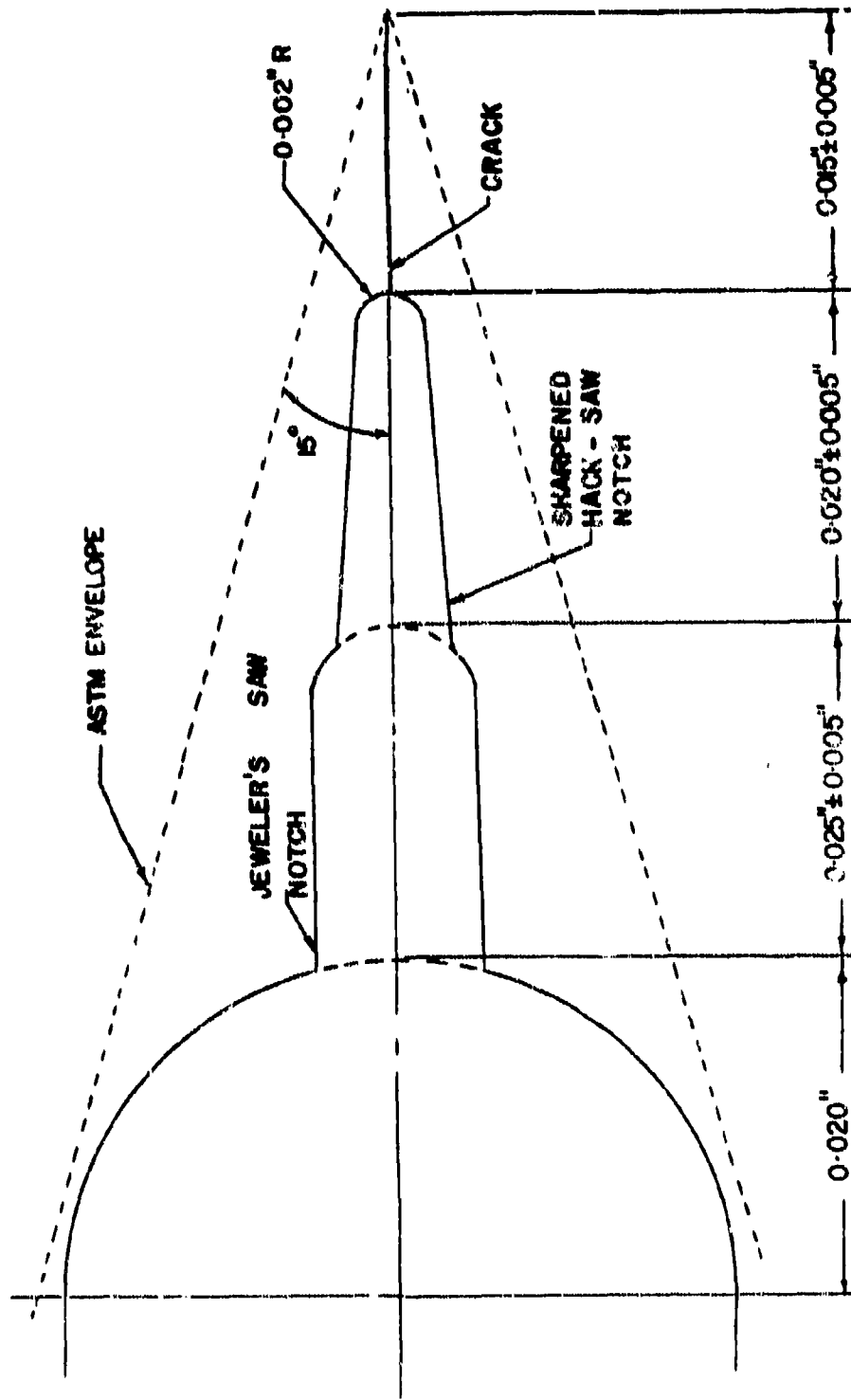


Figure 4. The shape of the final crack tip.

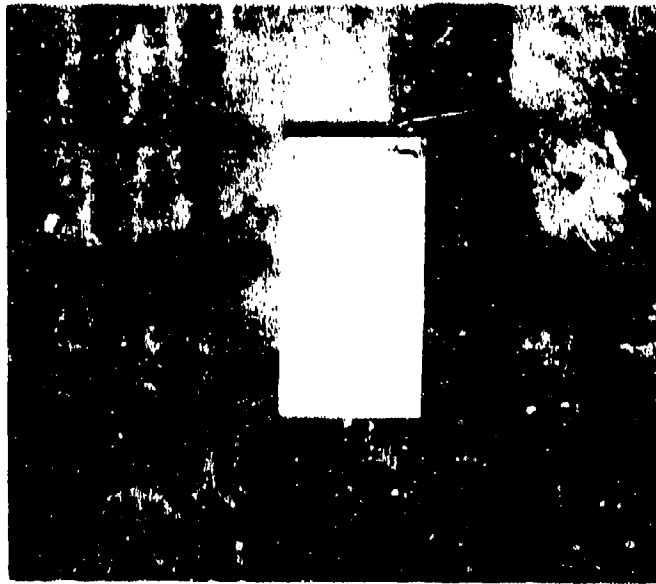


Figure 5. The mid-plane inhomogeneity.

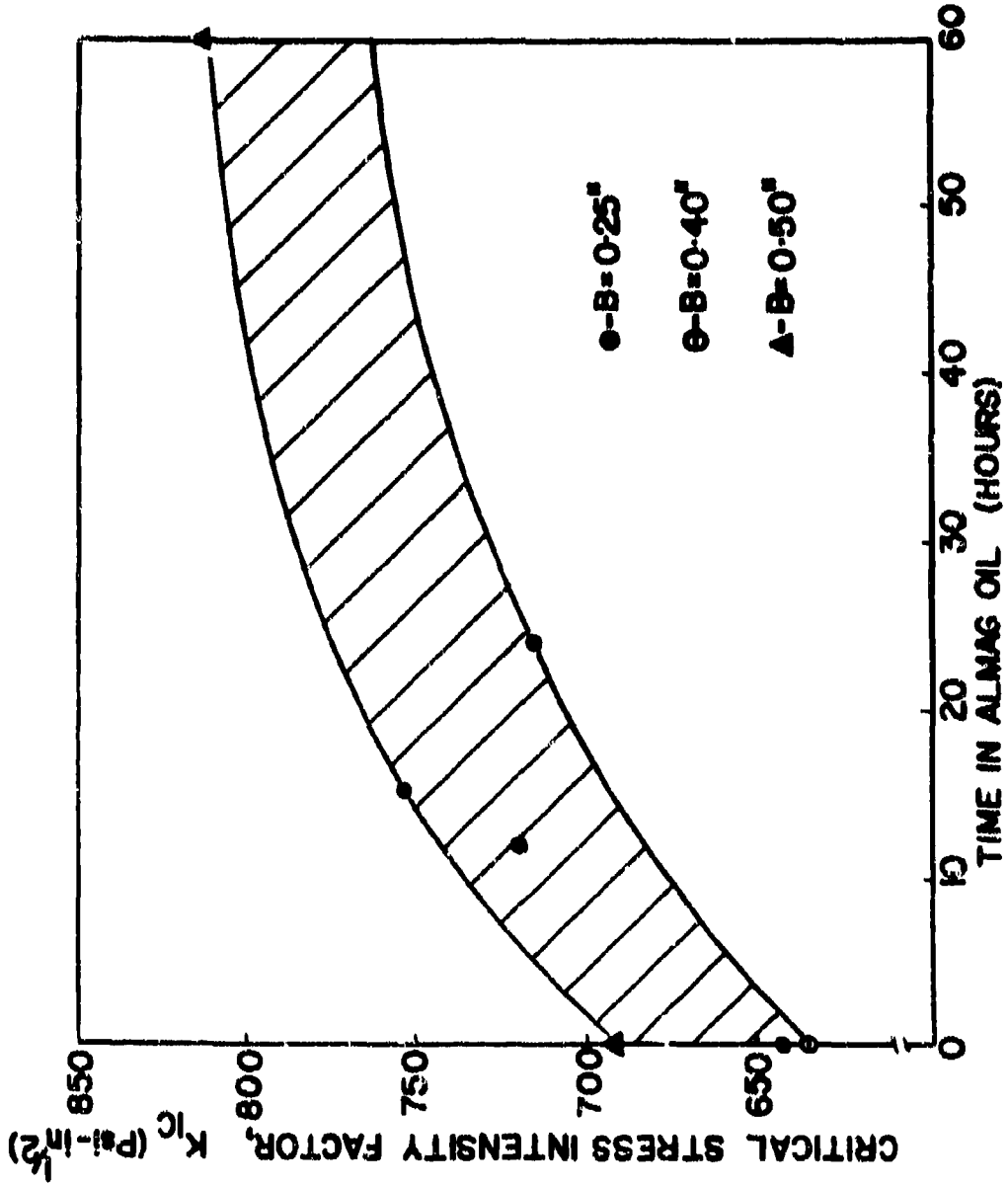
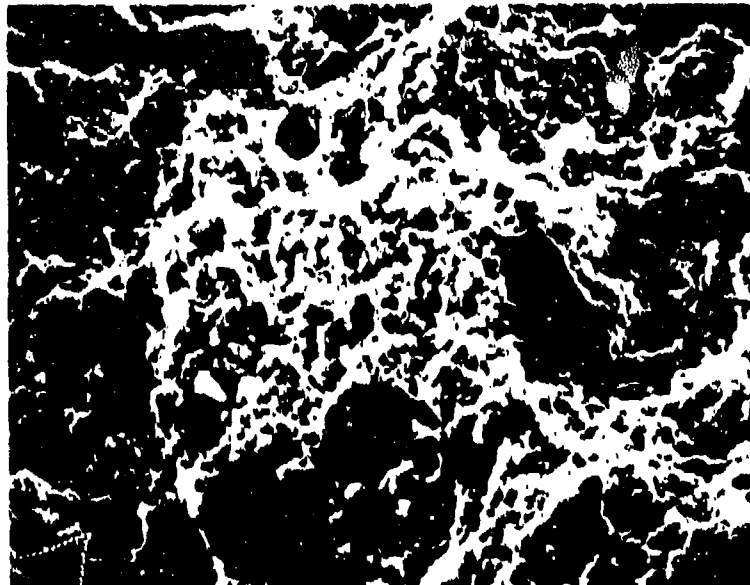
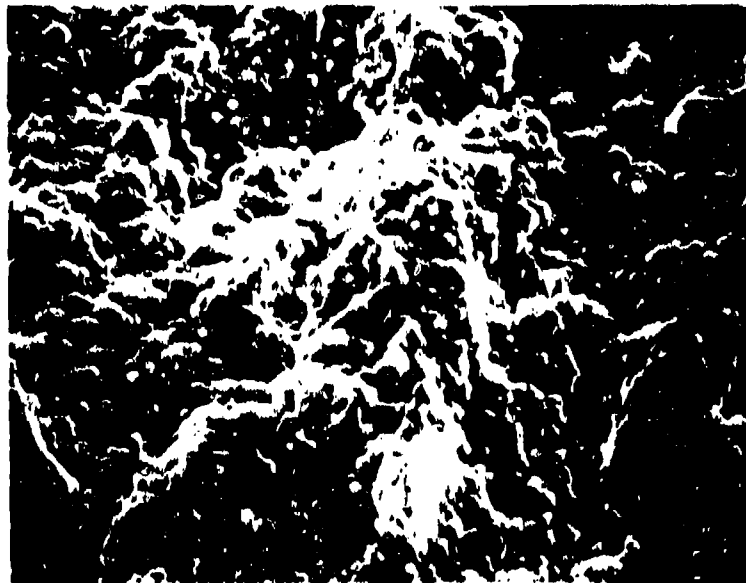


Figure 6. The improvement of the fracture strength of SCFS due to soaking in Almag oil.

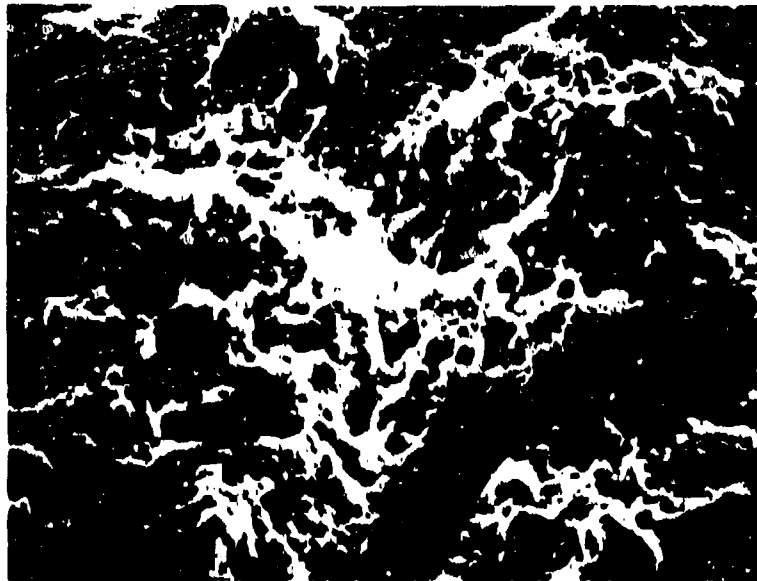


(a) Fracture surface of dry sample - 700X.

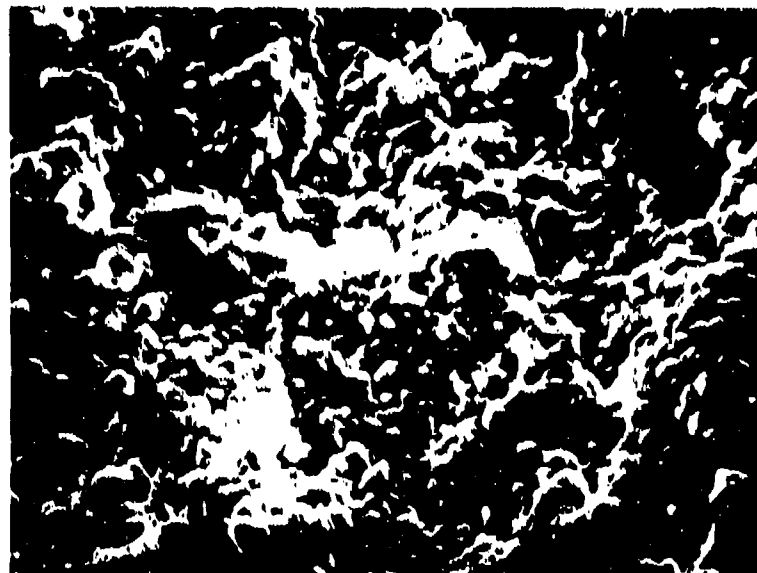


(b) Fracture surface of 12-hour oil-soaked sample - 700X.

Figure 7. Scanning electron micrographs showing comparisons of dry and 12-hour oil-soaked fracture surfaces.



(a) Fracture surface of dry sample - 700X.



(b) Fracture surface of 15-hour oil-soaked sample - 700X.

Figure 8. Scanning electron micrographs showing comparison of dry and 15-hour oil-soaked fracture surfaces.

D-1

APPENDIX D

PROBABILITY MODEL FOR RAIN EROSION DAMAGE

by Leland L. Long

I. INTRODUCTION

Natural rainfall exhibits all the properties necessary to be classified as a stochastic process. Thus, probability modeling is the only effective means whereby the process can be adequately described mathematically.

This report presents such a modeling approach with particular emphasis on rain erosion damage caused by high-velocity impact. A model is also developed which displays the interrelationship between rainfall rate, drop diameter range, and distance traveled as they affect the cumulative probability of exactly K impacts in a circular surface of radius r as it travels through the rainstorm.

Curves are presented which graphically display the information available from the mathematical results.

II. PROBABILITY MODEL FOR DISTRIBUTION OF RAINDROPS WITH DROP SIZE

Considerable work has been done in the study of the distribution of raindrops with size. Most of this effort has been directed toward applying the results to weather observation and related atmospheric problems. However, these results are applicable to the present study and have been used with good results.

The keynote article on drop size distribution is a paper by Marshall and Palmer [1] which established what has come to be a standard reference for most other studies involving this subject. They concluded that, except

for small drop diameters (less than 0.5 mm), the drop size distribution is well described by the exponential distribution function

$$p(x) = N_0 e^{-Ax} \quad \frac{\text{drops}}{\text{mm}^3/\text{mm}} \quad (1)$$

where

$$N_0 = 8000$$

$$A = 4.1R^{-.21}$$

R = Rainfall rate (mm/hr)

x = Drop diameter (mm).

Since p(x) represents a continuous type distribution, it follows that the corresponding probability density function (p.d.f.) is

$$f(x) = \begin{cases} 8000 c \exp(-4.1R^{-.21}x), & x > 0 \\ 0, & \text{elsewhere.} \end{cases}$$

The constant c is obtained from

$$8000 c \int_0^{\infty} \exp(-4.1R^{-.21}x) dx = 1$$

which gives

$$c = 4.1R^{-.21}/8000.$$

Therefore

$$f(x) = \begin{cases} 4.1R^{-.21} \exp(4.1R^{-.21}), & x > 0 \\ 0, & \text{elsewhere} \end{cases} \quad (2)$$

Now let X be a continuous type random variable with p.d.f. given by (2), then

$$\Pr(X = x_1) = 0$$

where x_1 is a fixed drop diameter. Thus, the only measure of probability which can be established is with reference to an interval. That is,

$$\Pr(a < X < b) = \int_a^b f(x) dx$$

In this study most results are based on probability measure for drop diameters greater than a preset value. Hence, if x_0 represents the smallest

drop diameter to be considered, then

$$\Pr(X > x_0) = \int_{x_0}^{\infty} f(x) dx$$

It is also important to realize that, based upon the assumed continuous probability distribution, the number of drops of given diameter must be considered within a drop size interval. For example, the expected number of drops per m^3 in the interval 1 mm to 2 mm is

$$N = \int_1^2 p(x) dx$$

This concept is used in the development of expressions for accumulated volume of erosion and accumulated eroded area.

III. ACCUMULATED AREA OF EROSION

If a water drop strikes a given surface with energy $E(\text{ft-lb})$, then the resulting crater area is (see Section IV of main report)

$$A_c = C_a E^{0.55} \text{ in}^2$$

where C_a is a constant which depends on the given material being impacted.

It can be shown that

$$E = C_e x^3 v_n^2 \text{ ft-lb}$$

where C_e is a conversion constant and

x = drop diameter (mm)

v_n = normal component of the impact velocity (ft/sec)

Therefore,

$$\begin{aligned} A_c &= C_a (C_e x^3 v_n^2)^{0.55} \\ &= C_a C_e^{0.55} x^{1.55} v_n^{1.1} \text{ m}^2. \end{aligned}$$

Now subdividing the Marshall-Palmer equation (1) into subintervals of equal length for $x > x_0$ gives

$$n_i = p(x_i) \Delta x \text{ drops/m}^3$$

as an approximation of the number of drops per m^3 in the drop interval x_{i-1} to x_i . If these drops are intercepted by a nose cone traveling at a velocity v ft/sec, then

$$v_n = v \sin \theta$$

where θ is the angle of the nose cone with the horizontal. Since the drops will be deflected by the shock wave along the nose cone, we write

$$v_n = v \sin(\theta - \delta(z, x))$$

where

- δ = deflection angle
- z = position along nose cone.

Now the crater area is

$$A_c = C_a C_e^{0.55} v^{1.1} [\sin(\theta - \delta(z, x))]^{1.1} x^{1.65} \text{ in}^2. \quad (3)$$

The number of drops per m^2 (in the drop-size interval x_{i-1} to x_i) which the nose cone will intercept when traveling a distance S (meters) through a given rain field is

$$n_i' = Sp(x_i) \sin \theta \Delta x \text{ drops/m}^2.$$

The net effect of these intercepted drops in relation to eroded area is

$$\Delta A_e = A_c n_i' \text{ in}^2/\text{m}^2$$

or

$$\begin{aligned} \Delta A_e &= C_a C_e^{0.55} v^{1.1} [\sin(\theta - \delta(z, x_i))]^{1.1} x_i^{1.65} Sp(x_i) \sin \theta \Delta x \\ &= C_a C_e^{0.55} S v^{1.1} \sin \theta [\sin(\theta - \delta(z, x_i))]^{1.1} x_i^{1.65} p(x_i) \Delta x. \end{aligned}$$

Taking the Riemann sum limit, the accumulated area of erosion caused by drops having diameter $x > x_0$ is

$$A_e = C_a C_e^{0.55} S v^{1.1} \sin \theta \int_{x_0}^{\infty} [\sin(\theta - \delta(z, x))]^{1.1} x^{1.65} p(x) dx \text{ in}^2/\text{m}^2. \quad (4)$$

Conversion to in^2/in^2 gives

$$A_e' = (2.54)^2 \times 10^{-4} A_e \text{ in}^2/\text{in}^2. \quad (5)$$

Thus, the percentage area of erosion is

$$P = 100A_e'.$$

IV. ACCUMULATED VOLUME OF EROSION

If a water drop strikes a given surface with energy $E(\text{ft-lb})$, then the resulting crater volume is (see Section IV of main report)

$$V_c = C_v E^{1.44} \times 10^{-4} \text{ in}^3,$$

where C_v is a constant which again depends on the material being impacted.

As with the crater area derivation,

$$E = C_e x^3 v_n^2 \text{ ft-lb}$$

Thus,

$$V_c = C_v C_e^{1.44} v_n^{2.88} x^{2.88} \times 10^{-4} \text{ in}^3$$

Taking a nose cone at angle θ , we use

$$E = C_e x^3 v_n^2 \sin^2 \theta, \text{ ft-lb}$$

It follows that the crater volume is

$$\begin{aligned} V_c &= C_v C_e^{1.44} x^{4.32} [v^2 \sin(\theta - \delta(z, x))]^{1.44} \times 10^{-4} \text{ in}^3 \\ &= C_v C_e^{1.44} v^{2.88} [\sin(\theta - \delta(z, x))]^{1.44} x^{4.32} \times 10^{-4} \text{ in}^3 \end{aligned}$$

Again, there are

$$n_i' = S p(x_i) \sin \theta \Delta x$$

drops/ m^2 in the drop diameter interval x_{i-1} to x_i which impact the nose cone. Therefore, the volume eroded by these drops is

$$\Delta V_e = V_c n_i' \text{ in}^3/\text{m}^2$$

or

$$AV_{\bullet} = C_v C_{\bullet}^{1.44} S_v^{2.88} \sin^2[\min(\theta - \delta(z, x))]^{1.44} x_i^{4.32} p(x_i) \Delta x \times 10^{-4} \text{ in}^3/\text{m}^2. \quad (7)$$

Taking the Riemann sum limit, the accumulated volume of erosion caused by drops having drop diameter $x > x_0$ is

$$V_{\bullet} = C_v C_{\bullet}^{1.44} S_v^{2.88} \sin^2 \theta \int_{x_0}^{\infty} [\sin(\theta - \delta(z, x))]^{1.44} x^{4.32} p(x) dx \times 10^{-4} \text{ in}^3/\text{m}^2. \quad (8)$$

It is convenient again to convert to in^3/in^2 . Therefore

$$V_{\bullet}' = (2.54)^2 \times 10^{-4} V_{\bullet} \text{ in}^3/\text{in}^2$$

is the accumulated volume of erosion (in^3) from one square inch of material.

Finally, the total eroded volume as a function of V_{\bullet}' and P is given by the relation

$$V_t = V_{\bullet}' (2 - \exp(-3P/(132-P))) \text{ in}^3/\text{in}^2. \quad (9)$$

V. PROBABILITY MODEL FOR RAINDROP IMPACTS

If rainfall rate is fixed at a constant value, then it is legitimate [2] to assume that the number of drops per unit volume is represented statistically as a Poisson process. Let the random variable Y represent the number of drops impacting a given surface area, A , which travels through the given rainfield a distance S . Then the probability density function of Y is

$$f(y) = \begin{cases} \frac{\lambda^y e^{-\lambda}}{y!}, & y = 0, 1, 2, 3, \dots \\ 0, & \text{elsewhere} \end{cases} \quad (10)$$

where

$$\lambda = NSA.$$

Note that N represents the average number of drops per unit volume.

It should be recalled that N will depend on the drop size interval being considered. That is, if x_0 and x_m represent, respectively, the smallest drop and the largest drop diameters being considered, then

$$N = \int_{x_0}^{x_m} p(x) dx$$

where $p(x)$ is again the function representing drop size distribution.

If it is desired to consider all drops having diameters greater than x_0 , then

$$N = \lim_{x_m \rightarrow \infty} \int_{x_0}^{x_m} p(x) dx$$

$$= \int_{x_0}^{\infty} p(x) dx.$$

Now consider the area, A , to be that of a circle of radius r so that $A = \pi r^2$. Let the random variable R represent the radius of the circle with exactly k raindrop impacts. Then,

$$\Pr(R > r) = \Pr(Y=0) + \Pr(Y=1) + \dots + \Pr(Y=k-1)$$

$$= \sum_{y=0}^{k-1} \Pr(Y=y)$$

$$= \sum_{y=0}^{k-1} \frac{(N\pi r^2)^y e^{-N\pi r^2}}{y!}.$$

It follows that

$$\Pr(R \leq r) = 1 - \Pr(R > r)$$

$$= 1 - \sum_{y=0}^{k-1} \frac{(N\pi r^2)^y e^{-N\pi r^2}}{y!}.$$

But, by definition, the cumulative distribution function of the random variable R is

$$G(r) = \Pr(R \leq r).$$

Therefore,

$$G(r) = 1 - \sum_{y=0}^{k-1} \frac{(N\pi r^2)^y e^{-N\pi r^2}}{y!}. \quad (11)$$

As an example, consider the case where $k = 1$ (i.e., one impact).

Then,

$$G(r) = 1 - e^{-NS\pi r^2}. \quad (12)$$

It follows that the probability density function of R is

$$g(r) = G'(r) = \begin{cases} 2NS\pi r e^{-NS\pi r^2}, & r > 0 \\ 0, & \text{elsewhere.} \end{cases} \quad (13)$$

Two interpretations are possible in regard to the expression $G(r)$ for a given value of k . These are:

1. Fix the value of $r = r_0$ and calculate $G(r_0)$. For example, suppose $G(r_0) = .80$ and $k = 4$. Then if 100 samples are taken for a circular region having radius r_0 , it should be true that, on the average, for 80 of these samples the radius to the k th hit will be $\leq r_0$.
2. Fix $G(r_1) = .95$ (or any chosen probability) for a given value of k and obtain the resultant value $r = r_1$. Then, if 100 samples are taken for a circular region having radius r_1 , it should be true that, on the average, for 95 of these samples the radius to the k th hit will be $\leq r_1$.

It is important to note that the parameters which control $G(r)$ are

- (a) Rainfall rate (contained in $p(x)$),
- (b) Minimum drop diameter, x_0 ,
- (c) Number of impacts, k , and
- (d) Distance, S .

Solving Eq. (12) for N gives

$$N = \frac{1}{\pi S r^2} \ln \left(\frac{1}{1-G(r)} \right). \quad (14)$$

The value of N may be obtained by the use of Eq. (1) so that

$$\begin{aligned}
 N &= \int_{x_0}^{x_m} N_0 e^{-\lambda x} dx \\
 &= \frac{N_0}{\lambda} (e^{-\lambda x_0} - e^{-\lambda x_m}).
 \end{aligned}
 \tag{15}$$

Setting the two expressions for N equal to each other and solving for S gives

$$S = \frac{\lambda \ln\left(\frac{1}{1-G(r)}\right)}{\pi N_0 r^2 (e^{-\lambda x_0} - e^{-\lambda x_m})}
 \tag{16}$$

Equation (16) is very important since, for a given rainfall rate and radius r, it establishes the distance S for which the probability is G(r) that a single raindrop having diameter between x_0 and x_m will strike the surface.

VI. DISCUSSION OF RESULTS

The resultant erosion formulas which are developed in Sections II, III, IV, and V of this appendix are used extensively in the report. Thus, for a fuller appreciation of their usefulness, it is necessary to refer to the corresponding graphical presentations and computer calculations which are presented there.

Also, reference should be made to the discussion of FORTRAN subroutines presented in Appendix G. In particular, SUBROUTINE PCTA and SUBROUTINE VONE produce outputs, respectively, which are given by the formulas in Sections II, III, IV, and V. That is:

PCTA → Percentage of area eroded

VONE → Accumulated volume of erosion.

The results agree quite well with available experimental data.

The results of Section V of this appendix are shown graphically in Figures 1 through 5. As stated, Eq. (11) gives the cumulative probability,

$$G(r) = 1 - \sum_{y=0}^{k-1} \frac{(NS\pi r^2)^y e^{-NS\pi r^2}}{y!},$$

of exactly k raindrop impacts in a circular region of radius r , for a given rainfall rate and distance travelled.

The graph of Figure 1 shows the effect on $G(r)$ versus r when different values of k are assumed. Here the rainfall rate is 2.5 in/hr and the distance is 500 ft.

Figure 2 demonstrates the shift in the $G(r)$ curves when distance is used as a parameter with a rainfall rate of 2.5 in/hr and $k = 1$. In Figure 3, the same effect is noted with a rainfall rate of 2.5 in/hr but with $k = 2$.

Changes in rainfall rate will also affect $G(r)$. This is noted in Figure 4 which shows $G(r)$ versus r for various rainfall rates. Here $k = 1$ and $S = 500$ ft.

Since

$$N = \int_{x_0}^{\infty} p(x) dx,$$

then changes in x_0 will also cause a shift in the graphs of $G(r)$ versus r . This is demonstrated in Figure 5, where rainfall rate is again 2.5 in/hr, $k = 1$, and $S = 500$ ft.

These results were all obtained by use of SUBROUTINE PROB (see Section VII). Similar graphs are available through use of this subroutine with choice of parameters left to the user.

Equation (16),

$$S = \frac{\lambda \ln\left(\frac{1}{1-G(r)}\right)}{8000\pi r^2} \cdot \frac{1}{\exp(-\lambda x_0) - \exp(-\lambda x_0)},$$

is also very useful as is demonstrated in Figure 6. Here, the rainfall rate is set at 2.5 in/hr and $x_m = 10$ mm. The resultant graphs show how $S(\text{ft})$ changes with increasing value of the minimum drop diameter, x_0 . To use the curves, let it be assumed that a nose cone is to travel through a rainstorm of 2.5 in/hr and suppose that a raindrop size greater than 8 mm in diameter must be avoided (at a given velocity). Also, assume that it is desired that the probability of impact with a single drop ($k = 1$) be small (.05). Then the vertical intercept ($x_0 = 8$ mm) with the desired probability curve ($G = .05$) will give the resultant distance on the $S(\text{ft})$ axis. Obviously there are variations on the use of these curves as for example the distance might be fixed by the extent of a given rainstorm through which the vehicle is to travel.

If other values of rainfall rate, etc., are to be used, then similar families of curves can be obtained by use of SUBROUTINE BGDROP. The listing of this subroutine follows in Section VII.


```
50 CONTINUE
55 INC=FLOAT(N)/20.
   IF(INC.EQ.0)INC=1
   RI=1000.+02*INC
   R44=0.0
   DO 55 J=INC,M,INC
     RM4=RM4+RI
     AREA=PI*RM4**2/25.4**2
55 WRITE(6,4)RM4,M(J),AREA
40 F=F+I
   2 FORMAT(1X,'NUMBER OF DROPS IN RADIUS=',I10//)
   3 FORMAT(1X,'RADIUS (M4)      CUMULATIVE PROBABILITY
   1 AREA (IN**2)'/1X,'*****
   2*****')
   4 FORMAT(1X,F10.2,F14.3,14X,E14.6)
   RETURN
   END
```

REFERENCES

1. Marshall, J. S., and Palmer, W. McK. (1948), "The Distribution of Raindrops with Size," Journal of the Atmospheric Sciences, v. 5, pp. 165-166.
2. Yoshio, S. (1965), "On the Probabilistic Analysis of Precipitation Particles," Proc. International Conference on Cloud Physics, Tokyo and Sapporo, pp. 254-259.

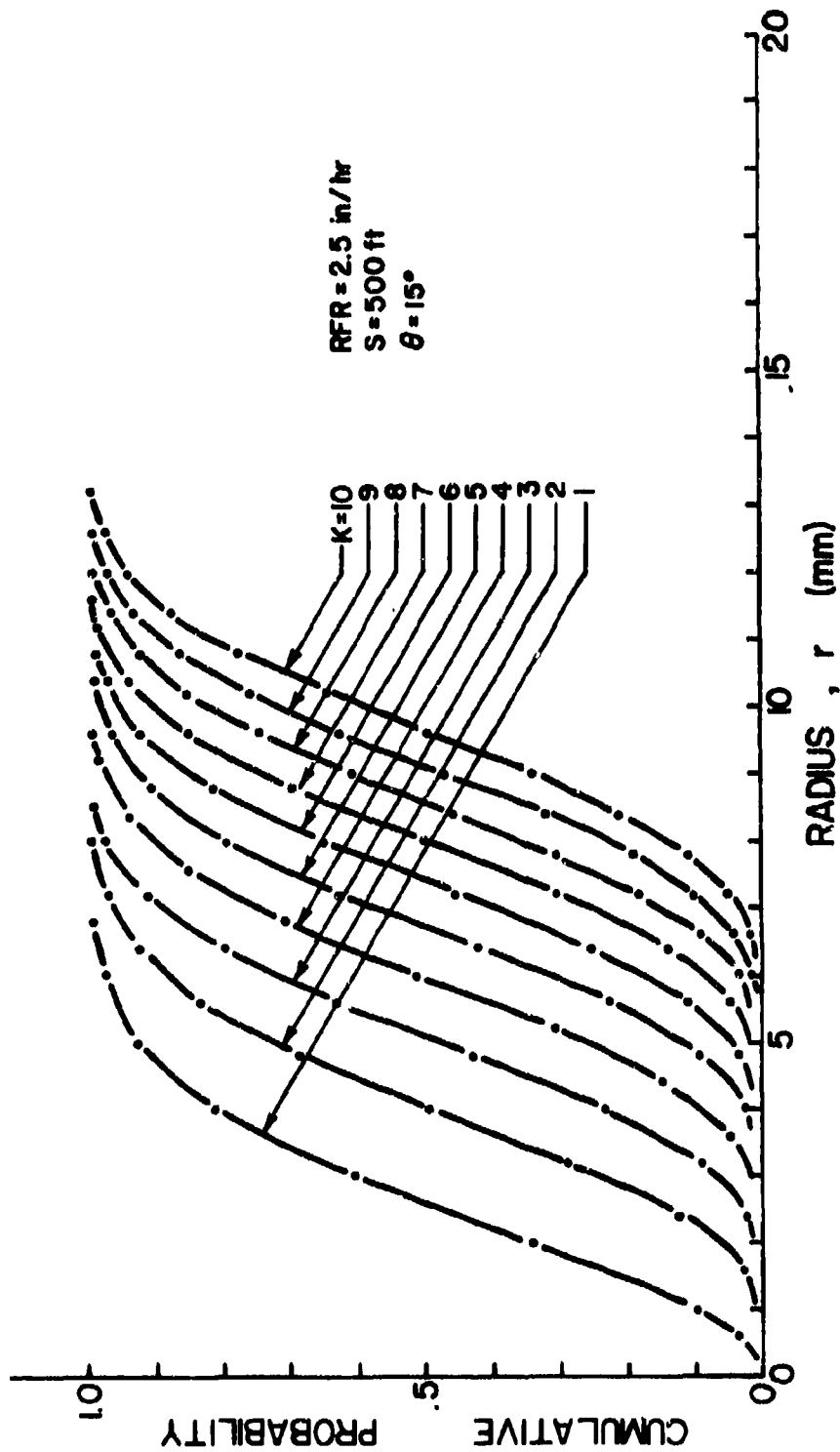


FIGURE 1. CUMULATIVE PROBABILITY, $G(r)$, AT K IMPACTS IN A RADIUS OF r (mm).

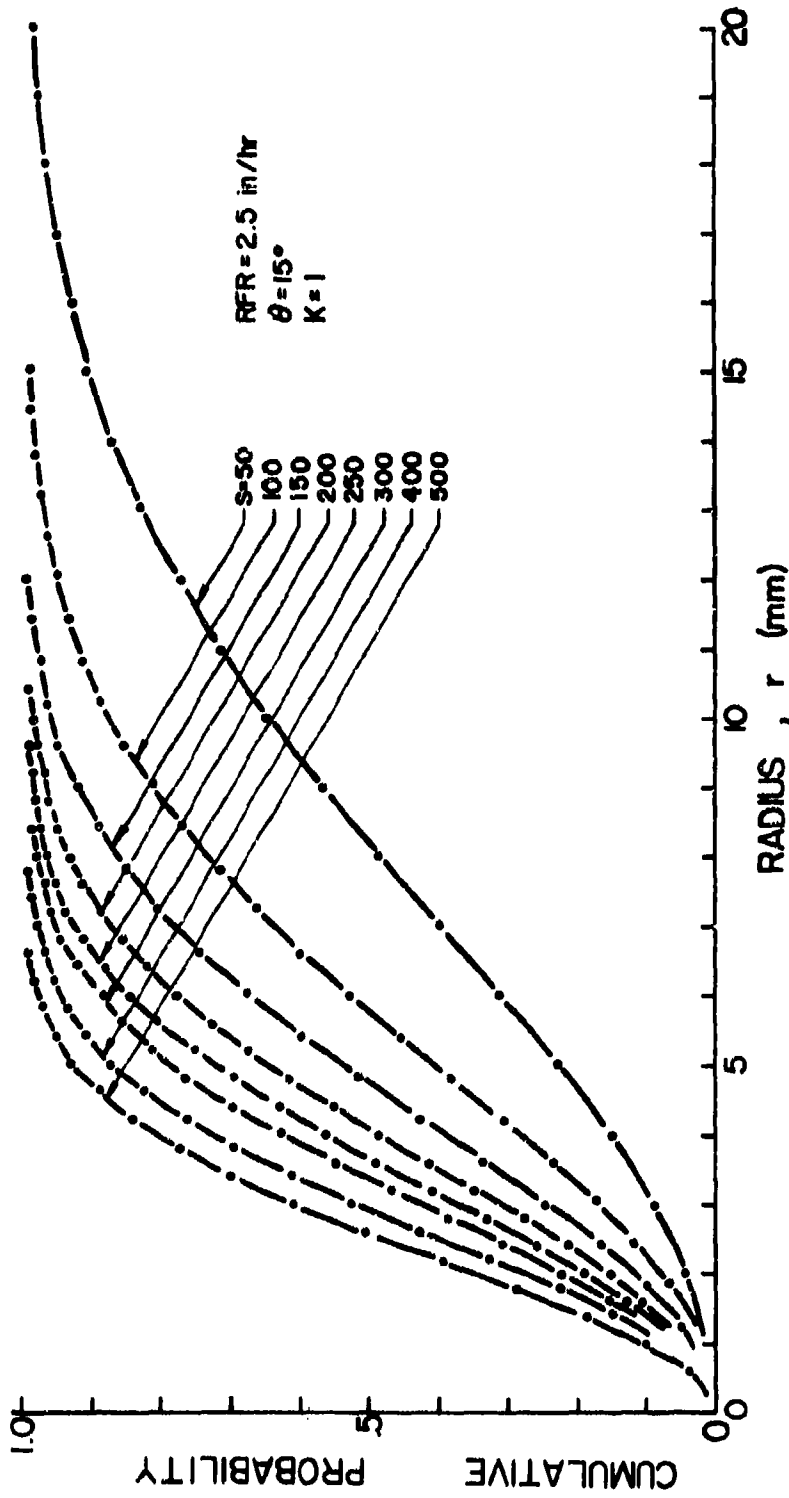


FIGURE 2. CUMULATIVE PROBABILITY, $G(r)$, VERSUS RADIUS, r , WITH DISTANCE AS A PARAMETER.

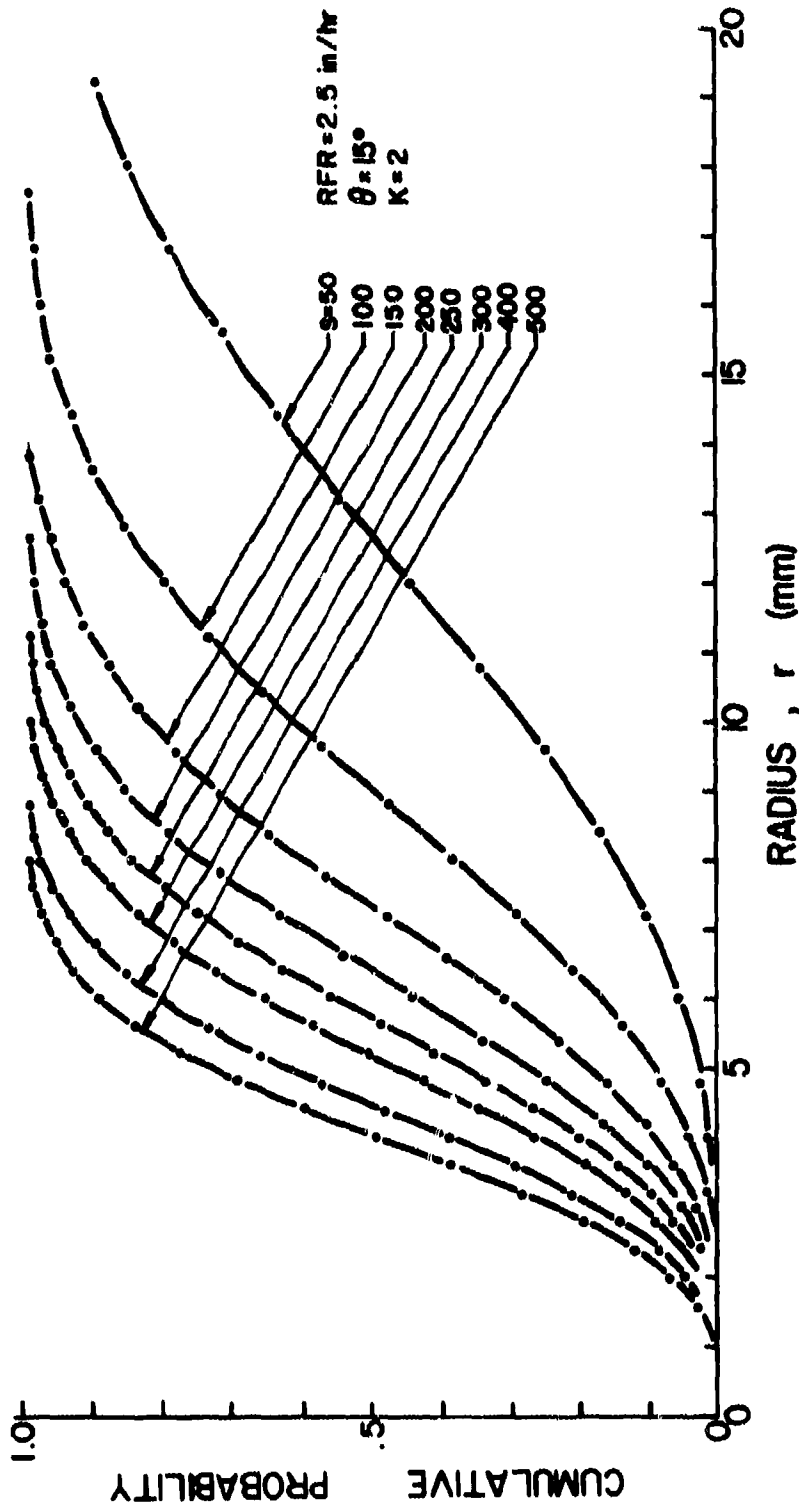


FIGURE 3. CUMULATIVE PROBABILITY, $G(r)$, VERSUS RADIUS, r , WITH DISTANCE AS A PARAMETER.

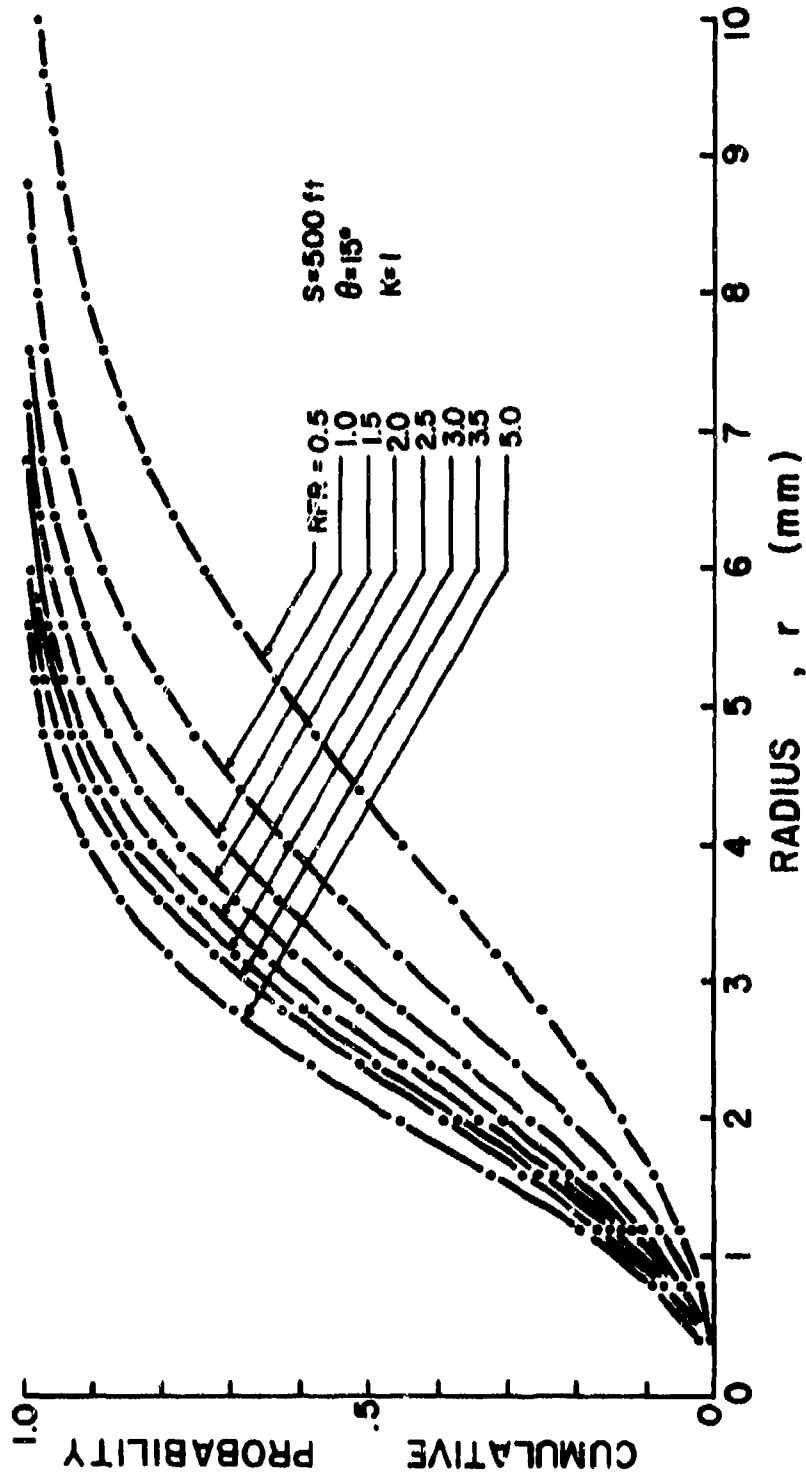


FIGURE 4. CUMULATIVE PROBABILITY, $G(r)$, VERSUS RADIUS, r , WITH RAINFALL RATE AS A PARAMETER.

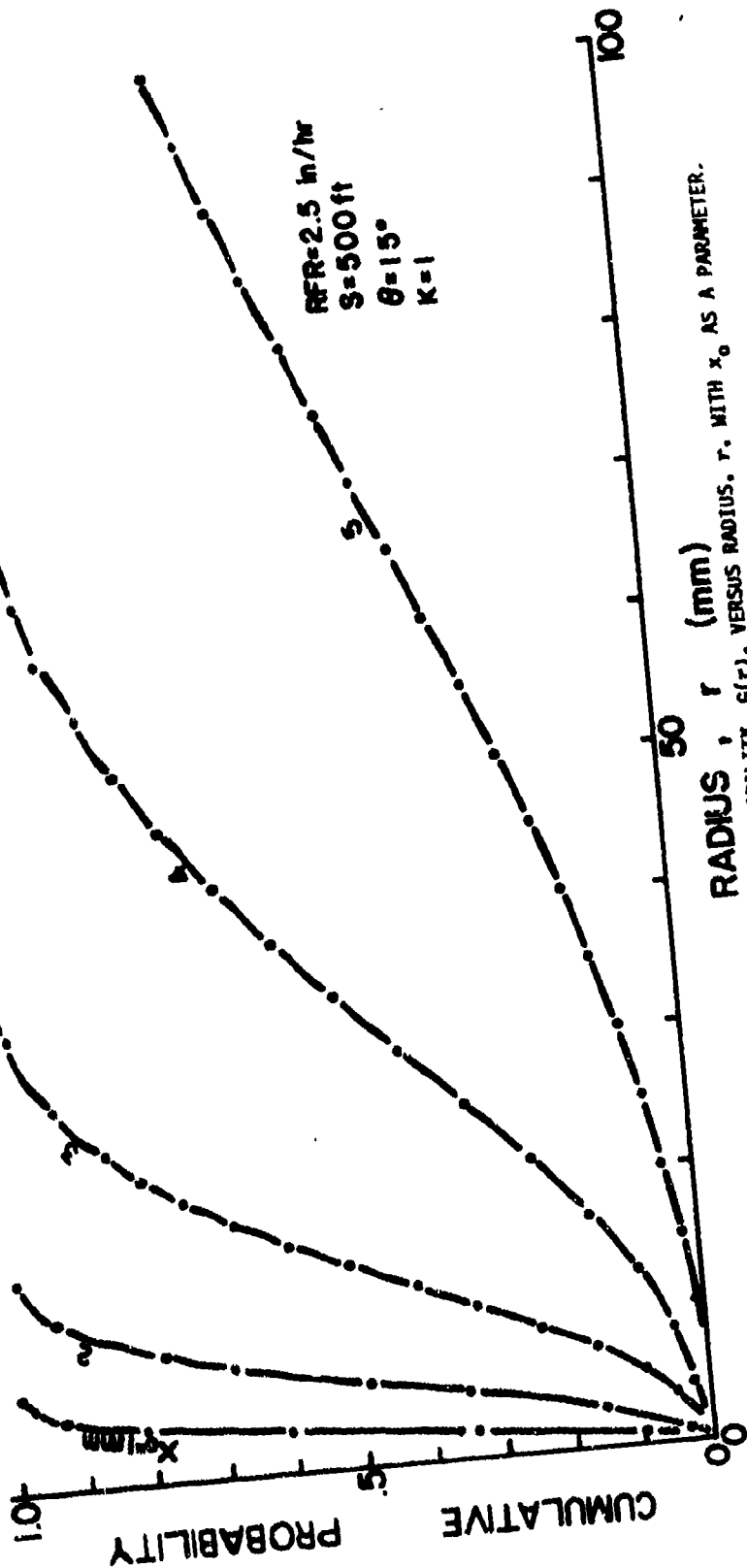


FIGURE 5. CUMULATIVE PROBABILITY, $G(r)$, VERSUS RADIUS, r , WITH x_0 AS A PARAMETER.

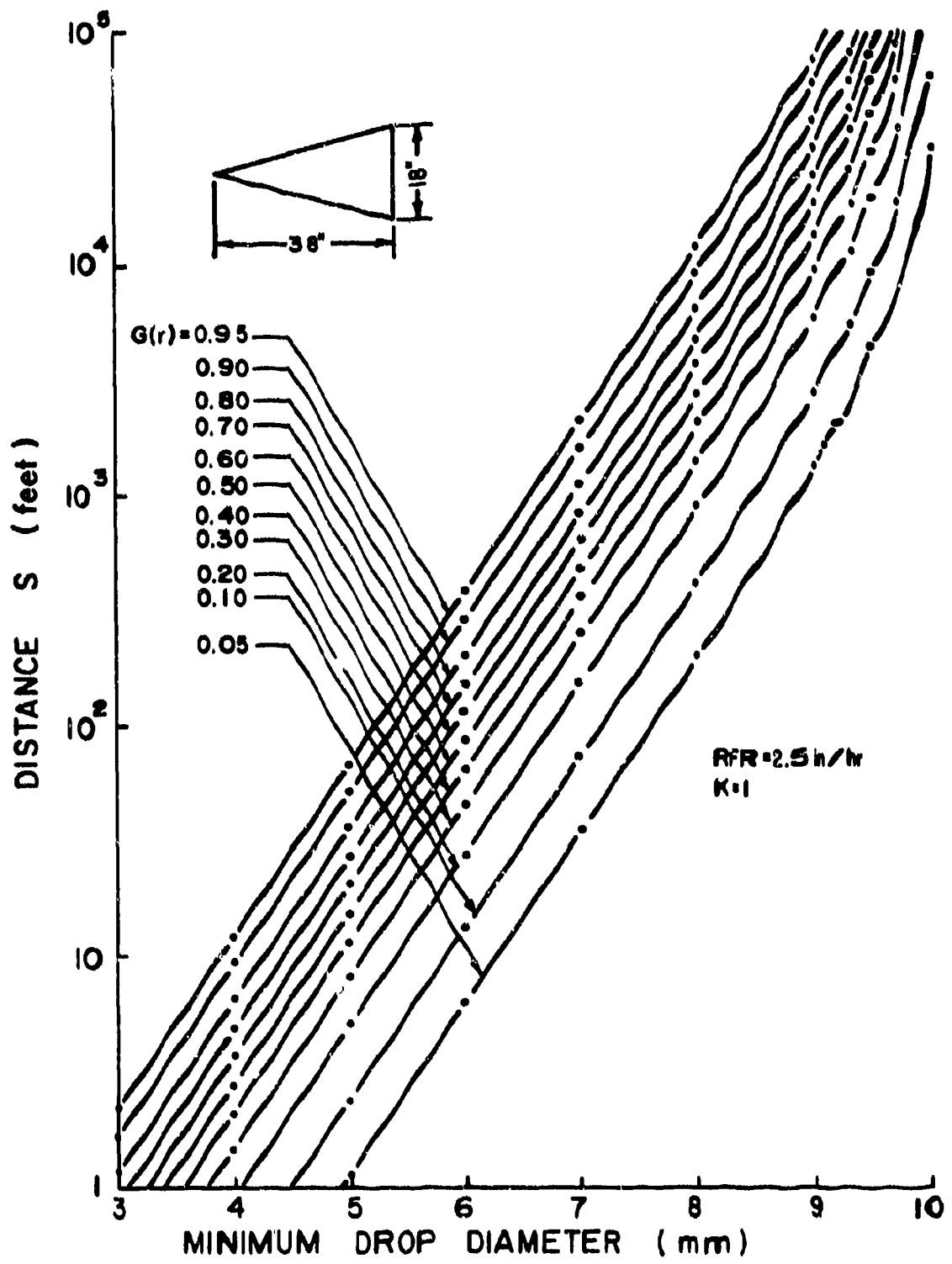


FIGURE 6. DISTANCE, S , VERSUS MINIMUM DROP DIAMETER, x_0 , WITH $G(r)$ AS A PARAMETER.

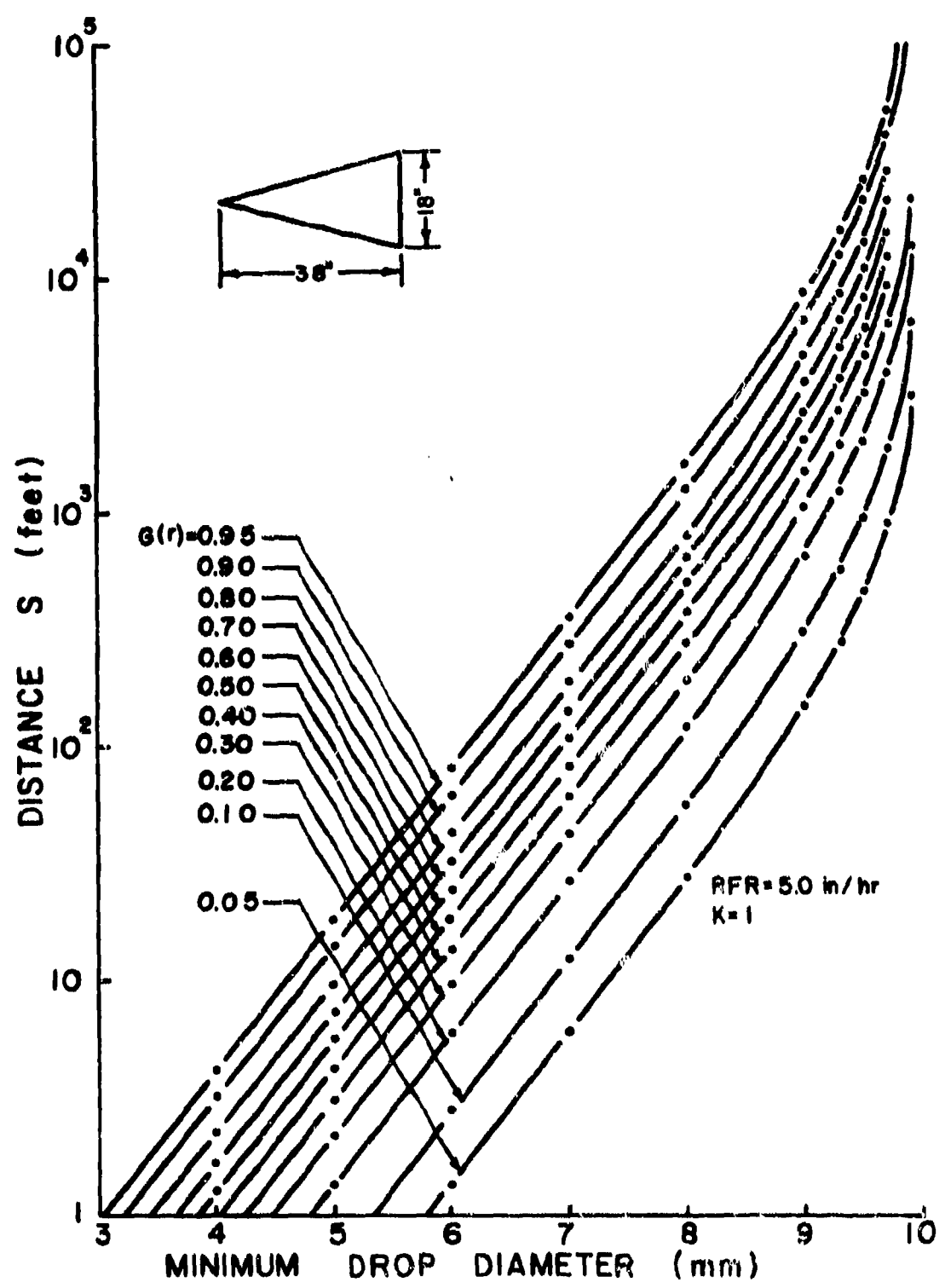


FIGURE 7. DISTANCE, S, VERSUS MINIMUM DROP DIAMETER, x_0 , WITH $g(r)$ AS A PARAMETER.

E-1

APPENDIX E

GAS-PARTICLE FLOW IN SUPERSONIC SHOCK LAYERS

by

John Peddieson, Jr. and Chung-Hsein Lyu
Associate Professor and Research Assistant, Respectively

Department of Engineering Science
Tennessee Technological University
Cookeville, Tennessee 38501

TABLE OF CONTENTS

Chapter	Page
1. INTRODUCTION	E1
2. GOVERNING EQUATIONS	E5
3. SHOCK LAYERS ON THIN WEDGES AND CONES	E10
ANALYTICAL SOLUTIONS FOR THIN WEDGE	E10
NUMERICAL SOLUTIONS FOR THIN SHOCK LAYERS	E15
4. GENERAL WEDGE-SHAPED AND CONICAL SHOCK LAYERS	E20
GOVERNING EQUATIONS FOR GENERAL SHOCK LAYERS	E20
NUMERICAL SOLUTIONS FOR ARBITRARY SHOCK LAYERS	
ON WEDGES AND CONES	E22
APPROXIMATE ANALYTICAL SOLUTIONS FOR THIN	
SHOCK LAYERS	E26
5. SPHERICAL AND CYLINDRICAL SHOCK LAYERS	E29
GOVERNING EQUATIONS IN POLAR COORDINATES	E29
NUMERICAL SOLUTIONS AT STAGNATION LINE	E32
APPROXIMATE ANALYTICAL SOLUTIONS AT STAGNATION LINE	E37
APPROXIMATE SOLUTIONS FOR $\alpha_1 > \alpha_{1c}$	E39
NUMERICAL SOLUTIONS AWAY FROM STAGNATION LINE	E41
APPROXIMATE ANALYTICAL SOLUTIONS AWAY FROM	
STAGNATION LINE	E46
6. INVESTIGATION OF ASSUMPTIONS	E48
EFFECTS OF FINITE VOLUME FRACTION	E48
DISTRIBUTION OF PARTICLE SIZES	E50

Chapter	Page
7. SHOCK LAYERS ON GENERAL BODIES	E53
8. SHOCK LAYERS ON BODIES WITH ATTACHED SHOCKS	E66
9. CONCLUSION	E71
REFERENCES	E72
TABLE I	E74
LIST OF FIGURES	E76

Chapter 1

INTRODUCTION

The problem of supersonic flow of an air-particle suspension (the particles being raindrops, ice, or dust) past a solid body has become of great importance to a wide range of technological applications in aeronautics and rocketry because high-speed impacts of such particles with a vehicle flying through the atmosphere can cause significant erosion and cratering of its surface. To get an accurate estimate of the cratering and erosion damage, it seems important to know the relative velocities with which the particles strike the vehicle, the particle trajectories, and the distribution of particle properties over its surface. In this report these quantities are computed theoretically for the cases where the body is a wedge, a right circular cone, a circular cylinder, or a sphere. These problems are chosen because their geometries are simple, their solutions in the single-phase case are well known (see Sims [1] and Hayes and Probstein [2]), and because both the conical and spherical shock layers represent good approximations to many realistic flow fields experienced by rockets and guided missiles. While the problems of flow past a wedge or a circular cylinder have no direct applications to rocketry, some results for these cases are also presented so that the properties of plane and axisymmetric two-phase flows of this type can be compared and also because they provide rough approximations to the flow fields over certain wings.

In the atmosphere the mass fraction of the suspended particles is usually so small that the presence of the particles does not significantly affect the motion of the air. Thus the two-phase flow problem discussed above is simplified to that of computing the motion of the particles moving through a known gas flow field. (In this report, as in all previous work on this and related problems, it is assumed that the gas flow field is sufficiently well described by that appropriate to an inviscid compressible fluid.) To do this, the particle cloud is treated in the present work as a pseudo-continuum. That is, it is assumed that a volume element, as shown in Figure 1, of the suspension, whose dimensions are small compared to the characteristic dimensions of the shock layer, contains a number of particles large enough to allow the formation of meaningful averages of the particle properties within the volume element. It is then treated mathematically as a differential element and the averages are treated as continuous variables. General discussions of the governing equations appropriate to such two-phase flows are given in the books by Wallis [3] and Soo [4] and the review article by Marble [5].

Several papers on two-phase hypersonic flow have appeared in the last five years. Probst and Fassio [6] analyzed flows past thin wedges and cones and in the stagnation regions of the cylinders and spheres. They employed the constant density approximation (see Hayes and Probst [2]) to the gas flow field in their work. Their equations were solved analytically for the wedge and numerically for the other cases. Waldman and Reinecke [7] considered two-phase flow in a conical shock layer and in the stagnation region of a spherical shock layer. They fitted analytical expressions to known exact numerical solutions of the governing equations for the gas and used these to describe the fluid-phase motion. They

obtained approximate analytical solutions by a coordinate perturbation method. Spurk and Gerber [8] discussed the flows in shock layers on power-law bodies. Slender-body theory was used to describe the gas flow field. The particle-phase governing equations were solved numerically. These authors also performed some calculations using the exact solution for inviscid flow of a perfect gas past a cone to check their results based on slender-body theory.

All three of these papers used the Lagrangian viewpoint to formulate the governing equations for the particle phase. None computed the particle-phase density distribution, and Probstein and Fassio [6] did not find the particle-phase temperature distribution. These three papers were concerned primarily with determining the overall collection efficiencies of the body shapes they discussed. (The overall collection efficiency of a body is the rate at which particulate mass actually strikes the body surface divided by the rate that would occur if the motion of the particles was unaffected by the shock layer.)

In addition to the papers mentioned previously, an extensive literature exists concerning related subsonic two-phase flow problems having to do with such applications as dust collection, aerosol sampling, ice formation on aircraft, and erosion of turbine blades. For a review of some of the literature (which is concerned primarily with overall collection efficiency calculations), see Peddieson [9] and the references cited therein.

In Chapter 2 a set of equations governing the motion of the particle phase of an air-particle mixture is formulated using the Eulerian description. In Chapter 3 a procedure for solving these equations numerically to obtain the particle velocities, streamline patterns, density

distributions, and temperature distributions is outlined for the cases of flow past thin wedges and cones. This method is verified by comparison with an analytical solution for flow over a thin wedge. In Chapter 4 this method is applied to problems of two-phase flow in general wedge-shaped and conical shock layers over wedges and cones that are not required to be thin. Both approximate analytical solutions (valid for thin shock layers) and exact numerical solutions are obtained. The application of the above procedure to two-phase flow in shock layers on blunt-nosed (spherical and cylindrical) vehicle shapes is discussed in Chapter 5. In Chapter 6 calculations are carried out to investigate the sensitivity of the solution variables to the value of nonnegligible particle-phase volume fractions (the ratio of particle volume to the total mixture volume) and to the distribution of particle sizes present within the mixture. In Chapters 7 and 8 flows past bodies having general symmetric shapes are considered. The governing equations are put in a general form which is convenient for such problems in Chapter 7. Chapter 8 deals with a simple set of equations which, however, is only applicable to flow past bodies with attached shock waves. Concluding remarks are contained in Chapter 9.

Chapter 2

GOVERNING EQUATIONS

Since it is assumed, as mentioned previously, that the gas-phase motion is unaffected by the presence of the particles, it may be regarded as known from existing work (such as that reported by Sims [1]), and it is only necessary to solve the governing equations for the particle phase. This chapter is devoted to the derivation of these equations.

The appropriate governing equations for analysis of the behavior of the particle phase are found from balances of mass, linear momentum, and energy. These are respectively

$$\begin{aligned} \rho_p',t + \vec{\nabla} \cdot (\rho_p \vec{u}_p) &= A \\ \rho_p (\vec{u}_p',t + \vec{u}_p \cdot \vec{\nabla} \vec{u}_p) &= \vec{B} \\ \rho_p (e_p',t + \vec{u}_p \cdot \vec{\nabla} e_p) &= C \end{aligned} \quad (2.1)$$

where Eq. (2.1a) results from balance of mass, Eq. (2.1b) from balance of linear momentum, and Eq. (2.1c) from balance of energy. In Eqs. (2.1) ρ_p , \vec{u}_p , and e_p are respectively the particle-phase in-suspension density, velocity vector, and internal energy while A , \vec{B} , and C are respectively the rates per unit volume of interphase mass, linear momentum, and energy transfer from the gas phase to the particle phase; t is time; and a comma in Eqs. (2.1) denotes partial differentiation with respect to the following subscript. In writing Eqs. (2.1) it has been assumed that the

particle-phase stress tensor vanishes (which is true for the dilute suspensions under discussion here) and that body forces are negligible. To render Eqs. (2.1) determinate, constitutive equations for A , \vec{B} , C , and e_p are required. For the internal energy, it is assumed (see Marble [5]) that

$$e_p = c_p T_p \quad (2.2)$$

where c_p is the heat capacity of the particle phase, T_p is its temperature. In the present report the mass, momentum, and heat transfer terms are taken to be

$$\begin{aligned} A &= 0 \\ \vec{B} &= N_1 \rho_p |\vec{u}_p - \vec{u}|^{(1-b)} (\vec{u} - \vec{u}_p) \\ C &= N_2 c_p (T - T_p) \end{aligned} \quad (2.3)$$

where \vec{u} and T are respectively the velocity vector and temperature of the gas phase, c is the gas-phase specific heat at constant pressure, and N_1 , N_2 , and b are constitutive coefficients. The next three paragraphs will be devoted to discussion of Eqs. (2.3).

Mass loss from the particle phase can occur because of evaporation or stripping and eventual breakup of liquid drops and from melting of ice or dust particles. Calculations performed by Waldman and Reinecke [7] indicate that melting of solid particles is minimal in many situations. Theories of two-phase flow incorporating mass transfer through evaporation of liquid drops have been developed by Lu and Chiu [10], Panton [11], Panton and Oppenheim [12], and Marble [5]. This mass-loss mechanism, however, does not appear to be important for flow in shock

layers associated with flight vehicles, as pointed out several years ago by Wheelahan [13]. He also stated that drop breakup was not significant; but recent experimental work, such as that reported by Waldman, Reinecke, and Glenn [14], shows that this is not true in certain high-Mach-number situations. At present the information needed to formulate a realistic constitutive equation for A based on the breakup mechanism is not available. Thus it seems reasonable to neglect mass loss in the present work as indicated by Eq. (2.3a). The solutions obtained in this way will be accurate for the many situations in which appreciable mass loss does not occur and will also serve as standards of comparison for the predictions of more comprehensive future theories which account for particulate mass loss.

Equation (2.3b) has a form consistent with that of equations that can be fitted to the standard drag curve for steady incompressible flow past a single rigid sphere (see Probst and Fassio [6] and Spurk and Gerber [8]). In principle the coefficients N_1 and b can be determined from a knowledge of the microscopic properties of the suspension. It can be shown, for example, that if the particle phase consists of identical rigid spheres of mass m and radius a which are sufficiently far apart to preclude interference between the flows past neighboring particles, if the local Reynolds number for flow past each particle is very small, and if the fluid phase is incompressible; then $b = 1$ and $N_1 = (6\pi a \mu / m)$, where μ is the viscosity of the fluid phase. In general, definitive information about the microscopic properties of the suspension is not available. Even if it were, the standard drag curve cannot be applied to suspension flows with complete confidence because it does not account for lift, flow unsteadiness, finite particle volume fractions, deviations from spherical

particle shapes, nonuniformity of particle size and mass, fluid compressibility, deformability of particles (important, for example, in the case of liquid drops), and several other effects. While some of these can (at least approximately) be taken into consideration (see, for instance, the drag formulas discussed by Spurr and Gerber [8]), no expression presently available accounts for all of them; and none is to be expected in the near future. It seems reasonable, therefore, to choose forms of the constitutive equations for \vec{B} guided by the forms of equations that fit the standard drag curve, but to regard the coefficients appearing therein (in this case N_1 and b) as macroscopic properties of the suspension which are to be determined so as to maximize the agreement between theoretical predictions and experimental results. This is the approach adopted in this report in employing Eq. (2.3b). It should be pointed out that the values of N_1 and b , based on particular idealized microscopic models of the suspension, are still very useful in estimating the orders of magnitude of these parameters. Such estimates are simply not regarded as definitive.

The approach discussed in the previous paragraph applies equally well to the interphase heat-transfer term. Thus N_2 in Eq. (2.3c) is thought of as a macroscopic property of the suspension. For the idealized model of the suspension mentioned in the above example that heat is transferred from the fluid phase to a single rigid sphere, then the value of N_2 is equal to $(4\pi a \kappa)/(mc)$. κ is the fluid-phase thermal conductivity. For the sake of simplicity, N_1 , N_2 , and b are taken to be constant in the remainder of this work.

Substituting Eqs. (2.2) and (2.3) into Eqs. (2.1) leads to

$$\rho_p \dot{t} + \vec{\nabla} \cdot (\rho_p \vec{u}_p) = 0$$

Eq

$$\dot{u}_p \cdot t + \dot{u}_p \cdot \dot{u}_p = N_1 |\dot{u} - \dot{u}_p|^{(1-b)} (\dot{u} - \dot{u}_p)$$

$$T_p \cdot t + \dot{u}_p \cdot \dot{T}_p = N_2 (c/c_p) (T - T_p) \quad (2.4)$$

Chapter 3

SHOCK LAYERS ON THIN WEDGES AND CONES

In this chapter the problem of two-phase flow past thin wedges and cones is considered. First an analytical solution is found for flow past a thin wedge. Then the numerical procedure to be used in the present work is introduced and applied to flow past both thin wedges and thin cones. The numerical and analytical solutions for the wedge are compared and found to be in excellent agreement. This verifies that the numerical method is accurate. In the next chapter this method is applied to problems of two-phase flow in wedge-shaped and conical shock layers over bodies that are not required to be thin.

ANALYTICAL SOLUTIONS FOR THIN WEDGES

Consider the steady supersonic flow of a gas-particle suspension past a wedge of surface length L and half-angle θ_b at zero angle of attack. The shock wave is known to be a straight line making an angle (for a thin shock layer)

$$\theta_s = \theta_b / (1 - \epsilon) \quad (3.1)$$

with the center line of the wedge, where ϵ denotes the ratio of the gas-phase density before the shock to that after the shock. Figure 2 shows the geometry of the flow field. The free-stream velocity of each phase is U_∞ , the density of the particle phase just behind the shock is $\rho_{p\infty}$,

and free-stream temperature of the mixture is T_∞ . This problem is conveniently described in terms of cartesian coordinates x and y with x measured parallel to the body surface and y measured normal to it. It is convenient to define the following dimensionless variables

$$\begin{aligned} s &= x/L, & n &= y/L \\ F_p^+ \mathbf{e}_s^+ + G_p^+ \mathbf{e}_n^+ &= \mathbf{u}^+/U_\infty, & F_p^+ \mathbf{e}_s^+ + G_p^+ \mathbf{e}_n^+ &= \mathbf{u}_p^+/U_\infty \\ Q_p &= \rho_p/\rho_{p\infty} \\ H &= T/T_\infty, & H_p &= T_p/T_\infty \end{aligned} \quad (3.2)$$

where \mathbf{e}_s^+ and \mathbf{e}_n^+ are unit vectors associated with the s and n axes. The process of nondimensionalizing the governing Eqs. (2.4) yields

$$\begin{aligned} (Q_p F_p^+)_s + (Q_p G_p^+)_n &= 0 \\ F_p^+ F_p^+ \mathbf{e}_s^+ + G_p^+ F_p^+ \mathbf{e}_n^+ &= \alpha_1 ((F_p^+)^2 + (G_p^+)^2)^{(1-b)/2} (F_p^+ \mathbf{e}_s^+) \\ F_p^+ G_p^+ \mathbf{e}_s^+ + G_p^+ G_p^+ \mathbf{e}_n^+ &= \alpha_1 ((F_p^+)^2 + (G_p^+)^2)^{(1-b)/2} (G_p^+ \mathbf{e}_n^+) \\ F_p^+ H_p^+ \mathbf{e}_s^+ + G_p^+ H_p^+ \mathbf{e}_n^+ &= \alpha_2 (H_p^+ \mathbf{e}_n^+) \end{aligned} \quad (3.3)$$

Here the two dimensionless parameters α_1 and α_2 measure the rates at which momentum and energy are respectively transferred between the gas and particle continuum. They are evaluated by the following expressions:

$$\alpha_1 = (N_1 L)/U_\infty^b, \quad \alpha_2 = (N_2 L/U_\infty)(c/c_p) \quad (3.4)$$

The gas flow variables are modeled by the inviscid solution for supersonic flow past a wedge. This solution is known exactly and for a thin shock layer (which occurs when θ_p and ϵ are small) has the form

$$F = 1, \quad G = 0, \quad H = H_s = \epsilon((1+\epsilon)M_\infty^2\theta_s^2 - 1) \quad (3.5)$$

where the subscript s denotes the value of the variables on the downstream side of the shock wave, and M_∞ is the free-stream Mach number. The solution of Eqs. (3.3) must satisfy the boundary conditions

$$F_p = 1, \quad G_p = -\theta_b, \quad H_p = 1, \quad Q_p = 1 \quad (3.6)$$

on the shock wave which is the line

$$n = (\theta_s - \theta_b)s \quad (3.7)$$

This problem is most easily solved using a Von Mises transformation familiar from boundary-layer theory. This is done by defining a stream function ψ_p such that

$$\psi_p's = -Q_p G_p, \quad \psi_p'n = Q_p F_p \quad (3.8)$$

and converting the independent variables from s and n to ψ_p and z where $z = n$. The total differential of ψ_p is

$$d\psi_p = \psi_p's ds + \psi_p'n dn = -Q_p G_p ds + Q_p F_p dn \quad (3.9)$$

Solving Eq. (3.9) for ds yields

$$ds = -(1/(Q_p G_p))d\psi_p + (F_p/G_p)dz \quad (3.10)$$

Now regarding s as a dependent variable which is a function of ψ_p and z, it is clear that

$$s_{,\psi_p} = -1/(Q_p G_p), \quad s_{,z} = F_p/G_p \quad (3.11)$$

Converting the derivatives in Eqs. (3.3) and rewriting Eq. (3.11b) one obtains

$$\begin{aligned} G_p F_p' z &= \alpha_1 ((1-F_p)^2 + G_p^2)^{(1-b)/2} (1-F_p) \\ G_p G_p' z &= \alpha_1 ((1-F_p)^2 + G_p^2)^{(1-b)/2} G_p \\ G_p H_p' z &= \alpha_2 (H_s - H_p) \\ G_p s' z &= F_p \end{aligned} \quad (3.12)$$

where Eqs. (3.5) have been used. Substituting Eqs. (3.6) and Eq. (3.7) into Eq. (3.9), integrating along the shock wave, and assuming $\psi_p(0,0) = 0$ yields

$$\psi_p = \theta_s z_s / (\theta_s - \theta_b) \quad (3.13)$$

It is convenient to replace ψ_p by z_s as one of the independent variables. When this is done Eq. (3.8a) reads

$$Q_p = -\theta_s / ((\theta_s - \theta_b) G_p s' z_s) \quad (3.14)$$

The initial conditions are

$$F_p = 1, \quad G_p = -\theta_b, \quad Q_p = 1, \quad H_p = 1, \quad s = z_s / (\theta_s - \theta_b) \quad (3.15)$$

on $z = z_s$. Since Eqs. (3.12) contain no derivatives with respect to z_s , they can be integrated like ordinary differential equations along the streamlines (lines of constant z_s). The dependence of the solution on z_s enters through the application of the boundary conditions. For all values of b the solution for the tangential velocity is

$$F_p = 1 \quad (3.16)$$

The other variables have different forms depending on the value of b. For three realistic values of b, they are

$$\begin{aligned}
 b = 1 : s &= (z_s / (\theta_s - \theta_b)) - (1/\alpha_1) \log(1 - (\alpha_1/\theta_b)(z_s - z)) \\
 G_p &= -\theta_b + \alpha_1(z_s - z) \\
 H_p &= H_s - (H_s - 1)(1 - (\alpha_1/\theta_b)(z_s - z))^{\alpha_2/\alpha_1} \\
 Q_p &= 1 / (1 - (\theta_b/\theta_s)(1 - (\alpha_1/\theta_b)(z_s - z))) \quad (3.17)
 \end{aligned}$$

$$\begin{aligned}
 b = 0.5 : s &= (z_s / (\theta_s - \theta_b)) - (5 / (2\alpha_1 \theta_b^{2/5})) \times \\
 &\quad (1 - (1 - (3\alpha_1 / (5\theta_b^{3/5}))(z_s - z))^{-2/3}) \\
 G_p &= -\theta_b (1 - (3\alpha_1 / (5\theta_b^{3/5}))(z_s - z))^{5/3} \\
 H_p &= H_s - (H_s - 1) \exp(- (5\alpha_2 / (2\alpha_1 \theta_b^{2/5})) \times \\
 &\quad ((1 - (3\alpha_1 / (5\theta_b^{3/5}))(z_s - z))^{-2/3} - 1)) \\
 Q_p &= 1 / (1 - (\theta_b/\theta_s)(1 - (1 - (3\alpha_1 / (5\theta_b^{3/5}))(z_s - z))^{-2/3})) \quad (3.18)
 \end{aligned}$$

$$\begin{aligned}
 b = 0 : s &= (z_s / (\theta_b - \theta_s)) - (1/(\theta_b \alpha_1))(1 - \exp(\alpha_1(z_s - z))) \\
 G_p &= -\theta_b \exp(-\alpha_1(z_s - z)) \\
 H_p &= H_s - (H_s - 1) \exp(-(\alpha_2 / (\alpha_1 \theta_b)) \times \\
 &\quad (\exp(\alpha_1(z_s - z)) - 1)) \\
 Q_p &= 1 / (1 - (\theta_b/\theta_s)(1 - \exp(\alpha_1(z_s - z)))) \quad (3.19)
 \end{aligned}$$

Results equivalent to Eqs. (3.17a, b), (3.18a, b), and (3.19a, b) have been given by Probstein and Fassio [6]. They used a Lagrangian

description. The temperature and density results are new. The use of an Eulerian description facilitates the determination of the particle-phase density and the location of the body surface (it is at $z = 0$). These results were used as a check on the numerical calculations to be described subsequently.

NUMERICAL SOLUTIONS FOR THIN SHOCK LAYERS

In this section the symbol j is introduced to differentiate between plane and axisymmetric flow. For the former, $j = 0$; while for the latter, $j = 1$. The discussion will be for the conical case, but the resulting equations are also valid for wedge flows if j is set equal to zero. Figure 2 depicts either a wedge-shaped or conical shock layer.

For numerical work it is found convenient to use a system of polar coordinates r and θ with $r = 0$ at the leading edge of the body and $\theta = 0$ on the axis of symmetry of the cone. Defining the dimensionless variables

$$\xi = r/L, \quad \eta = \theta$$

$$F_p \vec{e}_\xi + G_p \vec{e}_\eta = \vec{u}/U_\infty, \quad F_p \vec{e}_\xi + G_p \vec{e}_\eta = \vec{u}_p/U_\infty \quad (3.20)$$

where \vec{e}_ξ and \vec{e}_η are unit vectors associated with ξ and η , substituting Eqs. (3.20) and (3.2c,d) into Eqs. (2.4), and combining the results yields

$$(\xi(\xi\eta)^j Q_p F_p),_\xi + ((\xi\eta)^j Q_p G_p),_\eta = 0$$

$$F_p F_p,_\xi + (G_p/\xi) F_p,_\eta - G_p^2/\xi = \alpha_1 ((F-F_p)^2 + (G-G_p)^2)^{(1-b)/2} (F-F_p)$$

$$F_p G_p,_\xi + (G_p/\xi) G_p,_\eta + F_p G_p/\xi = \alpha_1 ((F-F_p)^2 + (G-G_p)^2)^{(1-b)/2} (G-G_p)$$

$$F_p H_p,_\xi + (G_p/\xi) H_p,_\eta = \alpha_2 (H_s - H_p) \quad (3.21)$$

The gas flow variables are modeled by the constant density approximation (see Probst and Fassio [6]).

$$F = 1, \quad G = -(1+j)(\eta - \theta_b), \quad H = H_s = \epsilon((1+\epsilon)M_\infty^2 \theta_s^2 - 1) \quad (3.22)$$

(Note that, within the thin-shock-layer approximations, these expressions are exact for $j = 0$.) The shock wave is a cone making an angle

$$\theta_s = \theta_b / (1 - (\epsilon / (1+j))) \quad (3.23)$$

with the axis of symmetry. The boundary conditions

$$F_p = 1, \quad G_p = -\theta_s, \quad H_p = 1, \quad Q_p = 1 \quad (3.24)$$

must be satisfied on the shock wave. As will be pointed out in the next chapter, some terms in the foregoing equations can be neglected for thin shock layers. This was not done, however, in this chapter to insure that the analytical and numerical results for wedge flows were solutions to exactly the same governing equations. Thus any discrepancy between the numerical and analytical solutions would be due to inaccuracy of the numerical method and not due to the differences in the sets of equations being solved.

Again it is useful to employ a Von Mises transformation. Defining a stream function ψ_p such that

$$\psi_p, \xi = -(\xi \eta)^j Q_p G_p, \quad \psi_p, \eta = \xi (\xi \eta)^j Q_p F_p \quad (3.25)$$

and converting to the independent variables ψ_p and $z = \eta - \theta_b$ one obtains

$$G_p F_p z - G_p^2 = \alpha_1 \xi ((1-F_p)^2 + ((1+j)z + G_p)^2)^{(1-b)/2} (1-F_p)$$

$$G_p G_p z + F_p G_p = -\alpha_1 \xi ((1-F_p)^2 + ((1+j)z + G_p)^2)^{(1-b)/2} ((1+j)z + G_p)$$

$$G_p H_p z = \alpha_2 (H_s - H_p)$$

$$G_p \xi_z = \xi F_p$$

$$Q_p = -1 / ((\xi(z + \theta_b))^j G_p \xi, \psi_p) \quad (3.26)$$

The relationship between ψ_p and ξ_s (the radial coordinate at which the particle-phase streamline $\psi_p = \text{constant}$ enters the shock layer) is easily found, using Eq. (3.25a), to be

$$\psi_p = (\theta_s^{1+j} / (1+j)) \xi_s^{1+j} \quad (3.27)$$

Using this expression Eq. (3.26e) can be written as

$$Q_p = -(\xi_s / \xi)^j (\theta_s / (z + \theta_b))^j (\theta_s / (G_p \xi, \xi_s)) \quad (3.28)$$

Equations (3.26a, b, c, d) are numerically integrated simultaneously along various streamlines using a fourth-order Runge-Kutta algorithm. Since each streamline represents a line of $\xi_s = \text{a constant}$, the partial derivatives with respect to z can be treated as ordinary derivatives in this calculation. After the determination of F_p , G_p , H_p , and ξ , Q_p is obtained from the algebraic Eq. (3.28). The derivative with respect to ξ_s is approximated by a two-point backward difference quotient. Equation (3.28) is then solved along the given streamline. A discussion of the numerical results obtained by this method is the subject of the next two paragraphs.

Figures 3 and 4 show the distribution of the particle-phase normal velocity and the particle-phase density along the vehicle surface. These calculations are for a vertex half-angle $\theta_b = 0.1$ and a gas density ratio $\epsilon = 0.1$. Results are plotted for various values of the dimensionless drag parameter α_1 and for the linear drag law $b = 1$. Figure 3 pertains to wedges while Fig. 4 pertains to conical shock layers. It can be seen that for small values of the drag parameter the particle-phase normal velocity and the particle-phase density are nearly constant along the surface. This represents a situation in which the motion of the particles is almost unaffected by the presence of the shock layer. As α_1 increases, significant deviations from the free-stream values of the variables quickly become apparent. It is clear that this effect is greater for the wedge than for the cone. Figure 3 represents either the numerical solution or the analytical solution represented by Eqs. (3.17a, b, d). For the step sizes used in this work [$\Delta\xi_s = 0.005$, $\Delta z = (\theta_s - \theta_b)/100$] it was found that the numerical and analytical solutions were indistinguishable. Reductions in the step sizes failed to produce any change in the solution variables. Thus the wedge results do exhibit the correct qualitative behavior and are especially useful to serve as a check on the numerical results.

Figure 5 shows some comparisons of the results obtained in different drag regimes (different values of b) for $\theta_b = 0.1$ and $\epsilon = 0.1$. The lines labeled $b = 1$ correspond to the linear law, while those labeled $b = 0.6$ and $b = 0$ pertain to the intermediate and quadratic laws respectively. Obviously the sensitivity of the solution variables to the value of b increases as α_1 increases because b is contained only in the drag terms whose magnitude is determined by the value of α_1 . It is clear from

the plotted data that for $\alpha_1 = 10$ significantly different values of the flow variables exist in different regimes of the standard drag curve.

The computer program actually calculates the flow variables at all points in the shock layer. The results are presented here only for the values of the variables on the body surface because these are thought to be of primary interest in applications.

Chapter 4

GENERAL WEDGE-SHAPED AND CONICAL SHOCK LAYERS

It is now desired to eliminate any assumption that either the body angle or the shock layer is thin. Before beginning the analysis of this chapter a notational correction is pointed out. In all subsequent equations a subscript s will indicate the value of a variable at the shock wave while a subscript b will indicate the value of a variable on the body surface.

GOVERNING EQUATIONS FOR GENERAL SHOCK LAYERS

It is desired to investigate collisions of particles with the body surface occurring between $r = 0$ and $r = L$. The governing Eqs. (3.21) are now replaced by

$$\begin{aligned}
 & (\xi(\xi \sin \eta)^j Q_{p p}^j F_p),_{\xi} + ((\xi \sin \eta)^j Q_{p p}^j G_p),_{\eta} = 0 \\
 & F_p F_{p,\xi} + (G_p/\xi) F_{p,\eta} - G_p^2/\xi = \alpha_1 ((F-F_p)^2 + (G-G_p)^2)^{(1-b)/2} (F-F_p) \\
 & F_p G_{p,\xi} + (G_p/\xi) G_{p,\eta} + F_p G_p/\xi = \alpha_1 ((F-F_p)^2 + (G-G_p)^2)^{(1-b)/2} (G-G_p) \\
 & F_p H_{p,\xi} + (G_p/\xi) H_{p,\eta} = \alpha_2 (H-H_p)
 \end{aligned} \tag{4.1}$$

where α_1 and α_2 are given by Eqs. (3.4). In this case the particle-phase stream function is defined so as to satisfy Eq. (4.1a) by

$$\psi_{p,\xi} = -(\xi \sin \eta)^j Q_{p p}^j G_p, \quad \psi_{p,\eta} = \xi(\xi \sin \eta)^j Q_{p p}^j F_p \tag{4.2}$$

Converting Eqs. (4.1) to the independent variables ψ_p and η and writing all the governing equations (using a procedure identical to that discussed in Chapter 3) in terms of new independent variables ξ_s and

$$z = (\theta_s - \eta) / (\theta_s - \theta_b) = (\theta_s - \eta) / \theta_L \quad (4.3)$$

(which transforms the region $\theta_b < \eta < \theta_s$ into the region $1 > z > 0$), the modified governing Eqs. (3.26) finally replaced by

$$\begin{aligned} G_p F_p' z + \theta_L G_p^2 + \alpha_1 \theta_L \xi ((F - F_p)^2 + (G - G_p)^2)^{(1-b)/2} (F - F_p) &= 0 \\ G_p G_p' z - \theta_L F_p G_p + \alpha_1 \theta_L \xi ((F - F_p)^2 + (G - G_p)^2)^{(1-b)/2} (G - G_p) &= 0 \\ G_p \xi' z + \theta_L \xi F_p &= 0 \\ G_p H_p' z + \alpha_2 \theta_L \xi (H - H_p) &= 0 \\ Q_p &= -((\xi_s \sin \theta_s) / (\xi \sin(\theta_s(1-z) + \theta_b z)))^J \sin \theta_s / (G_p \xi_s \xi_s) \end{aligned} \quad (4.4)$$

where $\theta_L = \theta_s - \theta_b$. The appropriate boundary conditions are (since it is assumed that the particles are unaffected by passage through the shock)

$$\begin{aligned} F_p(\xi_s, 0) &= \cos \theta_s, & G_p(\xi_s, 0) &= -\sin \theta_s \\ \xi(\xi_s, 0) &= \xi_s, & H_p(\xi_s, 0) &= 1, & Q_p(\xi_s, 0) &= 1 \end{aligned} \quad (4.5)$$

It should be noted that Eqs. (4.4a, b, c, d) contain no derivatives with respect to ξ_s . Thus when integrated along a given particle-phase streamline ($\xi_s = \text{a constant}$), they can be treated as ordinary differential equations.

NUMERICAL SOLUTIONS FOR ARBITRARY
 SHOCK LAYERS ON WEDGES AND CONES

In this section the exact numerical solution of Eqs. (4.4) is discussed. Equations (4.4a, b, c, d) and Eq. (4.4e) are solved numerically using the method discussed earlier. The solution begins at $\xi_s = 0$ with the initial conditions

$$\begin{aligned} F_p(0,z) &= \cos(\theta_s(1-z)+\theta_b z), & G_p(0,z) &= -\sin(\theta_s(1-z)+\theta_b z) \\ H_p(0,z) &= 1, & \rho_p(0,z) &= 1 \end{aligned} \quad (4.6)$$

[Equations (4.6) are the solutions to Eqs. (4.4a, b, d, e) with $\xi = 0$] and marches from streamline to streamline in the direction of increasing ξ_s . The fluid phase is taken to be an inviscid perfect gas with constant specific heats and specific heat ratio $\gamma = 1.4$. (The thin viscous boundary layer near the body surface is unlikely to have a pronounced effect on the behavior of the particle phase and is neglected.) The gas-phase flow variables are modeled by the linear functions

$$F = F_s(1-z)+F_b z, \quad G = G_s(1-z)+G_b z, \quad H = H_s(1-z)+H_b z \quad (4.7)$$

where F_s , H_s , and ϵ have the following forms:

$$\begin{aligned} F_s &= \cos \theta_s, & G_s &= -\epsilon \sin \theta_s \\ H_s &= \epsilon(1+(1-\epsilon)\gamma M_\infty^2 \sin^2 \theta_s) \\ \epsilon &= ((\gamma-1)M_\infty^2 \sin^2 \theta_s + 2)/((\gamma+1)M_\infty^2 \sin^2 \theta_s) \end{aligned} \quad (4.8)$$

(see Liepmann and Roshko [15]). The transverse velocity is normal to the

body surface at $z = 1$ so $G_b = 0$. The exact values for F_b and H_b (as tabulated by Sim [1]) are used to complete the description of the gas-phase flow field. The quantities F_b , H_b , and θ_s can be found from Ref. [1] once the free-stream Mach number M_∞ and the body angle θ_b are specified. Since the gas-phase solution is independent of ξ (see Liepmann and Roshko [15]), F_b and H_b are constants. The exact numerical solution for the gas flow field could have been used directly, but utilization of Eqs. (4.7) saves considerable computer storage, and comparison with some results obtained by Spurk and Gerber [8] shows that the loss of accuracy involved is insignificant.

A parametric study involving M_∞ , θ_b , α_1 , α_2 , and b was carried out and some representative results of these calculations are presented graphically in Figs. 6 through 10. Most pertinent to the evaluation of cratering and erosion damage are $F_p(\xi_s, 1) = F_{pb}$, $G_p(\xi_s, 1) = G_{pb}$, and $Q_p(\xi_s, 1) = Q_{pb}$. It was found from the numerical results that $\cos \theta_s < F_{pb} < (\cos^2 \theta_s + \epsilon^2 \sin^2 \theta_s)^{1/2}$ (the lower limit corresponds to $\alpha_1 = 0$, the upper limit to $\alpha_1 = \infty$). Since this estimate of F_{pb} is available in closed form, for the sake of brevity no numerical results are present for this quantity and attention is directed toward G_{pb} and Q_{pb} . In addition a few results are given for $H_p(\xi_s, 1) = H_{pb}$ and the local collection efficiency E (the actual rate at which particulate mass strikes the surface between the cone vertex and $\xi(\xi_s, 1) = \xi_b$ divided by the rate that would occur if the particle phase was unaffected by the shock layer). It can be shown that the value of E associated with the streamline $\xi_s = \text{constant}$ is

$$E = ((\xi_s \sin \theta_s) / (\xi_b \sin \theta_b))^{1+j} \quad (4.9)$$

Since the results of particle-phase variables for the wedge flows ($j = 0$) were found qualitatively very similar to that for cone flows ($j = 1$), for the sake of brevity the discussion will be confined to the conical case.

The basic features of the flow field are illustrated by Figs. 6 and 7. Increasing ξ_g (which increases the length of the particle-phase streamline $\xi_g = \text{constant}$) and increasing α_1 both increase the effectiveness of the interphase momentum transfer which tends to bring the particles into equilibrium with gas and thus deflect them away from the body. The magnitude of the particle-phase normal velocity component $-G_{pb}$ is, therefore, a decreasing function of both ξ_b (since ξ_b increases with ξ_g) and α_1 as can be seen from Fig. 6. The decrease in $-G_{pb}$ is accompanied by a compression of the particle phase as indicated by the behavior of Q_{pb} in Fig. 6. Some particles which would strike the body in the region $0 < \xi_b < 1$ in the absence of interphase momentum transfer are deflected enough so that they now do not strike the body in this region. Thus the collection efficiency is reduced as shown in Fig. 7. The decrease in $-G_{pb}$ causes an increase in the time spent by each particle in the shock layer in which interphase heat transfer can bring the particle-phase temperature closer to equilibrium with the (higher) gas temperature. Thus, as can be seen from Fig. 7, H_p is an increasing function of α_1 and ξ_b . It can be observed that the theory predicts large increase in Q_{pb} as $-G_{pb}$ becomes small. It is therefore possible that for a particular suspension the free-stream mass fraction of particles would be small enough to justify the neglect of the presence of the particles on the motion of the fluid but the computed results for the particle-phase density within the shock layer would violate this assumption. Thus the calculation of the particle-phase density (which was omitted by previous

investigators) can serve as an important check on the validity of the theory.

Figure 8 serves as a supplement to Fig. 6. Taken together they show that the particle phase is considerably more sensitive to interphase momentum transfer for $b = 1$ than for $b = 0$. Qualitative differences in behavior can be seen to exist between the results for these two values of b . For a given value of $-G_{pb}$ at $\xi_b = 1$ the curve for $b = 0$ appears to approach that final value more rapidly than does the one for $b = 1$. The corresponding density curves exhibit an always increasing slope for $b = 1$ but possess a region of increasing slope (difficult to detect because of the scale of the drawing) followed by a region of decreasing slope for $b = 0$. Qualitative observations such as these should be helpful in determining appropriate values of N_1 , N_2 , and b for various flow conditions and suspensions.

Increasing θ_b increases the shock angle and thus thickens the shock layer. The resulting increase in $-G_{pb}$ is not made up for by the resulting increase in the effectiveness of interphase momentum transfer, and increased impact velocities all along the body surface are the result as shown in Fig. 9. In addition the density of the particle phase Q_{pb} is also an increasing function of θ_b . Thus whether erosion and cratering are caused by individual high-speed impacts or a number of lower speed impacts occurring in the same place, increasing θ_b will increase the likelihood of damage to the body surface.

Increasing the free-stream Mach number M_∞ decreases θ_b and therefore the effectiveness of interphase momentum transfer. Thus $-G_{pb}$ is an increasing function of M_∞ while Q_{pb} is a decreasing function of this parameter as shown in Fig. 10. The results for $M_\infty = 10$ are representative

of hypersonic flight conditions. Sled tests, on the other hand, are often carried out at much lower Mach numbers and the results for $M_\infty = 2$ are intended to be representative of these conditions. The results presented in Fig. 10 serve to further illustrate qualitative differences between solutions corresponding to $b = 0$ and $b = 1$.

APPROXIMATE ANALYTICAL SOLUTION FOR THIN SHOCK LAYERS

In this section Eqs. (4.4) are simplified for thin shock layers. These are situations for which the inequalities

$$\theta_L \ll 1 \quad \text{and} \quad \theta_L/\theta_D \ll 1 \quad (4.10)$$

are satisfied. (Note that it is not required that $\theta_D \ll 1$ as was done in Chapter 3.) Such situations exist when $M_\infty \gg 1$. The resulting approximate equations can be solved analytically. Toward this end it is assumed, following Probstein and Fassiio [6], that

$$G_p/G \gg 1, \quad H_p/H \ll 1, \quad F \doteq F_S = \cos \theta_S, \quad H \doteq H_S \quad (4.11)$$

For $M_\infty \gg 1$ a large decrease in G and a large increase in H occur across the shock wave. The quantities G_p and H_p , on the other hand, are continuous across the shock wave. These facts provide the motivation for assumptions (4.11a, b). Assumptions (4.11c, d) are motivated by a desire to simplify the form of the analytical solutions to the maximum extent possible while retaining the correct qualitative behavior. Substituting assumptions (4.11c, d) into Eqs. (4.4), estimating the order of magnitude of each term in the resulting equations, using assumptions (4.11a, b) and (4.10) [but allowing for the possibilities $\alpha_1 \theta_L = O(1)$, $\alpha_2 \theta_L = O(1)$], and retaining only terms of $O(1)$ leads to

$$G_p F_p' z + \alpha_1 \theta_L \xi ((\cos \theta_s - F_p)^2 + G_p^2)^{(1-b)/2} (\cos \theta_s - F_p) = 0$$

$$G_p G_p' z - \alpha_1 \theta_L \xi ((\cos \theta_s - F_p)^2 + G_p^2)^{(1-b)/2} G_p = 0$$

$$G_p \xi_p' z = 0$$

$$G_p H_p' z + \alpha_2 \theta_L \xi H_p = 0$$

$$Q_p = -(\xi_s / \xi)^J \sin \theta_s / (G_p \xi, \xi_s) \quad (4.12)$$

Equations (4.12a, c) can be solved, subject respectively to Eqs. (4.5a, c), to yield

$$F_p = \cos \theta_s, \quad \xi = \xi_s \quad (4.13)$$

Substituting Eqs. (4.13) into Eqs. (4.12b, d, e) one obtains

$$G_p G_p' z + \alpha_1 \theta_L \xi_s (-G_p)^{2-b} = 0$$

$$G_p H_p' z + \alpha_2 \theta_L \xi_s H_p = 0$$

$$Q_p = -\sin \theta_s / G_p \quad (4.14)$$

Solving these equations for some realistic values of b (see Probstein and Fassio [6]) gives

$$b = 0 : G_p = -\sin \theta_s \exp(-\alpha_1 \theta_L \xi_s z)$$

$$H_p = 1 + (\alpha_2 H_s / (\alpha_1 \sin \theta_s)) (\exp(\alpha_1 \theta_L \xi_s z) - 1)$$

$$Q_p = \exp(\alpha_1 \theta_L \xi_s z) \quad (4.15)$$

$$b = 3/5 : G_p = -\sin \theta_s (1 - 3\alpha_1 \theta_L \xi_s z / (5 \sin^{3/5} \theta_s))^{5/3}$$

$$H_p = 1 + (5\alpha_2 H_s / (2\alpha_1 \sin^{2/5} \theta_s)) \times$$

$$(1 / (1 - 3\alpha_1 \theta_L \xi_s z / (5 \sin^{3/5} \theta_s)))^{2/3 - 1}$$

$$Q_p = 1 / (1 - (3\alpha_1 \theta_L \xi_s z / (5 \sin^{3/5} \theta_s)))^{5/3} \quad (4.16)$$

$$b = 1 \quad : \quad G_p = -\sin \theta_s (1 - (\alpha_1 \theta_L \xi_s z / \sin \theta_s))$$

$$H_p = 1 + (\alpha_2 H_s / \alpha_1) \log(1 / (1 - (\alpha_1 \theta_L \xi_s z / \sin \theta_s)))$$

$$Q_p = 1 / (1 - (\alpha_1 \theta_L \xi_s z / \sin \theta_s)) \quad (4.17)$$

These solutions should be useful because they demonstrate some of the qualitative features of the exact numerical solutions and provide quick estimates of the properties of two-phase flow without having to engage in extensive numerical calculations for thin shock layers. It should be noted that Eqs. (4.16a) and (4.17a) predict that

$$G_p = 0 \quad \text{at} \quad z_c = (\sin^b \theta_s / (b\alpha_1 \theta_L \xi_s)) \quad (4.18)$$

This would indicate that the particles coming from shock wave are brought to rest at this value of z and that a particle-free zone exists for $z_c < z < 1$. This prediction must be discounted, however, because when $G_p = 0$ assumption (4.11a) is obviously violated. Only results for which G_p is negative everywhere in the shock layer can be taken seriously.

Chapter 5

SPHERICAL AND CYLINDRICAL SHOCK LAYERS

The present chapter is concerned with the motion of the particle phase in the vicinity of a sphere or a circular cylinder. The flow configuration is shown in Fig. 11. Since a sphere is the geometrically simplest example of a blunt body, the results computed in the present work are of fundamental interest in estimating the cratering and erosion damage that will be experienced by blunt-nosed vehicles flying through particle-laden regions of the atmosphere. Since the shock wave is detached from the body surface in such cases, one would expect that the effectiveness of the interphase drag force in slowing down the particles before they strike the vehicle surface would be greater for a spherical shock layer than for a conical shock layer. This, in turn, would lead to less likelihood of damage to vehicle surfaces. Calculations of the flow variables for this case will be carried out by a method very similar to that discussed in the previous chapters. Some results for the case for cylindrical shock layers are also presented in this chapter to provide a basis for comparisons of flow variables between plane and axisymmetric two-phase flows.

GOVERNING EQUATIONS IN POLAR COORDINATES

Consider the steady supersonic flow of an air-particle suspension past a sphere of radius r_b . To describe the motion, polar coordinates r and θ (with associated unit vectors \vec{e}_r and \vec{e}_θ) are used. The polar

coordinate system lies in the plane of symmetry of the flow, has origin at the center of the sphere, and is oriented so that the line $\theta = 0$ is coincident with the forward stagnation line of the gas motion. Using Eqs. (2.4) and introducing the transformations

$$\begin{aligned} r &= r_b \xi, & \theta &= \eta \\ \vec{u} &= U_\infty (F_p^+ \vec{e}_r + G_p^+ \vec{e}_\theta), & \vec{u}_p &= U_\infty (F_p^+ \vec{e}_r + G_p^+ \vec{e}_\theta) \\ T &= T_\infty H, & T_p &= T_\infty H_p, & \rho_p &= \rho_p Q_p \end{aligned} \quad (5.1)$$

leads to

$$\begin{aligned} &(\xi(\xi \sin \eta)^j Q_p F_p^+),_{\xi} + ((\xi \sin \eta)^j Q_p G_p^+),_{\eta} = 0 \\ F_p^+ F_p^+,_{\xi} + (G_p^+ / \xi) F_p^+,_{\eta} - G_p^+{}^2 / \xi &= \alpha_1 ((F_p^+)^2 + (G_p^+)^2)^{(1-b)/2} (F_p^+) \\ F_p^+ G_p^+,_{\xi} + (G_p^+ / \xi) G_p^+,_{\eta} + F_p^+ G_p^+ / \xi &= \alpha_1 ((F_p^+)^2 + (G_p^+)^2)^{(1-b)/2} (G_p^+) \\ F_p^+ H_p^+,_{\xi} + (G_p^+ / \xi) H_p^+,_{\eta} &= \alpha_2 (H - H_p) \end{aligned} \quad (5.2)$$

where $\alpha_1 = (N_1 r_b / U_\infty^b)$, $\alpha_2 = (N_2 r_b / U_\infty)(c/c_p)$, and $j = 1$. As previously stated, the dimensionless parameters α_1 and α_2 are measures of effectiveness of interphase momentum and heat transfer respectively. For plane flow past a circular cylinder of radius r_b , the same equations result with $j = 0$. Equations (5.2) have the same form as do Eqs. (4.1). It should be noted that in this chapter the normal velocity with which particles strike the body is found by evaluating F_p^+ at the vehicle surface while the tangential impact velocity is found by evaluating G_p^+ at the surface. This is the opposite of the notation employed in previous chapters where the normal impact velocity was found by evaluating G_p^+ at the vehicle surface while the tangential impact velocity was found by computing the

value of F_p . It is easily shown that local collection efficiency is

$$E(\eta) = -((1+j)/\sin^{(1+j)\eta}) \int_0^\eta Q_p(1,\sigma) F_p(1,\sigma) \sin^j \sigma d\sigma \quad (5.2)$$

where σ is a dummy variable.

In order to solve Eqs. (5.2), F , G , and H must be specified. Following Waldman and Reinecke [7], these flow variables are modeled by the linear functions of ξ .

$$\begin{aligned} F &= ((F_s - F_b)/\Delta_s)(\xi - 1) + F_b \\ G &= ((G_s - G_b)/\Delta_s)(\xi - 1) + G_b \\ H &= ((H_s - H_b)/\Delta_s)(\xi - 1) + H_b \end{aligned} \quad (5.4)$$

where Δ_s is the radial distance from the body surface to the shock wave (the standoff distance) made dimensionless by the body radius r_b . To determine the dependence of the quantities appearing in Eqs. (5.4) on η , reference is made to the modified constant density theory for an inviscid gas discussed by Hayes and Probstein [2]. According to this theory, Δ_s is independent of η and has the form

$$\Delta_s = \lambda_1 / (1 - \lambda_1) \quad (5.5)$$

In Eq. (5.5)

$$\lambda_1 = \begin{cases} (\epsilon/2) \log(4/3\epsilon) + (\epsilon/2)^2 (\log(4/3\epsilon) - 1), & j = 0 \\ \epsilon / (1 + (8\epsilon/3)^{1/2}), & j = 1 \end{cases} \quad (5.6)$$

where ϵ is the ratio of the gas density just before the shock wave to the

gas density just behind the shock wave at $\eta = 0$. The constant density theory also yields the expressions

$$\begin{aligned} \epsilon &= ((\gamma-1)M_\infty^2+2)/((\gamma+1)M_\infty^2) \\ F_s &= -\epsilon \cos \eta, \quad F_D = 0 \\ G_s &= \sin \eta, \quad G_D = ((\gamma-j)\epsilon/S)^{1/2} \sin \eta \\ H_s &= \epsilon(1+\gamma M_\infty^2(1-\epsilon)\cos^2\eta) \\ H_D &= \epsilon(1+\gamma M_\infty^2(1-(\epsilon/2)-\lambda_2\sin^2\eta)) \end{aligned} \quad (5.7)$$

where

$$\begin{aligned} \lambda_2 &= (3/2)(1+(\epsilon/2)\log(4/3\epsilon)-1), \quad j = 0 \\ \lambda_2 &= (4/3)(1+(\epsilon/4)(1-(8/3)(8\epsilon/3)^{1/2})), \quad j = 1 \end{aligned} \quad (5.8)$$

As previously stated, M_∞ is the free-stream Mach number and γ is the ratio of specific heats for a perfect gas. In all calculations performed it was assumed that $\gamma = 1.4$.

If it is assumed that the shock wave has no effect on the particle-phase variables, the boundary conditions are

$$F_{ps} = -\cos \eta, \quad G_{ps} = \sin \eta, \quad Q_{ps} = 1, \quad H_{ps} = 1 \quad (5.9)$$

NUMERICAL SOLUTIONS AT STAGNATION LINE

To start the numerical method to be discussed in the following sections, the solutions for the particle-phase flow variables in the vicinity of the forward stagnation line of the gas flow field are needed. These solutions are also of interest in themselves because they illustrate many of the basic features of blunt-body two-phase flows of the type under

discussion in the present chapter. This section is, therefore, devoted to an analysis of the particle-phase flow field near $\eta = 0$. To begin the analysis, the following expansions are employed

$$\begin{aligned} F_p(\xi, \eta) &= F_{p0}(\xi) + O(\eta^2) \\ G_p(\xi, \eta) &= \eta(G_{p0}(\xi) + O(\eta^2)) \\ Q_p(\xi, \eta) &= Q_{p0}(\xi) + O(\eta^2) \\ H_p(\xi, \eta) &= H_{p0}(\xi) + O(\eta^2) \\ \cos \eta &= 1 + O(\eta^2) \\ \sin \eta &= \eta(1 + O(\eta^2)) \\ E &= E_0 + O(\eta^2) \end{aligned} \tag{5.10}$$

Substituting Eqs. (5.10) into Eqs. (5.2) - (5.9), equating the coefficient of each power of η appearing in each of the resulting equations to zero individually in the usual way, writing all the equations involving the first terms of the series (5.10a, b, c, d, g) in terms of the new independent variable

$$z = (1 + \Delta_s - \xi) / \Delta_s \tag{5.11}$$

[which transforms the interval $(1 < \xi < 1 + \Delta_s)$ into the interval $(1 < z < 0)$], and dropping the subscript 0 for convenience yields the differential equations

$$(F_p Q_p)' - (1+j)(\Delta_s / (1 + \Delta_s (1-z)))(F_p + G_p) Q_p = 0$$

$$F_p F_p' + \alpha_1 \Delta_s |F - F_p|^{(1-b)} (F - F_p) = 0$$

$$\begin{aligned}
 &F_p G_p' - (\Delta_s / (1 + \Delta_s (1-z))) (F_p + G_p) G_p \\
 &+ \alpha_1 \Delta_s |F - F_p|^{(1-b)} (G - G_p) = 0 \\
 &F_p H_p' + \alpha_2 \Delta_s (H - H_p) = 0
 \end{aligned} \tag{5.12}$$

(where a prime denotes differentiation with respect to z), the initial conditions

$$F_p(0) = -1, \quad G_p(0) = 1, \quad Q_p(0) = 1, \quad H_p(0) = 1 \tag{5.13}$$

and the expressions

$$\begin{aligned}
 E &= -F_p(1)Q_p(1) \\
 F &= F_s(1-z) + F_b z \\
 G &= G_s(1-z) + G_b z \\
 H &= H_s(1-z) + H_b z
 \end{aligned} \tag{5.14}$$

where

$$\begin{aligned}
 F_s &= -\epsilon, \quad F_b = 0, \quad G_s = 1, \quad G_b = ((9-j)\epsilon/3)^{1/2} \\
 H_s &= \epsilon(1 + \gamma M_\infty^2(1-\epsilon)), \quad H_b = \epsilon(1 + \gamma M_\infty^2(1-(\epsilon/2)))
 \end{aligned} \tag{5.15}$$

The governing Eqs. (5.12) are nonlinear, and it seems highly unlikely that analytical solutions can be found. Thus these equations were numerically integrated using a fourth order Runge-Kutta procedure. Numerical solutions were obtained for a variety of values of α_1 , α_2 , and M_∞ for both $b = 0$ and $b = 1$. Some typical results of these calculations are shown in Figs. 12 - 17.

Figures 12 and 13 show the radial velocity and density profiles of the particle phase predicted by approximate (will be discussed later) and exact solution methods for $b = 1$. It can be seen that the decrease in the radial velocity of the particles increases with increasing α_1 and is associated with a compression of the particle phase which also increases as α_1 increases.

In Figs. 14 and 15 the particle-phase flow variables at the vehicle surface are plotted versus α_1 for $b = 1$. It can be seen that $-F_p(1)$ is a decreasing function of α_1 and an increasing function of M_∞ . This is because both increases in α_1 and decreases in M_∞ increase the importance of interphase momentum transfer, the former directly and the latter indirectly by thickening the shock layer. These effects are considerably more pronounced for plane than for axisymmetric flow. For a given M_∞ the radial impact velocity vanishes at a finite value $\alpha_1 = \alpha_{1c}$ and remains zero for $\alpha_1 > \alpha_{1c}$. Thus for $\alpha_1 > \alpha_{1c}$ no cratering and erosion damage will occur because no particles strike the surface of the vehicle. This situation is in contrast to that occurring in cone flows (see Chapter 4) where particles strike the body surface for any finite amount of interphase momentum transfer. It is evident that blunting of flight vehicles is an option open to designers desirous of reducing cratering and erosion damage.

As pointed out when viewing the Figs. 12 and 13, decreases in $F_p(1)$ are accompanied by rapid increases of $Q_p(1)$. The value of $Q_p(1)$ is indicative of the number of impacts per unit time that will be experienced by the surface of the vehicle in the vicinity of the forward stagnation point. The range of parameters for which the greatest cratering and erosion damage will occur depends on the damage mechanism. If damage

is caused primarily by single particles impacting at high speeds, one would expect the most severe damage for the smaller values of α_1 and the larger values of M_∞ where $-F_p(1)$ is the largest. If, on the other hand, damage is primarily due to repeated impacts in the same area (fatigue damage, for example) the greatest damage would be expected for the larger values of α_1 and the smaller values of M_∞ where $Q_p(1)$ is the largest. Of course, as previously stated, no damage will occur for $\alpha_1 > \alpha_{1c}$.

If both of the damage mechanisms discussed above are of equal importance, the collection efficiency E [which is the product of $-F_p(1)$ and $Q_p(1)$] might be a suitable measure of the severity of cratering and erosion damage. To the authors' knowledge, however, no such correlation has so far been established. It can be seen that E is a decreasing function of α_1 and an increasing function of M_∞ . For a given M_∞ it is clear that E must vanish when $\alpha_1 = \alpha_{1c}$. This value is considerably lower for plane flow than it is for axisymmetric flow.

The particle-phase temperature $H_p(1)$ is an increasing function of both α_1 and M_∞ . The former effect is due to the fact that increasing α_1 decreases $-F_p(1)$ and thus decreases the importance of the convective term in Eq. (5.12d). The latter is a result of the fact that the gas temperature at any point in the shock layer is an increasing function of M_∞ . When $-F_p(1)$ vanishes, $H_p(1)$ is brought into equilibrium with the temperature of the gas phase as indicated by the constant-temperature portions of the curves in Fig. 15.

Figures 16 and 17 depict numerical results for $b = 0$ similar to those just discussed for $b = 1$. It can be seen that the trends of the data are identical to those found for $b = 1$ but that the flow variables are predicted to be less sensitive to changes in α_1 and M_∞ for $b = 0$

than for $b = 1$. It is also interesting that the shapes of the curves are somewhat different. The curves of $-F_p(1)$ versus α_1 , for example, exhibit more curvature for $b = 0$ than for $b = 1$. Comparisons such as this are useful in determining the value of b which best fits a given set of experimental data.

APPROXIMATE ANALYTICAL SOLUTIONS AT STAGNATION LINE

If certain simplifying assumptions are made, approximate analytical solutions to the governing Eqs. (5.12) can be found. Because these solutions illustrate some of the interesting features of the particle-phase flow field and because they can be used to obtain quick estimates of the particle-phase flow variables, they will now be presented.

The basic simplifying assumptions are (1) that the shock layer is thin, and (2) that the shock is strong. These two assumptions imply

$$\Delta_s \ll 1, \quad F_p/F \gg 1, \quad H_p/H \ll 1 \quad (5.16)$$

(see Probstein and Fassiò [6]). Using these assumptions to simplify Eqs. (5.12) and assuming (to simplify the forms of the analytical solutions) that G and H can be represented to a sufficient degree of accuracy by the expressions

$$G = G_s = 1, \quad H = H_s = \epsilon(1 + \gamma M_\infty^2(1 - \epsilon)) \quad (5.17)$$

leads to the approximate equations

$$(F_p Q_p)' = 0$$

$$F_p F_p' + \alpha_1 \Delta_s (-F_p)^{(2-b)} = 0$$

$$F_p G_p' + \alpha_1 \Delta_s (-F_p)^{(1-b)} (1-G_p) = 0$$

$$F_p H_p' + \alpha_2 \Delta_s H_p = 0 \quad (5.18)$$

Note that, even though it has been assumed that $\Delta_s \ll 1$, the possibility that $\alpha_i \Delta_s = O(1)$ ($i = 1, 2$) has been allowed for. Solving Eq. (5.18c) subject to Eq. (5.13b) yields

$$G_p = 1 \quad (5.19)$$

Solving Eqs. (5.18a, b, d) subject to Eqs. (5.13a, c, d) for some realistic values of b (see Probstein and Fassis [6] and Spurk and Gerber [8]), one obtains

$$\begin{aligned} b = 1 & : F_p = -(1 - \alpha_1 \Delta_s z) \\ Q_p & = 1 / (1 - \alpha_1 \Delta_s z) \\ H_p & = 1 + (\alpha_2 H_s / \alpha_1) \log(1 / (1 - \alpha_1 \Delta_s z)) \end{aligned} \quad (5.20)$$

$$\begin{aligned} b = 3/5 & : F_p = -(1 - (3\alpha_1 \Delta_s z / 5))^{5/3} \\ Q_p & = 1 / (1 - (3\alpha_1 \Delta_s z / 5))^{5/3} \\ H_p & = 1 + (5\alpha_2 H_s / (2\alpha_1)) ((1 / (1 - (3\alpha_1 \Delta_s z / 5)))^{2/3} - 1) \end{aligned} \quad (5.21)$$

$$\begin{aligned} b = 0 & : F_p = -\exp(-\alpha_1 \Delta_s z) \\ Q_p & = \exp(\alpha_1 \Delta_s z) \\ H_p & = 1 + (\alpha_2 H_s / \alpha_1) (\exp(\alpha_1 \Delta_s z) - 1) \end{aligned} \quad (5.22)$$

Note that in order for Eqs. (5.20a) and (5.21a) not to violate the assumption (5.16b), it is necessary that $\alpha_1 < 1/(b\Delta_s)$.

The comparisons of the approximate results with the numerical solutions obtained for $b = 1$ are shown in Figs. 12 and 13. The agreement is satisfactory for small and moderate values of α_1 . The degree of agreement decreases as α_1 increases. The agreement is somewhat worse for plane flow than axisymmetric flow. This is because for a given value of M_∞ the standoff distance Δ_g is larger for plane flow than for axisymmetric flow. Thus the assumption $\Delta_g \ll 1$, upon which the approximate analytical solutions are based, is better satisfied in the latter case than in the former. It is interesting to note that for axisymmetric flow the values $c = 0.175$ and $\Delta_g = 0.116$ are associated with $M_\infty = 10$. Thus the assumptions employed to obtain the approximate analytical solutions are only moderately well satisfied for the data presented in Fig. 12. In view of this, the agreement between the exact and approximate solutions is pleasantly surprising.

APPROXIMATE SOLUTIONS FOR $\alpha_1 > \alpha_{1c}$

For $\alpha_1 > \alpha_{1c}$ the numerical solutions to Eqs. (5.12) appeared to indicate a singularity in $Q_p(1)$. In order to investigate this matter, an approximate analytical solution valid near the vehicle surface was sought. This solution will now be discussed. Writing Eqs. (5.12) in terms of the independent variable $n = 1-z$, assuming that the dependent variables have the forms

$$F_p = -c_1 n, \quad G_p = c_2, \quad Q_p = c_3/n^w \quad (5.23)$$

for $n \ll 1$ (where c_1 , c_2 , c_3 , and w are constants), substituting Eqs. (5.23) into (5.12), expanding for $n \ll 1$, and retaining only the largest term in each expansion leads to the algebraic equations (for $b = 1$)

$$\begin{aligned}
 c_1^2 - \alpha_1 \Delta_s c_1 + \alpha_1 \Delta_s \epsilon &= 0 \\
 c_2^2 + \alpha_1 c_2 - \alpha_1 G_b &= 0 \\
 (1-\omega)c_1 - (1+j)\Delta_s c_2 &= 0
 \end{aligned}
 \tag{5.24}$$

which have the solutions

$$\begin{aligned}
 c_1 &= (\alpha_1 \Delta_s / 2) (1 - (1 - (4\epsilon / (\alpha_1 \Delta_s)))^{1/2}) \\
 c_2 &= (\alpha_1 / 2) ((1 + (4G_b / \alpha_1))^{1/2} - 1) \\
 \omega &= 1 - (1+j) ((1 + (4G_b / \alpha_1))^{1/2} - 1) / (1 - (1 - (4\epsilon / (\alpha_1 \Delta_s)))^{1/2})
 \end{aligned}
 \tag{5.25}$$

Because of the local nature of the solution, c_3 cannot be determined. Inspection of Eq. (5.25c) shows that the possibility of a solution exhibiting a singularity in Q_p is confirmed (it can be shown that $0 \leq \omega \leq 1$). Inspection of Eq. (5.25a) reveals that a solution of this form exists only for $\alpha_1 \geq 4\epsilon / \Delta_s$. It should be noted that this analysis shows only that a local solution of the form Eq. (5.23) exists, not that it is the limit of the actual solution for small n . It is found, however, that some of the numerical solutions computed in the present thesis do exhibit behavior consistent with Eqs. (5.23) and (5.25). Consider the case of $j = 1$ and $M_\infty = 10$ for which it was previously stated that $\epsilon = 0.175$ and $\Delta_s = 0.116$. Thus solutions of the form Eq. (5.23) are possible for $\alpha_1 \geq 6.04$. The numerical results indicate that such behavior actually occurs for $\alpha_1 \geq 10.6$. For this range of values of α_1 , the computed data show that $F_p(1) = 0$ and indicate a singularity in $Q_p(1)$. Furthermore, the predicted profile of G_p becomes constant for small n and assumes a value in excellent agreement with that indicated by Eq. (5.25b). These

considerations increase confidence in the proposition that Eqs. (5.23) and (5.25) describe the behavior of the particle-phase flow field in the cases where $F_p(1) = 0$. These formulas cannot be used, however, to predict the value of α_{1c} .

The presence of an algebraic singularity in the particle-phase density profile indicates a breakdown of the theory in the vicinity of the vehicle surface, because this prediction is in obvious disagreement with the assumption that the mass fraction of the particles must be small. When this is not so, the effect of the existence of the particles on the motion of the air must be accounted for (in a thin boundary layer adjacent to the body surface in the present situation). Since the primary concern of this report is the case for which particles do strike the surface of the vehicle (that is: $\alpha_1 < \alpha_{1c}$), this matter is not pursued further at the present time.

NUMERICAL SOLUTIONS AWAY FROM STAGNATION LINE

In this section attention is given to solution of Eqs. (5.2) away from stagnation line. This is facilitated, as previously stated, by a Von Mises transformation of the type familiar from boundary-layer theory. Toward this end a stream function ψ_p is defined such that

$$\xi(\xi \sin \eta)^j Q_p F_p = \psi_p, \eta, \quad (\xi \sin \eta)^j Q_p G_p = -\psi_p, \xi \quad (5.26)$$

Finding the total differential of ψ_p yields

$$d\psi_p = -(\xi \sin \eta)^j Q_p G_p d\xi + \xi(\xi \sin \eta)^j Q_p F_p d\eta \quad (5.27)$$

Reversing the roles of ψ_p and η (that is treating ψ_p as an independent variable and η as a dependent variable) Eq. (5.27) becomes

E42

$$d\eta = (1/(\xi(\xi \sin \eta)^j Q_p F_p)) d\psi_p + (G_p / (\xi F_p)) d\xi \quad (5.28)$$

from which it follows that

$$\eta_{,\psi_p} = 1/(\xi(\xi \sin \eta)^j Q_p F_p), \quad \eta_{,\xi} = G_p / (\xi F_p) \quad (5.29)$$

The solution is desired in the region $0 \leq \eta \leq \eta_f$. The new independent variable $\phi = \eta/\eta_f$ maps this region into $0 \leq \phi \leq 1$. This variable will be used for the rest of this section. Converting Eqs. (5.2b, c, d) to the independent variables ψ_p and ξ , then writing all the governing equations and boundary conditions in terms of the new independent variables ϕ_s (the angular coordinate at which the particle-phase streamline $\psi_p = \text{constant}$ enters the shock layer) and z defined by Eq. (5.11), one finally obtains (with the aid of the expression $d\phi_s/d\psi_p = -1/(\eta_f \xi_s \cos(\eta_f \phi_s) \xi_s \sin(\eta_f \phi_s))^j$) which is found by evaluating Eq. (5.26a) on the shock and noting that $Q_{ps} = 1$ and $F_{ps} = -\cos(\eta_f \phi_s)$)

$$\begin{aligned} F_p F_{p,z} + (\Delta_s / (1 + \Delta_s (1-z))) G_p^2 + \alpha_1 \Delta_s ((F - F_p)^2 + (G - G_p)^2)^{(1-b)/2} (F - F_p) &= 0 \\ F_p G_{p,z} - (\Delta_s / (1 + \Delta_s (1-z))) F_p G_p + \alpha_1 \Delta_s ((F - F_p)^2 + (G - G_p)^2)^{(1-b)/2} (G - G_p) &= 0 \\ F_{p\phi,z} + (\Delta_s / (\eta_f (1 + \Delta_s (1-z)))) G_p &= 0 \\ F_p H_{p,z} + \alpha_2 \Delta_s (H - H_p) &= 0 \\ Q_p = -((1 + \Delta_s) / (1 + \Delta_s (1-z)))^{1+j} (\sin(\eta_f \phi_s) / \sin(\eta_f \phi))^j \times \\ (\cos(\eta_f \phi) / (F_{p\phi, \phi_s})) & \quad (5.30) \end{aligned}$$

and

$$\begin{aligned}
 F_p(\phi_s, 0) &= -\cos(\eta_f \phi_s), & G_p(\phi_s, 0) &= \sin(\eta_f \phi_s) \\
 \phi(\phi_s, 0) &= \phi_s, & H_p(\phi_s, 0) &= 1
 \end{aligned}
 \tag{5.31}$$

where F, G, and H are determined by combining Eqs. (5.7) and (5.14). It can be seen that no derivatives with respect to ϕ_s appear in Eqs. (5.30a-d). Thus when integrated along the particle-phase streamline $\phi_s = \text{constant}$, they may be treated as ordinary differential equations.

In terms of the independent variables ϕ_s and Δ , the definition (5.3) of the collection efficiency E is difficult to employ. A more convenient expression can be found by applying the principle of balance of mass to the particle-phase material contained in the region bounded by the line $\phi = 0$ and the streamline $\phi_s = \text{constant}$. Doing this it is easily shown that the collection efficiency at the point on the body surface where the particle-phase streamline $\phi_s = \text{constant}$ strikes the vehicle is

$$E(\phi_s) = (1 + \Delta_s)^{(1+j)} (\sin(\eta_f \phi_s) / \sin(\eta_f \phi(\phi_s, 1)))^{(1+j)} \tag{5.32}$$

The governing Eqs. (5.30a-d) were solved by employing a fourth-order Runge-Kutta method. The term ϕ_s appearing in Eq. (5.30e) was evaluated using a two-point backward difference quotient, and Q_p was determined from the resulting algebraic equation. The solution procedure marches forward in ϕ_s from streamline to streamline using the stagnation-line ($\phi_s = 0$) solutions found in previous sections as initial conditions. Some typical results of these calculations are presented in Figs. 18 - 23. Since the constant-density expressions used to describe the gas flow field are reasonable only over the forward part of the vehicle, η_f was taken to be 30° in all the calculations performed. It should be pointed out that

the numerical procedure is in no way dependent on the expressions used to represent F , G , and H .

Computed data for $b = 1$ (solid lines) are presented in Figs. 18 and 19, together with two cases corresponding to $b = 0$ (dashed lines) for comparison. It can be seen that $-F_{pb} = -F_p(\phi_s, 1)$ is a decreasing function of $\phi_b = \phi(\phi_s, 1)$ and that the sensitivity of $-F_{pb}$ to ϕ_b is a decreasing function of α_1 . The flattening effect is more pronounced for $b = 0$ than for $b = 1$. The greatest curvature occurs for $\alpha_1 = 0$ when the solution is $-F_{pb} = \cos(\eta_f \phi_b)$. As α_1 increases, $-F_{pb}$ is decreased for all ϕ_b . The effect of interphase momentum transfer, however, increases with decreasing ϕ_b because the streamline curvature of the gas phase, and thus the relative velocity between the phases, increases as the stagnation line is approached. The greatest decrease in $-F_{pb}$, therefore, occurs at $\phi_b = 0$ where the effect of the interphase momentum transfer is greatest. This produces the flattening effect that can be observed in Fig. 18. These results indicate that $-F_{pb}$ will reach zero at all points along the surface of the vehicle simultaneously. Thus to determine the range of parameters for which no erosion and cratering damage will occur, it is necessary to consider only the stagnation-line solutions discussed in the previous section.

The stagnation-line solutions indicated that decreases in $-F_{pb}$ are accompanied by increases in $Q_{pb} = Q_p(\phi_s, 1)$. That this is true for all values of ϕ_b between zero and unity when $\eta_f = 30^\circ$ can be seen from Fig. 18. This compression of the particle phase increases with increasing ϕ_b and α_1 and is more pronounced for $b = 1$ than for $b = 0$.

The collection efficiency of the portion of the vehicle surface between the stagnation line and the point where the particle-phase

streamline $\phi_g = \text{constant}$ intersects the surface is a decreasing function of ϕ_b . The sensitivity of E to the value of ϕ_b increases sharply with increasing α_1 and is greater for $b = 1$ than for $b = 0$.

The particle-phase temperature $H_{pb} = H_p(\phi_g, 1)$ can be either an increasing or decreasing function of ϕ_b , depending on the values of α_1 and b . The behavior that actually occurs depends on the interaction of a variety of factors, and no simple explanation is obvious to the present author.

Figures 20 and 21 present results for $b = 0$ (solid lines) with two cases corresponding to $b = 1$ (dashed lines) for comparison. The trends of the data are identical to those inferred from inspection of Figs. 18 and 19. It seems clear that all of the variables are more sensitive to the values of α_1 and ϕ_b for $b = 1$ than for $b = 0$.

Figure 22 illustrates the influence of the free-stream Mach number M_∞ on the values of $-F_{pb}$ and Q_{pb} . Inspection of the plotted data shows that $-F_{pb}$ is an increasing function of M_∞ while Q_{pb} is a decreasing function of M_∞ . Also the curvature of $-F_{pb}$ versus ϕ_b increases as M_∞ increases. All of these trends are explained by the fact that increasing M_∞ decreases Δ_g and thus decreases the effect of interphase momentum transfer.

Figure 23 shows the influence of the parameter α_2 on H_{pb} . When $\alpha_2 = 0$, the solution is $H_{pb} = 1$. As α_2 increases, the influence of the gas temperature (which is a function of ϕ_b) increases, and H_{pb} becomes increasingly sensitive to the value of ϕ_b . Also as α_2 increases, the interphase heat-transfer mechanism becomes more effective in moving the particle phase toward thermal equilibrium with the gas phase (which is at a higher temperature). Thus H_{pb} is an increasing function of α_2 .

These results have been computed assuming that no mass loss from the particle phase occurs. They should, therefore, serve as useful standards of comparison for the prediction of more sophisticated theories which allow for particle vaporization.

APPROXIMATE ANALYTICAL SOLUTIONS AWAY FROM STAGNATION LINE

As has been said previously, it is interesting to find approximate analytical solutions for thin shock layers. To do this the assumptions

$$F_p/F \gg 1, \quad H_p/H \ll 1$$

$$G = G_s = \sin(\eta_f \phi_s), \quad H = H_s = \epsilon(1 + \gamma M_\infty^2(1 - \epsilon)\cos^2(\eta_f \psi_s)) \quad (5.33)$$

are invoked. Equations (5.30) then simplify to

$$F_p F_{p,z} - \alpha_1 \Delta_s (F_p^2 + (G_s - G_p)^2)^{(1-b)/2} F_p = 0$$

$$F_p G_{p,z} + \alpha_1 \Delta_s (F_p^2 + (G_s - G_p)^2)^{(1-b)/2} (G_s - G_p) = 0$$

$$F_p \phi_{,z} = 0$$

$$F_p H_{p,z} + \alpha_2 \Delta_s H_s = 0$$

$$Q_p = -(\sin(\eta_f \phi_s) / \sin(\eta_f \phi))^j (\cos(\eta_f \phi / (F_p \phi_{,z}))) \quad (5.34)$$

Solving Eqs. (5.34b, c) subject to Eqs. (5.31b, c) yields

$$G_p = G_s = \sin(\eta_f \phi_s), \quad \psi = \phi_s \quad (5.35)$$

Using Eq. (5.35a) simplifies Eq. (5.34a, e) to

$$F_p F_{p,z} + \alpha_1 \Delta_s (-F_p)^{(2-b)} = 0$$

$$Q_p = -\cos(\eta_f \phi) / F_p \quad (5.36)$$

Solving Eq. (5.36a) subject to Eq. (5.31a), substituting the result into Eqs. (5.34d) and (5.36b), and using Eq. (5.31d) one obtains for some realistic values of b

$$\begin{aligned} b = 1 & : F_p = -\cos(\eta_f \phi_s) (1 - (\alpha_1 \Delta_s z / \cos(\eta_f \phi_s))) \\ Q_p & = 1 / (1 - (\alpha_1 \Delta_s z / \cos(\eta_f \phi_s))) \\ H_p & = 1 + (\alpha_2 H_s / \alpha_1) \log(1 / (1 - (\alpha_1 \Delta_s z / \cos(\eta_f \phi_s)))) \quad (5.37) \end{aligned}$$

$$\begin{aligned} b = 3/5 & : F_p = -\cos(\eta_f \phi_s) (1 - (3\alpha_1 \Delta_s z / (5 \cos^{3/5}(\eta_f \phi_s))))^{5/3} \\ Q_p & = 1 / (1 - (3\alpha_1 \Delta_s z / (5 \cos^{3/5}(\eta_f \phi_s))))^{5/3} \\ H_p & = 1 + (5\alpha_2 H_s / (2\alpha_1 \cos^{2/5}(\eta_f \phi_s))) ((1 / (1 - (3\alpha_1 \Delta_s z / (5 \cos^{3/5}(\eta_f \phi_s)))))) - 1) \quad (5.38) \end{aligned}$$

$$\begin{aligned} b = 0 & : F_p = -\cos(\eta_f \phi_s) \exp(-\alpha_1 \Delta_s z) \\ Q_p & = \exp(\alpha_1 \Delta_s z) \\ H_p & = 1 + (\alpha_2 H_s / (\alpha_1 \cos(\eta_f \phi_s))) (\exp(\alpha_1 \Delta_s z) - 1) \quad (5.39) \end{aligned}$$

As discussed previously, these solutions are useful both because they indicate some of the qualitative features of the exact solutions and because they provide quick estimates of the flow variables for thin shock layers.

Chapter 6

INVESTIGATION OF ASSUMPTIONS

For the sake of simplicity, all previous calculations were carried out under conditions equivalent to the assumptions that volume fraction of the particle phase was negligible and that all the suspended particles were identical spheres. In the present chapter these restrictions are relaxed and calculations are carried out to investigate the importance of nonnegligible particle-phase volume fraction and the distribution of particle sizes within the mixture.

EFFECT OF FINITE VOLUME FRACTION

When the volume fraction $(\rho_p/\bar{\rho}_p)$ ($\bar{\rho}_p$ being the true density of particle material) of suspended particles is not negligible, it is found that the constitutive Eqs. (2.3) must be modified to allow \vec{B} and C to depend on the particle-phase volume fraction. In this section the importance of such a modification is investigated. One of the few cases for which the modified forms of \vec{B} and C have been determined is that of an idealized suspension satisfying the following conditions: (1) the volume fraction of the particle phase is finite but small, (2) the particle phase consists of identical nondeformable spheres of radius a , mass m , and thermal conductivity κ , (3) the Reynolds number and Mach number for the microscopic flow past each individual particle are infinitesimal, (4) the gas viscosity μ in the vicinity of each particle can be treated

as a constant. Under these conditions the following constitutive equations are appropriate

$$\begin{aligned} \vec{B} &= N_1 \rho_p (1 + R_1 (\rho_p / \bar{\rho}_p)^{1/3}) (\vec{u} - \vec{u}_p) \\ C &= N_2 \rho_p c (1 + R_2 (\rho_p / \bar{\rho}_p)^{1/3}) (T - T_p) \end{aligned} \quad (6.1)$$

It can be shown (see Marble [5] who carries out the derivation for the case of $R_1 = R_2 = 0$) that $N_1 = 6\pi\mu/m$ and $N_2 = 4\pi\kappa/mc$. Several authors have addressed themselves to the question of determining R_1 . Happel and Brenner [16] give the value $R_1 = 3/2$. Using a method equivalent to that employed by Happel and Brenner [16], the present authors have obtained the result $R_2 = 1$.

Because the flow in the vicinity of the forward stagnation line of a sphere or cylinder is governed by ordinary differential equations, the problem of determining this flow serves as a useful test case when investigating the importance of modification such as the one under discussion in the present section. Using Eqs. (6.1) the dimensionless Eqs. (5.12) are replaced by

$$\begin{aligned} (F_p Q_p)' - (1+j)(\Delta_s / (1+\Delta_s(1-z)))(F_p + G_p) Q_p &= 0 \\ F_p F_p' + \alpha_1 \Delta_s (1 + \beta_1 Q_p^{1/3})(F - F_p) &= 0 \\ F_p G_p' - (\Delta_s / (1+\Delta_s(1-z)))(F_p + G_p) G_p + \alpha_1 \Delta_s (1 + \beta_1 Q_p^{1/3})(G - G_p) &= 0 \\ F_p H_p' + \alpha_2 \Delta_s (1 + \beta_2 Q_p^{1/3})(H - H_p) &= 0 \end{aligned} \quad (6.2)$$

where $\beta_1 = (3/2)(\rho_{p^\infty} / \bar{\rho}_p)^{1/3}$ and $\beta_2 = (\rho_{p^\infty} / \bar{\rho}_p)^{1/3} = 2\beta_1/3$.

It can be seen that for finite volume fractions the velocity components are not independent of density as they are when volume fraction is negligible.

Equations (6.2) were solved for a variety of values of β_1 . Some typical results of these calculations are presented in Figs. 24 and 25. It can be seen that the value of β_1 has no qualitative effect on the dependence of the dependent variables on α_1 . Thus it appears that the effect on finite volume fractions could be accounted for by modifying the values of N_1 and N_2 appearing in the original constitutive Eqs. (2.3). In the idealized situation under discussion here, this approximation is unnecessary because the forms of the corrections for finite volume fractions are known [Eqs. (6.1)]. For actual suspensions the microscopic details of the suspension properties [and thus the form of the corrections to Eqs. (2.3)] are unknown. In general, therefore, there is no alternative to the procedure of modifying N_1 and N_2 to obtain the best fit to experimental data. The results of the present section indicate that this method is qualitatively correct. The computed results also indicate that the amount of modification necessary will be substantial for the larger values of β_1 . Unfortunately, the larger values of β_1 shown in Figs. 24 and 25 probably exceed the range of validity of Eqs. (6.1). The possibility of reaching a definitive conclusion about this matter is, therefore, precluded.

DISTRIBUTION OF PARTICLE SIZES

If the particle cloud of a suspension consists of a distribution of particles of different sizes, the values of N_1 and N_2 will not be the same as those appropriate to the situation in which all the particles

have identical sizes. The purpose of this section is to investigate the amount of difference that will occur. Toward this end, consider an idealized particle phase made up of N subphases. Each subphase contains enough particles to be treated as a continuum and obeys the constitutive equations

$$\vec{B}_i = N_{1i} \rho_{pi} (\vec{u} - \vec{u}_{pi}), \quad C_i = N_{2i} \rho_{pi} c (T - T_{pi}) \quad (6.3)$$

where the subscript i denotes the i th subphase and $N_{1i} = 6\pi a_i \mu / m_i$, $N_{2i} = (4\pi a_i \kappa_i) / (m_i c)$. Thus each subphase has a negligible volume fraction and obeys conditions (2), (3), and (4) of the previous section. Note that the expression for N_{1i} can also be written as $N_{1i} = 9\mu / (2\bar{\rho}_p a_i^2)$. From this it can be seen that the parameter N_{1i} (or $\alpha_{1i} = N_{1i} r_b / U_\infty$) is a function only of the particle size a_i associated with the i th subphase. It can be shown that the stagnation-line collection efficiency for such a suspension is

$$E = - \sum_{i=1}^N \rho_{pi} Q_{pi}(1) F_{pi}(1) / \sum_{i=1}^N \rho_{pi} \quad (6.4)$$

The collection efficiency associated with the i th subphase is

$$E_i = -Q_{pi}(1) F_{pi}(1) \quad (6.5)$$

Defining the mass ratio of the i th subphase to be

$$R_i = \rho_{pi} / \sum_{i=1}^N \rho_{pi} \quad (6.6)$$

and combining Eqs. (6.4), (6.5), and (6.6) yields

$$E = \sum_{i=1}^N R_i E_i \quad (6.7)$$

Several calculations of sphere collection efficiencies have been performed for the case of $N = 5$ and $M_{\infty} = 10$. Some typical results are displayed in Table I. The quantity $E(\bar{\alpha}_1)$ represents the collection efficiency associated with a particle phase consisting of identical particles for which $\alpha_1 = \bar{\alpha}_1 = (\sum_{i=1}^N \alpha_{1i})/N$. The quantity E is computed from Eq. (6.7). It can be seen that for all the entries in Table I the results based on the equivalent $\bar{\alpha}_1$ are within five percent of those based on Eq. (6.7). It is likely that the agreement would be even better for actual suspensions because the spread of the properties assumed for the calculations is unrealistically large. It thus appears that values of N_1 and N_2 based on the average properties of the particle phase are quite adequate for the types of calculations performed in the present report. (Probstein and Fassis [6] had reached this same conclusion employing a different approach involving the use of the normal distribution function to represent the distribution of particle sizes.)

Chapter 7

SHOCK LAYERS ON GENERAL BODIES

In Chapters 3, 4, 5, and 6 solutions have been presented for some simple body shapes. The simplified nature of the geometry in these problems has helped to focus attention on the various interesting physical phenomena which occur in supersonic two-phase flows. In this chapter and the next one it is desired to put the governing equations for the particle phase in forms that will be useful to engineers concerned with two-phase flows over a wide range of body shapes. In this chapter the governing equations are simplified for the case of plane or axisymmetric flow past a symmetric body at zero angle of attack. Several transformations of independent variables are made until a form of the equations is reached which is convenient for numerical solution of problems involving arbitrary symmetric body shapes. The final form of the governing equations is one of the main results of this chapter. Besides being convenient for numerical work, the equations when written in this form lend themselves readily to simplification for the case of thin shock layers. It is found to be possible to obtain analytical solutions to the simplified equations. These solutions are valid for any body shape. As a simple application of the complete equations, they are applied to the problem of flow past a wedge. The results of this analysis are used to illustrate various parametric trends and to evaluate the thin-shock-layer solution discussed previously.

In the next chapter and the next one it will be assumed that $b = 1$ in Eqs. (2.4). This is done for simplicity and does not affect any of the subsequent analysis.

SHOCK-LAYER EQUATIONS

Consider axisymmetric, steady, supersonic, two-phase flow past a symmetric body. The geometry of the system is shown in Fig. 26 which serves to define the tangential and normal coordinates x and y , the body radius $R(x)$, the tangential and normal velocity components u_p and v_p , the body transverse curvature $h(x)$, the body angle $\theta_b(x)$, the shock angle $\theta_s(x)$, and the shock wave $y_s = y_s(x)$. In terms of x and y Eqs. (2.4) have the forms

$$\begin{aligned} & ((R+y \cos \theta_b)^j \rho_p u_p)_{,x} + ((1+hy)(R+y \cos \theta_b)^j \rho_p v_p)_{,y} = 0 \\ & (u_p/(1+hy))u_{p,x} + v_p u_{p,y} + (hu_p v_p/(1+hy)) = N_1(u-u_p) \\ & (u_p/(1+hy))v_{p,x} + v_p v_{p,y} - (hu_p^2/(1+hy)) = N_1(v-v_p) \\ & (u_p/(1+hy))T_{p,x} + v_p T_{p,y} = N_2(c/c_p)(T-T_p) \end{aligned} \quad (7.1)$$

where $j = 1$. For plane flow one obtains the same equations with $j = 0$. Suppose that the free-stream velocity is U_∞ , the free-stream temperature is T_∞ , the free-stream particle density is $\rho_{p\infty}$, and it is desired to investigate collisions of particles with the body surface between $x = 0$ and $x = L$. It is convenient to define dimensionless quantities as follows:

$$\begin{aligned} \xi &= (x/L), \quad \eta = (y/L), \quad F_p = (u_p/U_\infty), \quad G_p = (v_p/U_\infty) \\ H_p &= (T_p/T_\infty), \quad F = (u/U_\infty), \quad G = (v/U_\infty), \quad H = (T/T_\infty) \\ Q_p &= (\rho_p/\rho_{p\infty}), \quad r = (R/L), \quad \kappa = hL \end{aligned} \quad (7.2)$$

Substituting Eqs.(7.2) into Eqs.(7.1) yields

$$\begin{aligned} & ((r+\eta \cos \theta_b)^j Q_p F_p)_{,\xi} + ((1+\kappa\eta)(r+\eta \cos \theta_b)^j Q_p G_p)_{,\eta} = 0 \\ & (F_p/(1+\kappa\eta))F_{p,\xi} + G_p F_{p,\eta} + (\kappa F_p G_p/(1+\kappa\eta)) = \alpha_1(F-F_p) \\ & (F_p/(1+\kappa\eta))G_{p,\xi} + G_p G_{p,\eta} - (\kappa F_p^2/(1+\kappa\eta)) = \alpha_1(G-G_p) \\ & (F_p/(1+\kappa\eta))H_{p,\xi} + G_p H_{p,\eta} = \alpha_2(H-H_p) \end{aligned} \quad (7.3)$$

where

$$\alpha_1 = (N_1 L/U_\infty), \quad \alpha_2 = (c/c_p)(N_2 L/U_\infty) \quad (7.4)$$

Equations (7.3) can be put in a more convenient form by the use of a Von Mises transformation. Toward this end, a dimensionless stream function ψ_p is defined which satisfies Eq. (7.3a). Thus

$$\begin{aligned} (1+\kappa n)(r+n \cos \theta_b)^j Q_p G_p &= \psi_p \cdot \xi \\ (r+n \cos \theta_b)^j Q_p F_p &= -\psi_p \cdot \eta \end{aligned} \quad (7.5)$$

The total differential of ψ_p is

$$d\psi_p = (1+\kappa n)(r+n \cos \theta_b)^j Q_p G_p d\xi - (r+n \cos \theta_b)^j Q_p F_p d\eta \quad (7.6)$$

Reversing the roles of ψ_p and ξ yields

$$d\xi = (d\psi_p / ((1+\kappa n)(r+n \cos \theta_b)^j Q_p G_p)) + (F_p d\eta / ((1+\kappa n)G_p)) \quad (7.7)$$

From Eq. (7.7) it is seen that

$$\begin{aligned} \xi_{,\psi_p} &= 1 / ((1+\kappa n)(r+n \cos \theta_b)^j Q_p G_p) \\ \xi_{,\eta} &= F_p / ((1+\kappa n)G_p) \end{aligned} \quad (7.8)$$

Transforming Eqs. (7.3b), (7.3c) and (7.3d) and rearranging Eqs. (7.8) produces

$$\begin{aligned} G_p F_{p,\eta} + (\kappa F_p G_p / (1+\kappa n)) &= \alpha_1 (F - F_p) \\ G_p G_{p,\eta} - (\kappa F_p^2 / (1+\kappa n)) &= \alpha_1 (G - G_p) \\ G_p H_{p,\eta} &= \alpha_2 (H - H_p) \\ G_p \xi_{,\eta} &= F_p / (1+\kappa n) \\ Q_p &= 1 / ((1+\kappa n)(r+n \cos \theta_b)^j G_p \xi_{,\psi_p}) \end{aligned} \quad (7.9)$$

It can be seen that Eqs. (7.9a-d) contain no derivatives with respect to ψ_p .

Thus, if they are integrated along a particle-phase streamline (a line of $\psi_p =$ constant) they can be treated as ordinary differential equations. Once this is done, the density Q_p can be found along the streamline from Eq. (7.9e). It should be recalled that κ , r , F , G , and H are functions of ξ which is now one of the dependent variables. The degree of nonlinearity inherent in the transformed equations is considerably greater than that exhibited by the original equations.

For convenience in numerical integration of Eqs. (7.9) two further transformations of coordinates were found to be helpful. Both are suggested by the

experience gained from the work described in previous chapters with simpler but analogous sets of equations. The first defines a new normal coordinate z by

$$z = 1 - (\eta/\eta_s) \quad (7.10)$$

This maps the interval $0 \leq \eta \leq \eta_s$ into the region $1 \geq z \geq 0$. In terms of the independent variables ψ_p and z the governing equations are found to have the form

$$\begin{aligned} D_1 G_p F_{p,z} - \kappa \eta_s D_2 F_p G_p + \alpha_1 \eta_s (F - F_p) &= 0 \\ D_1 G_p G_{p,z} + \kappa \eta_s D_2 F_p^2 + \alpha_1 \eta_s (G - G_p) &= 0 \\ D_1 G_p H_{p,z} + \alpha_2 \eta_s (H - H_p) &= 0 \\ D_1 G_p \xi_{,z} + D_2 \eta_s F_p &= 0 \\ Q_p &= D_2 / (D_1 D_3^j G_p \xi_{, \psi_p}) \end{aligned} \quad (7.11)$$

where

$$\begin{aligned} D_1 &= 1 - ((\eta_s'(1-z)F_p) / ((1+\kappa\eta_s(1-z))G_p)) \\ D_2 &= 1 / (1+\kappa\eta_s(1-z)) \\ D_3 &= r + \eta_s(1-z)\cos \theta_b \end{aligned} \quad (7.12)$$

In Eqs. (7.12) a prime denotes differentiation with respect to ξ .

The last transformation involves the replacement of the stream function ψ_p by the coordinate ξ_s at which the streamline $\psi_p = \text{constant}$ intersects the shock wave. On the shock wave

$$F_{ps} = \cos \theta_{bo}, \quad G_{ps} = -\sin \theta_{bo}, \quad Q_{ps} = 1 \quad (7.13)$$

where

$$\theta_{bo} = \theta_b(\xi_s) \quad (7.14)$$

Evaluating Eq. (7.6) on the shock yields

$$d\psi_p = -(D_{10} D_{30}^j / D_{20}) \sin \theta_{bo} d\xi_s \quad (7.15)$$

where

$$\begin{aligned}
 D_{10} &= 1 + ((\eta'_{s0} \cos \theta_{bo}) / ((1 + \kappa_o \eta_{s0}) \sin \theta_{bo})) \\
 D_{20} &= 1 / (1 + \kappa_o \eta_{s0}) \\
 D_{30} &= r_o + \eta_{s0} \cos \theta_{bo}
 \end{aligned} \tag{7.16}$$

In Eqs. (7.16)

$$\kappa_o = \kappa(\xi_s), \quad r_o = r(\xi_s), \quad \eta_{s0} = \eta_s(\xi_s), \quad \eta'_{s0} = \eta'_s(\xi_s) \tag{7.17}$$

Thus

$$\xi_{,\psi}_p = (\xi_s, \xi_s) (d\xi_s / d\psi_p) = -(D_{20} / (D_{10} D_{30}^j \sin \theta_{bo})) \xi_s, \xi_s \tag{7.18}$$

This transformation affects only Eq. (7.12e). The final set of governing equations in terms of the independent variables ξ_s and z is

$$\begin{aligned}
 D_{1p} G_p F_{p,z} - \kappa \eta_s D_{2p} F_p G_p + \alpha_1 \eta_s (F - F_p) &= 0 \\
 D_{1p} G_p G_{p,z} + \kappa \eta_s D_{2p} F_p^2 + \alpha_1 \eta_s (G - G_p) &= 0 \\
 D_{1p} G_p H_{p,z} + \alpha_2 \eta_s (H - H_p) &= 0 \\
 D_{1p} G_p \xi_{,z} + D_{2p} \eta_s F_p &= 0 \\
 Q_p = -(D_2 / D_{20}) (D_{30} / D_3)^j (D_{10} / D_1) (\sin \theta_{bo} / G_p \xi_s, \xi_s) & \tag{7.19}
 \end{aligned}$$

The appropriate initial conditions are

$$F_p(\xi_s, 0) = \cos \theta_{bo}, \quad G_p(\xi_s, 0) = -\sin \theta_{bo}, \quad H_p(\xi_s, 0) = 1, \quad \xi(\xi_s, 0) = \xi_s \tag{7.20}$$

The governing equations have now been put in a form which is convenient for any symmetric body shape. It should be pointed out that the transformations discussed in this section do not depend on the specific forms of the interphase momentum and heat transfer laws that are used.

A quantity of interest in problems of the kind under consideration in the present paper is the local collection efficiency $E(\xi_s)$. This is defined to be the rate at which particle-phase material actually strikes the surface of the body between $\xi = 0$ and $\xi = \xi_b = \xi(\xi_s, 1)$ divided by the rate that would occur if interphase momentum transfer were absent. It is easily shown that

$$E = (D_{30} / D_{3b})^{1+j} \tag{7.21}$$

where

$$D_{3b} = r_b = r(\xi_b) \quad (7.22)$$

THIN SHOCK LAYERS

As a first application of the equations derived in the last section, consideration will be given to thin shock layers, that is shock layers for which

$$\eta_s \ll 1, \quad \eta_s' \ll 1 \quad (7.23)$$

Using Eqs.(7.23), Eqs.(7.12) and (7.16) can be simplified to

$$D_1 = D_2 = D_{10} = D_{20} = 1, \quad D_3 = r, \quad D_{30} = r_0 \quad (7.24)$$

Substituting Eqs.(7.23) and (7.24) into Eqs.(7.19) yields

$$G_p F_{p,z} + \alpha_1 \eta_s (F - F_p) = 0$$

$$G_p G_{p,z} + \alpha_1 \eta_s (G - G_p) = 0$$

$$G_p H_{p,z} + \alpha_2 \eta_s (H - H_p) = 0$$

$$\xi_{,z} = 0$$

$$Q_p = (r_0/r)^J (\sin \theta_{bo}/G_p \xi_{, \xi_s}) \quad (7.25)$$

In obtaining Eqs.(7.25) the possibilities that $\alpha_1 \eta_s = O(1)$ and that $\alpha_2 \eta_s = O(1)$ have been allowed for. Equation (7.25d) can be immediately integrated subject to Eq.(7.20d) to yield

$$\xi(\xi_s, z) = \xi_s \quad (7.26)$$

This shows that

$$\begin{aligned} r(\xi) &= r(\xi_s) = r_0, & F(\xi, z) &= F(\xi_s, z) = F_s \\ G(\xi, z) &= G(\xi_s, z) = G_s, & H(\xi, z) &= H(\xi_s, z) = H_s \end{aligned} \quad (7.27)$$

For thin shock layers it will be assumed that the gas variables are independent of z . That is

$$F_s = F_{s0} = F(\xi_s, 0), \quad G_s = G_{s0} = G(\xi_s, 0), \quad H_s = H_{s0} = H(\xi_s, 0) \quad (7.28)$$

If the air is treated as a perfect gas the ratio of the gas density in the free stream to the gas density just behind the shock is

$$\epsilon = ((\gamma-1)M_\infty^2 \sin^2 \theta_s + 2)/((\gamma+1)M_\infty^2 \sin^2 \theta_s) \quad (7.29)$$

where γ is the ratio of specific heats for a perfect gas and M_∞ is the free-stream Mach number. In terms of these quantities it can be shown that

$$\begin{aligned} F_{so} &= \cos \theta_{so} \cos \theta_{Lo} + \epsilon \sin \theta_{so} \sin \theta_{Lo} \\ G_{so} &= \cos \theta_{so} \sin \theta_{Lo} - \epsilon \sin \theta_{so} \cos \theta_{Lo} \\ H_{so} &= \epsilon(1 + (1-\epsilon)\gamma M_\infty^2 \sin^2 \theta_s) \end{aligned} \quad (7.30)$$

where $\theta_{Lo} = \theta_{so} - \theta_{bo}$

For a thin shock layer $\theta_{Lo} \ll 1$ and

$$F_{so} = \cos \theta_{bo}, \quad G_{so} = -\epsilon \sin \theta_{bo} \quad (7.31)$$

Substituting Eq.(7.31a) into Eq.(7.25a) and solving subject to Eq.(7.20a) yields

$$F_p = F_{so} = \cos \theta_{bo} \quad (7.32)$$

Following Probstein and Fassiio [6] assume that $|G_p| \gg |G|$ and $H_p \ll H$ for a thin shock layer.

Simplifying Eqs.(7.25b) and(7.25c) accordingly and using Eq.(7.26) results in

$$\begin{aligned} G_p z + \alpha_1 \eta_{so} &= 0 \\ G_p H_p z + \alpha_2 \eta_{so} H_{so} &= 0 \end{aligned} \quad (7.33)$$

Solving these equations and using the initial conditions(7.20b) and(7.20c) one obtains

$$\begin{aligned} G_p &= -\sin \theta_{bo} (1 - (\alpha_1 \eta_{so} z / \sin \theta_{bo})) \\ H_p &= 1 + (\alpha_2 H_{so} / \alpha_1) \log(1 / (1 - (\alpha_1 \eta_{so} z / \sin \theta_{bo}))) \end{aligned} \quad (7.34)$$

Substituting Eqs.(7.26),(7.27c), and(7.34c) into Eq.(7.25) yields

$$Q_p = 1 / (1 - (\alpha_1 \eta_{so} z / \sin \theta_{bo})) \quad (7.35)$$

Substituting Eqs.(7.24) and(7.26) into Eq.(7.21) shows that to the order of approximation of the present solution

$$E = 1 \quad (7.36)$$

These simple closed-form solutions are applicable to symmetric bodies of any shape and should be useful both for obtaining quick estimates of the

properties of two-phase shock-layer flows and for demonstration of various parametric trends. In using these solutions it should be noted that only positive values of $(1 - (\alpha_1 \eta_{s0} z / \sin \theta_{b0}))$ are meaningful. When this quantity vanishes the assumption $|G_p| \gg |G|$ is already violated.

FLOW PAST A SYMMETRIC WEDGE

As an example of the application of the complete Eqs.(7.19) the flow past a symmetric wedge is considered. The geometry of this problem is shown in Fig. 27. The wedge is an important aerodynamic shape and it is the only body for which an exact closed-form solution to even the inviscid equations of motion for the gas phase is known. For the latter reason this problem makes a useful test case for calculations of the type under discussion in the present paper. It is, therefore, of both theoretical and practical interest.

From Fig.27 it can be seen that

$$\kappa = 0, \quad \eta_s = \xi \tan \theta_L, \quad \eta'_s = \tan \theta_L, \quad r = \xi \sin \theta_b \quad (7.37)$$

where θ_b and $\theta_L = \theta_s - \theta_b$ are now constants. Substituting Eqs. (7.12), (7.16), (7.17), and (7.37) into Eq.(7.19) yields

$$\begin{aligned} ((1-z)F_p \tan \theta_L - G_p)F_{p,z} - \alpha_1 \xi (F - F_p) \tan \theta_L &= 0 \\ ((1-z)F_p \tan \theta_L - G_p)G_{p,z} - \alpha_1 \xi (G - G_p) \tan \theta_L &= 0 \\ ((1-z)F_p \tan \theta_L - G_p)H_{p,z} - \alpha_2 \xi (H - H_p) \tan \theta_L &= 0 \\ ((1-z)F_p \tan \theta_L - G_p)\xi_{,z} - \xi F_p \tan \theta_L &= 0 \\ Q_p = 1/((\sin \theta_b + \tan \theta_L \cos \theta_b) ((1-z)F_p \tan \theta_L - G_p)\xi_{,z}) & \quad (7.38) \end{aligned}$$

If it is assumed that the velocity components and temperature of the air can be represented to a sufficient degree of accuracy by the solution for flow of an inviscid perfect gas (with $\gamma = 1.4$) one has

$$Q_p = (\cos^2 \theta_b + \sin^2 \theta_b)^{1/2}, \quad G = 0, \quad H = H_s \quad (7.39)$$

where ϵ and H_s are given by Eqs.(7.29) and(7.30c)respectively and θ_s is now regarded as a constant. The shock angle θ_s can be found as a function of the body angle θ_b by making use of tables or charts such as those given by Liepman and Roshko [15]. To complete the formulation of this problem it is noted that the local collection efficiency is

$$E = (\xi_s / \xi_b) \tag{7.40}$$

Equations(7.38) were solved numerically subject to Eqs.(7.20). Eqs.(7.30a-d)were integrated numerically along various streamlines (lines of $\xi_s = \text{constant}$) starting at $\xi_s = 0$. On a given streamline the numerical integration was carried out using a fourth order Runge-Kutta method starting at $z = 0$ and proceeding to $z = 1$. After Eqs.(7.30a-d) were solved along the streamline, Eq.(7.38e) was solved for Q_p . The partial derivative with respect to ξ_s was replaced by a two-point backward difference formula to convert Eq.(7.38e) to an algebraic equation. Some typical results of these numerical calculations are presented graphically in Figs. 28-35.

Figure 28 shows results for the quantities of the most importance in estimating the cratering and erosion damage likely to be experienced by a flight vehicle; namely, the particle-phase normal velocity at the body surface $G_{pb} = G_p(\xi_s, 1)$ and the particle-phase density at the vehicle surface $Q_{pb} = Q_p(\xi_s, 1)$. These quantities are plotted versus the distance from the leading edge of the wedge ξ_b . Figure 28 pertains to a free-stream Mach number of ten and a wedge half-angle of five degrees. It can be seen that the impact velocity decreases and the density increases as the distance from the leading edge increases. When α_1 (the measure of the effectiveness of interphase momentum transfer) is small, both G_{pb} and Q_{pb} are nearly constant. As α_1 increases, the variations of G_{pb} and Q_{pb} become

increasingly pronounced. The variation of the normal velocity illustrates the transition from a state of frozen flow (the particle-phase motion is independent of that of the gas phase) at $\xi = 0$ toward a state of equilibrium flow (the two phases have identical motions) which is nearly achieved at $\xi_b = 1$ for the larger values of α_1 . This behavior is due to interphase momentum transfer which tends to bring the normal particle-phase velocity into equilibrium with the normal gas-phase velocity which is zero in this case. For a given ξ_b interphase momentum transfer is enhanced by increasing α_1 and for a given α_1 interphase momentum transfer is enhanced by increasing ξ_b (which increases the length of the streamline that a particle must traverse to reach the wall). It appears that for a wedge or cone complete equilibrium flow is never reached even if the body is infinitely long. This is in contrast to the two-phase flow past a sphere or cylinder where complete equilibrium flow is possible near the body surface for certain combinations of parameters (refer to Chapter 5.) It can be seen that the decrease in particle-phase normal velocity is accompanied by a compression of the particle phase which increases in severity as either α_1 or ξ_b is increased. This is significant because it shows that the particle-phase mass fraction may be negligible in the free stream but non-negligible near the surface of the body. In such a situation the theory employed in the present paper would be inadequate and it would be necessary to solve the coupled equations governing the air and particle motions simultaneously. Thus, computation of the particle-phase density (which has not been carried out by most previous investigators) not only provides information about the distribution of impacts on a vehicle surface, but also provides an important check on the self-consistency of the theory.

Figures 29 and 30 present data for a free-stream Mach number of ten and a wedge angle of fifteen degrees. Increasing the wedge angle increases the thickness of the shock layer (and thus the effectiveness of interphase momentum transfer for a fixed α_1) and also increases the normal velocity of the particle phase at the shock. A comparison of the results for G_{pb} in Figs. 28 and 29 reveals that the latter effect is predominant as far as G_{pb} is concerned. That is, for a given α_1 the surface velocities increase with increasing θ_b . For a fixed α_1 the surface densities are also an increasing function of θ_b which shows that the behavior of Q_{pb} is primarily dependent on the effectiveness of interphase momentum transfer. Figure 30 shows numerical results for the particle-phase temperature at the surface of the wedge $H_{pb} = H_p(\xi_b, 1)$ and the local collection efficiency E . It can be seen that the surface temperature is increased by increasing α_1 (because increasing the effectiveness of interphase momentum transfer lengthens the time required by each particle to traverse the shock layer and thus provides more time for heat to be transferred from the warmer gas phase to the cooler particle phase). The collection efficiency decreases along the body surface and with increasing α_1 . It can be seen that for a given α_1 E approaches its equilibrium limit (zero) much more slowly than does G_{pb} . This is, of course, due to the corresponding increase in Q_{pb} .

In Fig. 31 results are presented for a free-stream Mach number of ten and a thirty-degree wedge angle. Here both the numerical solution (solid lines) and the analytical thin-shock-layer solution (dashed lines) are plotted. Comparison of the solid lines with the data previously discussed tends to confirm the statements made earlier concerning the influence of θ_b on the values of G_{pb} and Q_{pb} . For air ($\gamma = 1.4$) no shock layers on

wedges are particularly thin. In this case the value of θ_L is eight degrees so $(\theta_L/\theta_b) = 0.267$. The value of the shock wave density ratio is $\epsilon = 0.189$. Thus none of the assumptions $\eta_g \ll 1$, $\eta_g' \ll 1$, or $(G_p/G) \gg 1$ is very well satisfied and this constitutes an extreme test for the thin-shock-layer solution. Substituting Eqs. (7.37) into Eqs. (7.34) and (7.35) and replacing $\tan \theta_L$ by θ_L yields

$$\begin{aligned} G_p &= -\sin \theta_b (1 - (\alpha_1 \theta_L xz / \sin \theta_b)) \\ H_p &= 1 + (\alpha_2 H_{so} A_1) \log(1 / (1 - (\alpha_1 \theta_L xz / \sin \theta_b))) \\ Q_p &= 1 / (1 - (\alpha_1 \theta_L xz / \sin \theta_b)) \end{aligned} \quad (7.41)$$

Equations (7.41a) and (7.41c) were evaluated numerically to obtain the dashed lines shown in Fig. 31. It can be seen that for $\alpha_1 \leq 1$ the approximate and exact solutions are in good agreement. For larger values of α_1 the approximate solutions still predict the correct qualitative trends but deviate increasingly from the exact values as α_1 increases. Considering the fact that the test case exhibits rather poor satisfaction of the assumptions underlying the thin-shock-layer solution, the agreement between the exact and approximate solutions seems acceptable. A similar conclusion was reached in Chapter 5 in which was previously obtained the special case of Eqs. (7.34) and (7.35) corresponding to flow past a circular cylinder or a sphere. It will be interesting to compare the predictions of Eqs. (7.34) and (7.35) with exact results for two-phase flow in thin shock layers when such results become available.

Figure 32 illustrates the effect of the freestream Mach number on the behavior of G_{pb} and Q_{pb} . It can be seen that for a given θ_b and α_1 the particle-phase normal impact velocity is an increasing function of M_∞ and the particle-phase density is a decreasing function of M_∞ . This is because

the shock layer thickness (and thus the effectiveness of interphase momentum transfer) decreases as M_∞ increases.

As expected, the numerical results presented here are qualitatively similar to those for supersonic two-phase flow past a right circular cone obtained in Chapter 4. Comparison of the results for G_{pb} given in Fig. 29 with the corresponding results reported in Fig. 6 shows that the normal impact velocity is smaller for wedge flow than for cone flow. This is because the shock layer is thicker for the plane flow than for the axisymmetric flow and because the normal velocity of the fluid phase vanishes for wedge flow but does not for the cone flow. The difference discussed above can be significant. At $\xi_b = 1$ $|G_{pb}|$ is about 9 percent lower for plane than for axisymmetric flow for $\alpha_1 = 1$, about 55 percent lower for $\alpha_1 = 5$, and about 90 percent lower for $\alpha_1 = 10$. This behavior suggests that for a given profile an airfoil (over which the flow is approximately two-dimensional except near the edges) will experience less cratering and erosion damage per unit of surface area than will a corresponding axisymmetric body, provided that the magnitude of the normal impact velocity is the main determining factor of such damage.

Chapter 8

SHOCK LAYERS ON BODIES WITH ATTACHED SHOCKS

The equations given in Chapter 7 can be used to analyze two-phase flow past any symmetric body. It is often difficult, however, to write the equation of the shock surface so that its normal coordinate is given explicitly as a function of its tangential coordinate. It is more likely that the radial shock coordinate will be known explicitly as a function of the axial distance from the nose of the body. Rather than convert this information to normal and tangential coordinates, it seems wise to take advantage of this situation when possible. This can be done for bodies with attached shocks and is the subject of the present chapter.

GOVERNING EQUATIONS

Figure 33 depicts the geometry of the problem and serves to define the axial coordinate x , the radial coordinate r , the gas velocity components u and v , the particle-phase velocity components u_p and v_p , the body surface $r_b(x)$, the shock surface $r_s(x)$, the body angle $\theta_b(x)$, the shock angle $\theta_s(x)$, the length of the region in which impacts are to be investigated L , and the free-stream velocity U_∞ , temperature T_∞ , and particle-phase density $\rho_{p\infty}$. In this coordinate system Eqs. (2.4) for steady axisymmetric flow can be written as

$$(r^j \rho_p u_p)_{,x} + (r^j \rho_p v_p)_{,r} = 0$$

$$\rho_p (u_p u_p)_{,x} + v_p u_p)_{,r} = \rho_p N_1 (u - u_p), \quad \rho_p (u_p v_p)_{,x} + v_p v_p)_{,r} = \rho_p N_1 (v - v_p)$$

$$\rho_p c_p (u_p T_p'x + v_p T_p'r) = \rho_p c N_2 (T - T_p) \quad (8.1)$$

For plane flow the same equations result with $j = 0$.

It is convenient to define the following dimensionless variables.

$$\xi = (x/L), \quad \eta = (r/L), \quad F = (u/U_\infty), \quad F_p = (u_p/U_\infty) \\
G = (v/U_\infty), \quad G_p = (v_p/U_\infty), \quad H = (T/T_\infty), \quad H_p = (T_p/T_\infty) \quad (8.2)$$

Substituting Eqs (8.2) into Eqs. (8.1) yields

$$(\eta^j Q_p F_p)_{,\xi} + (\eta^j Q_p G_p)_{,\eta} = 0 \\
F_p F_p'_{,\xi} + G_p F_p'_{,\eta} = \alpha_1 (F - F_p), \quad F_p G_p'_{,\xi} + G_p F_p'_{,\eta} = \alpha_1 (G - G_p) \\
F_p H_p'_{,\xi} + G_p H_p'_{,\eta} = \alpha_2 (H - H_p) \quad (8.3)$$

where $\alpha_1 = (N_1 L / U_\infty)$ and $\alpha_2 = (c/c_p)(N_2 L / U_\infty)$. The appropriate boundary conditions are

$$F_{ps} = Q_{ps} = H_{ps} = 1, \quad G_{ps} = 0 \quad (8.4)$$

Here, and in what follows, a subscript s will denote the value of a variable on the shock surface while a subscript b will denote its value on the body surface.

Equations (8.3) can be put in a more convenient form by the use of a Von Mises transformation. Toward this end a dimensionless stream function ψ_p satisfying Eq. (8.3a) is defined such that

$$\eta^j Q_p F_p = -\psi_p'_{,\eta}, \quad \eta^j Q_p G_p = \psi_p'_{,\xi} \quad (8.5)$$

Finding the total differential of ψ_p and reversing the roles of ξ and ψ_p (that is, regarding ξ as a dependent variable and ψ_p as an independent variable) results in

$$d\xi = (d\psi_p / (\eta^j Q_p G_p)) + (F_p d\eta / G_p) \quad (8.6)$$

from which it follows that

$$\xi_{,\psi_p} = 1 / (\eta^j Q_p G_p), \quad \xi_{,\eta} = (F_p / G_p) \quad (8.7)$$

Transforming Eqs. (8.3b,c,d) and rearranging Eqs. (8.7) produces

$$\begin{aligned} G_p F_p', \eta &= \alpha_1 (F - F_p), & G_p G_p', \eta &= \alpha_1 (G - G_p), & G_p \xi', \eta &= F_p \\ G_p H_p', \eta &= \alpha_2 (H - H_p), & Q_p &= 1/(\eta^j G_p \xi', \psi_p) \end{aligned} \quad (8.8)$$

Since no derivatives with respect to ψ_p appear in Eqs. (8.8a, b, c, d), they can be treated as ordinary differential equations along the dispersed-phase streamlines (lines of constant ψ_p).

In order to make the radial distance from the body surface to the shock surface constant, it is convenient to define a new independent variable

$$z = (\eta_s - \eta)/(\eta_s - \eta_b) \quad (8.9)$$

which maps the region $\eta_b \leq \eta \leq \eta_s$ into the region $1 \geq z \geq 0$. It is also useful to replace ψ_p by the coordinate ξ_s at which the particle-phase streamline associated with ψ_p intersects the shock surface. Evaluating Eq. (8.6) on the shock with the aid of Eqs. (8.4) yields

$$d\psi_p = -\eta_{so}^j d\eta_{so} = -\eta_{so}^j (d\eta_{so}/d\xi_s) d\xi_s = -\eta_{so}^j \tan(\theta_{so}) d\xi_s \quad (8.10)$$

where $\eta_{so} = \eta_s(\xi_s)$ and $\theta_{so} = \theta_s(\xi_s)$. Transforming Eqs. (8.8) to the final independent variables ξ_s and z , using Eqs. (8.9) and (8.10), one obtains

$$\begin{aligned} F_p', z + (\alpha_1 D_1/D_2)(F - F_p) &= 0, & G_p', z + (\alpha_1 D_1/D_2)(G - G_p) &= 0 \\ \xi_s', z + (D_1 F_p/D_2) &= 0, & H_p', z + (\alpha_2 D_1/D_2)(H - H_p) &= 0 \\ Q_p &= ((D_{20}/D_2)(D_{30}/D_3)^j / \xi_s, \xi_s) \end{aligned} \quad (8.11)$$

where

$$\begin{aligned} D_1 &= \eta_s - \eta_b, & D_2 &= G_p - F_p((1-z)\tan(\theta_s) + z \tan(\theta_b)), & D_{20} &= -\tan(\theta_{so}) \\ D_3 &= (1-z)\eta_s + z\eta_b, & D_{30} &= \eta_{so} \end{aligned} \quad (8.12)$$

Equations (8.11) must be solved subject to the boundary conditions

$$F_p(\xi_s, 0) = H_p(\xi_s, 0) = -1, \quad G_p(\xi_s, 0) = 0, \quad x_p(\xi_s, 0) = \xi_s \quad (8.13)$$

Equations (8.11) combine the main advantage of the Lagrangian description used by Probstein and Fassio [6] Waldman and Reinecke [7] and Spurk and Gerber [8] (i.e., that the flow variables can be determined from the solutions of ordinary differential equations) with the main advantage of the Eulerian description (i.e., that the shock surface and the body surface correspond to known values of the independent variable). In addition, the distance from the shock to the body is constant when the variable z is used, and Eq. (8.11e) which determines the density, is algebraic. For these reasons it is believed that Eqs. (8.11) are convenient for numerical work, and it is hoped that they will prove useful to future investigators concerned with problems of this type.

NUMERICAL SOLUTIONS

Equations (8.11a,b,c) can be solved simultaneously subject to Eqs. (8.13a,c,d) by any numerical method for initial value problems. In the present work a fourth-order Runge-Kutta routine was used. The same method was used to solve Eq. (8.11d) subject to Eq. (8.13b). Equation (8.11e) was solved by approximating the partial derivative appearing therein by a two-point backward difference quotient. The general axisymmetric body shape considered was

$$\eta_b = BR(\xi); \quad R(0) = 0, \quad R(1) = 1 \quad (8.14)$$

An approximate description of the gas flow field was obtained by employing expressions for F , G , and H similar to those suggested by Waldman and Reinecke [7] and by assuming that the shock surface could be represented by the equation $\eta_s = SR(\xi)$ where R is the same function appearing in Eq. (8.14) and the quantity (S/B) is the same as that for a cone with

base-radius-to-length ratio B. (A more accurate description of the gas flow field could be used without affecting the solution procedure in any way, but this would necessitate numerical analysis of the gas-phase governing equations which the authors did not want to undertake in connection with the present work.) Numerical solutions were obtained for the specific body shapes

$$R = \xi^\beta, \quad (\text{power law}) \quad (8.15)$$

$$R = (2\xi - C\xi^2)/(2-C), \quad (\text{parabolic series}) \quad (8.16)$$

$$R = ((\cos^{-1}(1-2\xi))/\pi)^{\frac{1}{2}}, \quad (\text{Von Karman}) \quad (8.17)$$

$$R = (((1+B^2)^2 - (2B(1-\xi))^2)^{\frac{1}{2}} - (1-B^2))/(2B^2), \quad (\text{ogive}) \quad (8.18)$$

where β and C are constants.

Numerical results are presented in Figure 34 for the local collection efficiency (the rate at which particulate mass is actually collected by the body surface divided by the rate that would exist in the absence of interphase momentum transfer)

$$E(\xi_b) = \left(\int_0^{\xi_b} Q_{pb} (F_{pb} \tan(\theta_b) - G_{pb}) n_b^j d\xi_b \right) / \left(\int_0^{\xi_b} \tan(\theta_b) n_b^j d\xi_b \right) \quad (8.19)$$

for bodies with a base-diameter-to-length ratio of one third. For all calculations presented, the perfect-gas specific heat ratio $\gamma = 1.4$, the free-stream Mach number $M_\infty = 10$, and the momentum transfer coefficient $\alpha_1 = 1$. It can be seen that E is a decreasing function of ξ_b with the detailed shapes of the curves depending on the particular body to which the results correspond.

Chapter 9

CONCLUSION

In the present report a continuum theory of two-phase supersonic flow of a gas containing small particles has been formulated for the case of negligible particle-phase mass fraction. First, the governing equations for the particle phase were solved for flow past a right circular cone (or a plane wedge) at zero angle of attack. Approximate analytical solutions (valid only for thin shock layers) and exact numerical solutions of these equations were obtained. Secondly, the application of this procedure was applied again to the case of two-phase supersonic flow past a sphere (or a circular cylinder). Numerical solutions for this type of flow were found starting at the forward stagnation line of the air motion and marching downstream. Some calculations for the problem of flow past a wedge or circular cylinder were also carried out simply to show the comparisons of flow properties between plane and axisymmetric two-phase flows. Results having relevance to the estimation of cratering and erosion damage suffered by high-speed vehicles flying in the atmosphere and to the experimental determination of constants involved in the theory were presented graphically and discussed for these two different flow configurations respectively. The importance of nonnegligible particle-phase volume fractions and distributions of particle sizes within the particle phase were also discussed. Finally, two forms of the governing equations which facilitate the numerical solution of problems involving gas-particle flow past bodies having general symmetric shapes are discussed.

REFERENCES

1. Sims, J. L., "Tables for Supersonic Flow around Right Circular Cones at Zero Angle of Attack," NASA SP-3004, National Aeronautics and Space Administration, Washington, D. C., 1964.
2. Hayes, W. D., and Probst, R. F., Hypersonic Flow Theory, Vol. 1, Inviscid Flows, Academic Press, New York and London, 1966, pp. 217-263.
3. Wallis, G. G., One Dimensional Two-Phase Flow, McGraw-Hill, 1969.
4. Soo, S. L., Fluid Dynamics of Multiphase Systems, Blaisdell Publishing Co., 1967.
5. Marble, F. E., "Dynamics of Dusty Gases," Annual Review of Fluid Mechanics, 2, 1970, p. 397.
6. Probst, R. F., and Fassio, F., "Dusty Hypersonic Flow," AIAA Journal, 8, 1970, p. 772.
7. Waldman, G. D., and Reinecke, W. G., "Particle Trajectories, Heating and Breakup in Hypersonic Shock Layers," AIAA Journal, 9, 1971, p. 1040.
8. Spurk, J. H., and Gerber, N., "Dust Collection Efficiency for Power Law Bodies in Hypersonic Flight," AIAA Journal, 10, 1972, p. 755.
9. Peddieson, J., "Dust Collection at Moderate Void Fractions," Proceedings of Annual Technical Meetings of the Institute of Environmental Sciences, 19, 1973, p. 488.
10. Lu, H. Y., and Chiu, H. H., "Dynamics of Gases Containing Evaporable Liquid Droplets under Normal Shock," AIAA Journal, 4, 1966, p. 1008.
11. Panton, R., "Flow Properties for the Continuum Viewpoint of a Non-Equilibrium Gas-Particle Mixture," Journal of Fluid Mechanics, 31, 1968, p. 273.
12. Panton, R., and Oppenheim, A. K., "Shock Relaxation in a Particle-Gas Mixture with Mass Transfer Between Phases," AIAA Journal, 6, 1968, p. 2071.
13. Wheelahan, E. J., "State-of-the-Art Survey of Raindrop Erosion," AMC RS-TR-67-13, U. S. Army Missile Command, Redstone Arsenal, Huntsville, Alabama, 1967.

14. Waldman, G. D., Reinecke, W. G., and Glenn, D. C., "Raindrop Breakup in the Shock Layer of a High-Speed Vehicle," AIAA Journal, 10, 1972, p. 1200.
15. Liepmann, H. W., and Roshko, A., Elements of Gas Dynamics, John Wiley and Sons, New York, London, Sidney, 1957, p. 84-88, 120-123.
16. Happel, J., and Brenner, H., Low Reynolds Number Hydrodynamics, Prentice-Hall, 1965.

TABLE I.
 STAGNATION-POINT COLLECTION
 EFFICIENCIES FOR DISTRIBUTION OF PARTICLE SIZES

R_1	R_2	R_3	R_4	R_5	E	$E(\bar{\alpha}_1)$
$\alpha_1=0.5, \alpha_2=0.8, \alpha_3=1, \alpha_4=1.2, \alpha_5=1.5$						
.2	.2	.2	.2	.2	0.990	0.990
.1	.2	.4	.2	.1	0.990	0.990
.05	.15	.6	.15	.05	0.990	0.990
0	.1	.8	.1	0	0.990	0.990
.1	.2	.2	.4	.1	0.989	0.990
.1	.4	.2	.2	.1	0.990	0.990
.05	.15	.15	.6	.05	0.988	0.990
.05	.6	.15	.15	.05	0.991	0.990
$\alpha_1=2.5, \alpha_2=4.0, \alpha_3=5.0, \alpha_4=6.0, \alpha_5=7.5$						
.2	.2	.2	.2	.2	0.924	0.931
.1	.2	.4	.2	.1	0.927	0.931
.05	.15	.6	.15	.05	0.929	0.931
0	.1	.8	.1	0	0.931	0.931
.1	.2	.2	.4	.1	0.923	0.931
.1	.4	.2	.2	.1	0.931	0.931
.05	.15	.15	.6	.05	0.915	0.931
.05	.6	.15	.15	.05	0.937	0.931
$\alpha_1=1, \alpha_2=3, \alpha_3=5, \alpha_4=7, \alpha_5=9$						
.2	.2	.2	.2	.2	0.909	0.931
.1	.2	.4	.2	.1	0.913	0.931
.05	.15	.6	.15	.05	0.924	0.931
0	.1	.8	.1	0	0.929	0.931
.1	.2	.2	.4	.1	0.908	0.931
.1	.4	.2	.2	.1	0.925	0.931
.05	.15	.15	.6	.05	0.900	0.931
.05	.6	.15	.15	.05	0.939	0.931

TABLE 1. (Continued)

R_1	R_2	R_3	R_4	R_5	E	$E(\bar{\alpha}_1)$
$\alpha_1=8.5, \alpha_2=8.8, \alpha_3=9.0, \alpha_4=9.2, \alpha_5=9.5$						
.2	.2	.2	.2	.2	0.774	0.778
.1	.2	.4	.2	.1	0.776	0.778
.05	.15	.6	.15	.05	0.777	0.778
0	.1	.8	.1	0	0.778	0.778
.1	.2	.2	.4	.1	0.772	0.778
.1	.4	.2	.2	.1	0.779	0.778
.05	.15	.15	.6	.05	0.769	0.778
.05	.6	.15	.15	.05	0.784	0.778
$\alpha_1=8, \alpha_2=8.5, \alpha_3=9, \alpha_4=9.5, \alpha_5=10$						
.2	.2	.2	.2	.2	0.761	0.778
.1	.2	.4	.2	.1	0.768	0.778
.05	.15	.6	.15	.05	0.772	0.778
0	.1	.8	.1	0	0.777	0.778
.1	.2	.2	.4	.1	0.758	0.778
.1	.4	.2	.2	.1	0.775	0.778
.05	.15	.15	.6	.05	0.750	0.778
.05	.6	.15	.15	.05	0.787	0.778

LIST OF FIGURES

Figure	Page
1. A Differential Volume Element	E78
2. Shock Layer on Wedge or Cone	E78
3. Particle-Phase Normal Velocity and Density at Wedge Surface	E79
4. Particle-Phase Normal Velocity and Density at Cone Surface	E80
5. Particle-Phase Normal Velocity and Density at Cone Surface	E81
6. Particle-Phase Normal Velocity and Density at Cone Surface	E82
7. Local Collection Efficiency and Particle-Phase Temperature at Cone Surface	E83
8. Particle-Phase Normal Velocity and Density at Cone Surface	E84
9. Particle-Phase Normal Velocity and Density at Cone Surface	E85
10. Particle-Phase Normal Velocity and Density at Cone Surface	E86
11. Shock Layer on Sphere or Circular Cylinder	E87
12. Comparison of Exact and Approximate Stagnation- Line Solutions	E88
13. Comparison of Exact and Approximate Stagnation- Line Solutions	E89
14. Stagnation-Point Values of Particle-Phase Normal Velocity and Density	E90
15. Stagnation-Point Values of Particle-Phase Collection Efficiency and Temperature	E91
16. Stagnation-Point Values of Particle-Phase Normal Velocity and Density	E92

Figure

Page

17. Stagnation-Point Values of Particle-Phase Collection Efficiency and Temperature	E93
18. Particle-Phase Normal Velocity and Density at Sphere Surface	E94
19. Particle-Phase Collection Efficiency and Temperature at Sphere Surface	E95
20. Particle-Phase Normal Velocity and Density at Sphere Surface	E96
21. Particle-Phase Collection Efficiency and Temperature at Sphere Surface	E97
22. Particle-Phase Normal Velocity and Density at Sphere Surface	E98
23. Particle-Phase Temperature at Sphere Surface	E99
24. Stagnation-Point Values of Particle-Phase Normal Velocity and Density for Finite Volume Fractions	E100
25. Stagnation-Point Values of Particle-Phase Collection Efficiency and Temperature for Finite Volume Fractions	E101
26. Geometry and Coordinate System for General Symmetric Body	E102
27. Geometry and Coordinate System for Symmetric Wedge	E102
28. Particle-Phase Normal Velocity and Density at Wedge Surface	E103
29. Particle-Phase Normal Velocity and Density at Wedge Surface	E104
30. Particle-Phase Temperature at Wall and Local Collection Efficiency	E105
31. Particle-Phase Normal Velocity and Density at Wedge Surface	E106
32. Particle-Phase Normal Velocity and Density at Wedge Surface	E107
33. Geometry and Coordinate System	E108
34. Collection Efficiencies for Various Body Shapes	E109

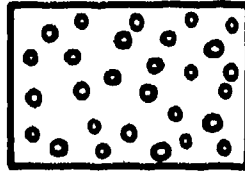


Figure 1. A Differential Volume Element

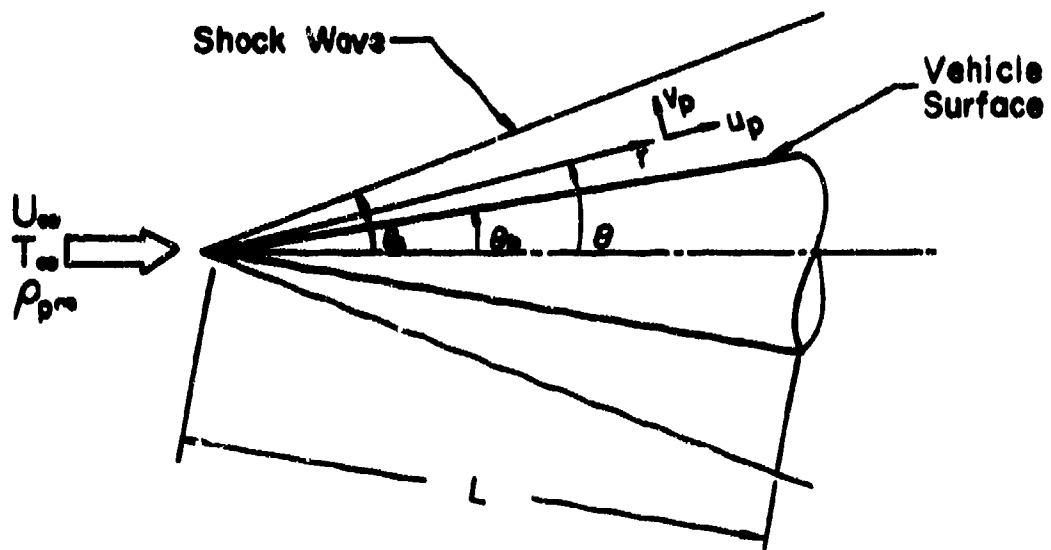


Figure 2. Shock Layer on Wedge or Cone

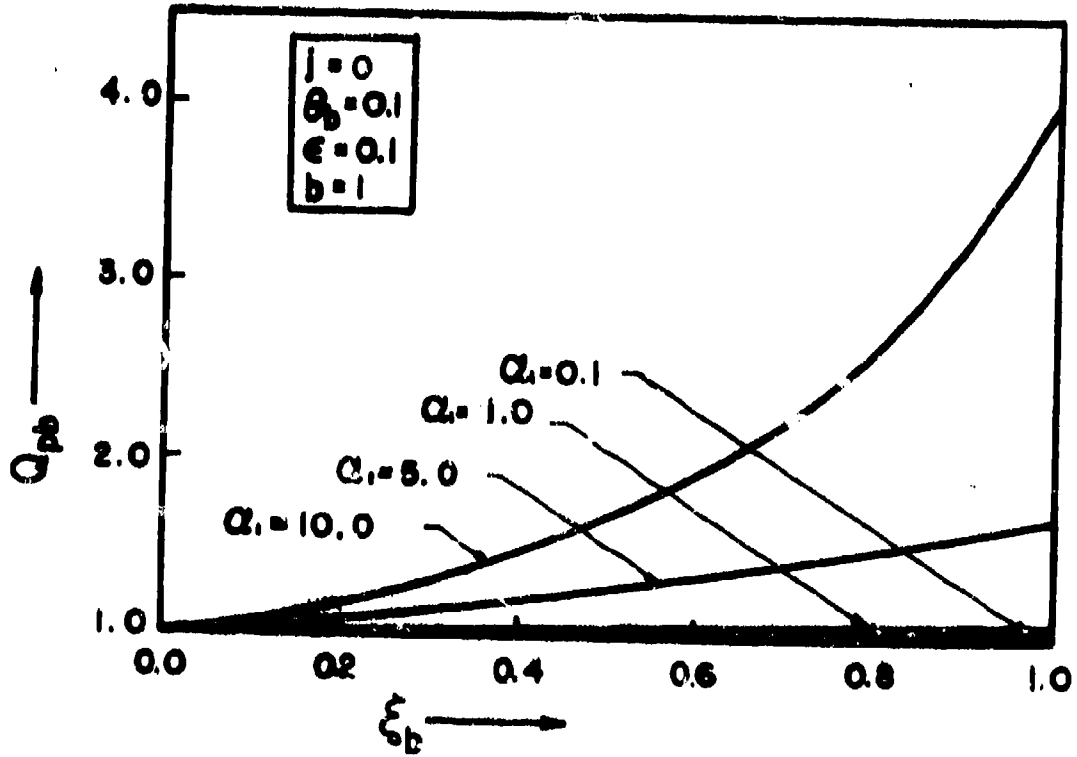
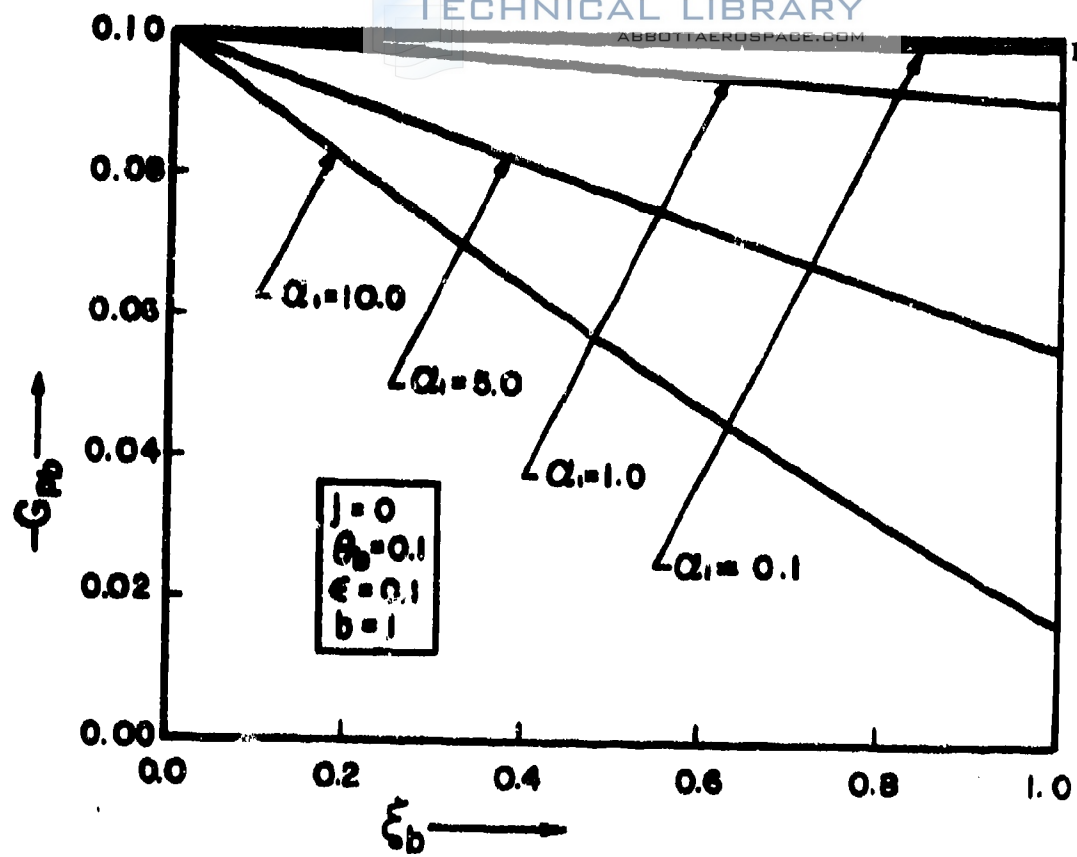


Figure 3. Particle-Phase Normal Velocity and Density at Wedge Surface

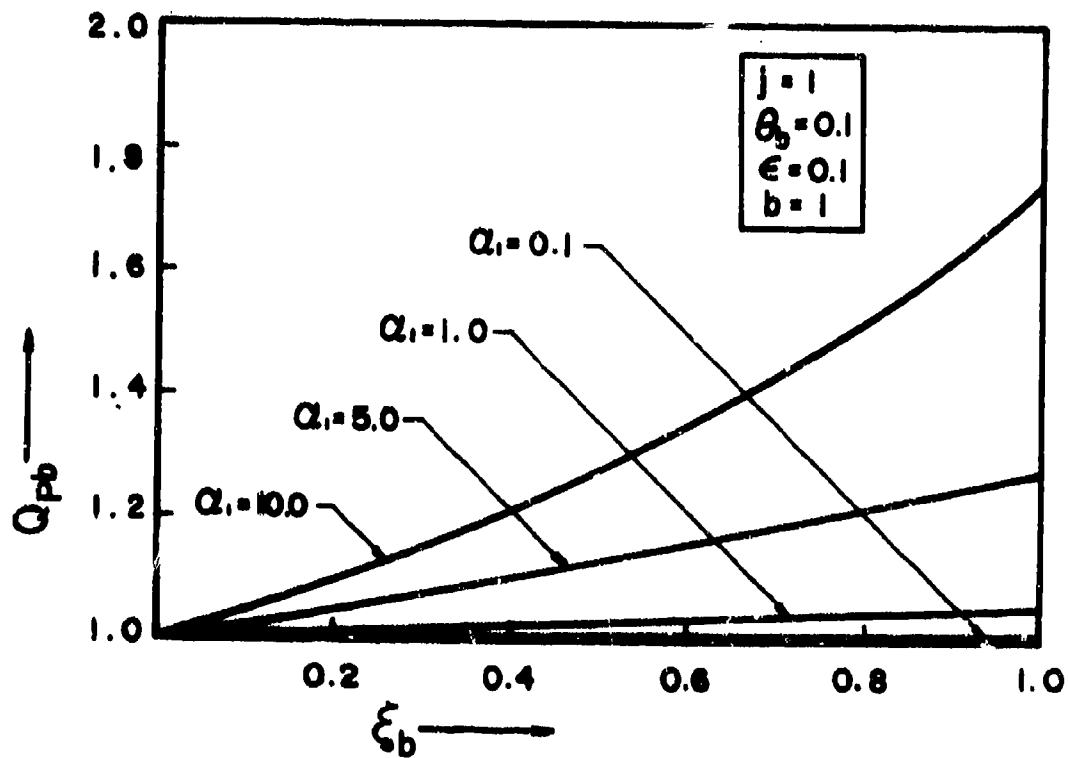
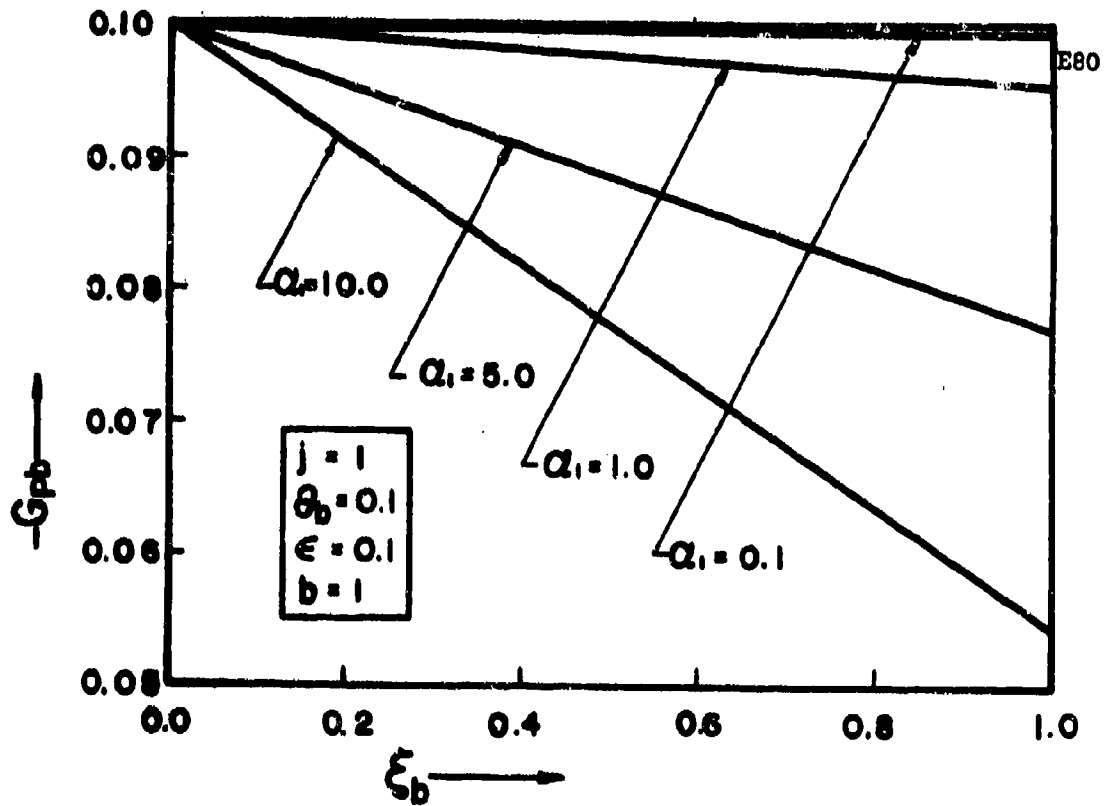


Figure 4. Particle-Phase Normal Velocity and Density at Cone Surface

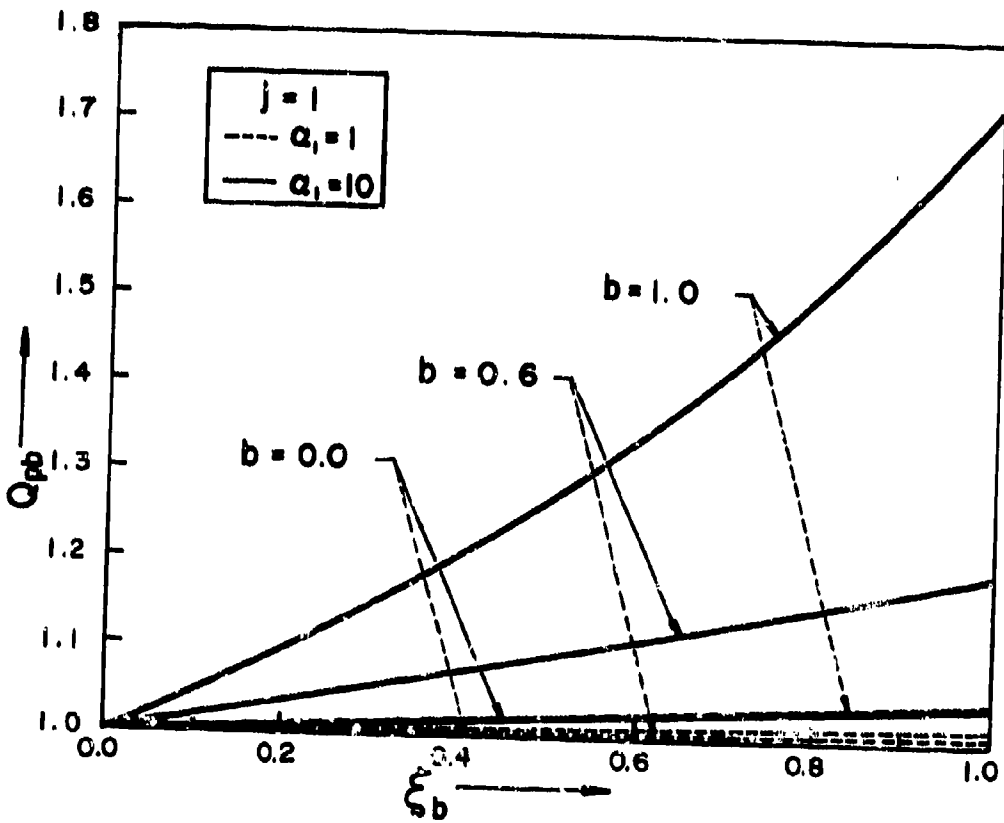
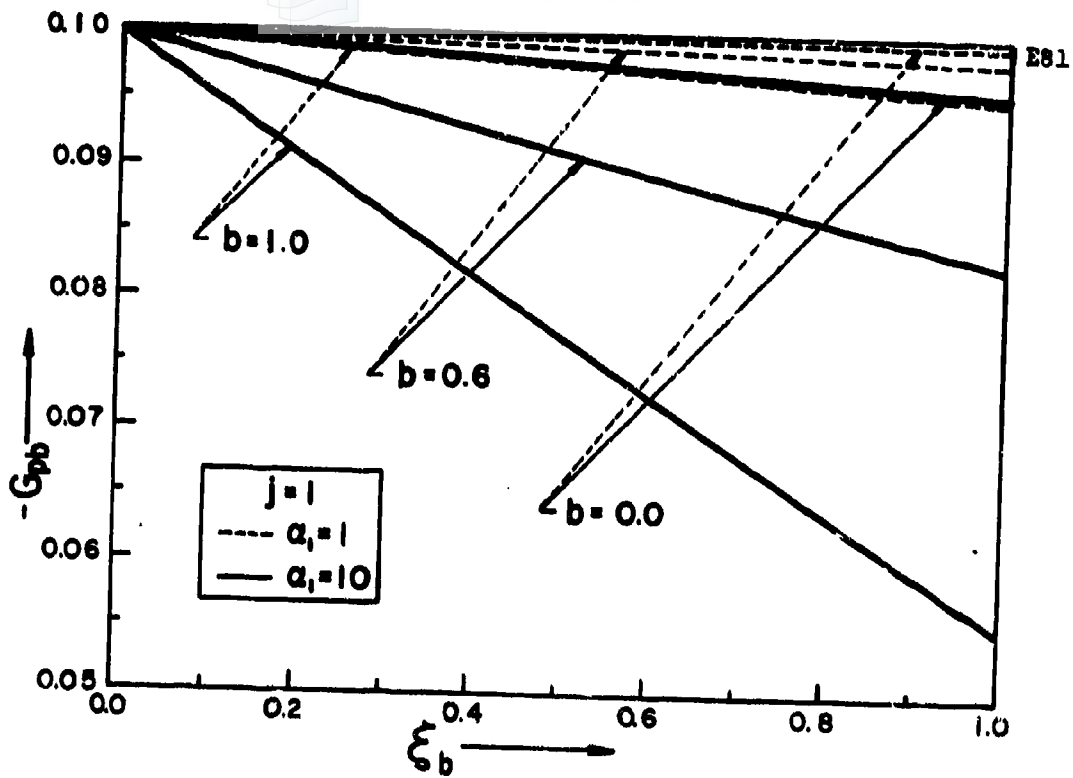


Figure 5. Particle-Phase Normal Velocity and Density at Cone Surface

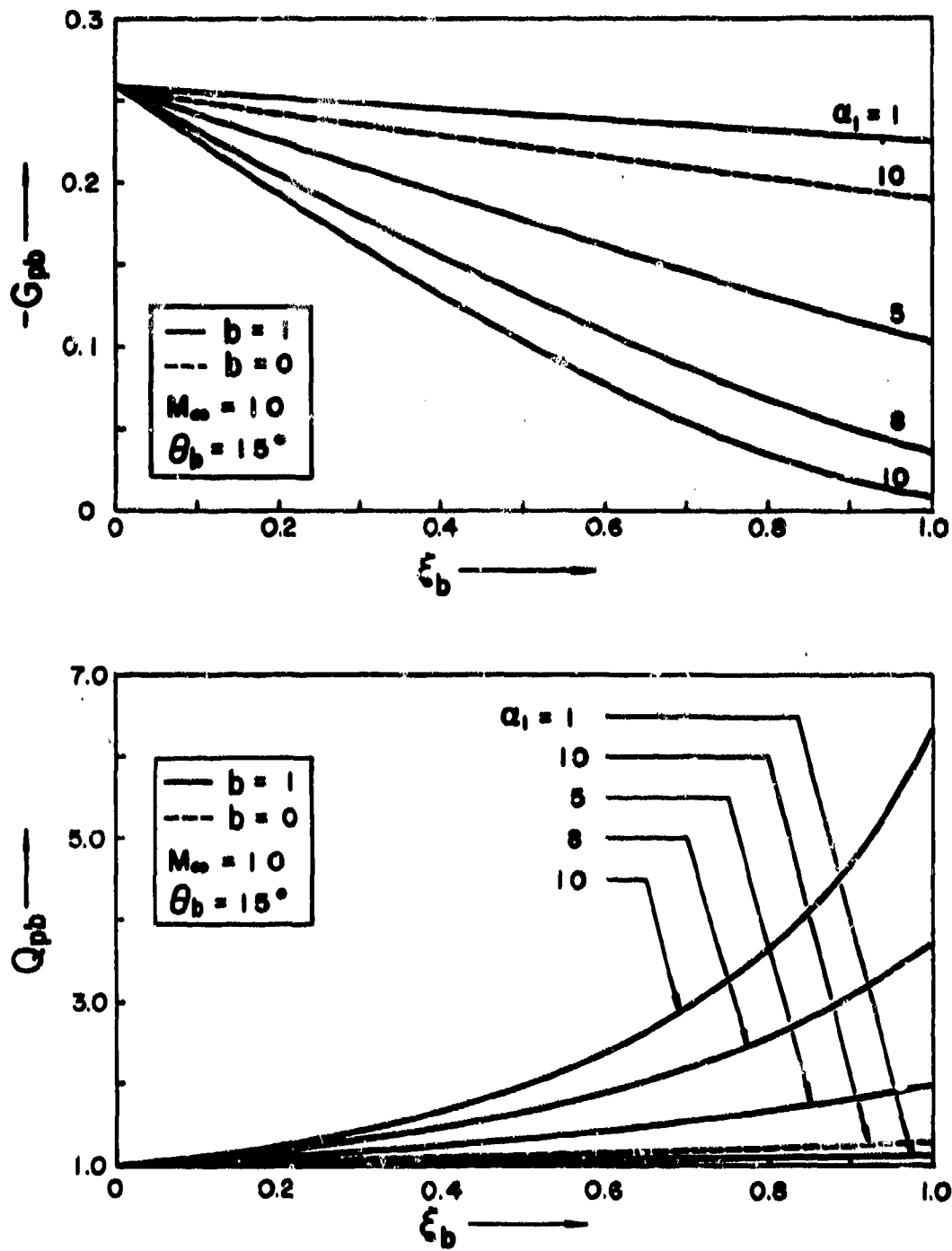


Figure 6. Particle-Phase Normal Velocity and Density at Cone Surface

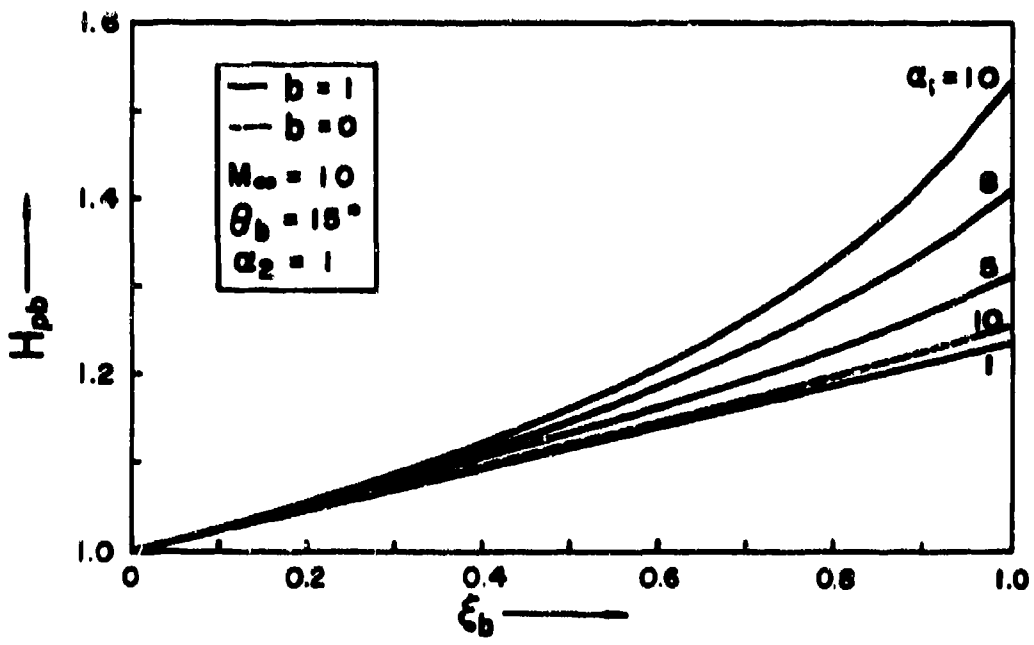
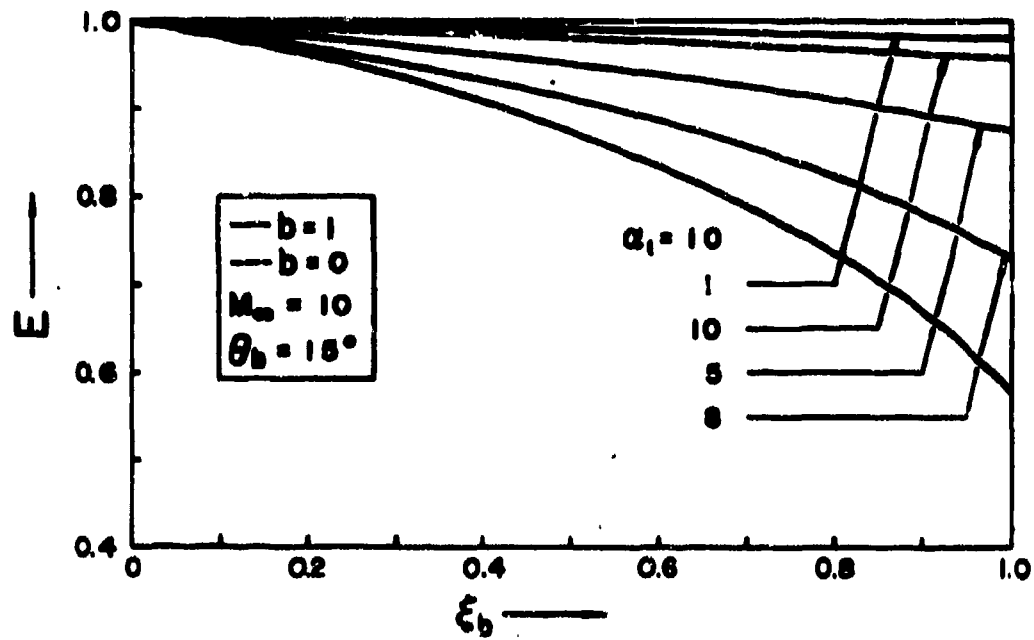


Figure 7. Local Collection Efficiency and Particle-Phase Temperature at Cone Surface

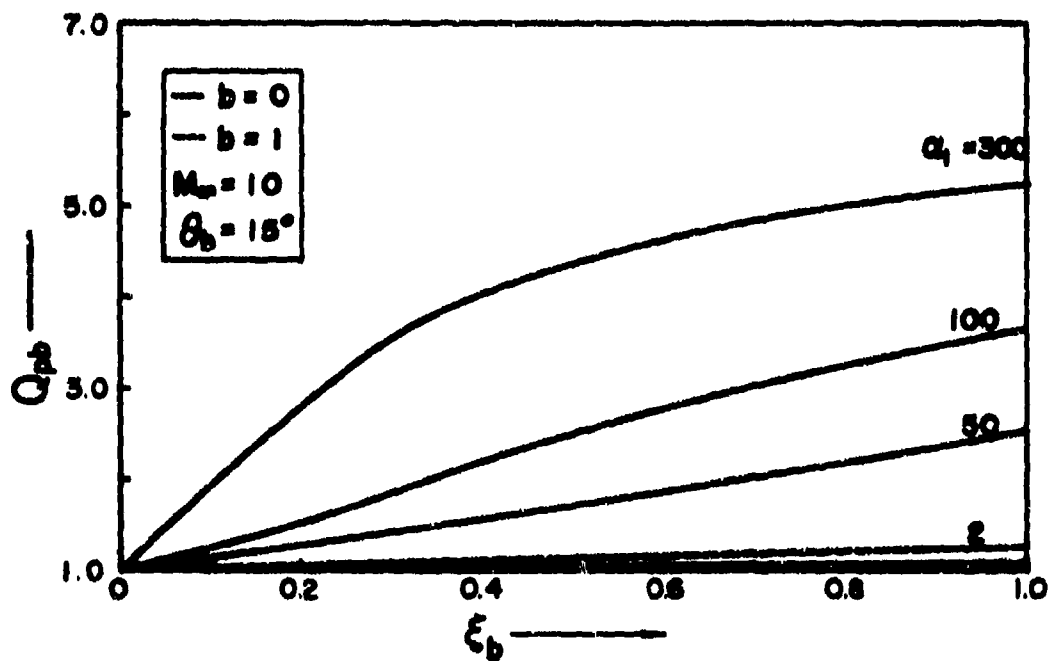
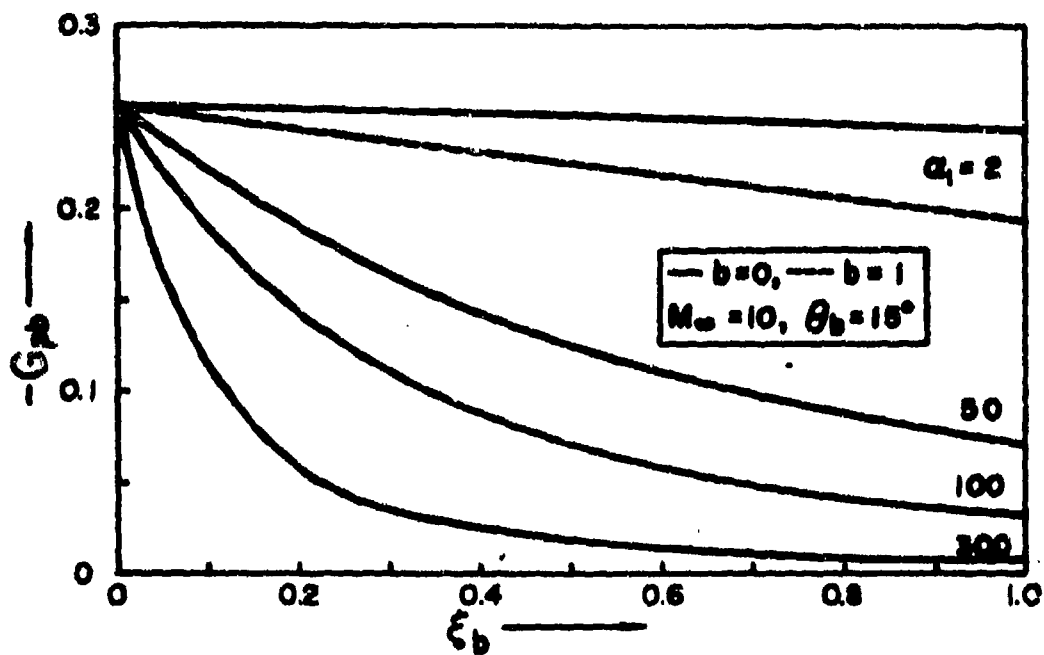


Figure 8. Particle-Phase Normal Velocity and Density at Cone Surface

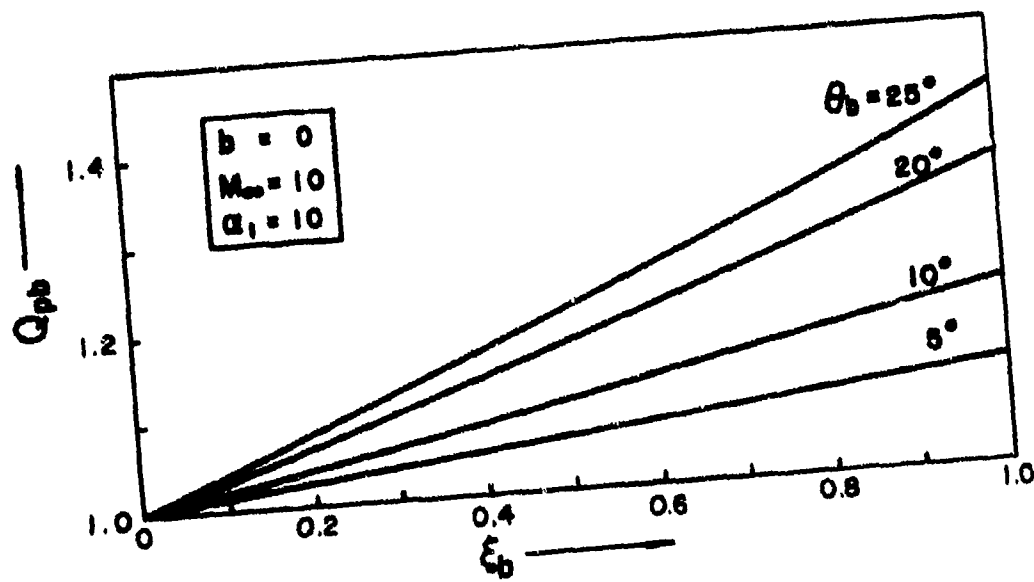
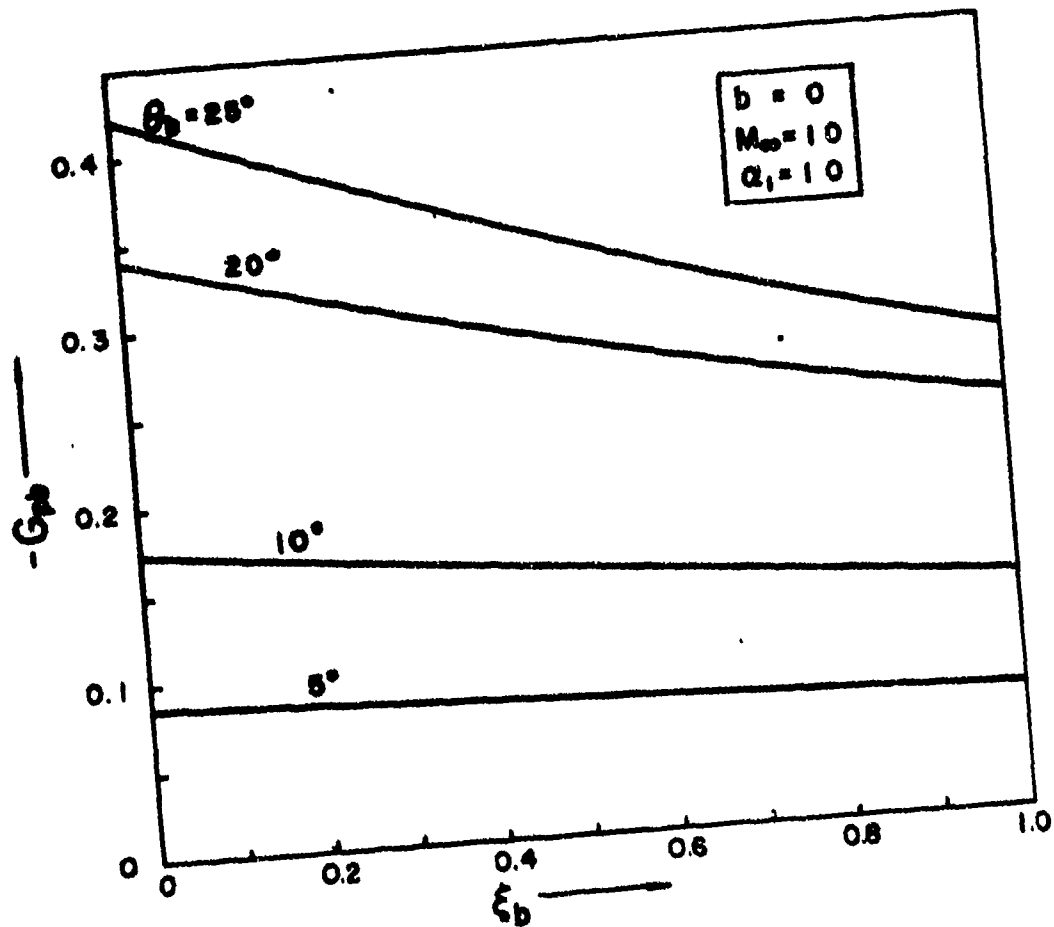


Figure 9. Particle-Phase Normal Velocity and Density at Cone Surface

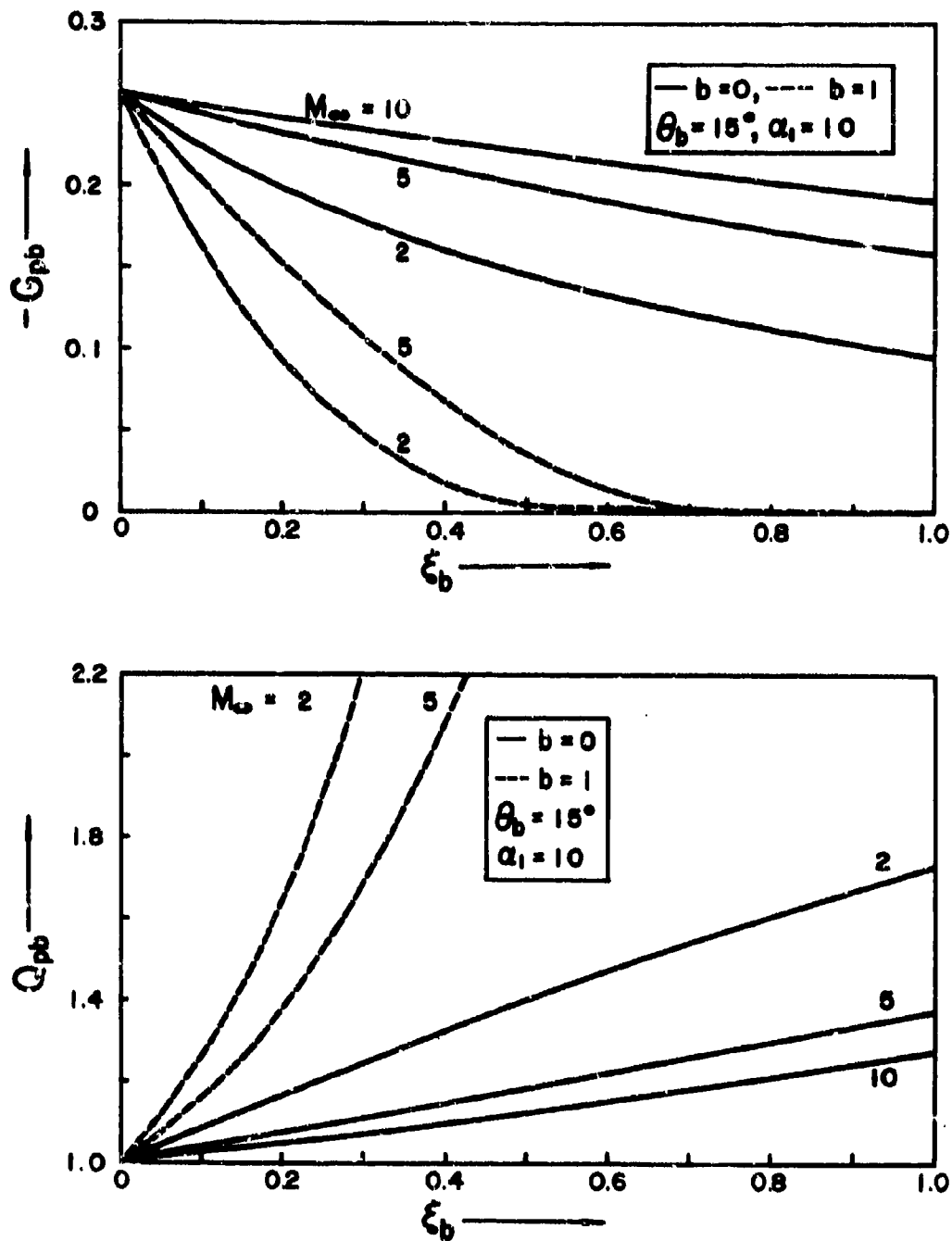


Figure 10. Particle-Phase Normal Velocity and Density at Cone Surface

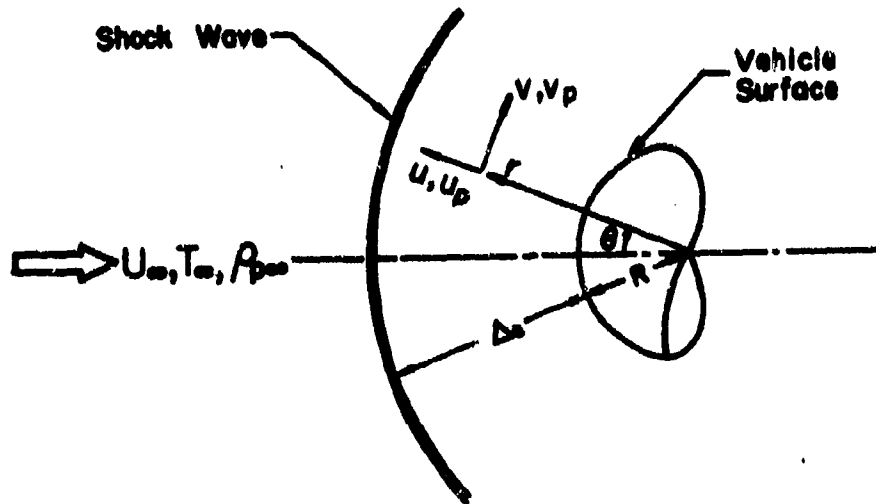


Figure 11. Shock Layer on Sphere or Circular Cylinder

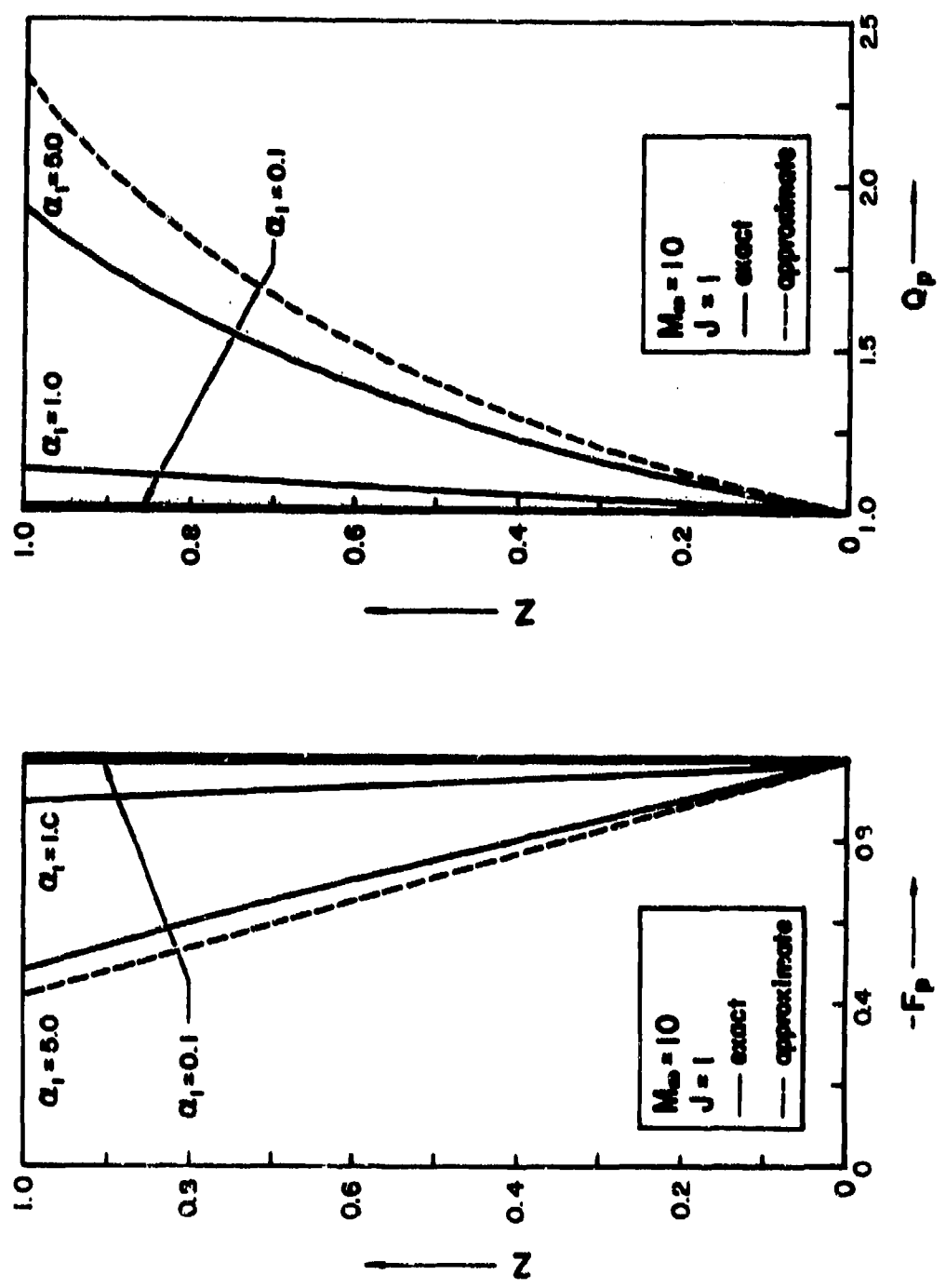


Figure 12. Comparison of Exact and Approximate Stagnation-Line Solutions

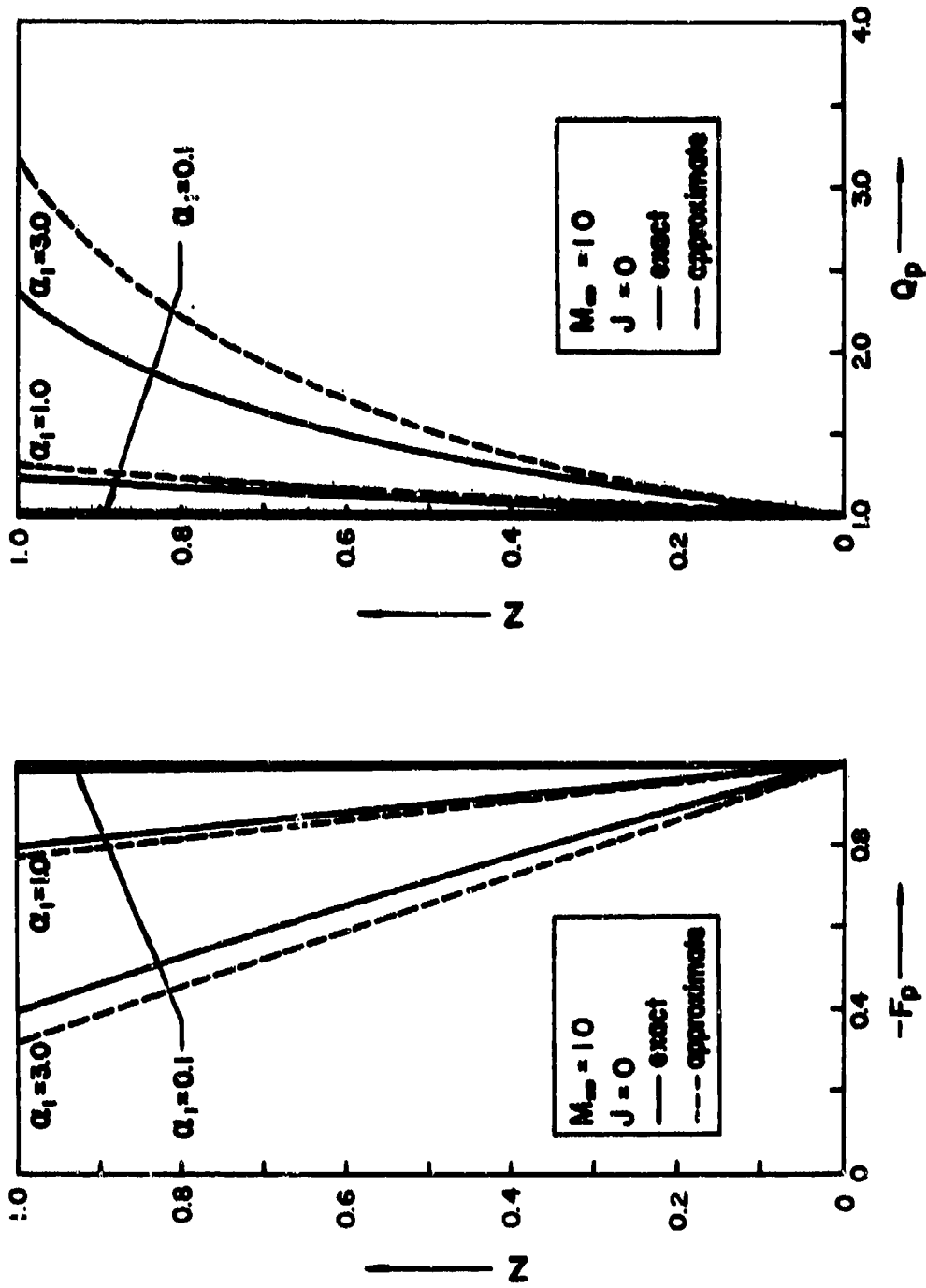


Figure 13. Comparison of Exact and Approximate Stagnation-Line Solutions

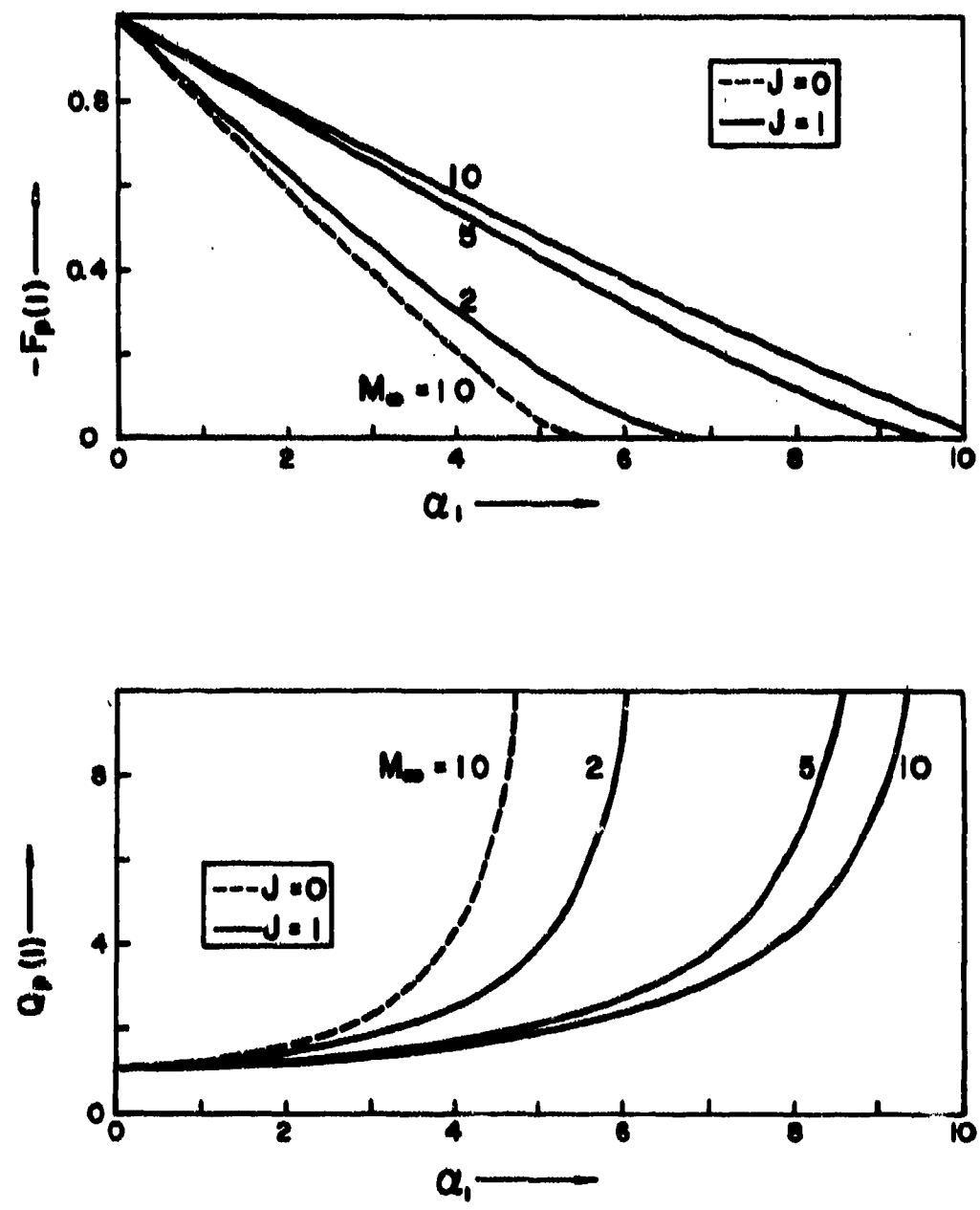


Figure 14. Stagnation-Point Values of Particle-Phase Normal Velocity and Density

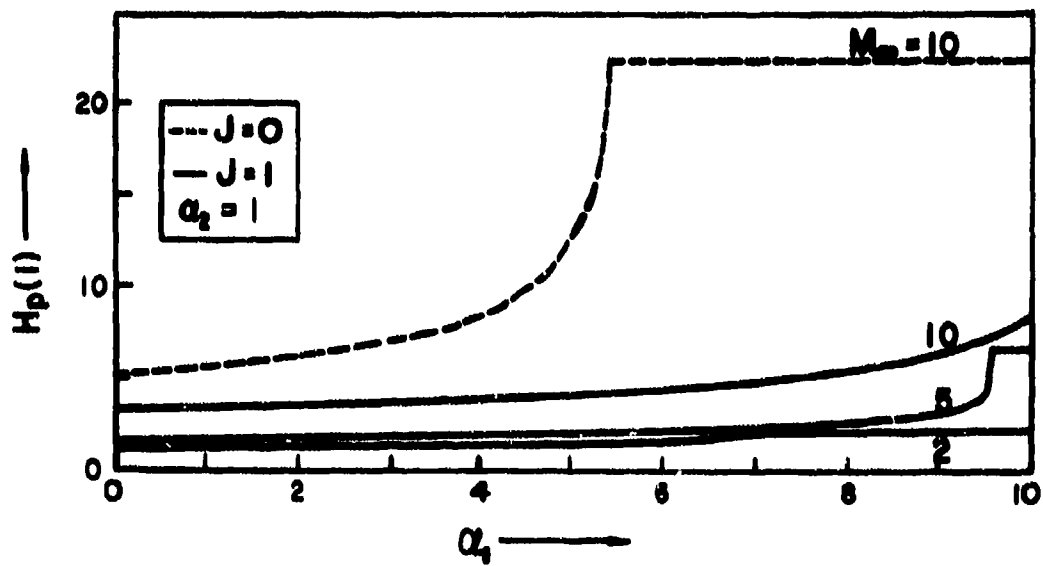
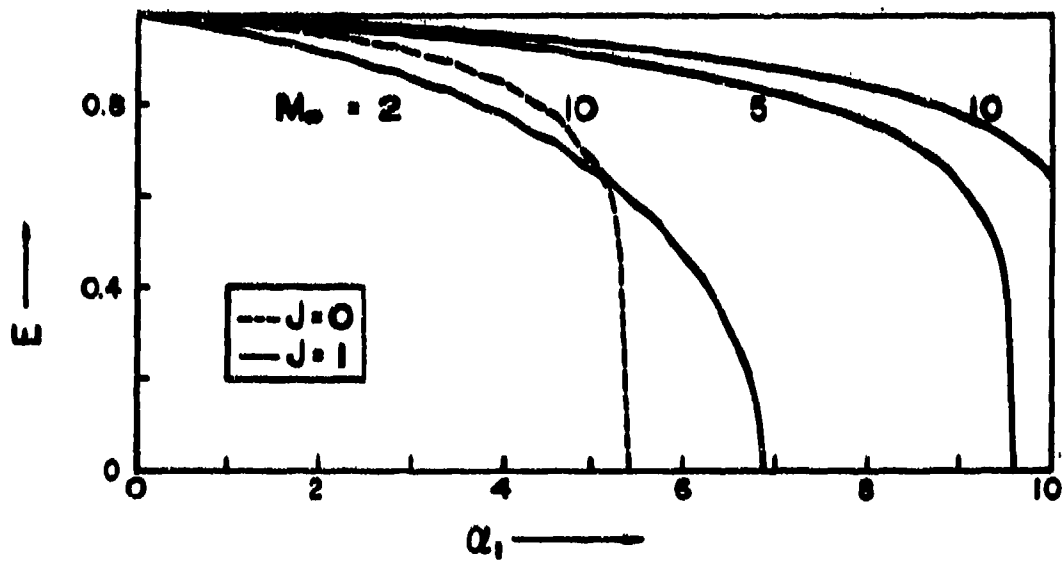


Figure 15. Stagnation-Point Values of Particle-Phase Collection Efficiency and Temperature

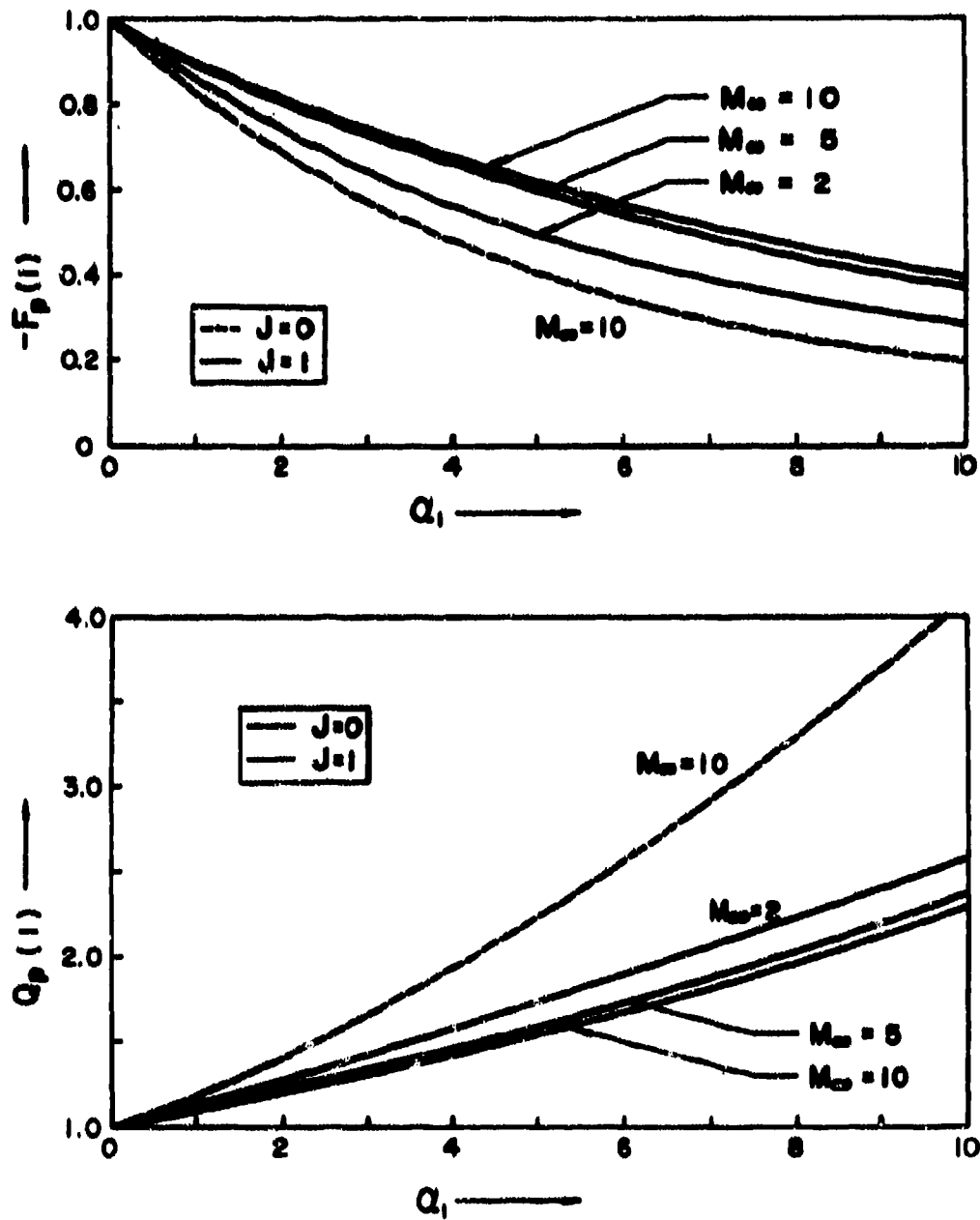


Figure 16. Stagnation-Point Values of Particle-Phase Normal Velocity and Density

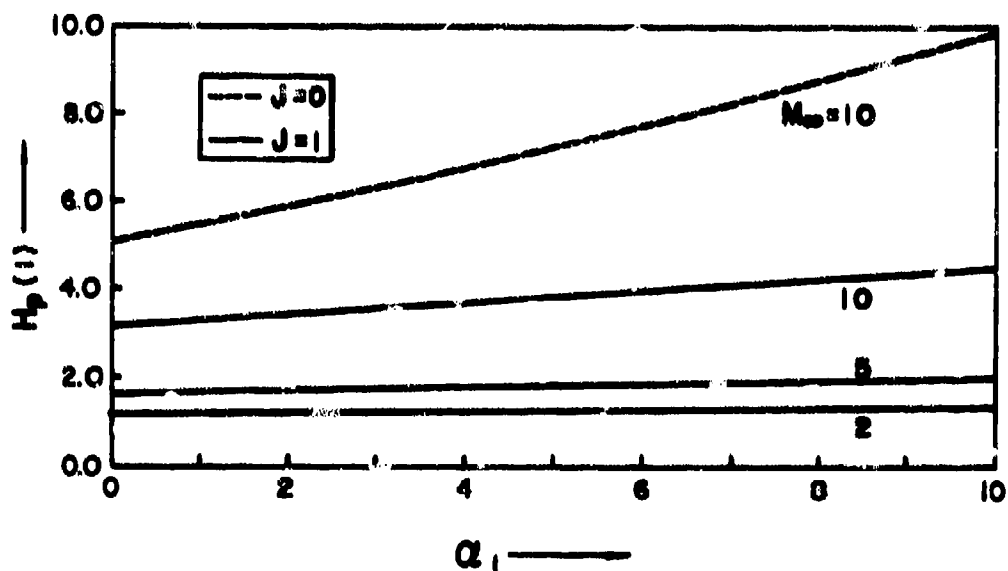
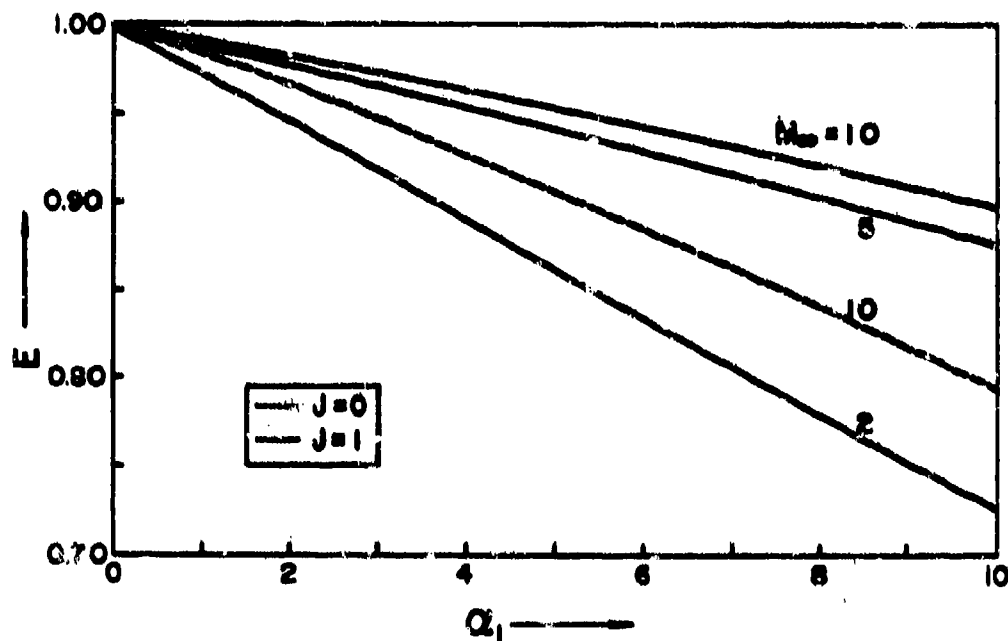


Figure 17. Stagnation-Point Values of Particle-Phase Collection Efficiency and Temperature

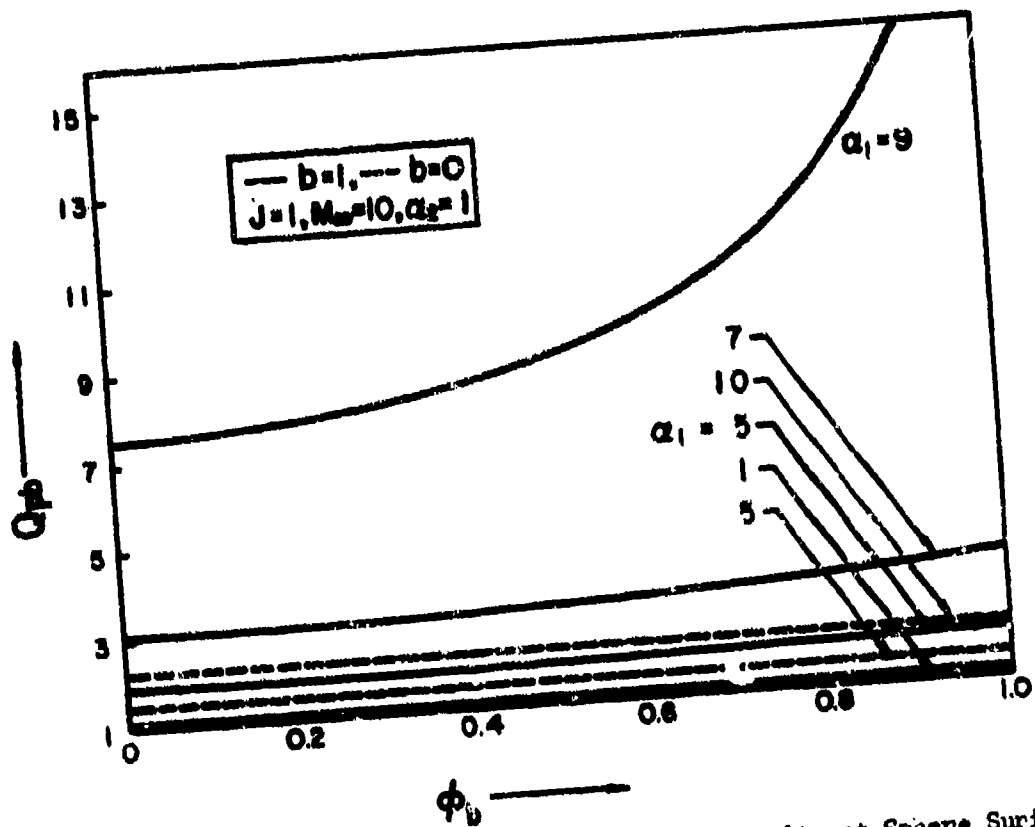
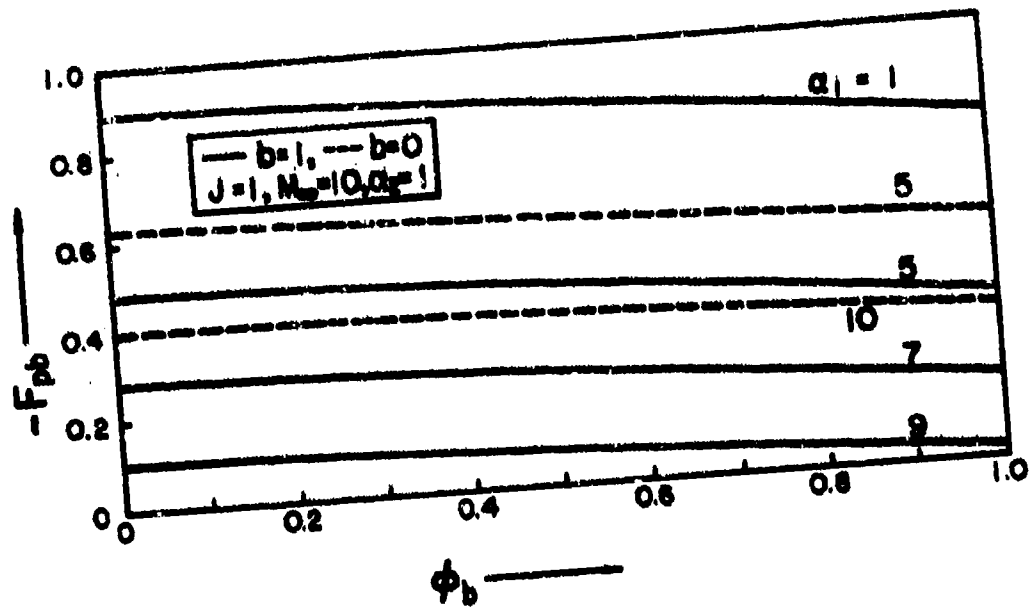


Figure 18. Particle-Phase Normal Velocity and Density at Sphere Surface

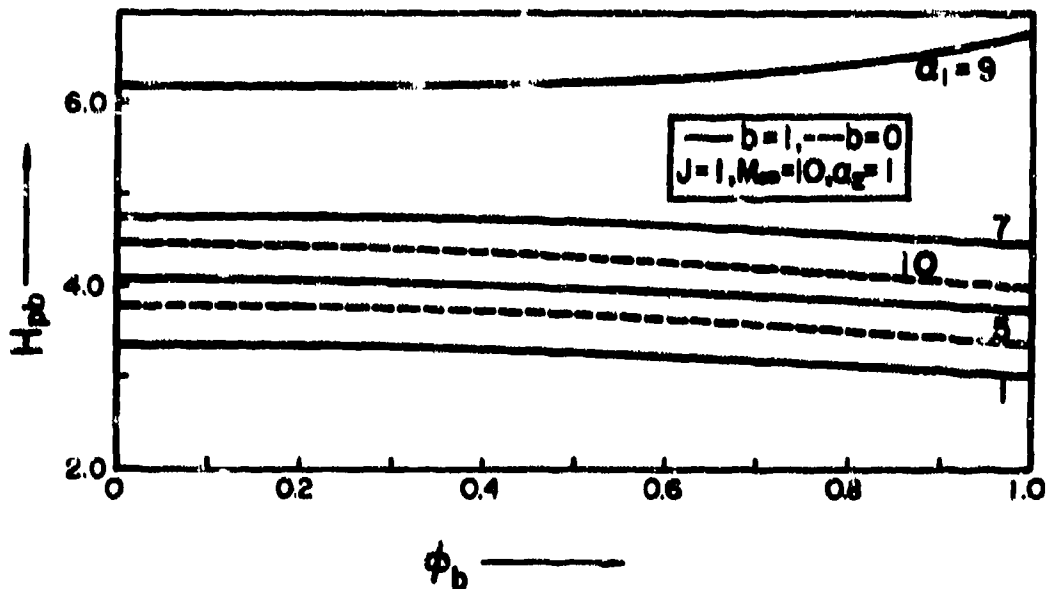
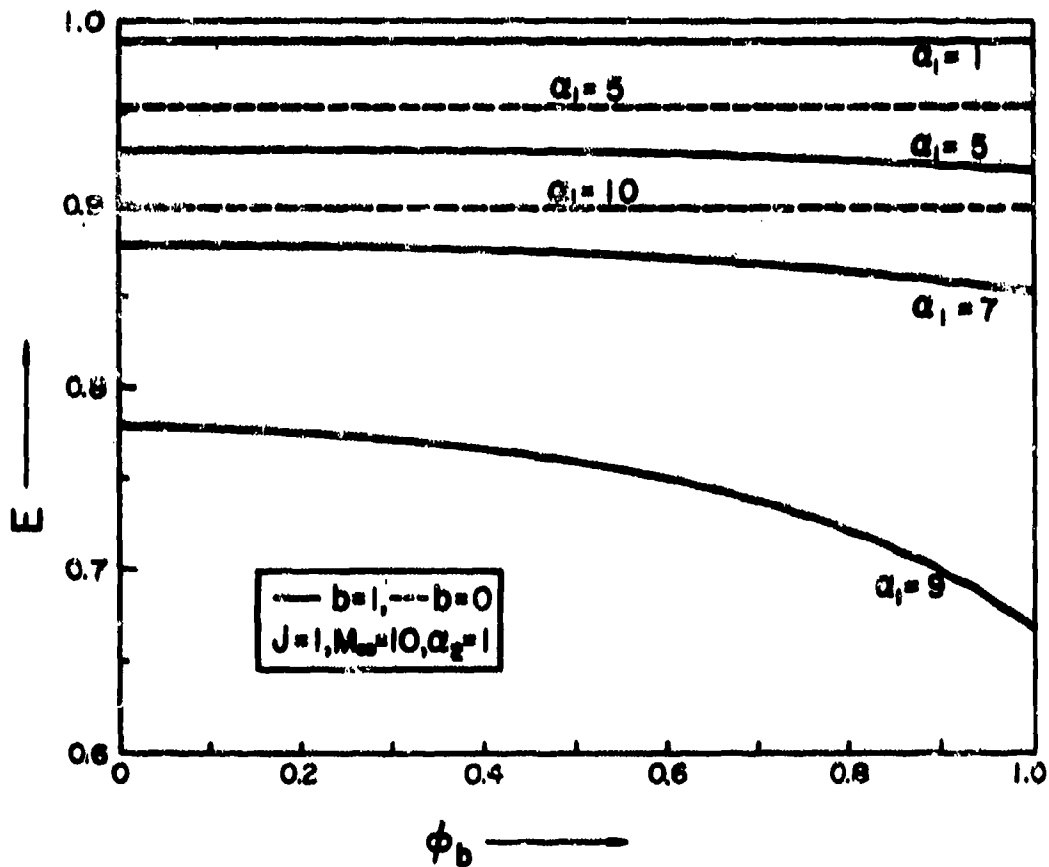


Figure 19. Particle-Phase Collection Efficiency and Temperature at Sphere Surface

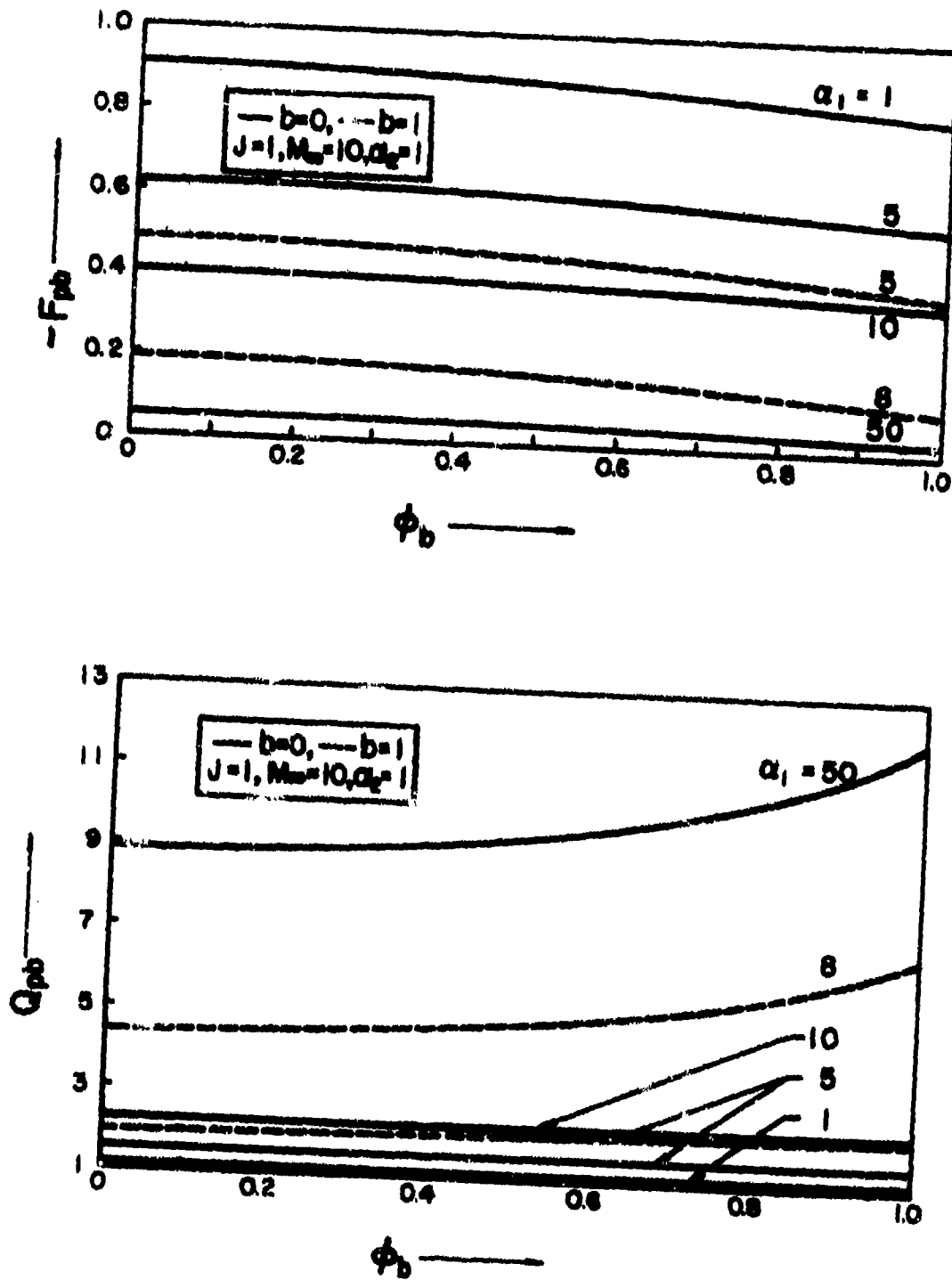


Figure 20. Particle-Phase Normal Velocity and Density at Sphere Surface

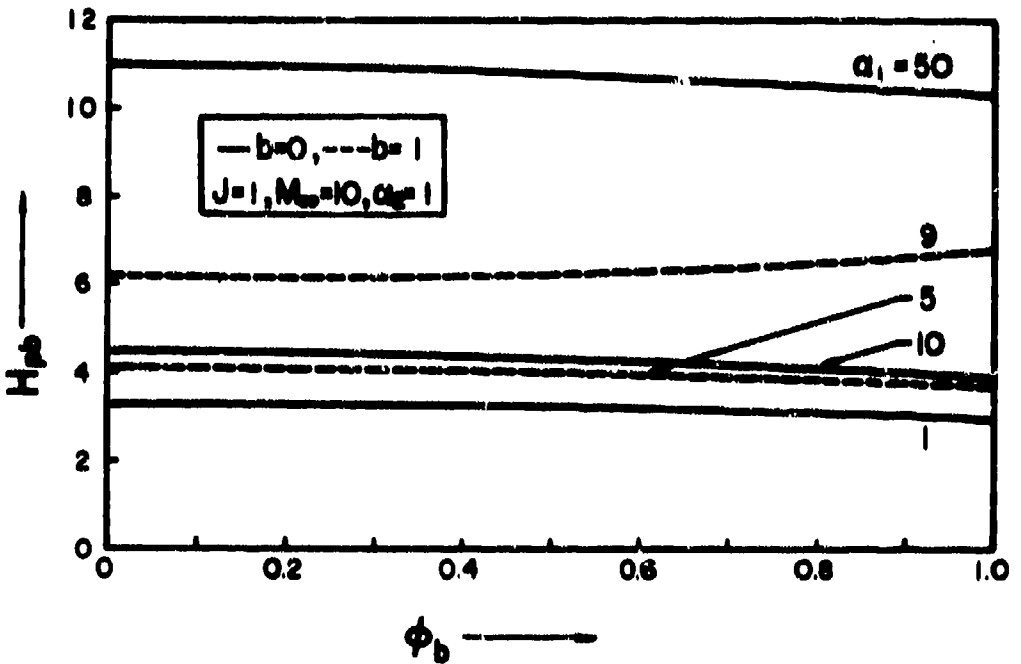
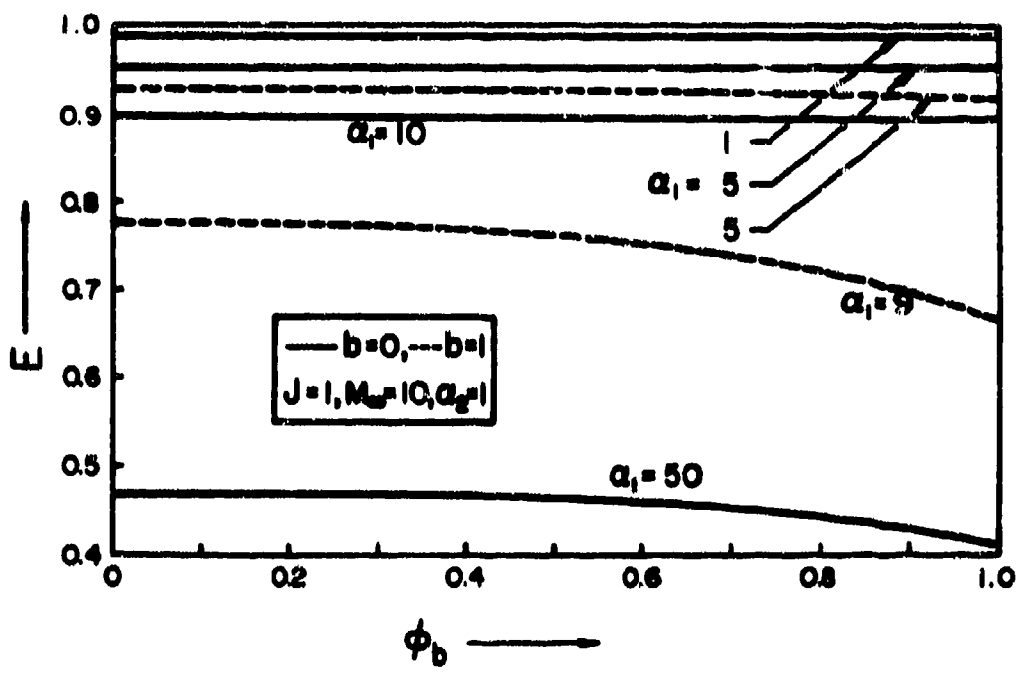


Figure 21. Particle-Phase Collection Efficiency and Temperature at Sphere Surface

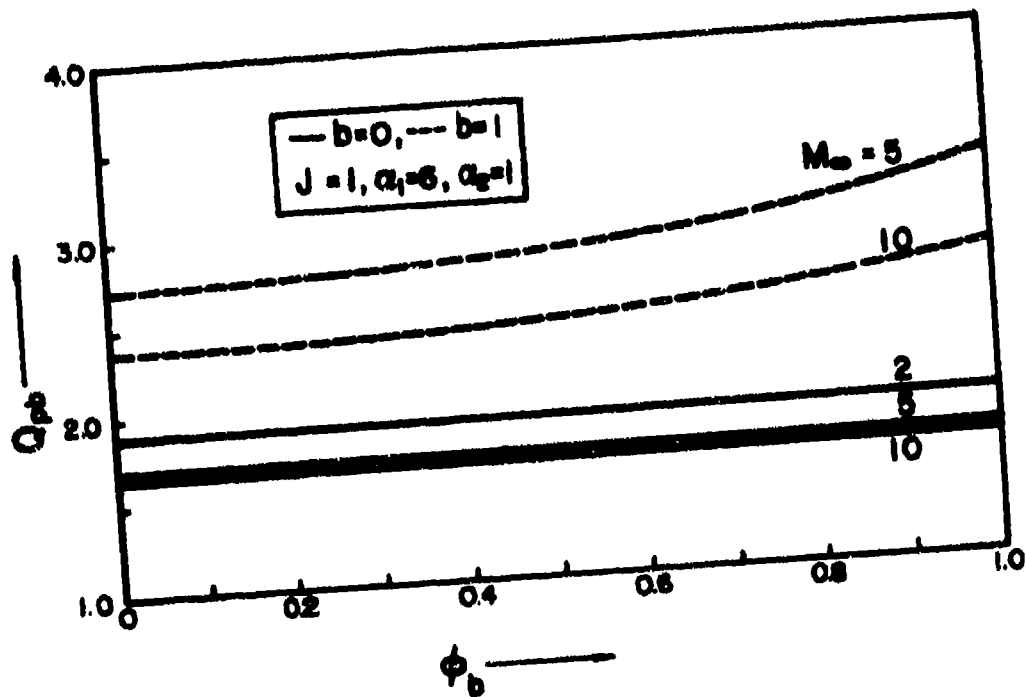
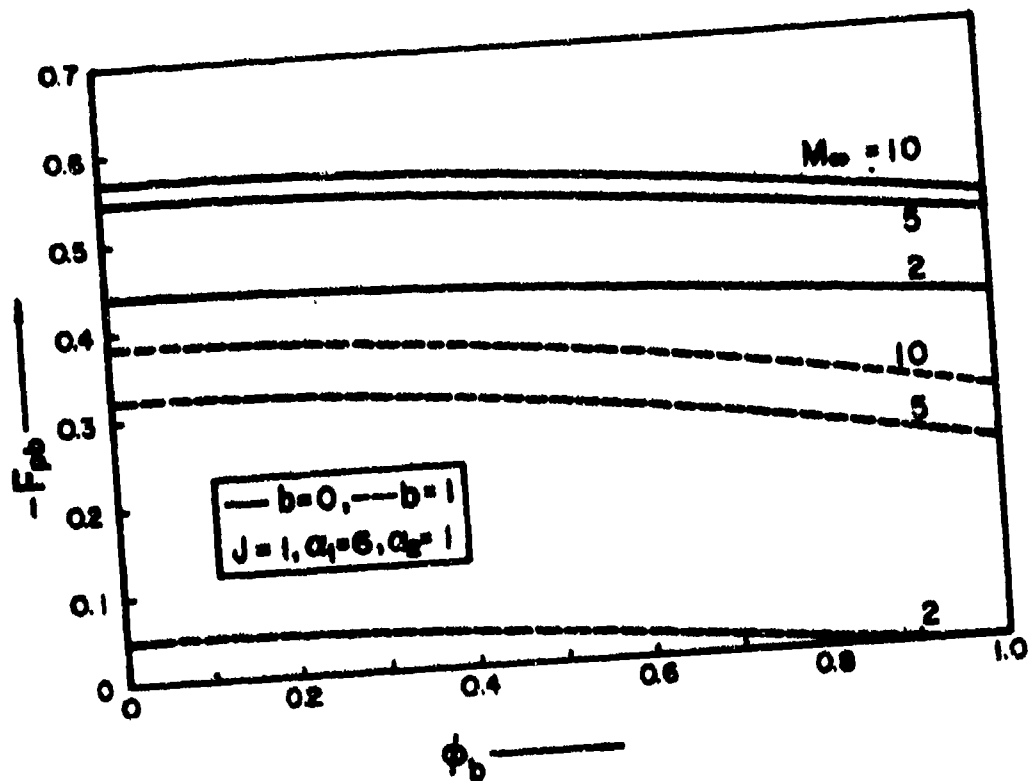


Figure 22. Particle-Phase Normal Velocity and Density at Sphere Surface

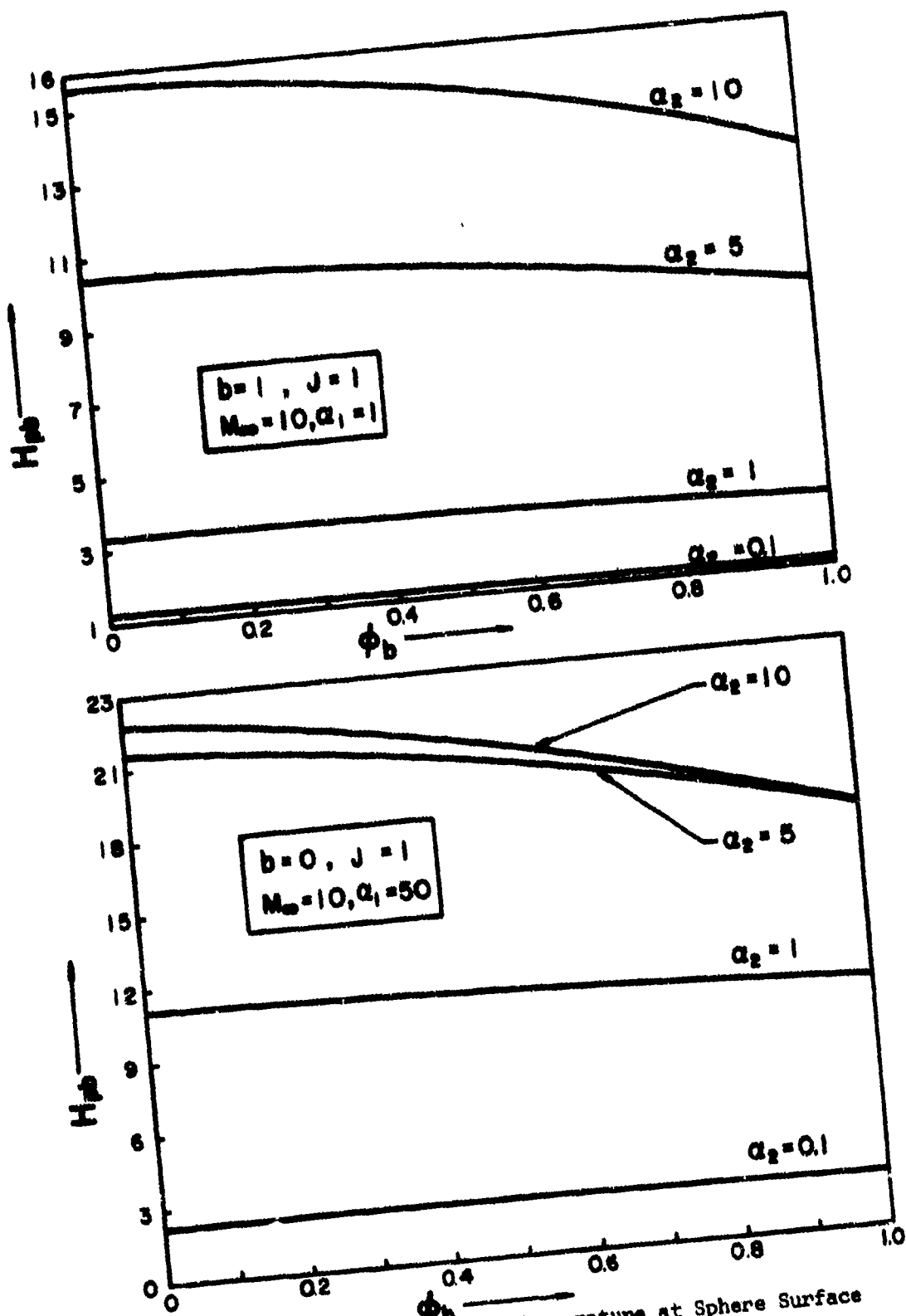


Figure 23. Particle-Phase Temperature at Sphere Surface

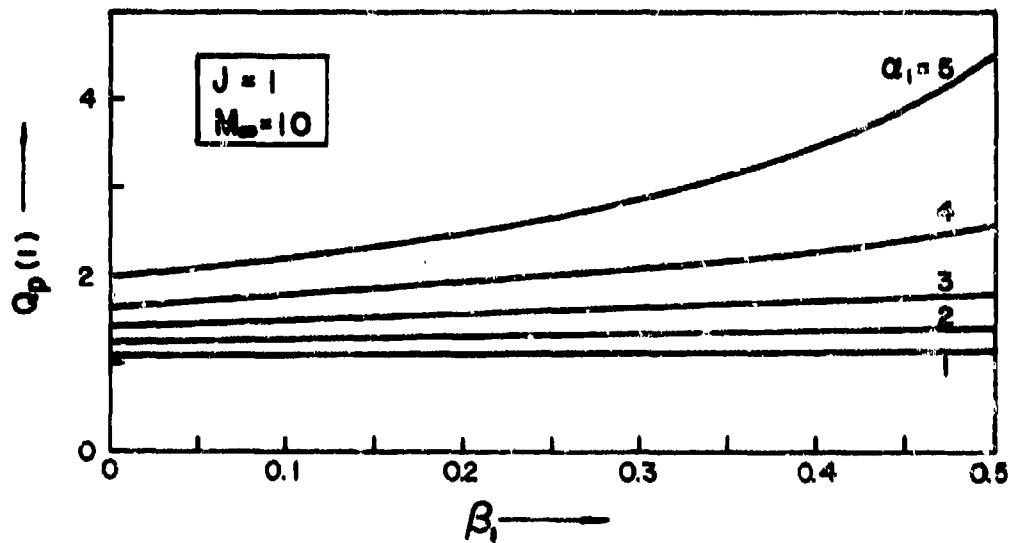
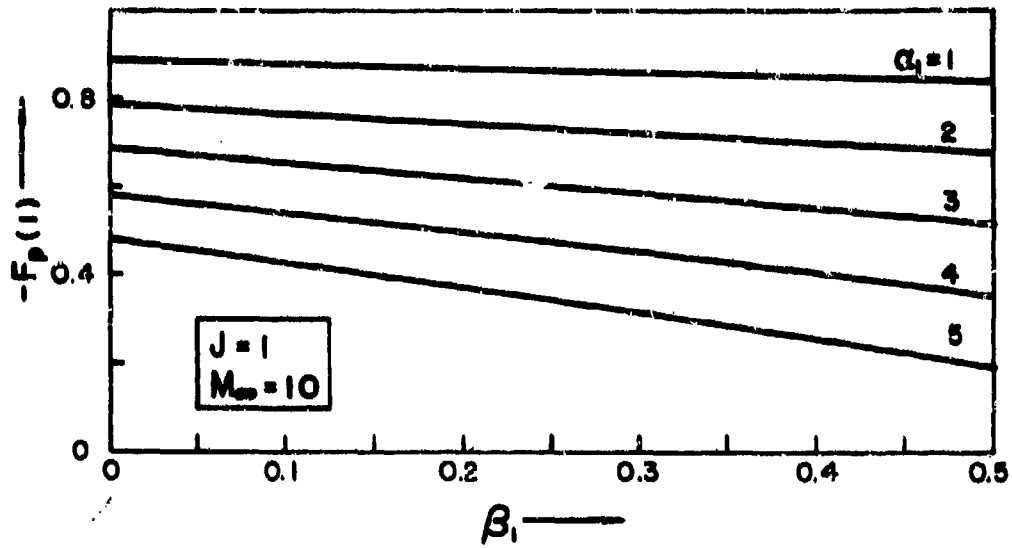


Figure 24. Stagnation-Point Values of Particle-Phase Normal Velocity and Density for Finite Volume Fractions

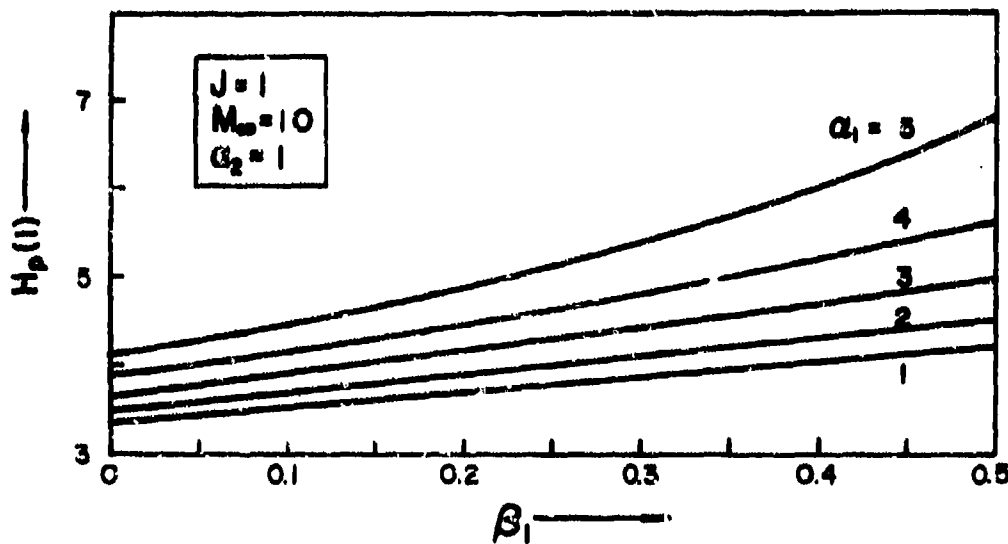
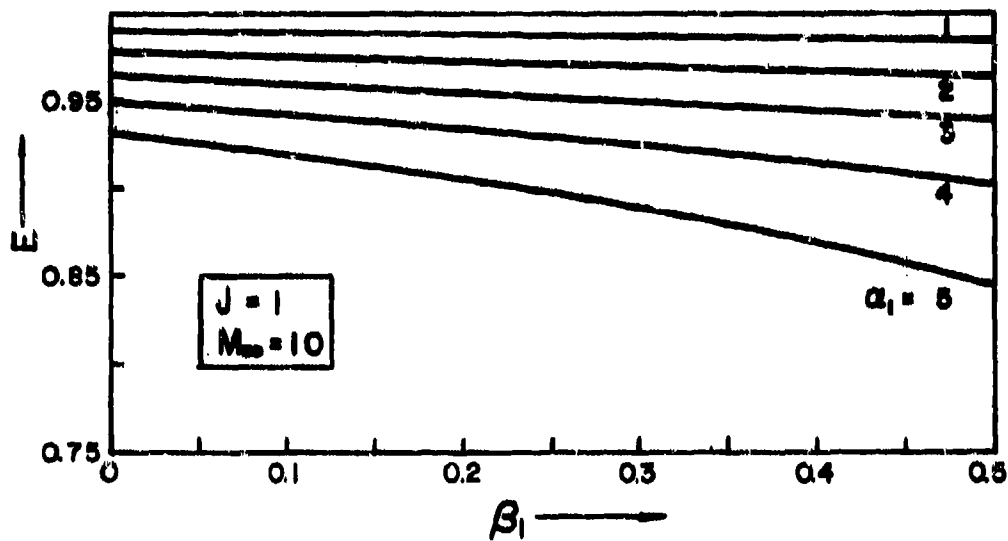


Figure 25. Stagnation-Point Values of Particle-Phase Collection Efficiency and Temperature for Finite Volume Fractions

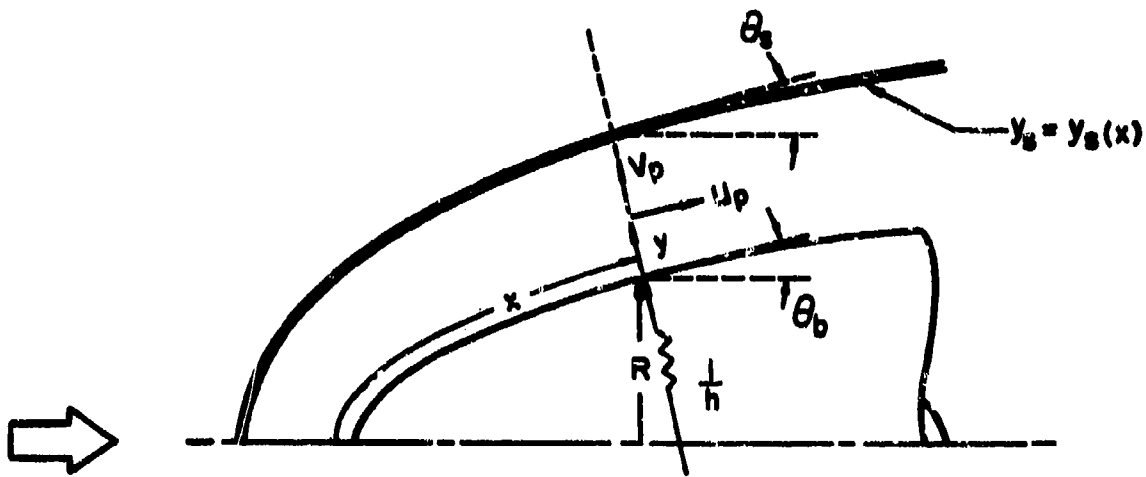


Figure 26. Geometry and Coordinate System for General Symmetric Body

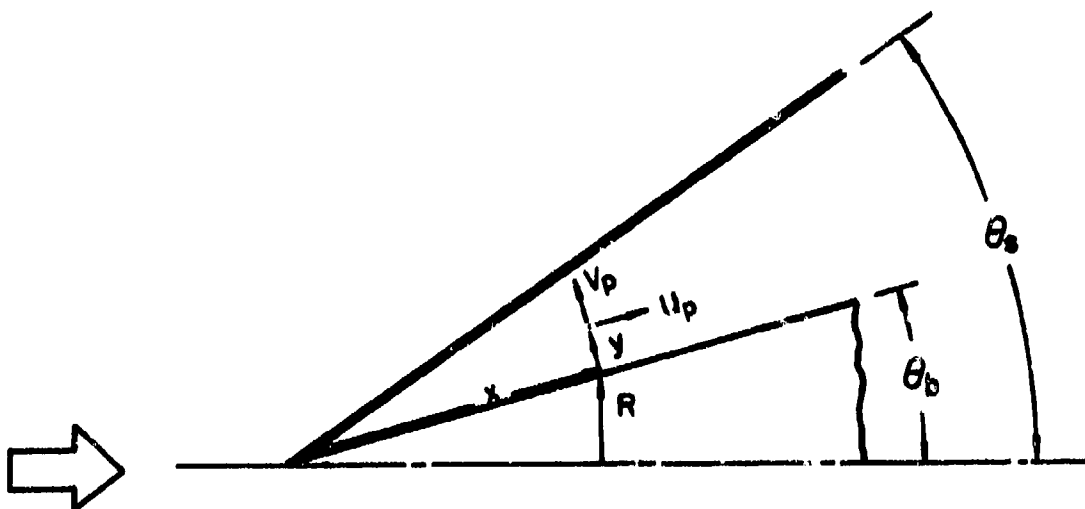


Figure 27. Geometry and Coordinate System for Symmetric Wedge

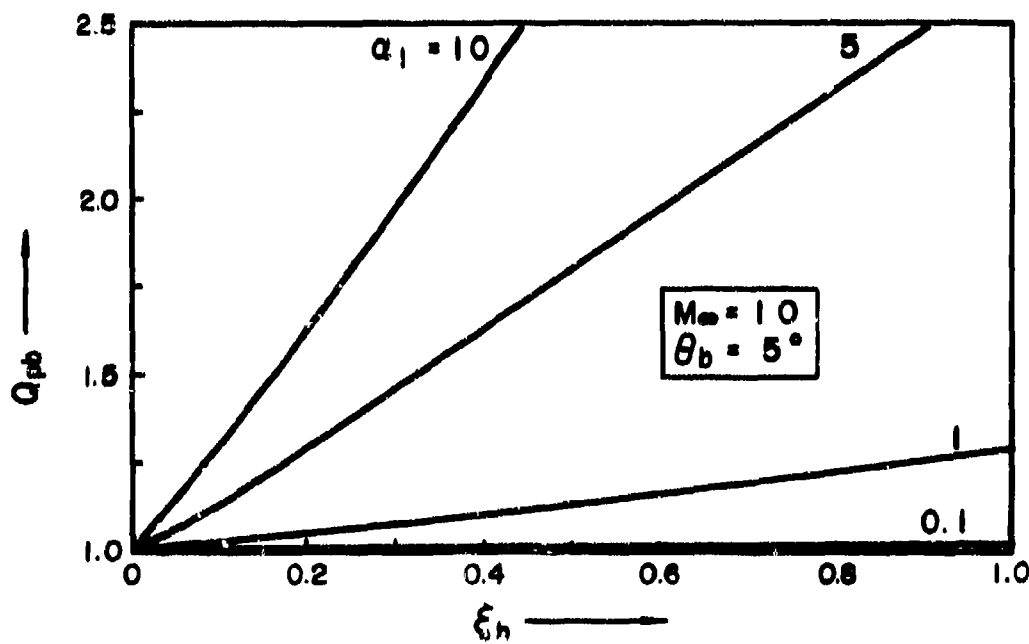
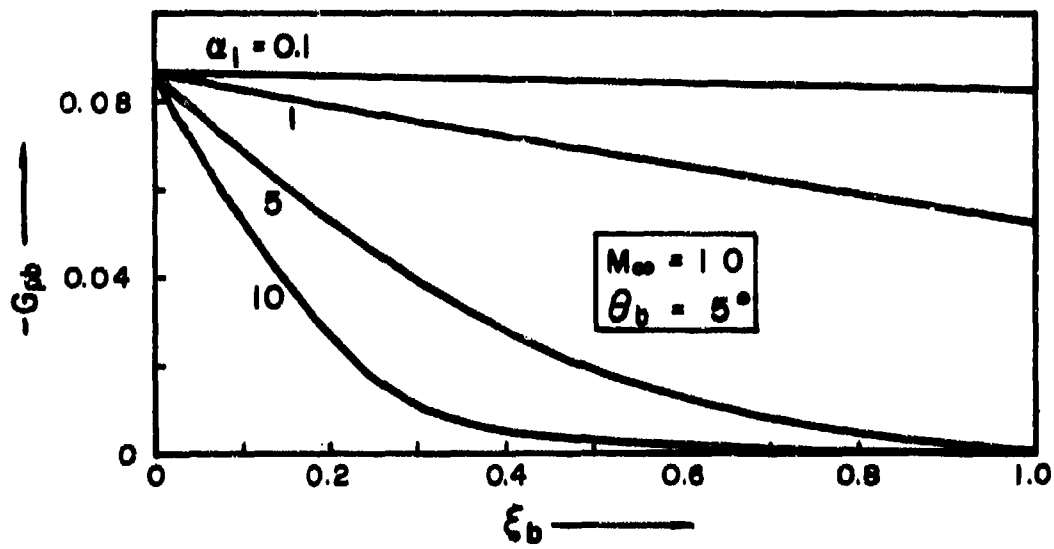


Figure 28. Particle-Phase Normal Velocity and Density at Wedge Surface

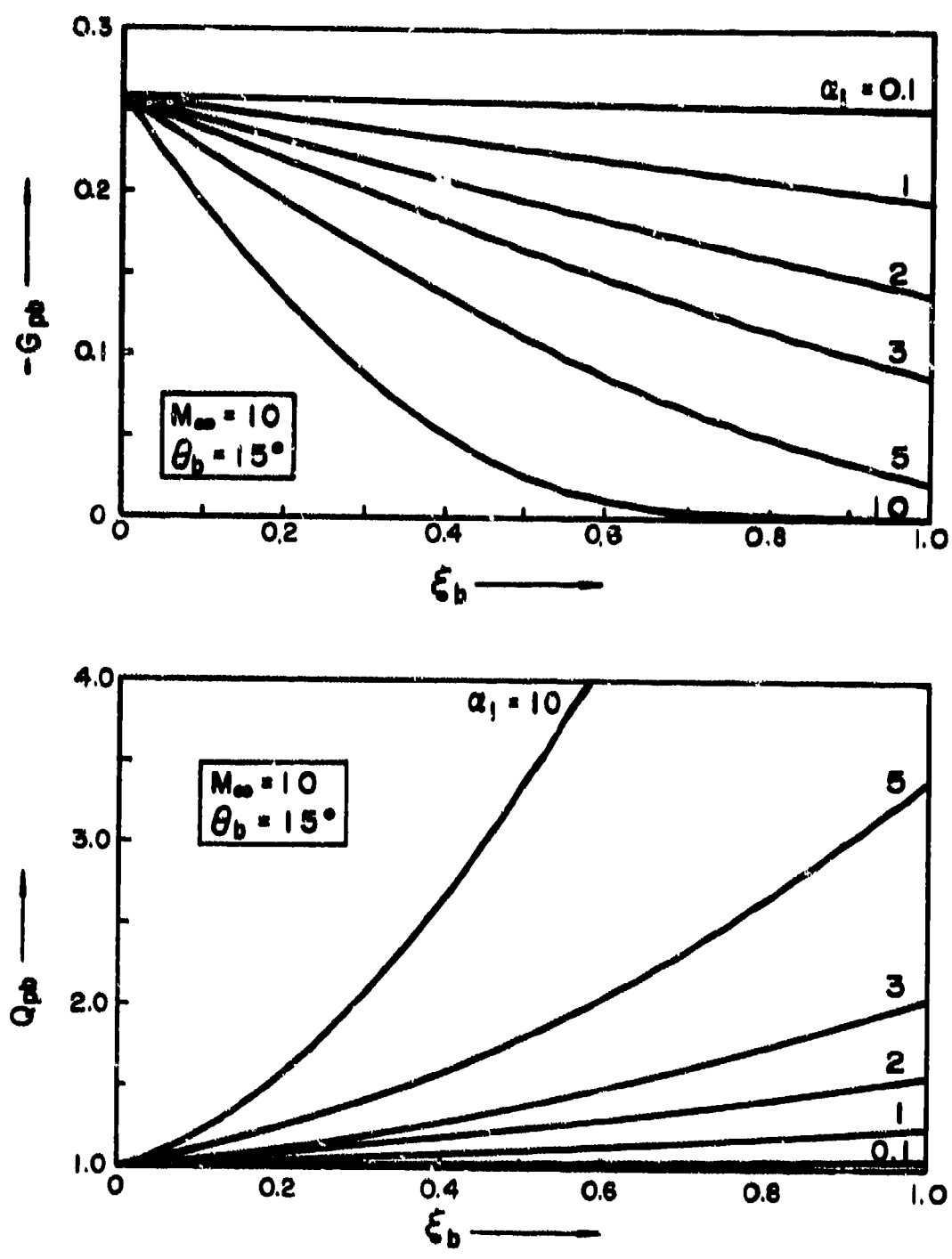


Figure 29. Particle-Phase Normal Velocity and Density at Wedge Surface

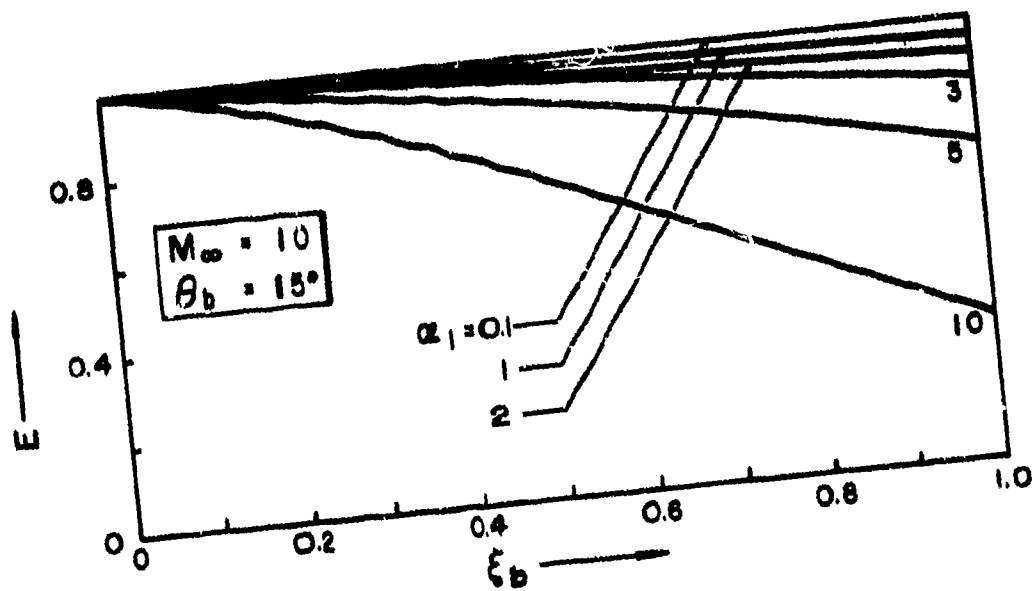
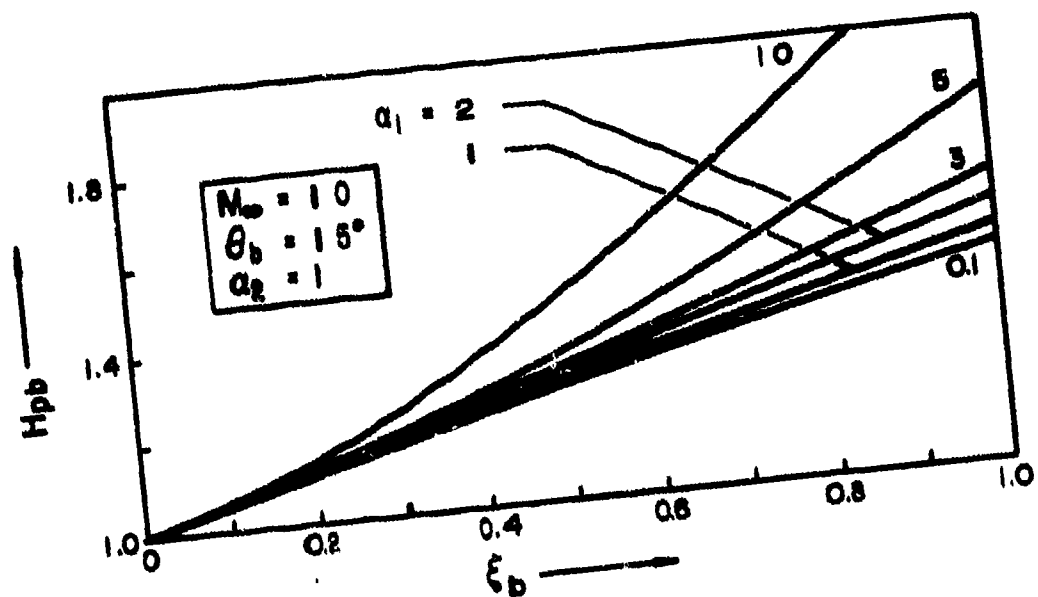


Figure 30. Particle-Phase Temperature at Wall and Local Collection Efficiency

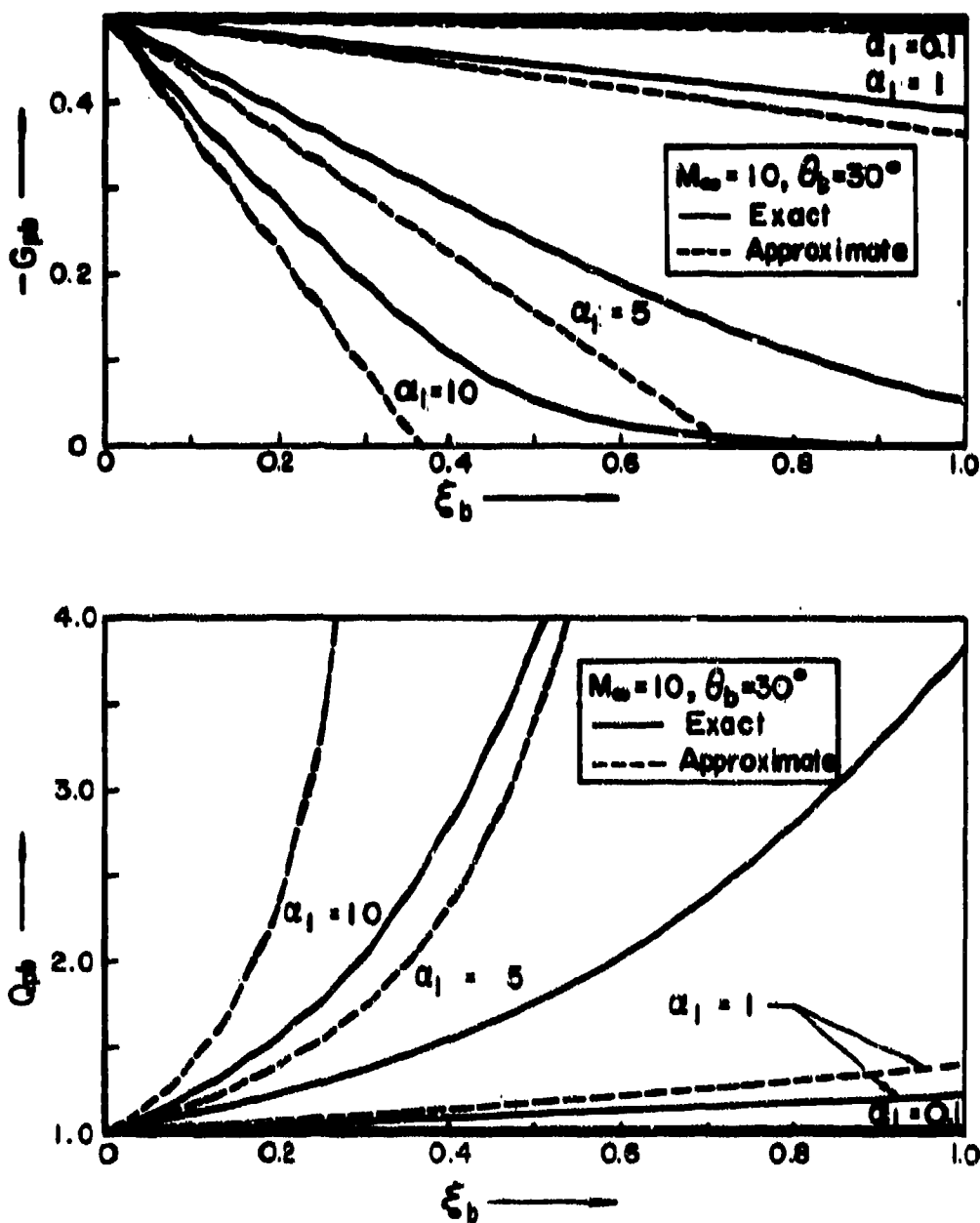


Figure 31. Particle-phase normal velocity and density at wedge surface

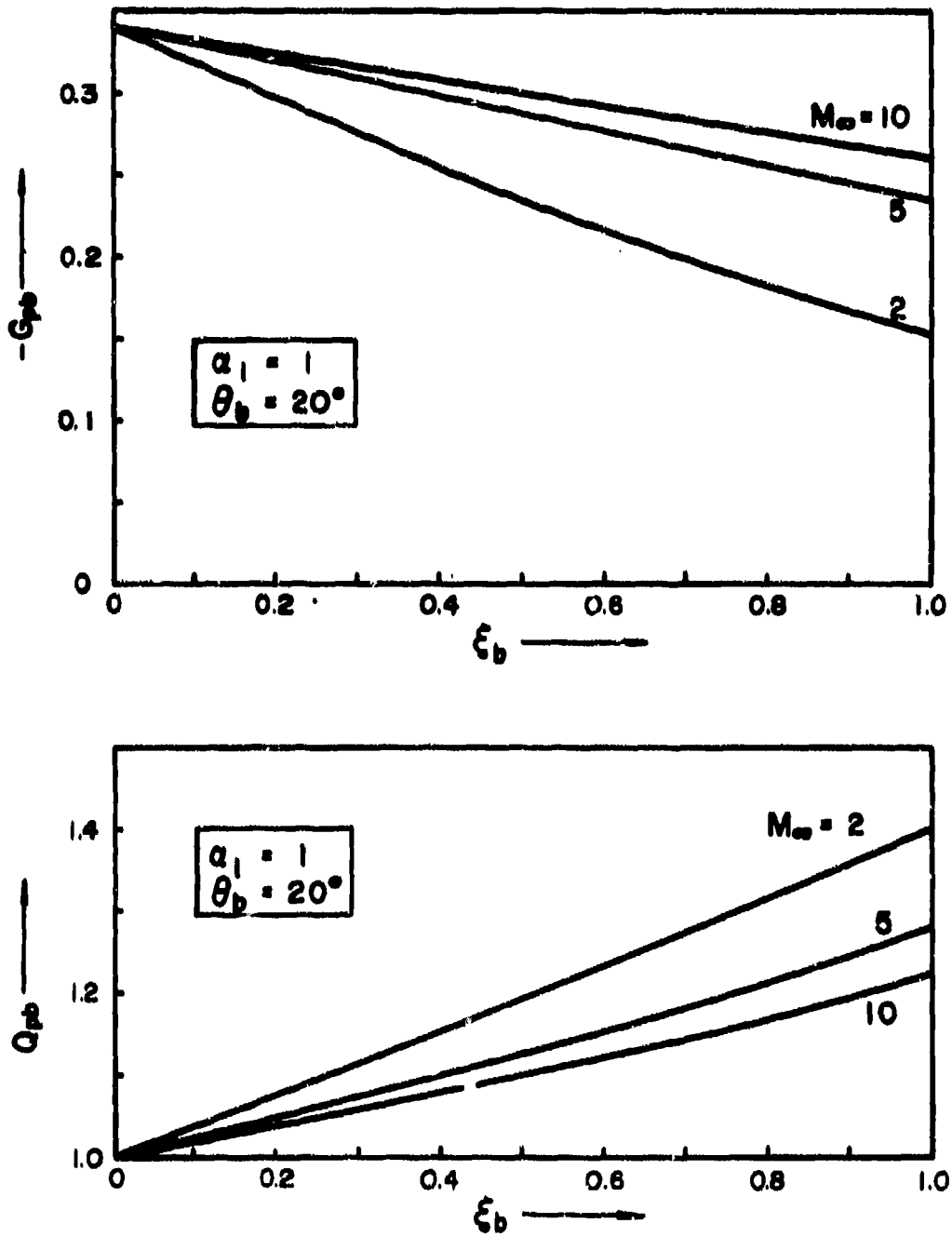


Figure 32. Particle-Phase Normal Velocity and Density at Wedge Surface

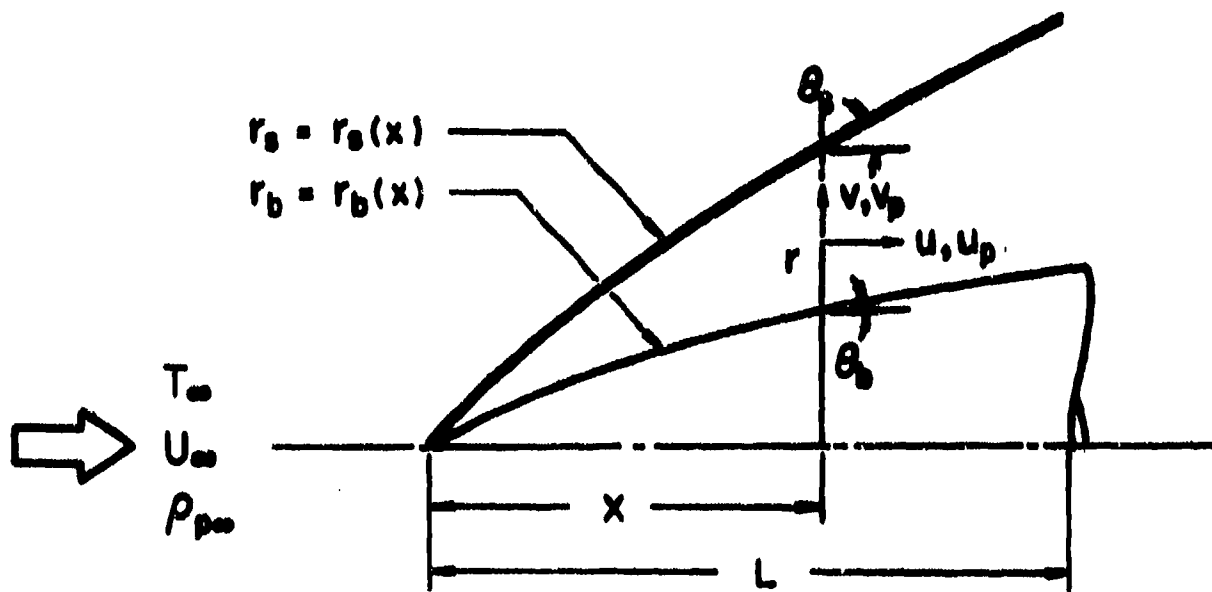


Figure 33. Geometry and Coordinate System.

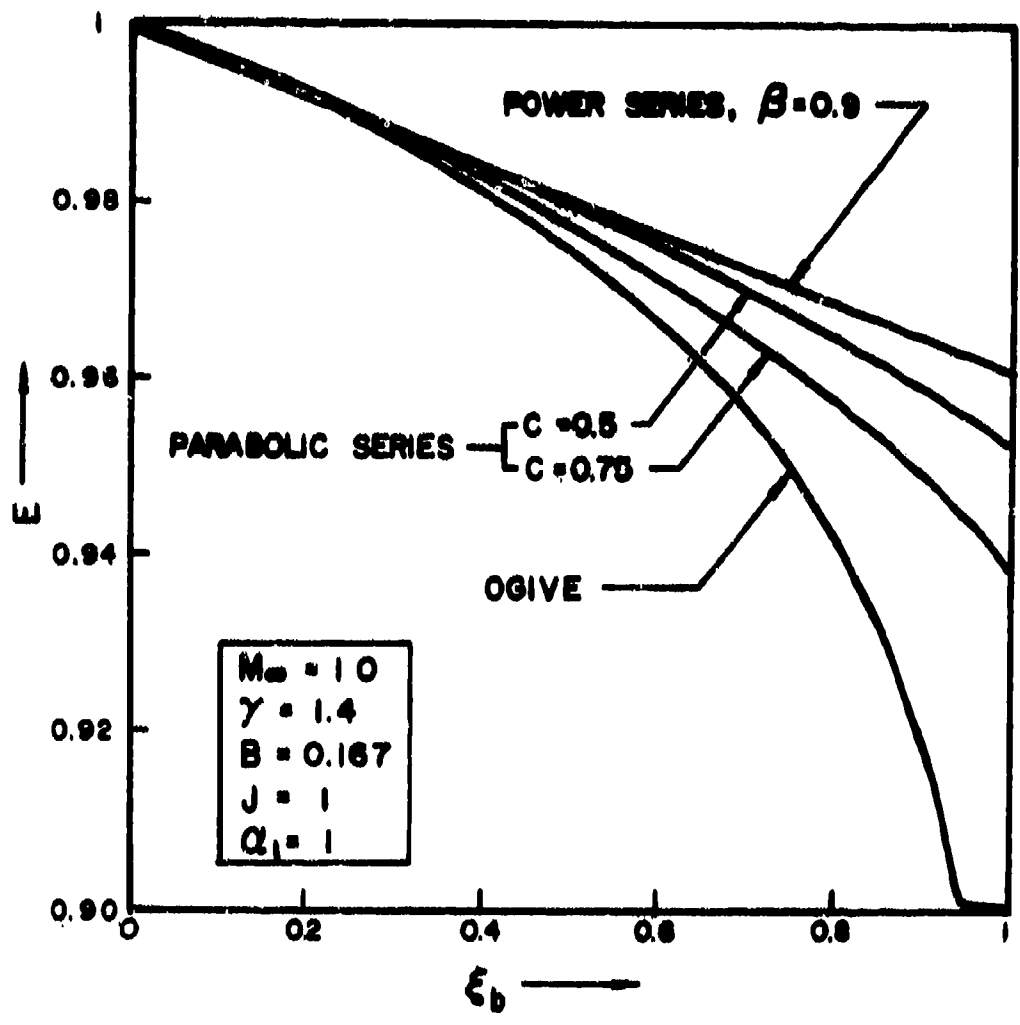


Figure 34. Collection Efficiencies for Various Body Shapes.

F-1

APPENDIX F

COMPUTER CODE FOR STRESS ANALYSIS OF
HYPERVELOCITY IMPACT

by

G. R. Buchanan and J. C. Huang
Associate Professors of Engineering Science
Tennessee Technological University
Cookeville, Tennessee 38501

APPENDIX F
 COMPUTER CODE FOR STRESS ANALYSIS OF
 HYPERVELOCITY IMPACT

by G. R. Buchanan and J. C. Huang

THEORETICAL ANALYSIS

The mathematical model for generating spherical elastic waves has been described by Kinslow [2]. To summarize briefly, it is assumed that there is a hollow, hemispherical cavity in the layer of material with its center at the point of impact and that a time-varying pressure or forcing function is applied to this imaginary cavity surface which generates stress waves in the material. The pressure applied to the surface of the cavity is an impulse described by the relation

$$P = P_0 \sum K_i e^{-\alpha_i t} \quad (1)$$

where P_0 is the pressure, α_i are decay constants, t is the time, and the K_i are constants. In this report only two terms have been considered and Eq. (1) reduces to

$$P = P_0 (K_1 e^{-\alpha_1 t} - K_2 e^{-\alpha_2 t}) \quad (2)$$

The propagation of spherical dilatational waves in a homogeneous, isotropic material can be studied using the spherical wave equation

$$\nabla^2 \phi = \frac{1}{c^2} \frac{\partial^2 \phi}{\partial t^2} \quad (3)$$

where ϕ is a scalar displacement potential, c is the wave speed, and t is time. The solution of Eq. (3) may be written as in [1]

$$\phi = \frac{P_0 r_0}{\rho_p [\omega_0^2 + (\alpha_0 - \alpha)^2]} e^{-\alpha r} + e^{-\alpha_0 r} \left(\cos \omega_0 \tau + \frac{\alpha_0 - \alpha}{\omega_0} \sin \omega_0 \tau \right) \quad (4)$$

where P_0 is peak pressure, α is a time-decay constant, time t is measured from arrival time of wave front, r_0 is radius of cavity, ν is Poisson's ratio, and

$$\alpha_0 = \frac{c(1-2\nu)}{r_0(1-\nu)} \quad (5)$$

$$\omega_0 = \frac{c(1-2\nu)^{\frac{1}{2}}}{r_0(1-\nu)} \quad (6)$$

$$\tau = t - (r - r_0)/c \quad (7)$$

$$c = (\lambda + 2\mu)/\rho \quad (8)$$

where λ and μ are Lamé's constants and ρ is the density of target material.

The radial and tangential stresses at a given point P inside the target are given by the following relations

$$\sigma_r = (\lambda + 2\mu) \frac{\partial u}{\partial r} + 2\lambda \left(\frac{u}{r}\right) \quad (9)$$

$$\sigma_{t_\theta} = \sigma_{t_\phi} = \lambda \frac{\partial u}{\partial r} + 2(\lambda + \mu) \left(\frac{u}{r}\right) \quad (10)$$

where $u = \frac{\partial \phi}{\partial r}$ is the particle displacement.

Consider the coordinate system of Figure 1. The location of an impact on a plane surface (the x - y plane) is designated as O_1 and is given by the coordinates (x_{01}, y_{01}) . The location of any point P at which the principal stresses are desired is specified by the coordinates (x, y, z) or (PX, PY, PZ) . For the computation of stresses resulting from an impact at O_1 , the coordinates (x_1, y_1, z_1) are employed, where

$$x_1 = PX - X_{01} \quad (11)$$

$$y_1 = PY - Y_{01} \quad (12)$$

$$z_1 = PZ \quad (13)$$

The location of P may also be specified by the coordinates (r_1, θ_1, ϕ_1) .

The following derivation of the components of stress at point P are relative to the O_1 coordinate system. For the sake of simplicity the subscript is omitted from the following equations.

The relations between the (x_1, y_1, z_1) and the (r_1, θ_1, ϕ_1) coordinates are

$$x = r \sin\phi \cos\theta \quad (14)$$

$$y = r \sin\phi \sin\theta \quad (15)$$

$$z = r \cos\phi \quad (16)$$

The direction cosines of the positive r-axis have components in the (x, y, z) system as follows

$$\cos(x, r) = \partial x / \partial r = \sin\phi \cos\theta \quad (17)$$

$$\cos(y, r) = \partial y / \partial r = \sin\phi \sin\theta \quad (18)$$

$$\cos(z, r) = \partial z / \partial r = \cos\phi \quad (19)$$

Similarly, the direction cosines of the tangential θ and ϕ axes are respectively

$$\cos(x, t_\theta) = (1/r \sin\theta)(\partial x / \partial \theta) = -\sin\theta \quad (20)$$

$$\cos(y, t_\theta) = (1/r \sin\theta)(\partial y / \partial \theta) = \cos\theta \quad (21)$$

$$\cos(z, t_\theta) = 0 \quad (22)$$

and

$$\cos(x, t_\phi) = (1/r)(\partial x / \partial \phi) = \cos\phi \cos\theta \quad (23)$$

$$\cos(y, t_\phi) = (1/r)(\partial y / \partial \phi) = \cos\phi \sin\theta \quad (24)$$

$$\cos(z, t_\phi) = (1/r)(\partial z / \partial \phi) = -\sin\phi \quad (25)$$

where

$$r = \sqrt{x^2 + y^2 + z^2} \quad (26)$$

$$\sin\phi = \sqrt{x^2 + y^2} / r \quad (27)$$

$$\cos\phi = z / r \quad (28)$$

$$\sin\theta = y / \sqrt{x^2 + y^2} \quad (29)$$

$$\cos\theta = x/\sqrt{x^2 + y^2} \quad (30)$$

As the spherical wave propagates through the material, the radial and tangential stresses having values given by Eqs. (9) and (10), respectively, are shown acting on an elemental volume in Figure 2. At any point, P, and for any time, the six cartesian components of stress relative to the

$[\sigma, \kappa, y, z]_1$ coordinate system may be computed from the following relations

$$[\sigma_x]_1 = [\sigma_{t\theta} \cos^2(x, t_\theta) + \sigma_{t\phi} \cos^2(x, t_\phi) + \sigma_r \cos^2(x, r)]_1 \quad (31)$$

$$[\sigma_y]_1 = [\sigma_{t\phi} \cos^2(y, t_\phi) + \sigma_r \cos^2(y, r) + \sigma_{t\theta} \cos^2(y, t_\theta)]_1 \quad (32)$$

$$[\sigma_z]_1 = [\sigma_r \cos^2(z, r) + \sigma_{t\theta} \cos^2(z, t_\theta) + \sigma_{t\phi} \cos^2(z, t_\phi)]_1 \quad (33)$$

$$[\tau_{xy}]_1 = [\sigma_{t\theta} \cos(x, t_\theta) \cos(y, t_\theta) + \sigma_{t\phi} \cos(x, t_\phi) \cos(y, t_\phi) + \sigma_r \cos(x, r) \cos(y, r)]_1 \quad (34)$$

$$[\tau_{yz}]_1 = [\sigma_{t\phi} \cos(y, t_\phi) \cos(z, t_\phi) + \sigma_r \cos(y, r) \cos(z, r) + \sigma_{t\theta} \cos(y, t_\theta) \cos(z, t_\theta)]_1 \quad (35)$$

$$[\tau_{zx}]_1 = [\sigma_r \cos(z, r) \cos(x, r) + \sigma_{t\phi} \cos(z, t_\phi) \cos(x, t_\phi) + \sigma_{t\theta} \cos(z, t_\theta) \cos(x, t_\theta)]_1 \quad (36)$$

These components of stress resulting from each of the several impacts could be added as follows:

$$\sigma_x = [\sigma_x]_1 + [\sigma_x]_2 + [\sigma_x]_3 + \dots \quad (37)$$

$$\sigma_y = [\sigma_y]_1 + [\sigma_y]_2 + [\sigma_y]_3 + \dots \quad (38)$$

$$\sigma_z = [\sigma_z]_1 + [\sigma_z]_2 + [\sigma_z]_3 + \dots \quad (39)$$

$$\tau_{xy} = [\tau_{xy}]_1 + [\tau_{xy}]_2 + [\tau_{xy}]_3 + \dots \quad (40)$$

$$\tau_{xz} = [\tau_{xz}]_1 + [\tau_{xz}]_2 + [\tau_{xz}]_3 + \dots \quad (41)$$

$$\tau_{yz} = [\tau_{yz}]_1 + [\tau_{yz}]_2 + [\tau_{yz}]_3 + \dots \quad (42)$$

These six components of stress are now substituted in the following cubic equation:

$$S^3 - (\sigma_x + \sigma_y + \sigma_z)S^2 + (\sigma_x\sigma_y + \sigma_y\sigma_z + \sigma_z\sigma_x - \tau_{xy}^2 - \tau_{yz}^2 - \tau_{zx}^2)S - (\sigma_x\sigma_y\sigma_z - \sigma_x\tau_{yz}^2 - \sigma_y\tau_{zx}^2 - \sigma_z\tau_{xy}^2 + 2\tau_{xy}\tau_{yz}\tau_{zx}) = 0 \quad (43)$$

The roots of this equation are the three principal stresses.

DEFINITION OF VARIABLES

ALPHA(1) = α_1 , time-decay constant

ALPHA(2) = α_2 , time-decay constant

AMDA = λ , Lamé's constant

C1 = $(\frac{\lambda+2\mu}{\rho})^{\frac{1}{2}}$, dilatational wave speed

C2 = $(\frac{\mu}{\rho})^{\frac{1}{2}}$, shear wave speed

D = Raindrop diameter

E = Young's modulus

ICODE = 1 for calling subroutine DATGEN to calculate P_0 , α_1 , α_2 , and r_0

JCODE = 1 for calling subroutine PRIDIR to calculate principal direction for the maximum tensile stress

JJJJ = Problem number counter

NINI = Total number of problems to be run

NUMBER = Number of ALPHA terms used

POWER = Exponential power of the weighted function for peak pressure P_0

PR = Poisson's ratio

PSUBO = P_0 , peak pressure of cavity

PX = x-coordinate of point P where stress is to be calculated

PXINC = Increment of PX

PXMAX = Maximum value of PX to be incremented

PY = y-coordinate of point P

PYINC = Increment of PY
PYMAX = Maximum value of PY
PZ = z-coordinate of point P
PZINC = Increment of PZ
PZMAX = Maximum value of PZ
RHO = ρ , density of radome material
RSUBO = r_0 , initial radius of cavity
SG(1) = Plus sign
SG(2) = Minus sign
TDELAY = Delay time
TIME = t, time variable
TINCR = Time increment
TMAX = Maximum time to be considered
TMIN = Initial time
TF = Target thickness
X1 = $x_01 - PX$
X01 = x-coordinate of impact cavity
Y1 = $y_01 - PY$
Y01 = y-coordinate of impact cavity
Z1 = PZ
ZR = Recess value of z to simulate normal pressure distribution
caused by impact of a raindrop on surface of target

EXPLANATION OF SUBROUTINES

CARTST Calculates the cartesian components of the stresses at point P resulting from the direct and reflect waves.
DISCOS Determines the direction cosines between impact cavities and point P.
PULSE Calculates the radial and tangential stresses from the wave's equation.

- THETA Calculates the angles ϕ_1 and ϕ_2 as shown in Figure 3.
- FRIDIR Calculates the principal direction for maximum tensile stress.
- DATGEN Generates the values P_0 , r_0 , α_1 , and α_2 .
- PRIST Calculates the principal stresses.
- CUBIC Solution of a cubic equation.
- QUAD Solution of a quadratic equation.

GUIDE FOR INPUT DATA

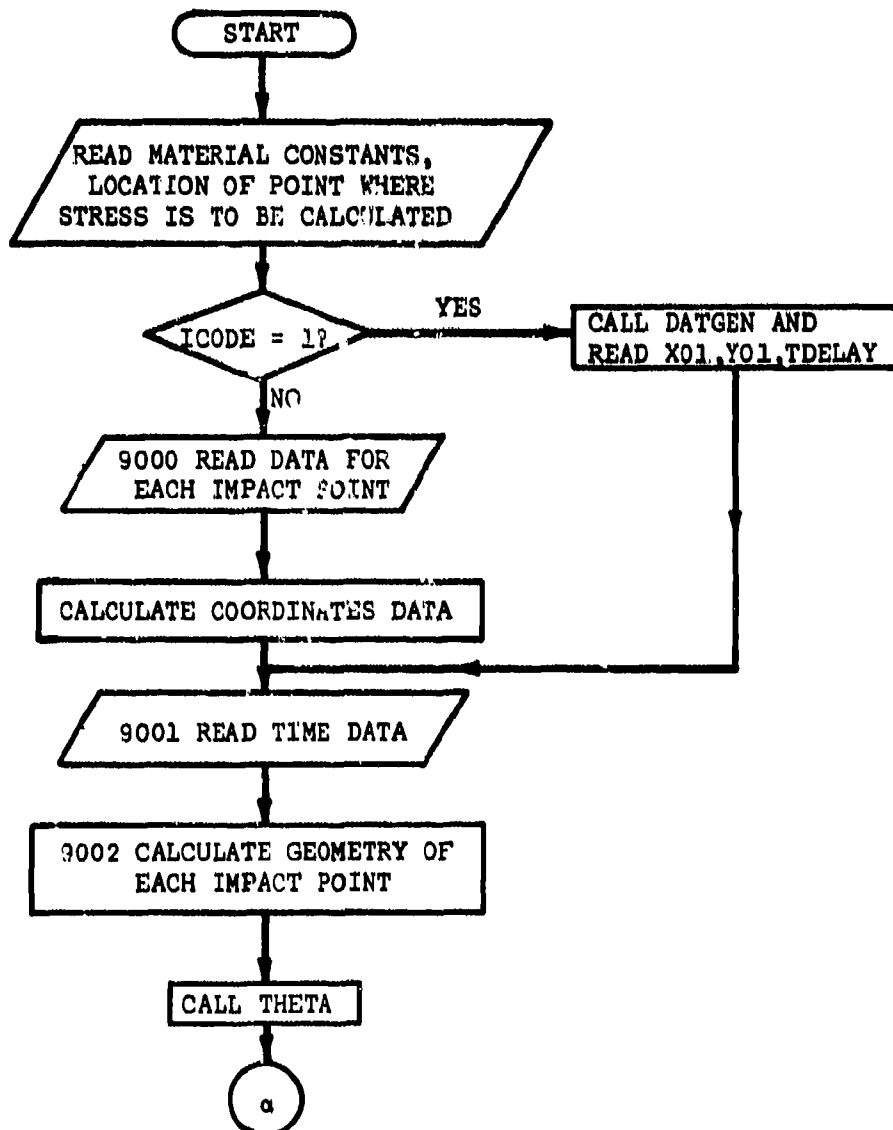
<u>Card</u>	<u>Fortran Name and Column Number</u>		<u>Format and Remarks</u>
1	NINI	1 - 2 (Right justified)	(I2)
2	E	1 - 10	(3F10.0)
	RHO	11 - 20	
	PR	21 - 30	
3	PX	1 - 10	(4F10.0)
	PY	11 - 20	
	PZ	21 - 30	
	ZR	31 - 40	
4	PXINC	1 - 10	(6F10.0)
	PXMAX	11 - 20	These six values
	PYINC	21 - 30	increment the initial
	PYMAX	31 - 40	coordinates given in
	PZINC	41 - 50	card 3
	PZMAX	51 - 60	
5	TT	1 - 10	(F10.0)
6	POWER	1 - 10	(F10.0,2I5,2F10.0)
	ICODE	11 - 15 (Right justified)	Omit cards 7, 8, 9 if
	JCODE	16 - 20 (Right justified)	ICODE = 1
	V	21 - 30	
	D	31 - 40	
7	NUMBER	1 - 2 (Right justified)	(I2,2F10.0)
	PSUBO	3 - 12	Omitted if ICODE = 1
	RSUBO	13 - 22	repeated for each
			impact location if
			ICODE \neq 1
8	ALPHA(1)	1 - 10	(2F10.0)
	SG(?)	11 - 20	Omitted if ICODE = 1
			repeated for each
			impact location if
			ICODE \neq 1

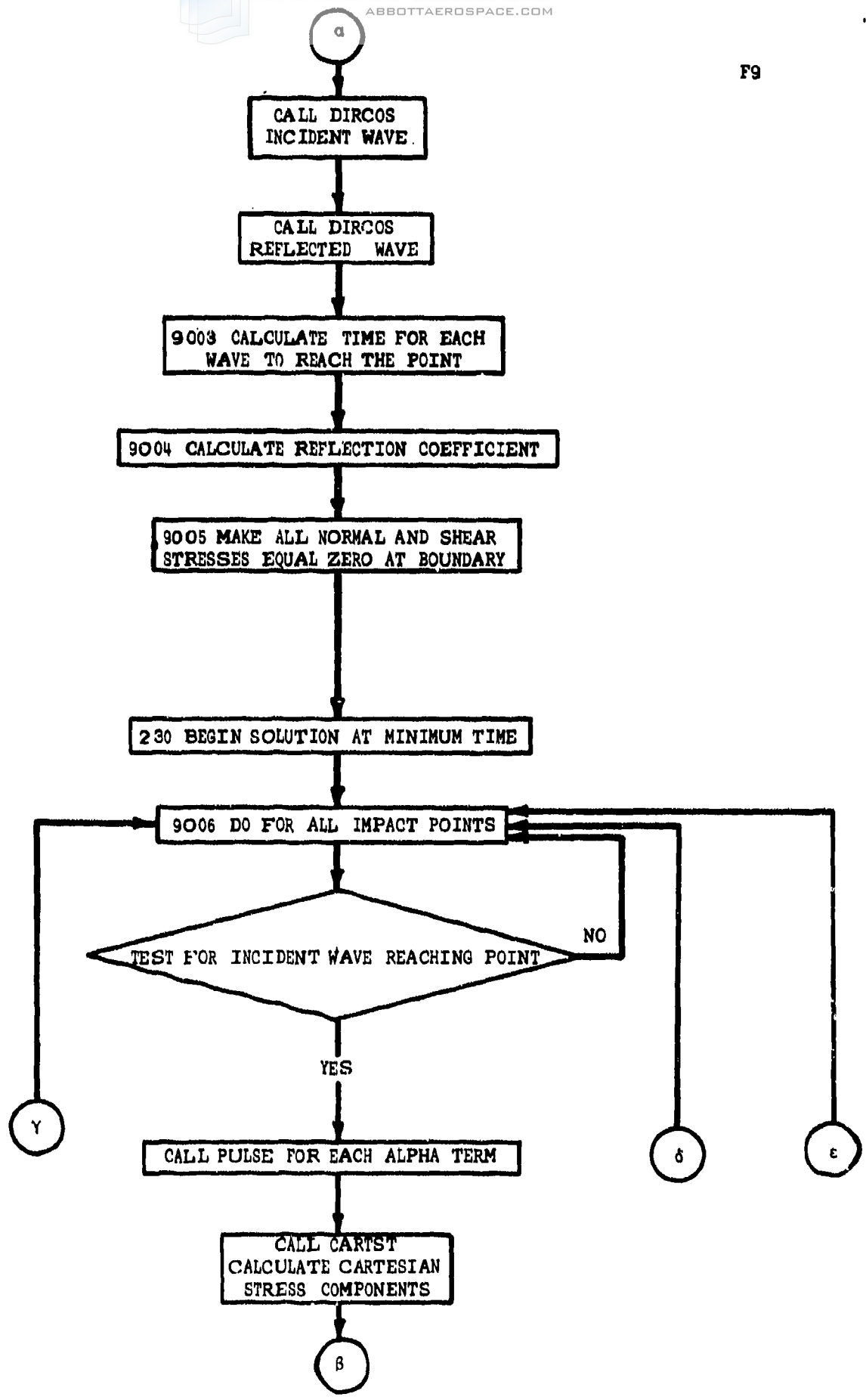
9	ALPHA(2) 1 - 10 SG(2) 11 - 20	(2F10.0) Omitted if ICODE = 1 repeated for each impact location if ICODE ≠ 1
10	X01 1 - 10 Y01 11 - 20 TDELAY 21 - 30	(3F10.0) Repeated for each impact location

Cards 7, 8, 9, and 10 are repeated for each impact location if ICODE ≠ 1. Otherwise only card 10 is repeated.

Last Card	TMIN 1 - 10 TINCR 11 - 20 TMAX 21 - 30	(3F10.0)
-----------	--	----------

FLOW CHART





DISCUSSION OF THE PROGRAM

The computer program is composed of the mainline program and nine subroutines. The mainline program is divided into three basic DO loops. The first DO loop reads the load functions and coordinate location of the impact points. The second DO loop computes the geometrical relations between the impact locations and the point where the stresses are to be calculated. The third DO loop calculates the normal and shear stresses due to each impact. The principal stresses and directions are then calculated and the computer goes through a series of logical comparisons to determine if another solution is desired for a different time or location.

The detailed discussion of the program will begin with the mainline program and will be referenced to the various comment statements and statement numbers.

The program is limited to an analysis using twenty impact locations. This number can be increased by merely changing the dimension size of the variables in the dimension statements. The number of Alpha exponents as given in Eq. (1) is limited to two, but can be increased by increasing the dimensions of Alpha and Sg.

The statements which appear as $SIN(X) = DSIN(X)$ merely change the standard library functions to double precision.

The first READ statement defines Young's modulus, material density, and Poisson's ratio (E, RHO, PR) which are constant for any given material. The second data card contains the actual number of impacts (IMPACS). The third data card gives the coordinate location of the point where the stresses are to be calculated, (PX, PY, PZ), as illustrated in Eqs. (11) through (13) and Figure 1, and ZR, the recess value of Z, to simulate the normal pressure distribution of a raindrop. The fourth data card allows

the coordinate location of PX, PY, or PZ to be changed in order to calculate stresses at more than one point. The fifth data card contains the target thickness (TT) which is the thickness of the layer of material. The sixth data card specifies POWER, which allows the peak pressure P_0 at each impact cavity to be weighted, and ICODE, JCODE, V, and D. Subroutine DATGEN will be called to generate the values of P_0 , r_0 , α_1 , and α_2 if ICODE = 1. Subroutine PRIDIR will be called to determine the principal direction of the maximum tensile stress if JCODE = 1. V is the velocity of the radome in ft/sec. D is raindrop diameter in mm.

If ICODE \neq 1, additional data cards are read in the first DO loop, which ends at statement 500. There are four data cards for each impact location: the first contains NUMBER, which is the number of Alpha terms in Eq. (1); PSUB0, the pressure P_0 in Eq. (1); and RSUB0 the radius of the spherical cavity, r_0 . The following data cards are determined by NUMBER. For Eq. (2), NUMBER is equal to 2; therefore, two data cards follow--the first contains α_1 and K_1 , the second contains α_2 and K_2 corresponding to Eq. (2). These quantities are named ALPHA (I,J) and SG(I,J) in the program. If both K_1 and K_2 in Eq. (2) are equal to one, then $SG(1,J) = 1$ and $SG(2,J) = -1$. The next data card contains the location of the impact cavity (X01,Y01) as given in Eqs. (11) and (12) and TDELAY which is the delay time for that cavity. If TDELAY is zero for all impacts, they will occur simultaneously; however, by specifying a positive delay time, the impacts may occur at random times. This sequence of data cards is repeated for each impact.

The remaining data card contains the time at which the solution should begin (TMIN), the time increment for intermediate solutions (TINCR), and the maximum time (TMAX). It should be noted that time quantities are entered in units of microseconds; hence, each time quantity is multiplied by 10^{-6} . Similarly, α_1 and α_2 are multiplied by 10^6 .

The second DO loop ends on statement 501 and generates the geometrical relations for each impact location. The first statement in the DO loop determines R1 given by Eq. (26). Subroutine THETA then calculates the angles ϕ_1 and ϕ_2 as illustrated in Figure 3. These angles are named T1 and T2, respectively, in the subroutine. The value of Z2 (Figure 3) is calculated for later use. In Figure 3, the point O' is the location of the spherical cavity which generates the reflected wave. This technique of solution is discussed in detail by Kinslow [3].

The subroutine DIRCOS is called next to determine the direction cosines for the impact cavity on the surface of the layer and then called again to calculate the direction cosines for the fictitious cavity, O', which generates the reflected dilatational wave. The subroutine DIRCOS corresponds directly to Eqs. (17) through (30). The notation in the mainline program may be interpreted as CXT1 meaning $\cos(X, \theta)$ where the 1 denotes the cavity on the surface, CXT2 denotes $\cos(X, \theta)$ for the fictitious cavity at O' (Figure 3).

The pressure input can be modified after the $\cos \phi$ has been calculated in subroutine DIRCOS for the cavity on the surface. The pressure input P_o can be weighted as

$$P_o = P_o (\cos \phi_1)^P \quad (44)$$

where p is the quantity called POWER in the program. Equation (44) appears in the program as

$$PSUBO(J) = (CZF1(J))*POWER$$

If this modification is not desirable, POWER may be read in as zero.

The quantities T1STRT and T2STRT are the times required for the incident wave and reflected wave to reach point P, respectively. The quantities ALSUBO and WLSUBO denote α_o and ω_o respectively (see Eqs. (5) and (6)). The

reflection coefficients are calculated next according to the theory developed by Kinslow [3]. The equations (31 and 32) given by Kinslow [3] are

$$1 + \bar{K}_1[1 + (1-2\nu)\cos 2\phi_2] + 2\bar{K}_2(1-\nu)\sin 2\phi_s = 0$$

and

$$1 - \bar{K}_1[(1-2\nu)\sin 2\phi_2] + 2\bar{K}_2(1-\nu)\cos 2\phi_s = 0$$

where \bar{K}_1 is COEFF1 the reflection coefficient for the dilatational wave, \bar{K}_2 is COEFF2 the reflection coefficient for the reflected shear wave, ϕ_2 is defined in Figure 3, and ϕ_s is the corresponding angle of reflection for a shear wave. The shear wave has been omitted in the analysis; hence, ϕ_s is not illustrated in Figure 3 and COEFF2 is not used in the program, except to calculate COEFF1. Note that the value of ϕ_2 is calculated in the subroutine THETA and is designated T2 in that subroutine; but appears as T1 in the mainline program.

The next sequence of statements merely initializes all radial and tangential stresses to zero.

The third DO loop, which ends at statement 502, contains the necessary operations to calculate the stresses. First, the time (TAU1) is calculated, which is the real time minus the time required for the wave to reach the point, minus the delay time. The subroutine PULSE is called twice, in a DO loop ending at statement 11, once for the α_1 term and once for the α_2 term. SR1 and ST1 are the radial and tangential stresses calculated in subroutine PULSE. The subroutine CARTST is then called to calculate the cartesian components of stress. Subroutine CARTST relates to Eqs. (31) through (36). Next, the computer will calculate the time (TAU2) required for the reflected dilatational wave to reach the point. If the reflected wave has reached the point in question, subroutine PULSE is

again used to calculate the radial and tangential stresses. If TAU2 is negative, indicating that the reflected wave has not reached the point, the computer will bypass the stress calculation. If the reflected wave is to be included, the stresses calculated in subroutine PULSE are multiplied by the proper reflection coefficient and subroutine CARTST is called to calculate the stresses in the cartesian coordinate system.

The next DO loop, ending on statement 503, sums up all the stresses due to multiple impacts at a given time according to Eqs. (37) through (42). Subroutine PRIST is called, and the principal stresses are calculated by solving for the roots of Eq. (43). The principal stresses are then printed, along with other identifying information, and the computer will compare the time for the calculation just completed with the maximum time (TMAX) to determine if another solution is desired. If the time comparison indicates that TMAX has been reached, the computer will test the current value of PZ against PZMAX to determine if additional solutions are desired. If so, PZ is increased by PZINC and the time is set equal to TMIN, and new solutions are obtained for each time increment. If PZ is equal to PZMAX, a comparison is made using PX and PXMAX, then a comparison using PY and PYMAX. If PZ, PX, and PY have reached their maximum values, the computer calls the EXIT routine and ends.

REFERENCES

1. Allen, W. A. and Goldsmith, W. (1955), "Elastic Description of a High-Amplitude Spherical Pulse in Steel," J. of Appl. Physics, Vol. 26, No. 1, pp. 69-74.
2. Kinslow, R. (1963), "Properties of Spherical Stress Waves Produced by Hypervelocity Impact," AEDC-TDR-63-197 (AD 421 57D).
3. Kinslow, R. (1969), "Properties of Reflected Stress Waves," AIAA, Hypervelocity Impact Conference, Cincinnati, Ohio, AIAA Paper No. 69-363.
4. Kinslow, R., Sahai, V., and Peddieson, Jr., J. (1972), "Preliminary Investigation of High-Velocity Liquid Impact Damage," Tenn. Tech. Univ., TTU-ES-72-2.

LISTING OF THE COMPUTER PROGRAM

```

C          SPHERICAL WAVE PROPAGATION
C          M A I N L I N E
C          IMPLICIT REAL*8(A-H,O-Z)
C          LIMIT OF IMPACT POINTS IS 20
C          NUMBER OF ALPHA EXPONENTS IN EACH INPUT FUNCTION IS
C          2
COMMON/CONTR/ PX, PY, PZ, IMPACT
COMMON      RSUBO(20), PWSUBO(20), ALPHA(2,20), SG(2,20)
1, NUMBER(20)      , X01(20), Y01(20), X1(20), Y1(20), Z1
2(20)              , TDELAY(20) , PSAVE(20)
DIMENSIONR1(20), SRZ(20), ST1(20), STR(20), Z2(20)
DIMENSIONR1(20), RXY(20), T1D(20), T2D(20), R2(20)
DIMENSIONT1STRT(20), T2STRT(20), ALSUBO(20), WLSUBO(20)
1, COEFF1(20), COEFF2(20)
DIMENSIONSX1(20), SY1(20), SZ1(20), TXY1(20), TYZ1(20)
1, TZX1(20)
DIMENSIONSX2(20), SY2(20), SZ2(20), TXY2(20), TYZ2(20)
1, TZX2(20)
DIMENSIONCXT1(20), CYT1(20), CZT1(20), CXP1(20), CYP1(20)
1, CZP1(20), CXR1(20), CYR1(20), CZR1(20), CXT2(20), CYT2(20)
2, CZT2(20), CXP2(20), CYP2(20), CZP2(20), CXR2(20), CYR2(20)
3, CZR2(20)
SIN(X)=DSIN(X)
COS(X)=DCOS(X)
ATAN(X)=DATAN(X)
SQRT(X)=DSQRT(X)
EXP(X)=DEXP(X)
ABS(X)=DABS(X)
ARCSIN(X)=DASIN(X)
C          NOTE: "JJJJ" AND "NINI" CONSTITUTE A COUNTER FOR EASE
C          OF OPERATION
C          "NINI" IS THE NUMBER OF PROBLEMS TO BE RUN.
C          READ(5,130) NINI
C          JJJJ= 1
C          READ YOUNGS MOD., DENSITY, POI. RATIO
33 CONTINUE
WRITE(6,51) JJJJ, NINI
51 FORMAT('1', ' THIS IS PROBLEM', I5, 'X', ' OF', I5, 'X'
1, ' PROBLEMS: ' //)

C          IF E= 500 000.0 AND RHO= 0.00011 ARE ENTERED ON DATA
C          INPUT CARDS I
C          THIS PROGRAM, THEN THE COMPUTER ASSUMES:
C
C          E= 500 000.0 PSI
C          AND RHO= 0.11 X 10**9 (LB)*(MICROSEC**
C          *2)*(INCH**4)
    
```



```

C           ALSUBO AND WLSUBO ARE DEFINED IN
C           SUBROUTINE PULSE
C           ALSUBO(J)=DUM*C1/RSUBO(J)
C           DUM=SQRT(1.-2.*PR)/(1.-PR)
C           WLSUBO(J)=DUM*C1/RSUBO(J)

C           CALCULATE REFLECTION COEFFICIENTS COEFF1 AND
C           COEFF2
9004 AK=(1.+(1.-2.*PR)*COS(2.*T1))
      STS=SIN(T1)/C3
      TS=ASIN(STS)
      BK=2.*SIN(2.*TS)*(1.-PR)
      CK=(1.-2.*PR)*SIN(2.*T1)
      DK=2.*COS(2.*TS)*(1.-PR)
      COEFF2(J)=2.*CK/(DK+(BK*CK)/AK)
      COEFF1(J)=1.-COEFF2(J)*BK/AK
9005 SX1(J)=0.
      SY1(J)=0.
      SZ1(J)=0.
      TX1(J)=0.
      TY1(J)=0.
      TZ1(J)=0.
      SX2(J)=0.
      SY2(J)=0.
      SZ2(J)=0.
      TX2(J)=0.
      TY2(J)=0.
      TZ2(J)=0.
501 CONTINUE

C           STATEMENT 501 ENDS THE LOOP WHICH CALCULATES THE
C           GEOMETRY OF
C
C           THE IMPACT POINTS
C
C
C           BEGIN SOLUTION WHEN FIRST WAVE REACHES POINT P
230 TIME=TMIN
      IF((TMAX-TMIN)/TINCR.LT.15.)GO TO 519
      WRITE(6,3015)
3015 FORMAT('1')
      GO TO 520
519 WRITE(6,800)
800 FORMAT('1'////)
520 PZZ=PZ-ZR
      WRITE (6,1301) ZR
1301 FORMAT (5X,' RECESS VALUE OF Z = ',F10.5,/)
      WRITE (6,3005) PX,PY,PZZ
3005 FORMAT('14X'PX=',F8.3,4X,'PY=',F8.3,4X,'PZ=',F8.3,/,
1 4X'TIME'7X'BX'9X'BY'9X'BZ' 8X'TXY' 8X'TYZ'8X'TZX'9X'P
21'9X'P2'9X'P3'4X'MAX SHEAR'2X'THETA'2X'PHI'/)
    
```

```

      SXMAX=0.
      SZMAX=0.
      SYMAX=0.
      SZMAXT =0.
30 CONTINUE
9006 DO 502 J=1,IMPACS
      SR1(J)=0.
      SR2(J)=0.
      ST1(J)=0.
      ST2(J)=0.
      TAU1=TIME-T1STRT(J)-TDELAY(J)
      IF(TAU1) 502,21,21
C      IF TAU IS NEGATIVE THE WAVE HAS NOT
C REACHED THE POIN
21 CONTINUE
      NUM=NUMBER(J)
C      NUMBER DEFINES THE NUMBER OF ALPHA TERMS
C IN EACH
C INPUT FUNCTION
      DO 11 I=1,NUM
      ALPH=ALPHA(I,J)
      CALL PULSE(ALPH,PSUBO(J),RSUBO(J),WLSUBO(J),ALSUBO(J)
      ,1,RHO,TAU1,C1,R1(J),G,AMDA,U,V,W,SRR,STT)
      SR1(J)=SR1(J)+SQ(I,J)*SRR
11 ST1(J)=ST1(J)+SQ(I,J)*STT
      CALL CARTST(SR1(J),ST1(J),ST1(J),CXR1(J),CYR1(J),CZR1
      1(J),CXT1(J),CYT1(J),CZT1(J),CXP1(J),CYP1(J),CZP1(J)
      2, SX1(J),SY1(J),SZ1(J),TXY1(J),TYZ1(J),TZX1(J))
13 TAU2 =TIME-T2STRT(J) -TDELAY(J)
      IF (TAU2) 502,113,113
113 CONTINUE
      DO 14 I=1,NUM
      ALPH=ALPHA(I,J)
      CALL PULSE(ALPH,PSUBO(J),RSUBO(J),WLSUBO(J),ALSUBO(J)
      ,1,RHO,TAU2 ,C1,R2(J),G,AMDA,U,V,W,SRR,STT)
C
C
      SR2(J)=SR2(J)+SQ(I,J)*SRR
14 ST2(J)=ST2(J)+SQ(I,J)*STT
      SR2(J)=SR2(J)+COEFF1(J)
      ST2(J)=ST2(J)+COEFF1(J)
      CALL CARTST(SR2(J),ST2(J),ST2(J),CXR2(J),CYR2(J),CZR2
      1(J),CXT2(J),CYT2(J),CZT2(J),CXP2(J),CYP2(J),CZP2(J)
      2, SX2(J),SY2(J),SZ2(J),TXY2(J),TYZ2(J),TZX2(J))
12 CONTINUE
502 CONTINUE
      SXTOT=0.
      SYTOT=0.
      SZTOT=0.
      TXYTO=0.
      TYZTO=0.

```

```

TZXT0=0.
9007 DO 503 J=1,IMPAC6
      SXTOT=SXTOT+SX1(J)+SX2(J)
      SYTOT=SYTOT+SY1(J)+SY2(J)
      SZTOT=SZTOT+SZ1(J)+SZ2(J)
      TXYTO=TXYTO+TXY1(J)+TXY2(J)
      TYZTO=TYZTO+TYZ1(J)+TYZ2(J)
      TZXT0=TZXT0+TZX1(J)+TZX2(J)
503  CONTINUE
      IF(SXTOT.EQ.0.0.AND.SYTOT.EQ.0.0.AND.SZTOT.EQ.0.0) GO
1    TO20
      SXTOT=-SXTOT
      SYTOT=-SYTOT
      SZTOT=-SZTOT
      IF(SXTOT.EQ.SYTOT.AND.SYTOT.EQ.SZTOT.AND.SZTOT.EQ.SXTO
1    T)P1=SXTOT;P2=SYTOT;P3=SZTOT; GO TO 504
      CALL PRIST(SXTOT,SYTOT,SZTOT,TXYTO,TYZTO,TZXT0,P1,P2
1    ,P3,SMAX)
504  CONTINUE
      IF(JCODE.EQ.0) P=0.0; GO TO 601
      CALL PRIDIR(SXTOT,SYTOT,SZTOT,TXYTO,TYZTO,TZXT0,P1,P2
1    ,P3,P,TH1,PH1)
601  CONTINUE
C    WRITE THE PRINCIPAL STRESSES AND TIME
      TYME=TIME+1.0E+06
      IF(ABS(P1).LT.1.0 .AND. ABS(P2).LT.1.0 .AND. ABS
1    (P3).LT.1.0 .AND. ABS(SMAX).LT.1.0) GO TO 20
      IF(P.EQ.0.0) WRITE(6,2000) TYME,SXTOT,SYTOT
1    ,SZTOT,TXYTO,TYZTO,TZXT0,P1,P2,P3,SMAX; GO TO 20
      WRITE(6,2000) TYME,SXTOT,SYTOT,SZTOT,TXYTO
1    ,TYZTO ,TZXT0,P1,P2,P3,SMAX,TH1,PH1
2000 FORMAT(' ' F7.3 ,10F11.2,2F7.2)
20  CONTINUE
      TIME= TIME+TINCR
      IF(TIME=TMAX) 32,31,31
32  CONTINUE
      IF(SXTOT.LT.SXMAX) SXMAX=SXTOT
      IF(SZTOT.LT.SZMAX) SZMAX=SZTOT
      IF(SYTOT.LT.SYMAX) SYMAX=SYTOT
      IF(SZTOT.GT.SZMAXT) SZMAXT=SZTOT
      GO TO 30
31  CONTINUE
      IF (SZMAXT .EQ. 0.0) GO TO 6100
      WRITE (6,6003) SZMAXT
6003 FORMAT (5X,/, 'THE MAX. COMPRESSIVE STRESS =',F20.5)
      WRITE (6,6004)
6004 FORMAT (/,3X, 'THE MAX. TENSILE STRESSES: ',/)
      WRITE(6,6001) SXMAX,SZMAX,SYMAX
6001 FORMAT(1X, 'SXMAX=',F20.5,4X, 'SZMAX=',F20.5,4X,
1    'SYMAX=',F20.5//)
6100 CONTINUE
    
```

```

IF(PZINC.EQ.0.0) GO TO 508
IF(PZ.GE.PZMAX) GO TO 508
PZ=PZ+PZINC
IF(PZ.LE.TT) GO TO 600
PZ=TT
600 GO TO 511
508 IF(PX.GE.PXMAX) GO TO 509
IF(PXINC.EQ.0.0) GO TO 509
PX=PX+PXINC
PZ=PZONE
GO TO 511
509 IF(PY.GE.PYMAX) GO TO 505
IF(PYINC.EQ.0.0) GO TO 505
PY=PY+PYINC
PX=PXONE
PZ=PZONE
511 DO 507 J=1,IMPACT
X1(J)=PX-X02(J)
Y1(J)=PY-Y02(J)
507 Z1(J)=PZ
GO TO 506
505 JJJJ=JJJJ+1
IF(JJJJ.LE.NINI) GO TO 33
CALL EXIT
END
IMPLICIT REAL*8(A-H,O-Z)
SUBROUTINE CARTST(SR,ST,SP,CXR,CYR,CZR,CXTT,CYTT,CZTT
1,CXTP,CYTP,CZTP,IX,IB,IZ,IXY,ITY,ITZ)
SUBROUTINE TO CALCULATE THE CARTESIAN
COMPONENTS
OF STRESS
EQUATIONS 4.32 THROUGH 4.37
BX=ST+CXTT**2+SP*CXTP**2+SR*CXR**2
BY=ST+CYTT**2+SP*CYTP**2+SR*CYR**2
BZ=ST+CZTT**2+SP*CZTP**2+SR*CZR**2
TXY=ST*CXTT*CYTT+SP*CXTP*CYTP+SR*CXR*CYR
TYZ=SP*CYTP*CZTP+SR*CYR*CZR+ST*CYTT*CZTT
TZX=SR*CZR*CXR+ST*CZTP*CXTP+SP*CZTT*CXTT
R E T U R N
E N D
IMPLICIT REAL*8(A-H,O-Z)
SUBROUTINE DIRCOS(X1,Y1,Z1,R1,RIX,CXTT,CYTT,CZTT,CXTP
1,CYTP,CZTP,CXR,CYR,CZR)
SUBROUTINE TO CALCULATE DIRECTION
COSINES BETWEEN
THE IMPACT POINT AND MATERIAL POINT
THE COORDINATES X1, Y1, Z1 IN MAINLINE
ARE USED
EQUATIONS 4.27 THROUGH 4.31 WILL BE
EVALUED
IF(X1.EQ.0.0.AND.Y1.EQ.0.0) CXTT=1./CYTT=0./CZTT=0./CX

```

C
C
C
C

C
C
C
C
C
C

```

1 TP=0./CYTP=1./CZTP=0./ CXR=0./CYR=0./CZR=1./ GO TO 5
  SINP=RX/R1
  COSP=Z1/R1
3  SINT=Y1/RXY
  COST=X1/RXY
  CXTT=-SINT
  CYTT=COST
  CZTT=0.
  CXTP=COSP+COST
  CYTP=COSP+SINT
  CZTP=-SINP
  CXR=SINP+COST
  CYR=SINP+SINT
  CZR=COSP
5  CONTINUE
   RETURN
    
```

```

1  END
  IMPLICIT REAL*(A-H,O-Z)
  SUBROUTINE PULSE(ALPHA,PSUBO,A,WSUBO,ASUBO,RHO,TAU,C1
1, R,AMU,AMDA,U,V,W,SR,ST)
  SIN(X)=DSIN(X)
  COS(X)=DCOS(X)
  ATAN(X)=DATAN(X)
  SQRT(X)=DSQRT(X)
  EXP(X)=DEXP(X)
  ABS(X)=DABS(X)
  ARSIN(X)=DARSIN(X)
  ASQ=WSUBO+WSUBO+(ASUBO-ALPHA)*(ASUBO-ALPHA)
  AA=SQRT(ASQ)
  BETA= ARSIN((ASUBO-ALPHA)/AA)
  B=PSUBO+A / (RHO+ASQ+WSUBO)
  IF ( ALPHA+TAU=90. 174. ) C=0.0/ GO TO 11
  C=WSUBO/EXP( ALPHA+TAU)
11 CONTINUE
  EAT=EXP(ASUBO+TAU)
  WMBETA=WSUBO+TAU-BETA
  D=AA+COS(WMBETA)/EAT
  H=AA+WSUBO+SIN(WMBETA)/EAT
  U2=-B*(D-C)
  F=ALPHA+C+ASUBO+D+H
  G=ALPHA+ALPHA+C+(WSUBO+WSUBO-ASUBO+ASUBO)+D=2.*ASUBO+H
  U1=B+F/C1
  V1=B+G/C1
  V2=B+F
  W1=-V1/C1
  W2=-2.*U1
  W3=-2.*U2
  RSQ=R*R
  U=U1/R+U2/RSQ
  V=V1/R+V2/RSQ
    
```

```

RCUBE=R*RBG
W=W1/R+W2/RBQ+W3/RCUBE
BR=(AMDA+2.*AMU)*W+2.*AMDA*U/R
** BT=AMDA*W+2.*(AMDA+AMU)*U/R
    
```

C
C
C
C

SEE - ALLEN AND GOLDSMITH, J OF APPL. PHYSICS,
 VOL.26, NO 1 J
 A=CAVITY RADIUS
 AMU= SHEAR MODULUS

```

RETURN
END
SUBROUTINETHETA(R1,RXY,X1,Y1,Z1,T1D,T2D,R2,TT,T2,Z2)
RXY=SQRT(X1*X1+Y1*Y1)
IF(RXY.EQ.0.0) GO TO 18
IF(Z1.EQ.0.0) T1=1.5708)GO TO 19
T1=RXY/Z1
T1=ATAN(T1)
GO TO 19
18 T1=0.
19 T1D=T1*180./3.1416
2 T2= RXY/(2.*TT-Z1)
T2=ATAN(T2)
T2D=T2*180./3.1416
IF(T2)4,5,4
5 R2=2.*TT-Z1
GO TO 6
4 R2=RXY/SIN(T2)
6 CONTINUE
Z2=Z1-Z.*TT
RETURN
END
IMPLICIT REAL*8(A-H,O-Z)
SUBROUTINE PRIDIR (SX,SY,SZ,TTY,TYZ,TZX,P1,P2,P3,P,TH1,PH1)
P=0.0
IF(P1.LT.P) P=P1
IF(P2.LT.P) P=P2
IF(P3.LT.P) P=P3
IF (P.EQ.0.0) TH1=0.0)PH1=0.0)GO TO 200
IF(TXY.EQ.0.0.AND.TYZ.EQ.0.0.AND.TZX.EQ.0.0.AND.SX.EQ.
1P.AND. SY.EQ.P) TH1=0.0)PH1=90.) GO TO 200
IF(TXY.EQ.0.0.AND.TYZ.EQ.0.0.AND.TZX.EQ.0.0.AND.SZ.EQ.
1P.AND. SY.EQ.P) TH1=0.0)PH1=0.0) GO TO 200
SXX=-SX+P
SYY=-SY+P
SZZ=-SZ+P
D=SYY+SZZ-TYZ+TYZ
IF(DABS(D).LT.1.0D-16) GO TO 400
Y=(TYZ+TZX-SZZ+TTY)/D
Z=(TXY+TYZ-SYY+TZX)/D
TH1=DATAN(Y)*180./3.1415927
    
```

```

        IF(DABS(Z).LT.1.0D-16)          PH1=90.; GO TO 200
        PH1=DATAN((1.+Y*Y)+*0.5/Z)*180./3.1415927
        GO TO 200
400  D=SXX+BYZ=TXZ+TXZ
        IF(DABS(D).LT.1.0D-16)          GO TO 300
        X=(TXZ+TYZ=TYZ+SXX)/D
        Y=(TXZ+TZS=TYZ+SXX)/D
        IF(DABS(X).LT.1.0D-16)          TH1=90.; GO TO 450
        TH1=DATAN(Y/X)*180./3.1415927
450  PH1=DATAN((X*X+Y*Y)+*0.5/Z)*180./3.1415927
        GO TO 200
300  D=SXX+SZZ=TXZ+TXZ
        IF(DABS(D).LT.1.0D-16)          TH1=0.;PH1=0.;P=0.; GO TO
1 200
        X=(TXZ+TYZ=TXZ+SZZ)/D
        Z=(TXZ+TZS=TYZ+SXX)/D
        IF(DABS(X).LT.1.0D-16)          TH1=90.; GO TO 350
        TH1=DATAN(Z/X)*180./3.1415927
350  IF(DABS(Z).LT.1.0D-16)          PH1=90.; GO TO 200
        PH1=DATAN((1.+X*X)+*0.5/Z)*180./3.1415927
200  RETURN
    END
    IMPLICIT REAL*(A-H,O-Z)
    SUBROUTINE DATGEN(V,D)
    COMMON/CONTR/ PX,PY,PZ,IMPACS
    COMMON  RSUBO(20),PSUBO(20),ALPHA(2,20),SG(2,20)
1,NUMBER(20)          ,X01(20),Y01(20),X1(20),Y1(20),Z1
2(20)                ,TDELAY(20) ,PSAVE(20)
    DIMENSION AF(2),SN(2)
    AF(1)=2.686/D
    AF(2)=4.5*AF(1)
    TR=0.16*D
    PO=119.7*V
    RO=0.0085*D
    SN(1)=+1.
    SN(2)=-1.
    DD 4777 J=1,IMPACS
    NUMBER(J)=2
    PSUBO(J)=PO
    RSUBO(J)=RO
    PSAVE(J)=PSUBO(J)
    LIMIT=NUMBER(J)
    DO 40 I=1,LIMIT
    ALPHA(I,J)=AF(I)+1000000.
    SG(I,J)=SN(I)
40  CONTINUE
    READ(5,250) X01(J),Y01(J),TDELAY(J)
250  FORMAT(3F10.0)
    X1(J)=PX=X01(J)
    Y1(J)=PY=Y01(J)
    Z1(J)=PZ
    
```

```

WRITE(6,303 )J,X01(J),Y01(J),PSUBQ(J),RSUBD(J),ALPHA(1
1,J),ALPHA(2,J), TDELAY(J)
303  FORMAT(' 4X12, 9XF9.3,6XF9.3,5XG15.8,3XF9.3,3X2Q15.8
1,3XF9.3/)
TDELAY(J)=TDELAY(J)*1.0E=06
OUTPUT(6) V,D,TR
4777 CONTINUE
RETURN
END
IMPLICIT REAL*(A-H,O-Z)
SUBROUTINE PRIST(S11,S22,S33,S44,S55,S66,P1,P2,P3,P4)
C          SUBROUTINE TO FIND THE PRINCIPAL STRESSES
DIMENSION W(3),B(4),XR(3)
ABS(X)=DABS(X)
S111=S11-S22
S222=S22-S33
S333=S33-S11
IF(ABS(S111).LT.1.E=04.AND.ABS(S222).LT.1.E=04.AND.ABS
1(S333).LT.1.E=04) P1=S11/P2=S22/P3=S33)GO TO 901
IF (ABS(S44).LT.1.E=04.AND.ABS(S55).LT.1.E=04.AND.ABS
1(S66).LT.1.E=04) W(1)=S11/W(2)=S22/W(3)=S33)GO TO
2 9011
B(1) = 1.
B(2) = -(S11+S22+S33)
B(3)=S11+S22+S22+S33+S33+S11-S44**2-S55**2-S66**2
B(4) = -(S11+S22+S33-S11+S55**2-S22+S66**2-S33+S44**2
1+2.*S44+S55+S66)
CALL CUBIC (B,XR,XI)
W(1) = XR(1)
W(2) = XR(2)
W(3) = XR(3)
9011 CONTINUE
IF (W(1).GE.W(2).AND.W(2).GE.W(3))P1=W(1)/P2=W(2)/P3=W
1(3))GO TO 31
IF (W(1).GE.W(3).AND.W(3).GE.W(2))P1=W(1)/P2=W(3)/P3=W
1(2))GO TO 31
IF (W(2).GE.W(1).AND.W(1).GE.W(3))P1=W(2)/P2=W(1)/P3=W
1(3))GO TO 31
IF (W(2).GE.W(3).AND.W(3).GE.W(1))P1=W(2)/P2=W(3)/P3=W
1(1))GO TO 31
IF (W(3).GE.W(1).AND.W(1).GE.W(2))P1=W(3)/P2=W(1)/P3=W
1(2))GO TO 31
IF (W(3).GE.W(2).AND.W(2).GE.W(1))P1=W(3)/P2=W(2)/P3=W
1(1))GO TO 31
901 CONTINUE
31 P4 = (P1-P3)/2.
RETURN
END
SUBROUTINE CUBIC (A,XR,XI)
C          SOLUTION OF A CUBIC EQUATION

```

```

C      A(1)*X**3 + A(2)*X**2 + A(3)*X + A(4) = 0.
C
      DIMENSION A(4),XR(3),AQ(3)
      IPATH = 2
      EX = 1./3.
      IF(A(4)) 1006,1004,1006
1004  XR(1) = 0.
      GO TO 1034
1006  AR = A(1)**2
      B = (27.*AR*A(4) - 9.*A(1)*A(2)*A(3) + 2.*A(2)**3)/
      1(54.*AR*A(1))
      IF (B) 1010,1008,1014
1008  Z = 0.
      GO TO 1032
1010  B = -B
      IPATH = 1
1014  P = (3.*A(1)*A(3) - A(2)**2)/(9.*AR)
      ARG = P**3 + B**2
      IF (ARG) 1016,1018,1020
1016  Z = -B.*SQRT(-P)*COS(ATAN(SQRT(-ARG)/B)/3.)
      GO TO 1028
1018  Z = -B.*B**EX
      GO TO 1028
1020  SARG = SQRT(ARG)
      IF (P) 1022,1024,1026
1022  Z = -(B + SARG)**EX - (B - SARG)**EX
      GO TO 1028
1024  Z = -(2.*B)**EX
      GO TO 1028
1026  Z = (SARG-B)**EX - (SARG + B)**EX
1028  GO TO (1030,1032), IPATH
1030  Z = -Z
1032  XR(1) = (3.*A(1)*Z - A(2))/(3.*A(1))
1034  AQ(1) = A(1)
      AQ(2) = A(2) + XR(1)*A(1)
      AQ(3) = A(3) + XR(1)*AQ(2)
      CALL QUAD (AQ,XR(2),XR(3),XI)
      RETURN
      END
      SUBROUTINE QUAD (A,XR1,XR2,XI)

```

```

C
C
C      SOLUTION OF THE QUADRATIC EQUATION
      A(1)*X**2 + A(2)*X + A(3) = 0.
C
      DIMENSION A(3)
      X1 = -A(2)/(2.*A(1))
      DISC = X1**2 - A(3)/A(1)
      IF (DISC) 10,20,20
10  XR2 = SQRT(-DISC)
      XR1 = X1
      XR2 = X1

```

```
XI = X2  
GO TO 30  
20 X2 = SQRT(DISC)  
XR1 = X1 + X2  
XR2 = X1 - X2  
XI = 0  
30 RETURN  
END
```

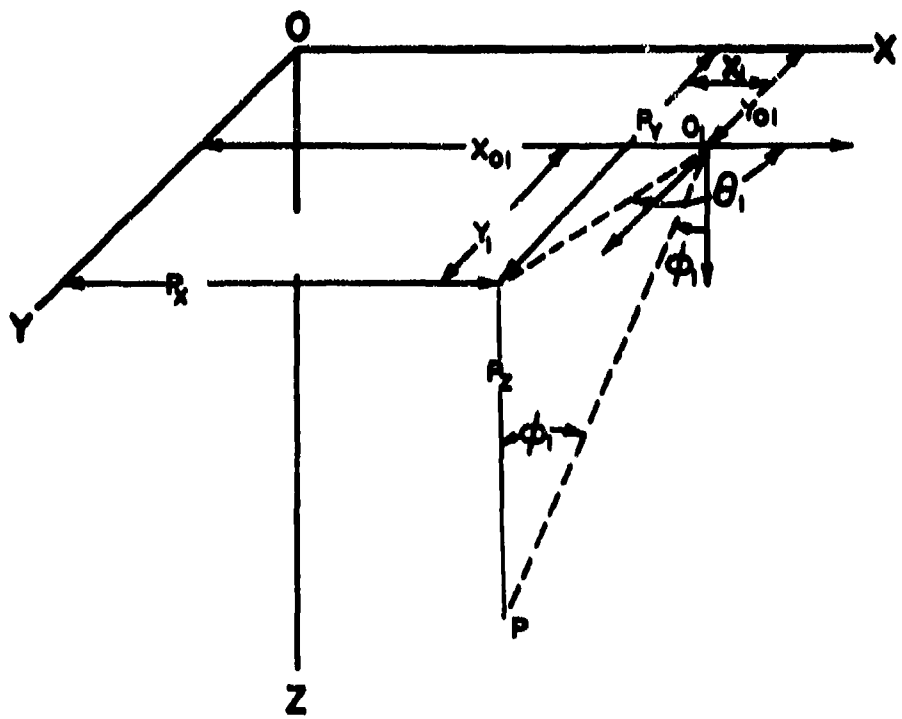


FIGURE 1 IMPACT COORDINATE SYSTEM

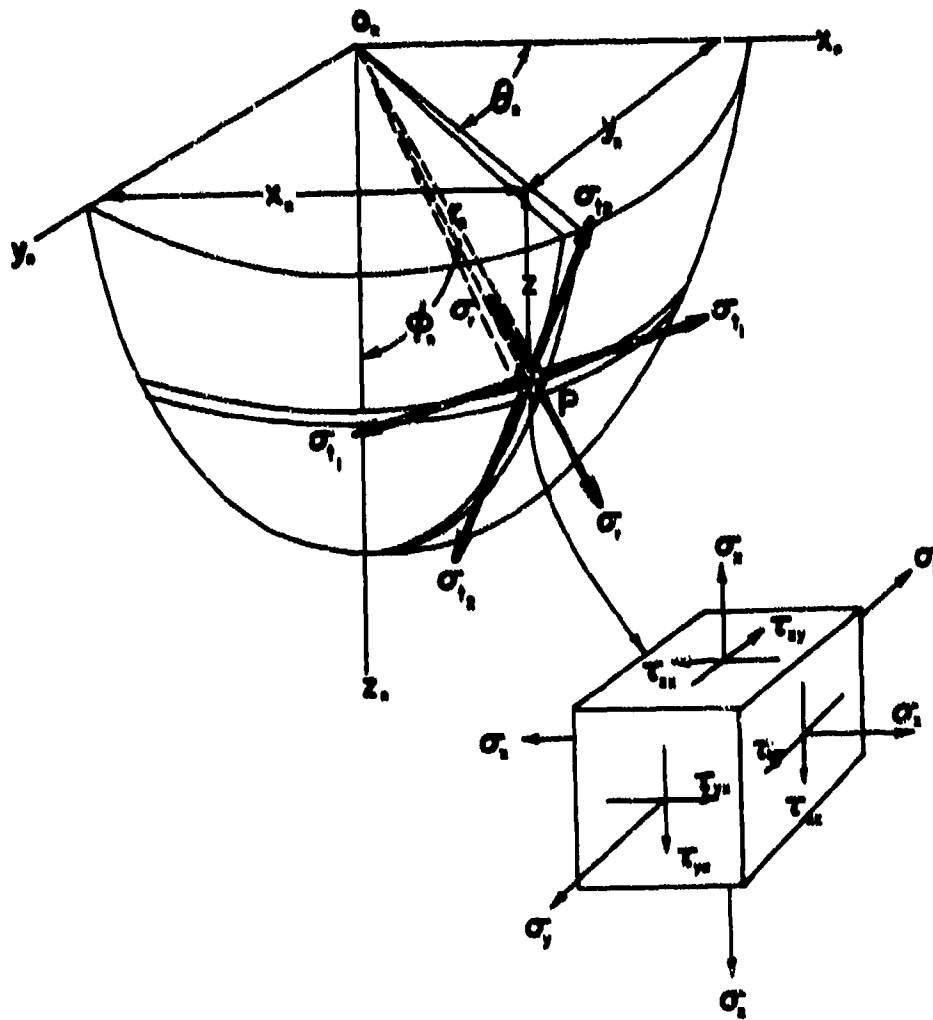


FIGURE 2 STRESSES CREATED BY SPHERICAL STRESS WAVES

G-1

APPENDIX G

COMPUTER CODE FOR CALCULATING RAIN EROSION
OF MISSILE RADOMES AT SUPERSONIC
SPEEDS (REMRASS)

by

Ju-chin Huang
Associate Professor of Engineering Science
Tennessee Technological University
Cookeville, Tennessee 38501

APPENDIX G

COMPUTER CODE FOR CALCULATING RAIN EROSION OF MISSILE RADOMES AT SUPERSONIC SPEEDS (REMRASS)

by Ju-chin Huang

INTRODUCTION

When a vehicle flies through a rain field, the erosion damage to the vehicle depends on the relative velocities of the raindrops, the angle of impact θ_1 , and the distribution of drops along the surface. The theoretical analysis has been given in detail in the report. This computer code--Rain Erosion of Missile Radomes at Supersonic Speeds (REMRASS)--was developed to solve numerically the governing equations derived previously and to determine the angle of impact of a raindrop and the position at which it strikes the vehicle surface. The percentage area of erosion and the total volume eroded were then calculated.

DEFINITION OF VARIABLES

- AL = Length of the tip portion of radome
- AJ = Parameter for plane and axisymmetric flow
- AM = Free stream Mach number
- ALTH = Length of radome in mm
- B = Dimensionless body radius at the end of radome with respect to the length of radome
- Bl = Base diameter of radome in inches
- C = Parameter in equation of radome surface
- Cl = Length of curved portion of radome in inches
- CA = Area conversion constant
- CC = Shock wave angle in radians

CCD = Shock wave angle in degrees

CV = Volume conversion constant

DDIA = Raindrop diameter step size in mm

DDIS = Increment distance traveled in rain field (ft)

DIAØ = Initial raindrop diameter in mm

DIAMAX = Upper limit of the integration with respect to drop diameter

DIS = Distance traveled in rain field (ft)

DISMAX = Maximum distance traveled in rain field (ft)

DXS = Streamline step size

ER = Volume erosion rate per sq. in. (in./sec.)

ER1 = $ER/(\sin\theta)^2$

GM = Ratio of specific heats for a perfect gas

K = Number of streamline along which solution has been found

KINC = Increment of K

JJ = Station number counter

L = Length of radome in inches

M = Number of intervals used in Runge-Kutta method

N = Number of integration points in Runge-Kutta method

PCT = Percentage of area eroded

POS = Dimensionless axial position at which streamline intersects radome

POSL = Axial position in inches

R = Rainfall rate (in./hr.)

RFR = Rainfall rate (in./hr.)

RATIO = $VOL/V1$

S = Dimensionless shock radius at the end of radome

T1 = Half-angle of cone in radians

- THETA = Half-angle of cone in degrees
- V = Velocity of vehicle (ft./sec.)
- V1 = Intermediate value for calculating volume eroded
- VOL = Total volume eroded (in.³)
- X θ = Dimensionless length of conical portion of radome
- XF = Initial abscissa of the last streamline that hits the radome
- XS = Initial abscissa of a streamline

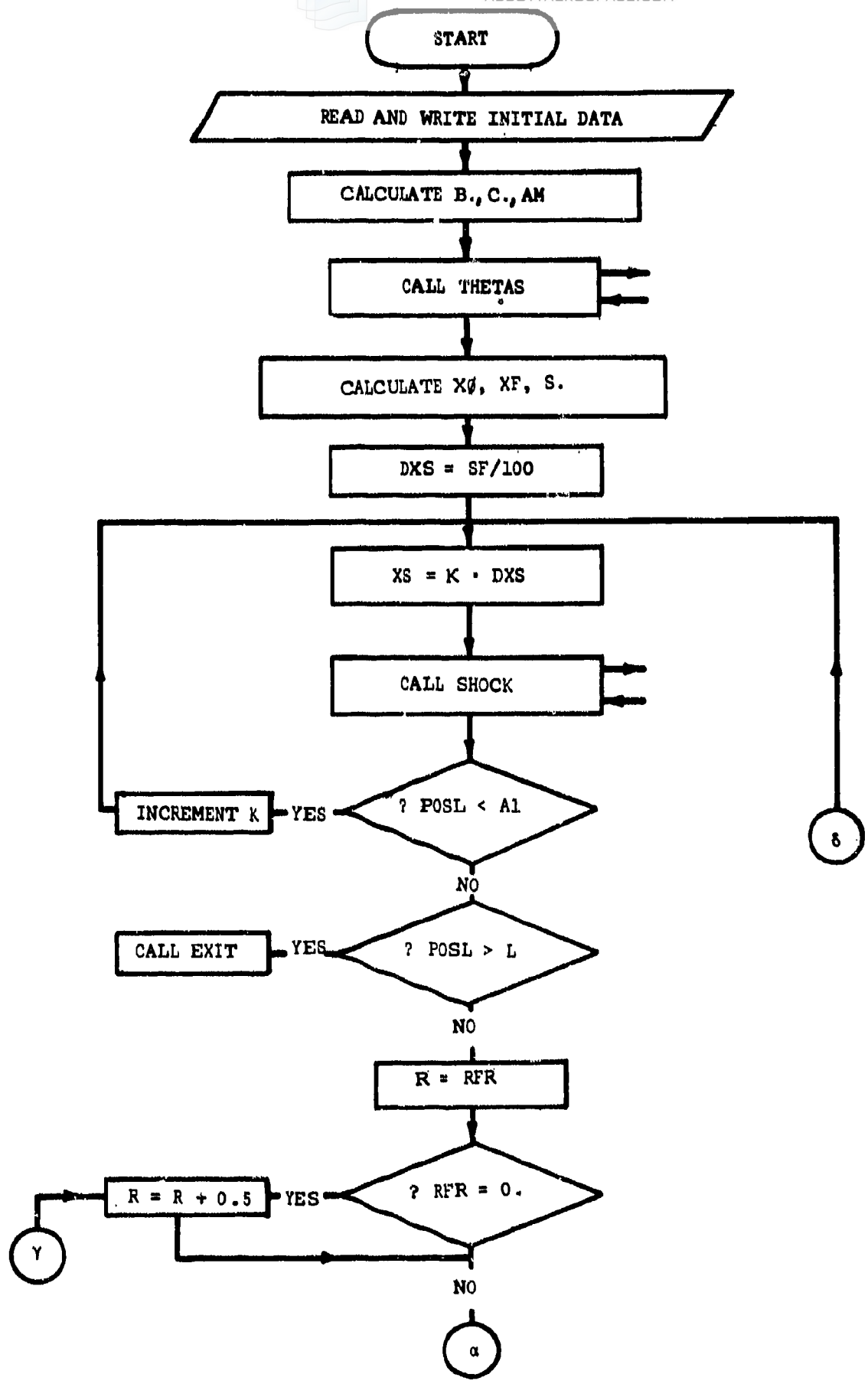
EXPLANATION OF SUBROUTINES

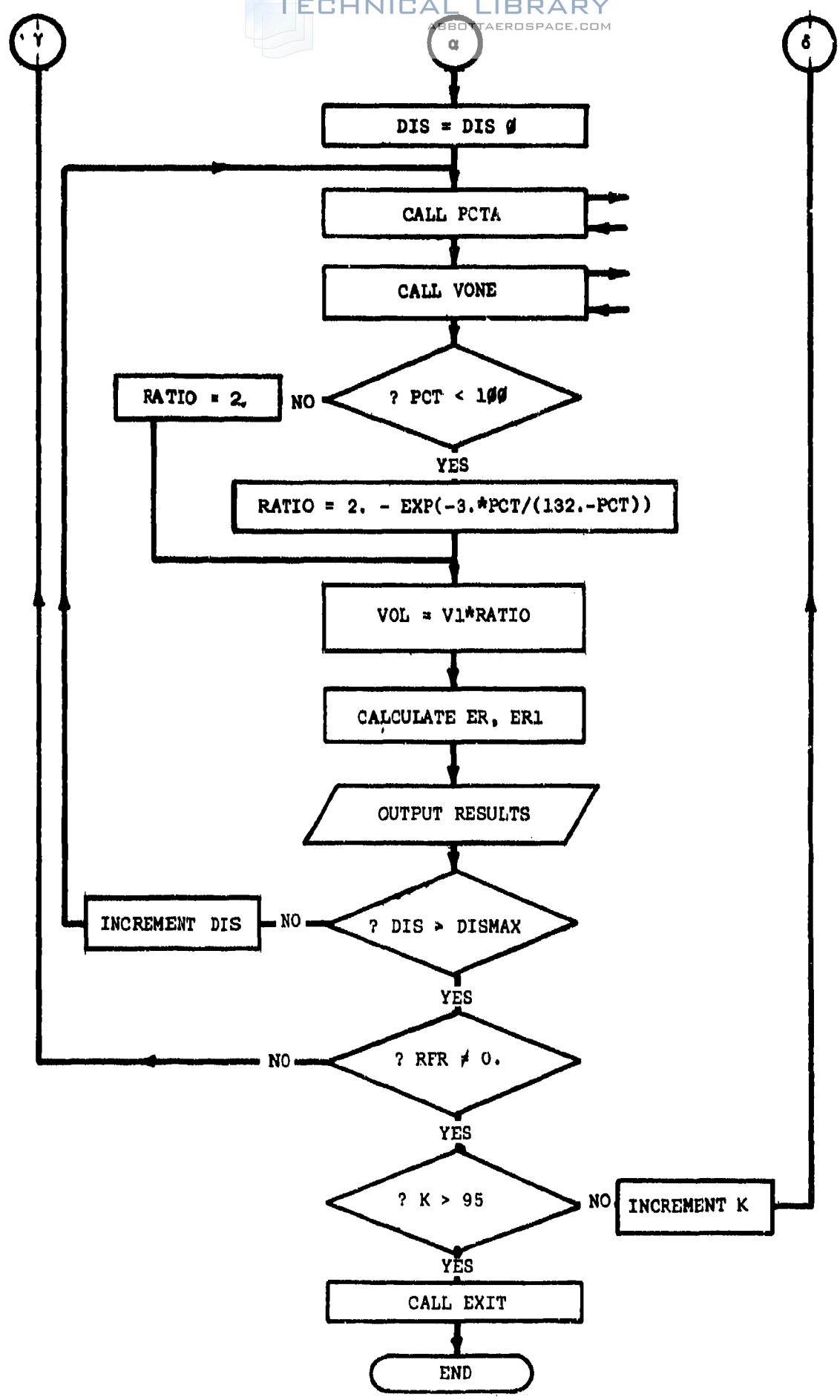
Most of the computation steps are carried out in the four subroutines of the program. These subroutines are controlled by the main routine. Following is a list of the subroutines with an explanation of their functions.

- THETAS Interpolates shock wave angle θ_g by means of Lagrange interpolation function.
- SHOCK Uses fourth-order Runge-Kutta method to solve for impact angle θ_i and axial position of impact.
- PCTA Computes the percentage of area eroded of the radome during the time of flight in a rain field.
- VONE Calculates the total volume eroded of the radome.

GUIDE OF INPUT DATA

<u>Card</u>	<u>Fortran Name and Column No.</u>	<u>Format and Remark</u>
1	A1 1 - 10	(5F10.0)
	B1 11 - 20	
	C1 21 - 30	
	L 31 - 40	
	THETA 41 - 50	
2	AJ 1 - 10	(5F10.0) If RFR is left blank, the program will start with R=0.5 and incre- ment it until R=5in/hr.
	GM 11 - 20	
	CA 21 - 30	
	CV 31 - 40	
	RFR 41 - 50	
Last Card	V 1 - 10	(F10.0)





DISCUSSION OF THE PROGRAM

The three data statements in the main routine specify the values of distance traveled in a rain field, diameters of raindrops, number of intervals used in the numerical calculation, and their increment. These values should be changed for a different problem. The lower limits of $DIAG$ and $DDIA$ should not exceed 0.1 and the upper limit of DZ is 0.01. The other two data statements in subroutine THETAS contain the values of free stream Mach numbers and their corresponding shock wave angles θ_s for a 15-degree cone angle. These values must be replaced if another cone angle is used. A table of shock wave angle versus free stream Mach number is given in Table I or see Ref. 1.

The first read statement defines radome geometry: A_1 is the length of tip portion, B_1 the base diameter, C_1 the length of curved portion, L the length of radome, and $THETA$ is the cone angle. The second data card contains AJ , GM , CA , CV , and RFR . $AJ = 0$ for plane flow and 1 for axisymmetric flow. GM is the ratio of specific heat for a perfect gas. CA and CV are conversion constants for area and volume respectively. RFR is rainfall rate. If RFR is left blank, the program will increment the rainfall rate from 0.5 to 6 in./hr. The last data gives the velocity of the radome in ft./sec. The program first calculates the values of B , C , and AM , and then calls subroutine THETAS to interpolate shock wave angle θ_s for use in calculating S . The calculation of XF requires the body surface function. Statements 300 and 301 relate to the radome configuration. The streamline step size DXS is made equal to $XF/100$. The value of XS , the initial abscissa of a streamline, is then set equal to K times DXS . Subroutine SHOCK is called to calculate the impact angle θ_i and the axial position of impact of raindrops. Statements 110-113 in SHOCK specify the

radome surface function. In this program a combination of 15-degree cone and an ogival shell was used. For other configurations to be considered, the body surface function must be modified accordingly. After the axial position of impact and impact angle of raindrops are found, the program proceeds to determine the percentage area of erosion and the total volume eroded by calling the subroutine PCTA and VONE respectively. Subroutines PCTA and VONE perform the numerical integration of the following integrals.

$$I_A = \int_0^{\infty} (\sin\theta_i)^{0.5} (D)^{1.65} P(D) dD$$

and

$$I_V = \int_0^{\infty} (\sin\theta_i)^{1.0} (D)^{4.32} P(D) dD$$

where

$$P(D) = \text{EXP}[-4.1(R)^{-0.21} D]$$

The percentage of area eroded and the total volume eroded are given as

$$\text{PCT} = 100 A_e$$

$$\text{VOL} = V1(\text{RATIO}) = V1(2 - e^{3\text{PCT}/(132-\text{PCT})})$$

where

$$A_e = [C_A(\text{DIS})V^{1.1} \sin\theta] I_A$$

$$V1 = [C_V(\text{DIS})V^{2.88} \sin\theta] I_V$$

REFERENCES

1. Tables for Supersonic Flow Around Right Circular Cones at Zero Angle of Attack, NASA SP-3004, Scientific and Technical Information Div., NASA, Washington, D. C., 1964.

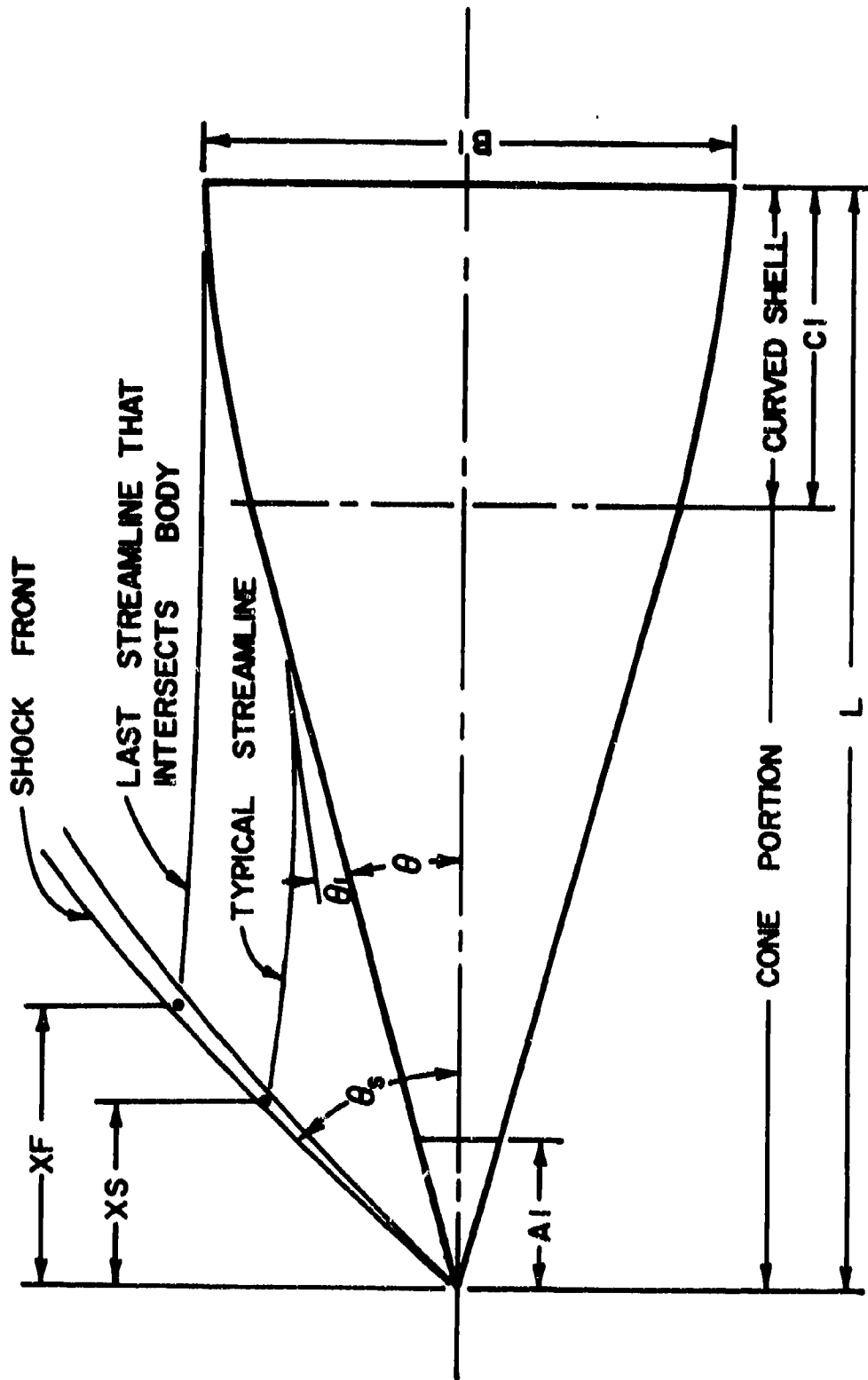


Figure 1. Shock Wave and Radome Configuration.

TABLE I.
VALUES OF SHOCK-WAVE ANGLE θ_s

M_a	θ_b	2.5°	5.0°	7.5°	10.0°	12.5°	15.0°	17.5°	20.0°	22.5°	25.0°	27.5°	30°
1.5		.72979225	.73078309	.73489674	.74466072	.76158205	.78592365	.81737375	.85571959	.90132794	.95578504		
1.75		.60832317	.60952726	.61444903	.62563831	.64398586	.66900117	.69978538	.73560474	.77605995	.82114418	.87135164	.92802044
2.0		.52369890	.52524879	.53140177	.54464827	.56518145	.59192180	.62370115	.65966167	.69928055	.74232301	.78882392	.83913453
2.5		.41168587	.41425491	.42357796	.44136238	.46630615	.49662600	.53101645	.56864312	.60899456	.65177773	.69686390	.74427222
3.0		.34011057	.34409993	.35701069	.37899374	.40763084	.44085123	.47752193	.51687237	.55844619	.60196673	.64728576	.69436247
3.5		.29017134	.29591943	.31238763	.33790128	.36539419	.40494077	.44344094	.48423753	.52692147	.57123978	.61704946	.66429713
4.0		.25329402	.26104195	.28078488	.30918220	.34295689	.38032070	.42028295	.46225228	.50585840	.55087169	.59716180	.644467684
4.5		.22495268	.23483710	.25747371	.28822452	.32383435	.36256044	.40389119	.44671754	.49107302	.53666064	.58336450	.63114000
5.0		.20251780	.21458047	.23972546	.27241579	.30952796	.34954864	.39164866	.43533264	.48029511	.52635069	.57339789	.62140105
6.0		.16936998	.18564567	.21481181	.25049160	.28990367	.33173775	.37527812	.42010459	.46596496	.51271277	.56027373	.60862959
7.0		.14622532	.16627981	.19846161	.23632593	.27739747	.32051775	.36506213	.41067349	.45714479	.50436191	.55227301	.60087454
8.0		.12931031	.15261801	.18711985	.22663938	.26894684	.31300625	.35827161	.40443925	.45133986	.49888523	.54704135	.59581671
10.0		.10660326	.13498608	.17279866	.21462672	.25860856	.30390795	.35010593	.39698293	.44442555	.49238318	.54084699	.58984179
12.0		.09237825	.12439992	.16443793	.20775907	.25278296	.29883132	.34558101	.39287165	.44062723	.48882168	.53746203	.58658328
15.0		.07917793	.11497084	.15726234	.20192526	.24789127	.29460009	.34182829	.38947389	.43749622	.48589157	.53468140	.583991003
20.0		.06734690	.10697188	.15127223	.19723448	.24400089	.29125730	.33887635	.38680903	.43504579	.48360210	.53251169	.58182628

LISTING OF PROGRAM

```

0001 C MAIN PROGRAM
0002     IMPLICIT REAL*8(A-H,O-Z)
0003     REAL*8 L
0004     COMMON/BET1/XB,DXB,XO,ALTB,AM,GM,AJ,B,C,K
0005     COMMON ALPHAP(101)
0006     DATA DIBO,DDIB,DISMAK/50.0,50.0,5000.0/
0007     DATA DIAO,DDIA,DIAMAK/0.5,0.5,10.0/
0008     DATA M,N,KINC,DZ/100,101,5,0.01/
0009     SIN(X)=DSIN(X)
0010     EXP(X)=DEXP(X)
0011 C
0012 C READ IN GEOMETRICAL DATA I
0013 C A1= LENGTH OF TIP
0014 C B1= BODY DIAMETER AT X=L
0015 C C1=LENGTH OF THE OGIVAL PORTION
0016 C L= LENGTH OF RADOM
0017 C THETA= ANGLE OF THE CONE
0018 C
0019 C READ (5,11) A1,B1,C1,L,THETA
0020 C
0021 C READ IN PHYSICAL QUANTITIES:
0022 C AJ=0. FOR PLAN FLOW AND 1.0 FOR AXISYMMETRIC FLOW
0023 C GM= RATIO OF SPECIFIC HEATS FOR A PERFECT GAS
0024 C CA,CV = CONVERSION CONSTANT
0025 C RFR=RAIN FALL RATE
0026 C
0027 C READ (5,11) AJ,GM,CA,CV,RFR
0028 C
0029 C READ IN VELOCITY OF CRAFT
0030 C
0031 C READ (5,11) V
0032 11 FORMAT(5F10.0)
0033     OUTPUT(6) CA,CV
0034     WRITE(6,1900)
0035 1900 FORMAT(1X,' GEOMETRY OF BODY '///)
0036     OUTPUT(6) A1,B1,C1,L
0037     IF(AJ.EQ.0.) WRITE(6,1901)
0038     IF(AJ.EQ.1.) WRITE(6,1902)
0039 1901 FORMAT(//1X,' PLAN FLOW IS ASSUMED IN THIS CALCULATION'///)
0040 1902 FORMAT(//1X,' AXISYMMETRIC FLOW IS ASSUMED IN THIS CALCULATION'///)
0041     M=M*5
0042     T1=THETA*3.14159/180.
0043     TANT1=DTAN(T1)
0044     B=B1/2./L
0045     C=C1*ANT1/B
0046     AM=V/1100.
0047     IF(AM.LT.7.0) CALL THETAS(AM,CC,1,12)
0048     IF(AM.GE.7.0) CALL THETAS(AM,CC,11,16)
0049     CCD=CC*180./3.14159
0050     TANTS=DTAN(CCD)
0051     S=TANTD/C
0052     ALTB=L*25.4
0053     XO=(L-C1)/L
0054     XFR=B/(C+D)
0055     IF(XF.LT.XO) GO TO 300
0056     GO TO 302
0057 300 D1=1-CX(1.0-XO)*(1.0-XO)/(1.0-C1)+2.0*XO
0058     D2=KX*XL-(8*(1.0-XO)*(1.0-XO)/(B*(1.0-C1))
0059     SUD=DSQRT(1.0+(4.0*D2/(D1*D1)))
0060     XFR=(D1/2.0)*(1.0+SUD)
0061     IF(XF.LT.XO) GO TO 301
0062     IF(XF.GT.1.0) GO TO 301
0063     GO TO 302
0064 301 XFR=(D1/2.0)*(1.0-SUD)
0065     XFR=
0066     DXE=XFR*X*
0067     J=1
0068     WRITE (6,2) V,THETA
0069 2 FORMAT(2X,' VELOCITY='F10.2,' FT/SEC')17X,' ANGLE OF CONE='F10.2,' IN
0070     ' DEGREES'///)
0071     WRITE(6,3) AM,CCD
    
```

```

0072 1 FORMAT(1X,' FREE STREAM MACH NUMBER = ',F10.2,' SHOCK ANGLE =
0073 1 ',F10.2,' DEGREES',//)
0074 K=KINC
0075 3000 CONTINUE
0076 K=K+DX
0077 CALL SHOCK(POS,NE,DIAG,ODIA,DIAMAX,DZ,M,N)
0078 ND=INZ=1//2
0079 POSL=POS*V
0080 IF(POSL-UT*A1) GO TO 2009
0081 IF(POSL-RE*L1) GO TO 2002
0082 WRITE(6,400) JJ
0083 400 FORMAT(1//1X,' STATION NO=',I2//)
0084 WRITE(6,14) POSL
0085 14 FORMAT(1X,' LOCATED AT A DISTANCE X = ',F10.2,' IN FROM TIP'//)
0086 R=FR
0087 CONTINUE
0088 IF(RFR-ES*0.0) R=R+0.5
0089 WRITE(6,41R
0090 4 FORMAT(1//1X,' RAIN FALL RATE = ',F10.2,' IN/HR'//)
0091 WRITE(6,5)
0092 5 FORMAT(1X,' DISTANCE (FT)',5X,' PCT AREA',5X,' VOLUME (IN**3/IN**2)
0093 1 ',5X,' R (IN/SEC)',5X,' EC/(SIN(THETA))**2'//)
0094 DIS=DIS0
0095 SINC=DIS
0096 DO 10 I=1,50
0097 CALL PCTAIR(DIS,V,THETA,DIAG,ODIA,CA,PCT,NE)
0098 CALL VONEIR(DIS,V,THETA,DIAG,ODIA,CV,V1,NE)
0099 IF(PCT=100)BU,60,60
0100 60 RATIO=2.
0101 GO TO 70
0102 RATIO=2.*EXP(-3.*PCT/(1.25+PCT))
0103 70 VOL=V1*RATIO
0104 IF (PCT .GT. 100.00) PCT=100.00
0105 ER=VOL/(DIS*V)
0106 ER1=ER/(SIN(THETA))**2.0
0107 WRITE(6,6) DIS,PCT,VOL,ER,ER1
0108 6 FORMAT(1X,F10.2,5X,F10.2,7X,E14.6,6X,E14.6,7X,E14.6)
0109 IF(DIS-01.460-0) SINC=10.*DIS
0110 IF(DIS-3E-DISMAX) GO TO 2000
0111 DIS=DIS+SINC
0112 SINC=DIS
0113 10 CONTINUE
0114 2000 CONTINUE
0115 IF(MFR-NE*0.0) GO TO 201
0116 IF(N-ES*0.0) GO TO 201
0117 GO TO 200
0118 201 CONTINUE
0119 IF(K+GE-M*100 TU 2002
0120 WRITE(6,202)
0121 202 FORMAT(1//1X,' *****
0122 1 *****
0123 2009 CONTINUE
0124 K=K+KINC
0125 JJ=JJ+1
0126 UD TO 3000
0127 3000 CALL EX11
0128 END
    
```

```

0001 SUBROUTINE THETA(M,CC,NI,VR)
0002 IMPLICIT REAL*8(A-H,O-Z)
0003 DIMENSION Z(10),Y(16)
0004 DATA Z/1.5,1.75,2.0,2.5,3.0,3.5,4.0,4.5,5.0,6.0,7.0,8.0
0005 1 ,10.0,12.0,15.0,20.0/
0006 DATA Y/7.8592368, .66300117, .5912180, .49662600, .44025123,
0007 1 .40496377, .38032170, .36266044, .34954844, .33173775, .32051775,
0008 2 .31300625, .30790795, .29983132, .29460009, .29125730/
0009 CC=0.
0010 DO 3 I=NI,VR
0011 Z1=Z(I)
0012 M=1.
0013 DO 2 J=NI,VR
0014 IF(I-ES*0) GO TO 2
0015 Z2=Z(J)
0016 AA=(X+Z2)/(Z1+Z2)
    
```

```

0017      P=PMAX
0018      CONTINUE
0019      BB=BB*(I)
0020      1   CC=CC+BB
0021      RETURN
0022      END

0001      SUBROUTINE SHOCK(PUB, N2, DIA0, DIA, DIAMAX, DZ, H, N )
0002      IMPLICIT REAL*8(A-H, O-Z)
0003      COMMON /SET1/ XB, DXB, X0, ALTH, AM, DM, AJ, B, S, C, K
0004      COMMON ALPHAP(101)
0005      DIMENSION Z(101), FP1(101), GP1(101), HP1(101),      X1(101)
0006      DIA=DIA0
0007      UIN=3048747
0008      AF1=0.000404*(ALTH/DIA)
0009      AF2=0.00672*(ALTH/(UIN+DIA+DIA))
0010      FP1(1)=1.0
0011      GP1(1)=0.0
0012      HP1(1)=1.0
0013      Z(1)=0.0
0014      KK=1
0015      DO 24 I=1, N
0016      ALPHAP(I)=0.
0017      24   X1(I)=0.0
0018      300  CONTINUE
0019      X1(1)=XB
0020      DO 198 I=2, N
0021      J=1
0022      FPA=FP1(I-1)
0023      GPA=GP1(I-1)
0024      HPA=HP1(I-1)
0025      KA=X1(I-1)
0026      ZA=Z(I-1)
0027      110  **KA
0028      IF(I=3) GO TO 112
0029      R= C+K
0030      HP= C
0031      112  CONTINUE
0032      H= C+K*(1.0=C)*(1.0=NO)*(1.0=NO)/(1.0=NO)+(1.0=NO))
0033      R= C+2.0*(1.0=C)*(1.0=NO)/(1.0=NO)+(1.0=NO))
0034      113  CONTINUE
0035      RB=H+R
0036      RHP=B+RP
0037      TR=RB
0038      CTB=1.0/(1.0+TTB+TTB)+*(1.0/2.0)
0039      STB=TR+CTB
0040      RB=H+R
0041      RHP=B+RP
0042      TR=RB
0043      CTB=1.0/(1.0+TTB+TTB)+*(1.0/2.0)
0044      STB=TR+CTB
0045      AM=AM+STB
0046      CP=(1.0=J)*AM*(AM+2.0)/(1.0+1.0)*AM*(AM)
0047      EP=C*(1.0=CTB)+EP*(1.0=STB)
0048      FB=CTB+CTB
0049      GP=(1.0=EP)+CTB+STB
0050      HP=C*(1.0=H)
0051      HPA=H*(1.0+(1.0=EP)+GM*(AM+AM))
0052      **AM
0053      FA=FB*(1.0=ZA)+FB*ZA
0054      JA=JB*(1.0=ZA)+JB*ZA
0055      HA=HS*(1.0=ZA)+HB*ZA
0056      PI=PS+IS
0057      H=TTB*(1.0=JA)+TTB*JA
0058      HPA=HPA+FA+FA+PP
0059      118  FB=FA+FA+FA*(FA=FA)
0060      GB=JA+JA+JA*(JA=JA)
0061      FB=GB+RT*(FF+GD)
0062      114  FA=FA*(1.0=FB)+(FA=FA)
0063      GA=HA*(1.0=GB)+(GA=GA)
0064      HA=HA*(1.0=GA)+(HA=HA)
0065      FA=FA+FA
0066      GO TO (120, 130, 140, 150) J

```

```

0068      120      AK1=FPP*OZ
0069      A1=1*GPP*OZ
0070      AM1=HPP*OZ
0071      A01=KP*OZ
0072      FPA=FP1(I=1)+(AK1/2*O)
0073      GPA=GP1(I=1)+(AL1/2*O)
0074      HPA=HP1(I=1)+(AM1/2*O)
0075      KA=X1(I=1)+(A01/2*O)
0076      ZA=Z(I=1)+(OZ/2*O)
0077      J=2
0078      GO TO 110
0079      130      AK2=FPP*OZ
0080      A12=GPP*OZ
0081      AM2=HPP*OZ
0082      A02=KP*OZ
0083      FPA=FP1(I=1)+(AK2/2*O)
0084      GPA=GP1(I=1)+(AL2/2*O)
0085      HPA=HP1(I=1)+(AM2/2*O)
0086      KA=X1(I=1)+(A02/2*O)
0087      ZA=Z(I=1)+(OZ/2*O)
0088      J=3
0089      GO TO 110
0090      140      AK3=FPP*OZ
0091      A13=GPP*OZ
0092      AM3=HPP*OZ
0093      A03=KP*OZ
0094      FPA=FP1(I=1)+AK3
0095      GPA=GP1(I=1)+AL3
0096      HPA=HP1(I=1)+AM3
0097      KA=X1(I=1)+A03
0098      ZA=Z(I=1)+OZ
0099      J=4
0100      GO TO 110
0101      150      AK4=FPP*OZ
0102      A14=GPP*OZ
0103      AM4=HPP*OZ
0104      A04=KP*OZ
0105      FP1(I)=FP1(I=1)+(AK1+2*O*AK2+2*O*AK3+AK4)/6*O
0106      GP1(I)=GP1(I=1)+(AL1+2*O*AL2+2*O*AL3+AL4)/6*O
0107      HP1(I)=HP1(I=1)+(AM1+2*O*AM2+2*O*AM3+AM4)/6*O
0108      X1(I)=X1(I=1)+(A01+2*O*A02+2*O*A03+A04)/6*O
0109      Z(I)=Z(I=1)+OZ
0110      M=X1(I)
0111      198      CONTINUE
0112      FPB1=FP1(I)*CTB+GP1(I)*NTB
0113      FPD1=FP1(I)*BTB+GP1(I)*DTB
0114      IF(FPB1*BTB+O*CI) GO TO 2000
0115      TFP1=FPB1/FPBT
0116      FPR1=DA1*V1/TFP1
0117      IF(DIA+D2*DIA*AK) GO TO 2000
0118      A1=PHAP1(K)=TFP1
0119      DIA=DIA+D2DIA
0120      J14=304888
0121      AF1=O.000404*(AL1H/DIA)
0122      AFR=O.00672*(AL1H/(J14*DIA*DIA))
0123      KK=KK+1
0124      GO TO 500
0125      2000      CONTINUE
0126      POS=X1(I)
0127      V2=KK
0128      RETURN
0129      END
    
```

```

0001      SUBROUTINE PCTAIR(B,V,T,HETA,K0,DX,CA,PCT,N2)
0002      IMPLICIT REAL*8(A-H,O=7)
0003      COMMON A,PHAP(101)
0004      DIMENSION J(3)
0005      EXPR(X)=DEXP(X)
0006      SIN(X)=DSIN(X)
0007      F(X)=EXP(X)*.65*EXP(-.4*1.875**X+.2*1.X)
0008      H=25.4*H
0009      V1=3.14159
0010      ALPHA=T*HETA*PI/180.
0011      S=.3048*F5
    
```

```

0012      CF=62.43*PI/(386.4*304.8**3)
0013      C1=CA*CE**0.55*SIN(ALPHA)*V**1.1
0014      X=XO
0015      BETA =ALPHAP(1)
0016      G(1)=SIN(BETA )**0.5*F(X)
0017      AI=0.
0018      DO 10 I=1,N2
0019      DO 20 J=2,3
0020      X=X+DX
0021      IJ=2*(I-1)+J
0022      BETA =ALPHAP(IJ)
20      G(IJ)=SIN(BETA )**0.5*F(IJ)
0024      DAR=DX*(G(1)+4.*G(2)+G(3))/3.
0025      AI=AI+DAR
0026      10      G(1)=G(3)
0027      AI=5000.*AI
0028      AI=C1*84*AI*2.54**2*1.E=4
0029      PCT=100.*AI
0030      RETURN
0031      END
    
```

```

0001      SUBROUTINE VONE(R,B,V,THETA,XO,DX,CV,V1,N2)
0002      IMPLICIT REAL*8(A-H,O-Z)
0003      COMMON ALPHAP(101)
0004      DIMENSION G(3)
0005      SIN(X)=DSIN(X)
0006      EXP(X)=DEXP(X)
0007      F(X)=X**4.32*EXP(-4.1+2**4*(=-21)*X)
0008      PI=3.14159
0009      RMM=25.4*R
0010      ALPHA=THETA*PI/180.
0011      EM=.3048*B
0012      CE=62.43*PI/(386.4*304.8**3)
0013      C1=CV*CE**1.44*SIN(ALPHA)*V**2.88
0014      X=XO
0015      BETA =ALPHAP(1)
0016      G(1)=SIN(BETA )**1.00*F(X)
0017      V1=0.
0018      DO 10 I=1,N2
0019      DO 20 J=2,3
0020      X=X+DX
0021      IJ=2*(I-1)+J
0022      BETA =ALPHAP(IJ)
20      G(IJ)=SIN(BETA )**1.00*F(IJ)
0024      DVOL=DX*(G(1)+4.*G(2)+G(3))/3.
0025      V1=V1+DVOL
0026      10      G(1)=G(3)
0027      V1=5000.*V1
0028      V1=C1*64*V1*2.54**2*1.E=8
0029      RETURN
0030      END
    
```